Improving Continuous Crystallisation Using Process Analytical Technologies: Design of a Novel Periodic Flow Process

Keddon Andre Powell

Supervisors: Prof. Chris D. Rielly and Prof. Zoltan K. Nagy

A thesis submitted for the degree of Doctor of Philosophy at the Department of Chemical Engineering, Loughborough University, United Kingdom.

Submitted: October 19th, 2015.

Dedication

This work is Dedicated to the late Jennifer 'Claire' Gowie

My friend, my angel and wonderful mother.

Declaration

I declare that the work as presented in this thesis is my own except as acknowledged in the text and has not been submitted either in whole or in part, for a degree at this or any other institution.

Acknowledgements

Late evenings, long nights, weekends and holidays, what a life it is to be a PhD student, or was it just me? I can't say I would do anything any differently, the sweat, the tears, the highs and lows, the YES! moments have all led to this final piece. Need I say it, the Doctoral Thesis! I can safely say it was all worth it! I would like to express my deepest gratitude to all those who contributed invaluably to the work presented herein and to those who helping me get though the phases, the good, the bad and the in-between times. To my academic supervisors Prof. Chris Rielly and Prof. Zoltan Nagy, thank you immeasurably for granting me the opportunity to embark on this challenging, but fulfilling experience with you. I want to thank you for your invaluable advice, direction, encouragement and for discussions which clarified my thoughts and approach to this research project and other more matters. Thank you for allowing me the freedom to pursue different projects without interference.

A very special thank you to the academic, research, technical, administrative and ancillary staff in the Chemical Engineering Department. Tony Ayre for his fun friendly spirit, his patience and understanding, and assistance with designing and building my experimental rig, Sean Creedon and lab technician team for assistance with procuring the consumables for my project and for providing training on various pieces of equipment in the department. Yasmin, what would I do without you, with your cheeky sense of humour, cheerful and infectious personality, thank you.

To my colleagues in the crystallisation group and the wider CMAC community past and present, Ali Saleemi, Ani, Qing Lin, Akos and Elena (Loughborough University), Kate Wittering and Chick Wilson (University of Bath), Natalia Dabrowska (University of Strathclyde), thank you for the advice on several aspects of my project and your contribution to this work.

My friends William, Flora, Dimitris and Emmanuel, thank you for all the fun times in Loughborough and elsewhere. I had a blast hanging out with all of you, cheers to summer barbeques, great nights, a party or two, a drink or few and all the lively discussions on various subjects. Thank you also for organising the many social events that made my experience at Loughborough University truly memorable.

To Sean and the subwarden team and the Campus Living staff in Butler Court, thank you all for making my experience in Halls a truly amazing one, I will surely miss you all. I had a great time during my subwardenship and have learnt so much from the experience.

To my family and friends in Jamaica, USA, Canada, Ireland, Germany, the Czech Republic and the Dutch Caribbean who offered words of encouragement through the tough times and for

sharing a joke or two to cheer me up, thank you for your love and support, for always being there and listening to my troubles Brie (my best), April, Saba, Dermot, Florian, Henry and Ronald.

Finally, I would like to express special thanks to the EPSRC, ERC and the wonderful people at CMAC for financial support and equipment thought my PhD project.

Abstract

In this thesis novel configurations and operating strategies in the mixed suspension mixed product removal (MSMPR) crystalliser are investigated, aided by integrated process analytical technologies (PAT) and crystallisation informatics system (CryPRINS) tools. The MSMPR is an idealised crystalliser model that assumes: steady-state operation; well mixed suspension with no product classification, such that all volume elements contain a mixture of particles (small and large) and crystal size distribution (CSD) that is independent of location in the crystalliser and is identical of the product withdrawn; and uniform supersaturation thought, leading to constant nucleation and growth rates. Single-stage MSMPR designs with continuous recycle/recirculation and modified heat exchanger were investigated and found to minimise fouling, encrustation and transfer line blockages. In particular, a modified MSMPR with baffled heat exchanger was found to significantly reduce the temperature between incoming feed hot feed solution and the cooled crystalliser, leading to a significant reduction in fouling, encrustation and blockages.

In addition, the concept of the periodic mixed suspension mixed product removal (PMSMPR) crystallisation process is demonstrated for the first time *viz* single- and multi-stage cascaded operations. This method of operation involves the periodic transfer of slurry (addition and withdrawal) at high flow rates from either a single stirred vessel or between a number of stirred vessels arranged in series. The PMSMPR is therefore characterised by periodic withdrawals of product slurry. Similar to the MSMPR, the product withdrawn from a PMSMPR has exactly the same composition as the vessel at the time of removal. The rapid withdrawal of slurry at high flow rates in PMSMPR operation leads to the prevention of particle sedimentation and blockage of transfer lines. The transfer of slurry (to/from) the PMSMPR is followed by a holding (or pause) period when no addition or withdrawal of slurry takes place. The holding period extends the mean residence time of the PMSMPR relative to a typical MSMPR, thereby increasing the yield and productivity of crystallisation as more time is allowed for consumption of available supersaturation *viz* crystal growth and nucleation. A “state of controlled operation” (SCO) in the periodic flow process, defined as a state of the system that maintains itself despite regular, but controlled disruptions was characterised using the PAT tools and CryPRINS within an intelligent decision support (IDS) framework.

The crystallisation of paracetamol (PCM) from isopropyl alcohol (IPA) using different configurations of a single-stage continuous MSMPR crystalliser that incorporated continuous recycle and recirculation loop, and a novel design with baffled heat exchanger was

investigated. Crystallisations of PCM-IPA carried out in the MSMPR without heat exchanger suffered from severe fouling, encrustation and blockage problems due to the high level of supersaturation (S = 1.39) in the crystalliser, which was required for the initial burst of nucleation to generate enough particles for later growth, as well as the large temperature difference between the incoming feed (45 ^{o}C) and the crystalliser (10 ^{o}C). Using the modified MSMPR design with baffled heat exchanger, the challenges of fouling, encrustation and blockage were significantly reduced due to the rapid lowering of the feed stream temperature prior to entering the crystalliser. In addition, the closed loop system led to conservation of material, which is a great benefit since large amounts of materials would otherwise be required if the MSMPR was operated with continuous product removal. This design is great for research purposes, in particular, to investigate process design and optimisation.

Continuous crystallisation of PCM in the presence of hydroxyl propyl methyl cellulose (HPMC) additive was investigated in the modified MSMPR design with heat exchanger. HPMC was found to improve the crystallisation performance, leading to complete avoidance of fouling, encrustation and blockages at a concentration of 0.05 wt%. However, the yield of crystallisation was significantly reduced (28.0 %) compared to a control experiment (98.8 %, biased due to fouling/encrustation) performed without additive addition. Regardless, the productivity of crystallisation was more than four times that achieved in batch linear cooling (LC) (0.62 – 0.86 g/L-min) and batch automated dynamic nucleation control (ADNC) (0.24 – 0.25 g/L-min) runs.

Aspects of the periodic flow crystallisation of single- and multi-component (co-crystals) molecular systems have also been examined to demonstrate the concept of “state of controlled operation”. The single component systems studied were PCM and glycine (GLY), each representative of compounds with slow and fast growth kinetics, respectively. The co-crystal systems investigated were urea-barbituric acid (UBA) and p-Toluenesulfonamide-Triphenylphosphine oxide (p-TSA-TPPO). UBA is a polymorphic co-crystal system with three known forms (I, II and III). Form I UBA was successfully isolated in a three-stage periodic flow PMSMPR crystalliser. This study demonstrates the capability of periodic flow crystallisation for isolation of a desired polymorph from a mixture. p-TSA-TPPO exists in two known stoichiometric co-crystal forms, 1:1 and 3:2 mole ratio p-TSA-TPPO, respectively. The two crystalline forms exhibit solution mediated transformation, which proves to be a difficulty for separation. For this study, the implementation of temperature cycles in batch and flow control in semi-batch and periodic PMSMPR crystallisers were investigated to isolate pure 1:1 and 3:2 p-TSA-TPPO, respectively. Different regions of the ternary diagram of p-TSA, TPPO and acetonitrile (MeCN) were investigated. The desired co-crystal form was isolated all

crystallisation platforms investigated. However, greater consistency was observed in the semi-batch and PMSMPR operations respectively.

Periodic flow crystallisation in PMSMPR is a promising alternative to conventional continuous MSMPR operation, affording greater degrees of freedom operation, slightly narrower RTD profiles, consistent product crystal quality (size, shape and distribution), longer mean residence times, higher yield and productivity and significant reduction in fouling, encrustation and transfer line blockages over prolonged operating periods. Furthermore, the PMSMPR is a versatile platform that can be used to investigate a range of different molecular systems. Relative to batch operation, the PMSMPR can operate close to equilibrium, however, this is dependent on the system kinetics. In addition, retrofitting of batch crystallisers to operate as PMSMPRS fairly simple and require only subtle changes to the existing design space.

The integrated array of PAT sensors consisted of attenuated total reflectance ultra violet/visible spectroscopy (ATR-UV/vis), attenuated total reflectance Fourier transform infrared spectroscopy (ATR-FTIR), focused beam reflectance measurement (FBRM), particle vision microscopy (PVM) and Raman spectroscopy. The results from the studies reported here illustrate very well the use of PAT and information system tools together to determine when the continuous and periodic MSMPR operations reaches a steady-state or state of controlled operation (i.e. periodic steady-state). These tools provided a better understanding of the variables and operating procedures that influence the two types of operations.

Graphical Abstract

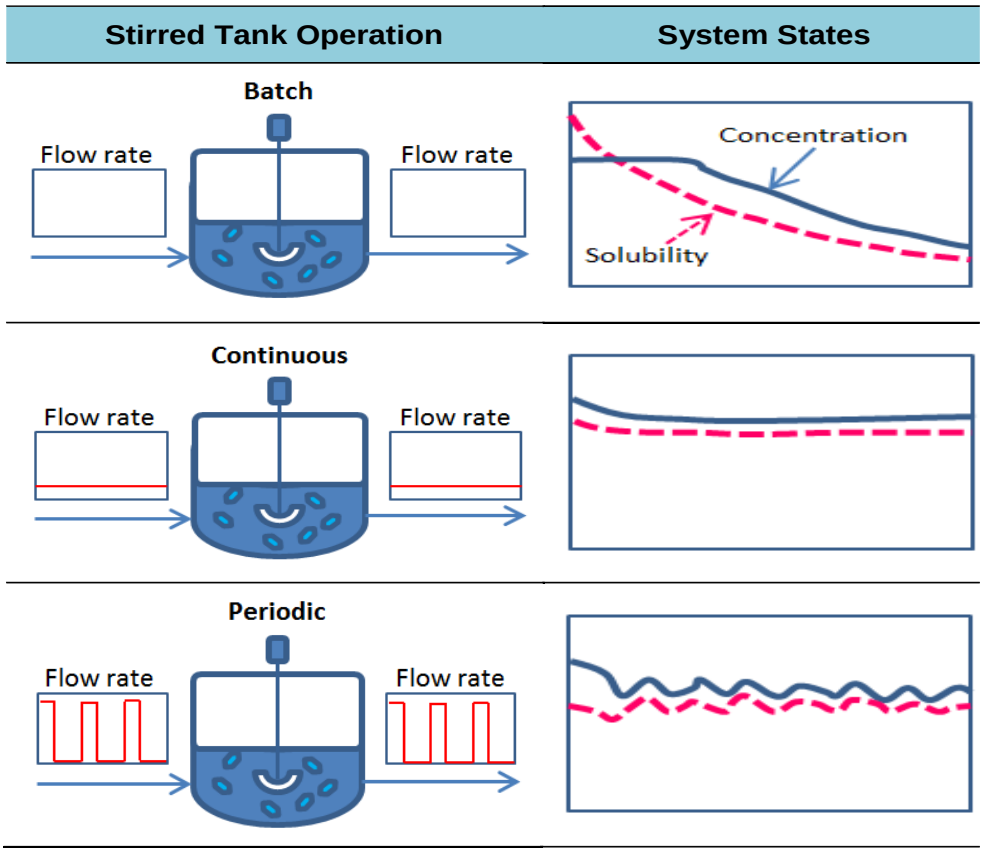

Comparison of batch, continuous MSMPR and periodic flow PMSMPR operations.

Table of Contents

List of Figures

List of Tables

Abbreviations

ADNC	*Automated direct nucleation control*
AMGN	*Amgen*
ANN	*Artificial neural networks*
API	*Active pharmaceutical ingredient*
HPLC	*High performance liquid chromatography*
ATR	*Attenuated total reflectance*
BA	*Barbituric acid*
BFDM	*Backward finite difference method*
BVI	*Bulk video imaging*
CCA	*Canonical correlation analysis*
CLD	*Chord length distribution*
CMAC	*Centre for Innovative Manufacturing in Continuous Manufacturing and Crystallisation*
COBC	*Continuous oscillatory baffled crystalliser*
CPP	*Critical process parameters*
CQA	*Critical quality attributes*
CryPRINS	*Crystallization process informatics system*
CSA	*Composite sensor array*
CSD	*Crystal size distribution*
CV	*Coefficient of variation*
DoE	*Design of experiment*
DSC	*Differential scanning calorimetry*
DTB	*Draft tube baffle*
EMA	*European Medicines Agency*
FBRM	*Focused beam reflectance measurement*
FC	*Forced circulation*
FDA	*Food and Drug Administration*
FTIR	*Fourier transform infra-red*
GLY	*Glycine*
GLY-H_2O	*Glycine-water*
GSK	*GlaxoSmithKline*
HPLC	*High performance liquid chromatography*
HSM	*Hot stage microscopy*
IDS	*Intelligent decision support*
IPA	*Isopropyl alcohol*
ISPT	*The Netherlands Institute of Sustainable Process Technology*
JNJ	*Johnson & Johnson*
LALLS	*Low angle light scattering*
LC	*Linear cooling*
LDA	*Linear discriminant analysis*
MeCN	*Acetonitrile*
MeOH	*Methanol*
MIR	*Mid-infrared*
MLR	*Multiple linear regression*
MS	*Mass Spectroscopy*

MSMPR	*Mixed suspension mixed product removal*
MSWCL	*Mean square weighted mean chord length*
MSZW	*Metastable zone width*
MSMA-PFC	*Multi-segment multi-addition plug-flow crystalliser*
NPLS	*Non-linear partial least squares*
NIR	*Near infra-red*
NL GUTS	*The Netherlands Group of Users of Technology for Separation*
NVS	*Novartis*
PAT	*Process analytical technology*
PCA	*Principal component analysis*
PC	*Principal component*
PCM	*Paracetamol*
PCR	*Principal component regression*
PDE	*Partial differential equation*
PFC	*Plug flow crystalliser*
PLS-DA	*Partial least squares discriminant analysis*
PLSR	*Partial least squares regression*
PMSMPR	*Periodic flow mixed suspension mixed product removal*
PSE	*Process System Enterprise*
p-TSA	*p-Toluenesulfonamide*
p-TSA-TPPO	*p-Toluenesulfonamide-Triphenylphosphine*
PVM	*Particle vision microscopy*
PVI	*Process video imaging*
PXRD	*Powder X-ray diffraction*
QA	*Quality assurance*
QbD	*Quality by design*
QbT	*Quality by testing*
RMSEP	*Root mean squared error of prediction*
RT	*Residence time*
RT_{PO}	*Residence time of periodic flow*
RTD	*Residence time distribution*
SCO	*State of controlled operation*
SEM / EDS	*Scanning electron microscopy / Energy dispersive X-ray spectroscopy*
SFI	*Science Foundation Ireland*
SIMCA	*Soft independent modelling of class analogy*
SNV	*Standard normal variate*
SSC	*Supersaturation control*
SSPC	*Solid State Pharmaceutical Cluster*
SWCLD	*Square weighted chord length distribution*
SME	*Small-medium enterprises*
TPPO	*Triphenylphosphine Oxide*
UBA	*Urea-barbituric acid*
UV/Vis	*Ultra violet/visible*
VCI	*Vibrational chemical imaging*
VRTX	*Vertex Pharmaceuticals*

Symbols

B	*birth*
c	*concentration*
c_i	*initial concentration*
D	*death*
G	*growth*
dL	*crystal size interval*
E_j *(t, θ)*	*residence time distribution of* j^{th} *exceeding stream*
$f(L)$	*normalised one-dimensional distribution function*
F_i *(t, θ)*	*residence time distribution of* i^{th} *stream*
L	*crystal size*
S, s or σ	*supersaturation*
t	*time*
T	*temperature*
V	*volume*
$\dot{V}_i$	*inlet flow rate*
$\dot{V}_o$	*outlet flow rate*
$\partial\hat{n}$	*population density of crystals*
τ, θ	*residence time*
k_v	*volume shape factor*
ρ	*crystal density*
μ_i	i^{th} *moment of distribution*
δ	*Dirac delta function*
W (t, θ)	*residence time distribution*

Chapter 1

Thesis Overview

Aspects of the industrial crystallisation and manufacture of speciality fine chemicals, specifically, pharmaceutical and agrochemical active ingredients are discussed. In particular, an assessment of crystallisation methods (batch and continuous), specifically, the benefits and limitations of implementing continuous crystallisation methodologies are addressed. Process monitoring and control strategies, and the implementation of process analytical technologies (PAT) in the design space to tailor product critical quality attributes (CQA) applying quality by design principles (QdD) are highlighted. Gaps have been identified where process improvements could be made through implementation of innovative continuous crystallisation operating strategies, and control approaches aided by PAT. In this thesis, viable solutions are proposed that could facilitate a transition from batch to continuous manufacturing and crystallisation. A novel continuous crystallisation process known as periodic flow mixed suspension mixed product removal (PMSMPR) crystallisation is introduced. A new concept "state of controlled operation", rather than "steady-state" is used to describe when the periodic operation is under control. An automated intelligent decision support (IDS) framework, enabled by PAT and information systems that were used to monitoring and control the periodic flow process is discussed. Experimental investigations and mathematical modelling aspects are also reported. The overall aim is to provide an engineering design that is amenable to adoption in commercial plants and robust on scale-up to industrial production capacity. An overview of the fundamental aspects of the thesis objectives is henceforth presented, and the significant contributions of the work highlighted. An outline of the thesis structure is presented toward the end of this chapter.

1.1 Motivation

Crystallisation is an important unit operation in the chemical industries, widely used for separation and purification of active pharmaceutical ingredients (APIs), active agrochemical ingredients (AAIs), intermediates and food products, petrochemicals and various other speciality and high value products. The primary objective of crystallisation is to produce high quality crystalline material from liquids (melt or solution). The process requires specific attention to yield, size, shape, distribution and purity of the product crystals. These critical quality attributes (CQA) can have a significant impact on downstream unit operations such as

filtration, washing, drying, milling and product formulation as well as impact on the physicochemical properties of the crystalline material, for example, the solubility, rate of dissolution and permeability [1]–[4]. In addition to the aforementioned, pharmaceutical products require special attention to the API solid form, specifically: polymorphism (e.g. metastable forms), salts, solvates, glycosylated derivatives (i.e. acetals of saccharides), and more recently multi-component molecular systems such as co-crystals. Invariably, the properties of an API solid form are directly linked to the oral bioavailability of a drug, which is very important to pharmaceutical manufacturers, since this will ultimately determine the commercial success of the drug product [3]. Figure 1.1 summarises the main aspects of industrial crystallisation, and includes the objectives (or functions), product properties (or CQA), modes of operation and kinetics of crystallisation.

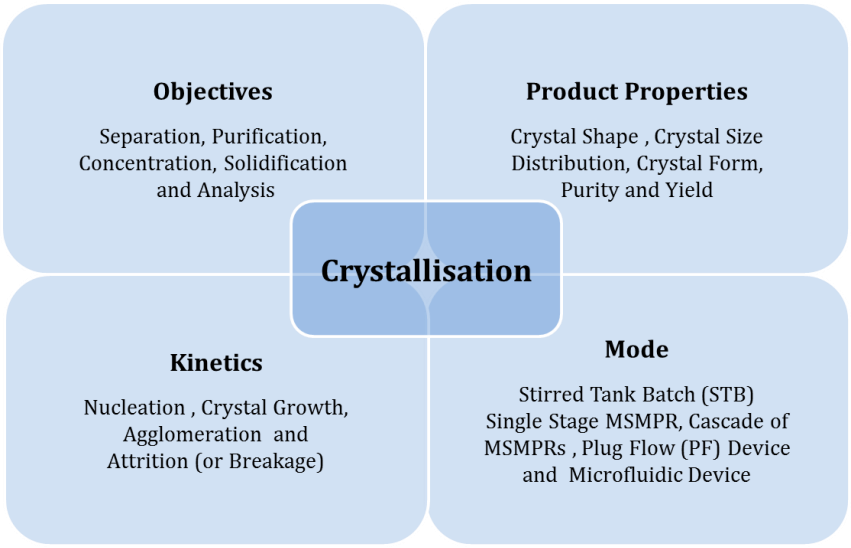

Figure 1.1: Schematic showing the main aspects of crystallisation including, objectives (or functions), product properties (or CQA), operation modes, and kinetics of crystallisation.

On an industrial scale, crystallisation may be achieved using batch or continuous operation. The choice of operation depends largely on the process requirements, for example, the physicochemical characteristics of the material to be crystallised, desired production capacity, type of solvent system, operating temperature and pressure, supersaturation level, desired mixing characteristics, heat exchange and other energy requirements, construction materials, cleaning requirements and the desired crystal size distribution (CSD) [5], [6]. In addition, the economics of the process is another important factor to consider, for example, the costs of construction, materials, utilities and labour [2], [7]. In the fine chemicals sector, crystallisation is typically achieved using large stirred tank batch or semi-batch crystallisers. While the methodologies for developing these processes are reasonably well understood, there are still significant issues with batch-to-batch variability, which leads to disruption of downstream unit

operations [8], [9] due to the production of off-spec product that either requires rework or has to be discarded. Consequently, in recently years the case for a transition from batch to continuous manufacturing and crystallisation has gained momentum. The benefits of continuous relative to batch operation is a well debated topic [2], [10]–[12]. For example, continuous processes operate at “steady-state”, which could potentially lead to more consistent product quality. Other benefits include, smaller equipment size leading to a reduction in capital expenditure; and the capacity for recycling, for example, spent process liquor and fines to reduce wastage and raw materials usage [2], [13]. However, continuous manufacturing (specifically crystallisation) has been an *ad hoc* research field for the past decade, in which there have been campaigns for the development and adoption of next generation continuous technologies for pharmaceutical and fine chemical industries [14], [15]. In order to develop a good continuous process, all the unit operations being considered should be first studied separately in order to develop a better understanding [16]. Generally, there are two types of continuous crystallisers that are most investigated, namely the tubular and the stirred-tank designs [17]. These two designs help to achieve, ideally, the plug-flow [18] and the mixed-suspension mixed-product removal (MSMPR) operations [19], respectively. While derivatives of these two designs have resolved some of the practical concerns related to continuous crystallisation processes, such as the continuous oscillatory baffled crystalliser (COBC) to deal with sedimentation of crystals due to low Reynolds number in straight tubes [20], the multi-segment multi-addition plug-flow crystalliser (MSMA-PFC) to implement supersaturation control [21], [22] or fines dissolution along the tube [23] and cascaded multi-stage continuous MSMPR crystallisers to enhance product yield [13], [24] there remains some unresolved challenges. For example, the important issue of material residence time in these two continuous crystallisation platforms has rarely been addressed. In addition, persistent fouling and encrustation on vessel walls and process equipment and transfer line blockage [13], [25] are challenges that need to be addressed to successfully demonstrate the merits of continuous over batch operation. This thesis project seeks to address some of these challenges by providing alternative engineering designs that facility process optimisation and control, whilst avoiding some practical operating problems. To this end, a novel periodic flow crystalliser was developed using mixed suspension mixed product removal (MSMPR) operation. Usually, MSMPR crystallisers are operated with continuous feed supply and product withdrawal to and from the vessel(s). With a certain amount of operating volume, it is often necessary to reduce the stream flow rates of MSMPR crystallisers to obtain enough residence time for crystals to grow, which often leads to particle setting, fouling and transfer line blockages between stages. In a periodic flow MSMPR or periodic mixed suspension mixed product removal (PMSMPR) crystalliser, periodic disruptions are applied to the inlet and outlet flows of an otherwise continuous MSMPR, either synchronously or asynchronously, to

manipulate the RTD profile. This is achieved by implementing a holding (or batch) period between flow disruptions, which, for example, is able to significantly increase the mean residence time for slow growing crystallisation systems. By intermittently increasing stream flow rates between stages, sedimentation, fouling and line blockages can be avoided. Notably, the PMSMPR crystalliser is a hybrid of batch and continuous MSMPR, and if the transient effects caused by periodic flow are controlled within narrow limits in the design space, then the final crystal product attributes will be maintained in a “state of controlled operation” (SCO), as required by FDA regulations [26].

In recent years, the development of *in situ* sensors, that is, process analytical technologies (PAT) has led to the widespread application of various measurement techniques in pharmaceutical and fine chemical research laboratories [27]–[29]. PAT tools (or sensors) are often used simultaneously to monitor crystallisation processes, but often the data acquired are not combined, interpreted and applied in real time [29], [30]. Recently, the concept of composite sensor arrays (CSA) was introduced [30]. CSA is based on the idea that all sensors used in a crystallisation process are components of a single global sensor, which allows simultaneous signal acquisition from all devices for the purposes of automation, real-time decision support, and feedback control of the process. In the current work, the various sensors of the CSA are coordinated by a crystallisation process informatics system tool (CryPRINS) [31]. Figure 1.2 (adapted from Nagy *et al* [29]) provides a schematic showing how multiple process and quality properties can be monitored in real-time, and simultaneously using all signals from a number of sensors for automated intelligent decision support (IDS), and direct feedback control of a crystallisation process.

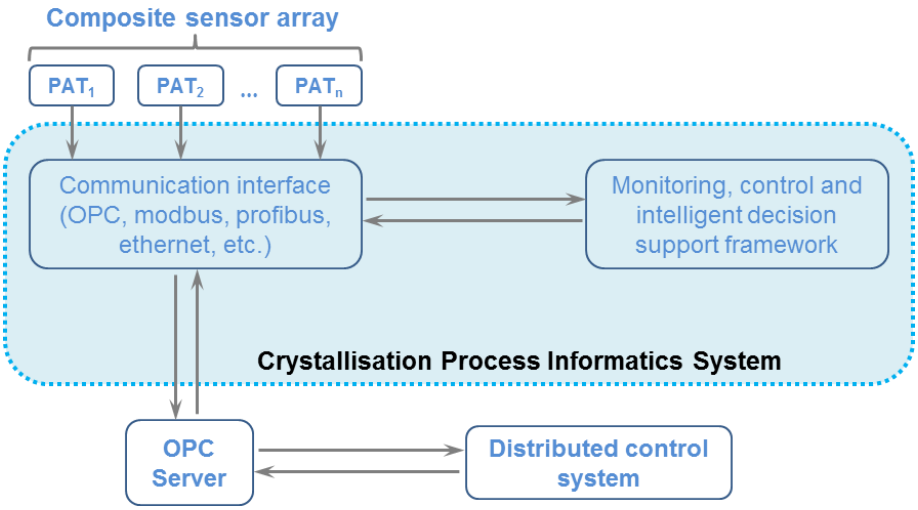

Figure 1.2: Schematic showing the architecture of the crystallisation process informatics system with composite sensor array and industry standard communication interface with distributed control system. Adapted from [29], [31].

The application of CSA in the continuous manufacturing and crystallisation design space could potentially revolutionise the pharmaceutical and fine chemical processing by directly facilitating the Food and Drug Administration's (FDA) Quality by Design (QbD) principle, and leading to better control of product CQA. Until now, the PAT and CSA approach has only been applied to batch crystallisers. In this thesis project, an array of PAT tools, including sensors for monitoring particle size, distribution and form, as well as temperature and concentration sensors integrated with a CryPRINS software tool were used to monitor and improve batch, continuous and periodic flow crystallisation processes. In particular, the continuous and period flow processes were monitored and controlled in real-time and "steady-state" and "state of controlled operation" (SCO) determined viz. the implementation of an IDS framework.

1.2 Aim and Objectives

The overall aim of this thesis is to provide novel alternative engineering designs of the continuous MSMPR crystalliser that are amenable to adoption in commercial plants and robust on scale-up to industrial production capacities. The objectives that support the principal aim of this thesis are as follows:

I. Highlight gaps in the literature where process improvements could be made toward the design and development of the next generation of continuous crystallisation technologies.

II. Design and application of a novel periodic flow mixed suspension mixed product removal (PMSMPR) crystalliser that addresses the issue of limited residence time distribution (RTD) control in continuous MSMPR operation. This PMSMPR operation lends itself to robust process control *viz*. controlled periodic disruption of the feed and outlet flow rates.

III. A further aim is to mitigate fouling, encrustation, and line blockages issues often encountered in continuous MSMPR operations, by using innovative operating strategies in the PMSMPR. Furthermore, the performance characteristics of PMSMPR crystalliser compared to batch and continuous equivalents in terms of residence time, yield, productivity, product critical quality attributes (i.e. size, shape and distribution) and polymorph control are examined.

IV. The effect of the amplitude of perturbations caused by PMSMPR operation are examined by investigation and comparison of different operating strategies, including: operating with and without recycle stream (concentrate or non-concentrated), seed

type and loading, and aspects of coupled (or synchronous) versus de-coupled (non-synchronous operation).

V. Demonstrate the use of the periodic flow crystallisation process in single-stage and multi-stage cascaded PMSMPR operations for the crystallisation of single-component and multi-component (i.e. co-crystal) molecular systems that exist as polymorphs or other crystalline forms.

VI. Introduce the concept of “state of controlled operation” (SCO) (or “periodic steady-state”) instead of “steady-state” operation to describe when the PMSMPR operation is under control. Furthermore, experimental and mathematical evaluation of the PMSMPR crystallisation process is investigated, aided by PAT and CryPRINS to improve process understanding for optimisation of product properties. Parameter estimation, process simulation and modelling aspects were implemented using Process Systems Enterprise (PSE) gCRYSTAL 4.0 software package.

VII. Develop multivariate calibration models from spectroscopy data (namely, attenuated total reflectance ultraviolet/visible (ATR-UV/vis) and Fourier transform infrared (ATR-FTIR), and Raman spectroscopy) using statistical approaches such as principal component regression (PCR), partial least squares regression (PLSR) and multiple linear regression (MLR) for real-time concentration determination and quantification of polymorphic or other crystalline forms during batch, continuous and PMSMPR crystallisations.

VIII. Demonstrate the application of an integrated array of PAT tools inclusive of particle monitoring techniques, such as focused beam reflectance measurement (FBRM) and particle vision microscopy (PVM); and spectroscopy techniques, including ATR-FTIR and ATR-UV/vis (used for solution phase monitoring) and Raman (polymorphic form identification and solution phase monitoring) together with CryPRINS software within an IDS framework for monitoring and implement control in batch, continuous and PMSMPR operations.

1.3 Research Methods

The modified MSMPR crystalliser design reported in this thesis incorporates a baffled heat exchanger to minimise temperature fluctuations as hot feed solution enters the pre-cooled MSMPR crystalliser. MSMPR provides a different supersaturation trajectory though the phase diagram compared to batch operation, which could allow better product crystal CQA to be

attained, that is, in terms of mean size and CSD, polymorphic form and purity [32], whilst operating at steady-state. The effect of different operating regimes, in terms of initial saturation temperature of feed, MSMPR stage temperatures, seeding and anti-solvent addition are investigated.

The novel periodic flow PMSMPR crystallisation process can create customised elaborate RTD profiles in order to tailor the product CQA while applying QbD principles in the design space, that is, quality assured by better product and process understanding. Usually, the MSMPR is operated with continuous feed supply and product withdrawal to and from the crystalliser viz. the continuous MSMPR crystallisation operation. By convention, in order to maintain a constant operating volume and sufficient residence time for the crystals to grow in the continuous MSMPR, it is necessary to reduce the stream flow rates, which often leads to transfer line fouling and blockage issues. The periodic flow crystallisation process using MSMPR (or PMSMPR) crystalliser is a novel operation whereby periodic disruptions are applied to the inlet and outlet flows of an otherwise continuous MSMPR, either synchronously or asynchronously, to manipulate the RTD. In this method of operation, a holding (or batch) period is implemented between flow disruptions, which for example is able to significantly increase the mean residence time for slow growing systems. In addition, it also benefits from the intermittent increase of stream flow rates, which helps to alleviate the usual transfer line fouling and blockage issues encountered in existing continuous operations. Periodic flow operation can also be applied to cascaded multi-stage PMSMPR crystallisers to facilitate controlled nucleation and gradual crystal growth in the phase diagram. Different operating strategies are investigated in the PMSMPR to manipulate the product CQA, namely, the length of the batch cycle, seed loading and supersaturation (viz. stage temperature manipulation). Factors such as temperature, supersaturation, nucleation, growth, breakage and agglomeration were controlled by applying different cooling and/or anti-solvent crystallisation strategies. Mathematical modelling approaches combined with experimental investigations using PAT tools and multivariate statistical methods are also exploited in order to improve process understanding. The information gained can then be applied to optimise the MSMPR and PMSMPR operations to target specific product CQA.

1.4 Research Contribution

The significant contributions of this work are as follows:

I. Different combinations of pre-treatment/processing methods for chemometrics model building, including derivatives, mean centering, auto-scaling, normalisation routines

and scatter correction techniques were applied to the spectral data obtained viz. ATR-UV/vis, ATR-FTIR and Raman spectroscopy, principally for noise reduction and baseline correction. Following data pre-treatment, different combinations of model development algorithms were (PCR, PLSR and/or MLR) were applied to extract information pertaining to the concentration of the analyte (or solute) of interest. Multivariate models were developed to determine the concentration of a single analyte or multi-analytes concomitantly. This study also demonstrates that Raman spectroscopy is capable of monitoring solution concentration when the appropriate multivariate techniques are applied to the spectral data.

II. The IDS framework consisting of integrated array of PAT tools and CryPRINS informatics systems software proved very useful for monitoring and control of the various crystallisation processes investigated in this thesis whilst also giving an indication of when a controlled state of operation (i.e. steady-state or SCO) is achieved. The IDS was also able to detected process disturbances and drifts arising from transfer line blockages, flow rate changes and fouling. These effects were easily captured as large signal fluctuations of the PAT and temperature sensor signals.

III. The novel periodic PMSMPR crystalliser design shows great promise in addressing many of the challenges of adopting current generation continuous crystallisers, such as fouling and encrustation, classified slurry withdrawal and insufficient residence time for crystal growth. The PMSMPR is a hybrid operation that incorporates the beneficial aspects of batch (long residence time for crystal growth) and continuous crystallisation (consistent product quality) operation. If the transient effects caused by periodic flow operation are controlled within narrow limits in the design space, then the final crystal product attributes will be maintained in a “state of controlled operation” (SCO), as required by FDA regulations. “State of controlled operation” (SCO) is demonstrated in this work for the first time. PMSMPR is able to significantly increase the mean residence time for slow growing crystallisation systems without further broadening the CSD (i.e. relative to continuous MSMPR operation). There are also benefits from the intermittently operated feed addition and slurry withdrawal streams: increasing the flow rates of these streams over short periods, helps to alleviate the usual classified product withdrawal and transfer line fouling and blockage problems often experienced in conventional MSMPR operations. A dynamic residence time distribution model was applied to simulate RTD profiles of conventional MSMPR and periodic flow PMSMPR crystallisers, respectively. It was proven that the latter extends the mean residence time of slurry in the crystalliser without further broadening the RTD.

IV. The periodic flow PMSMPR operation was used for the crystallisation of fast and slow growing single-component systems, namely, glycine (GLY) and paracetamol (PCM); and multi-component co-crystals systems, namely, urea-barbituric acid (UBA) and p-Toluenesulfonamide-Triphenylphosphine (p-TSA-TPPO). Crystal growth of PCM was marginal in the PMSMPR, whereas significant increase in size was observed for GLY. In both cases, narrow CSD were obtained relative to the seed crystals used. UBA co-crystal polymorphs, form I and III that exhibit strikingly similar solubilises and overall physicochemical properties were crystallised in the PMSMPR and the conditions for isolation of UBA form I optimised. The 3:2 and 1:1stoichiometric co-crystals of the p-TSA-TPPO system were both successfully isolated using the PMSMPR by manipulating the mass fraction composition of the starting materials in the crystalliser viz. flow rate adjustments. These examples demonstrate the versatility and flexibility of the PMSMPR compared to batch and continuous MSMPR operations.

1.5 Thesis Outline

This work has sought to improve continuous crystallisation with the aid of PAT tools. In this thesis alternative engineering designs of continuous MSMPR crystallisers are presented and that were fully characterised using integrated PAT and informatics systems tools to achieve better process understanding. This thesis consists of a further seven chapters organised as follows:

I. **Chapter 2: Literature Review: Continuous Crystallisation and Multivariate Statistical Process Monitoring**. This chapter provides a detailed review of the literature on different aspects of continuous crystallisation, including the operating principles of the different platforms available, application of PAT and multivariate methods for process characterisation, parameter estimation and mathematical modelling, crystallisation kinetics, polymorphism and co-crystallisation.

II. **Chapter 3: Materials and Experimental Methods.** In this chapter detailed descriptions of the materials (chemicals and solvents), analytical techniques and experimental methodologies employed in the studies reported in this thesis are provided. It includes a description of the instrumentation used and experimental parameters implemented. Details of multivariate calibration model development using various spectroscopy techniques are also included.

III. **Chapter 4: Comparative Investigation of Batch and Continuous Crystallisation of Paracetamol Using PAT.** In this chapter, optimised batch (*viz*. linear cooling (LC)

and automated dynamic nucleation control (ADNC)) and continuous crystallisation (*viz*. different MSMPR configurations, including the modified MSMPR) methods are investigated and compared on the bases of product mean size and CSD, extent of agglomeration, process yield, and productivity for the crystallisation of PCM form isopropyl alcohol (IPA) and water (used both as solvent and anti-solvent). MSMPR seeded crystallisation experiments were carried out in single-stage and two/three-stage cascaded crystallisers with or without recycle employed. Where a recycle stream was used, concentrated or non-concentration streams, respectively, were investigated.

IV. **Chapter 5: Periodic Flow Crystallisation of Paracetamol: Example of a Slow Growing API.** In this chapter a novel periodic flow crystallisation process, that is, PMSMPR, is designed and built. The PMSMPR was used to investigate the crystallisation of PCM from IPA. PCM is a well-known slow growing single-component API system. Different configurations of the PMSMPR, including, single-stage and two/three-stage cascades operated either with or without recycle stream are investigated. In addition, the effect of supersaturation, seed type and seed loading are investigated. The effects on the different operating strategies on the crystallisation outcome are quantified and compared to batch operation. The concepts of "state of controlled operation" (SOC) or "periodic steady-state" are introduced and used to describe when the PMSMPR operation achieves a controlled state of operation aided by PAT tools and CRYPRINS.

V. **Chapter 6: Periodic Flow Crystallisation of Glycine: Example of a Fast Growing API.** In this chapter, the novel concept of periodic flow crystallisation which is described in detail in Chapter 5 was applied to the crystallisation of GLY from water. Dynamic RTD models of the continuous single-stage MSMPR and the periodic PMSMPR crystallisers are developed and compared. Experimental evaluation of the PMSMPR was carried out using single-stage and three-stage cascades. Coupled and decoupled modes of period operation were investigated. The effect of product withdrawal location (bottom valve versus outlet tube withdrawal) on the product attributes are investigated and compared. Mathematical models of the PMSMPR crystallisers are developed using Process System Engineering's gCRYSTAL 4.0 software. The crystallisation mechanisms and kinetics of the GLY-H_2O system are estimated from batch crystallisations and validated with periodic flow crystallisations in three-stage PMSMPR.

VI. **Chapter 7: Periodic Flow Crystallisation of Co-Crystals Using PMSMPR: Case of Urea-Barbituric Acid**. In this chapter the periodic flow crystallisation concept is

extended to the crystallisation of the multi-component co-crystal system UBA. Co-crystals can often have several polymorphs, just as in single-component molecular systems. In this study, the co-crystallisation and isolation of desired polymorphs of the UBA co-crystal system, which has three known polymorphic forms, I, II and III is investigated and the experimental conditions optimised. Different start-up strategies and temperature sets are investigated using different configurations of a three-stage cascaded PMSPMR. PAT and off-line solid-state characterisation methods are employed to determine when SCO is achieved and to determine the co-crystallisation outcomes.

VII. **Chapter 8: Design of Agrochemical Co-Crystallisation Processes: Isolation and Characterisation of 1:1 and 3:2 Co-Crystals of p-Toluenesulfanomide /Triphenylphosphine Oxide.** In this chapter, the selective co-crystallisation and subsequent characterisation of stoichiometric forms of the p-Toluenesulfanomide /Triphenylphosphine (p-TSA-TPPO) agrochemical co-crystal system is investigated. Different regions of the ternary phase diagram of the co-crystals system are explored and the conditions optimised for producing the desired form of p-TSA-TPPO in batch, semi-batch and PMSMPR crystallisers. Temperature cycling (via direct feedback control using a Raman sensor) and flow rate manipulation are investigated to control the co-crystallisation outcome in the different crystalliser platforms and the results compared.

Chapter 2

Literature Review: Continuous Crystallisation and Multivariate Methods

In the pharmaceuticals sector, batch crystallisation is a simplified tried and true approach that has been used for decades and has served well for both industry and regulatory bodies [33]*. In comparison, other industries such as petrochemical and food manufacturing have moved to continuous crystallisation technologies for the production of a range of materials, driven mainly by cost and quality considerations. A recent comparison of batch and continuous manufacturing by Kossik* [34] *highlights some of the reasons, other than tradition, why the pharmaceutical industry is dominated by batch processes. The primary driver for other industries that adopt continuous manufacturing is the reduction in operational costs due to the economies of scale (i.e. high tonnage, but low value), reduction in labour costs and increased use of automation. Other factors that influenced the decision to adopt continuous manufacturing include the desire to reduce the size of and number of manufacturing plants, enhanced reproducibility and control of physical characteristics of the product and the ability to respond rapidly to market demand (i.e. with respect the amount of material required/produced). In recent years the pharmaceutical industry and FDA have both come to an agreement that an overhaul of the manufacturing regulations that apply to innovative processing methods will prove beneficial for the patient that both of them serve* [35]*. In fact the industry and the FDA are working together in several joint initiatives to apply new Quality by Design (QdD) approaches to replace existing and less effective Quality by Testing (QbT) methods* [36]*. In this chapter a brief, but detailed review of the current-state-of-the-art in continuous manufacturing and crystallisation, including aspects related to process analytics and multivariate, structure-based design and isolation of different crystalline forms is presented.*

2.1 Introduction

Continuous crystallisation has long been a standard method used for the purification of bulk commodity chemicals such as salt and sugar due to the many practical and economic benefits [6]. The earliest attempt at continuous crystallisation was reported back in 1908 by the Ukrainian Zapiski Orosianikov who operated eight crystallisers in series for 50 days at a sugar

factory in Mironovka, Kiev [37]. In the pharmaceutical and fine chemicals industries, continuous crystallisation has only recently become a focus [38], [39]. Historically, pharmaceutical companies have competed solely on the basis of innovation through new drugs for medical needs [10], [33], [40]. According to a recent study by Tufts Centre for the Study of Drug Development capitalising out of pocket costs to the point of marketing approval yields a total pre-approval cost estimate of US $ 2.6 billion per new drug [41], a 145 % increase (corrected for inflation) over the estimate of US $ 802 million reported in 2003 [42]. This huge increase has been attributed to annual increases in total capitalised cost and out-of-pocket cost per approved new compound of 8.5 and 9.3 %, respectively. In a best case scenario, the R&D costs can be expected to remain the same or increase in the future if the industry does not adopt more efficient technologies for drug discovery and development. When combined with other factors, such as increases in competition, further increases in proportion of generic utilization, opening of new markets, and the socioeconomic pressures for price controls, it is evident that the industry is facing significant challenging ahead.

Currently, new technologies and techniques, including proteomics, genomics, and the use of biomarkers, appear to be creating a future where blockbusters, as we currently define them, may or may not exist. The future instead will consist of many "customised" small volume drugs that take into consideration a patient's specific subcategory of disease and genetic makeup. These overall shifts will translate into manufacturing many more new products. When all of the above factors are summarised, the same cost and quality drivers that have affected other industries are forcing the pharmaceutical industry to look for ways to improve quality while maintaining or reducing research and development (R&D) costs. Continuous manufacturing technologies provide one possible path forward for the pharmaceutical industry to reduce the cost of manufacturing, with the objective to convert selected unit operations and processes from batch to continuous along with appropriate real time characterization using state-of-the-art process analytical technologies (PAT) [10], [33], [43], [44]. However, any transition to continuous manufacturing will require process re-design and re-validation [16]. Pharmaceutical companies are required by the FDA and EMA to validate their processes and equipment to demonstrate that the design space in which they operate can produce drug products that conform to design specifications, as described in the following section.

2.1.1 Regulatory Considerations

The pharmaceutical industry is heavily regulated, which has led to a culture of conservatism that has stifled innovation in process technology development to improve manufacturing [10]. According to the FDA regulatory definition, a batch or lot is a specific quantity of a drug or

other material that is intended to have uniform character and quality, within specified limits, and is produced according to a single manufacturing process during the same cycle of manufacture [45]. It would appear from this definition that the regulatory framework is already in place to support the concept of a period of time (which is defined by the time required to achieve a controlled state of operation and obtain desirable product critical quality attributes) being a “batch” for the purpose of tracking and quality assurance. If this interpretation is accepted, then it would be an opportunity to make the case for moving to continuous or at least periodic (hybrid batch and continuous) manufacturing, which is by definition a single processing cycle. Although there are currently no specific regulations or guidance for continuous manufacturing, other than the definition of “lot” [45], there is nothing stated that prohibits continuous manufacturing of pharmaceutical intermediates or active ingredients. However, the FDA has expressed concern about the concept of steady-state which is associated with continuous manufacturing. Unlike batch processes which typically attain an equilibrium condition, continuous processes operate at steady-state when material properties in the system remain constant with time [46]. The time to achieve steady-state largely depends upon the flow properties of a system. Therefore, several questions arise, for example: When is a product acceptable or not to collect? How to start-up and shut-down a continuous process? If disturbances occur in the system (e.g. spike in feed rate), how will rejects be handled? When do all component concentrations and physical properties reach steady-state? – This may necessitate the measurement of process variables other than concentration of the active ingredient(s). The FDA’s most recent position on this issue is that a well-defined system for process performance and product quality monitoring should be applied to assure performance within a “state of control” (rather than steady-state) and to identify improvement areas[26], [47]. Application of PAT tools with integrated information systems, direct design and model based design approaches may provide solutions to the challenges of continuous processing as posed in the questions earlier. With the appropriate technologies and application of robust methodologies, robust systems can be designed to monitor and control/maintain steady-state in continuous operations and deliver the desired product critical quality attributes (CQA) consistently. There are already well established methodologies that are implemented in batch systems that could potentially be applied to continuous operations. For example, the use of PAT and information system tools for the control of particle size (or aspect ratio) as demonstrated by Saleemi *et al* [48] using focused beam reflectance measurement (FBRM) *viz* dynamic nucleation control and attenuated total reflectance ultraviolet/visible (ATR-UV/vis) spectroscopy *viz* supersaturation control. Others have demonstrated the application of Raman spectroscopy for active polymorphic feedback control using [49]. Currently, there are only a few examples of the application of PAT and information tools in continuous processing to gain process understanding and implement control over

product CQA. Recently, the application of FBRM implement to DNC for particle size/aspect ratio control in a cascade of mixed suspension mixed product removal (MSMPR) crystallisers was demonstrated [50].

Regarding direct design control approaches, there are currently many studies on this topic in the area of continuous crystallisation. For example, impurity control using nano-filtration membrane [51], polymorphism control by tuning stage temperatures and the residence time in a MSMPR crystalliser [52], and particle size control using an inverted dissolution device with a MSMPR [53]. More recently, direct design has been applied for particle engineering purposes to tailor particle shape/size by spherical continuous crystallisation [54], [55]. However, no of these studies have looked into direct design approaches to deal with critical issues such as level changes, residence time, flow control, blockages in transfer lines or fouling and encrustation. Model-based design approaches are already well established for batch processes [30], [56]. In recent years there has been increasing interest in developing model-based understanding of continuous processes [13], [21], [57], but to date there are no studies on the application to process design.

Overall, the issue of new technology introduction in pharmaceutical manufacturing has been very constrained. However, this has been changing quite rapidly from a regulatory perspective. For example, the FDA's draft guidance to the pharmaceutical industry in "Guidance for Industry: PAT – A Framework for Innovative Pharmaceutical Manufacturing and Quality Assurance" [35] describes a regulatory framework on which industry and government can work together to increase the level of innovative pharmaceutical manufacturing technologies by the removal of actual and perceived barriers [33]. The draft guidance document states: "Process Analytical Technology, or PAT, should help manufacturers develop and implement new efficient tools for use during pharmaceutical development, manufacturing, and quality assurance while maintaining or improving the current level of product quality assurance." The background of this guidance is centered on the concept that while conventional pharmaceutical manufacturing is accomplished using batch mode, new opportunities exist to improve the efficiency and quality of the pharmaceutical manufacturing process. This is an attempt to introduce 21st century technology into the pharmaceutical industry to better respond to the rapidly changing marketplace for pharmaceutical products. The utilizing of new approaches to pharmaceutical manufacturing, while maintaining the concept that quality cannot be tested into a product, but must be built in by design [33], [44], leads to the concept of continuous manufacturing. More specifically, the draft guidance document on PAT states that a desired goal of the framework is to assist in "Facilitating continuous processing to improve efficiency and manage variability – for example, use of dedicated small-scale

equipment (to eliminate certain scale-up issues)." These regulatory statements are reassuring and should encourage pharmaceutical manufacturers to exploit the benefits of continuous manufacturing.

2.1.2 Continuous Manufacturing and Crystallisation: Processes and Technologies

Drug Substance Manufacture: The manufacture of a drug substance or active pharmaceutical ingredient (API) involves several unit operations or processes. Typically, the initial stage involves several molecular synthesis and reaction work-up steps, often involving unstable intermediate (s) [43]. In some cases, downstream processing of the reaction mixture is required, for example *viz.* distillation, filtration etc. prior to the next reaction step. The final reaction mixture (or mother liquor), goes through multiple stages of downstream processing to produce the desired API in solid form. These stages almost always involve distillation, precipitation (or reactive crystallisation), crystallisation, filtration, washing, drying and milling. Figure 2.1 show a schematic of the typical sequence of stages involved in the primary manufacture of an API. Of these, the milling process is inherently continuous in nature. Additionally, filtration and distillation can be made to operate in continuous mode without much difficulty. In the case of filtration, two equivalent units can be operated alternately to achieve continuous operation. Once a fixed pressure drop is reached for the first filtration unit, the feed stream can be diverted to the second filter, while the first unit is serviced. Continuous distillation is the norm for oil refining and most commodity chemical processes [33]. The remaining stages of precipitation, crystallisation, washing and drying may also be converted to continuous, but with some challenges which will be discussed later. For the purpose of this literature review, a particular focus will be placed on continuous crystallisation processes and technologies.

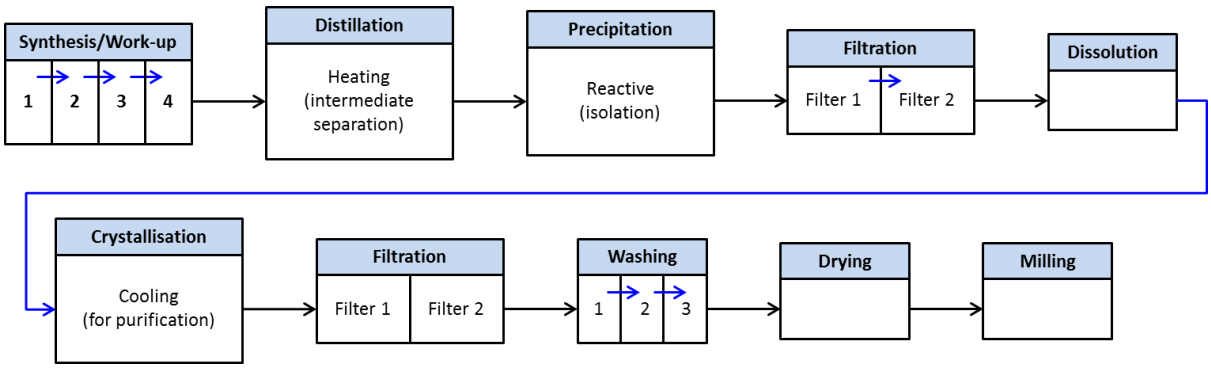

Figure 2.1: Schematic showing the primary manufacturing process for a typical API.

R&D and Continuous Drug Manufacture: Recently, there has been a significant shift in R&D focus from batch to continuous processes as more and more researchers report on the application of continuous manufacturing [13], [19]–[21], [24], [58]–[63]. The change has been realised due to a growing number of enterprising collaborative research initiatives between established technology companies, pharmaceutical manufacturers, SMEs, academic institutions and government agencies. A particularly good example that highlights the extent of collaboration is the EPSRC Centre for Innovative Manufacturing in Continuous Manufacturing and Crystallisation (CMAC) in the UK. This initiative was established in 2011 to develop and advance technologies to facilitate a change from batch to continuous manufacturing. This national centre initially consists of a team of 14 leading academics from across 7 UK institutions and working with a number of multinational pharmaceutical manufacturers, technology companies and small-medium enterprises (SMEs). The CMAC centre aims to bridge the gaps between development of continuous processes and technologies and their implementation in the pharmaceutical industry. So far, the centre has pioneered a multi-disciplinary approach to continuous manufacturing and crystallisation, which includes: chemical and process engineering; synthetic, physical, analytical, structural and materials chemistry; crystallisation science; pharmaceutical science; and manufacturing and operations management. The core areas of research within the CMAC centre are outlined in Figure 2.2. Continuous crystallisation is a central feature and the primary area of R&D. There is a commitment to developing continuous crystallisers for consistent production of high quality crystals for later secondary processes and to determinate the most suitable approaches for their implementation in the pharmaceutical industry. A further example of enterprising collaborative research is the Dutch sustainable manufacturing initiative, which saw a Scottish technology company (NiTech), The Netherlands Institute of Sustainable Process Technology (ISPT) and three member companies of The Netherlands Group of Users of Technology for Separation (NL GUTS) joining forces to investigate the feasibility of scale-up and operation of COBCs and other continuous manufacturing technologies [62]. In the Republic of Ireland, the Solid State Pharmaceutical Cluster (SSPC) was established as a strategic collaborative research initiative between Science Foundation Ireland (SFI), five top Irish universities and several pharmaceutical companies. The aim is to carry out research in the area of pharmaceutical crystallisation. In addition to the aforementioned research initiatives, the Novartis-MIT collaboration is worthy of mention. This 10-year initiative, which started in 2007 is one of the first to be established for the sole purpose of investigating continuous manufacturing alternatives for implementation in the pharmaceutical industry.

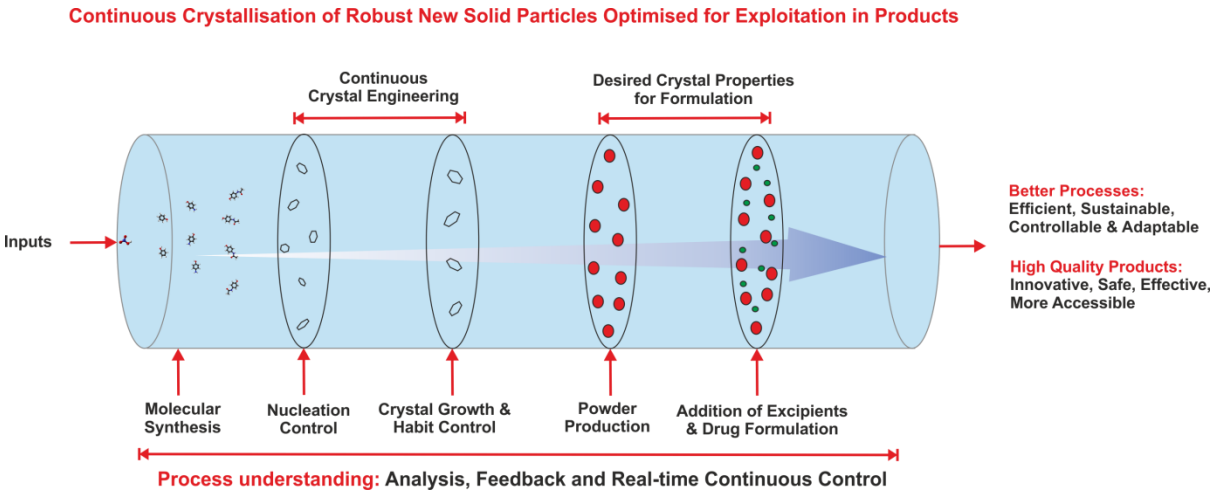

Figure 2.2: Key R&D areas within the CMAC centre spanning initial inputs and molecular synthesis through to crystallisation, formulation and final product manufacture.

As a result of the many research initiatives mentioned earlier a turning point toward continuous processing is now being realised, with many pharmaceutical manufacturers starting to adopt continuous processes, converting some unit operations into compact systems with a higher degree of automation and fewer manual interventions. For example, secondary production steps such as milling, blending, granulation and compression [64]–[66] that were previously performed sequentially in batch mode are now being integrated into single a continuous process. Primary processing, that is continuous flow chemistry is also well established [43], [67], [68]. Companies such as Vertex Pharmaceuticals (VRTX), Amgen (AMGN), GlaxoSmithKline (GSK), Novartis (NVS), Johnson & Johnson (JNJ) and others have started to build continuous drug manufacturing facilities. For example, GSK is building a US $ 29 million continuous manufacturing plant in Singapore, which is expected to come online in 2016. Amgen recently announced it was using some continuous manufacturing processes in its plant in Singapore as well. Vertex indicated that its continuous tablet compression process could allow the production of 100,000 tablets of a cystic fibrosis drug in an hour, compared to 4 to 6 weeks using batch processing [69]. The majority of these projects are for making finished products and not active ingredients, although Novartis has announced a prototype called “Technikum” for beginning-to-end continuous manufacturing, which it has proposed will continuously transform raw materials into finished tablets without interruption (24 h/day) in just two days, using a single facility with a footprint 1/10 of existing batch plants.

Continuous Crystallisation: Continuous crystallisers have the built-in flexibility to enable the control of temperature, supersaturation, nucleation, crystal growth and other process parameters that influence crystal size distribution (CSD). In some cases, continuous has advantages when batch is unacceptable, for example where there are highly toxic substances

or where mixtures of polymorphs are formed, due ease of automation and consistence. There is also the advantage of significant reduced in inventory levels. Intermittent (or semi-continuous) crystallisation processes often combine the best features of both batch and continuous operation, and deserve definite attention. In the past decade, continuous crystallisation has been a highly active research field, as part of the campaign aimed at developing the next generation continuous manufacturing technologies for the pharmaceutical industry [14], [15], [70].

Generally, there are two types of continuous crystallisers that are most investigated, *viz*, the tubular and the stirred-tank designs [2], [17]. Regardless of recycling, these two designs help to achieve idealised flow patterns, namely the plug-flow [18], [21], [71]–[75] and the mixed-suspension mixed-product removal (MSMPR) operations [8], [13], [19], [24], [53]. Typically, continuous stirred tank crystallisers such as the MSMPR operated with continuous feeding of a saturated solution to and withdrawing of slurry from the vessel. There are no real crystallisers capable of fully representing the MSMPR complete mixing flow model or PF model, but some crystallisers behave close enough to the ideal [5]. Recent studies have investigated different designs of stirred tank crystallisers to achieve mixing conditions closer to the idealised MSMPR model. For example, the introduction of baffles to efficiently shear slurry for more improved mixing [76]; fine-tuning of the agitator conditions for better particle suspension [25], [77]; and adjustment of the addition and withdrawal point to achieve representative isokinetic slurry withdrawal [25]. The relationship between mean residence time and batch mixing time [78] has also been investigated in MSMPR. However, a meaningful correlation was not established in this study. Although derivatives of the PF and MSMPR crystalliser designs have resolved some of the practical concerns over continuous crystallisation, such as the use of: (1) a cascade of MSMPR vessels linked in series (slurry flows from one stage to another), with gradual temperature change across each succeeding stage leading to direct control over supersaturation and enhanced product yield [8], [13], [70] (however a systematic approach to selecting stage temperatures for MSMPR cascade has not been demonstration); (2) a continuous oscillatory baffled crystalliser (COBC) to deal with the sedimentation of crystals at low through-flow Reynolds number in a straight tube [20], [79]; (3) a slug-flow crystalliser design wherein liquid and gas are introduced into one end of the tube to spontaneously generate alternating slugs of liquid and gas to generate large uniform crystals [80]. Other examples include: (4) the multi-segment multi-addition plug-flow crystalliser (MSMA-PFC) to tackle problems with supersaturation control [21], [22], [57] or fines dissolution along the tube [23]; (5) a continuous MSMPR crystalliser with a fines trap and a product classifier to achieve a high production rate and a low polydispersity of the crystals [81]; (6) similar work was also reported using an “inverted” product classifier unit in a modified continuous MSMPR

crystalliser, wherein small crystals are withdrawn as product, and larger crystals recycled to a dissolver [53]; (7) rapid and intermittent pneumatic transfer of slurry in a single-stage MSMPR for isokinetic withdrawal and polymorphism control [32], [51], [82]. In continuous crystallisation recycle is often used as a means of conserving material and for improving process yield by manipulating the recycle ratio, which is defined as the ratio of the volumetric flow rates of the recycle stream to that of the feed stream [19]. However, the recycle ratio needs to be carefully selected in order to avoid impurity build-up. One way of addressing this issue is to apply nano-filtration membranes to purge impurities [51] from the recycle stream. Recycling may also affect the product crystal properties (i.e. size and CSD), for example the impact of concentrated versus non-concentrated recycle stream has not been sufficiently addressed in the literature and will be focused on in Chapter 4 of this Thesis.

One the more important issues for the two continuous crystalliser designs mentioned earlier is the material mean residence time and the residence time distribution (RTD). For example, although a narrow RTD can be achieved, in a tubular crystalliser, a relatively long tube is necessary for slow growing crystals to achieve sufficient residence time and to reach a desired large mean particle size. Furthermore, the long tube design also makes difficult the delicate control of supersaturation by either multi-section jacket cooling or multi-addition of anti-solvent [22], [23], [81]. In contrast, the broad RTD of continuous MSMPR operation adversely affects the critical quality attributes of the final products by broadening the crystal size distribution (CSD). In order to extend the material RT, large-scale MSMPR crystallisers have to be implemented, in which the scaling up of a stirred tank imposes the additional problem of slurry mixing uniformity [83]. Based on these observations, continuous crystallisation is seen as the limiting step for beginning-to-end continuous manufacturing of drug products [84]. Therefore, the main objectives of the work presented in this thesis are to: (1) tailor the RTD and operating conditions in MSMPR crystallisers to enhance the critical quality attributes (CQA) of crystals; (2) demonstrate a “state of controlled operation” (SCO) in novel designs of single and cascaded multi-stage MSMPR crystallisers, thereby promoting a Quality by Design (QbD) paradigm shift, such that quality may be assured by better product and process understanding for the design of beginning-to-end continuous manufacturing in the pharmaceutical and fine chemical industries. Recent studies have examined how to change the mean residence time and width of the RTD in MSMPR in order to control polymorphism [82] and crystal size and distribution [77]. Typically, long mean residence times lead to crystal growth, however the settling of particles in transfer lines becomes an issue [25].

Where a MSMPR crystalliser is used, for a given operating volume it is often necessary to reduce the net inlet and outlet stream flow rates in order to obtain enough RT for the crystals

to grow; however, this approach often leads to transfer line fouling and blockage. In this thesis periodic flow operation of MSMPR crystallisers whereby periodic disruptions are applied to the inlet and outlet flows, either synchronously or asynchronously, will be demonstrated and fully explored, with the dual aims of retaining slurry in the crystalliser for longer and to facilitate isokinetic (i.e. representative) withdrawal of the product. This approach is different from intermittent withdrawal procedures reported in the literature [32], [77], [85], [86], since the slurry addition and withdrawal cycle(s) and batch period are tuneable, leading to several more degrees of freedom in operation.

Comparatively speaking, temperature control of an MSMPR is relatively straightforward unlike a PFC. In addition, the maintenance of an MSMPR is relatively simple, and the cost of operating them quite low. Conversely, PFCs are often more efficient (requires less material and gives better yield) than MSMPRs of the same volume [87]. However, temperature control is more complicated and expensive with PFCs, and plugging (or blockage) is a common problem [2], [88]. In terms of flow and mixing pattern, the MSMPR may be described as a completely mixed vessel characterised by a well-defined RTD of exponentially decaying function, and possessing identical fluid elements (in terms of liquid and solid composition and CSD) in the outlet flow and inside the crystalliser [5], [6]. Randolph and Larson [9] were the first to introduce the term MSMPR to represent this ideal flow and mixing crystalliser configuration. The flow and mixing pattern of a PFC on the other hand may be characterised by uniform velocity and equal residence time of all fluid elements inside the crystalliser [5], [89]. For example, the flow patterns achieved in oscillatory baffled flow devices, static and high intensity mixers, and Couette-Taylor flow devices under restricted operating flow conditions may be approximated to plug flow [5].

Recently, several unconventional continuous crystalliser designs have been investigated, including:

(a) Microfluidic devices – typically sub-millimetre scale that are based on the precise control and manipulation of fluid flow through micro-fabricated channels [90], [91];

(b) Solid hollow fibre devices – these consist of several non-porous hollow fibres bundled together and enclosed in a shell. The feed solution for crystallisation in these devices is passed through the spaces inside (i.e. hollow fibres) [71], [72], [92], [93];

(c) Static and high intensity mixers – are typically used for the mixing of two fluids. These devices consist of a series of mixing elements enclosed in a pipe or tube [21], [94]–

[96] and are often used in tandem with other crystallisation equipment. For example, as demonstrated recently by Myerson et al [21] in their study on the continuous crystallisation of three APIs in a plug flow device consisting of four jacketed tubular glass sections packed with Kenics type static mixing elements (to enhance mixing and aid particle suspension);

(d) Couette-Taylor devices – typically consist of two rotating concentric cylinders. Couette (or Azimuthal) flow is generated when a viscous fluid is brought into the space between the rotating cylinders. Couette and later Taylor [97] were the first to use this type of device to investigate the behaviour of viscous fluids;

(e) Tubular or laminar flow devices – typically these devices have a close resemblance to a tube-in-tube heat exchanger. The fluid is transported through the inner tube, while a coolant flows counter- or co-currently through the outer tube [98]. Laminar flow often dominates fluid motion in these devices, and is characterised by the orderly movement of all elements in a straight line parallel to the tube wall with high momentum diffusion (axial mixing) and low momentum convection [99].

Although there are many promising alternative technologies to conventional MSMPR and PFC these are not yet mature. For example, to these devices are not amenable to commercial applications and are difficult to scale, whereas industry is more likely to consider retrofitting current batch stirred tank reactors into continuous MSMPRs.

2.1.3 MSMPR Crystallisers: Key Features and Kinetic Considerations

In many early works, MSMPR crystallisers were most often used for the measurement of crystallisation kinetics. In 1980 Garside and Shah [100] published a comprehensive review of the literature on crystallisation kinetics derived from MSMPRs and compared nucleation and growth rate measurements on a common basis. They found that in general, the range of variables studied (for example, supersaturation, slurry density and stirrer speed) for any given system were extremely limited. Furthermore, the experimental conditions, particularly those related to crystalliser hydrodynamics, were usually poorly defined. Consequently, the scale-up of kinetics based on such results would often not be possible. Since this review there has been significant improvements in the determination of crystallisation kinetics using MSMPR [8], [13], but there is still a lack of understanding of the correlation between kinetics and crystalliser hydrodynamics. Chen and Larson [86] investigated the kinetics of calcium nitrate tetrahydrate in a single stage MSMPR over a wide range of mean residence times and slurry densities and obtained kinetic data for the system using the population balance model (PBM)

approach. In later work, Jones et al [101] reported on the crystallisation kinetics of potassium sulphate. In their study, the supersaturation and slurry density were the independent variables investigated, but strong curvature was exhibited in the population density plot (which suggest size-dependent product removal). Jones and Mydlarz [102] compared methods proposed in the literature for the determination of crystallisation kinetics from CSDs for a number of systems that exhibited size-dependent growth rates. These investigators found wide variations in inferred kinetic parameters depending on the analytical methods used. Improvements in the estimated nucleation and growth rates were observed when the investigators used size-dependent growth rate models for direct fitting of the differential population density data. Larson *et al* [103] developed a mathematical model relating CSD from a MSMPR to the distribution of growth rates (i.e. growth rate dispersion). This same model was used by Ramanarayanan [104] to derive analytical expressions for all cases between the completely mixed MSMPR to near plug flow state (a cascade of MSMPRs). More recently, Moore *et al* [105] used X-ray scattering technique to determine the kinetics of various forms of perovskite (calcium titanium oxide). Zahedi *et al* [106] used a similar technique to study the kinetics of a binary compound of a calcia–alumina (calcium and aluminium oxide).

Notable kinetic studies on organic systems include work by Sikdar and Randolph [107] who reported on secondary nucleation and growth kinetics of citric acid and correlated the results to supersaturation and product CSD of the MSMPR. Jinyang and Shuzhong [108] studied L-glutamic acid crystallisation from fermentation broth and found that the kinetics of the process conformed to a size-independent model (McCabe ΔL law). Alamdari and Tabkhi [109] determined the kinetic parameters for the reactive crystallisation of the pharmaceutical intermediate hexamine (Meissner process) using data from an industrial MSMPR with a fines dissolution loop. The growth and nucleation kinetic parameters were determined by applying PBM. Kougoulos *et al* [110] used a modified MSMPR with product recycle loop to estimate 'pure' crystallisation kinetics of an organic fine chemical. The effects of supersaturation, slurry density, impeller speed and configuration on the growth and nucleation rates were examined. Hao *et al* [111] investigated the kinetics of the reactive crystallisation of dexamethasone sodium phosphate, an anti-inflammatory and immunosuppressant using a MSMPR. The investigators found the growth of product crystals to be size dependent. Wierzbowska *et al* [112] investigated the kinetics for the cooling crystallisation of L(+)-ascorbic acid from water in a laboratory draft-tube (DT) MSMPR. The kinetic parameters were found to conform to McCabe ΔL law, which assumes that the crystal growth rate is independent of crystal size. Note that the MSMPR gives rate information at a fixed set of conditions (i.e. at steady-state), which means that it is difficult to cover a wide range of initial conditions (e.g. supersaturations and residence time). In the study mentioned earlier, the effect of supersaturation on the growth

and nucleation rates and mean residence time on the extent of crystal growth and nucleation were examined. It was found that with increased supersaturation mean crystal size decreased while longer mean residence times led to a 3-fold increase in linear growth rate (size dependent growth) and 7-fold decrease in nucleation rate. The explanation for these observations is that higher supersaturation leads to increased secondary nucleation, on the other hand growth is promoted with longer residence times as small crystals dissolve and larger ones grow at their expense. Generally, the growth and nucleation kinetics of a given system are highly specific and depends on a number of factors, for example the solute-solvent system and sensitivity to the hydrodynamics and scale of operation.

The model identification process is very important since the inclusion of additional effects, such as secondary nucleation, agglomeration and breakage can have a strong effect on the kinetic parameters for growth and primary nucleation. The growth rate kinetics are derived from fundamental rate equations, whereby growth rate is expressed in terms of the free energies of the various molecular configurations that the crystal surface passes through during growth [113]. Recently, empirical approaches have become more common place for growth rate estimation [114]. Regardless of the approach used, inconsistences in the use of either size-dependent (proportionate) or size-independent (constant) growth is evident thought the literature. These two growth laws can be differentiated as follows; size-dependent growth: the relative size difference among crystals is maintained during proportionate growth, leading to constant size variance for a CSD as mean crystal size increases; size-independent growth: the absolute size difference among crystals is maintained during constant growth, resulting in a decrease in size variance [114], [115]. It has been shown that size-dependent growth occurs in stirred systems, whereas constant growth occurs in non-stirred systems [115]. It is thought that the mechanism of size-dependent growth is related the supply of solution phase solute molecules to the surface of crystals by advection, whereas size-independent growth is related to supply by diffusion. However, it has been shown that some systems show either size-dependent or size-independent growth under both stirred and non-stirred conditions. Many recent studies have simply assumed size-independent growth for simplification [8], [24]

A number of assumptions are often associated with the MSMPR model; the most notable is that all fluid elements are well mixed with no spatial variation in solution concentration, solids concentration or particle size distribution. Invariably, the mixing characteristics of a given system will have an effect on local kinetic processes as demonstrated by Rielly and Marquis [116]. The study argued that the fluid mechanical environment is not uniform in a MSMPR and hence the kinetic rates deduced are a complex weighted average of localised kinetic rates. Furthermore, if the distribution of localised kinetic rates changes on scale up, then the design

of large scale units could be problematic. Several assumptions are also made when deriving crystallisation kinetics from population balance models (PBMs). For example, the influence of agglomeration and breakage kinetics are usually ignored. The net result of these assumptions is the derivation of widely varying kinetic parameters for a given system. Furthermore, agglomeration and breakage can significantly influence product quality, especially for dense particle systems and should not be neglected during model development [117].

Despite those nuances the MSMPR is perhaps the most amenable to incorporation into existing plant designs, that is, by retrofitting batch crystallisers [2]. There are a wide variety of MSMPR designs available, with configuration being dependent on product specification and desired throughput [5], [6]. There are two broad category classifications for MSMPRs based on their usage in bulk chemical manufacturing; these are, forced circulation (FC) and draft tube baffled (DTB) crystallisers. MSMPR crystallisers used for the investigation of pharmaceutical actives are typically of the conventional stirred tank type, with no elaborate designs reported in the literature apart from cascaded multi-stage designs [85], and the so called “inverted RZ” design reported by Griffin *et al* [53]. However, many interesting studies are beginning to emerge using single- and multi-stage MSMPRs, including: continuous spherical agglomeration [54], [55], non-linear model predictive control with cooling and anti-solvent addition [118], [119], start-up optimisation of a multi-stage MSMPR operated *viz* combined cooling anti-solvent addition [120], chiral separation [121], polymorph isolation [82], impact of recycle and the application of membrane filtration on yield and purity [51], relationship between seed loading and nucleation kinetics [122], and feedback control approaches to stabilise MSMPR operation [123]. Quon *et al* [24] recently reported high yield (92%) and purity (99%). However, the residence time per MSMPR stage investigated were quite long, ranging from 2 and 13.33 h, and furthermore the product crystals properties obtained showed little difference to the batch. Arguably, at the operation is a series of batch crystallisers and proved no significant operational advantage. Alvarez *et al* [13] conducted a similar study using a three-stage MSMPR cascade with and without recycle stream for the cooling crystallisation of cyclosporine (an immunosuppressant drug). In this study, the residence time of each MSMPR stage was 2.93 h (i.e. 8.8 h combined). The yield and purity of the product obtained from with recycle (87% and 94%) and without recycle (71% and 96%) were comparable to batch (74% and 95%). Arguably, for the aforementioned MSMPR operations to be considered viable alternatives to batch, much shorter mean residence times and superior product CQA needs to be demonstrated. Table 2.1 below highlights the main advantages, disadvantages and promising features of conventional MSMPR technology. In this thesis, novel operating strategies and configurations of MSMPR crystallisers will be

demonstrated to improve on the current-state-of-the-art in continuous crystallisation aided by PAT and informatics system tools.

Table 2.1: A perspective on the advantages, disadvantages and promising features of conventional MSMPR operation.

Advantages	Disadvantages	Promising Features
• Steady state operation gives more consistent product. • Allows for fast cooling or anti-solvent addition while maintaining low supersaturation. • Some configurations allow for classified withdrawal of product and fines dissolution resulting in narrow CSD. • Several MSMPR in series may approximate near plug flow behaviour. • Ease of temperature control minimises hotspots.	• Mixed removal of product may result in large coefficient of variation (CV) in the CSD. • Limited multi-product flexibility compared to batch crystallisers. • Sampling systems for quality assurance (QA) not fully developed. • Pumping of slurry between crystallisers may lead to temperature control issues and crystal breakage. • Introduction of recycle stream may lead to impurity build-up, but purges may be used for impurity control.	• Potential to eliminate certain downstream processes such as milling due narrow achievable CSD. • For the same yield as a batch system, a smaller volume crystalliser may be employed. • Product yield could be increased by employing liquor recycle stream. • MSMPRs may be more amenable to automated control, however, these technologies are not yet fully developed. • Flexibility with the level of throughput. • Reduced down time, energy costs and operator involvement. • Lower operating costs than batch crystallisation. • Reduction in solvent consumption compared to batch crystallisation.

Process Modelling and Simulation: The steady-state CSD for a continuous MSMPR may be derived from the population and mass balance equations, as describe in many of the studies mentioned earlier. For simplicity, the following assumptions are usually made: perfect mixing of the crystalliser contents, constant volume, initial seeding (at t = 0), isothermal behaviour with no crystals in the feed stream, all crystals and nuclei have the same shape, size independent growth rate of crystals and no agglomeration or breakage. Randolph and Larson [9] proposed the following one-dimensional population balance from a transiently operated MSMPR with continuous inflow and outflow:

$$\frac{\partial \hat{n}}{\partial t} + G(S)\frac{\partial}{\partial L}(\hat{n}) + \frac{\partial \hat{n}}{V\partial t} + D(L) - B(L) + \sum_k \frac{\dot{V}_i \hat{n}_i}{V} = 0 \qquad 2.1$$

for which B is the birth function that describes nucleation (or agglomeration if not ignored), D is the death function that describes dissolution or attrition (or breakage if not ignored) and V

is the volume of the crystalliser. The remaining terms have the usual meaning as described for the batch population balance. The expression $\partial\hat{n}/\partial t$ describes the change in population density, however, this term reduces to zero for a continuously operated steady state MSMPR. The expression $G(S)\partial(\hat{n})/\partial L$ describes the difference between crystals growing into and out of a crystal size interval *dL* due to the crystal growth rate $G = dL/dt$. Finally, the expression $\sum_k \frac{\dot{V}_i \hat{n}_i}{V}$ gives the sum of the particles flowing in and out of the crystalliser.

Eqn. 2.1 is difficult to solve since *B* and *D* cannot be formulated in a general way, as events such as attrition (or crystal breakage) are brought about by mechanical and fluid dynamic processes and the kinetics of crystallisation. Where fragmented particles exist in a supersaturated solution they can grow and their growth rate will then be influenced by supersaturation. The rather complex interaction of mechanical and kinetic effects leads to the difficulty in describing the birth and death functions [124]. Hence, the terms *B(L)* and *D(L)* in Eqn. 2.1 are often disregarded. The steady-state population balance then reduces to:

$$G(S)\frac{\partial}{\partial L}(\hat{n}) + \sum_k \frac{\hat{n}_i \dot{V}_i}{V} = 0 \qquad 2.2$$

Usually the solution fed to MSMPR is free of crystals (i.e. unseeded) and only one volumetric flow $\dot{V}_i$ is removed. The population balance therefore reduces to:

$$G(S)\frac{\partial}{\partial L}(\hat{n}) + \hat{n}\frac{\dot{V}_i}{V} = 0 \qquad 2.3$$

The ratio between the volume *V* and outlet flow rate $\dot{V}_i$ is equivalent to the mean residence time τ of the suspension that is assumed to be ideally mixed (not that $\dot{V}_i = \dot{V}_0$, where $\dot{V}_0$ is the inlet flow rate), and so Eqn. 2.3 becomes:

$$G(S)\frac{\partial}{\partial L}(\hat{n}) + \frac{\hat{n}}{\tau} = 0 \qquad 2.4$$

From Eqn. 2.4, it is assumed that both the crystals and the solution have the same mean residence time in the crystalliser. However, in principle the crystal growth rate *G* can depend on particle size [6], [124]. In addition to other factors, this can be linked to the fact that the mass transfer coefficient of particles in the grain size area of 100 µm < L < 2000 µm is slightly

influenced by particle size in the case of diffusion limited growth [124]. In many systems the crystal growth rate is only slightly affected by the size of the crystals and the parameter *G* (which is in reality a mean growth rate) may be expressed independently of crystal size *L* (McCabe Δ*L* Law) as above. In order to solve Eqn. 2.4 additional information is required on the initial distribution (or density of crystals), nucleation and growth rate respectively, as well as on the mass balance of solute being crystallised. The initial distribution of particles sizes, the density of nuclei and growth rate are represented by the following equations:

$$\hat{n}(0, L) = f(L) \tag{2.5}$$

$$\hat{n}(t, 0) = \frac{B_0(S)}{G\ (S)} \tag{2.6}$$

$$G = G(S) \tag{2.7}$$

where $f(L)$ is the normalised one-dimensional distribution function and *c* is the solute concentration. The mass balance of the solute may be written:

$$\frac{dc}{dt} = \frac{\dot{V}_i c_i}{V} - \frac{\dot{V}_o c}{V} - \frac{d}{dt}\left(\rho_c k_v \int_0^\infty \hat{n} L^3 dL\right) \tag{2.8}$$

where *c* is the solute concentration. Applying the method of moments and further reduction gives the following expression:

$$\frac{dc}{dt} = \frac{1}{\tau}(c_i - c) - 3k_v \rho_c G \mu_2 \tag{2.9}$$

where μ_2 is the second moment of (*L*), which represents the total crystal surface area. The kinetic and population balance equations for a well-mixed isothermal MSMPR have been extensively studied [102], [119]. Many of these studies, in particularly those on organic systems are not suitable for scale-up purposes since they are often based on several assumptions (some of which were described earlier). The same can be said for studies carried out using non-isothermal MSMPR. In this thesis aspects of kinetic parameter estimation (using batch experiments) and process modelling for a novel operating strategy *viz* the periodic flow MSMPR crystallisation approach are examined in Chapters 6. Given the uncertainties with

parameter estimation from MSMPR as highlighted earlier, the alternative approach using batch crystallisation experiments was explored.

2.2 Process Analytical Technologies: Analytical Quality by Design Approaches

In the last decade there has been a rapid increase in the number of PAT and informatics systems tools to implement QdB for improve product quality, safety and efficacy [125]. Recent FDA guidance, for example, ICH guidelines Q8 to Q11 and PAT framework discuss the implementation of PAT and QbD for API synthesis and formulation development. The "Guidance for Industry PAT — A Framework for Innovative Pharmaceutical Development, Manufacturing, and Quality Assurance" [35] clearly highlights the importance of PAT for the design and development of well understood process, which is consistent with the basic tenet of QbD. Further to this, the ICH Q11 guidelines clearly discuss QbD approach for API manufacture with examples [126]. As per ICH guidance, QbD is defined as "A systematic approach to development that begins with predefined objectives and emphasizes product and process understanding and process control, based on sound science and quality risk management". The QbD life cycle has different tools such as ATP (Analytical Target Profile), CQA, Risk Assessment, Method Optimisation and Development with design of experiment (DoE), Method Operable Design Region (MODR), Control Strategy and Risk Assessment, QdB Method Validation, and Continuous Method Monitoring; Figure 2.3 show the QbD life cycle with each of these tools. Detailed discussion on each of the tools can be found in the recent review by Raman *et al* [125].

PAT and informatics systems tools can be used for designing, analysing, and controlling manufacturing processes through timely measurements (i.e. during processing) of critical quality and performance attributes [35], [127]. The measurements may be on raw materials, intermediates and products, but often they are of key process parameters which affect the efficiency of the process and the quality of the final product of the process [127]. PAT measurements can be taken in one of three ways: at-line, where the sample is removed and analysed close to the process stream; on-line, where the sample is diverted from the manufacturing process to an analyser and possibly returned to the stream; and in-line, an invasive or non-invasive process that analyses the sample while it is a part of the process stream. A detailed review of the different types of PAT sensors will not be attempted here since there are already numerous review papers on this subject [127]–[134] addressing a wide range of topics including, spectroscopy [133]: Raman [49], [135]–[137], attenuated total reflectance Fourier transform infrared (ATR-FTIR) [32], [138]–[140], attenuated total reflectance

ultraviolet/visible (ATR-UV/vis) [141], [142], near infrared (NIR) [135], [143]–[145], terahertz [146]–[148]; and imaging and particle monitoring sensors: particle vision microscopy (PVM) [135], vibrational chemical imaging (VCI) [149]–[151], process video imaging (PVI) [152], endoscopy [153], *in-situ* microscopy for bioprocess monitoring [154]; focused beam reflectance measurement (FBRM) [135], [155]–[157].

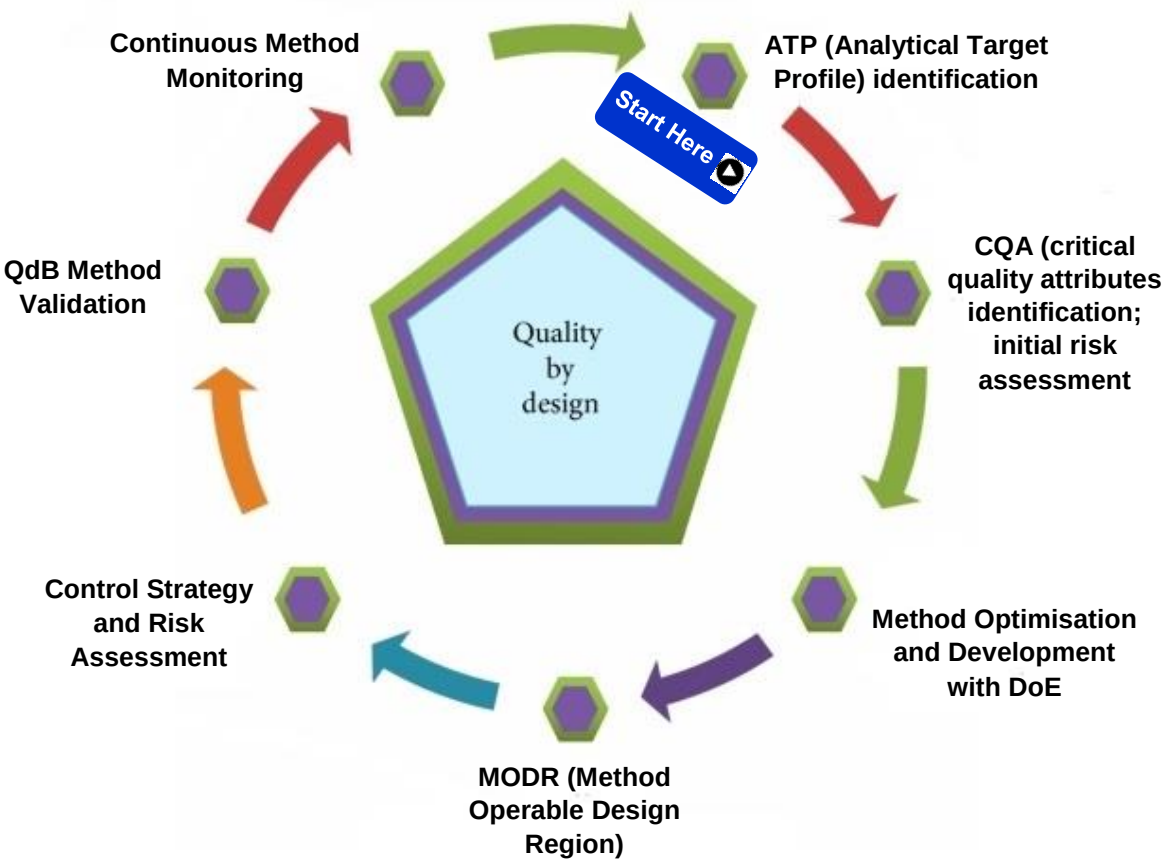

Figure 2.3: QbD tools and life cycle (Adopted from Raman *et al* [125]).

The application of various PAT tools for crystallisation monitoring and control of critical process parameters (CPP) is well documented in the literature [27], [49], [135], [158]–[162]. In these studies many essential crystallisation process parameters are examined, for example: polymorphic transformations [49], [163], [164]; phase transformations other than polymorphism [165], crystal size, morphology and distribution [166], [167]; quantitative monitoring of solute composition in solid and liquid phase [136], [168]–[170], and impurity detection and quantification [171], [172]. All of the aforementioned studies involve batch systems, and only recently has there been an interest in applying PAT to monitoring, control and develop continuous crystallisation processes. In this thesis several aspects of continuous crystallisation monitoring, control and development will be investigated applying integrated PAT and a crystallisation informatics systems (CryPRINS) tool. The aim is to bring

pharmaceutical crystallisation to a state were processes are well understood and demonstrated *viz* control of CPP, which must be within a particular range for the product to meet the desired CQA. By bringing the key crystallisation parameters (supersaturation, crystal properties (size, shape, distribution and form), yield and purity), to a desired "state of controlled operation" (SCO), improved product uniformity and quality can be assured as the process is made more consistent.

2.3 Multivariate Data Analysis

The interactions in even a single step in a process can be very complex, and there are any number of different variables that could be adjusted [173]. Multivariate data analysis (or chemometrics) can identify the variable(s) having the greatest effect on the changes/variations observed during a process and which factors interact. Multivariate data analysis is a particularly useful tool for maximising the information obtained from PAT tools in implementation. Multivariate methods have been used to analyse data obtained from various instruments including Raman [174], [175], NIR [145], ATR-FTIR [176], ATR-UV/vis [162], high performance liquid chromatography (HPLC) [177], and terahertz pulse spectroscopy [178]. These techniques have been used in the quality assurance and quality control of pharmaceutical solid dosage forms [179]. Applications have also been reported in real-time image analysis [180]. However, there are questions over how to handle the vast amounts of data generated by PAT tools. The answer lays with data management (or informatics) systems. These systems are capable of handling the large volumes and types of data generated by a range of PAT tools. In this thesis, the CryPRINS informatics system mentioned in Chapter 1 was integrated with ATR-UV/vis and FBRM to monitor and implement temperature control in MSMPR crystallisers. In this context CryPRINS is used as an automated data acquisition and synchronization system. One of the greatest hurdles involved in almost any analysis is generation, integration and organization of data. This is particularly true for the pharmaceutical industry where data are often stored in vast repositories but rarely, if ever, retrieved and used [181].

In this thesis, the commonly used multivariate methods for the analysis of spectroscopy data (Raman, ATR-PTIR, ATR-UV/vis and NIR) will be described. There are typically three main techniques that are involved in the analysis of spectral data [182], namely:

1. **Mathematical pre-processing:** used to enhance the information from spectra, and decrease the influence of the noise and other redundant information contained in the spectra. Since spectra pre-processing is well established in the literature [136], [151],

therefore a detailed description will not be provided here. Classical pre-processing methods are normalizations, derivatives and smoothing. For more details, readers are referred to [181], [183], [184]. Selection of the appropriate pre-processing techniques depends on the instrumentation and experimental conditions employed. Pre-processing method selection is covered in greater detail in Chapter 3 of this thesis.

2. **Classification methods**: used to group samples together according to their spectra. Classification methods can be divided into either of two categories, unsupervised and supervised. In the former case, samples are classified without prior knowledge except for the spectral information, whereas the opposite is true for the latter [48].

3. **Regression methods**: applied to link the spectra to quantifiable properties of the samples. Regression analysis is a statistical process for estimating the relationships among variable. It includes many techniques for modelling and analysing several variables simultaneously [185], [186].

Principal Component Analysis: The basis of most multivariate statistical methods is principal component analysis (PCA). PCA was first described by Pearson [187] as a method to find the closest fit of lines and planes to points in space. Since then a number of researchers have contributed to making PCA an advanced statistical technique for analysis and pattern recognition of multivariate data sets [186], [188]–[190]. Through a number of examples, it is shown in this thesis that PCA can successful detect similarities and differences between spectral data. PCA is a method able to reduce the dimensionality of a problem by projecting a high-dimensional space onto a lower dimension space [182], [188]. PCA takes advantage of the fact that most industrial data display a high degree of correlation. The principal components (PCs) define a space in which the scores (i.e. the projected data) are linear combinations of the original measurements and constitute pseudo variables that capture the major mechanisms of the process [182]. By reducing the space, irrelevant information (i.e. selected variables) are disregarded, however, this does not mean that information is wasted. In fact, the fundamental principle of PCA is that adequate information is represented by the principal components, whilst the irrelevant information is considered as noise. Usually, data are mean centred and scaled so that measurements of different units and numerical amplitudes may be compared. If this step is not performed, a variable with high numerical significance can affect the model in a disproportionate way. PCA is particularly useful when visualizing data. Figure 2.4 shows the application of PCA to a three-dimensional data set, which are mainly located within a two-dimensional subspace. PCA was used to visualise these data by reducing the dimensionality such that the three original independent variables are reduced to a lower number of two new variables (i.e. independent variables) termed (i.e. PCs).

Such two-dimensional visualization of the data allows for qualitative conclusions to be drawn about the separability of experimental conditions (marked by different colours) [191].

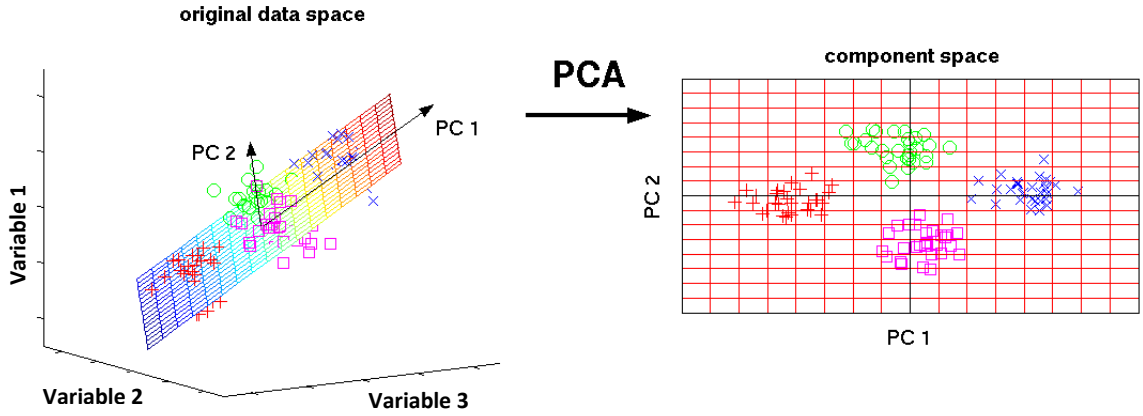

Figure 2.4: Application of PCA to a three-dimensional data set gives a two dimensional plane that optimally describes the highest variance of the data. Adopted from [191].

Unsupervised Classification Methods: these methods are typically used to try and find hidden structure in unlabelled data. Since the data given to the learner are unlabelled, there is no error or reward indicator to evaluate a potential solution. This distinguishes unsupervised learning from supervised learning and reinforcement learning. Many of the methods employed in unsupervised learning are based on data mining approaches used to pre-process data. Methods of unsupervised learning include clustering techniques such as k-means [192], Gaussian mixture models [193], hierarchical clustering, for example density based spatial clustering of applications with noise (DBSCAN) [194] or Kohonen neural network [195].

Supervised Classification Methods: There are three different types of supervised pattern recognition algorithms: (1) discriminant methods, such as linear discriminant analysis (LDA), and those that place an emphasis on similarity within a class, for example, soft independent modelling of class analogy (SIMCA); (2) Linear and non-linear methods, such as neural methods; (3) Parametric and non-parametric computations techniques. For the parametric techniques such as LDA, statistical parameters of the normal distribution of samples are used in the decision rules. The classical methods for the supervised classification are correlation based methods, distance based methods, LDA, SIMCA, partial least squares discriminant analysis (PLS-DA), and bilinear methods, for example, principle component regression (PCR) and partial least squares regression (PLSR) which will be discussed in the thesis [144], [179]. The development of bilinear models involves arranging the data in matrices so that each vertical column has variables and each horizontal row contains samples [196].

Partial least squares regression (PLSR): these are a widely accepted class of methods used for modelling the relations between different sets of observed variables by means of latent variables [179], [197]. Projections of the observed data to its latent structure by means of PLSR were developed by Wold *et al* [198], [199]. The basis of PLSR is that it modifies relations between sets of the observed variables by a small number of latent variables (not directly observed or measured) by incorporating regression, dimension reduction techniques, and modelling tools. Generally, these latent vectors maximise the covariance between different sets of variables. PLSR is similar to canonical correlation analysis (CCA) and can be applied as a discrimination tool and dimension reduction method, similar to principal component analysis (PCA) [179]. It can also be related to other regression methods like principal component regression (PCR), ridge regression (RR), and multiple linear regression (MLR); all these methods can be cast under a unifying approach called continuum regression (CR) [183], [200], [201]. PLSR has great acceptance in the field of multivariate data analysis. In fact, quite a wide spectrum of chemical data analysis problems are processed using this algorithm [178], [190], [202], [203]. However, where there is substantial nonlinearity in a data set, PLSR tends to give large prediction errors thereby making nonlinear calibration techniques such as nonlinear partial least squares (NPLS), locally weighted regression (LWR), alternating conditional expectations (ACE), and artificial neural networks (ANN) more useful in such cases[179].

Principal Component Regression (PCR): PCR is similar to PLSR in many ways and the theoretical relationship between them has been treated extensively in the literature [204], [205]. Like PLSR, PCR models the relations between different sets of observed variables by means of latent variables. In PCR, data decomposition is done using only the independent variables, while PLS employs independent variables (e.g. spectra) and dependent variables (e.g. concentration values). Historically, PCR predates PLS, however, since its introduction, PLS appears by most accounts to have become the method of choice among chemists [205] and engineers.

2.4 Conclusions

Continuous manufacturing and crystallisation is a rapidly developing field in the pharmaceutical sector. Unlike batch operation, there are several degrees of freedom in continuous (as well as semi-continuous) operation. However, continuous crystallisation is a highly complex aspect of drug manufacture that requires PAT and informatics systems tools for systems characterisation and process understanding. This is necessary to implement monitoring and control strategies in order to determine when steady-state or at least as

controlled state of operation is achieved as well as to maintain critical process parameters (CPP) within acceptable bounds to make sure that the CQA of the product stream are maintained. Furthermore, this will have implications for the achievable product yield and quality. Therefore, multivariate data analysis is essential for capturing adequate information to inform process control, monitoring and optimisation strategies (inclusive of process modelling aspects). MSMPR operation is identified as one of the most adaptable continuous crystallisation techniques since existing batch capacity can be easily retrofitted to operate as continuous stirred tanks that fulfil the MSMPR requirement. However, there are several issues with attaining the right mean residence time for crystal growth and improved yield. Furthermore, issues such as fouling, encrustation and transfer line blockages are not currently well resolved. In order to resolve these issues, novel MSMPR designs and operating strategies are required, which will likely encourage uptake in the pharmaceutical industry and facilitate “beginning-to-end” continuous manufacturing.

Chapter 3

Materials and Experimental Methods

3.1 Materials

In this chapter, the materials used and experimental methods employed in the studies reported in Chapters 4 through 8 are described. All substances used in the crystallisation studies reported in this thesis were obtained from approved suppliers and are listed in the categories chemicals and solvents below:

Chemicals:

Measures were taken to obtain chemicals from the same supplier were possible. In some cases, chemicals were ordered from the same supplier, but the country of origin differed. All chemicals were used as obtained and were of the.

- Paracetamol (PCM): 4-acetaminophenol, 98 % purity was purchased from Sigma Aldrich UK (raw materials originated from China, France and USA).
- Glycine (GLY; α-Form): ≥ 99 % purity was purchased from Fisher Scientific UK Sigma Aldrich UK (raw materials originated from China, Belgium and USA).
- Barbituric Acid (BA; Form II): ≥ 99 % purity was purchased from Fisher Scientific UK (sourced from Acros Organics China).
- Urea (U): ≥ 99 % purity was purchased from Fisher Scientific UK (sourced from Acros Organics Spain).
- p-Toluenesulfanamide (p-TSA): 99 % purity was purchased from Fisher Scientific UK (sourced from Acros Organics Republic of Korea)
- Triphenylphosphine oxide (TPPO): 99 % purity was purchased from Fisher Scientific UK (sourced from Acros Organics Germany)

Solvents:

- Isopropyl alcohol (IPA): propan-2-ol, analytical reagent grade, 99.97 % was purchased from Fisher Scientific UK.
- Deionised (DI) water: tap water was purified using either a Millipore Elix® Advantage or a Millipore Direct-Q3 Ultrapure water purification system, and use as dispensed.

- Methanol (MeOH): analytical reagent grade, 99.9 % was purchased from Fisher Scientific UK.
- Acetonitrile (MeCN): analytical reagent grade (99.9 %) and HPLC grade were purchased from Fisher Scientific UK.
- Formic acid: ACS reagent grade (88 – 91 %) was purchased from Sigma Aldrich.

3.2 Materials Characterisation

A combination of off-line solid-state characterisation tools and on-line PAT tools were applied in each of the studies reported in this thesis, as described in the following sections. Where appropriate and when necessary, analytical equipment were calibrated according to the recommended methodology of supplier, unless otherwise stated. The instrument analytical conditions were adjusted according to the properties of the sample under investigation. A detailed description of the analytical procedures employed for each analysis is provided in the relevant sections of this thesis.

3.2.1 Powder X-Ray Diffraction

Powder X-ray diffraction (PXRD) is a semi-quantitative technique frequently used for solid state characterisation and identification of crystalline samples by their diffraction patterns. The technique is based on the elastic scattering of X-rays hitting the sample. Since X-rays are electromagnetic radiation with wavelengths of similar size to crystal lattice spacings, crystals can act as diffraction gratings. Relative to other solid state methods, PXRD allows for rapid non-destructive analysis of multi-component mixtures, without extensive sample preparation [206].

PXRD patterns of raw materials and crystalline samples collected from the cooling crystallisation runs were collected using either a Bruker D8 Advanced or Bruker D2 Phaser bench-top X-ray diffractometer unit, each equipped with Cu K_α radiation source (λ = 1.54056 Å), For each analysis, a 3 mm anti-scatter slit was used with a programmable divergent slit of 1 mm. A 1.5^o Soller slit was employed and diffractograms collected between 5 and 90^o 2θ with a step size of 0.02^o. In preparation for PXRD analysis, samples were mounted and spread evenly onto 6 or 12 mm discs, depending on the quantity available. Data analysis was carried out using the Bruker's DIFFRAC.EVA version 3.1 software.

3.2.2 Differential Scanning Calorimetry

Differential scanning calorimetry (DSC) is a thermoanalytical technique that monitors heat effects associated with phase transitions and chemical reactions as a function of temperature. In a DSC analysis the difference in heat flow required to increase the temperature of a sample and a reference is recorded as a function of temperature. The sample and reference are both heated at a constant rate, and thus maintained at the same temperature during analysis. Typically, the reference is an inert material such as alumina (aluminium pan). Since the DSC operates at constant pressure, heat flow is equivalent to enthalpy changes [207].

DSC analyses were carried out using a Thermal Advantage DSC Q20 fitted with a Thermal Advantage 90 cooling system, using nitrogen gas at a flow rate of 18 cm^3/min. Data were collected and processed using the Instruments-Waters LLC Advantage Qseries version 5.4.0 software package supplied with the instrument.

3.2.3 Raman and Hot Stage Microscopy

Raman spectroscopy is a widely used solid state characterisation technique that observes vibrational, rotational, and other low frequency modes in a system [208]. The technique is commonly used to provide a “fingerprint” by which molecules can be easily identified. Raman relies on inelastic scattering (or Raman scattering) of monochromatic light, typically from laser in the visible, near infrared, or near ultraviolet range. Typically, a sample is illuminated with a laser beam and the electromagnetic radiation scattered from the sample is collected with a lens and then sent to a monochromator (detector). Elastic or Rayleigh scattered radiation at wavelengths corresponding to the laser is filtered out and the remaining light is collected and dispersed onto the detector.

A Thermo Scientific DXR™ Raman Microscope equipped with 780 nm laser, Olympus TH4 200 optical component, and Linkam THMS600 heating/freezing stage was used for phase identification, polymorph characterisation and image analysis. The full spectral range of the instrument (3500 – 50 cm^{-1}) was capture with a single exposure of the charged-coupled-device (CCD). Samples for polymorph screening and imaging were mounted on glass slides and analysed using x 4, x 10 or x 50 objective, resulting in spot sizes of 7.9, 3.8 and 1.3 µm, respectively. Raman spectra were collected using the 50 µm slit and a laser setting of 15 mW. The number of scans and exposure time for each sample was 10 x 10 s. The instrument settings led to estimated resolution of 4.7 – 8.7 cm^{-1}. Data processing and analysis was carried out using Thermo Scientific OMNIC™ Series Raman software and TQAnalyst™ version 8.0 software.

Hot stage microscopy (HSM) studies were carried out using the Linkham THMS600 unit. The stage body fitted with a quick-to-fit gas port was connected to a LNP95 cooling pump to control the sample atmosphere using a dry nitrogen flow. Samples were loaded onto a 0.17 mm thick cover slip and placed on a highly polished pure silver heating element to ensure good heat transfer and sensitive temperature measurements. Samples were heated to 100 ^{o}C and equilibrated, followed by stepwise heating at a rate of 1 ^{o}C/min to 180 ^{o}C, holding at each step for 5 minutes. Images and Raman spectra were captured whenever phase changes were detected.

A Kaiser Optical Systems Raman RXN2 Hybrid with PHAT probe (785 nm Invectus™ NIR laser), spectral range 1875 – 100 cm^{-1}, was used to analyses samples taken from the crystallisation processes to determine the crystalline form and polymorphic purity. Data processing and analysis were carried out with Kaiser iC Raman version 4.1 and TQAnalyst™ version 8.0 software packages.

3.2.4 Attenuated Total Reflectance Fourier Transform Infrared Spectroscopy

Solid state analyses with off-line attenuated total reflectance Fourier transform infrared spectroscopy (ATR-FTIR) is widely used to study the interaction of molecules with infrared radiation by measuring the absorption, emission and reflection patterns. Specific frequencies of the absorbed radiation match the transition energy of the bond or functional group that vibrates. ATR-FTIR is a complementary technique to Raman spectroscopy, and is used to identify molecules based on their unique vibration patterns.

Samples were analysed using a Thermo Scientific Nicolet™ iS™50 FT-IR benchtop spectrometer with a KBr beam splitter and DTGS ATR detector. The spectral range of the instrument was 4000 – 400 cm^{-1}. Prior to analysis a background reading (5 scans averaged) was taken in air to eliminate interferences from CO_2, H_2O and other atmospheric gases. Samples were then mounted on the ATR iS50 window and fixed in place with the sample holder supplied with the instrument. The instrument was set to absorbance mode and 10 scans were recorded and averaged over 10 seconds per sample, leading to a spectral resolution of 4 cm^{-1}. Data processing and analysis was carried out using Thermo Scientific OMNIC™ Series FT-IR software and TQAnalyst™ version 8.0 software.

3.2.5 Scanning Electron Microscopy (SEM) and Energy Dispersive X-ray Spectroscopy (EDS)

In scanning electron microscopy (SEM) an electron beam is focused and scanned across a sample's surface. When the electrons strike the sample, they interact with the atoms, which emit a variety of signals that can be detected. Specific signals (secondary electrons, backscattered electrons and X-rays) contain information about the sample surface topography and composition and are combined to produce an image. The detection and measurement of energy from the sample surface as described earlier, permits elemental analysis, that is, energy dispersive spectroscopy (EDS). EDS provides rapid quantitative analysis of elemental composition with a sampling depth of 1 – 2 µm. X-rays may also be used to form lines, profiles or maps, showing the elemental distribution on the sample surface.

SEM/EDS studies were carried out using a Carl Zeiss 1530 VP high resolution field emission gun scanning electron microscope (FEGSEM) fitted with a high energy EDS for chemical analysis and an electron backscattering system (EBSD). Samples were prepared for SEM/EDS analysis using a bench-top Quorum Q150T ES gold sputter coater/carbon evaporator coating system with turbo-molecular pump. The system was used to coat each sample with a thin film of gold-palladium prior to analysis. Samples were then mounted on a stage in the SEM instrument chamber and analysed under vacuum.

3.2.6 High Performance Liquid Chromatography and Mass Spectrometry

High performance liquid chromatography (HPLC is an analytical technique used to separate and quantify the components in a mixture. The technique relies on high pressure pumps to pass the liquid solvent (mobile phase) containing the sample mixture through a column packed with solid adsorbent material (stationary phase). Each component of the sample mixture interacts differently with the adsorbent material, leading to different flow rates for the different components and hence their separation.

Mass spectrometry (MS) is an analytical chemistry technique used to identify the quantity and type of molecules in a sample by measuring the molecular mass [209]. In order to measure the characteristics of individual molecules, the mass spectrometer converts them to ions so that they can be manipulated by external electric and magnetic fields. These ions are extracted into the analyser region of the mass spectrometer where they are separated according to their mass-to-charge ratios (m/z). The separated ions are detected and the signal sent to a data system where the m/z ratios are stored together with their relative abundance for presentation in the

format of an m/z spectrum. The spectrum can then be used to elucidate the chemical composition and structure of molecules present in the sample.

Method 1: analyses on PCM samples for impurities were performed using an Accela 600 HPLC chromatograph, combined with an Exactive (Orbitrap) MS unit, both from Thermo Fisher Scientific (Bremen, Germany). UV detection was performed at 254 nm using HPLC, but due to low sensitivity, MS was also implemented. An electro spray ionisation method was used to monitor the positive $[M-H]^+$ ions. Mass parameters were optimised as follows: capillary temperature 350 °C, sheath gas 50 psi, ion spray (IS) voltage 4500 V. An ACE 111-1503 column (100 Å, 3.0 µm, 3.0 mm×150 mm) obtained from HiChrom (Reading, UK) was employed. 0.1 % formic acid in water was used as for mobile phase A, and 0.1% formic acid in MeCN for mobile phase B. The flow rates of the mobile phases were each set to 300 µL/min. PCM samples were dissolved in methanol to a concentration of 5 mg/mL, followed by dilution with water to 1.25 mg/mL. The sample injection volume was 10 µl, and a gradient elution program was applied as shown in Table 3.1. Prior to analysis the column was equilibrated for each HPLC condition by running two solvent blanks (mixture of methanol and water (3:1, v/v)).

Table 3.1: Gradient program

Time (min)	% Mobile Phase A	% Mobile Phase B
0	90	10
30	0	100
31	90	10
35	90	10

HPLC-MS data were screened based on the exact mass of impurities. The list of potential impurities has been developed from an extensive literature review and exact mass has been calculated using ChemBioOffice software.

Method 2: analyses on p-TSA and TPPO samples were performed using a Hewlett Packard HP1100 Series chromatograph with a DAD.G1315A diode array detector using a Waters Spherisorb C8 Column (80 Å, 5 µm, 4.6 mm × 250 mm) eluting with MeCN:H_2O (80:20) at 1 mL/min and UV detection at 254 nm. A small quantity of each sample was dissolve in MeCN, the injection volume was 100 µl.

3.2.7 Laser Diffraction Analyses: Malvern Mastersizer®

Laser diffraction analysis, otherwise known as laser diffraction spectroscopy (LDS) is one of the most popular methods used to determine particle size. The technology utilizes diffraction

patterns of a laser beam passed through a dispersed particulate sample to measure particle size distributions by calculating the angular variation in intensity of light diffracted as the laser beam strikes particles in the sample [210]. Laser diffraction analysis utilizes the Mie theory of light scattering to calculate the particle size distribution, assuming a volume equivalent sphere model [210], [211]. Mie theory is a closed form solution to Maxwell's electromagnetic equations for scattering from spheres. The solution includes sensitivity to smaller sizes (wide angle scatter), a wide range of opacity (that is, light absorption) and light that refracts thorough the particle (secondary scattering). Mie theory requires knowledge of the optical properties (that is, refractive indices) of the particle and dispersing medium.

A Malvern Mastersizer® 2000 instrument fitted with Hydro SM dispersion unit was used for particle size analysis by laser diffraction. Dried crystalline samples were dispersed in IPA or H_2O, and introduced into the flow cell of the Mastersizer unit via a circulation system for measurement by laser diffraction. Three representative measurements of each sample were performed and the average values reported.

3.3 On-line Process Analysis

Each of the crystallisation study reported in this thesis were analysed on-line using different arrangements of a composite process analytical technology (PAT) array with crystallisation informatics systems (CryPRINS) software tool.

3.3.1 On-line Raman Spectroscopy

On-line Raman analyses of crystallisations were carried out using either a Kaiser Optical Systems RamanRXN analyser with MultiRXN immersion probe (785 nm Invectus™ NIR laser), spectral range 3425 – 100 cm^{-1} or Kaiser Optical Systems RamanRXN2 Hybrid with MR immersion probe (785 nm Invectus™ NIR laser), spectral range 1875 – 100 cm^{-1}. Data processing and analysis was carried out with Kaiser iC Raman 4.1 software package and Thermo Scientific TQAnalyst version 8.0. Chemometric analyses were performed on the acquired spectral data for principal component analyses and multivariate model development to characterise both the solid and liquid phases of the crystallisations.

3.3.2 On-line ATR-FTIR Spectroscopy

On-line ATR-FTIR spectroscopy was used as a complementary technique to Raman for monitoring the solution phase of the crystallisations. A Thermo Scientific FT-IR spectrometer

with KBr beam splitter, MCT/A detector and artphotonics ATR Silicium SN 210 immersion probe was employed. The spectral range of the unit was 2800 – 650 cm^{-1}. Prior to each analysis a background reading was taken in the solvent at room temperature. For each analysis 23 scans were collected over 30, 60 or 90 s and averaged, leading to a spectral resolution of 4 cm^{-1}. Data analysis and processing was carried out using Thermo Scientific TQAnalyst version 8.0 software.

3.3.3 On-line ATR-UV/vis Spectroscopy

Ultraviolet/visible spectroscopy is a technique used to measure absorbance or reflectance in the ultraviolet/visible spectral region. Molecules containing π-electrons or non-bonding electrons (n-electrons) can absorb ultraviolet or visible light to excite these electrons to higher anti-bonding orbitals and produce an absorbance spectrum in the process.

On-line attenuated total reflectance ultra violet/visible (ATR-UV/vis) was used as a complementary technique to Raman and ATR-FTIR for monitoring solution phase of the crystallisations. A Carl Zeiss Multi-Channel MSC621 UV-VIS/CLD 600 spectrometer fitted with either a Helma 661.822 or Katana 6 ATR-UV immersion probe was used. The spectral range of the unit was 700 – 185 nm. The unit was coupled with an in-house developed LabView software program for real-time display of data and for process monitoring.

3.3.4 Focused Beam Reflectance Measurement Analysis

Focused beam reflectance measurement (FBRM) is an *in situ* particle monitoring technique. It provides real-time measurements that reflect the number, size and distribution of particles. During FBRM analysis a laser beam is focused onto the surface of the probe window in contact with the suspended particles and is rotated at a constant speed. The beam scans across individual particles or particle structures (such as agglomerates) that pass in front of the window. The particles backscatter the laser light which is detected by the probe as a pulse. The duration of the pulse of backscattered light multiplied by the rotation speed of the laser gives a measure of the length of the intersected particle, referred to as a chord length. After numerous scans, a chord length distribution is generated, which shows the number of individual chords measured per second as a function of the chord length dimension. The chord length distribution is strongly dependent on particle shape, with different distributions generated for spheres, ellipsoids or cubes, for example. The technique is capable of measuring particle sizes in the range 1 – 1000 µm and can be used to measure the trends in

size distributions that evolve with time due to breakage, agglomeration, growth or nucleation of particles

Analyses were carried out using either a Mettler Toledo Lasentec® D600L FBRM® fitted with a 19 x 400 mm immersion probe or a ParticleTrack G400 FBRM® fitted with a 14 x 200 mm immersion probe during the cooling crystallisation studies reported in this thesis. Each instrument consisted of an infrared laser, with a wavelength of 785 nm and scan speed of 2 m/s. Data were record and saved either every 10 or 30 s depending on the system under investigation. Mettler Toledo FBRM® Acquisition version 6.7.0 (D600L) software or iC FBRM™ software (G400) was used to acquire and save the data. Data analysis and processing was carried out using either Mettler Toledo FBRM® Review version 6.7.0 (D600L) software or iC FBRM™.

3.3.5 Particle Vision Microscopy Analysis

Particle vision microscopy (PVM) is complementary *in situ* particle monitoring technique to FBRM. This technique is capable of measuring particle sizes from 2 – 1000 µm and provides real-time image analysis to quantify particle dimensions or aspect ratios.

PVM image acquisition and particle analysis was carried out using a Mettler Toledo V819 PVM® unit fitted with a 19 x 400 mm immersion probe. Mettler Toledo PVM® Image Acquisition software 8.3 version software was used to track the particle properties of the system under investigation. Image analysis parameters such as thresholding, filter type and decimation factor were set using the “Blob analysis” algorithm in the software. The evolution of the particle properties, that is, number and size were tracked simultaneously using Mettler Toledo PVM® Acquisition software 6.7.0 version

3.4 Chemometrics: Multivariate Data Treatment and Analysis

Chemometrics involves performing mathematical and statistical analysis on data obtained from chemical measurements. It involves the use of linear or non-linear algebraic methods to make either qualitative or quantitative interpretation of chemical data, primarily spectra. Applications of chemometrics are varied, and include experimental design, data mining, multivariate data analysis, calibration, process modelling, pattern recognition and classification, signal correction and compression, and statistical process control [179], [212]. Chemometrics can be used to analyse the data obtained from various instruments including Raman, NIR, Terahertz, MIR, UV, and HPLC. In this thesis emphasis will be placed on the

use of chemometrics approaches for multivariate calibration model development and data analysis for Raman, IR and UV. Compared to classical univariate calibration methods, multivariate techniques use not only one wavelength / wavenumber, but the whole spectral range for the model development. The advantage of these types of calibration methods is the amount of spectral information used, so that even minor differences in the sample spectra can be identified and correlated to a specific phenomenon [153]. Furthermore, multivariate techniques are capable of measuring multiple analytes simultaneously. For this thesis project, chemometrics was a useful method for real-time in-process monitoring and characterisation and is viewed as a valuable process analytical tool.

3.4.1 Multivariate Calibration Models for Crystallisation Monitoring

Chemometrics offers a range of different techniques for data processing, evaluation and model building using a variety of algorithms. The different techniques may be divided into two main categories referred to as bilinear and multiway models (see Chapter 2). In this thesis various bilinear models were used to analyse data and develop multivariate calibrations for the qualitative and quantitative evaluation of the different cooling crystallisations that were studied. In bilinear modelling the data set is arranged in matrices so that each vertical column has variables and each horizontal row contains samples [179], [196]. The bilinear models that were applied in the cooling crystallisation studies included PCA, PCR and PLSR (see Chapter 2). Models were developed using either Thermo Scientific's TQAnalyst version 8.0 or MathWorks® 2012b or 2013a software packages.

3.4.2 Paracetamol (PCM): Raman and ATR-UV/vis Spectroscopy Multivariate Models

In order to build a robust calibration model for solution concentration measurement using Raman spectroscopy, a few factors must first be taken into account. Raman spectroscopy is a scattering technique based on vibrational, rotational, and other low-frequency modes in a system [208]. The laser is therefore capable of interacting with molecular excitations in both the solid and liquid phases. Therefore, when developing a calibration model for monitoring solution phase concentration, the effect of particle scattering on the Raman signal must be accounted for. By collecting spectra at known concentrations of PCM in IPA in the presence and absence of solid phase (crystallised PCM).

Raman spectroscopy is rarely used in crystallisation for solution concentration measurement [136]. The work reported here is a proof of concept approach whereby the capability of Raman

spectroscopy to distinguish solution from solid phase in a crystallisation process is demonstrated. Raman spectra of PCM dissolved in IPA solvent were collected using the Kaiser RamanRXN analyser unit in the range 3425 cm^{-1} to 100 cm^{-1} at a spectral resolution of 4 cm^{-1}. The number of scans and exposure time for each sample was 7 x 4.9 s over a total measurement time of 60 s. PCM-IPA solutions were prepared at saturation temperatures of 10, 15, 20, 30, 40 and 50 °C. The saturation temperature (T_{sat}) of PCM in IPA were estimated from solubility data published by Hojjati *et al.* [213]. The same solubility data were also used by Saleemi *et al*. [170] in a study on comparative batch crystallisation control strategies using PCM-IPA as a model system. The model equation used to determine the solubility (c) of PCM (g / g IPA) in IPA as a function of temperature T (°C) is:

$$c\,(T) = 2.742 \times 10^{-5} T^2 + 1.328 \times 10^{-3}\, T + 7.202 \times 10^{-2} \qquad 3.1$$

Figure 3.1 (a) and (b) show typical time diagrams for solid-free solution and solid-liquid suspension calibration and validation experiments respectively. Suspensions of PCM-IPA were heated to 10 °C above the desired T_{sat} and maintained for 15 min. The resulting solution was then cooled in steps of 5 °C and held at each step for 30 min. This was continued until nucleation was observed in the system. For each experiment, Raman spectra were collected from the solid-free solutions before the occurrence of nucleation and used as calibration samples in the model development process. For validation purposes, an additional experiment at 15 °C saturation was conducted, where solid-free solution Raman spectra were collected.

In addition to the solid-free calibration and validation experiments, an extended series of experiments were conducted whereby Raman spectra from solid-liquid suspensions were collected and used in the calibration model development and validation. In a typical experiment, shown in Figure 3.1 (b), a suspension of PCM-IPA was heated to 10 °C above the desired T_{sat} and maintained for 15 min. The resulting solution was then cooled to 5 °C at a rate of 0.5 °C/min and maintained until nucleation was observed. The system was then heated up in steps of 5 °C and held at each temperature step for 2 hours to allow the system to equilibrate. Raman spectra were collect from these solid-liquid suspensions prior to complete dissolution.

During each of the calibration experiments, ATR-UV/vis was used to measure solution phase concentration using a pre-existing multivariate model developed by Saleemi *et al.* [170]. FBRM was used to detect the onset of nucleation and to track the particle properties of the system over time. Solid-free solution spectra used in the calibration model were all taken prior to the onset of nucleation, as detected by FBRM (total counts/s) and ATR-UV/vis (concentration; g/g), as shown earlier in Figure 3.1 (a). Spectra from the solid-liquid suspension were used to

account for particle scattering effects on the Raman signal. Peaks were identified in the Raman spectra corresponding to the solution (peak at 1445 cm^{-1}) and solid (peak at 1668 cm^{-1}) phase, as shown on the time diagram, Figure 3.1 (b). The FBRM data captured during this experiment shows curvature in some regions of the ramping steps, which may be an indication that particles are sticking on the probe window. As the particle numbers in the system are reduced with each heating step, the curvature is noticeably diminished.

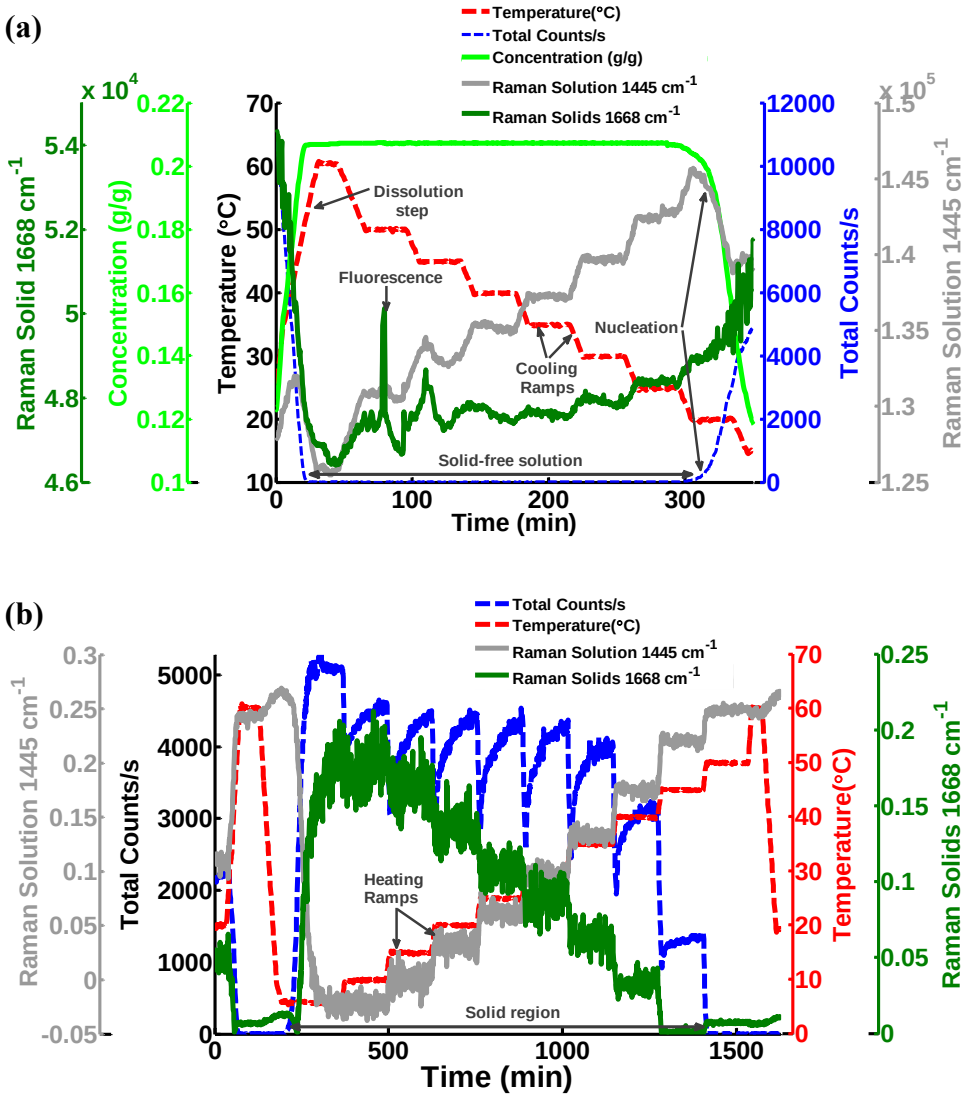

Figure 3.1: Time diagrams showing: (a) typical solid-free calibration/validation experimental run and (b) typical solid-liquid suspension calibration/validation experimental run.

The TQ Analyst version 8.0 software was used for Raman spectra pre-treatment, model development and concentration determination. Figure 3.2 shows the Raman spectra of PCM in IPA along with the selected range of wavenumbers (1750 – 100 cm^{-1}) used for model development and validation. In total, 2219 spectra (or samples) were used for the calibration model development and validation. Of these, 2009 samples were used as calibration

standards, 150 as solid-free validation standards and 60 as solid-liquid suspension validation standards.

The standard normal variate (SNV) normalisation algorithm in TQAnalyst was applied to pre-treat the Raman spectra. SNV compensated for differences in sample path-lengths and removed the effect of scattering caused by the presence of particles. The first derivative (1st DV) was then applied to the spectral data. Derivatives (e.g. first or second) are often used in multivariate data analysis to enhance spectral resolution, eliminate or reduce linear and constant baseline drift effects between samples and also to emphasise pronounced, but small spectral features relative to larger broader ones. [214]–[216]. Five regions within the selected range of wavenumbers highlighted in Figure 3.2 were used to develop the multivariate model post pre-processing.

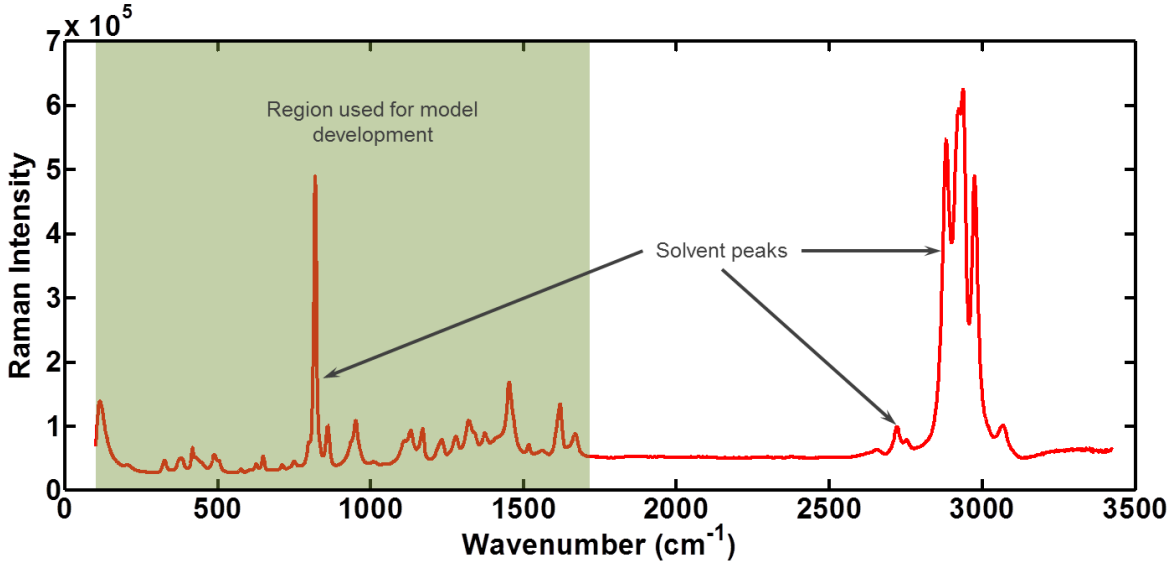

Figure 3.2: Typical Raman spectrum of PCM in IPA showing the regions selected for the multivariate calibration model development (100 – 1700 cm^{-1}).

The 'Partial least squares (PLS)' option in TQAnalyst was applied to build the calibration model with the selected regions. This model was used for real-time *in situ* concentration measurement of PCM in the liquid phase during each of the cooling crystallisation experiments. In the PLSR analysis, the spectra, temperature, and concentration data were first encoded in a matrix form and then reduced to only a few principal components according to [217]. In this study, 8 components were applied, which allowed sufficient data to be used to correlate changes in the spectra due to temperature and particle scattering effects to the sample concentration. Figure 3.3 (a) and (b), shows the calibration plot with validation points and percentage errors between the actual and predicted concentrations. For model validation, spectral data from solid-free solutions and suspensions containing solids were used. The

validation points are circled in Figure 3.3 (a); they indicate that the model is working effectively. The maximum error between the predicted and model determined concentration was 3.7%. The root mean square error of prediction (RMSEP), which is a measure of the model predictive accuracy, was 0.0074 g/g, which is based on the lowest concentration measurement.

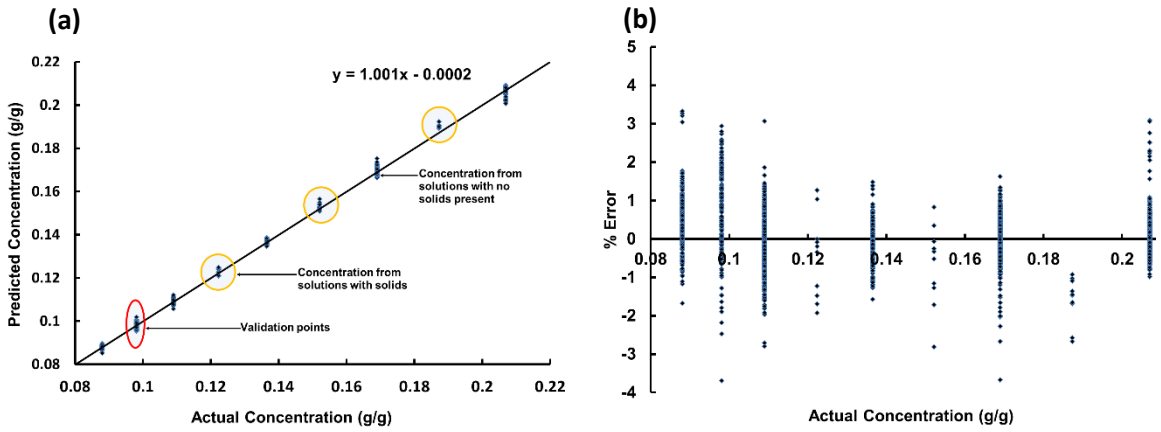

Figure 3.3: Raman concentration prediction plots derived from the multivariate calibration model development process showing: (a) predicted versus actual concentration values and circled model validation points. (b) error plot of predicted versus actual concentrations.

PLSR is a suitable multivariate method for this case as shown in Figure 3.3, since acceptable levels of accuracy were obtained using only 8 principal components to build the calibration model, which were 7 composites of Raman wavenumbers plus temperature as an additional variable.

A non-linear multivariate ATR-UV/vis model [170] was used to further validate the Raman model described above. The ATR-UV/vis model was of the form:

$$\mathrm{C} = b_o + b_1 d + b_2 T + b_3 d\,T \qquad 3.2$$

where C is the concentration in (g PCM/g IPA) and b_o, b_1, b_2, and b_3 are fitted regression coefficients with values of -0.0290, -3.7889, -0.0002 and -0.0248 respectively, d is the 1st DV of the absorbance at the selected wavelength (266 nm), and T is the process temperature (^{o}C). A simple non-linear term expressed as the product of the derivative of the absorbance and temperature was also included to improve the accuracy of the calibration model. Further details on the model development using ATR-UV/vis can be found in works by Saleemi *et al* [170], [218]. Figure 3.4 shows the predicted concentration for a batch linear cooling experiment showing both the Raman and ATR-UV/vis predicted concentration measurements from the respective multivariate models; the data shows good agreement between the two.

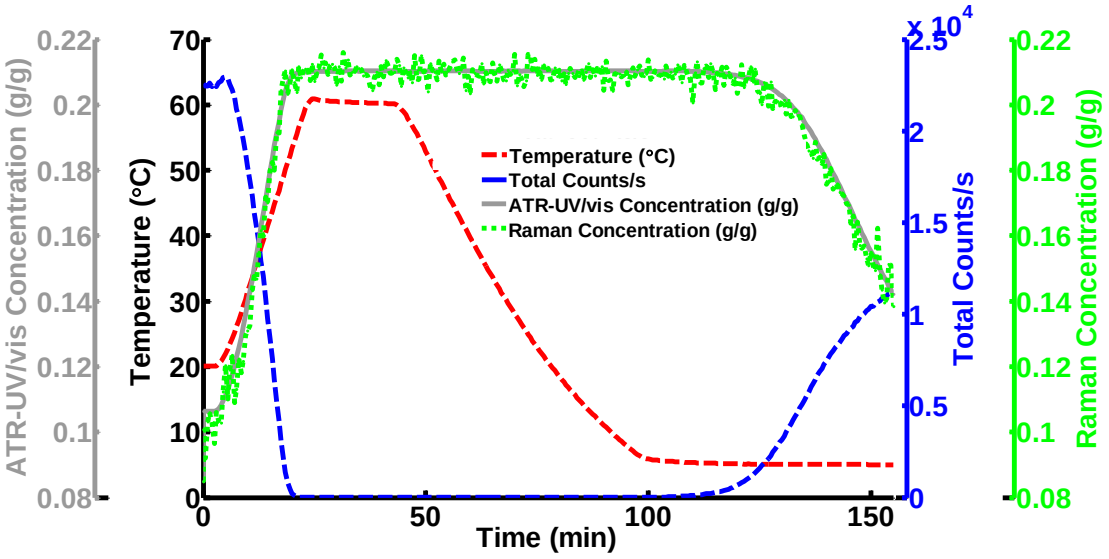

Figure 3.4: Time diagram of a linear cooling crystallisation run showing Concentration was monitored with Raman and ATR-UV/vis.

3.4.3 Glycine (GLY): Raman Spectroscopy Multivariate Calibration Model

Following the successful use of Raman spectroscopy to develop a multivariate calibration model for PCM solution phase concentration monitoring, a similar approach was applied to glycine-water (GLY-H_2O) system for quantitative measurement of GLY in solution during crystallisation. The Kaiser RamanRXN analyser unit was used in this study and spectra were collected in the range 3425 cm^{-1} – 100 cm^{-1} at a spectral resolution of 4 cm^{-1}. The number of scans and exposure time for each sample was 8 x 10 s over a total measurement time of 90 s. The for GLY is greater than that used for PCM, which is a direct result of the varying abilities of the two substances to scatter Raman light. Note that the exposure time refers to the time taken for the integration time for each pixel (i.e. frequency) of the Raman signal. Therefore, weak Raman scatters require longer exposure times for collection of a spectrum. Raman spectra of GLY were collected at known concentrations of GLY in water in the presence and absence of solid phase (crystallised GLY). Potential temperature effects were also considered by operating over a wide temperature range (5 – 60 ^oC). For the training data set GLY-H_2O solutions and suspensions were prepared at saturation temperatures of 5, 10, 20, 30, 40, 50 and 60 ^oC (concentrations, g GLY /g H_2O: 0.159, 0.181, 0.228, 0.277, 0.330, 0.385 and 0.446 respectively). For the validation data set, experiments were carried out at 15, 35 and 50 ^oC saturation (concentration, g GLY/g H_2O: 0.204, 0.303 and 0.385 respectively). A total of 1037 spectra were used for the calibration model development and validation, of these, 766 were used as calibration standards, 91 as solid-free validation standards and 180 as solid-liquid suspension validation standards. MathWorks Matlab® 2014a software pack was used for

spectral pre-processing and model development. A generic set of Matlab® codes used for multivariate model development can be found in Appendix I.

At the pre-processing stage, two methods were applied to select the spectral regions for later model development. The first was manual selection of the wavenumbers based on knowledge of the chemical shifts of GLY-H_2O as shown in Figure 3.5.

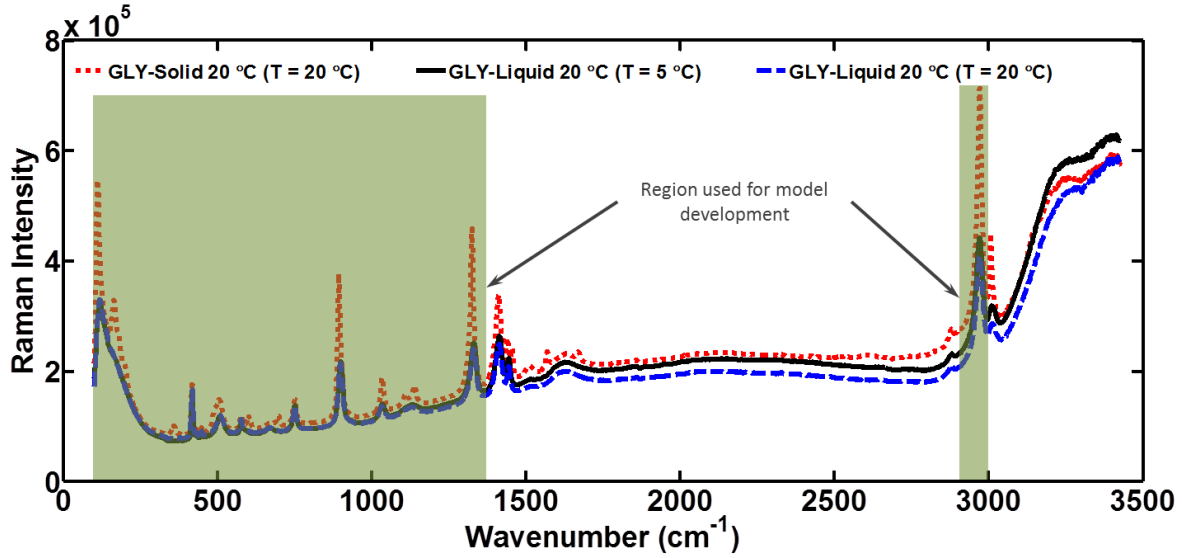

Figure 3.5: Typical Raman spectra of GLY in H_2O (T_{sat} of 20 °C) and collected in the presence and absence of solids (i.e. crystallised GLY) and at different operating temperatures (for solid-free solutions only) and constant temperature (for suspensions only). Operating temperatures are indicated in brackets. Highlighted regions were used for the model development.

Figure 3.5 displays three spectra corresponding to the same T_{sat} of 20 °C. The difference between the three spectra are seen from the change in baseline with change in operating temperature (T) and the appearance of peaks corresponding to the solid phase relative to solution phase spectra in the finger print region (1670 – 100 cm^{-1}), for example small peaks appearing at 327, 695, 1140, 1455 and 1564 cm^{-1}. Due to particle scattering, special scatter correction algorithms, for example, multiplicative scatter correction (MSC) or standard normal variate (SNV) have to be considered in order to eliminate this effect and prevent erroneous predictions.

The second region selection method involved the application of a statistical technique, stepwise multiple linear regression analysis (MLR) using the Stepwise Regression toolbox in Matlab® 2014a. This is a method for selecting predictor variables, by stepwise addition (forward MLR) or removal (backward MLR). The forward MLR method was applied whereby an initial screening of variables is performed. With this method, variables are added stepwise to the predictor data set by applying partial F-test statistical analysis. In forward MLR variables

are selected until no more can be justifiably added to the predictor data set. The cut-off point is applied when the root mean squared error (RMSE) can be reduced no further or the coefficient of determination (R^2) does not improve with the addition of new variables. RMSE is a measure of the difference between sample and population values predicted by a model and is described by the expression:

$$\mathrm{RMSE} = \sqrt{\sum (Y^{meas} - Y^{cal})^2} \qquad 3.3$$

where Y^{meas} and Y^{cal} are respectively, the measured and predicted values [217].

The limitations of MLR technique are well known and the final model is not guaranteed to be optimal in any specified sense. MLR procedure yields only a single set of predictor variables. The danger here is that selected variables may not be useful for prediction and useful ones may be ignore. Furthermore, it does not take into account a researcher's knowledge about the predictors. However, in practice, used appropriately in combination with appropriate multivariate techniques, for example PLSR and PCR, MLR can lead to the development of good quality robust calibration models.

Unless otherwise stated all mathematical treatments of the spectral data were performed using Matlab® 2014a software. Further mathematical pre-processing was done on the predictor variables selected by using the manual method or stepwise MLR method, techniques investigated included: SNV transformation, MSC, mean centering (MC) and auto-scaling (AS). First or second order derivative processing was applied to the data either before or after applying SNV or MSC followed my MC or AS. Mathematical pre-processing has several advantages that have been widely reported in the literature [136], [160], [216], [219]. Following pre-processing, multivariate calibration models were developed using either PCR or PLSR analysis. In model development an important step is to compare the performance between different methods to determine the most accurate and suitable approach. PCR and PLSR are the most widely used multivariate methods. Both methods are used to construct new predictor variables (components) by a linear combination of the original variables (pre-processed spectral data). In the case of PCR, the components are created to explain variability in the predictor variables without consideration of the response variable (in this case, concentration). PLSR on the other hand does take into account the response variable. Typically, PLSR leads to better models that are able to fit the response variable using fewer components compared to PCR [204], [205], [220]. However, both methods have been shown to give comparable results, although PCR sometimes uses more components for prediction [205]. The calibration models were validated using spectral data captured in the presence and absence of solids

according to the procedure outlined earlier. The same data selection and mathematical pre-treatment procedures were applied to the validation data set as the training set. Table 3.2 shows a summary of performance analysis on the best PCR and PLSR models identified, with remarks. Different combinations of spectral pre-processing methods were applied to achieve the best possible model performance. A PLSR model with the lowest RMSEP (0.0032 g/g) was selected for use, the maximum error between the predicted and model determined concentration was 3.4%. The statistical plots derived from the selected PCR and PLS multivariate calibration models can be found in Appendix I.

Table 3.2: Summary of performance indices for the best PLSR and PCR models

Model Type	Pre-Processing Applied	No. C*	RMSEP	R^2	% Error	Remarks
MLR-PLSR	MSC =>1stDV =>AS	10	0.0032	0.9999	± 3.4	optimum
MLR-PLSR	MSC =>1stDV =>AS	7	0.0034	0.9998	± 3.7	high rank
MLR-PLSR	MSC =>1stDV =>AS	5	0.0054	0.9996	± 3.8	high rank
MLR-PCR	MSC =>1stDV =>AS	5	0.0064	0.9914	± 5.0	high rank
Manual PLSR	SNV =>AS	9	0.0106	0.9993	± 4.8	outliers
MLR-PCR	MSC =>1stDV =>AS	10	0.0109	0.9991	± 4.7	outliers
Manual PCR	SNV =>AS	10	0.0124	0.9990	± 5.5	outliers
Manual PLSR	SNV =>1stDV =>AS	10	0.0234	0.9992	± 5.6	outliers
Manual PCR	SNV =>1stDV =>AS	10	0.0278	0.9992	± 5.7	outliers

C* = number of components; 1stDV = first derivative; AS = auto-scaling

3.4.4 Hierarchical Approach to Model Development

Multivariate calibration and classification models are ubiquitous in PAT and QbD [221]. They are used both in the development of processes and their permissible operating limits, (i.e. models used for relating the process design space to product quality), and in manufacturing (i.e. models used in process monitoring and control). The hierarchal approach to model development involves the division of variables into meaningful blocks to simplify the interpretation of multivariate models with many variables [190], [199], [222]. This is a simple idea whereby variables measured on the same part of a process or system (e.g. spectra), are put in the same block. The block sizes are selected to avoid significant overlapping; typically block sizes are kept below 50 [190]. This method is typically used to summarize a few components for each block using a PCA, PCR or PLSR model. The resulting block scores are then used as variables in the higher level of the hierarchical model [199]. This idea can be

easily extended to several levels, thus providing a more robust approach to modelling data sets with many variables. However, these algorithms have been shown to be equivalent to ordinary PCA or PLSR of all variables, followed by rescaling of the model parameters [202]. In this study, a slightly different hierarchical model development approach is proposed that consists of multiple levels of conventional bilinear PLSR models. It is based on a hierarchical approach whereby a parent model, which consists of four interconnected levels, is used to estimate the parameter of interest (in this case concentration) in a stepwise manner. This hierarchical approach is implemented for the glycine-H_2O system and is an extension of the model proposed in Section 3.2.1. The first level (Level 1) of the hierarchical model consists of a generic model that spans the range of concentration values of interest and is used for initial screening of the variables. For this purpose, the multivariate model described in Section 3.2.1 was used. The second level (Level 2) consists of three overlapping models, each of which spans different concentration ranges, and are characterised by a select set of samples (spectra). The spectra and their associated variables (wavenumbers) are first screened at Level 1 to establish their value (i.e. concentration). They are then sorted and assigned to different concentration ranges at Level 2. Where there are overlapping concentration values, predefined model selection criteria were applied using 'for' and/or 'if' statements in Matlab® 2014a. A schematic outlining the various stages of the hierarchical model development process is shown in Figure 3.6. Raman spectra, $\boldsymbol{X_i}$, are pre-screened by forward multiple linear regression (MLR) to minimise the number of variables to be used for calibration. Mathematical pre-processing is then applied to the selected variables, followed by application of a model development algorithm (e.g. PLSR) in Matlab® 2014a. This initial model is applied at Level 1 and provides the initial estimates of concentration, $\boldsymbol{\hat{y}_i}$ for the calibration set. The outputs ($\boldsymbol{\hat{y}_i}$) from Level 1 are further refined by apply three independent models (1, 2 and 3) at Level 2 of the hierarchy. These models are developed independently from each other, but using the same data from the Level 1 model, plus additional independently obtained spectra to expand the range of each model. The refined calibration set predictions from Level 2 ($\boldsymbol{y_{M1}}$, $\boldsymbol{y_{M2}}$ and $\boldsymbol{y_{M3}}$) can then be compared to the results from Level 1 to determine whether there is an improvement. The hierarchical model not only provides more accurate predictions, but can also act as its own internal fault detection system that can alert the user to changes in the predictive capability over time, due to any number of factors, including changes in sample matrices or the instrument response [221]. This can then inform the decision to revaluate, update and maintain the model as needed to preserve its predictive ability and robustness.

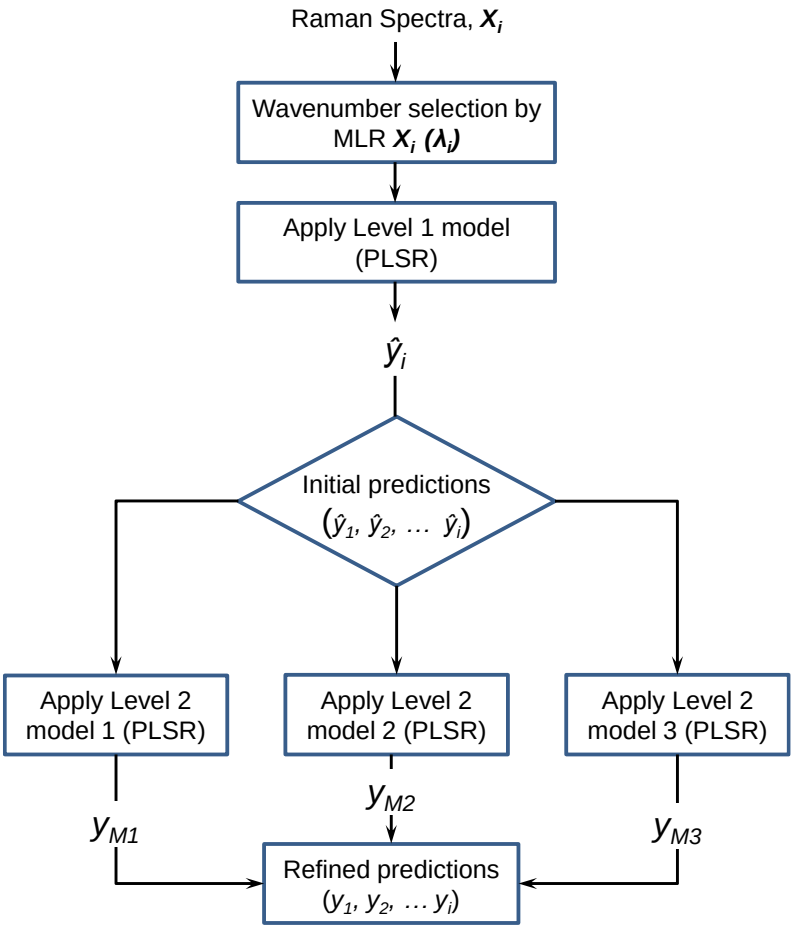

Figure 3.6: Schematic of the hierarchical model development process.

Hierarchical Model Structure: A detailed representation of the hierarchical model structure is shown in Figure 3.7, $\mathbf{k_o}$ represents the pre-processed variables of each sample that are separated and grouped into $\mathbf{X_i}$ predictor variables that are used to build the Level 1 model, $\mathbf{M_o}$ (MLR-PLSR). Matlab® 2014a was used to execute all mathematical pre-processing and model building algorithms. The predictor variables each represent a specific output value of ***y***. At Level 2 of the hierarchal model, $\mathbf{k_o}$ is divided into three overlapping subsets ($\mathbf{k_1}$, $\mathbf{k_2}$, and $\mathbf{k_3}$) corresponding to high, medium and low values of ***y***. These variables are combined with additional pre-processed variables within each range (new values of ***y*** but within the same range for each subset). Three independent multivariate models are built with each data set to construct Level 2 of the hierarchical model, that is, $\mathbf{M_1}$ (MLR-PLSR), $\mathbf{M_2}$ (MLR-PLSR) and $\mathbf{M_3}$ (MLR-PCR). Each model is used to predict a subset of ***y*** observations, that is, y_1, y_2, and y_3 respectively.

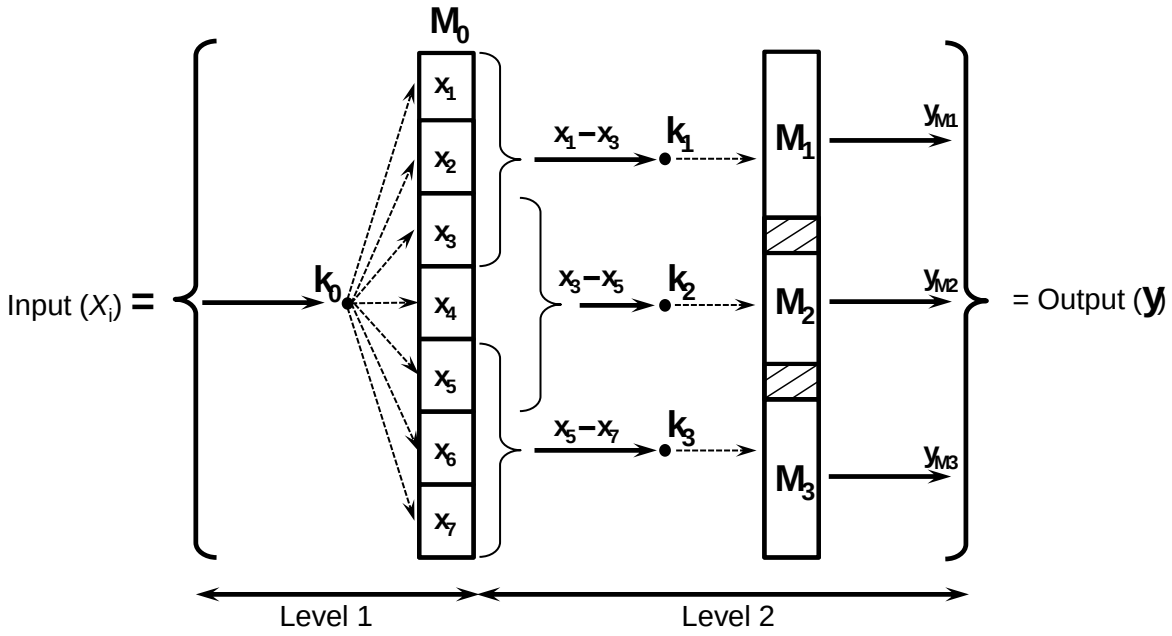

Figure 3.7: Hierarchical model structure.

Variable Selection, Pre-processing and Model Development: the mathematical expression of the MLR variable selection routine that was applied to the spectra is of the form:

$$\hat{c}_i = b_0 + b_1\lambda_{i1} + b_2\lambda_{i2} + \ldots + b_p\lambda_{ip} + e_i \qquad 3.4$$

where i = 1, 2 … n, $\hat{c}$ is the scalar dependent variable (known concentration values), and λ represents the explanatory variables (wavenumbers). The regression coefficients b_0, b_1, b_2 … b_p represent the independent contributions of each explanatory variable to the prediction of the dependent variable. This relationship is modelled taking into account the error term e_i. Following MLR, PCA analysis is carried out on each data set for outlier detection. The mathematical expression of the PCA model is:

$$x_{ik} = a_i + \sum_{j=1}^{A} b_{ij}t_{jk} + e_{ik} \qquad 3.5$$

The analysis corresponds to a least squares fitting of a straight line $(A = 1)$, where x_{ik} represents the scaled value of analysis i for sample k; a_i determines the centre (mean) of the data set; b_{ij} are the direction coefficients (one for each variable and component) of the line. For each sample k, the parameter t_{jk} describes the position of data points projected to the model. Hence, the t values (principal components) can be used to relate data points (samples) to each other. The values of b (loadings), together with the residuals e_{ik} give information on how much

descriptor variables contributes to the model. An important result of this empirical modelling is that the variance in the data can be described by fewer variables than in the original data set. Figure 3.8 shows the scores plots of PC1 vs PC2 obtained for the PCA analysis at levels 1 and 2 of the model hierarchy, that is, ***M₀*** (Level 1) and ***M₁***, ***M₂*** and ***M₃*** (Level 2). In all cases PC1 and PC2 combined account for greater that 80 % variance in the data.

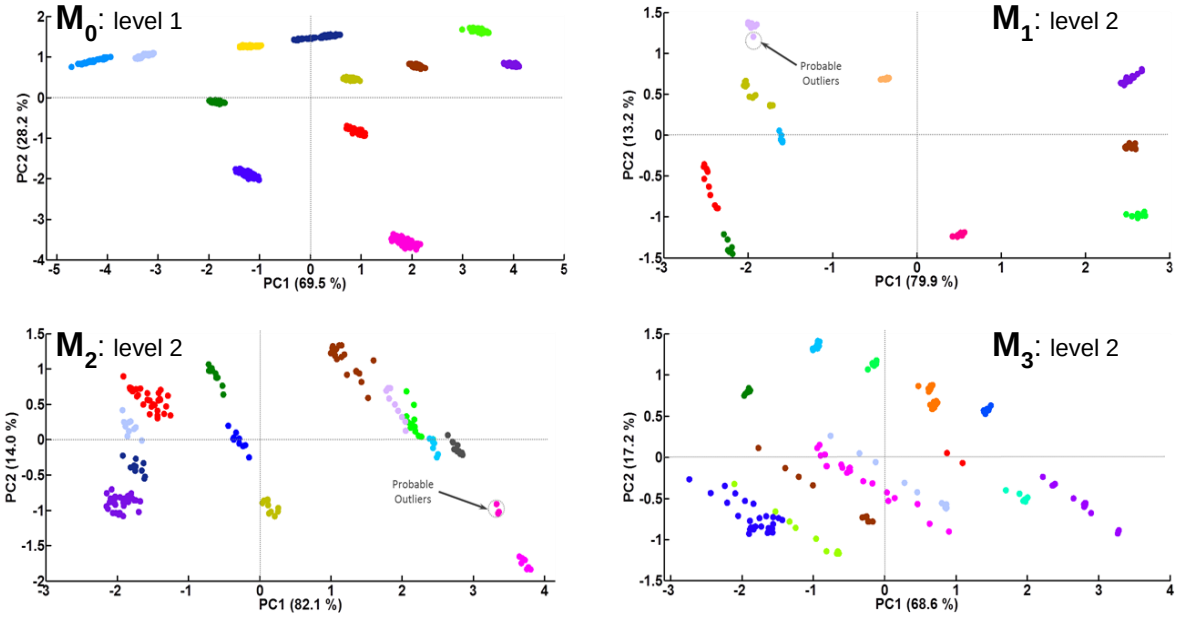

Figure 3.8: Scores plots of PC1 and PC2 for data used to build models M_0, M_1, M_2 and M_3. It shows clustering of variables that have similar characteristics.

The samples are "grouped" (clustered) according to their similarity to each other. At level 1 of the hierarchical model architecture, the samples show 12 distinctive clusters, each representing subsets of the original data set. At level 2 clusters are also observed, although some clusters are not as distinctive as at level 1, and there is evidence of possible outliers. The reason for this is that the PCA analysis is carried out on small subsets of the level 1 data set (albeit with some additional samples included), which means that even subtle differences between samples of the same subset are captured more easily. This also leads to the detection of "outliers" that can be examined further and removed from the sample sets if necessary. In this respect PCA is useful as an initial screening tool to identify "bad" samples.

The development of the Level 1 model of the in the hierarchy was described in Section 3.2.1. The Level 2 models were built using the same variables as at Level 1, with additional variables included as mentioned earlier. Following MLR and PCA analysis mathematical pre-processing was implemented using SNV or MSC, first or second derivative (2nd DV) and MC or AS algorithms in Matlab® 2014a. The pre-processed variables are shown in Figure 3.9. In

comparison to the variables with no pre-processing applied there is a constant baseline (i.e. where the first derivative is applied) and minimal sample drift effects.

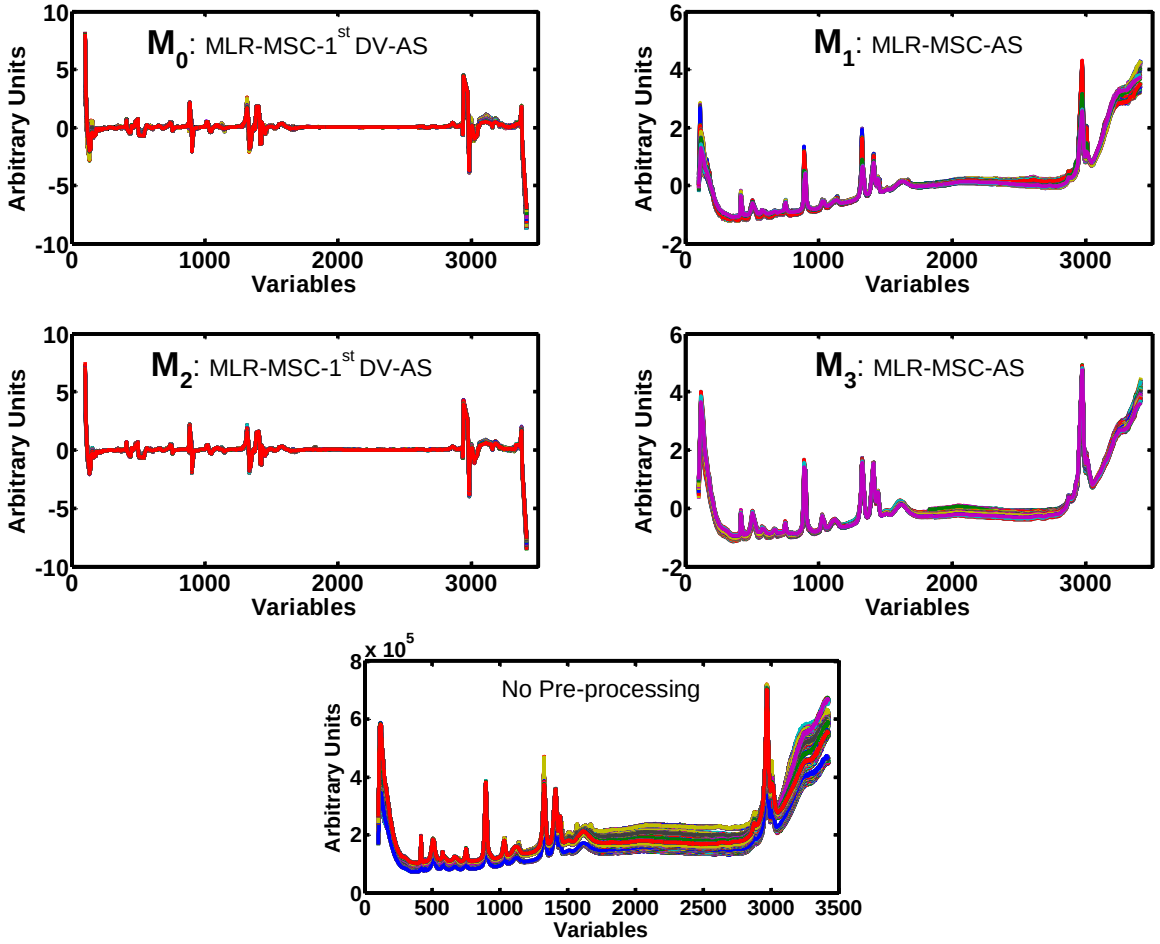

Figure 3.9: Variables (spectral regions) of multi-level hierarchical model pre-processed by different combinations of MSC, 1st DV and AS. Variables with no pre-processing applied are shown for comparison.

PLSR or PCR calibration algorithms were applied to the pre-processed data in Matlab® 2014a. *k*-fold cross validation was applied to the calibration or training data set. During *k*-fold cross-validation, the original sample set is randomly partitioned into *k* equal sized subsamples, with each subsample set used to validate the remaining *k* – 1 subsets that are used to build the calibration model. Figure 3.10 shows the predicted residual sum of squares (PRESS) plots, which reflects the predictive ability of the optimum PLSR and PCR models identified based on different the pre-processing methods, 10-fold cross validation was applied. This is a type of *k*-fold cross-validation whereby the calibration or training data set is partitioned into 10 equal sized data subsets. Of the 10 subsets, one subset is retained as validation data set for testing the model performance, and the remaining 9 subsets were used as calibration data. The cross-validation process was then repeated 10 times (that is, 10 folds), with each of the 10 subsets

used just once as the validation data set. The 10 results from the folds are averaged to produce a single estimation. The advantage of this method is that all samples are used for both calibration and validation. However, the method was used only as a guide to selecting the number of components, since it is an internal validation approach.

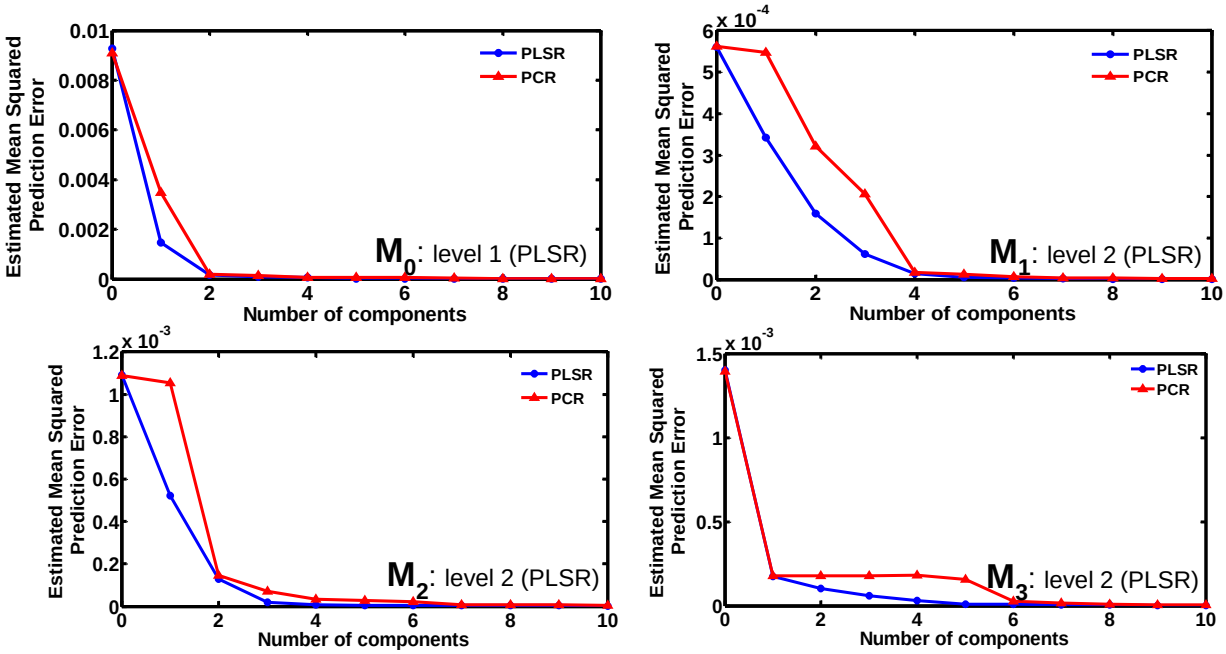

Figure 3.10: Predicted residual sum of squares (PRESS) plots of PLSR models for Level 1 (M_o) and Level 2 (M_1, M_2, and M_3) of the hierarchical model architecture.

The PRESS plots for PLSR models indicate that a minimum of three or four components are required to build useful models. On the other hand, for the PCR models at least five components are required to get the same or better prediction accuracy than PLSR. The addition of more and more components as demonstrated in the PRESS minimises the mean squared prediction error, leading to better calibration models for both PLSR and PCR. It is often useful to choose the number of components to minimise the predicted error when checking the response from future observations on the predictor variables (calibration or training set). Simply using a large number of components will do a good job in fitting the current observed data, but is a strategy that can lead to over-fitting, which then leads to poor prediction of variables for the validation data set (test set) [205], [223]. Therefore, care was taken when selecting the number of components to apply for the purpose of prediction.

Hierarchical Model Validation and Application: Figure 3.11 shows the calibration plots with external validation points for the four multivariate models that make-up the hierarchical model. The Level 1 model (M_0) spans the entire concentration rage of interest (0.159 – 0.443 g GLY/ g H_2O). This model was validated with 9 different concentrations of GLY in H_2O spanning the

calibration set concentration range. At level 2 of the model hierarchy the three constituent models constructed covered the concentration ranges 0.159 – 0.228 g GLY/ g H_2O (***M₁***), 0.228 – 0.330 g GLY/ g H_2O (***M₂***), and 0.330 – 0.443 g GLY/ g H_2O (***M₃***). The level 2 models were validated using the same data set applied at level 1 of the model hierarchy, except that the data were divided into three sets corresponding to the concentration ranges of each of the level 3 models.

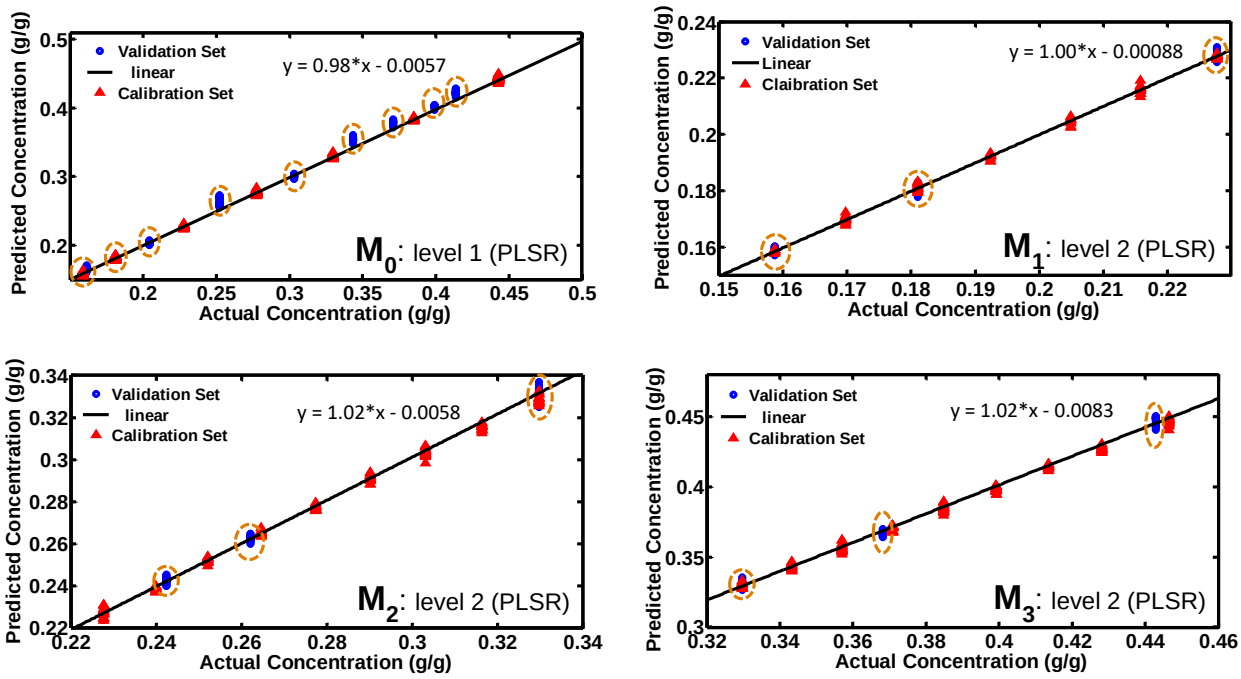

Figure 3.11: Multivariate calibration plots derived from the hierarchical models. The circled data points represent the validation sets. The data set used to validate the model at Level 1 (***M₀***) were split into three data sets according to concentration range and applied to validate the models at Level 2 (***M₁, M₂*** and ***M₃***).

Figure 3.11 gives an indication of the predictive accuracy of each model. For M_0 the validation set fits very well to the linear calibration fit at low concentrations (0.159 – 0.228 g GLY/ g H_2O), but drifts slightly at higher concentrations (0.251 – 0.443 g GLY/ g H_2O). In comparison, the validation sets fit very well with the linear calibration fits of ***M₁***, ***M₂*** and ***M₃*** at level 2 of the model hierarchy. These results indicate that the level 1 PLSR model does not capture sufficiently the differences between samples in the data set (which is quite large), leading to larger errors due to the requirement to fit all the data to the same model. The fitting of the data at level 2 is much improved, attributed to the splitting of the data into subsets, and the use of the most appropriate pre-processing methods and multivariate model to fit each subset in order to sufficiently capture, and account for the differences between samples. The models shown in Figure 3.11 gave the lowest RMSEP and error values of several tested models. The best obtained PLSR or PCR models were compared, and the model showing optimum performance based on the RMSEPs

and error values selected. Table 3.3 gives a summary of the statistical information indicating the predicative capability of the optimum PLSR models (as shown in Figure 3.11). The statistics for PCR models that show good performance (high) relative to the optimum PLSR models is also included for comparison. In general, the PCR approach to model development led to the use of significantly more components compared to PLSR. In some cases, the PCR models gave similar results to PLSR in terms of the RMSEP and % error values. However, PLSR models were selected at all levels of the model hierarchy due to consistently better results with fewer components compared to PCR. Another important observation from the results presented in Table 3.3 is the improvement in the prediction error by ~ 2 % for the Level 2 models ($\boldsymbol{M_1}$, $\boldsymbol{M_2}$, and $\boldsymbol{M_3}$) compared to the Level 1 ($\boldsymbol{M_0}$) model. This suggests that the strategy of dividing the data into smaller subsets at Level 2 and applying independent multivariate models to each set has leads to an improvement in the overall performance of the Hierarchical model. It is also interesting to note that different combinations of pre-processing methods were required to build the optimum models. This leads to the development of a distinctive set of principal components, thus making each model in the hierarchy unique. The improved predictive accuracy of the calibration model may lead to significant improvements in supersaturation monitoring and control of crystallisation processes.

Table 3.3: Summary of performance indices for the best PLSR and PCR models.

Model	Level	Model Type	Pre-Processing Applied	No. C*	RMSEP	R^2	% Error	Performance
M_0	1	MLR-PLSR	MSC =>1stDV =>AS	7	0.0032	0.9997	± 3.4	optimum
M_0	1	MLR-PCR	MSC =>1stDV =>AS	10	0.0067	0.9993	± 4.3	high
M_1	2	MLR-PLSR	MSC =>AS	9	0.0012	0.9994	± 1.3	optimum
M_1	2	MLR-PCR	MSC =>AS	10	0.0016	0.9987	± 1.7	high
M_2	2	MLR-PLSR	MSC =>1stDV =>AS	9	0.0023	0.9985	± 1.4	optimum
M_2	2	MLR-PCR	MSC =>1stDV =>AS	10	0.0026	0.9975	± 2.0	high
M_3	2	MLR-PLSR	MSC =>AS	8	0.0024	0.9992	± 1.0	optimum
M_3	2	MLR-PCR	MSC =>AS	10	0.0026	0.9977	± 1.6	high

C* = number of components; 1stDV = first derivative; AS = auto-scaling

Figure 3.12 (a) shows the prediction at Level 1 and Level 2 for the validation samples, using the hierarchal models $\boldsymbol{M_0}$ (Level 1), and $\boldsymbol{M_1}$, $\boldsymbol{M_2}$ and $\boldsymbol{M_3}$ (Level 2), respectively. Figure 3.12 (b) shows the Level 2 model of the hierarchy used to predict and refine the results from the Level 1 prediction. The Level 1 initial prediction shows significantly more noise in the data when compared to the Level 2 refined prediction, an indication of the improvement achieved by applying this hierarchical modelling approach. Figure 3.13 (a), (b), and (c) shows the application of the hierarchical model to predict concentration during an experimental run. For this

experiment, a saturated solution of 0.4729 g GLY/g H_2O was prepared by dissolving the required amount of materials in a 500 mL crystalliser.

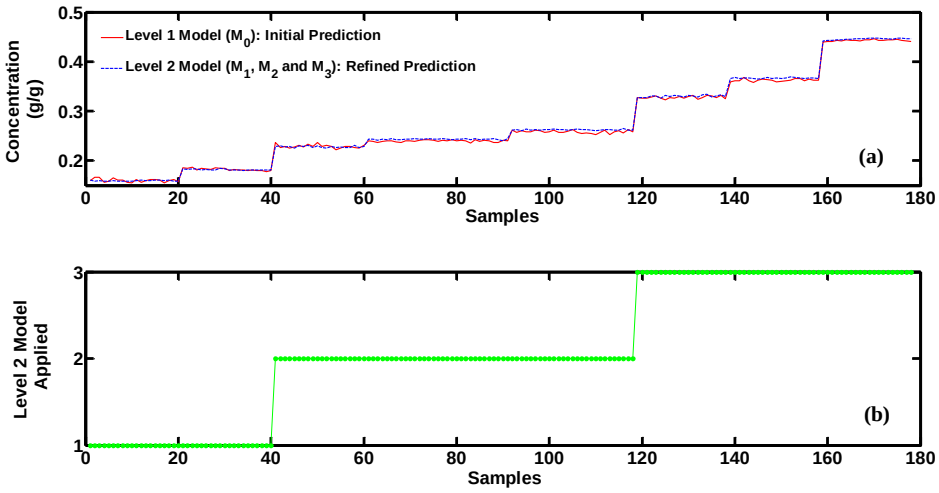

Figure 3.12: (a) Predicted concentration for 178 validation samples obtained from the Level 1 and Level 2 models and (b) Plot indicating the Level.

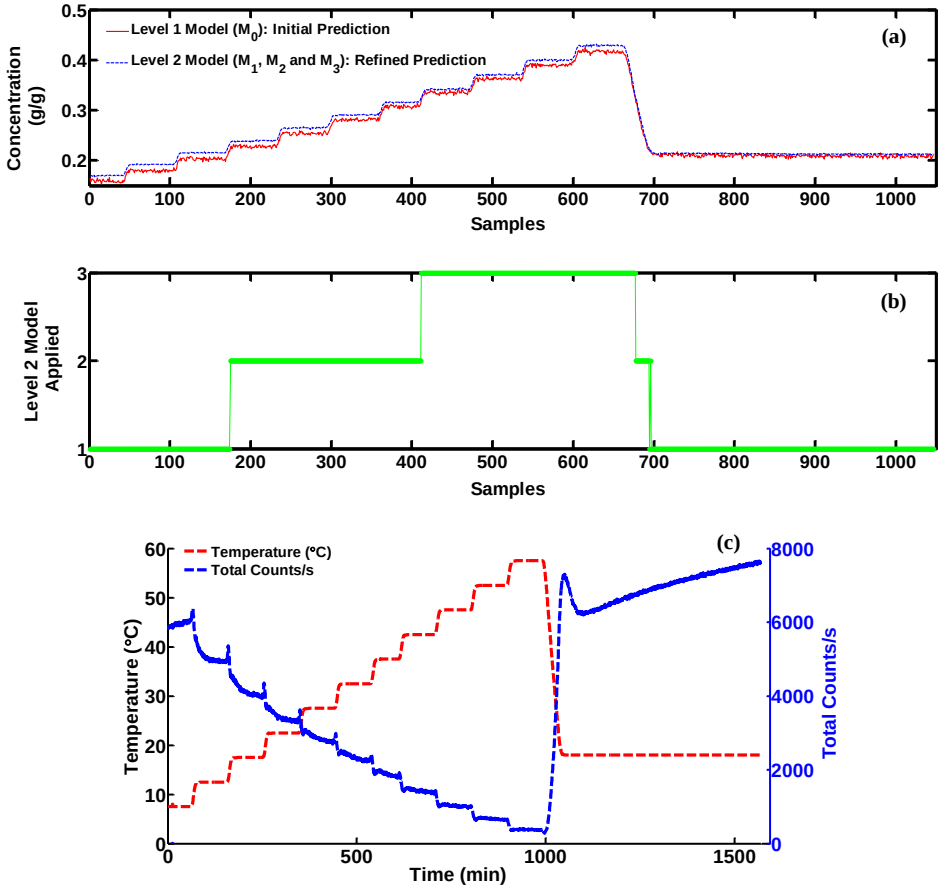

Figure 3.13: Application of hierarchical model predict concentration for an experimental run: (a) Level 1 and Level 2 initial and refined predictions; (b) Plot indicating the model applied for the refined predictions and (c) Time diagram of the experimental run.

Temperature ramps were implemented during the solids dissolution phase to test the robustness of the model to variations in the process conditions. Once dissolved, the solution was cooled at a rate of 1 ^{o}C/min until nucleation was detected by FBRM and held at 20 ^{o}C. From Figure 3.13 (b), it is clear that a different model was applied to refine the concentration prediction for each stage of this experiment. A significant advantage of the hierarchical approach is the capability of modelling large data sets. This means that hierarchical models are scalable, that is, applicable to larger and larger data sets. For the hierarchical model approach presented here, analogous "blocking" of samples rather than variables (proposed by Wold *et al* [199]) was applied in the observation (***y***) direction to give a series of cluster models, which grouped the observations together (that is, each cluster was summarised by a separate model). Each block of variables at the lower level (Level 2) of the hierarchical model architecture were summarised by scores from parts of the PLSR model at the higher level (Level 1). The block scores were used as variables to predict different ranges of ***y*** from Level 1 of the hierarchical model. These block scores were separate PLSR models that improved the predictive capability of the hierarchical model.

3.4.5 p-Toluenesulfonamide and Triphenylphosphine Oxide: ATR-FTIR and ATR-UV/vis Spectroscopy Multivariate Calibration Models

ATR-FTIR and ATR-UV/vis were used to build multivariate calibration models to monitor concomitantly the solution phase concentration of p-TSA and TPPO during batch, semi-batch and period flow MSMPR co-crystallisation studies. Spectra were obtained using the Thermo Scientific FT-IR and Carl Zeiss Multi-Channel UV/vis spectrometer units. The model development process for a multi-component system involves the same steps as discussed for the single-component systems PCM-IPA and GLY-H_2O. For the calibration data set, ATR-FTIR and ATR-UV/vis spectra of p-TSA and TPPO dissolved in MeCN were collected simultaneously from solutions with different initial concentrations of the two components. Spectra were collected at different temperatures to account for temperature effects on the absorbance measurements for both ATR-FTIR and ATR-UV/vis. The effect of particle scattering was taken into account by collecting spectra in suspensions of known concentrations of p-TSA and TPPO. The validation data set was collected in a similar way to the calibration set. The concentration of p-TSA and TPPO were varied in the range 0.010 – 0.285 g/g MeCN and 0.010 – 0.3084 g/g MeCN respectively, for both the calibration and validation sets. For the ATR-FTIR calibration model only, a separate validation data set was not acquired; instead cross-validation approach was used to verify the calibration model performance. MathWorks Matlab® 2014a software was used for spectral pre-processing and model development. This was done in order to test the model performance before carrying out

any further experiments since the performance of the ATR-FTIR spectrometer can be affected by slight movements of the fibre optic cable. This was found to affect the baseline of spectra and can often lead to erroneous predictions from a developed model.

In order to develop the calibrations models for simultaneously determine of p-TSA and TPPO concentrations variables (spectral regions) were selected manually prior to applying pre-processing algorithms in Matlab® 2014a. Pre-processing methods including, SNV, MSC, first or second derivative and MS or AS were applied to the selected regions of both ATR-FTIR and ATR-UV/vis spectra. Figure 3.14 shows the pre-processed ATR-FTIR variables in the region (1448 – 650 cm^{-1}). For comparison, those variables with no pre-processing applied are also shown. The no pre-processed variables show more variability between samples due to base line drift effects when compared to the pre-processed variables. An outlier is also detected, which was removed from the sample set prior to model development. Pre-processing of the variables in the order MSC, 1st DV and AS, led to the least variability between samples, an indication that this approach is the most suitable for further development of the multivariate model. The least reliable pre-processing method appears to be MSC and AS, for which there is still a significant baseline drift effect between samples compared to when no pre-processing was applied.

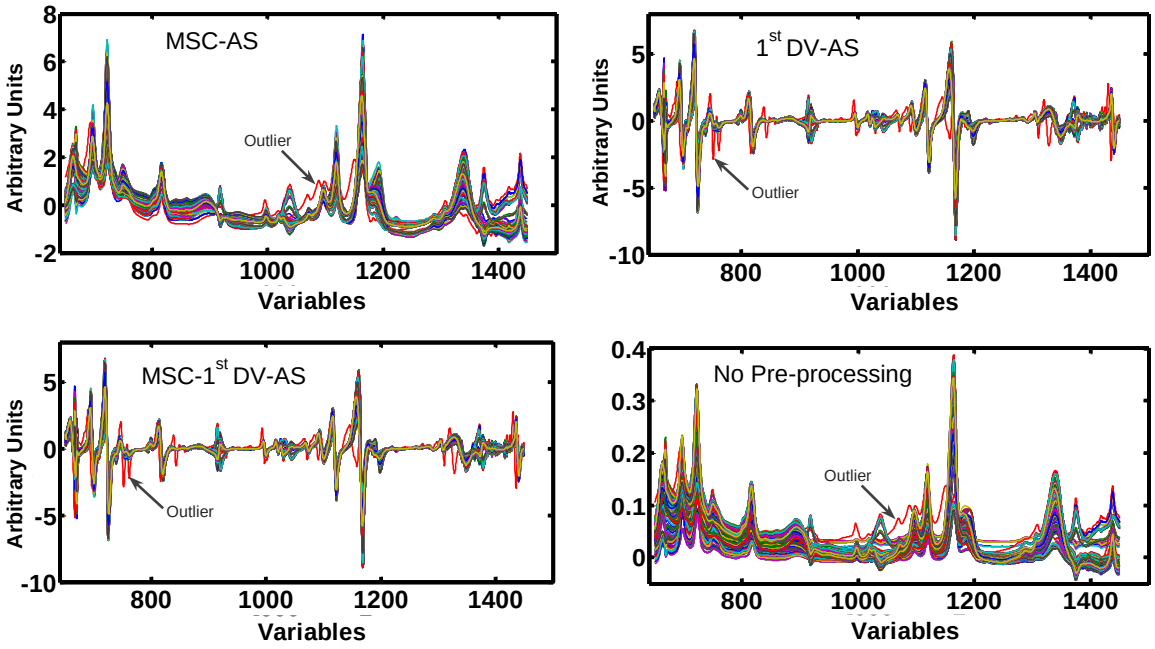

Figure 3.14: ATR-FTIR variables with pre-processing by (a) MSC and AS; (b) 1st DV and AS. Variables with no pre-processing (d) are shown for comparison.

PCR and PLSR models were built using the pre-processed variables described earlier. Table 3.4 gives a summary of the performance of the best obtained models for the prediction of p-TSA and TPPO concentrations respectively.

Table 3.4: Summary of performance indices for the best PLSR and PCR models

Model Type	Pre-Processing Applied	No. C*	RMSECV	R^2	% Error	Remarks
p-TSA Models						
PLSR	MSC =>AS	9	0.0017	0.9788	± 10.5	optimum
PLSR	MSC =>1stDV =>AS	9	0.0013	0.9778	± 12.9	outliers
PLSR	1stDV =>AS	9	0.0013	0.9778	± 12.9	outliers
PCR	MSC =>AS	10	0.0639	0.9660	± 13.2	outliers
TPPO Models						
PLSR	MSC =>AS	9	0.0043	0.9729	± 10.0	optimum
PLSR	MSC =>1stDV =>AS	9	0.0011	0.9805	± 11.2	outliers
PLSR	1stDV =>AS	9	0.0011	0.9805	± 11.2	outliers
PCR	MSC =>1stDV =>AS	10	0.0492	0.9665	± 14.0	outliers

C* = number of components; 1stDV = first derivative; AS = auto-scaling

In this study, the root mean squared error of cross validation (RMSECV) was the statistic used to compare model performance (i.e. instead of the RMSEP) since a separate validation data were not available. The error reported for the optimum model was outside an acceptable target limit of ± 5%. Due to poor accuracy, the multivariate model developed using ATR-FTIR data were not considered further for validation. Instead, PCR and PLSR models were developed using ATR-UV/vis data for the determination of p-TSA and TPPO concentration during the co-crystallisation studies. Figure 3.15 shows the variables selected (with and without pre-processing applied) that were used to develop multivariate models for p-TSA and TPPO prediction.

The 1st DV and MS were the pre-processing methods applied, which takes care of the baseline effects observed in the none pre-processed variables. Multivariate models were built applying PCR and PLSR algorithms in Matlab® 2014a using either variables with and without pre-processing. Table 3.5 gives a summary of the performance of the best obtained models for the prediction of p-TSA and TPPO concentrations respectively. The models providing the lowest RMSEP values (0.0029 g/g, p-TSA and 0.0019 g/g, TPPO) based on the lowest calibration standard, and the lowest error values were used for prediction of unknown samples. The error reported for the optimum p-TSA and TPPO models were ± 3.2 and ± 1.6 %.

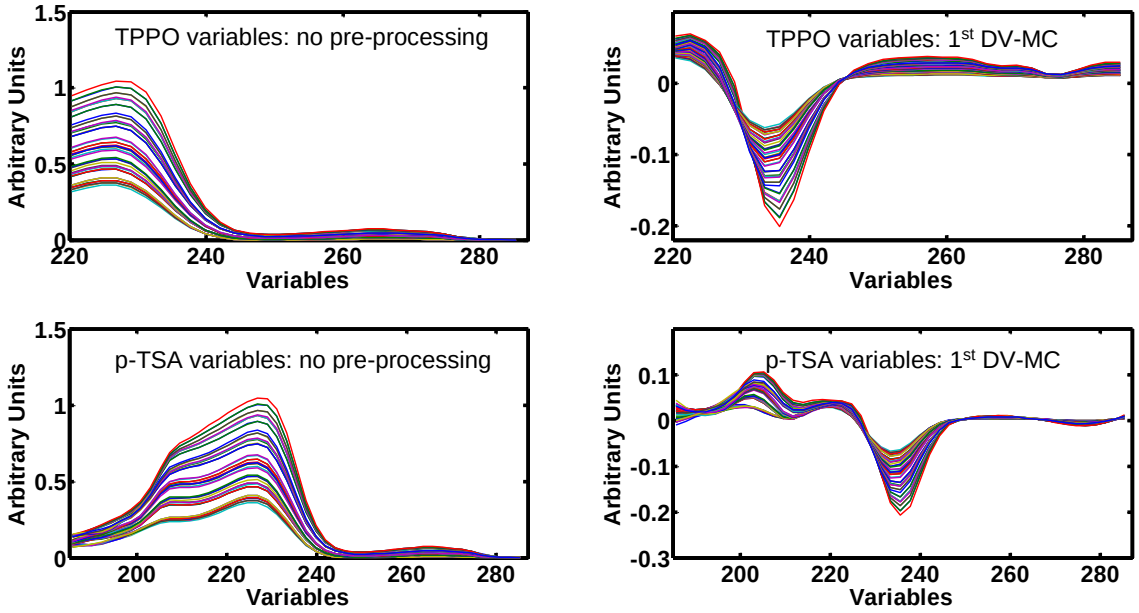

Figure 3.15: ATR-UV/vis variables with pre-processing (left) and with pre-processing by MSC and MC (right).

Table 3.5: Summary of performance indices for the best PLSR and PCR models

Model Type	Pre-Processing Applied	No. C*	RMSEP	R^2	% Error	Remarks
p-TSA Models						
PCR	AS => 1stDV	26	0.0029	0.9993	± 3.2	optimum
PCR	AS =>1stDV	20	0.0029	0.9993	± 4.0	high
PLSR	none	18	0.0048	0.9991	± 7.4	high
PCR	1stDV	23	0.0080	0.9991	± 6.7	high
TPPO Models						
PLSR	1stDV	17	0.0019	0.9988	± 1.6	optimum
PCR	1stDV	23	0.0020	0.9988	± 1.8	high
PCR	AS =>1stDV	21	0.0052	0.9991	± 3.8	high
PLSR	AS =>2ndDV	25	0.0060	0.9990	± 4.4	outlier

C* = number of components; 1stDV = first derivative; 2ndDV = second derivative; MS = mean centering

3.5 Summary on Multivariate Data Analysis

In sections 3.4 aspects of multivariate analyses applied to Raman, ATR-UV/vis and ATR-FTIR spectroscopy data were discussed. Multivariate analyses were performed in order to extract useful information from the different crystallisation processes investigated in this thesis pertaining to the change in concentration (i.e. the rate of desupersaturation). Additionally, Raman spectroscopy was used to determine the polymorphic form of the solid phases. The choice of spectroscopy technique for monitoring process concentration depended on the

properties of the system to be investigated. For PCM-IPA crystallisation both Raman and ATR-UV/vis spectroscopy were employed. The choice of Raman spectroscopy in this case was to demonstrate as proof of concept, its use for solution phase concentration measurement during a crystallisation process. Raman is typically used for solid phase monitoring and there are no robust and fully established multivariate methods in the literature for solution phase monitoring during crystallisation [164]. The multivariate Raman model was compared to an independently obtained ATR-UV/vis multivariate model in order to validate the developed method. The advantage of Raman when compared to ATR-UV/vis is that the spectral signal is more or less insensitive to temperature variations. On the other hand, ATR-UV/vis is insensitive to the presence of particles when compared to Raman, which leads to a high signal to noise ratio for the latter. In the case of GLY-H_2O system, Raman was the chosen technique since GLY is a non-conjugated system and is therefore not a good UV/vis absorber. For the p-TSA-TPPO co-crystals system, both ATR-UV/vis and ATR-FTIR were explored for monitoring the solution species concomitantly. The latter technique has been widely used in crystallisation for the past 10 years and multivariate methods are well established. However, ATR-FTIR is not the most reliable since is it is very sensitive to stresses or temperature changes along the length of the fibre optics [143] compared to other spectroscopy techniques. This often leads to problems such as loss of signal or low signal and noisy baseline. For the p-TSA-TPPO system, ATR-UV/vis was found to be more reliable when compared to ATR-FTIR, hence it was selected for monitoring the crystallisation process. The choice of multivariate pre-processing algorithms for application to the spectral data from the range of spectroscopy techniques investigated in this thesis depended on the effect spectral effects observed. For example, MSC or SNV scatter correction techniques were applied to Raman spectra to minimise the effect of particles on the spectral signal. First or second derivative pre-processing were applied to take care of baseline drift effects observed in in Raman, ATR-UV/vis and ATR-FTIR. Typically, only the first derivative was applied, since the increasing order of the derivative can lead to increase in spectral noise. The application of MC or AS to the spectral data from all techniques was also necessary to inform the selection of the most important variables for prediction.

3.6 Experimental Apparatus and Configurations

Different configurations of batch, semi-batch, continuous and period flow crystallisation equipment were employed to investigate the cooling crystallisation of the single- and multi-component molecular systems reported in this thesis. Details of the basic experimental set-up use for each mode of crystallisation operation are reported in the sections following. The configurations reported are indicative, since different layouts were used for each study. The reader is directed to the chapters following, for more detailed flow diagrams of the

experimental set-ups. An integrated array of PAT and in-house developed information systems software program, CryPRINS were combined and applied to monitor the crystallisations, Figure 3.16, for example to acquire and display real-time FBRM counts/s and ATR-UV/vis data and to implement process temperature control. Robust multivariate calibration models described earlier in this chapter were applied to determine solution phase concentration from Raman and ATR-UV/vis spectroscopy. An Automated Intelligent Decision Support (IDS) framework was established for monitoring and controlling each crystallisation process based on the concept of integrated PAT array (FBRM and ATR-UV/vis (with multivariate models)) in CryPRINS. The CryPRINS interface offers a unique environment that provides connectivity to a variety of PAT tools allowing comprehensive monitoring of crystallisation processes. The interface also allows for the implementation of a various control strategies to achieve desired crystallisation outcomes. The data generated in CryPRINS was combined with ancillary PAT (Raman (with multivariate models) and PVM) data to further characterise each of the crystallisation processes investigated in real-time. The IDS was used to control process temperature and to monitor solution concentration and particle size and shape properties. The IDS information display feature also allows the user to monitor and determine when a continuous process achieves steady-state or a batch process reaches equilibrium condition. In addition, the IDS framework can detect any system deviations due to perturbations caused for example by blockages, flow rate changes, fouling or impurity build-up.

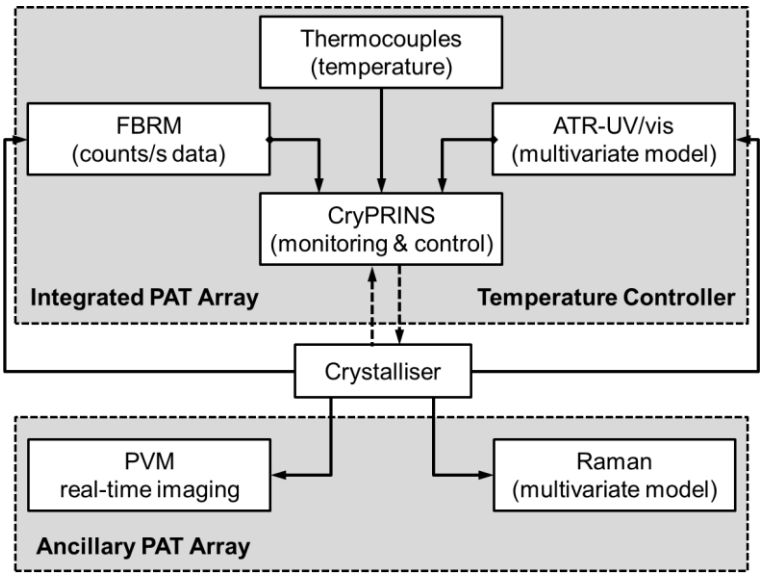

Figure 3.16: Real-time Intelligent Decision Support System with PAT Array and CryPRINS.

3.6.1 Batch and Semi-batch Crystallisation Apparatus

Batch and semi-batch cooling crystallisation studies were carried out using a 500 mL jacketed glass vessel. A schematic representation of the experimental set-up used is shown in Figure 3.17. The batch crystalliser was fitted with a PTFE lid with ports for insertion of an overhead PTFE pitch blade stirrer and five PAT probes. The jacket was connected to a Thermofluid bath (Huber ministat 230) for temperature control. Temperature profiles were implemented and data recorded using CryPRINS software. Raman immersion probes were used for *in situ* real-time measurement of both the liquid and solid phases. FBRM® and PVM® probes were used for nucleation and dissolution detection, and to tracking the evolution of crystal properties (size shape and distribution). ATR-UV/vis and ATR-FTIR immersion probes were used complementarily to monitor changes in the liquid phase.

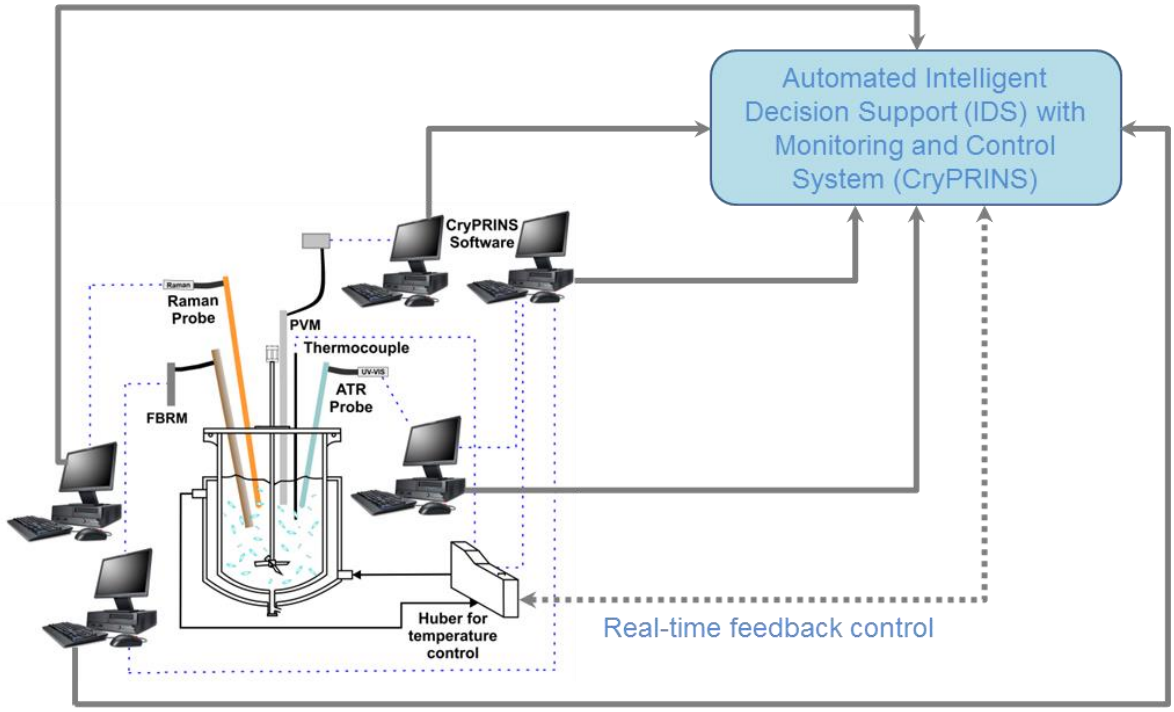

Figure 3.17: Schematic of batch crystalliser used for the cooling crystallisation experiments.

For a typical batch experimental run, the solvent and raw material(s) of interest were charged to the crystalliser and the contents heated at a fixed rate (typically 1 °C/min) until completely solubilised (typically 10 °C above the T_{sat} of the material). The crystalliser was then cooled at a pre-specified rate until nucleation was detected and then held for a pre-specified time period after which the product slurry was removed by releasing the bottom valve of the crystalliser and draining the contents. After each experimental run the vessel was cleaned thoroughly by washing with the solvent used to solubilise the starting material. Two to three passes with solvent was considered sufficient for cleaning as determined by visual inspection of the vessel.

3.6.2 Continuous and Periodic Flow Crystallisation Apparatus

Continuous and periodic flow cooling crystallisation studies were carried out using either single or multi-stage cascaded periodic mixed suspension mixed product removal ((P) MSMPR) crystalliser configurations consisting of 500 mL jacketed glass vessel(s) and a 5 L feed tank. Schematic representations of the typical (P) MSMPR experimental set-ups used for single-stage and three-stage cascaded studies are shown in Figure 3.18 (a) and (b).

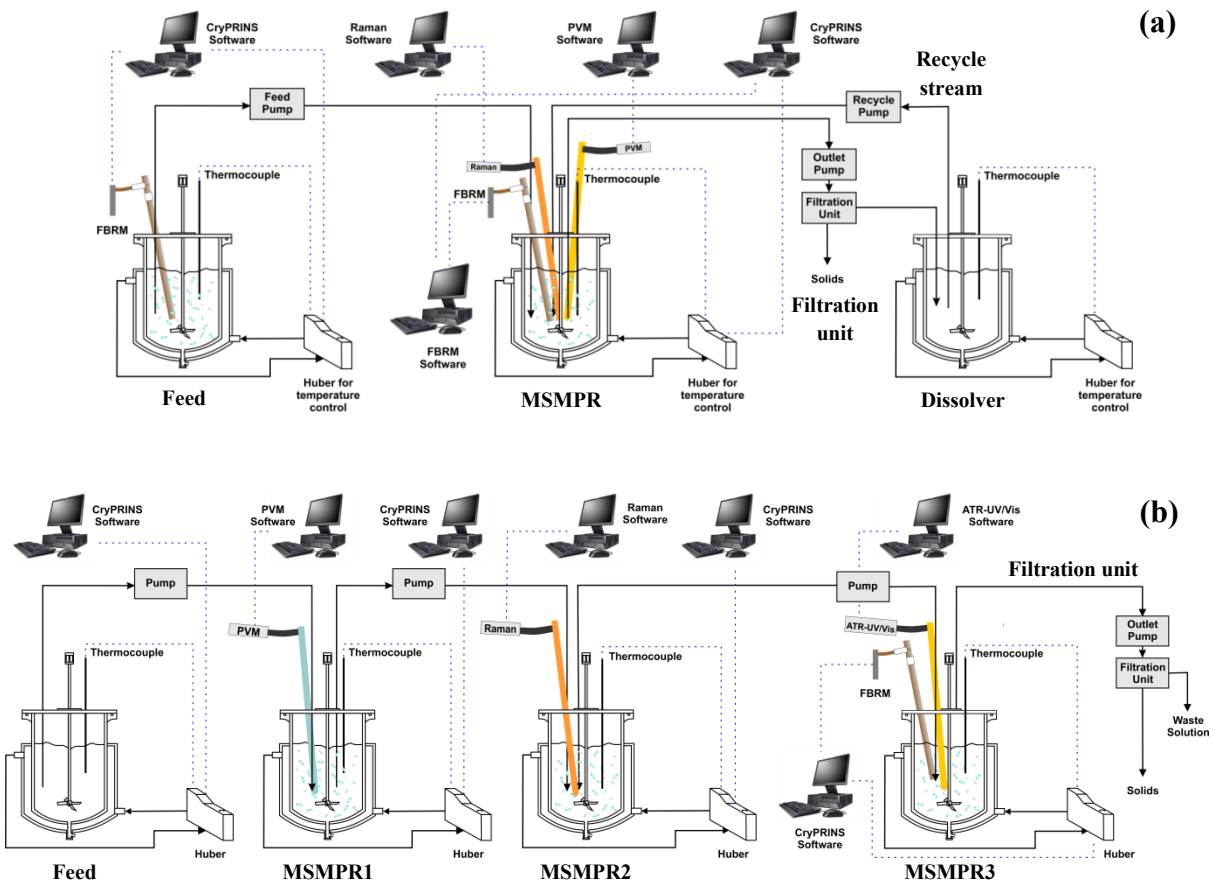

Figure 3.18: Schematic representations of (a) single-stage (P) MSMPR unit with recycle stream and (b) three-stage cascade of (P) MSMPRs used for the continuous and periodic flow cooling crystallisation experiments.

The single-stage (P) MSMPR unit was configured either with or without a recycle stream. The feed, (P) MSMPR and recycle units had independent temperature controllers. For the three-stage (P) MSMPR unit, the (P) MSMPRs were configured in series as a cascade, with each vessel assigned an independent temperature controller. Calibrated and pre-programmed Masteflex® pumps fitted with 3.1, 4.8 or 6.4 mm ID platinum cured silicone tubing were used to transfer solutions and slurry to/from each (P) MSMPR. Pumps were operated either in continuous (normal MSMPR operation) or time-dispense (periodic PMSMPR operation) mode.

When operated in time dispense mode the pumps were programmed to switch on and off over specific time intervals. The arrangement of PAT tools is indicative, as different combinations were employed for each study based on the properties of the molecular system under investigation and to acquire the most useful process data and determine when steady-state or at least a controlled state of operation is attained. The IDS framework described earlier was applied for process monitoring and temperature control.

Table 3.5 below gives a summary of the performance characteristics of the different *in situ* PAT tools used to monitor the batch, continuous and periodic flow crystallisation studies reported here. The best techniques for solid phase monitoring (i.e. crystal size shape and distribution) were FBRM and PVM. Solution phase monitoring was excellent with Raman (molecules with dipole moment only) and ATR-UV/vis (conjugated molecules only) probes, however, ATR-FTIR typically required higher solution concentration. The best technique for polymorphism and crystal form detection was Raman. FBRM and PVM could detect changes in particle shape, which is sometimes (but not always) indicative of change in crystal form.

Table 3.5: Summary of PAT application in Batch, Continuous and PMSMPR studies

Process Parameters Monitored	***In situ* PAT Techniques with Rating**				
	FBRM	**PVM**	**Raman***	**ATR-FTIR#**	**ATR-UV/vis^**
Solid Phase	Excellent	Excellent	Good	Poor	Poor
Solution Phase	Poor	Poor	Excellent	Good	Excellent
Polymorphism / Crystal Form	Good	Good	Excellent	Poor	Poor
Crystal Size / Shape	Very Good	Very Good	Good	Poor	Poor
Crystal Size Distribution	Good	Good	Poor	Poor	Poor

Raman* - excellent for molecules with dipole moment, not useful for polar molecules; ATR-FTIR# - Typically requires high concentrations and rigid/stable fibre optic; ATR-UV/vis^ - excellent for conjugated system only.

For a typical non-seeded continuous MSMPR experimental run, a feed solution at a pre-specified T_{sat} was prepared in a separate feed tank (5 L vessel for continuous removal experiments; or 500 mL for continuous dissolver/recycle experiments) and pumped to the first-stage crystalliser, which is typically held at a lower temperature in order to generate supersaturation required for crystallisation. The slurry from the crystalliser was either removed continuously and sampled or sent to a dissolver unit (held at high temperature to dissolve the solids) and recycled back to crystalliser, in effect creating a closed loop operation. When a multi-stage MSMPR was employed each crystalliser vessel was filled sequentially and the product slurry subsequently removed and sampled from the final stage. A dissolver unit was not employed for cascaded MSMPR studies. For seeded cooling crystallisation experiments

in MSMPR, a feed solution was prepared at a pre-specified T_{sat} by dissolving the raw material in solvent at 10 ^{o}C above the saturation point. The resulting solution was then cooled to 1 ^{o}C below T_{sat} and the required amount of seed material added to the vessel and aged typically for 30 min. The seeded feed suspension was then pumped to the first-stage MSMPR. For a cascade of MSMPRs, each vessel was filled sequentially and product slurry removed and sampled from the final-stage continuously. At the end of each experimental run, the slurry transfer pump between each MSMPR stage and the feed pump were switch off and each vessel drained sequentially and cleaned according to the same procedure described for the batch studies earlier.

Seeded cooling PMSMPR experiments were carried out in a similar way as described for the seeded MSMPR above. Feed preparation was exactly the same, however, the PMSMPR filling procedure was slightly different. The first-stage PMSPMR was filled by pumping slurry at a pre-specified rate over a fixed time interval. Once the vessel was filled, a holding period (or batch cycle) was implemented whereby the feed pump was switched off. For coupled periodic flow experiments in the PMSMPR, at the end of the holding period the feed and outlet pumps were switched on simultaneously. Slurry from the crystalliser outlet was sampled in a similar way to the MSMPR study described earlier. For a cascade of PMSMPRs, the filling procedure was sequential similar to MSMPR, but with cyclic pumping and holding periods. Decoupled PMSMPR experiments. Instead of applying simultaneous feed addition and slurry withdrawal, the process was staggered such that filling was always followed by removal (asynchronous). Typically, 50% of the crystalliser volume was removed and then refilled each cycle, followed by a holding period, which was similar to the coupled PMSMPR operation. The cleaning procedure for coupled and decoupled operation was the same as for MSMPR study. More details of the operating strategies are provided in the chapters that follow.

3.6.3 Co-Crystal Solubility Studies

The solubility studies were carried out using either turbidity measurement (i.e. percentage light transmission) or gravimetric technique. Real-time, through vial turbidity measurements were carried out using an Avantium Crystalline® SE reaction block consisting of 8 parallel ports with independent temperature control for insertion of 8 mL vials. For each analysis, an excess of the material to be analysed was added to each vial with solvent at 20 ^{o}C. The resulting suspension was equilibrated at 20 ^{o}C for 30 min, and then heated slowly at a rate of 0.25 ^{o}C/min with constant stirring (800 rpm) until the “clear point” was detected. Turbidity of the suspension in each reactor was measured independently by monitoring the percentage light transmission to determine when the “clear point" was achieved. CrystalClear® version 2.1.3

software package was used to set the temperature profiles and stirring rates of each reactor with a script. The same software tool was used to analyse the experimental data (experimental findings are presented in Chapter 6).

Solubility measurements by gravimetric analysis were carried out using a 100 mL jacketed batch reactor with ports for insertion of a thermocouple and ATR-UV/vis probe (Helma Katana 6 immersion probe). For each analysis, an excess of the material to be analysed was charged to solvent in the reactor at a specific temperature and equilibrated with constant stirring for 3 hr or until the absorbance measurements from the ATR-UV/vis probe indicated that equilibrium was attained. The stirrer was then stopped and the solids allowed to settle over a period of 1 hr. Three 2.5 mL samples of the clear solution were then collected in pre-weighed glass vials (X_1) and weighed (X_2). The solvent was allowed to evaporate in a vacuum oven at 25 ^{o}C for 24 h before weighing the final dry weight (X_3). The formula $(X_3 - X_1) / (X_2 – X_3)$ was used to obtain the solubility, expressed as g solid/ g solvent (experimental findings are presented in Chapter 7).

Chapter 4

Comparative Investigation of Batch and Continuous Crystallisation of Paracetamol Using PAT

In this chapter, batch and continuous crystallisation methods are investigated and compared on the bases of yield of crystallisation, productivity, crystal size and distribution. The dynamics of these crystallisation strategies are vastly different, due mainly to the difference in rate of supersaturation generation and the trajectory through the phase diagram. Since supersaturation is the driving force for crystallisation, the different trajectories that are accessible using different crystallisation methods can allow the exploitation of a wider range of product critical quality attributes (CQA) such as CSD, purity, habit, and, polymorphic or other crystalline forms [32], [170]*. In this study, batch and continuous crystallisations of paracetamol (PCM) from isopropyl alcohol (IPA) were performed. Batch experiments were carried out using two control strategies, namely, linear cooling (LC) and automated direct nucleation control (ADNC). Continuous cooling crystallisations were carried out with and without seeding using either a single-stage MSMPR or a modified version with recirculation loop incorporated to conserve materials. Due to difficulties experienced with fouling, encrustation and blockage in MSMPR, the additive hydroxyl propyl methyl cellulose (HPMC) was investigated to control these phenomena. Overall the results indicate that different CQA (mean size, CSD and habit) are attainable in the batch and continuous crystallisers. An advantage of the continuous MSMPR is that it operates at steady-state, leading to consistent product quality compared to batch. Although the yield of crystallisation was much lower compared to batch, the productivity of crystallisation was significantly higher in the steady-state MSMPR operation.*

4.1 Introduction

So far it has been established that fine chemicals and pharmaceuticals manufacturing and crystallisation are almost always conducted using batch processes, with each unit dosage form identified as coming from a unique batch [33]. However, the operation of batch processes is very costly and inefficient. In order to address this problem several researchers [31], [153], [168], [180], [224] have resorted to high level modelling, monitoring and control strategies often aided by process analytical technologies (PAT) to improve batch performance. However, similar concepts could be applied to continuous crystallisers, gaining the additional benefits

related to operating at steady-state [32], [152], [225], [226], or at least in a controlled dynamic state. In this study, an integrated array of PAT tools and CryPRINS informatics system software were used together within an IDS framework (described in Chapter 3) to monitoring and control the batch (via LC and ADNC) and continuous crystallisation. The solute considered was PCM, which is a widely used over-the-counter analgesic and anti-pyretic drug; it is also used as an intermediate in the manufacture of azo dyes and photographic chemicals [227]. A comparative analysis was conducted to determine the most suitable crystallisation approach for producing large uniform crystals at high yield. For the batch LC method, the time rate of change of temperature is kept constant by manipulating the coolant temperature to maintain a constant level of heat removal. Implementation of an unseeded crystallisation with LC requires solubility and metastable zone width (MSZW) information to determine the optimum cooling rate to achieve a desired CSD. However, with LC there is limited control over the system once nucleation occurs, and this leads to broad CSDs. Fines destruction/removal [6] or external seeding [9] methods may be employed to narrow the CSD and suppress nucleation. Alternatively, ADNC is a model-free approach that utilises FBRM for direct feedback control [170]. It utilises closed-loop feedback control based on a target value of total number of counts/s to improve the CSD, via implementation of heating/cooling cycles. ADNC leads to larger, more uniform and less agglomerated crystals and prevents solvent and impurity inclusion [170], [224]. For ADNC implementation only the solubility data are required to determine the level of supersaturation. However, a disadvantage of ADNC is that it can often lead to very long batch times (sometimes days) and is not appropriate for systems which are acicular or needle shape, because FBRM gives erroneous count/s measurements for these systems [157], [228].

An alternative strategy to batch approaches is continuous MSMPR crystallisation. With this approach there are several degrees of freedom in operation that can be exploited to control the supersaturation trajectory through the phase diagram (for example, when operated as a cascade), thereby controlling a range of product CQA. For example, the temperature, feed flow rate and operating volume of the MSMPR can be varied to achieve different crystallisation outcomes. In this study, different continuous cooling crystallisation approaches were investigated and compared to the batch approaches mentioned earlier. PAT tools in the form of ATR-UV/vis, FBRM and PVM were used to monitor each process. Due to fouling, encrustation and blockage issues in the continuous MSMPR, a two-pronged approach was taken to mitigate these problems. The first involved the design of a modified MSMPR, incorporating a baffled heat exchanger to minimise temperature variations in the crystalliser, this is, by avoiding a large temperature difference between the feed stream and slurry within the MSMPR as well as temporal variations. The second approach involved the use of a

polymeric additive, HPMC to control the crystallisation kinetics (nucleation and growth), and thereby avoid fouling and crust formation for extended operation of the MSMPR.

4.2 Experimental Methods

The aim of this study was to identify conditions for the production of large, uniform crystals with narrow CSD using different configurations of MSMPR crystallisers, and to compare their productivity and product crystal CQA to optimised batch crystallisers. PCM was crystallised by cooling from IPA in the batch studies. For the MSMPR studies, crystallisation of PCM was carried out by cooling from either pure IPA or H_2O. Equations for the multivariate models used to determine PCM solubility and concentration in IPA from Raman and ATR/UV/vis spectra were reported in Chapter 3 Section 3.4.2 (Eqn. 3.1 and 3.2, respectively). PCM solubility in water was estimated from data published by Braatz *et al* [229]. The solubility data were also used by Nagy *et al* [230] in their study on the crystallisation kinetics of PCM in water. The model equation for the solubility of PCM in water as a function of temperature (°C) is given by:

$$c(T) = 1.5846 \times 10^{-5}T^2 - 9.0567 \times 10^{-3}T + 1.3066 \qquad 4.1.$$

The impeller stirring rate for the experimental runs was set to either 300 or 400 rpm. The approximate power per unit volume were 0.056 kW/m^3 and 0.133 kW/m^3, respectively. There was no significant difference between particle suspension 300 or 400 rpm, based on visual observations. Hou *et al* [77] conducted a series of investigations to determine the agitation rate required to give homogeneous suspensions of PCM-IPA-H_2O system in a 530 mL continuous MSMPR. The study showed that impeller speeds ranging from 200 – 400 rpm (power output per unit volume ranged from 0.0186 – 0.1486 kW/m^3) produced homogeneous suspensions as confirmed by FBRM measurements from the top, centre and bottom of the continuous MSMPR. It is well known that for isokinetic withdrawal of slurry from MSMPR to be achieved, there is a requirement to maintain a homogeneous suspension in the crystalliser. There are also further requirements for high flow rate and optimal positioning of the outlet dip tube to ensure rapid and representative slurry withdrawal.

4.2.1 Batch Crystallisation Experiments

Batch experiments were carried out using the experimental configuration described in Chapter 3 Section 3.6.1 (Figure 3.14). As far as possible, experimental conditions were tailored to match those reported by Saleemi *et al* [170]. A target concentration of 0.207 g PCM/g IPA (i.e. saturation temperature (T_{sat}) of 50 °C) was selected for each experimental run. For each

run, 64.8 g of PCM and 314 g of IPA were added to the crystalliser taking care to ensure reagents were transferred as completely as possible. The crystalliser was then heated to 60 ^{o}C at a rate of either 1 or 2 ^{o}C/min and held for 15 min to ensure complete dissolution of PCM. For the batch LC experiments the resulting solution was cooled at a rate of either -1.0 ^{o}C/min (fast cooling) or -0.5 ^{o}C/min (slow cooling) to 10 ^{o}C, and held until nucleation was detected and stable counts/s observed from FBRM. For the ADNC experiments, the DNC temperature control option in CryPRINS was selected to initiate cooling of the solution from 60 ^{o}C at a rate specified in the software settings. Table 4.1 provides a summary of the experimental conditions employed for the LC and ADNC experimental runs, respectively.

Table 4.1: Summary of experimental conditions employed during the batch crystallisation of PCM from IPA.

Exp. No.	Exp. Type	PCM Raw Material	Stirring Rate	Heating / Cooling Rate (^{o}C/min)	k_h / k_c	ADNC Set-point (counts/s)	[+]Experiment Duration (min)
(1a) / (1b)	LC	FR_{new}	300 / 400	1.0 / -1.0	n/a	n/a	187
(2a) / (2b)	LC	FR_{new}	300 / 400	1.0 / -0.5	n/a	n/a	240
3	ANDC	FR_{new}	300	0.4 / -0.2	5 / 5	4000 ± 100	625
4	ANDC	FR_{new}	300	0.4 / -0.2	5 / 5	4000 ± 1000	1190
5a / 5b	ANDC	FR_{new}	300 / 400	0.2 / -0.4	5 / 5	4000 ± 100	642
6a / 6b	ANDC	FR_{new}	300 / 400	0.2 / -0.4	5 / 5	8000 ± 100	650
7	ANDC	CH_{new}	400	0.2 / -0.4	5 / 5	8000 ± 100	612
8	ANDC	CH_{new}	400	0.2 / -0.4	5 / 5	4000 ± 100	662
9	ANDC	DE_{old}	400	0.2 / -0.4	5 / 5	8000 ± 100	647
10	ANDC	DE_{old}	400	0.2 / -0.4	5 / 5	4000 ± 100	670
11	ANDC	US_{new}	400	0.2 / -0.4	5 / 5	8000 ± 100	569
12	ANDC	US_{new}	400	0.2 / -0.4	5 / 5	4000 ± 100	753
13	ANDC	FR_{old1}	400	0.2 / -0.4	5 / 5	8000 ± 100	611
14	ANDC	FR_{old1}	400	0.2 / -0.4	5 / 5	4000 ± 100	696
15	ANDC	FR_{old2}	400	0.2 / -0.4	5 / 5	8000 ± 100	654
16	ANDC	FR_{old2}	400	0.2 / -0.4	5 / 5	4000 ± 100	628

[+] Experiment time includes the holding period (typically 15 min); () Replicated experimental runs; FR_{new} = France new sample, FR_{old1} = France sample 1, FR_{old2} = France old sample2, CH_{new} = China new sample, DE_{old} = Germany old sample, US_{new} = United States new sample. k_h/k_c are the proportional gains for the heating and cooling phases.

The ADNC runs were performed using different PCM raw material samples obtained from the same supplier, but manufactured in different countries (see Chapter 3 Section 3.1). This aspect of the study was motivated by the fact that different numbers of ADNC cycles were obtained when compared to results of Saleemi *et al* [170], which suggested that the PCM sample characteristics, specifically the impurity profile was contributing to the contrasting results. Therefore, experiments were done to establish whether or not there was a link between the impurity profiles of the different PCM raw materials and the number of ANDC cycles. Industrially, PCM is manufactured by either of four routes, involving the following intermediates: Phenol, Nitrobenzene, *p*-Nitrochlorobenzene, and *p*-Hydroxy-acetophenone. By-products of the different synthetic routes include: Acetic acid, Aniline, and *p*-Nitrophenol sodium salt among other phenolic derivatives reported by Rao *et al* [231].

4.2.2 Continuous Crystallisation Experiments

Continuous crystallisation experiments were carried out using either a conventional MSMPR or a modified version incorporating a recirculation loop so that product slurry withdrawn from is sent to a dissolver, which also serves as a feed/recycle unit [19], [110], [152]. Importantly, this arrangement leads to the conservation of material and allows operation of the MSMPR as a continuous, unseeded system for long periods without using large quantities of material. This is particularly useful for research purposes at laboratory scale, given the large amounts of materials that can be consumed by continuous crystallisers. The added value of the modified MSMPR unit is that continuous crystallisation of high value APIs can be investigated using only a small amount of material, in particular, during the pre-clinical and phase I stages of drug development. Arguably, a limitation of this operation is the requirement to generate particles by primary nucleation, which is not always consistent and results in fouling, encrustation and line blockages due to the high supersaturation requirement. However, the use of an additive to control the crystallisation shows promise. A number of seeded crystallisation experiments were also carried out using conventional MSMPR crystallisers operated at low supersaturation for comparison with the proposed modified MSMPR operation. Operating at low supersaturation with seeding is advantageous for the alleviation of fouling and encrustation whilst producing crystals that exhibit consistent mean size and CSD. However, this is highly dependent on the continuous and consistent supply of uniform seed material.

Operation of Modified MSMPR: Figure 4.1 (a) and (b) show respectively, the flow diagram and photograph of the experimental set-up used (a schematic layout with PAT tools was present in Chapter 3 Section 3.6.2 (Figure 3.15). The modified MSMPR consisted of a 750 mL

crystalliser and 400 mL dissolver vessel each with independent temperature controllers. The MSMPR was connected to the dissolver using Masterflex® platinum cured silicon tubing (6.4 mm ID). A heat exchanger consisting of a jacketed 220 mm length glass tube with smooth periodic baffle constrictions (5 mm ID with 2.0 mm constrictions) connected to a thermofluid circulator bath cooled to 10 °C was incorporated in the design in order to cool the feed sent back to the crystalliser and mitigate rapid fouling and encrustation following nucleation. The baffled heat exchanger has a high surface, which leads to rapid removal of heat from the incoming feed solution. It is an important modification to the MSMPR unit since it prevents a large temperature gradient developing when hot solution from the dissolver enters the crystalliser held at a much lower temperature to provide the driving force for crystallisation.

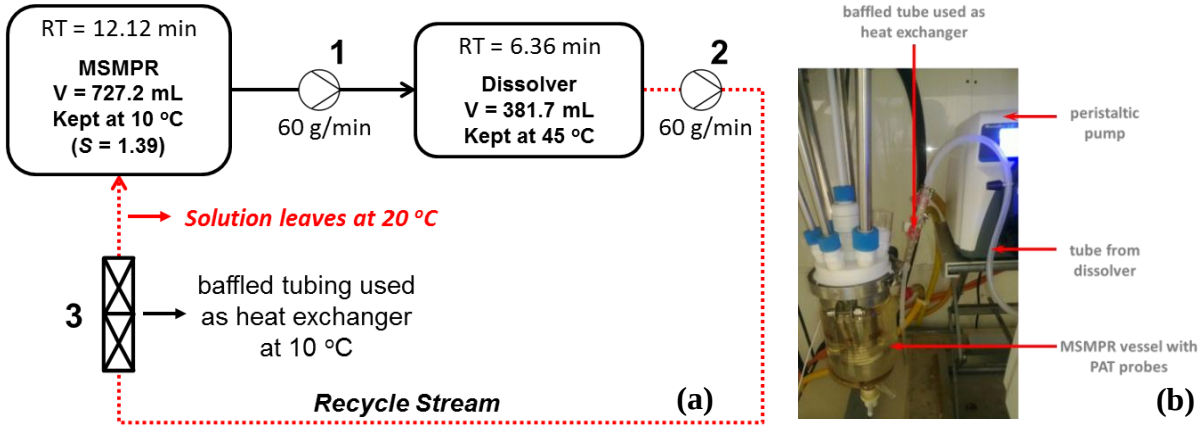

Figure 4.1: (a) Flow diagram of modified MSMPR indicating the operating conditions employed. (c) Photograph of the lab scale set-up used.

At start-up a suspension of 0.232 g PCM/g IPA in the MSMPR was heated to 65 °C and held for 15 min to allow complete dissolution of PCM. The resulting solution was then cooled to 45 °C, while simultaneously heating a solution of pure IPA in the dissolver to the same temperature. Once both vessels reached 45 °C the solution in each was pumped continuously between them using Masterflex® peristaltic pumps at a rate of 60 g/min to homogenise the vessel contents. In effect, this created a closed loop system, in which the final solution concentration was ~ 0.152 g PCM/g IPA (T_{sat} = 35 °C). Once the contents of the vessels were homogenised, as determined by real-time concentration measurement using multivariate calibration models described Chapter 3 Section 3.4.2, solution from the dissolver/feed vessel was sent to the baffled tube heat exchanger where it is cooled from 45 °C to 20 °C before entering the MSMPR crystalliser, which was cooled to 10 °C. This start-up strategy lead to generation of supersaturation required to drive primary nucleation and produce the initial start-up slurry, while preventing rapid crust formation. It took approximately 35 min for the MSMPR to reach 10 °C, i.e., inclusive of the initial start-up period. The MSMPR was maintained at 10

°C and the dissolver at 45 °C for the duration of each experiment. The experiments were carried out either with or without HPMC addition. A control experiment (no additive) was carried out using the experimental start-up and operating procedures described earlier. The flow rates employed were shown in Figure 4.1 (a), and resulted in mean residence times (RTs) of 12.12 and 6.38 min in the MSMPR and dissolver vessels respectively. The duration of each experiment was ~ 4.6 hours (inclusive of the start-up period). The process was operated for ~ 18 RTs from the point of nucleation detection in the MSMPR. Experiments with additive addition were carried out in a similar way with HPMC additive added to the system in order to control the crystallisation of PCM and prevent fouling, encrustation and potential line blockage issues. Fouling and encrustation problems were encountered during the initial development stages of the modified MSMPR and during the control experiments. Figure 4.2 shows the detrimental effect of fouling observed during preliminary development experiments with a closed loop MSMPR design without the heat exchanger modification. Severe fouling and crust formation occurred on the PAT probes and vessel walls of the MSMPR. Fouling in the MSMPR was a result of the rapid generation of high localised suspersaturation due to the large temperature difference between the incoming feed stream (at 45 °C) and the crystalliser (at 10 °C).

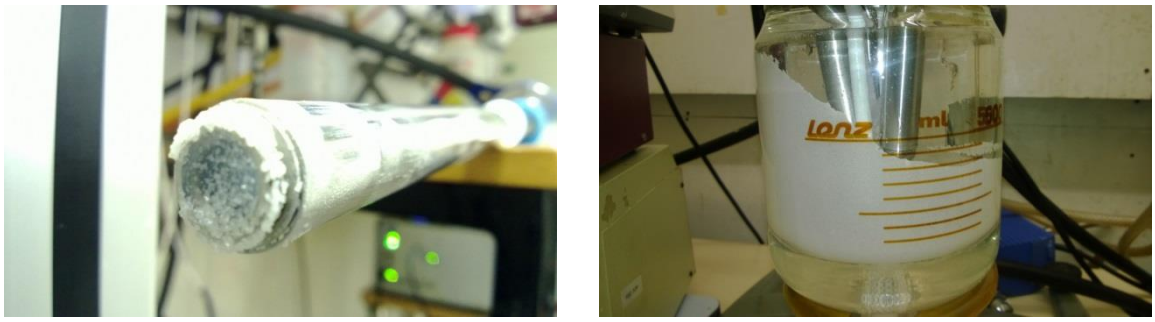

Figure 4.2: Extent of fouling and crust formation on PAT probe (left) and crystalliser wall (right) in MSMPR operated without the baffled tube heat exchanger.

Three concentrations of HPMC 0.001, 0.003 and 0.05 wt% (i.e., relative to mass of PCM) were investigated in the modified MSMPR. For each experiment, the required amount of HPMC was added to the MSMPR at the start of the 15 min homogenisation period. For the experiment in which 0.05 wt% HPMC was added, the dissolver temperature was elevated to 50 °C. This was due to incomplete dissolution of small amounts of large crystals as observed from visual inspection of material flowing through the recycle transfer line during preliminary experimental runs where the vessel was maintained at 45 °C.

Effect of HPMC on Raman and ATR/UV/vis Signals: *HPMC* was found to have no effect on the *in situ* Raman or ATR-UV/vis signals at all applied concentrations. Figure 4.3 shows the

Raman spectra of experiments carried out with 0.05 wt% HPMC and with no HMPC addition at similar PCM concentrations (0.153 and 0.156 g PCM/ g IPA, respectively). There is no evidence of extra peaks or any spectral features (such as peak broadening or distortion) related Raman scattering by HPMC. Therefore, the spectra collected during each experimental run are thought to be independent of the HPMC concentration. Furthermore, signal changes due to the presence of interference can be minimised or eliminated by applying mathematical pre-processing techniques (see Chapter 3; Section 3.4.2) to the data [216].

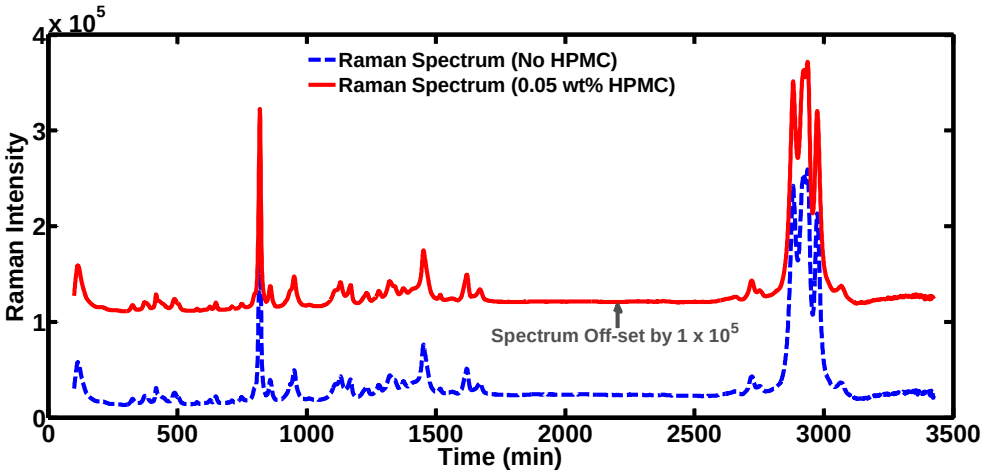

Figure 4.3: Raman spectra from solution phase for experiments carried out with 0.05 wt% HPMC (straight line) and No HPMC (dashed line) addition at concentrations of 0.153 and 0.156 g PCM/ g IPA respectively.

Conventional MSMPR Operation: a number of seeded cooling crystallisation experiments were carried out using a conventional continuous MSMPR crystalliser (500 mL). Figure 4.4 shows the flow diagram of the MSMPR set-up. Experiments were carried out with PCM using either water or IPA as solvent.

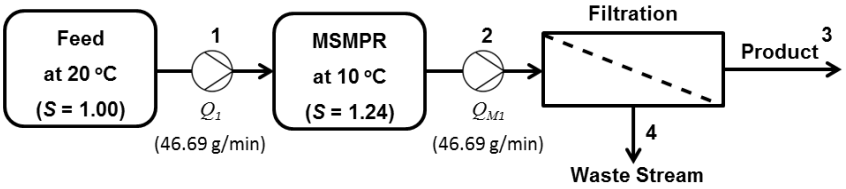

Figure 4.4: Flow diagram of the MSMPR units used for the crystallisation studies.

For the cooling crystallisation experiments using water as solvent, a fresh feed solution of PCM in water was prepared at 20 °C saturation (0.013 g PCM / g H_2O) in a 1 L feed vessel. Feed solution was pumped to the MSMPR crystalliser (kept at 10 °C) at a rate of 46.69 g/min On filling, the MSMPR was seeded once by manually addition of either 3.5 or 7.0 % (i.e., 1.5 or 3.0 g) PCM raw material. Following seed addition, a holding period of 30 min was

implemented for equilibration with solute in the liquid phase, crystal growth and healing. This was followed by restarting of the feed and withdrawal of slurry at a constant rate of 46.69 g/min, leading to a mean RT of 10.6 min. The feed vessel was replenished as required to give extended operation of the MSMPR. For the cooling crystallisation of PCM from IPA, the MSMPR was operated at low (20 ^{o}C saturation; 0.109 g PCM/g IPA) supersaturation (i.e. relative to the modified MSMPR), with continuous feed addition and withdrawal of slurry. The MSMPR was fed with a fresh feed each RT followed by rapid manual addition of 0.5 % (i.e., 0.24 g) portions of homogenised PCM raw material seed. The 1 L feed vessel was replenished every second RT to provide an uninterrupted supply solution to the MSMPR. The mean RT of slurry inside the MSMPR was 8.42 min due to lower density of the PCM-IPA suspension compared to PCM-H_2O. Slurry withdrawn from the MSMPR each RT was separated by vacuum filtration (20 µm pore filter). Recovered product crystals from all experimental runs (PCM-H_2O and PCM-IPA) were then dried at 40 ^{o}C for 24 hrs in a drying oven and image analysis carried.

4.3 Results and Discussion

4.3.1 Batch LC and ADNC Experiments

A summary of the crystallisation experiments performed was presented in Table 4.1. The batch LC experiments provided an initial benchmark of total counts/s generated from the nucleation of PCM. The total FBRM counts/s from all the LC runs were within the range 13000 to 16000 count/s. This benchmark range as well as the results reported by Saleemi *et al* [170] were taken into account when selecting the parameters for subsequent ADNC runs. No significant difference was observed between the counts/s and square weighted mean chord length (SWMCL) of crystals obtained from the LC experiments conducted at low or high stirring rates (300 or 400 rpm) and at fast or slow cooling rates (-1.0 and -0.5 ^{o}C/min) which was a surprising outcome. Table 4.2 provides a summary of results from the LC experiments

Table 4.2: Summary of results for batch LC experiments.

Exp No.	PCM Raw Material	Stirring Rate	Heating / Cooling Rate (°C/min)	Final FBRM counts/s	SWMCL (µm)
1a	FR_{new}	300	1 / -1.0	15585	48.5
1b	FR_{new}	400	1 / -1.0	13716	47.6
2a	FR_{new}	300	1 / -0.5	13007	46.3
2b	FR_{new}	400	1 / -0.5	15428	47.9

Figure 4.5 shows the time and phase diagrams respectively of the LC experiment carried out at 400 rpm and cooling rate of 0.5 °C/min. The FBRM total counts/s exceeds 16000 and the experiment duration was 240 min. The onset of nucleation is marked by a rapid increasing in particles over a short time period as expected.

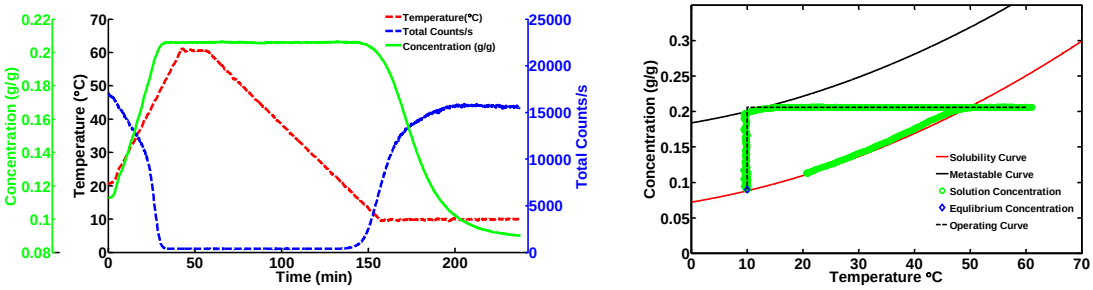

Figure 4.5: Time diagram (left) and phase diagram (right) of LC experiment.

Several ADNC experiments were carried out to investigate the effect of the impurity profiles of six different PCM starting materials on the number of heating/cooling cycles. The PCM samples were screened for impurities, based on exact masses using the HPLC-MS method described in Chapter 3 Section 3.2.6. A list of potential impurities was developed based on an extensive literature review [231]–[236]. The exact masses of impurities were calculated using ChemBioOffice software. Table 4.3 provides a summary of the HPLC-MS results, indicating the impurities found in each sample.

Table 4.3: Normalised % of impurities (based on PCM peak height) detected in PCM samples used in the LC and ADNC experiments.

Impurity	FR_{old1}	FR_{old2}	DE_{old}	CH_{new}	US_{new}	FR_{new}
N-phenylacetamide	-	-	5.86E-04	-	7.97e-04	-
Phenol	-	-	-	-	1.73e-04	-
p-nitrochlorobenzene	-	-	-	-	-	-
N-(4-hydroxyphenyl) propanamide	3.23e-04	3.99e-04	1.45E-04	5.17e-04	3.43e-04	4.38e-04
diacetylaminophenyl	7.98e-05	7.80e-05	4.06E-04	6.51e-05	5.88e-04	6.86e-05
Aniline	-	-	-	-	-	-
N-hydroxyparacetamol	-	-	-	1.31e-05	-	-
4-(Acetylamino)phenyl Acetate	-	-	-	-	-	-
p-chloroacetanilide	-	7.38e-07	-	-	-	5.64e-06
p-iminoquinone	-	-	-	-	-	-

FR_{old} and FR_{new} samples (each sourced from France) show strikingly similar impurity profiles. All other samples exhibit unique impurity profiles. However, *N*-(4-hydroxyphenyl)-propanamide and diacetylaminophenyl impurities were detected in all samples analysed. The diverse impurity profiles of the PCM samples suggest that they were produced by different synthesis routes. In spite of the diverse impurity profiles of the samples, the ANDC profiles were strikingly similar for experimental runs carried out at FBRM set-points of 4000 ± 100 and 8000 ± 100 counts/s, respectively. For example, the number of ADNC cycles obtained and the batch time (Table 4.1) were similar at each set-point investigated. The exceptions were experiments carried out using DE_{old} sample (sourced from Germany) at 4000 ± 100 counts/s set-point, and CH_{new} sample (sourced from China) at 8000 ± 100 counts/s set-point. Figure 4.6 show the ADNC time diagrams with temperature, FBRM counts/s and concentration measurements for the experimental sets carried out using DE_{old} and CH_{new} PCM, ADNC set-points are indicate on each diagram. Corresponding operating regions in the phase diagram for these ADNC runs are shown in Figure 4.7. With DE_{old} PCM only two ADNC temperature cycles were observed at set-point 4000 ± 100 counts/s (Exp. No. 10) before the system stabilised close to the target counts/s. This compares to a total of three temperature cycles all other experiments carried out at the same set-point (Table 4.1). For the experiment carried out with CH_{new} PCM at set-point 8000 ± 100 counts/s (Exp. No. 7) two temperature cycles are observed before the system reaches the target. This compares to only one cycle in all other experiment. The time diagrams (Figure 4.6) also show that the ADNC set-point of 8000 ± 100 counts/s was not achieved for Exp. No. 9 (DE_{old} 8000 ± 100), the measurement was 6901 counts/s. This experiment reflects the outcome of all experiments carried out at the ADNC set-point of 8000 ± 100 counts/s. All experiments carried out at ADNC set-point of 4000 ± 100

counts/s either achieved this target or was very close to it as shown in the summary of results presented in Table 4.4.

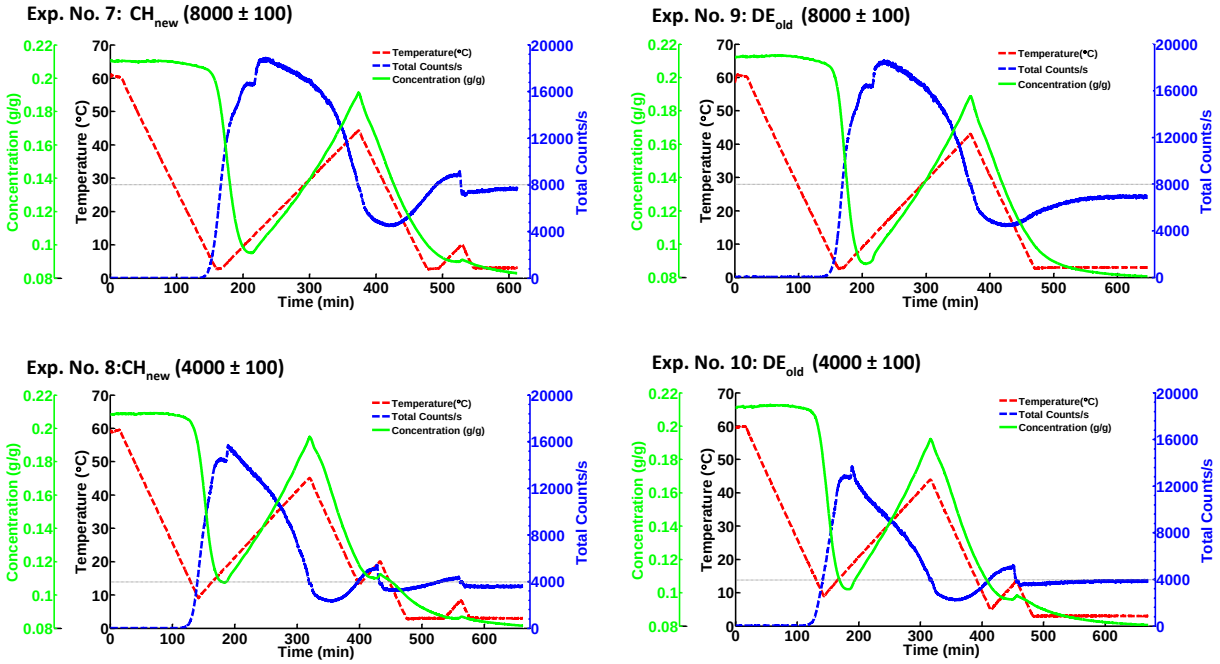

Figure 4.6: ADNC time diagrams showing the change in temperature, concentration and FBRM counts/s at set-points of 8000 ±100 counts/s (top) and 4000 ±100 counts/s.

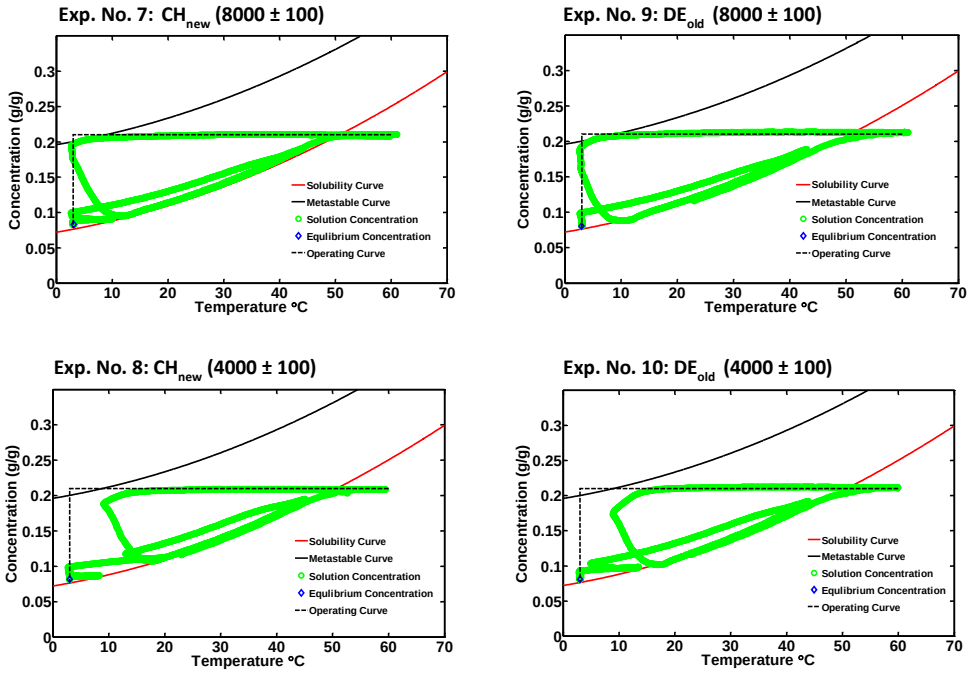

Figure 4.7: ADNC phase diagrams for experiments carried out with CH_{new} and DE_{old} PCM at set-points of 8000 ±100 counts/s (top) and 4000 ±100 counts/s.

Table 4.4: Summary of results for select ADNC experiments.

Exp No.	PCM Raw Material	Heating / Cooling Rate (°C/min)	ADNC Set-point (counts/s)	Final FBRM (counts/s)	SWMCL (µm)	No. of Cycles	Saleemi *et al*. [170] Cycles
3	FR_{new}	0.4 / -0.2	4000 ± 100	3665	90.0	1	n/a
4	FR_{new}	0.4 / -0.2	4000 ± 1000	3677	75.8	2	n/a
5b	FR_{new}	0.2 / -0.4	4000 ± 100	3573	84.5	1	n/a
6b	FR_{new}	0.2 / -0.4	8000 ± 100	6580	69.0	3	5
7	CH_{new}	0.2 / -0.4	8000 ± 100	7670	67.1	2	5
8	CH_{new}	0.2 / -0.4	4000 ± 100	3501	83.4	3	11
9	DE_{old}	0.2 / -0.4	8000 ± 100	6901	67.5	1	n/a
10	DE_{old}	0.2 / -0.4	4000 ± 100	3916	83.1	2	11

n/a = not applicable

Table 4 also shows the number of ADNC cycles obtained for each experiment and its equivalent from Saleemi *et al* [170]. The latter results show a far greater number of ADNC cycles, which is likely linked to the purity profile of the raw material used. The alternative explanation is that the different experimental outcomes in terms of numbers of ADNC cycles is a result of batch-to-batch variability. For experiments in which the set-points counts/s was not achieved, the observed counts/s when each of the systems stabilised was lower than the target value. This means that the implementation of a cooling cycle could have increased the number of particles via secondary nucleation in the system in order to achieve the target. However, in all cases the temperature recorded when the counts/s in the system stabilised was roughly 3 °C, which is also the lower temperature limit set in the DNC profile in CryPRINS. This means that no further cooling of the process vessel was possible to produce more particles. Therefore, each system remained at the final counts/s value and stabilised without the implementation of further ADNC cycles. The crystals obtained from experimental runs carried out at ADNC set-points 8000 ± 100 and 4000 ± 100 counts/s, respectively, were of a similar mean size (SWMCL) for all runs in the same category. However, the SWMCL of crystals obtained from 4000 ± 100 counts/s are noticeably larger compared to those from 8000 ± 100 counts/s. This is attributed to the greater extent of fines dissolution achieved at the lower ADNC set point, leading to the remaining crystals growing larger still at the expense of the dissolved fines. Figure 4.8 (a) shows the evolution of SWMCL with time over the last 400 min of Exp. No. 3, 4, 7, and 10. These trends confirm that the largest mean crystal size was obtained for Exp. No. 3 (4000 ± 100 counts/s). For this experiment, the ADNC heating/cooling rate settings were 0.4 / -0.2 °C/min, whereas for the other experiments they were 0.2 / - 0.4 °C/min. This suggests that low cooling growth is more favourable and with fast heating there is rapid dissolution of the fines. On assessment of Exp. No. 4 (4000 ± 1000 counts/s), the

mean crystal size is smaller compared to Exp. No. 3, a reflection of the wider ADNC boundary conditions employed. Figure 4.8 (b) shows the images of crystals obtained at the end of the ADNC runs described earlier.

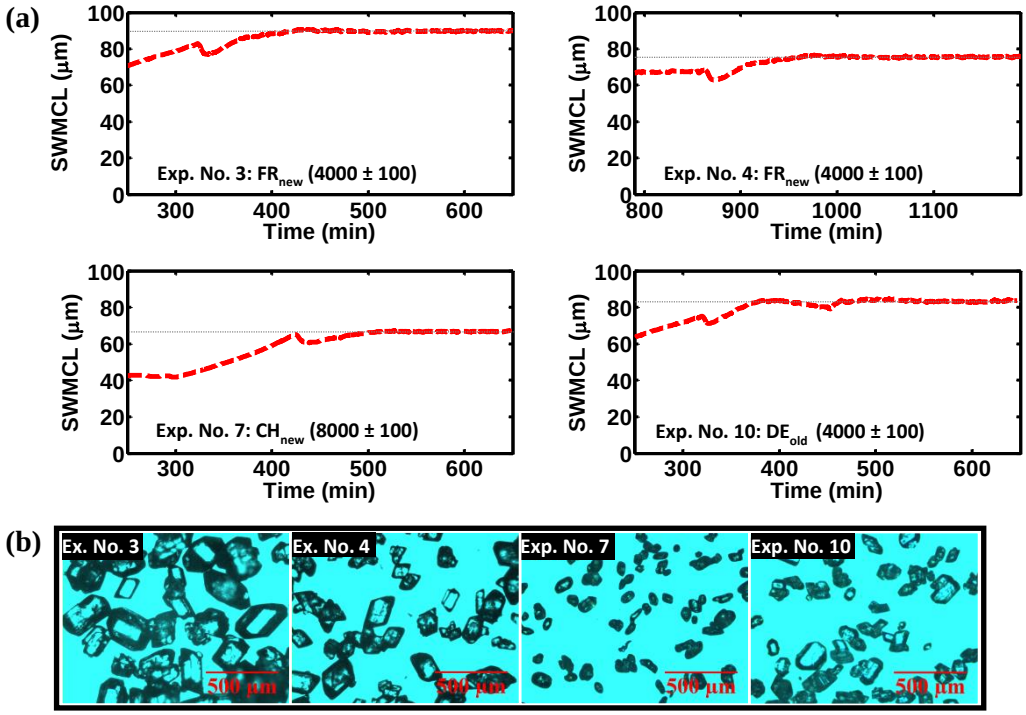

Figure 4.8: FBRM SWMCL measurements (a) and microscope images (b) for Exp. No. 3: FR_{new} (4000 ± 100), Exp. No. 4: FR_{new} (4000 ± 1000), Exp. No. 7: CH_{new} (8000 ± 100) and Exp. No.10: DE_{old} (4000 ± 100).

The crystals obtained from Exp. No. 3 show better CQA properties in terms of shape, size and extent of agglomeration when compared to crystals from the other experimental runs. Overall, the results present indicated that the impurity profile of the PCM samples does not significantly affect the behaviour of the system when ADNC control is applied. This is perhaps due to the very low impurity concentrations detected. However, the selected ADNC set-point and control setting, including the boundary conditions and heating/cooling rates all have an effect on the mean size and CSD of the final product.

4.3.2 Cooling Crystallisation in Conventional MSMPR

Seeded Cooling Crystallisation Experiments Using Water: PCM crystallisation was investigated in the single-stage MSMPR described in Section 4.2.2 (Figure 4.4). Figure 4.9 (a) and (b) show the time diagram for the seeding cooling crystallisation of PCM from water at 3.5 and 7.0 % seed loading, respectively. The data shows that there is unsteady behaviour of the FBRM counts/s and 1st derivative of the ATR-UV/vis signal. It appears the system is dominated

by secondary nucleation, leading to rapid depletion of concentration as indicated by an increase in the 1st derivative of the ATR-UV/vis absorbance at 266 nm. In the 3.5 % seed experiment there was an initial decrease in FBRM counts/s signal immediately after the holding period, an indication that some crystals were being washed out of the system. In comparison, the 7.0 % seed experiment shows a steady signal, followed by a steady increase soon after the commencement of slurry withdrawal. These experiments suffered from persistent fouling on the vessel walls and probes in spite of the low supersaturation employed. This can be attributed to the hydrophobicity of PCM crystals, which tended to form clusters in the presence of water. Figure 4.10 shows the microscope images of the homogenised raw material seed and product crystals obtained from the 3.5 and 7.0 % seed addition experiments, respectively. The product crystals appear larger than the seed crystals. However, there are clearly a lot of agglomerates present. This is attributed partly to the poor quality of the seed material, but also to the hydrophobicity of PCM in water leading to aggregation of the seed crystals.

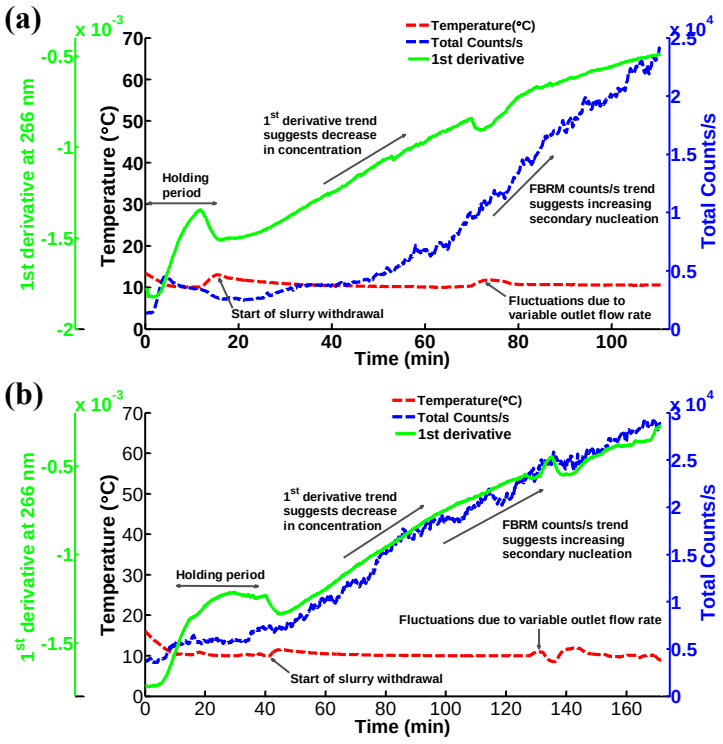

Figure 4.9: Time diagrams show the change in temperature, 1st derivative ATR-UV/vis absorbance at 266 nm and FBRM counts/s for PCM crystallisation from water: (a) 3.5 % seed added manually at start-up (b) 7.0 % seed added manually at start-up.

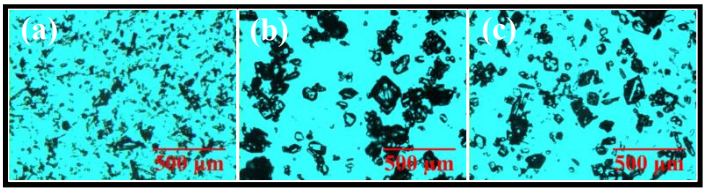

Figure 4.10: Microscope images of crystals (x4) of (a) seed material, (b) product crystals from of 3.5 % seed experiment, and (c) product crystals from 7.0 % seed experiment.

The product crystals from 3.5 % seed experiment appear larger in comparison to the 7.0 % seed experiment. This suggests that the amount of seed has an effect on the nucleation and growth kinetics of the system, where by at lower seed loading the growth of crystals appears to be favoured. Eder *et al* [75], [237] showed in their study that increasing seed loadings resulted in decreased differences between the mean seed and product crystal sizes. This is attributed to the fact that more particles are introduced into the system which leads to increased competition to consume the same amount of supersaturation available.

Seeded Cooling Crystallisation Experiments Using IPA: Figure 4.11 shows the time diagram for the seeding cooling crystallisation of PCM from IPA. The MSMPR was seeded periodically as opposed to once at the beginning to avoid washing out issues and uncontrolled secondary nucleation. Preliminary MSMPR experimental runs showed that the amount of crystals obtained from IPA solvent was greater, due to the higher solubility of PCM in this solvent compared to water. Furthermore, the CQA of the product crystals were much better for crystallisations from IPA, evidenced from the presence of fewer aggregates and more uniformly shaped and sized crystals in spite of the poor quality seed used. It was evident that the single-stage MSMPR required optimisation of the seed addition method, based on experience from the experiments carried out in water.

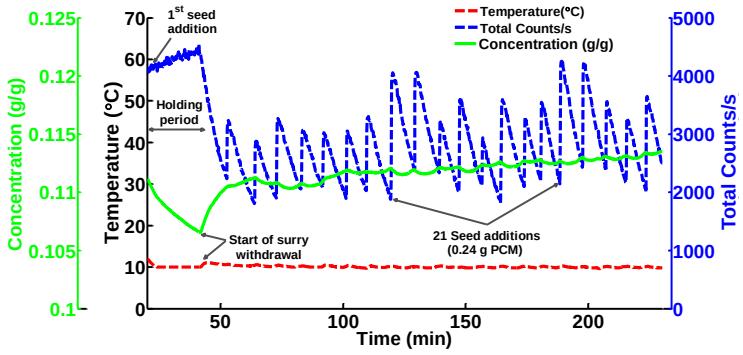

Figure 4.11: Time diagram showing the change in temperature, ATR-UV/vis concentration and FBRM counts/s for the seeded cooling crystallisation of paracetamol from IPA.

Figure 4.11 shows that manual periodic seed addition results in several spikes in the FBRM counts, and more minor fluctuations in the concentration, whilst the temperature remains constant. However, the change in concentration recorded from the second seed addition to the end of the experiment was ~ 2.66 %, although there is a slight increasing trend. This was a promising result, which indicated that the system may have achieved steady-state if the experiment was continued for a longer period, but this was not possible due to a limited supply of material. As intimated earlier, many published studies on MSMPR crystallisation have relied FBRM statistics [8], [13], [110], [152], periodic concentration measurement [19], [24], [53] and the yield of crystallisation [8], [13] to characterise steady-state behaviour. However, there are very few studies that have reported on real-time monitoring of concentration in the MSMPR coupled with particle monitoring techniques to determine the exact time to steady-state. In this study, it is clear that steady-state FBRM counts/s and concentration were not attained. This was perhaps due to the intermittent addition of seed to the system. According to Johnson et al [60] seeding is not required at steady-state, because there is steady-state birth rate of nuclei. Therefore, it is likely that the intermittent addition of seed prevented the attainment of steady-state in the MSMPR. However, it was shown earlier for PCM crystallisation from water that the seeding once at start-up approach did not work and instead encouraged secondary nucleation and prevented the attainment of steady-state. It is likely that further optimisation of the intermittent seeding strategy could lead to steady-state operation. For example, the use of a larger seeded feed vessel could minimise the variations caused by intermittent addition. This strategy will be explored further in Chapter 5. Figure 4.12 shows the change in SWCLDs between seed additions from the 2nd to 22nd RT. The results show that the distributions overlap significantly from the 2nd to 15th RT. Further information can be drawn from the microscope images of the product crystals shown in Figure 4.13 (b). There is a significant amount of crystal growth observed from the initial seed crystals through to the 2nd RT(45.15 min) and 22nd RT (230 min) sample. The crystals are also less agglomerated and more uniform in size compared to the product crystals obtained for PCM crystallisation from water.

The overall assessment of the cooling crystallisation experiments in water and IPA is that the seed addition method requires further improvement for better crystallisation outcomes in terms of attainment of steady-state. Recent studies using single-stage MSMPR have relied on intermittent pumping of feed solution or suspension, and lengthy residence times to achieve desired crystal properties [8], [13], [19], [24]. The crystallisation times in many of these studies are similar to that achievable in batch crystallisers. The challenge therefore is to develop an MSMPR process that produces crystals of the desired CQA within a short time scale to reduce residence time burden, whilst also achieving representative and isokinetic product withdrawal.

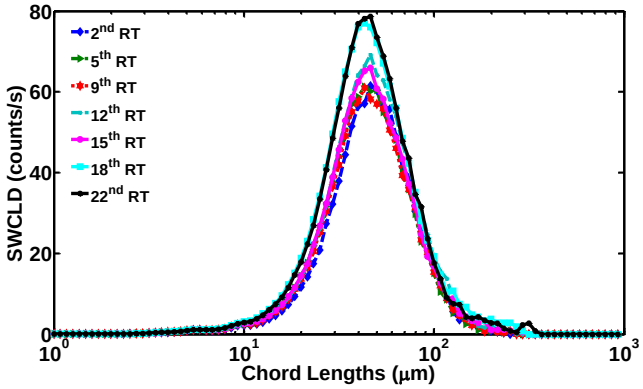

Figure 4.12: Evolution of SWCLD during the seed cooling crystallisation of PCM from IPA in a single-stage MSMPR.

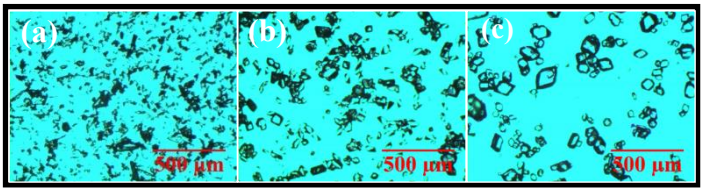

Figure 4.13: Microscope images of crystals (x4) of (a) seed material, (b) product crystals from the 2nd RT, and (c) 22nd RT.

Comparative Assessment of Batch and MSMPR Operations: In order to quantify the performance and efficiency of each crystallisation process reported in this study, the fractional yield (Eqn. 4.2) and productivity of crystallisation (Eqn. 4.4) were calculated.

$$Productivity\ of\ Crystallisation = \frac{Mass\ of\ Product\ Recovered}{Process\ Residence\ Time} \qquad 4.2$$

Note that for the fractional yield calculation of seeded crystallisation processes, c_o includes the seed contribution in addition to the initial solute concentration of feed solution. Table 4.5 provides a summary of the yield and productivity of crystallisation data for selected batch and continuous crystallisations. The data shows that while the yield of optimised LC and ADNC batch crystallisations are significantly high compared to the continuous MSMPR operated at steady-state (i.e., modified MSMPR with 0.05 wt% additive addition), the productivity of the latter is far superior. The steady-state MSMPR was ~ 16 times more productive than ANDC and ~ 5 times more productive than LC. Kim [238] reported productivity of crystallisation ~ 7 times greater than batch using a MSMPR crystalliser. Compared to the MSMPR, product crystals obtained from the LC runs show poor CQA due to variable crystal size and shape properties and broad CSD as shown in Figure 4.14 (a) and (b), respectively. The SWCLD plot

(Figure 4.14 (a)) confirm that larger mean crystal sizes are obtained from the batch ADNC experimental runs compared to the batch LC and continuous experimental runs, respectively. Although the SWCLD of the continuous crystallisation run is shifted towards smaller sizes, it is much narrower compared to all the batch experimental runs. It is also clear that the fast cooling batch LC run (Exp. No. 1a) produced much smaller particles when compared to the other experiments. In contrast, the slow cooling batch LC run (Exp. No. 2a) produced larger crystals, but the SWCLD is bimodal and significantly broadened. The microscope images (Figure 4.14 (b)) of crystals obtained from each of the experimental runs show good agreement with the SWCLD data.

Table 4.5: % Yield and volumetric productivity of batch and continuous crystallisations.

Exp. Type	Description	% Yield	Heating/ Cooling Rate (°C/min)	Residence Time (min)	Productivity of Crystallisation (g/L-min)
Batch LC	Exp. No 1a	98.5	1 / -1.0	187	0.8570
Batch LC	Exp. No 2a	95.7	1 / -0.5	240	0.6228
Batch ADNC	Exp. No. 3	95.0	0.4 / -0.2	625	0.2474
Batch ADNC	Exp. No. 6b	94.6	0.2 / -0.4	650	0.2366
Modified MSMPR	No Additive	98.8*	n/a	12.12	n/a*
Modified MSMPR	0.05 wt% HPMC	28.0	n/a	12.12	4.002
Conventional MSMPR	water; 3.5 % seed	88.6*	n/a	10.60	n/a*
Conventional MSMPR	water; 7.0 % seed	90.2*	n/a	10.60	n/a*
Conventional MSMPR	IPA; 0.5 % seed	18.6*	n/a	8.42	n/a*

n/a = not applicable; n/a* = not applicable due to unsteady state behaviour; * unsteady-state operation observed

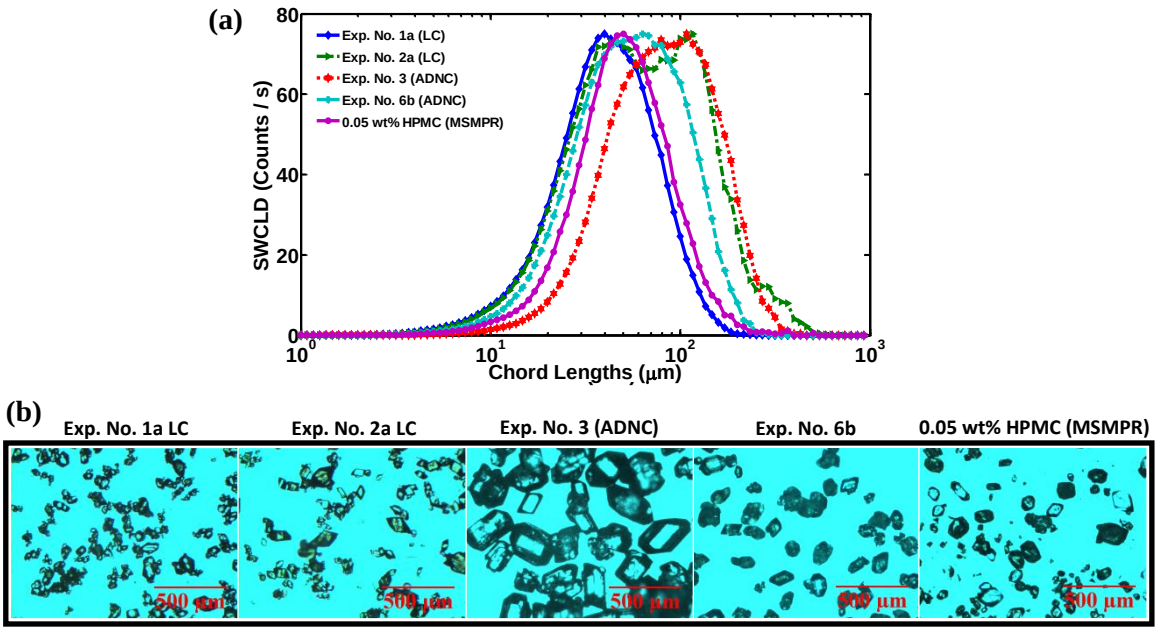

Figure 4.14: FBRM SWCLD measurements (a) and microscope images (b) Exp. No. 1a (LC), Exp. No. 2a (LC), Exp. No. 3 (ADNC), Exp. No. 6b (ADNC) and 0.05 wt% HPMC (MSMPR).

4.3.3 Continuous Crystallisation in Modified MSMPR

***Crystallisation in Modified MSMPR (No Additive)*:** Several challenges were encountered during the development stages of the continuous crystallisation apparatus: 1) particle settling and blockage of transfer lines, particularly at the peristaltic pump gears; 2) fouling and encrustation on the walls of the MSMPR and dip tube; and 3) fouling on PAT probes. These issues were mainly due to the narrow bore size of transfer lines (3 mm ID); low flow rate requirement to achieve long residence times leading to particle settling in product discharge lines; and operation of the MSMPR with a recirculation loop, which resulted in the creation of localised regions of high supersaturation, uncontrolled nucleation and eventually fouling and encrustation. The issues reported here have been encountered by several other investigators [13], [25], [32], but were largely avoided by using the modified MSMPR (Figure 4.1). However, fouling on the PAT probes and mild encrustation on the vessel walls persisted over prolonged operation. Figure 4.15 shows the process time diagram for a control experiment (no additive). The changes in temperature, FBRM counts/s and concentration are shown.

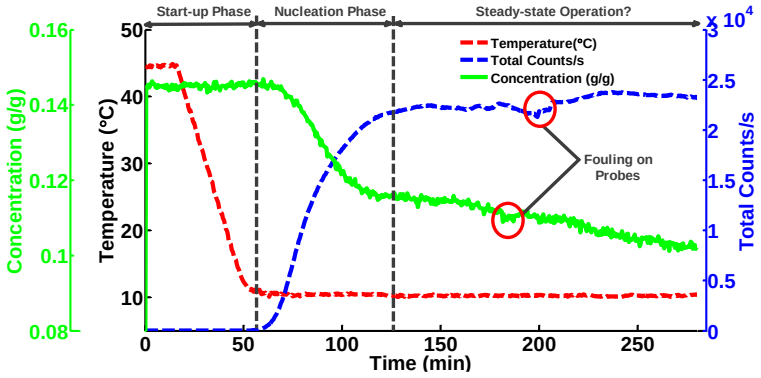

Figure 4.15: Time diagram showing temperature, FBRM counts/s and Raman concentration measurements obtained from the modified MSMPR.

Points during the process where fouling was detected on the PAT probes are indicated by circles. Periodic cleaning of the probes was necessary when to avoid the recording of erroneous results, a practice not often reported in the literature. The start-up phase is indicated as the initial period prior to nucleation. The nucleation phase and region of controlled operation (i.e. steady-state) are also indicated. The crystallisation proceeded without any washout issues, which are often reported in the literature [78]. This is attributed to the start-up method employed that was described in Section 4.2.2. During the nucleation phase there is rapid increase in FBRM counts/s; this dynamic state of the system leads to varied size distributions with time as confirmed by the SWCLD data shown in Figure 4.16 (a). After ~ 127 min (6th RT onwards) the FBRM counts stabilise and the system appears to arrives at a steady-state mean particle size and CSD. This is confirmed by overlapping of the SWCLD from the 6th to 18th RT onwards as shown in Figure 4.16 (b). The Raman concentration data (Figure 4.15) paints a different picture of the process when compared to the SWCLD data. There is a decreasing trend from the onset of nucleation (0.153 g PCM / g IPA) to the end of the experiment (0.089 g PCM/ g IPA). The ATR-UV/vis data also indicated that the concentration was decreasing over the period (Figure 4.17). Figure 4.17 shows the phase diagram of the process with the trajectory of concentration change. At the point of intersection with the indicative metastable curve, nucleation is observed. The final recorded concentration of the process indicated with a dot/arrow is close to the solubility curve, indicating that available supersaturation is almost completely depleted. The FBRM counts/s appear to show steady-state behaviour until a fouling event was detected at approximately 200 min (Figure 4.15). Following a cleaning procedure, an apparent drift from steady-state can clearly be observed, which complements the decrease in Raman concentration and is a further indication that the system is not at steady-state as suggested by the FBRM SWCLD measurements shown in Figure 4.16.

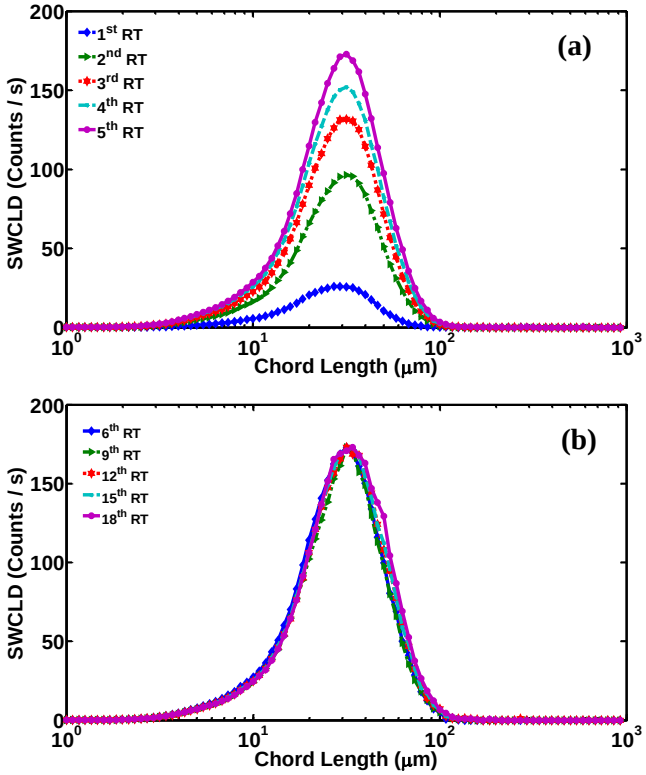

Figure 4.16: Evolution of SWCLD: (a) dynamic state of change in the MSMPR (1st to 5th RT); and (b) steady-state operation of the MSMPR (6th to 18th RT).

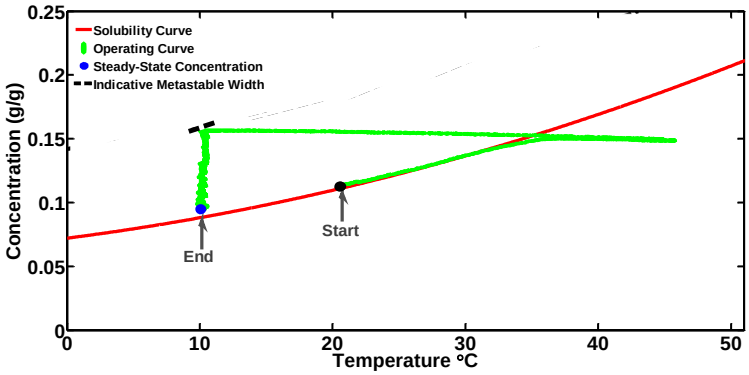

Figure 4.17: Phase diagram showing solubility and operating curves and indicative metastable width as displayed in CryPRINS. Initial (Start) and final (End) recorded concentrations are indicated by dots/arrows.

Raman and ATR-UV/vis with their respective multivariate calibration models gave similar concentration measurements. The concentration data from both methods (Figures 4.15 and 4.17) indicated that the system was in a dynamic state of change and that steady-state had not been attained. This is an important observation, since many recent studies on the subject of continuous crystallisation monitoring characterised steady-state by relying solely on FBRM [8], [20], [32], [77], [85], [110] and/or imaging techniques (for example, low angle light scattering (LALLS) and PVM[77], [78]) or “calibration free” spectroscopy approaches [32].

Arguably, real-time determination of concentration using multivariate models supported by on-line particle measurements provides a more robust measure of steady-state operation, as opposed to just tracking changes in FBRM statistics, or using 'calibration-free' methods. Since these are qualitative measures, they may not reliably determine the attainment of steady-state operation. In some studies, off-line concentration measurements [8], [21], [24] or gravimetric mass balance analysis and/or off-line particle size analysis[13], [225] [63] are used to determine steady-state operation. These methods are not only laborious, but prone to error due to the amount of sample handing involved. Furthermore, losses often occur during the sample filtration step. The use of PAT with multivariate models, as demonstrated here provides a robust approach for characterising the MSMPR operation in addition to using FBRM, and PVM technologies. Potentially, other image analysis techniques such as bulk video imaging (BVI) [239], [240] or endoscopy-stroboscopy [153] in concert with multivariate image analysis methods could replace PVM to provide more useful information for further process characterisation, in particular, of nucleation and growth phenomena. The advantages of multivariate methods is well documented for batch processes [141], [213], [241], however, the application in continuous processing remains limited.

Crystallisation in Modified MSMPR (HPMC Additive): Although many of the challenges encountered during the development stages of the MSMPR were alleviated by employing the modified configuration (Figure 4.1), problems persisted with fouling and mild encrustation in the MSMPR. The use of additive was therefore explored as a means of eliminating these problems. In a study on the effect of different polymers on the crystallisation of PCM from aqueous solutions Wen *et al* [242] showed that HPMC inhibited nucleation and growth to a significant degree by adsorbing on to the (010) face of monoclinic form I crystals. It was thought that HPMC developed hydrogen-bonding interactions with PCM crystals in the direction of the *a*-axis on the (010) face, thereby disrupting the surface diffusion of PCM molecules in this direction and changing the etching patterns on the crystal surface. HPMC was therefore seen as a variable additive to use for controlling PCM crystallisation and thereby prevent fouling and encrustation in the MSMPR. Figure 4.18 shows the process time diagram for the 0.05% HPMC continuous crystallisation experiment. The start-up phase was extended due to the presence of HPMC, when compared to the control experiment that was evaluated earlier. Following this is the nucleation phase where the FBRM counts/s increases rapidly with simultaneous depletion of concentration. The maximum FBRM counts/s attained in the nucleation phase was about 2,660 counts/s, which is almost an order of magnitude lower compared to the maximum value of 23,800 counts/s recorded during the control experiment (see Figure 4.15).

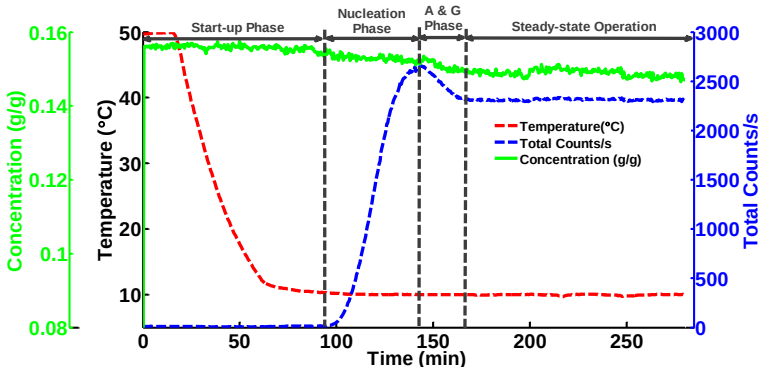

Figure 4.18: Time diagram showing temperature, FBRM counts/s and Raman concentration measurements obtained from the modified MSMPR. Start-up, nucleation, agglomeration and growth (A & G) phases and region of steady-state operation are indicated.

Figure 4.18 indicates that HPMC not only delays the onset of nucleation in the system, but also suppresses it significantly. These observations corroborate findings from previous studies [242]–[244] on HPMC suppression of PCM nucleation. The "A & G phase" as show in Figure 4.18 refers to a period when there is both agglomeration (A) and/or growth (G) taking place, indicated by a decrease in FBRM counts/s and corresponding decrease in concentration. Following the A & G phase, the system achieves steady-state whereby the FBRM counts and solute concentration are stabilised and remain constant for the duration of the experiment. Compared to the control experiment with no additive added (Figure 4.15), the change in concentration when nucleation occurs is small, a further confirmation that HPMC is suppressing nuclei formation. The concentration decreased gradually from start-up from the level of 0.156 to 0.150 g PCM/ g IPA after 154 min. The steady-state concentration (0.147 g PCM/ g IPA) was reached after ~ 170 min and was maintained at that level until the end of the experiment. The FBRM SWCLD also confirmed steady-state operation was attained as shown in Figure 4.19 (a) and (b) (1st to 15th RT). The significant overlap of the distributions between the 6th and 15th RT is an indication of steady-state.

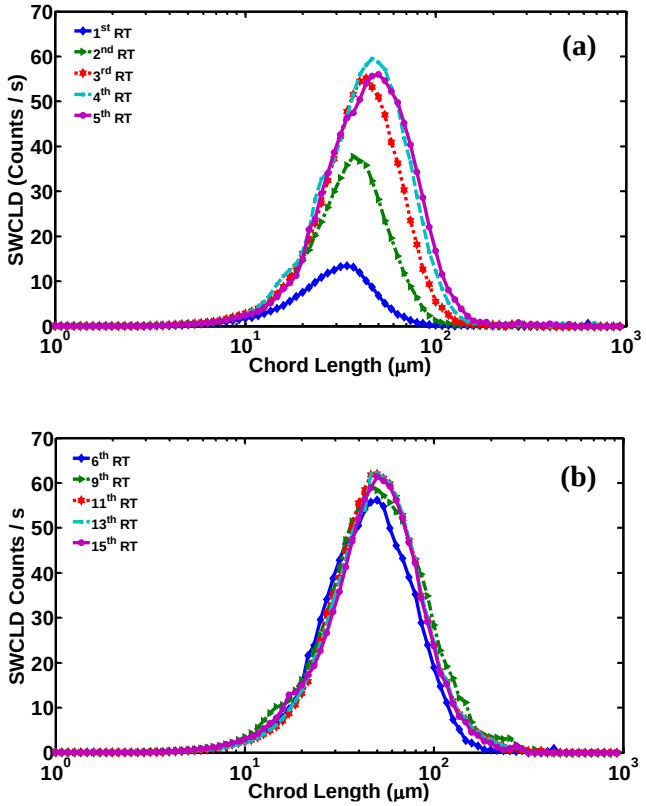

Figure 4.19: Evolution of SWCLD showing: (a) dynamic state of change in the MSMPR (1st to 5th RT); and (b) steady-state operation of the MSMPR (6th to 15th RT).

Figure 4.20 shows the phase diagram of the process, indicating the region of steady-state operation. Compared to the control experiment, the level of supersaturation remains quite high (S = 1.015 control; S = 1.665 HPMC at 0.05 %), confirming the effect of HPMC on the nucleation suppression [242], [243]. Due to the dramatic effect of 0.05 wt% HPMC on the delay and suppression of PCM nucleation, further investigations were conducted at lower concentrations (0.001 and 0.003 wt%). Table 4.5 gives a summary of the results from all experiments carried out using the modified MSMPR. The supersaturation (S) as reported is defined as c_i/c^*. The data shows that there is a direct correlation between HPMC concentration in the system and induction time. Conversely, and as expected, there is an inverse correlation between HPMC concentration and FBRM counts/s data and fractional yield (Y) of crystallisation.

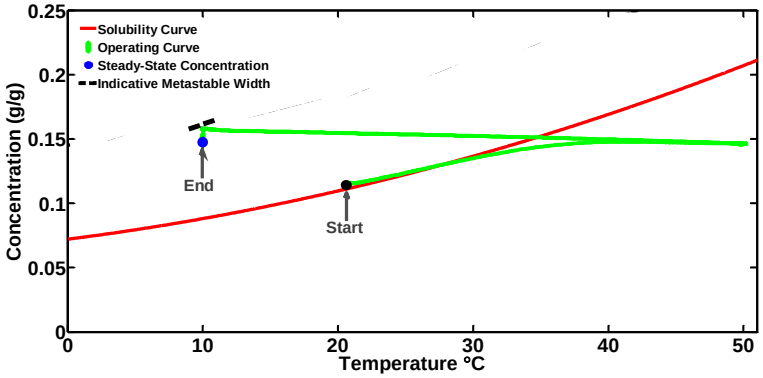

Figure 4.20: Phase diagram showing solubility and operating curves and indicative metastable width as displayed in CryPRINS. Initial (Start) and final (End) recorded concentrations are indicated by arrows/dots.

Eqn. 4.3 shows the formula used to calculate the Y. The fractional yield represents the amount of product obtained from each crystallisation process relative to the amount of available supersaturation, and is described as:

$$Y = \frac{c_o - c_i}{c_o - c_i^*} \times 100 \qquad 4.3$$

where c_o , c_i , and c^*, and are respectively, the dissolver/feed stream concentration (g PCM / g IPA), MSMPR steady-state concentration, and equilibrium concentration at the specified operating temperature, respectively. The data presented in Table 1 shows there is a direct correlation between the HPMC concentration and the level of supersaturation at which the MSMPR operates. Steady-state was not observed for either the 0.001 or 0.003 wt% HPMC additive experiments, due to the persistence of fouling and encrustation problems.

Table 4.6: Summary of experimental results showing the effect of HPMC additive on the continuous cooling crystallisation of PCM.

HPMC (wt%)	Induction time: from the onset of cooling (min)	Nucleation Phase Max. FBRM (counts/s)	Fractional Yield of Crystallisation (%)	Supersaturation (c_i/c^*)
0	58	23800	98.8	1.015
0.001	59	15119	56.6	1.314
0.003	64	7146	40.7	1.536
0.050	97	2656	28.0	1.665

Characterisation of Crystal Properties from FBRM Statistics and Image Analysis: CQA of product crystals obtained from the modified MSMPR crystalliser were investigated further using FBRM statistical trends, real-time PVM and off-line microscope image analysis. Figure 4.21 (a) to (d) provides a comparison between the FBRM statistical trends for the control and 0.05%

HPMC additive experiments. These time diagrams show the fraction of total counts/s for each size range. In the early stages of each experiment, just following the onset of nucleation, the 1 – 5 and 6 – 25 µm size fractions accounted for greater than 90 % of the total counts/s. However, as growth becomes the dominant crystallisation mechanism, a large reduction in the smaller size fractions for the 0.05 % HPMC experiment is observed. This compares to a much smaller reduction in the amount of fine crystals for the control experiment.

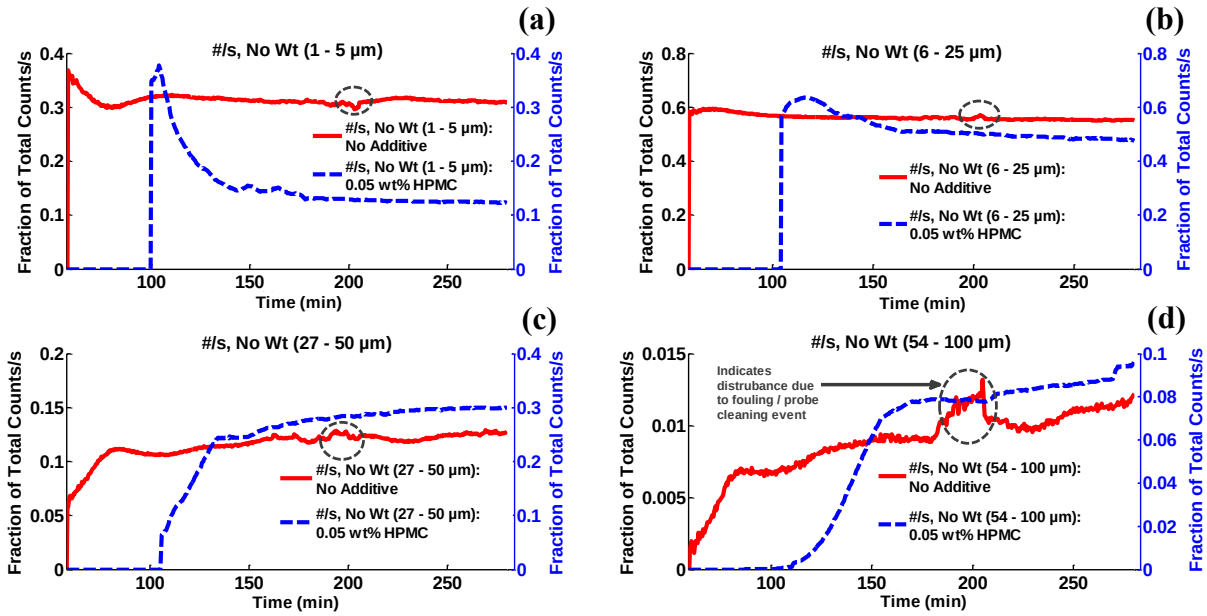

Figure 4.21: FBRM statistics showing the fraction of particle counts/s for a range of size fractions for the modified MSMPR control (No Additive) and 0.05 wt% HPMC experiments, respectively: (a). No weighted counts/s 1 – 5 µm; (b). No weighted counts/s 6 – 25 µm; (c). No weighted counts/s 27 – 50 µm; and (d). No weighted counts/s 54 – 100 µm.

The contribution of each size fraction to the CSD as the system approaches steady-state operation provides further evidence of the effect of HPMC on the suppression of nucleation and subsequent growth of crystals. Figure 4.21 (a) further indicates that the 1 – 5 µm size fraction contributes only a small amount (~ 13.1 %) to the total counts/s for the 0.05 wt% HPMC experiment. This compares to a much larger contribution (~ 31.3 %) to the total counts/s from crystals in the same size range for the control experiment. The 6 – 25 µm fraction contribution to the total counts/s for the control and 0.05 wt% HPMC additive experiments were similar (~ 55 % and 50 % respectively). The 27 – 50 µm and 54 – 100 µm fractions combined contributed ~ 35.3 % to the steady-state total counts/s for the 0.05 wt% HPMC experiment, while the contribution was only 13.7 % for the control experiment. These results indicate that whilst HPMC is suppressing nucleation to a significant degree and much larger product crystals are obtained compared to the control experiment. It is likely that due to the severe suppression of nucleation, the few crystals present in the system have less competition

for solute molecules and thus can grow larger. However, it is likely that the rate of growth of these crystals is also suppressed. Therefore, the overall deduction is that HPMC suppresses the nucleation, as well as growth kinetics of PCM. Femi-Oyewo and Spring [243] studied the effect of HPMC and other additives on PCM crystallisation from aqueous solutions and reported a high degree of nucleation and crystal growth inhibition. In this study, 'microcrystals' with low yield were observed. The investigators reported crystal size reduction from 4.28 mm (length) without HPMC addition (control) to between 0.3 and 0.42 mm (length) when HPMC additive in the concentration range 0.1 – 0.7 wt% was used. In these studies, the effect of HPMC on the product crystal size is rather dramatic compared to the results reported here. However, this is not surprising given the much higher concentrations that were employed in aqueous solution. Trends of the FBRM mean square weighted chord length (MSWCL) statistic shown in Figure 4.22, provide further evidence that larger product crystals are obtained from the 0.05 wt% HPMC experiment compared to the control experiment. The mean size of crystals at the end of the control experiment was 35.2 µm, which compares to 60.6 µm for the 0.05 wt% HPMC experiment.

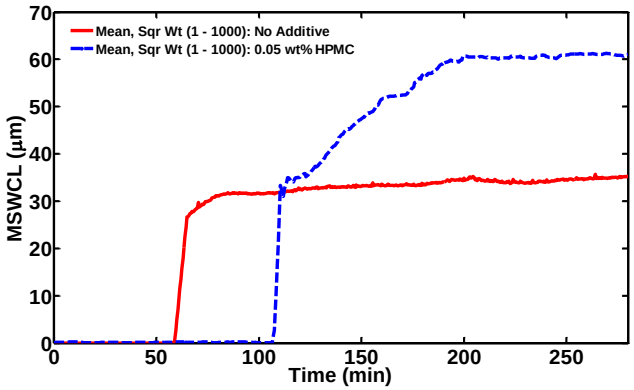

Figure 4.22: Real-time FBRM mean square weighted chord length (MSWCL) trends for the 0.05 wt% HPMC and control (No Additive) experiments respectively.

Real-time PVM images also indicate that there are larger crystals for the 0.05 wt% HPMC experiment relative to the control experiment. Figure 4.23 (a) shows the change in appearance of crystals from the onset of nucleation (~ 58 min) to the end of the control experiment. There is a rapid increase in the number of crystals up to 130 min, after which the PVM probe has become saturated due to the high particle density. On the other hand, Figure 4.23 (b) shows the change in crystal properties captured by PVM from the onset of nucleation (~ 97 min) to the end of the 0.05 wt% HPMC experiment. These crystals are clearly larger than those from the control experiment. PVM also indicated that steady-state was achieved from 170 min onwards, since the crystals are of similar size and shape. Figure 4.24 (a) and (b) show microscope images of samples taken from the control and 0.05 wt% HPMC experiments. The

differences in product crystal CQA between the two experimental runs can be more clearly identified. Comparatively, the crystals obtained from the 0.05 wt% HPMC run are significantly larger than those from the control run. It is also evident that the crystals are predominantly of a tabular habit with smoother edges, an indication that HPMC may be affecting the growth rate to a different degree on each crystal face.

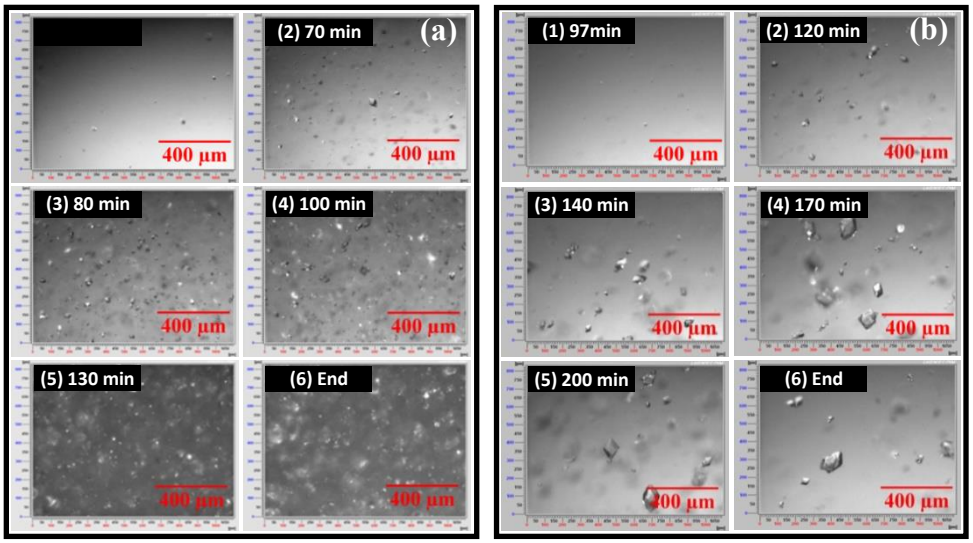

Figure 4.23: PVM images captured during: (a) the control experiment (No Additive), and (b) the 0.05 wt% HPMC additive experiment.

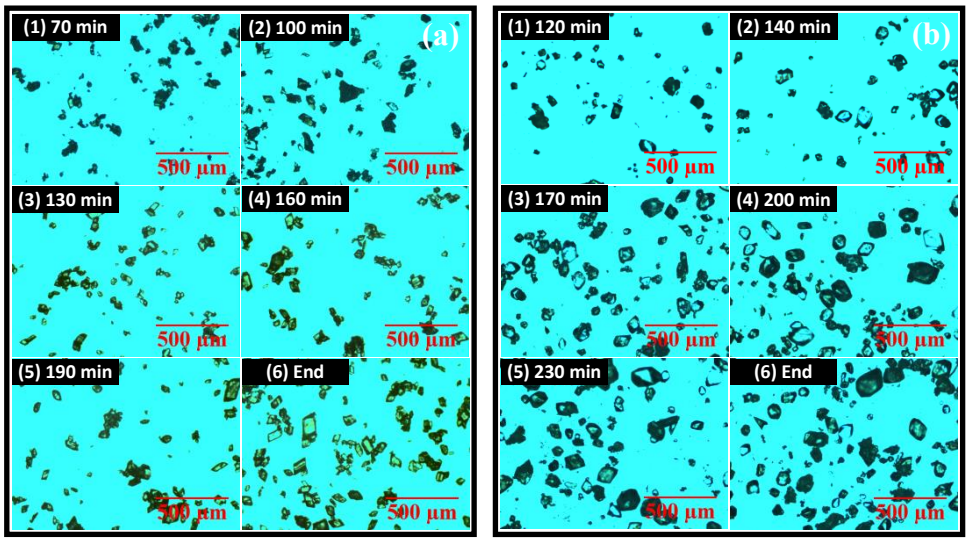

Figure 4.24: Offline microscope images of samples taken from the continuous crystallisation experiments: (a) control experiment and (b) 0.05 wt% HPMC.

The effect of additives on crystal growth and morphology is well documented in the literature [245]–[247]. Thompson et al [245] investigate the effect of structurally related additives on different crystal faces of form I PCM. They found that the growth of the (001) face, and hence the crystal morphology was affected to different extents by acetanilide and metacetamol

additives respectively, due to different interactions with the $NHCOCH_3$ and OH functional groups. It may be that at the applied concentration of HPMC, surface interactions that lead to suppression of growth on specific crystal faces occurs, leading to a subsequent change in the crystal habit. For the control experiment, the microscope images show crystals of several different habits, including, prismatic, tabular and cuboid morphologies. There is also evidence of agglomerated and twinned crystals present. Ristic *et al.* [248] examined the morphology of form I PCM crystals grown from aqueous solutions and concluded that the habit changes of PCM was due principally to changes in the growth mechanism of the (110) and (001) faces which exhibit markedly different growth rates at high and low supersaturations. Crystal growth was found to be dominant on the (110) face at low supersaturations, which gave way to increasing dominance of the (001) as the supersaturation increased. At low supersaturations (<10%) crystals exhibiting a columnar or prismatic morphology elongated along the (001) axis, while at high supersaturations (>15%) crystals of a tabular morphology were reported. Wen *et al* [242], [249] later showed that the mechanism of HPMC effect on PCM morphology was via hydrogen bonding interactions. It is likely that HPMC interacts differently with PCM on the different crystal faces at high and low supersaturations leading to the crystal control morphological evolution of PCM crystals. While these are interesting observations, investigation of those phenomena related to the crystal habit of PCM in the presence of HPMC were outside the scope of the study.

4.4 Conclusion

In this chapter, optimised batch and continuous crystallisation approaches were investigated under different operating conditions. Batch crystallisation of the model compound PCM from IPA solvent was investigated using two different control policies, LC and ADNC. As expected, the latter approach produced larger, uniform crystals with narrower CSD compared to the former, which showed more fines, agglomerates and broad CSD. However, although the crystallisation results were as expected, in the ADNC experiments, fewer temperature cycles and thus shorter batch times were observed when compared to results from Saleemi *et al* [170] with similar crystal CQA. It was initially conceived that the unusual outcome of the ADNC experiments reported here was due to the presence of impurities in the raw material used. HPLC-MS analyses on the PCM raw material sourced from the same manufacturer, but produce in several different countries showed different impurity profiles based on their origin. Further investigation of ADNC control policy using the different PCM raw materials revealed no clear link between the impurity profiles and the number of temperature cycles or the quality of the product crystals obtained.

The crystallisation of PCM was further investigated in a continuous MSMPR operation. These studies were carried out using either a modified MSMPR or a conventional MSMPR crystalliser. The modified MSMPR crystalliser configuration consisted of a dissolver/feed unit, in-line heat exchanger and recirculation loop was employed for the continuous cooling crystallisation of PCM. In this closed loop operation slurry is continuously dissolved and recycled/fed back to the MSMPR leading to the conservation of materials. The heat exchanger was able to minimise, but not completely eliminate fouling and encrustation at start-up, leading to prolonged operation. Furthermore, start-up of the MSMPR was achieved without any wash-out issues as is often reported in the literature[32], [78], since nuclei were generated by primary nucleation. Wash-out was avoided due to the start-up strategy employed, whereby material is circulated between the dissolver and MSMPR until nucleation is detected, as opposed to starting up with a suspension already in the MSMPR[77], [78]. Due to the persistence of fouling and encrustation issues over prolonged operation of the modified MSMPR, HPMC additive was explored as means of controlling the crystallisation and thereby preventing these problems. More stable operation of the MSMPR was observed in the presence of HPMC additive and steady-state was achieved more readily when compared to a control experiment. However, HPMC shows a significant effect on the suppression of PCM nucleation and crystal growth. In the presence of HPMC, the product crystals obtained were tabular shaped and of similar size. For the control experiment in which no HPMC was added, predominantly fine crystals with a range of different morphologies were obtained. A direct correlation was observed between HPMC concentration, induction time and MSMPR steady-state supersaturation, while an inverse relationship was found between HPMC concentration, the fractional yield and number of particles detected. The application of an IDS framework with integrated and ancillary PAT array, and informatics software CryPRINS tool were used to monitoring the MSMPR operation. Robust multivariate models were applied using Raman and ATR-UV/vis spectroscopy for solution concentration measurement. The application of multivariate methods for real-time monitoring of a continuous crystallisation process is rarely reported. Furthermore, Raman spectroscopy is rarely used in crystallisation to monitor solution phase concentration. The results further indicate that the combined use of PAT tools within the IDS framework can indicate when steady-state is achieved. The PAT array provides a more robust approach for characterisation of steady-state compared to the use of standalone PAT monitoring frameworks or ‘calibration-free’ approaches.

Due to the dramatic effect of HPMC on the suppression of PCM crystallisation in the modified MSMPR even at very low applied concentrations, another approach involving seeded cooling crystallisation in a conventional MSMPR crystalliser operated at low supersaturation was explored. In these studies, either water or IPA was used as solvent and different seeding

strategies were investigated. Steady-state was not achieved in any of the experimental runs conducted using water as solvent due to problems with aggregation of PCM during the crystallisation, leading to persistent fouling on the vessel walls and PAT probes and poor product crystal CQA. A secondary factor was the once-only seeding strategy employed at start-up, which meant that the system took a long time to achieve steady state due to wash-out issues. However, useful information was gained for further optimisation of the conventional MSMPR operation. According to Frawley *et al.* [237], the effect of seed loading and the mechanism of secondary nucleation is crucial to the successful operation of continuous crystallisers. For the cooling crystallisation of PCM from IPA a manual seeding policy was implemented whereby seed material was added to the MSMPR each RT, to avoid wash out in the initial stages of the operation and also to control the extent of secondary nucleation. Data acquired from each of the PAT tools employed to monitor the crystallisation show that the system experienced oscillations. In particular, the FBRM counts/s data showed the effect of the intermittent seed addition. However, the system appeared to have been close to achieving steady-state, which was supported by the ATR-UV/vis data, which showed that the concentration varied by no more than 2.66 % from the 1st RT to the end of the experiment. The product crystals obtained from this experiment were of better quality than previous experimental runs using water as solvent. Overall, the results from this experiment were promising, but optimisation of the seed addition method from intermittent manual addition to continuous addition may be necessary.

A comparison of batch crystallisation approaches with the conventional and modified MSMPR approaches was conducted. It was found that while the batch operations gave superior yield, the continuous crystallisation at steady-state lead to higher productivity of crystallisation. Furthermore, the product crystals obtained from the steady-state MSMPR had a narrower CSD compared to batch, although the mean crystal size was significantly smaller. Further work is required to optimise the single-stage MSMPR operation to achieve desired crystallisation outcomes, such as improved yields and better crystal properties in terms of size, shape and distribution. The results reported provide a better understanding of the parameters and operating procedures that influence the batch and continuous operations. The use of integrated PAT tools within an ISD framework with CryPRINS was very useful for real-time monitoring and control of the batch and continuous crystallisation operations. In addition, it gives an indication as to whether or not steady-state operation is achieved in the latter.

An overall assessment of the results presented so far in this Chapter indicate that steady-state MSMPR operation offers superior productivity, and much narrower CSD compared to optimised batch crystallisation processes, but suffers from low crystallisation yield. However,

a more useful comparison could have been made if steady-state operation was achieved in the majority of MSMPR experiments reported. The problems of encrustation, fouling and line blockage significantly hindered the MSMPR operation. Therefore, the design of an optimisation operation to overcome these challenges is critical. In Chapter 5 such an optimised MSMPR operation is proposed which could lead to significant improvements in continuous crystallisation outcomes in terms of attainment of steady-state or at least a controlled state of operation.

Chapter 5

Periodic Flow Crystallisation of Paracetamol: Example of a Slow Growing API

In Chapter 4 various operating strategies were explored for the crystallisation of paracetamol (PCM) with desired critical quality attributes (CQA) using continuous MSMPR operations. In this chapter, a novel concept involving periodic flow operation of a MSMPR is explored to achieve better control over the product CQA of PCM (a slow growing API) in IPA whilst avoiding the problems of fouling, encrustation, line blockage and limited residence time for crystal growth. The term periodic mixed suspension mixed product removal (PMSMPR) is used to describe the novel process reported here. A "state of controlled operation" in operation is attained in the system when the transient effects caused by the periodic operation (i.e. periodic, but controlled disruptions) are minimised such that consistent product CQAs are attained. This study further illustrates the concept of "state of controlled operation" (SCO) instead of "steady-state operation" as a state that can characterise a continuously or periodically operated process.

5.1 Introduction

During a periodic flow crystallisation controlled disruptions are applied to the inlet and outlet flow streams of an otherwise continuous MSMPR, either synchronously (viz. coupled addition and withdrawal) or asynchronously (viz. decoupled addition and withdrawal), with an aim to retain the slurry for a longer period in the crystalliser. In this way, the residence time distribution (RTD) can be manipulated by having a tuneable holding period within each periodic cycle, which, for example, is able to significantly increase the mean residence time for slow growing systems without broadening the crystal size distribution (CSD) too much. Unlike the idealised continuous MSMPR operation described by Randolph and Larson [9], [250], in which product slurry is continuously withdrawn and has exactly the same composition as the vessel, the PMSMPR operation is characterised by periodic transfer of slurry (addition and withdrawal) at high flow rates. Similar to a continuous MSMPR, the product withdrawn during the PMSMPR operation has exactly the same composition as the vessel at the time of withdrawal. The rapid transfer of slurry at high flow rates during the PMSMPR operation prevents particle sedimentation and transfer line blockages, and is more likely to lead to isokinetic product withdrawal. The transfer of slurry is followed by a holding (or pause) period when no addition or withdrawal of slurry to/from the crystalliser takes place, but the suspension continues to be agitated. Comparisons

of batch, continuous and periodic flow operations in a stirred tank crystalliser (STC) are summarised in Table 5.1.

Table 5.1: Comparison of batch, continuous and periodic flow operations in a stirred tank crystalliser (STC).

Stirred Tank Operation	System States	Remarks
Batch 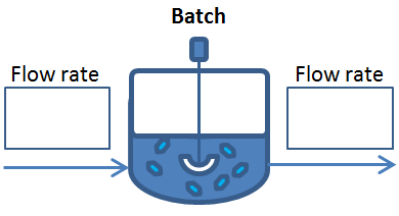	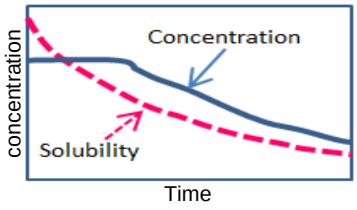	▪ Easy, flexible and universal ▪ Perfect control of residence time ▪ Accepted by regulators ▪ Batch-to-batch variations ▪ Low productivity ▪ Labour and cost intensive ▪ Significant inventory
Continuous 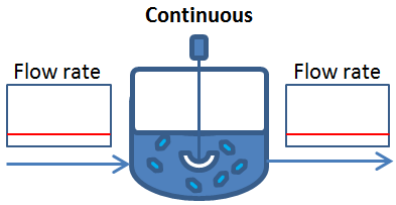	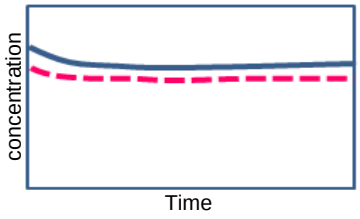	▪ Steady-state operation ▪ High productivity, but low yield ▪ Safe and agile ▪ Short mean residence time ▪ Broad RTD profiles ▪ Fouling and encrustation ▪ Transfer line blockage ▪ Resistance from industry
Periodic 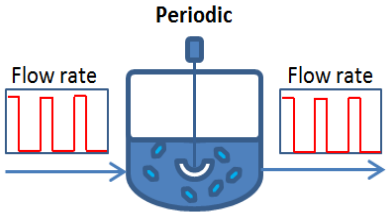	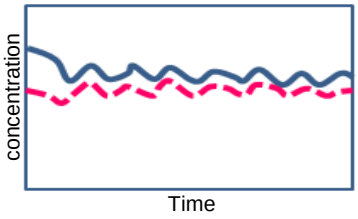	▪ Controlled state of operation ▪ High productivity and yield ▪ Hybrid of batch and continuous ▪ Improved control of RTD ▪ Broad RTD profiles, but better than continuous ▪ Reduced fouling, encrustation and transfer line blockages

A significant challenge associated with continuous crystallisation processes involves the generation of nuclei for later growth. Often seed nuclei are generated *in situ*, which demands high levels of supersaturation to encourage primary nucleation. The problem with this approach is that primary nucleation dominates the process at start-up and can ultimately lead to fouling on process equipment and encrustation problems. Furthermore, the preferential removal of fines and transfer line blockages are a common feature in continuous MSMPR operation due to the low flow rate and narrow transfer line requirements to achieve crystal growth, improve productivity and promote representative and isokinetic withdrawal of slurry. Preferential fines removal tends to occur due to the slower settling velocities and shorter response times of small crystals compared to larger crystals [25]. Furthermore, the varied properties of crystals represented by a given CSD in the MSMPR can lead to localised size distributions, in particular, where non-ideal mixing conditions predominate [25], [100]. Such classification phenomena ultimately lead to instabilities (i.e. oscillations) in the CSD, in which case high withdrawal velocities help to achieve representative sampling [25]. The effective control of slurry classification during withdrawal can lead to a narrower CSD with larger mean crystal size. A solution to the problems mentioned earlier is to operate the MSMPR at low supersaturation with

seed addition to encourage controlled secondary nucleation and growth. However, the limitation here is that the MSMPR productivity and yield are significantly reduced.

Periodic flow crystallisation is an alternative approach that could alleviate the problems typically encountered in continuous MSMPR operation. High productivity and yield of crystallisation could potentially be achieved by tuning the periodic addition, holding and withdrawal cycles of the periodic flow mixed suspension mixed product removal crystalliser (PMSMPR). Since there is direct control over the mean residence time of slurry in the PMSMPR crystalliser the CQA of product crystals can be better tuned to achieve desired specifications. For example, the mean residence time could be shortened or extended to control mean crystal size and CSD. The PMSMPR differs from MSMPR operation in that periodic disruptions are applied to the feed and product flow stream *viz* periodic shutting off of the transfer pumps for predefined time period. Effectively, the PMSMPR is a hybrid operation that combines the best aspects of the batch and continuous STC, respectively, that is, long mean residence time and flow of materials (albeit periodically) in a controlled state of operation. Additional benefits can be gained from the PMSMPR by using a multi-stage cascade of crystallisers to facilitate control over nucleation and growth mechanisms of the crystallisation, in particular for slow growing APIs, by carefully selecting the PMSMPR stage temperatures. The concept of periodic flow crystallisation demonstrated here is different from intermittent addition/withdrawal methods reported in the literature recently [32], [77], which involve the rapid addition/withdrawal of 10 % or less of the crystalliser volume every one tenth of the mean residence time. Such a strategy was developed to enable the isokinetic withdrawal of slurry, and prevent transfer line blockage in “continuous” MSMPR crystallisers some years ago [251]. In this study, the PMSMPR operation is demonstrated as proof of the period flow crystallisation concept for particle size control *viz*. the balance of growth and secondary nucleation for the model API system (PCM in IPA solvent). The PMSMPR crystalliser used in the study was configured and operated as a single- or multi-stage unit, and operated either with or without a recycle stream to determine the effect on product CSD during the crystallisations. Further aims were to determine the effect of seed properties (crystal size, shape and distribution) and supersaturation on the product CSD. During the process development stages feeding strategy, that is, constant versus intermittent feed supply was found to have an effect on the time to achieving a periodic steady-state operation (i.e. SCO) so these results are presented as a significant finding. The IDS framework described in Chapter 3 Section 3.6 was applied *viz*. CryPRINS and integrated array of PAT sensors (ATR-UV/vis, FBRM, PVM and Raman) to monitor and implement temperature control during the periodic flow crystallisations, and to determine when SCO was attained.

5.2 Experimental Methods

The cooling crystallisation of PCM from IPA in batch, continuous MSMPR and periodic flow PMSMPR crystallisers was investigated to provide a robust analysis of the different methods. Aspects related to seed properties (size, shape and CSD), seed loading, supersaturation, recycle and feed addition strategy were investigated. The aim is to demonstrate as a proof of concept study, the potential benefits of the periodic flow process in comparison to batch and continuous operations, respectively. The multivariate models used to determine solubility and concentration were reported in Chapter 3 Section 3.4.2. The experimental set-up used for the batch, continuous and period flow experiments were described in Chapter 3 Section 3.6. The impeller stirring rate for the experimental runs was set to 300 rpm with, power per unit volume as stated in Chapter 4 Section 4.2.

5.2.1. Seed Preparation

All crystallisation experiments reported were seeded. In order to determine the effect of seed properties (size and CSD) on the crystallisation outcomes for PCM, the seed crystals were prepared according to the following methods:

(1) Sieving raw material to within the size range 100 – 125 µm (referred to as “raw material seed”).
(2) Sieving recrystallised PCM to within the size range 75 – 125 µm (referred to as “recrystallised seed”.

Figure 5.1 shows the microscope images of PCM seed prepared from “raw material seed” (A) and “recrystallised seed” (B), respectively. The images clearly show the varied size and shape properties of the former compared to the latter. The recrystallised seed crystals were of better quality, showing more uniform size and shape crystals and fewer fines. For all experiments 2.5 % seed (relative to dissolved material) was used based on common industrial practice, whereby, between 0.1 and 10% seed loading is typically employed [155].

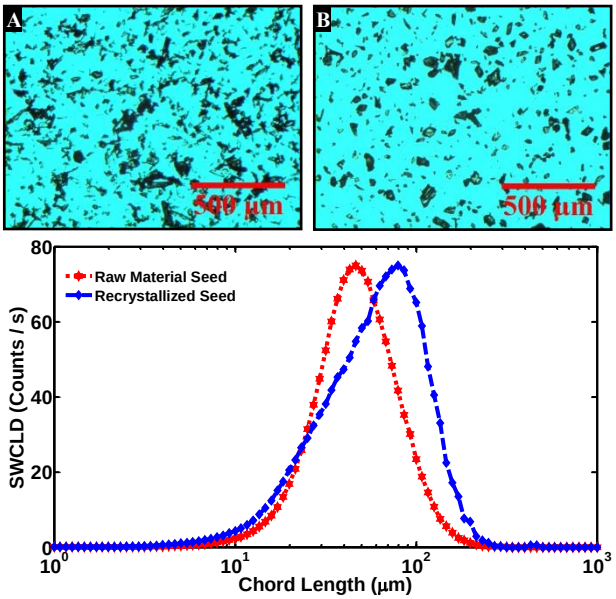

Figure 5.1: Top, microscope images of dry seed crystals used in the periodic flow crystallisation study: (A) “raw material seed” (100 – 125 µm fraction); and (B) “recrystallised” (75 – 125 µm fraction); Bottom, FBRM SWCLDs for raw material and recrystallised seed.

5.2.2. Periodic Flow Crystallisation Experiments

Periodic flow crystallisation experiments were carried out in single-stage, two-stage and three-stage PMSMPR crystalliser configurations. The PMSMPR can be operated in coupled or decoupled periodic flow mode. Figure 5.2 (a) and (b) provides schematic representations of the two different operating regimes, showing the change in operating volume with time. In the coupled operation, Figure 5.2 (a), the volume of the crystalliser remains unchanged due to simultaneous addition of feed and withdrawal of slurry. On the contrary, in the decoupled operation, Figure 5.2 (b), the volume of the crystalliser changes due to decoupling of the feed addition and slurry withdrawal cycles, providing an additional degree of freedom in operation compared to the coupled process. Additional benefits of the decoupled over the coupled periodic flow operation include, the ability to further extend the mean residence time of the PMSMPR, and minimise the amount of feed slurry to be directly washed out to the next stage, thus reducing the amount of fine crystals in the SCO product. In both the coupled and decoupled operations an adjustable holding or batch period is implemented in the PMSMPR to control the mean residence time of slurry inside the crystalliser. The batch operation cycle refers to that time period during which the pumps are switched off and there is no inflow of feed or outflow of slurry to/from the PMSMPR (coupled or decoupled). In this study, single-stage PMSMPR experiments were carried out in coupled operation mode. The operating volume of each single-stage PMSMPR was ~ 500 mL. Cascaded three-stage PMSMPR experiments were also performed, the operating volume of each stage was ~750 mL. The sum of the addition/withdrawal and batch

operation periods represents the periodic operation mean residence time (RT_{PO}) for each experimental run.

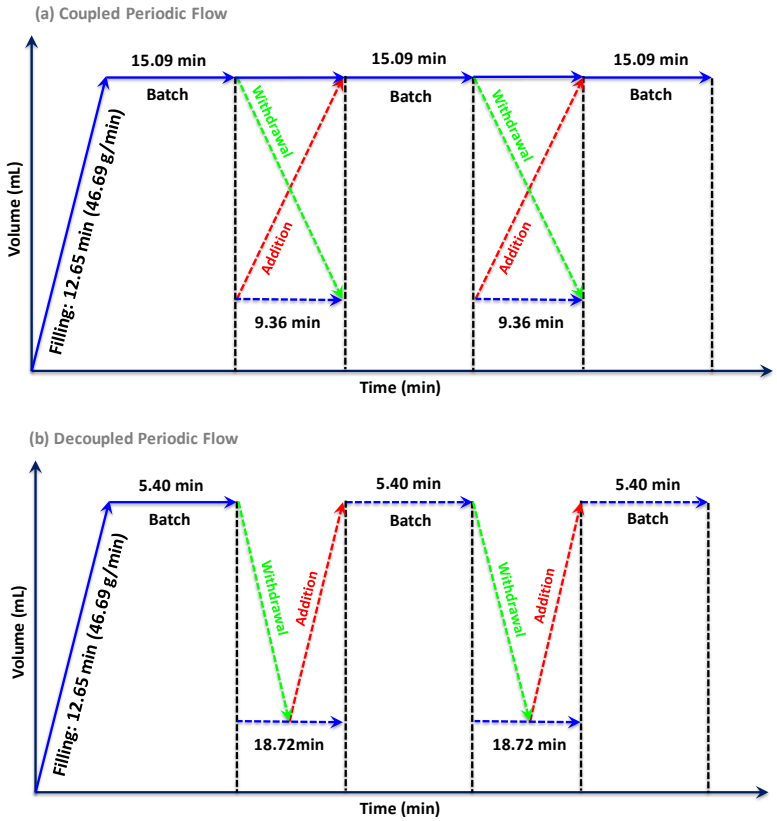

Figure 5.2: Schematic representations showing: (a) Coupled periodic flow operation of three-stage PMSMPR (constant operating volume); (b) Decoupled periodic flow operation of three-stage PMSMPR (variable operating volume due to asynchronous slurry addition and withdrawal at each stage).

The mean RT_{PO} of slurry in the single-stage PMSMPRs (coupled operations) was 20 min, corresponding to an addition/withdrawal cycle of 9.36 min, and holding cycle of 10.64 min. For the coupled three-stage PMSMPR operation (~750 mL per stage), the addition/withdrawal cycle (9.36 min) and holding cycle (15.09 min) led to a mean RT_{PO} of 24.45 min. In case of the de-coupled operation, the sum of the addition/withdrawal (18.72 min) and holding (5.40 min) cycles led to a mean RT_{PO} of 24.12 min. The RT_{PO} for the coupled operation was tuned to almost match that of the decoupled operation. In both operations, partial addition/withdrawal of 66.7 % of the PMSMPR (~ 500 mL) was implemented each cycle for all three stages. The decoupled operation had a shortened holding period of 5.40 min. Furthermore, due to the decoupling of the addition/withdrawal cycle, the pumping period was extended to 18.72 min (which corresponds to 9.36 min each for addition and subsequent withdrawal of material from each stage). Note that for the three stage PMSMPR operations, coupled and decoupled, 33.3 % (250 mL) of the crystalliser contents was retained each addition/withdrawal cycle, which would contribute a

further 4.68 min and 9.36 min, respectively to the mean RT_{PO}. However, for simplicity only the RT_{PO} of 500 mL operation has been considered. The overall aim of these studies is to demonstrate as proof of concept, the potential benefits of periodic flow cooling crystallisation using PMSMPR. Another important aim is to determine the experimental conditions that promote crystal growth and supress secondary nucleation in order to produce large crystals.

Periodic Flow Seeded Cooling Crystallisation in PMSMPR: The PMSMR unit, Chapter 3, Section 3.6.2, Figure 3.19 (a) was reconfigured as required to operate either as a single-stage or multi-stage cascade unit. Figure 5.3 shows the process flow diagrams of the single-stage PMSMPR configurations employed, and operated with and without recycle/dissolver stream, respectively. Also shown are the mass flow rates, Q (i.e. of slurry) employed as well as the operating temperature and supersaturation (*S*) for the feed and PMSMPR. *S* is the supersaturation ratio defined as c_o/c^*, where c_o is the initial solute concentration of the feed or PMSMPR and c^* is the equilibrium concentration at the specified operating temperature. For the feed stream, either a 1 L or 5 L vessel was used to deliver seeded saturated feed suspension to the first-stage PMSMPR. Masterflex® pumps operating in time dispense mode and platinum cured tubing (3.1 mm ID) were used for suspension transfer between vessels and from the PMSMPR to the filtration unit.

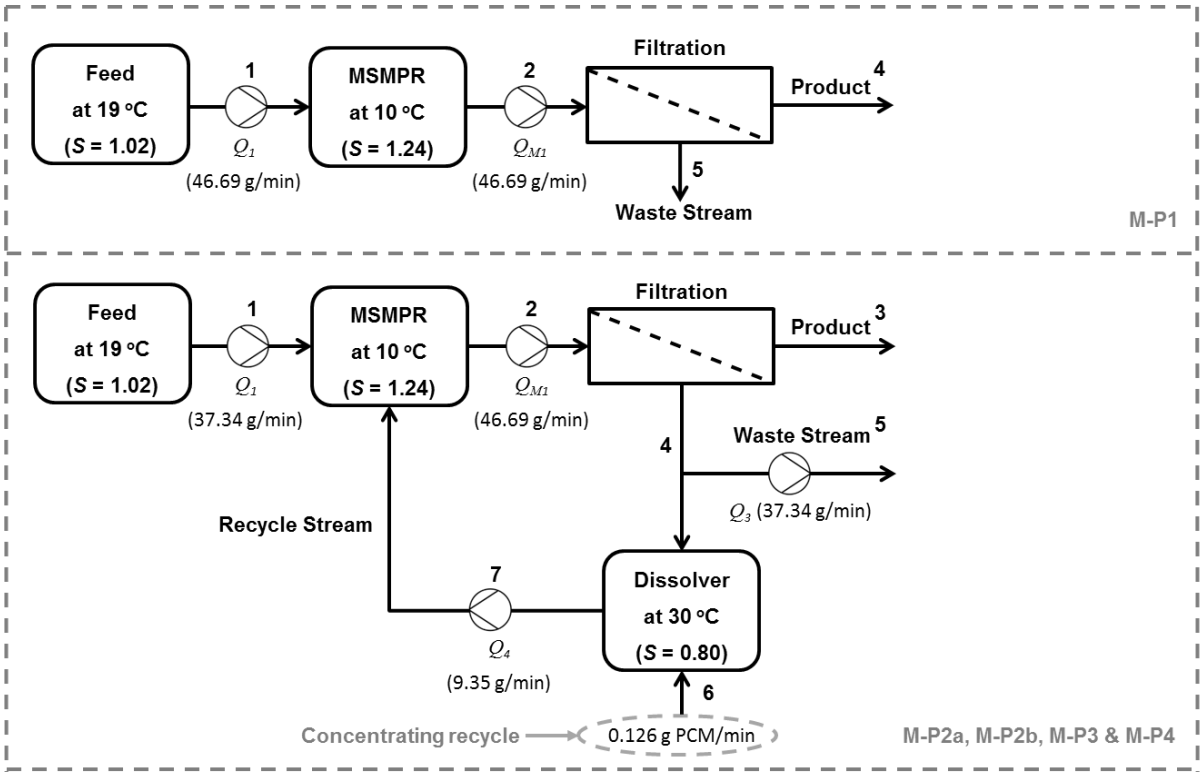

Figure 5.3: Flow diagrams showing the configuration of the single-stage PMSMPR units used for the periodic flow crystallisation studies. The PMSMPR was operated either without recycle stream (M-P1); or with recycle stream (M-P2a, M-P2b, M-P3 and M-P4).

Experimental Conditions for Batch and PMSMPR Crystallisations: Table 5.2 gives a detailed summary of the experimental conditions used for each of the batch and PMSMPR (single- and two-stage) cooling crystallisation experiments conducted during the study. Recycle ratio (Q4/ Q1) was set to 0.25 during the study to avoid significant dilution of the system and prevent impurity build-up that can occur for total recycle.

Table 5.2: Summary of experimental conditions used for the cooling crystallisation of PCM in the in singe- and two-stage PMSMPR and batch crystallisers.

Experimental Conditions	M-P1	M-P2a	M-P2b	M-P3	M-P4	M-P5	M-PC	M-PD	B-C1
Mode of operation	cp/no	cp/ncr	cp/ncr	cp/ncr	cp/cr	cp/no	cp/no	dc/no	n/a
Feed temp. (°C)	19	19	19	19	19	19	19	19	n/a
PMSMPR temp. (°C)	10	10	10	10	10	(15; 10)*	(17; 14; 10)*	(17; 14; 10)*	n/a
Dissolver temp. (°C)	n/a	30	30	30	30	n/a	n/a	n/a	n/a
Feed conc. (g/g)	0.110	0.112	0.110	0.111	0.111	0.110	0.111	0.111	n/a
Seed loading (%): raw material seed+	n/a	2.5	2.5	n/a	n/a	n/a	n/a	n/a	n/a
Seed loading (%): recrystallised seed++	2.5	n/a	n/a	2.5	2.5	2.5	2.5	2.5	2.5
Flow rate: feed stream, Q_1 (g/min)	46.69	37.34	37.34	37.34	37.34	46.69	46.69	46.69	n/a
Flow rate: MSMPR1 outlet, Q_{M1} (g/min)	46.69	46.69	46.69	46.69	46.69	46.69	46.69	46.69	n/a
Flow rate at MSMPR2 outlet, Q_{M2} (g/min)	n/a	n/a	n/a	n/a	n/a	46.69	46.69	46.69	n/a
Flow rate at MSMPR3 outlet, Q_{M3} (g/min)	n/a	n/a	n/a	n/a	n/a	n/a	46.69	46.69	n/a
Flow rate of recycle stream, Q_4 (g/min)	n/a	9.35	9.35	9.35	9.35	n/a	n/a	n/a	n/a
Recycle ratio (Q_4/ Q_1)	n/a	0.25	0.25	0.25	0.25	n/a	n/a	n/a	n/a
Addition and withdrawal period (min)	9.36	9.36	9.36	9.36	9.36	9.36	9.36	18.72	n/a
Holding period (min)	10.64	10.64	10.64	10.64	10.64	10.64	15.09	5.40	n/a
Mean residence time (min)	20	20	20	20	20	40	73.35	72.36	423
tube size (mm ID)	3.1	3.1	3.1	3.1	3.1	3.1	3.1	3.1	n/a
No. of PMSMPR stages	1	1	1	1	1	2	3	3	n/a
Seed type	recry	raw	raw	recry	recry	recry	recry	recry	recry

()*Temperature of 1st, 2nd and 3rd stage PMSMPR respectively; +100 – 125 µm raw fraction; and ++75 – 125 µm fraction; cp = coupled operation; dc = decoupled operation; no = no recycle; ncr = non-concentrated recycle; cr = concentrated recycle; recry = 2.5 % recrystallised seed; and raw = 2.5 % raw material seed).

Crystallisation in Single-stage PMSMPR without Recycle (M-P1): The process flow diagram of the experimental set-up used for the single-stage PMSMPR experiment is shown in Figure 5.3 (M-P1). Prior to start-up a fresh feed solution saturated at 20 ^{o}C (0.110 ± 0.002 g PCM/g IPA) was prepared in the feed vessel. The feed solution was then cooled to 19 ^{o}C, seeded with 2.5 % (11.19 g) "recrystallised seed" and held for 30 min to give the crystals time to heal by Ostwald ripening [252]. The supersaturation of the feed stream to the PMSMPR was 1.02. At start-up the single-stage PMSMPR was cooled to 10 °C, thereafter, feed suspension was added to give a SCO operating volume of 500 mL. This was then followed by a holding period of 10.64 min (batch period). Thereafter, a period of simultaneous addition of feed (at a rate of 46.69 g/min) to, and withdrawal of slurry (at a rate of 46.69 g/min) from the PMSMPR was initiated for a period of 9.36 min (continuous period). The slurry withdrawn from the PMSMPR was filtered and the product crystals collected and dried at 40 ^{o}C for 24 hours. The periodic addition/withdrawal and holding cycles were continued for the duration of the experiment. The holding cycle refers to that time period during which the pumps are switched off and there is no net inflow of feed or outflow of slurry to or from the PMSMPR. The sum of the addition/withdrawal time period (9.36 min) and the holding period (10.64 min) is defined as the mean RT_{PO} of the single-stage PMSMPR (20 min).

Single-stage PMSMPR Crystallisation with Recycle (M-P2a, M-P2b, M-P3 & M-P4): For these experiments, the feed preparation and seeding procedure was the same as that described for the single-stage PMSMPR without recycle (M-P1). The purpose of these experiments was to determine the effect of having a recycle stream on the yield of crystallisation. The single-stage PMSMPR configurations with recycle M-P2a, M-P2b, M-P3 and M-P4 were operated as follows:

> *M-P2a and M-P2b*: seeded with "raw material seed" and operated with a non-concentrated recycle stream, that is, without the use of stream 6 as shown in Figure 5.2 (M-P2a) and (M-P2b).
>
> *M-P3:* seeded with "recrystallised seed" and operated with a non-concentrated recycle stream, that is, without the use of stream 6 as shown in Figure 5.3 (M-P3).
>
> *M-P4:* seeded with "recrystallised seed" and operated with a concentrated recycle stream, that is, using stream 6 as shown in Figure 5.3 (M-P4).

The start-up procedure for each single-stage PMSMPR operated with recycle stream was exactly the same as described earlier for experiments carried out without recycle. The slurry withdrawn from the PMSMPR each cycle was filtered rapidly and the filtrate solution added to

the recycle vessel, which was kept at 30 ^{o}C to dissolve any fines present. Once sufficient filtrate was collected, the periodic addition and withdrawal operation of the PMSMPR was continued, but with an adjustment of flow rate from the feed stream to the PMSMPR, that is, reducing from 46.69 to 37.34 g/min. This was done to compensate for the additional inlet flow from the recycle stream at a rate of 9.35 g/min. This resulted in a recycle ratio of 0.25 (i.e. Q_4/Q_1; based on Figure 5.3), which was selected to minimise too much impurity build-up in the crystalliser and also to avoid too much dilution when non-concentrated filtrate is used for recycle. The effect of recycle stream supersaturation level on the crystallisation outcome was investigated *viz*. two methods:

(1) Non-concentrated whereby filtrate solution was added directly to the PMSMPR after filtration and dissolution; and

(2) Concentrated whereby PCM raw material was added to the filtrate solution and dissolved to increase the concentration level to the equilibrium concentration of the feed stream.

The experiment with concentrated recycle (M-P4) was designed to investigate the effect on process yield. For this study, the filtrate liquor collected from the waste stream of the experiment carried out with non-concentrated recycle stream (M-P3) was weighed and the concentration determined by ATR-UV/vis (0.104 ± 0.001 g PCM/g IPA). The filtrate liquor was then concentrated to the equilibrium concentration of the feed stream liquor entering the PMSMPR. The overall rate of addition of PCM to the recycle stream was estimated at 0.126 g/min as shown in Figure 5.3. The concentrated recycle stream liquor was added to the PMSMPR at a rate of 9.35 g/min Overall, the operating principle of M-P2a, M-P2b and M-P4 was the same as described for M-P1.

Two-stage PMSMPR Crystallisation without Recycle (M-P5): Figure 5.4 shows the process flow diagram of the two-stage PMSMPR crystalliser set-up. The feed preparation and start-up procedure were similar to those employed for the coupled single-stage PMSMPR study without recycle (M-P1), except that an additional PMSMPR vessel was used and at start-up the first- and second-stage PMSMPR vessels were cooled to 15 and 10 ^{o}C, respectively. After filling and equilibration in the first-stage PMSMPR, the pumps from the feed vessel to the first-stage and from the first-stage to the second-stage PMSMPR were switched on simultaneously for 9.36 min This procedure allowed sufficient time for one working volume of the first-stage to be transferred to the second stage. Following this, there was a holding period (10.64 min). Thereafter, the pumps for all transfer lines were operated periodically over the time intervals mentioned earlier, until the end of the experiment (i.e. coupled operation). Slurry withdrawn

from the second-stage PMSMPR vessel each period was filtered and the crystals collected and dried for off-line microscope image analysis. The sum of the addition/withdrawal time period (9.36 min) and the holding period (10.64 min) for each stage of the two-stage PMSMPR is defined as the mean RT_{PO}, which is 40 min

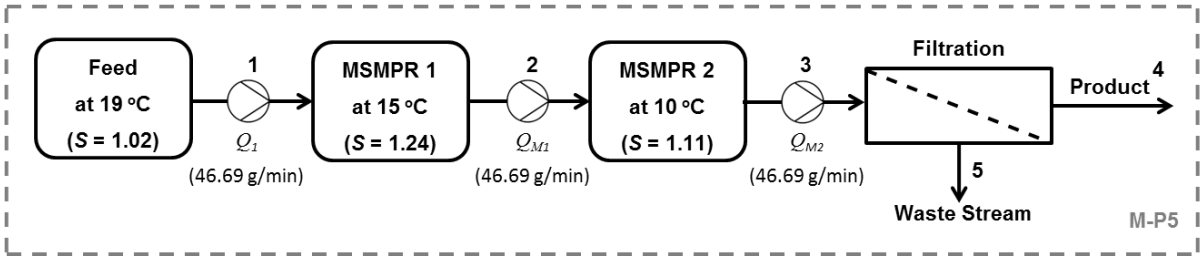

Figure 5.4: Flow diagram showing the block configurations of the two-stage PMSMPR unit used for periodic flow crystallisation studies without recycle stream (M-P5).

Three-stage PMSMPR Crystallisation Coupled and De-Coupled Periodic Flow Operations (M-PC and M-PD): Figure 5.5 shows the process flow diagram of the three-stage PMSMPR crystalliser set-up used for the coupled (M-PC) and de-coupled (M-PD) experimental runs, respectively. A description of the addition/withdrawal and holding cycles implemented was provided earlier. For the coupled PMSMPR operation the start-up and operating procedure was the same as employed for the two-stage process described earlier, but with an additional process stage and different temperatures implemented at each stage as indicated in Figure 5.5. The decoupled PMSMPR operation was carried out in 750 mL as opposed to 500 mL vessels to allow withdrawal of 500 mL of slurry each cycle without emptying the vessel. The coupled periodic flow experiment was also carried out 750 mL volume, in order to achieve similar RT_{PO} to the decoupled operation.

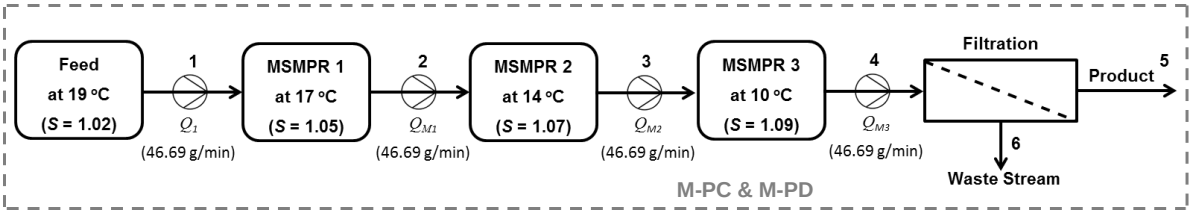

Figure 5.5: Flow diagram showing the block configurations of the three-stage PMSMPR unit used for the coupled and decoupled periodic flow crystallisation studies (M-PC and M-PD).

Batch Crystallisation of PCM (B-C1): A batch crystalliser was configured and used to conduct studies under similar conditions to those of the periodic flow studies. The seeded batch cooling crystallisation experiment was carried out for comparison with, and further characterisation of the PMSMPR. At start-up a suspension of 0.109 g PCM/g IPA was dissolved at 30 °C (10 °C above the desired saturation temperature) in a 500 mL vessel and

held for 15 min The solution was then cooled to 19 °C, seeded with 2.5 % PCM seed and held for 30 min The resulting seed suspension was then cooled to 10 °C and held for 423 min The batch crystallisation experiment can be used to examine further the crystallisation phenomena observed in the PMSMPR.

5.3 Results and Discussion

5.3.1 Periodic Flow Crystallisation in PMSMPR

Several challenges were encountered during the development of a continuous MSMPR crystalliser unit for the crystallisation of PCM from IPA, including washing out, fouling and encrustation, and transfer line blockages, as reported in Chapter 4. To overcome these difficulties a novel strategy involving periodic mixed suspension removal was developed, which leads to the illustration of the concept of SCO. This type of operation involves alternating periods of true continuous and batch operations; hence the RT_{PO} of crystals in the case of periodic operation can be extended with the duration of batch operation period (t_{batch}), which is combined with the addition/withdrawal period (RT_{conti}), such that $RT_{PO} = t_{batch} + RT_{conti}$. Note that RT_{conti} refers to addition/withdrawal period. The periodic flow method of operation has two main advantages:

(1) For a seeded system, it allows for addition of seed suspension and the high flow rates are more likely to lead to representative and isokinetic withdrawal of product crystals; and

(2) Extends the RT_{PO} of slurry inside the MSMPR, which can lead to improved yield and larger product crystals.

In addition, issues such as fouling on process equipment, encrustation and blockage of transfer lines are avoided, particularly when operating at low supersaturation with seeding. These advantages allow an extended operating time, without interruptions that necessitate, for example, cleaning of PAT probes, transfer lines or vessel walls due to the issues mentioned earlier. Figure 5.6 (a) – (f) shows the process time diagrams for the periodic flow crystallisation experiments conducted in the single- and two-stage PMSMPR configurations; the batch crystallisation experiment (B-C1) is also show for comparison.

Single-stage PMSMPR without Recycle (M-P1): Recrystallised seed was used in the study and the process time diagram for the single-stage PMSMPR experiment without recycle stream (M-P1) is shown in Figure 5.6 (a). The start-up period is rapid, leading to rapid

attainment of periodic conditions. The cyclic behaviour of the concentration, temperature and FBRM counts data reflects the periodic mode of operation.

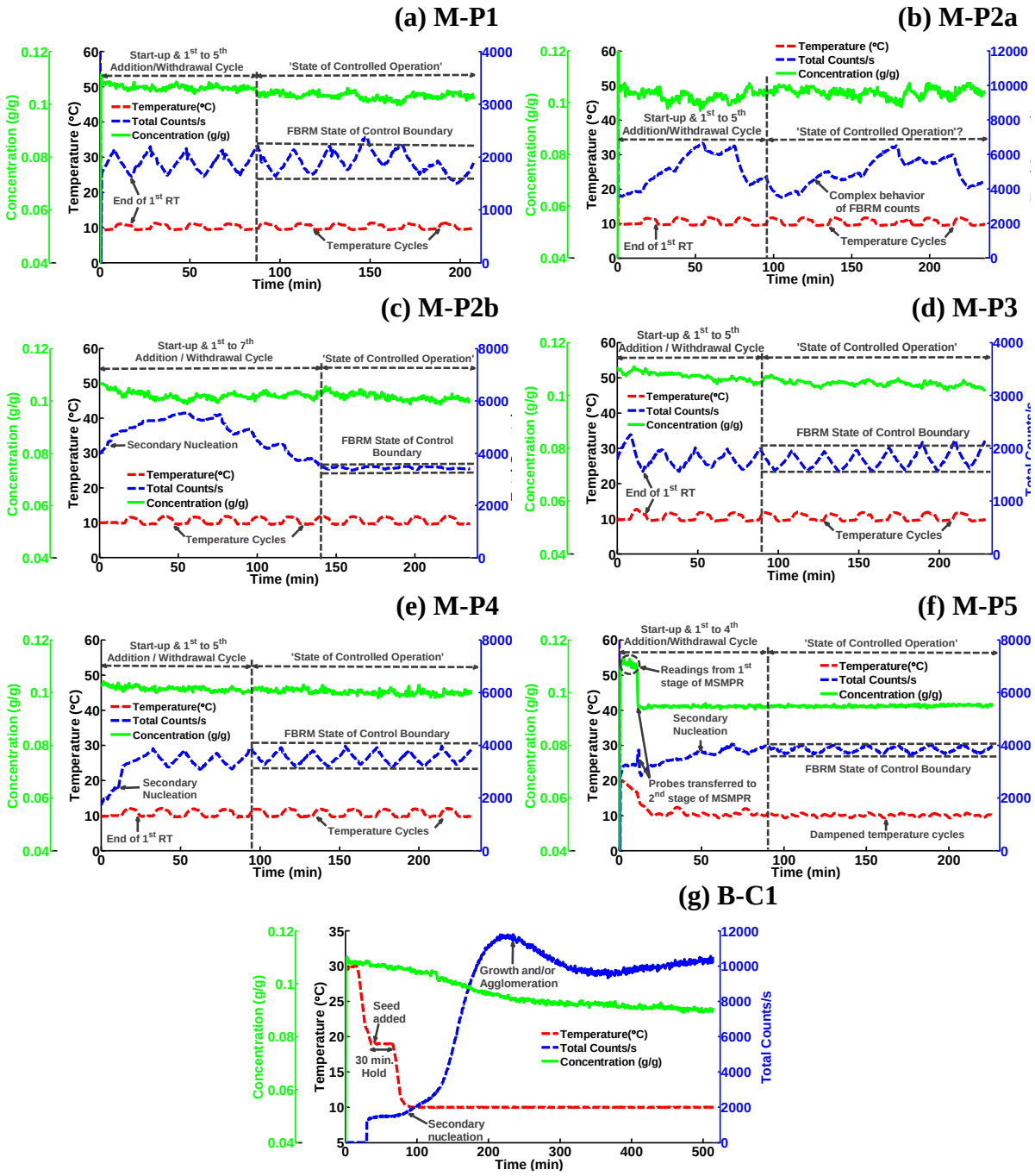

Figure 5.6: Process time diagrams showing real-time temperature, FBRM counts/s and Raman concentration data for: (a) M-P1: single-stage PMSMPR, no recycle stream; (b) M-P2a and (c) M-P2b: single-stage PMSMPR, non-concentrated recycle; (d) M-P3: single-stage PMSMPR, non-concentrated recycle; (e) M-P4: single-stage, concentrated recycle; (f) M-P5: two-stage PMSMPR, no recycle stream; (g) B-C1: Batch crystalliser.

The concentration in the PMSMPR decreased gradually from start-up until the 5th addition/withdrawal cycle, to a SCO value of 0.104 g PCM/g IPA (S = 1.07) as determined by

Raman measurements. This was a result of the seed material consuming available supersaturation, primarily by promoting secondary nucleation, but also growth on the surfaces of crystals surface already present. Thereafter, the concentration change was only small after the 5th addition/withdrawal cycle (marked by the vertical dashed line in Figure 5.6 (a)). The concept of periodic steady-state (or SCO) has not yet been defined in the literature in reference to MSMPR crystallisation. A SCO operating region is shown in Figure 5.6 (a), where the concentration changes by less than 3 %, a SCO FBRM boundary (± 270 counts/s) is also defined. The FBRM counts/s, concentration and temperature data from Figures 5.6 (a) – (f) also give an insight into the effect of periodic flow operation on the particle properties and supersaturation level of the system. At the start of each experiment the empty crystalliser is filled with slurry from the feed tank. The saving of data begins when the vessel has sufficient material to immerse all the PAT probes (i.e. from time, t = 0). After filling to the required operating volume the holding period commences. During each holding cycle there is a slow but sustained increase in the number of particles detected by FBRM. This is due to secondary nucleation occurring in the PMSMPR, which is the result of a rapid generation of supersaturation (S = 1.24) from the feed suspension added in the previous cycle that was subsequently cooled (i.e. 9 ^{o}C undercooling), thus leading to an increase in crystal density. On the other hand, during each addition/withdrawal cycle, there is a decrease in the FBRM counts/s, indicative of a reduction in crystal density. Slurry is withdrawn from the PMSMPR and the supersaturation reduced (S = 1.02) due to the addition of fresh feed which is at an elevated temperature (19 ^{o}C) relative to the PMSMPR (10 ^{o}C). The reduction of supersaturation in the PMSMPR then leads to suppression of secondary nucleation. Once the addition/withdrawal cycle ends and the equilibration cycle (or pause period) begins, the suspension cools more rapidly leading to high supersaturation, which leads to an increase in secondary nucleation. It appears that for PCM, secondary nucleation is the dominant crystallisation mechanism under the prevailing operating conditions. However, it appears that due to periodic operation, the extent of secondary nucleation is controlled. Evidence of this is drawn from the batch crystallisation experiment (Figure 5.6 (g); B-C1) process time diagram, which shows that as the system starts cooling from 19 ^{o}C, there is a slow increase in counts, indicative of secondary nucleation. Once the system cools to the final operating temperature (10 ^{o}C), a rapid and sustained increase in counts occurs, indicating the rapid onset of secondary nucleation. This temperature was selected to generate just enough supersaturation to encourage growth and avoid uncontrolled nucleation. With periodic operation, a rapid and sustained increase in the numbers of secondary nuclei is avoided and the system rapidly attains SCO due to simultaneous feed addition and slurry withdrawal.

Single-stage PMSMPR with Non-concentrated Recycle (M-P2a & M-P2b): The process time diagrams of the single-stage PMSMPR experiments with recycle stream, in which PCM raw material seed was used (M-P2a and M-P2b) are shown in Figures 5.6 (b) and (c), respectively. M-P2a was one of a series of initial process development experiments conducted to investigate periodic flow operation of the single-stage PMSMPR and was carried out using a 1 L feed vessel as opposed to the 5 L feed vessel used for M-P2b and all subsequent PMSMPR experiments reported. The process time diagram for M-P2a indicates a complex behaviour of the FBRM counts/s data and it appears that SCO has not been achieved. In contrast, the Raman concentration data indicates a decrease in concentration during the start-up phase, which then stabilises from the 5th addition/withdrawal cycle to a periodic steady-state (0.102 ± 0.002 g PCM/g IPA), that is, SCO until the end of the experiment. The FBRM counts/s data highlights an operating weakness in this initial PMSMPR crystalliser design (M-P2a). The use of the 1 L feed vessel to supply seed slurry to the PMSMPR may have led to variations in the mass fraction of seed crystals delivered. The 1 L tank had to be refilled periodically to continue supplying feed suspension to the 500 mL PMSMPR. For each refill, a fresh batch of saturated solution (1.2 L) was prepared in a separate vessel and cooled to 19 ^{o}C. This solution was then added to the feed tank, followed by addition of dry seed crystals (2.5 %) to make the seed slurry. In contrast, the 5 L tank used in M-P2b provided a more consistent supply of feed suspension, since only a single preparation of saturated solution and seed crystals was necessary. Moreover, the longer residence time of slurry in the 5 L feed tank, allowed for aging of the seed crystals and surface healing via Ostwald ripening mechanism.

A fundamental limitation of the FBRM technique is that it measures chord lengths rather than true particle sizes; typically, a large number of chords of different sizes can be obtained from any given particle [218]. Furthermore, different intensity profiles are often obtained from crystals of different sizes and shapes. Therefore, it is likely that in suspensions of crystals with a wide variety of morphologies, an even greater number of different chords may be obtained compared to a suspension of crystals with a more uniform shape. It is also likely that the frequency of refilling the 1 L feed vessel used to in M-P2a experiment contributed to the variations in the FBRM counts/s, due to non-uniform and inconsistent transfer of seed suspension to the PMSMPR. This may be attributed to changes in mass fraction content of seed crystals in the feed suspension during discharge from the feed vessel, as a result of variations that occurred in the seed slurry preparation each cycle, and changes in the properties of the seed slurry on refilling of the feed vessel due to the presence of small amounts of seed suspension left over from previous refills.

In contrast, the process time diagram of experiment M-P2b shows a FBRM counts/s profile that can be more easily interpreted: there is an initial increase in FBRM counts from start-up due to secondary nucleation. The same phenomena can be observed in the time diagram for M-P2a experiment. However, in M-P2b the FBRM counts/s profile then shows a steady, but sustained decrease in particle number until the 7th addition/withdrawal cycle, indicative of the occurrence of crystal growth and/or agglomeration in the system. From the 7th addition/withdrawal cycle onwards the counts/s levels off, except for the occurrence of dampened cycles due the periodic operation. In Figure 5.6 (c), this is highlighted as the point of attainment of SCO for M-P2b. This was also confirmed by the Raman concentration measurements, which showed that SCO was attained over the same period. The change in concentration from the 7th RT_{PO} to the end of the experiment was less than 4 % (± 0.0041 g PCM/g IPA). The results from M-P2b experiment suggests that the most probable cause of the complex behaviour of the FBRM counts/s data obtained from M-P2a experiment was the frequency of refilling the 1 L feed vessel. The results therefore indicate that selection of a stable and consistent feed delivery system is important from the perspective of attaining SCO in the PMSMPR. It is also evident from both M-P2a and M-P2b that the FBRM counts/s in both systems at start-up is more than twice that observed for the experiments in which recrystallised seed was used. The raw material seed contains many small particles in comparison to the recrystallised seed (Figure 5.1), even though it was sieved to a narrower size fraction (100 – 125 µm). This is because the dry raw material seed had a tendency to aggregate even during sieving. When added to the feed solution, the raw material seed aggregated even more initially, but these aggregates broke up over the aging time (30 min), revealing much finer particles. Another observation from M-P2b is that the system takes a longer time to achieve SCO, compared to the other PMSMPR experiments. This suggests that the seed properties have an effect on the time to achieving SCO. A reasonably straightforward phenomenon whereby the smaller sized raw material seed (SWMCL 49-50 µm; Figure 5.1) used in M-P2b (and M-P2a) is capable of consuming supersaturation more quickly compared to the recrystallised seed material (SWMCL 66 – 70 µm; Figure 5.1) used in the other PMSMPR experiments. Since the time required to achieve SCO depends on the kinetics of the crystallisation process, faster growth can lead to smaller time constants. It is accepted in general that smaller sized seeds exhibit larger overall active surface area thus higher active site concentration, which can lead to faster mean growth rates in an MSMPR exhibiting growth rate dispersion. The SCO product size of crystals from M-P2b was 67 µm. A mean SCO crystal product size could not be determined for M-P2a. This is because the process shows significantly amplified cyclic behaviour of the particle counts determined by FBRM, which is linked to the periodic refilling of the feed vessel, which leads to inconsistent delivery of seed to the PMSMPR. For experiment M-P2b, the SCO FBRM boundary (± 80 counts/s) is indicated

in Figure 5.6 (c). The FBRM cycles are significantly dampened on approach to SCO, due to a minimisation of disturbances affecting the system. This is an indication that the seed properties also have an effect on limiting the disturbances caused by periodic flow operation.

Single-stage PMSMPR with Non-concentrated Recycle (M-P3): The process time diagram of the single-stage PMSMPR experiment with non-concentrated recycle stream (M-P3) and using recrystallised seed supplied from a 5 L feed vessel is shown in Figure 5.6 (d). The system rapidly achieves periodic steady-state operation after the 5th addition/withdrawal cycle. The initial concentration of (recrystallised PCM) seed suspension delivered to the PMSMPR was (0.111 g PCM/g IPA). The process concentration decreased from start-up until the 5th addition/withdrawal cycle to 0.104 g PCM/g IPA. Thereafter, the concentration decreased only marginally from the 5th addition/withdrawal cycle, marked by the vertical dashed line in Figure 5.6 (d); periodic steady-state operating region was established and the concentration changes by less than 3 %. A periodic steady-state boundary (± 300 counts/s) is defined for the FBRM counts as indicated by parallel dashed lines in Figure 5.6 (d).

Single-stage PMSMPR with Concentrated Recycle (M-P4): The process time diagram, Figure 5.6 (e), of the single-stage PMSMPR experiment with concentrated recycle stream (M-P4) shows that the system rapidly achieves SCO after the 5th addition/withdrawal cycle, as indicated by the vertical dashed line. The concentration of the feed decreased from 0.111 g PCM/ g IPA to 0.101 g PCM/ g IPA by the 5th addition/withdrawal cycle in the PMSMPR and thereafter was changed by less than 3 %. The FBRM counts/s remained steady within a defined SCO boundary (± 400 counts/s) from the 5th addition/withdrawal cycle to the end of the experiment. The amplitude of the FBRM cycles are increased when compared to the experiment conducted with non-concentrated recycle (M-P3), an indication that secondary nucleation in the system has increased due to the increased concentration of PCM in the recycle stream to the PMSMPR.

Two-stage PMSMPR without Recycle (M-P5): The process time diagram of the two-stage PMSMPR without recycle and with recrystallised seed is shown in Figure 5.6 (f). The system achieves SCO after the 5th addition/withdrawal cycle in the second-stage PMSMPR. The concentration of seed suspension delivered to the first-stage PMSMPR was (0.111 g PCM/g IPA) and the feed concentration decreased to 0.109 g PCM/g IPA in the first-stage and then to 0.095 g PCM/g IPA in the second-stage PMSMPR. Figure 5.6 (f) shows the change in concentration and FBRM counts/s from 0 to 11 min in the first-stage PMSMPR. The probes were then transferred to the second stage PMSMPR as indicated in the time diagram. The temperature cycles as shown in Figure 5.6 (f) are dampened compared to the previous experiments where the single-stage PMSMPR unit was used, indicating more efficient

temperature control in the two-stage PMSMPR due to the smaller temperature difference (5 ^{o}C) between the feed and subsequent two stages. Figure 5.6 (f) further shows that attainment of SCO is rapid in the two-stage PMSMPR. Both the FBRM counts/s and the Raman concentration are stabilised from the 5th addition/withdrawal cycle (3rd RT_{PO}) until the end of the experiment, with a variation of less than 2 %, the FBRM SCO boundary (± 190 counts/s) is also shown.

Batch Crystallisation Study: The batch crystalliser was operated as close as possible to conditions employed during the periodic flow crystallisation experiments. Figure 5.6 (g) shows the process time diagram of the batch crystallisation experiment (B-C1). At start-up, a suspension of 0.110 g PCM/g IPA was dissolved at 30 ^{o}C and maintained at that temperature for 10 min The resulting solution was then cooled at a rate of 1 ^{o}C/min to 19 ^{o}C and seeded with 2.5 % recrystallised seed. At that stage in the process, the FBRM counts/s increased from 0 to 1750 counts/s. The vessel was maintained at 19 ^{o}C for 30 min and then cooled at a rate of 1 ^{o}C/min to 10 ^{o}C. On cooling, the concentration starts to decrease and there is a simultaneous increase in FBRM counts, which occurs gradually until the system reaches 10 ^{o}C, at which point there is a dramatic increase in the counts/s due to secondary nucleation. The increase in counts/s continues until ~225 min into the process. Thereafter, the FBRM counts/s starts to decrease as concentration continues to decrease, indicating that the system has entered a growth and/or agglomeration dominated phase. This is then followed by a period after ~460 min where the FBRM counts and concentration begin to stabilise. The batch crystallisation experiment gives some insights into the effect of periodic operation on the crystallisation outcome. In the PMSMPR, the addition/withdrawal cycles inadvertently impose control over the secondary nucleation kinetics of the system. In contrast, the batch process is dominated by uncontrolled secondary nucleation in the early stages of the process, which ultimately leads to fine particles and a broad CSD. In the periodically operated PMSMPR there is greater control over the CSD due to suppression of secondary nucleation during the addition/withdrawal cycles. A discussion on the FBRM square weighted chord length distributions (SWCLD), which gives an indication of the CSD obtained from each of the crystallisation experiments can be found in the section following. The batch process attains an equilibrium condition (close to the solubility curve), whereas MSMPR processes operate at steady-state at a fixed point in the metastable zone. Therefore, it is always possible to get a higher yield from a batch process (i.e. depending on the batch time) compared to a continuous MSMPR operated under similar conditions. However, a continuous MSMPR can be operated closer to the solubility curve if the residence time is extended. This is usually done by increasing the number of MSMPR stages (which may prove impractical for systems with slow growth kinetics) or by using low flow rates. The former may lead to a significant increase in the number of crystallisation process equipment and by

extension the overall cost of operation, whereas the latter option leads to sedimentation and therefore classified slurry withdrawal and eventual blockage of transfer lines [13]. Periodic flow operation extends the residence time of the MSMPR without the use of additional stages whilst also ensuring isokinetic withdrawal of slurry.

The following important observations were made based on the results assessed from all the PMSMPR experiments described in this chapter so far:

(1) Re-crystallised seed shows better quality properties in terms of size and shape relative seed prepared from PCM raw material.

(2) A consistent supply of seed slurry is required in order to avoid unsteady behaviour and encourage attainment of SCO in a short time frame.

(3) Generally, SCO is attained after 4 – 7 RT_{PO}, both in terms of the solute concentration and the FBRM count/s measurements.

5.3.2 Comparison of Crystallisation Methods

Product Crystal Size and Overall Process Yield: In this section the crystallisation experiments discussed earlier are compared. A summary of experimental results from each of the crystallisation experiments is presented in Table 5.3.

Table 5.3: Summary of results for the cooling crystallisation of PCM in the single- and two-stage PMSMPR and batch crystallisers.

Parameters Measured	M-P1	M-P2a	M-P2b	M-P3	M-P4	M-P5	B-C1
Mean SCO conc., c_1 (g/g)	0.103	0.102	0.101	0.104	0.101	0.095	0.089
% Yield of process	35.3 ± 1.9	43.3 ± 1.9	41.5 ± 1.1	31.1 ± 1.0	37.5 ± 0.5	68.9 ± 0.4	96.1 ± 0.1
Time to SCO (min / RT_{PO})	89.5 / 5th	n/a	140 / 7th	89.0 / 5th	90.0 / 5th	89.0 / 5th	460 / n/a
Seed Size: FBRM SWMCL (µm)	70.1 ± 0.1	48.7 ± 0.2	49.9 ± 0.7	70.1 ± 0.1	66.3 ± 0.1	70.1 ± 0.1	66.7 ± 0.2
SCO mean crystal size: FBRM SMWCL (µm)	74.5 ± 0.4	n/a	67.4 ± 0.3	71.5 ± 0.1	64.6 ± 0.1	77.7 ± 0.2	59.6 ± 0.1

M-P1 = Single-stage PMSMPR without recycle stream (2.5% recrystallised seed); M-P2a and M-P2b = Single-stage PMSMPR with non-concentrated recycle stream (2.5% raw material seed); M-P3 = Single-stage PMSMPR with non-concentrated recycle (2.5% recrystallised seed); M-P4 = Single-stage PMSMPR with concentrated recycle stream (2.5% recrystallised seed); M-P5 = Two-stage PMSMPR without recycle stream (2.5 % recrystallised seed); RT_{PO} = mean residence time; and n/a = not applicable.

The yield reported for each experiment is the fractional yield of crystallisation (*Y*), which refers to the amount of product obtained from the crystalliser relative to the amount of available supersaturation. *Y* is therefore defined as:

$$Y = \frac{c_i f_0 + c_{R1} f_{R1} - c_1 f_1}{c_i f_0 + c_{R1} f_{R1} - c^* f_1} \times 100 \qquad 5.1$$

where c_i , c_1 , c^* and c_{R1} are respectively, the feed stream concentration (g PCM / g IPA), PMSMPR SCO concentration, equilibrium concentration at the specified operating temperature, recycle stream concentrations (where the recycle stream is non-concentrated $c_{R1} = c_1$; otherwise c_{R1} is calculated using a mass balance around the dissolver unit in Figure 5.3). f_0, f_1 and f_{R1} are the solute free mass flow rates of IPA from the inlet, outlet, and recycle streams of the PMSMPR respectively, that is, based on time-averaged flow. The data shown in Table 5.3 indicates that the configuration of the PMSMPR (single- or two-stage), seeding strategy and the use of recycle stream (concentrated or non-concentrated) can affect the crystallisation outcome in terms of yield, mean crystal size and the achieve time to SCO. The time taken to reach SCO in each PMSMPR experiment is more or less similar (90 min), with the exception of M-P2b (as discussed in section 0). With respect to configuration, the highest SCO yield (68.9 ± 0.4 %) and SCO mean crystal size (77.7 ± 0.2 µm) is obtained from the two-stage PMSMPR without recycle stream (M-P5). Of the single-stage PMSMPR configurations the largest SCO mean crystal size (74.5 ± 0.4 µm) was obtained from M-P1 (operated without recycle stream), which was marginally larger than the seed material (70.1 µm) used. The process yield from M-P1 experiment was 35.3 ± 1.9 %. In comparison, the configuration with a non-concentrated recycle stream (M-P3) gave a marginally smaller SCO mean crystal size of 71.5 ± 0.1 µm and an overall SCO product yield of 31.1 ± 1.0 %. The single-stage PMSMPR configuration with concentrated recycle stream (M-P4) gave a higher yield of 37.5 ± 0.5 %. However, the mean crystal size was smaller (64.6 ± 0.1 µm) compared to the recrystallised seed material used (66.3 ± 0.1 µm) and products from experiments M-P1 and M-P3 for which the same seed material was used. This is an indication that concentrating the recycle stream improves the process yield, but leads to smaller crystals, because of additional secondary nucleation. In all of the PMSMPR experiments reported, there was evidence of growth of product crystals relative to the seed crystals used, except for M-P4 where the product crystals were marginally smaller than the seed material used. The extent of crystal growth observed in the PMSMPR was marginal for all experiments based on the FBRM SWMCL data, that is, with the exception of M-P2b where a significant increase in product crystal size (67.4 ± 0.3 µm) relative to the seed material (49.9 ± 0.2 µm) used is observed. In the batch crystallisation experiment, it is clear that the process yield is higher (96.1 ± 0.1 %) and the product crystal size (59.6 ± 0.1 µm) much smaller than obtained from all the

PMSMPR experiments. The issue of crystal growth in the PMSMPR experiments relative to seed crystals used (matured for 30 min in a 5 L vessel) will be discussed further in the section following. The process yield of M-P2a and M-P2b (43.3 ± 1.9 % and 41.5 ± 1.1 %) were higher compared to M-P3 even though the experimental conditions were almost identical. The main reason for this difference is down to the properties of the seed materials used. M-P3 was seeded with recrystallised PCM seed (75 – 125 µm) while M-P2a and M-P2b was seeded with PCM raw material (100 – 125 µm). Although sieved to within a narrower size fraction, the size of the seed obtained from the raw material was much smaller (Figure 5.1). This was due to the amorphous and powdery consistency of the raw material, which gave very fine crystals that had a tendency of sticking together and therefore were not broken up sufficiently in the sieving process. Aamir *et al* [142] showed that the material used to prepare seeds can affect the quality of the seed produced (the compound investigated was potassium dichromate); seed prepared from sieving recrystallised material had a distinctive shape, uniform size, and had fewer fine particles compared to seed prepared from sieving milled material. The higher process yield obtained from M-P2a and M-P2b is therefore attributed to the properties of the seed crystals used (PCM raw material), which has a large surface area due to the presence of many fine particles. Therefore, this fine seed is able to consume supersaturation and grow more rapidly than the larger recrystallised seed material used in other experiments. However, these small seeds can also promote secondary nucleation and agglomeration according to Fujiwara *et al* [229] in their study on the control of batch cooling crystallisation of PCM from aqueous seeded solutions. The investigators found that seeding the system with small seed crystals (less than 100 µm) resulted in the promotion of secondary nucleation and agglomeration leading to a product of varying sizes and broad CSD at 5 % seed loading. On the other hand, seeding with large seed crystals (sieve sizes 125 – 250 µm and 250 – 350 µm) led to the suppression of secondary nucleation and agglomeration, resulting in product crystals of more uniform size and shape and hence a narrower CSD. However, a limitation with using large seed as shown in the study is the long batch times that are required before significant growth is observed (3 – 5 hours). This would translate to impractically long residence times in the PMSMPR. Furthermore, the use of coarse as opposed to fine seed as demonstrated in this study, may lead to only marginal growth.

Operating Trajectories in the Phase Diagram: Figure 5.7 shows the process phase diagrams for each of the single- and two-stage PMSMPR and batch experiments. Shown are the solubility [170] and indicative metastable curves, PMSMPR operating points, the mean SCO point for PMSMPR operation / equilibrium point for batch operation, and the theoretical batch trajectory through the phase diagram. These results show that the dynamics of batch and PMSMPR operations are markedly different, both giving different trajectories through the phase diagram. Since supersaturation is the driving force for crystallisation, variations in the supersaturation

trajectory can allow for the exploitation of more crystal attributes in terms of size [32], shape, distribution and polymorphic form. This observation is particularly true for the PMSMPR crystalliser.

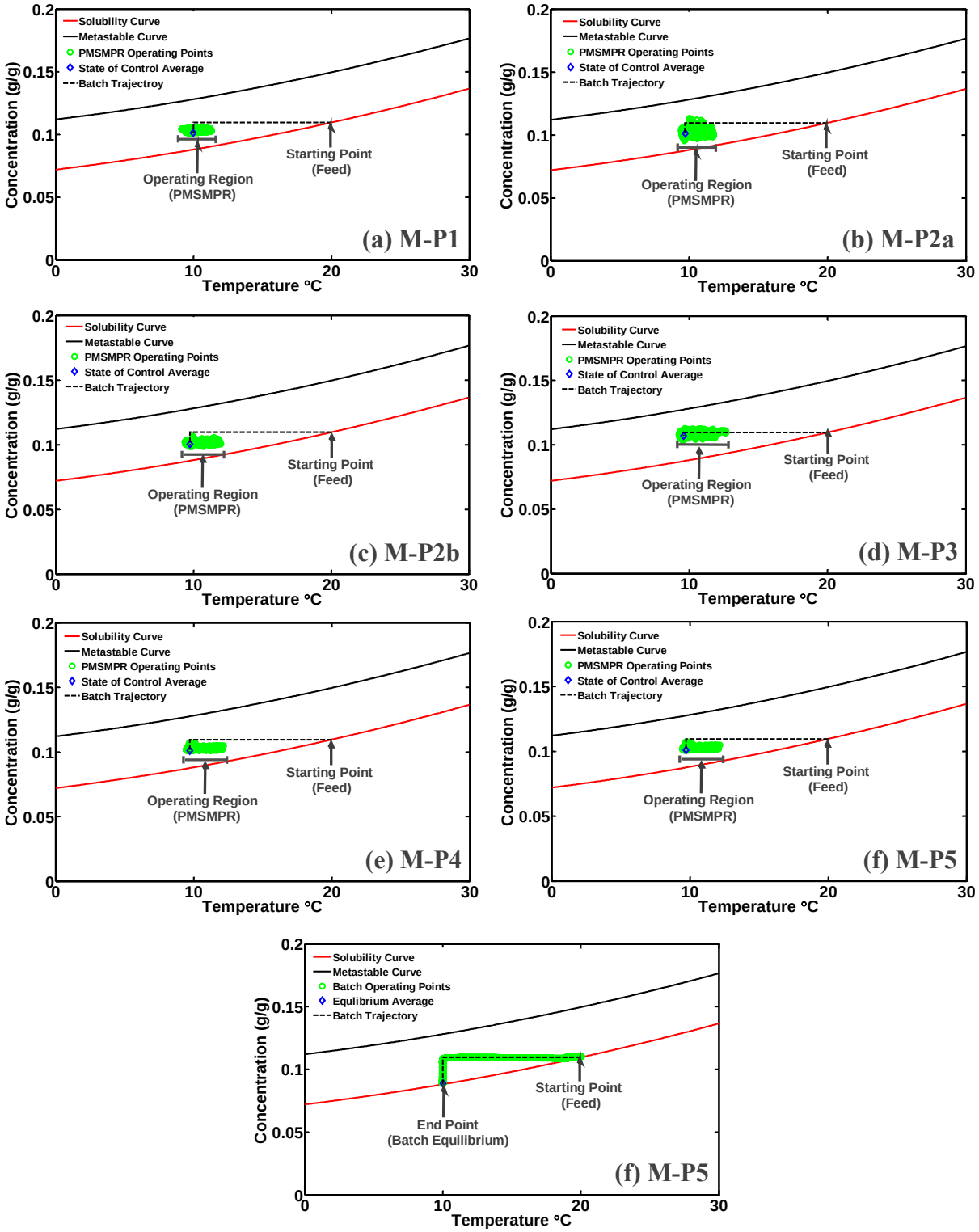

Figure 5.7: Process phase diagrams for the PMSMPR and batch crystallisation experiments showing operating region for each system: (a) M-P1: single-stage PMSMPR, no recycle stream; (b) M-P2a and (c) M-P2b: single-stage PMSMPR, non-concentrated recycle; (d) M-

P3: single-stage PMSMPR, non-concentrated recycle; (e) M-P4: single-stage, concentrated recycle; (f) M-P5: two-stage PMSMPR, no recycle stream; (g) B-C1: Batch crystalliser.

MSMPR crystallisers are usually operated continuously (at steady-state) or in this study periodically (at SCO), which means there is no progression in terms of time or spatial position. This means that the system is operated at a fixed supersaturation, which is also the point at which slurry is removed from the crystalliser. Compared to batch crystallisation, which operates towards an equilibrium there is no supersaturation continuum in the MSMPR. However, if the MSMPR is operated periodically as done in this study, then the supersaturation is no longer fixed, but oscillates periodically between upper and lower limit values. So long as the oscillations are small, the system can be controlled as shown in this study to maintain a narrow supersaturation limit range (controlled state of operation). It is also important to note that the trajectories for the PMSMPRs are all within the MSZW and quite far from the region of primary nucleation.

The phase diagrams for each of the PMSMPR experiments (Figure 5.7 (a) – (f)) show the effect of periodic operation as the system is disturbed at set time intervals due to slurry addition/withdrawal. Each system approaches the SCO condition rapidly as the supersaturation boundaries narrow. It is evident from the phase diagrams that the process yield from each PMSMPR is lower than that of the batch crystallisation process. M-P5 (two-stage PMSMPR, recrystallised seed) shows the least variation in steady-state concentration (measurements from second-stage PMSMPR) of all the PMSMPR operations. This is because of better temperature control due to the smaller temperature difference (5 ^{o}C) between stages, when compared to the single-stage PMSMPR operations (9 ^{o}C difference between PMSMPR and feed vessel). Of the single-stage PMSMPR operations, M-P1 (single-stage without recycle stream) shows the least variation in concentration in the operating region of the phase diagram, this is attributed to the absence of a recycle stream in this experiment. All of the single-stage PMSMPR experiments employing a recycle stream showed more variation in concentration due to the additional inlet flow creating slightly more disturbance in the system. Furthermore, this additional inlet flow from the recycle stream, is at a lower supersaturation (S ranges from 0.75 – 0.80) and higher temperature (30 ^{o}C) relative to the feed stream (S = 1.02, at 19 ^{o}C) and PMSMPR (S = 1.24, at 10 ^{o}C). These differences in supersaturation also contribute to the greater disturbance seen in each of the systems employing the recycle stream. However, these disturbances are maintained with reasonably narrow bounds, so that the operation is still being controlled within the metastabe zone. The merits of PMSMPR compared to continuous MSMPR have already been outlined. There also exists a significant potential with this mode of operation to explore different regions in the

phase diagram and to determine the effect on crystallisation outcomes in terms of product CQA.

***Comparison of FBRM SWCLD*:** Figure 5.8 shows the normalised FBRM SWCLD of the final products obtained from the batch crystallisation experiment and the SCO products from the PMSMPR crystallisation experiments. Compared to the batch experiment all the distributions obtained for the PMSMPR are shifted to the right (towards larger sizes). The distributions for M-P1, M-P3 and M-P5 are quite similar and appear to overlay, indicating that the product crystals are of similar mean size, in agreement with the SWMCL data reported in Table 5.3. The similarity between the SCO product SWCLDs for M-P1, M-P3 and M-P5 also indicates that the number of stages employed (single- or two-stage) and the mode of operation (with or without recycle) do not have a significant effect on the CSD in the PMSMPR. This is an interesting observation, since typically one would expect that an increase in the number of stages would lead to longer RT_{PO} and thus more time for crystals to grow. It must be noted, however, that although the distributions are similar for M-P1, M-P3 and M-P5, there is a very small but notable shift towards larger sizes in the two-stage PMSMPR (M-P5). Overall, the results suggest that the growth and secondary nucleation kinetics of PCM are the main variables affecting the crystallisation. It appears that the secondary nucleation kinetics of the system is the dominant crystallisation mechanism, while the growth kinetics is extremely slow. This was noticed early on in development studies in a seeded continuous MSMPR crystalliser (Chapter 4).

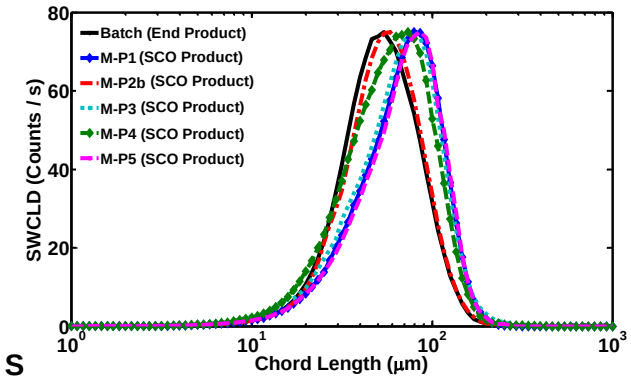

S

Figure 5.8: Comparison of FBRM SWCLD for the PMSMPR SCO products and batch crystalliser end stage product.

A strategy was developed employing low supersaturation and moderate seed loading (2.5 %) in the PMSMPR. Typically, seed loadings used in crystallisation processes range from as little as 0.1 % to as much as 5 % and even more depending on the requirements [253]. Although each PMSMPR was operated at low supersaturation with moderate seed loading, this strategy did not lead to significant crystal growth, with the exception of the M-P2b experiment where

significant growth appears to have occurred due to the larger surface area of the raw material seed used. It is well known that low seed loading can contribute to undesirable secondary nucleation, leading to an increase in the number of small particles in solution [254]. Therefore, an investigation of periodic flow crystallisation in the single-stage PMSMPR without recycle at a higher seed loading (5 % recrystallised seed) was conducted to determine the effect on the product crystal properties. The experimental conditions for this run were the same as reported for M-P1, only the seed loading was changed. Figure 5.9 shows a comparison between the SWCLD of the seed and product crystals from this experiment. The result indicates that even at a higher initial seed loading level, the product CSD has not shifted significant to the right (i.e. towards larger sizes) relative the seed CSD. It is also likely that due to the high density of crystals in the system the competition for solute molecules is sufficiently high that the product crystals show no noticeable increase in size. The mean size of seed and SCO product crystals, that is, the SWMCL observed for this experiment were 66.2 ± 0.3 µm and 61.8 ± 0.4 µm, respectively. The marginally smaller size of the product crystals relative to the seed crystals used confirms the deductions made earlier regarding the effect of secondary nucleation and competition for solute molecules. The results further confirm that the growth kinetics of PCM is extremely slow, whereas the secondary nucleation kinetics is much faster. Therefore, secondary nucleation may be the dominant crystallisation mechanism. An important variable that was no investigated in this study is the time allowed for the periodic flow addition/withdrawal and holding cycles. These cycles could be adjusted to determine the effect on crystal growth in future work.

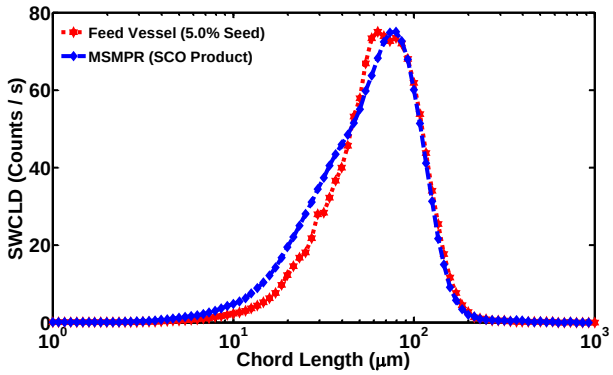

Figure 5.9: Comparison of SWCLD of seed material (5.0 %) and PMSMPR SCO product.

Figure 5.10 shows the normalised FBRM SWCLD of product crystals relative to the initial seed crystal distributions for the other PMSMPR experiments. Evidently, only marginal crystal growth is observed relative to the seed crystals used for M-P1, M-P3 and M-P5, respectively. This is indicated by a narrower SWCLD compared to the seed crystals. However, for M-P4 the product crystals obtained from the PMSMPR were marginally smaller than the seed crystals. Although the crystals were smaller, the SWCLD for M-P4 SCO product was narrower than that that of the seed crystals. For the batch experiment (B-C1) the product crystal SWCLD (not shown) showed

a significant shift to the left and was significantly broadened relative to the seed size distribution, which is further evidence that secondary nucleation is the dominant crystallisation mechanism for PCM. Overall the results indicate that the PMSMPR produces marginally larger crystals with narrower CSD when compared to seed crystals used; PCM is known to exhibit slow growth crystallisation kinetics [229]. It may be that longer RT_{PO} in cascaded PMSPMRs with narrow temperature transitions between process vessels is required to achieve significant crystal growth of PCM.

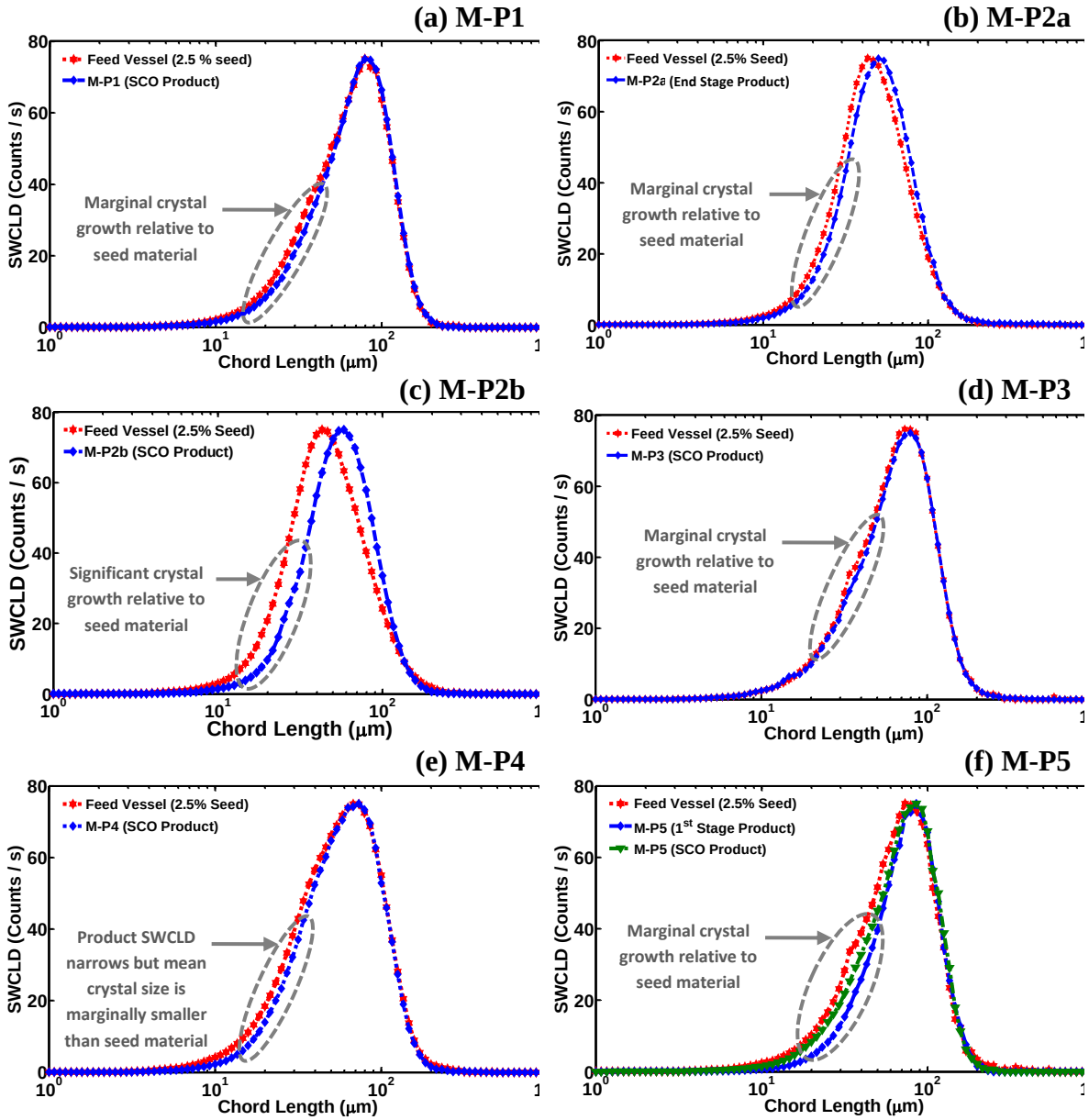

Figure 5.10: Comparison of FBRM SWCLD for seed material and PMSMPR SCO products and batch crystalliser end stage product.

It is evident from the results of M-P5 (two-stage PMSMPR) experimental run that the crystal size increases by extending the residence time in the PMSMPR simply by numbering up stages in a

cascade, which has the added advantage of applying more gradual stage temperature transitions. This allows for smaller changes in supersaturation, which is more suitable for slow growing systems [24] like PCM. Preliminary experiments in the PMSMPR unit with a fast growing system showed that significant growth of product crystals was achieved relative to seed crystals when compared to PCM (see Chapter 6), which further indicates that the slow growth kinetics of the latter system.

An important variable which affects the product crystal quality from the PMSMPR is the seeding protocol employed. In a recent review paper, O'Sullivan *et al* [253] highlighted some of the key seeding strategies used in industry to achieve desired product crystal attributes in batch crystallisers, which may also be applied to the PMSMPR. The authors highlighted that seeding with crystals of the correct size, mass and form at the right point in a process can lead to more consistent and repeatable crystallisations. Selecting the appropriate seeding conditions (for example, seeding temperature), at the appropriate supersaturation level can lead to improved crystallisation outcomes. Here, information on the metastable zone width (MSZW) of the crystallising system is necessary to determine whether to seed close to the solubility curve or the metastable curve. Another important consideration is the appropriate seed loading and seed size for a process, which depends on the desired product crystal size, distribution and polymorphic form. Typically, if large crystals are desired less seed material of larger size is added to encourage growth. On the other hand, if small crystals are desired then a large seed loading of small sized particles are used. In the PMSMPR experiments discussed earlier and preliminary experiments not reported here, both of these seeding strategies were utilised to determine the effect on the crystallisation outcome for the PCM-IPA system. The best results, in terms of crystal growth were observed using a lower seed loading of 2.5 % and either 75 – 125 µm recrystallised seed fraction or 100 – 125 µm raw material seed fraction. For the former case the overall CQA of the product crystals were better compared to the latter. However, only marginal growth was observed in the majority of experiments conducted.

Comparison of PVM and Off-line Microscope Images: PVM images were captured in real-time and off-line microscope images taken of the dried product crystals after each RT_{PO} in each of the PMSMPR experiments. Figure 5.11 shows the off-line microscope images and real-time PVM images of the seed and product crystals from the 1st and 10th RT_{PO}, respectively for M-P1 (single-stage PMSMPR without recycle), and M-P2a and M-P2b (single-stage PMSMPRs with non-concentrated recycle). The 1st and 10th RT_{PO} images for M-P1 show evidence of crystal growth relative to the seed crystals although there are also many fine crystals present, indicative of secondary nucleation, which contributes to reducing the overall SWMCL of the product, there are also agglomerated crystals present. Significantly more agglomerated crystals are observed

in the microscope images compared to the PVM images. This is not entirely surprising since microscope images were obtained after filtration and drying of product crystals. On filtration, crystals have a tendency to stick together, forming agglomerates due to cementation of crystals as mother liquor associated with the wet filter cake becomes supersaturated from solvent evaporation.

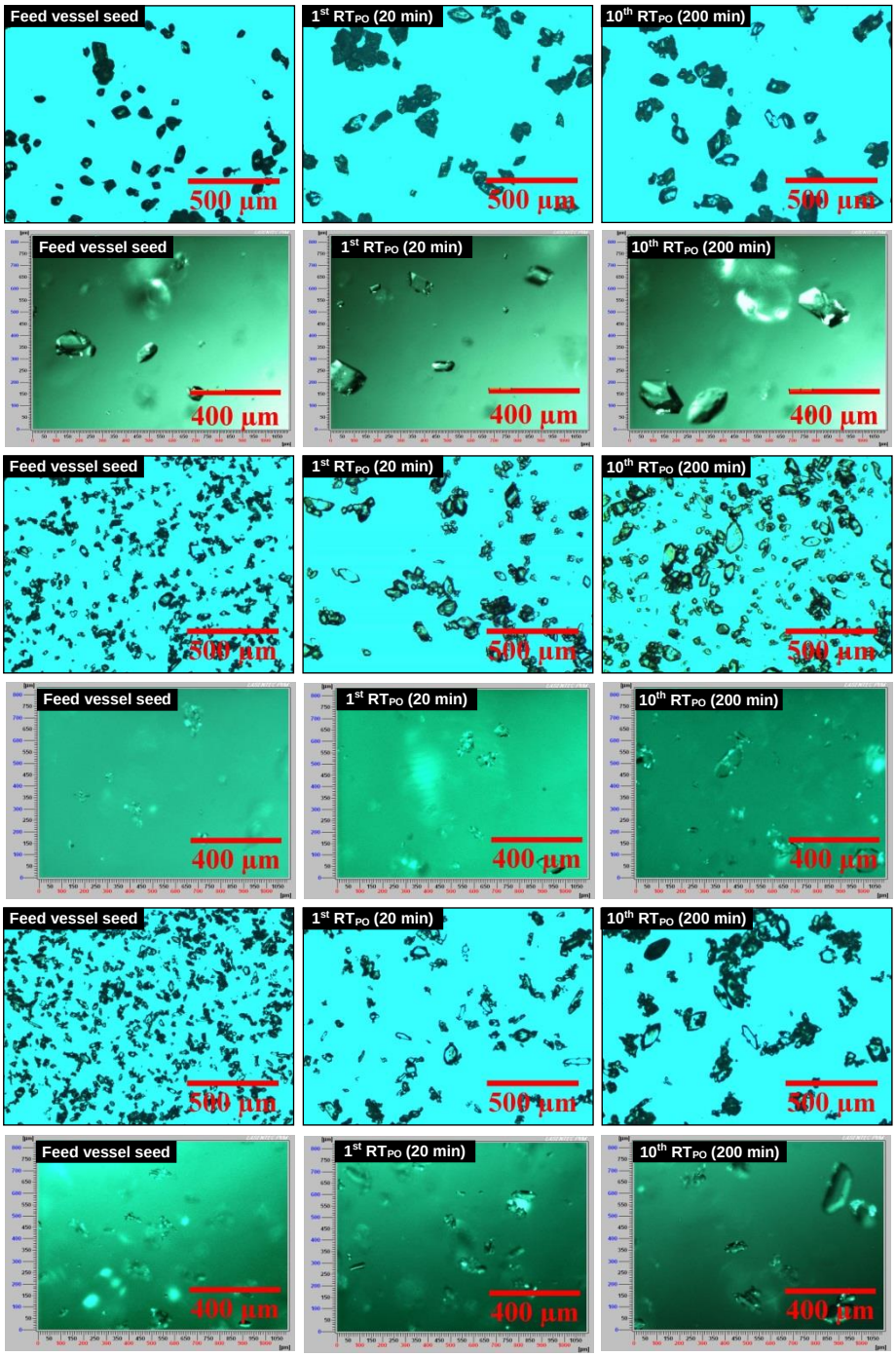

Figure 5.11: Microscope (rows from top 1, 3 and 5) and PVM images (rows 2, 4 and 6) of seeds crystals from feed stream, and crystals from the 1st RT_{PO} (20 min) and 10th RT_{PO} (200 min) for M-P1 (rows 1 and 2), .M-P2a (rows 3 and 4) and M-P2b (rows 5 and 6).

Furthermore, the outlet slurry is supersaturated when exiting the PMSMPR as shown from the operating region in the phase diagram (Figure 5.7). Compared to M-P1 seed which shows predominantly regular shaped and sized rhombic crystals, the M-P2a and M-P2b seed crystals appear irregular in shape and size.

As discussed earlier in this thesis, seed crystals used for M-P2a and M-P2b experimental run were prepared from PCM raw material rather than recrystallised material. The product crystals from the 1st and 10th RT_{PO} indicate that there is growth relative to the seeds evidenced from a number of large crystals present. However, there are also a number of agglomerates and fine crystals present. The fine particles present in both the 1st and 10th RT_{PO} products are indicative of some secondary nucleation, which was confirmed by the time diagrams, Figure 5.6 (b) and (c). These observations agree with the findings from the assessment of the FBRM SWMCL (Table 5.3) and SWCLD (Figures 5.8 and 5.10). The seed and product crystals from M-P3 and M-P4, that is, single-stage PMSMPR with non-concentrated and concentrated recycle, respectively, are shown in the Figure 5.12. The PMSMPR product crystals show a characteristic rhombic shape, similar to the recrystallised seed material used. Once again, there is evidence of agglomeration from the microscope images of both the seeds (sampled from feed stream) and product crystals, which may be due to the sample preparation process. However, this is not the only cause of crystal agglomeration. It appears that PCM has a natural tendency to agglomerate when many fine crystals are produced from secondary nucleation. There is evidence of agglomeration and crystal twinning from the *in situ* PVM images of the 1st and 10th RT_{PO} product crystals. The images of product crystals for M-P4 show more agglomerates and fines present, although there are also a few large crystals present as well. In particular, the PVM images of the 1st and 10th RT_{PO} samples show a significant number of fine crystals present as well as some large ones. This suggests that the contribution from secondary nucleation is more significant than from crystal growth, which is attributed to the concentration of the recycle stream. The operating supersaturation level in M-P4 is higher (1.28) than that of M-P3 (1.23), which was operated with a non-concentrated recycle stream. This is an indication that only a small change in supersaturation can significantly affect the crystallisation outcome. The large number of fines observed from the microscope and PVM images also support the SMWCL and SWCLD data from FBRM, both of which indicated that the mean size of the product crystals from M-P4 was smaller compared to the initial seed crystals used. The SCO product crystals obtained from the two-stage PMSMPR without recycle (M-P5) were of the best quality for all PMSMPR configurations investigated. The images show that relative to the seed crystals there is a small, but noticeable amount of crystal growth, which was also confirmed from FBRM SWMCL and SWCLD. Overall, the results from M-P5 indicate that with a more controlled and smaller stepwise temperature change in the

two-stage PMSMPR, led to better product properties in terms of crystal size and yield are attainable compared to the single-stage PMSMPR operated with and without recycle stream.

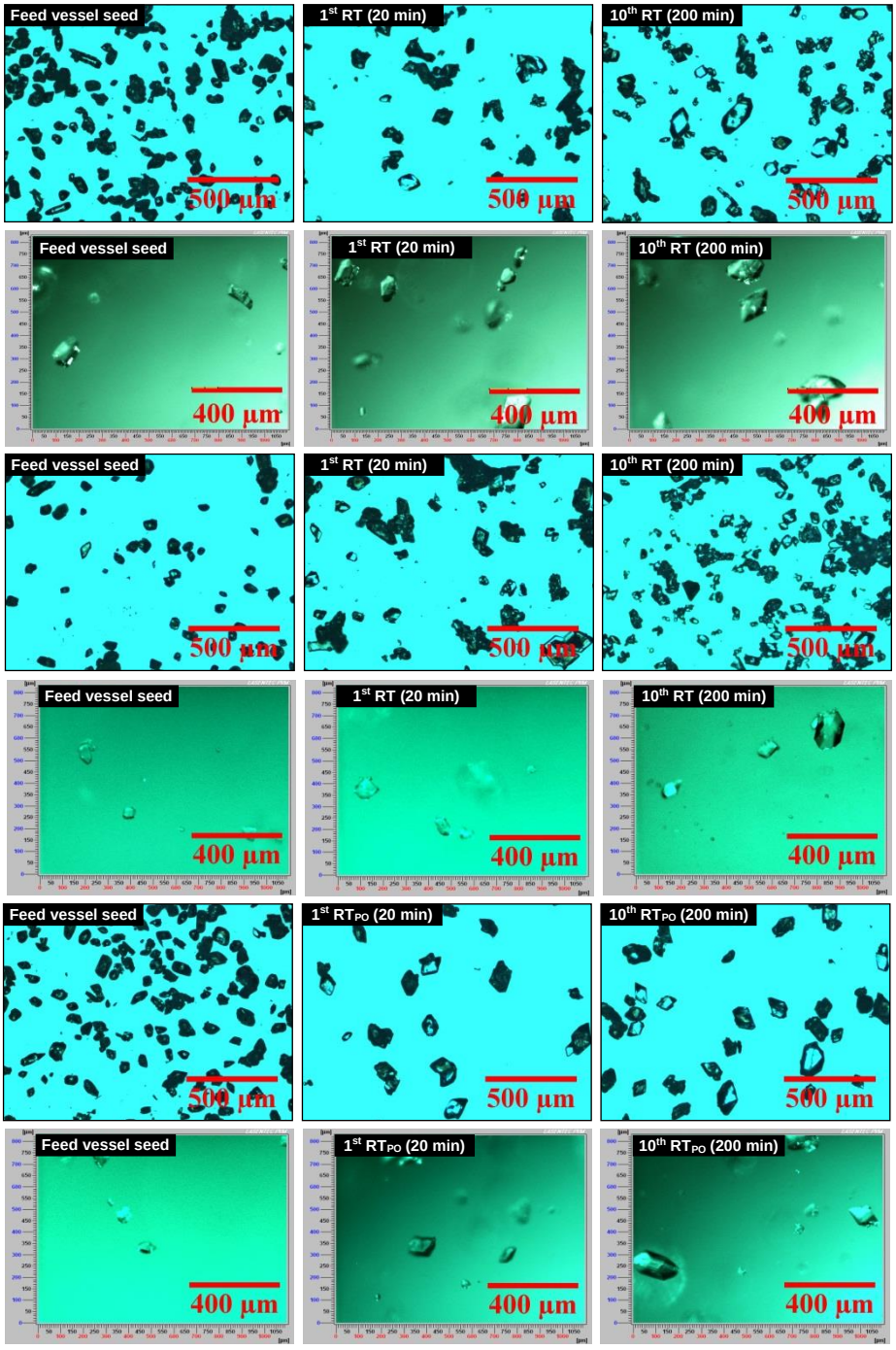

Figure 5.12: Microscope (rows 1, 3 and 5) and PVM images (rows 2, 4 and 6) of seeds aged crystals, and crystals from the 1st RT_{PO} (20 min) and 10th RT_{PO} (200 min) of the single-stage PMSMPR operated with non-concentrated (M-P3, rows 1 and 2) and concentrated (M-P4, rows 3 and 4) recycle stream, and two-stage PMSMPR without recycle (M-P5).

Period Flow Crystallisation in Coupled and Decoupled Three-stage PMSMPR (M-PC and M-PD): Table 5.3 provides a summary of the experimental results from the two experimental runs. The data shows that a higher process yield was obtained from the decoupled operation (M-PD), compared to the coupled operation (M-PC) due the extended RT_{PO} of the former compared to the latter. These experiments were conducted to see whether significant crystal growth of PCM could be achieved relative to the previous PMSMPR experiments.

Table 5.4: Summary of results for the cooling crystallisation of PCM in a three-stage PMSMPR operated in coupled and decoupled modes, respectively.

Exp.	Mean SCO Conc.(g/g)	SCO Conc. Change (g/g)	% Yield of Process	Seed Size: FBRM SWMCL (µm)	SCO Mean Crystal Size: FBRM SMWCL (µm)
M-PC	0.093	± 1.96	77.7 ± 0.3	66.8 ± 0.1	55.3 ± 0.3
M-PD	0.091	± 1.12	85.8 ± 0.2	68.0 ± 0.2	53.8 ± 0.1

The mean sizes of product crystal were similar for the coupled and decoupled operations. However, the product crystals obtained were of smaller size compared to the initial seed material used, which suggests that under the prevailing operating conditions, secondary nucleation is promoted over growth. The process time diagrams for M-PC and M-PD experiments are shown in Figure 5.13 (a) and (b), respectively. SCO was achieved in the former, but process deviations were detected in the latter, attributed to the difficulty in controlling the volume changes in the PMSMPR each RT_{PO}.

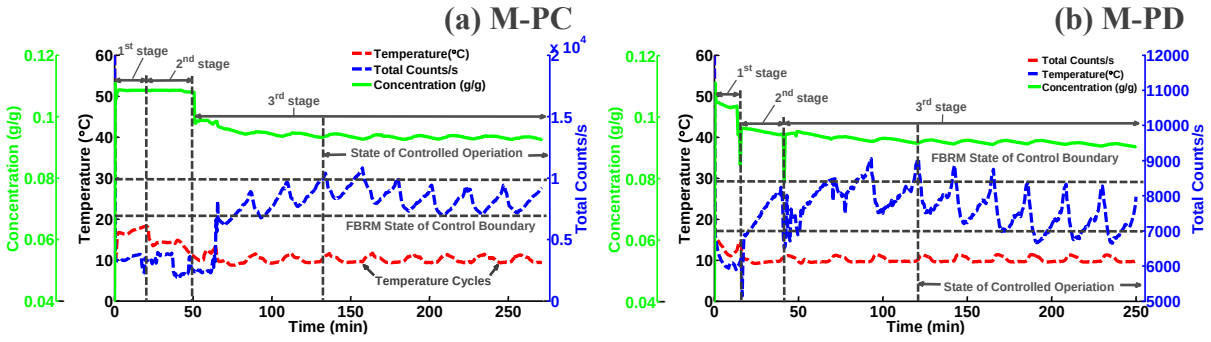

Figure 5.13: Process time diagrams showing real-time temperature, FBRM counts/s and Raman concentration data for coupled (M-PC) and decoupled (M-PD) experiments in a three-stage PMSMPR.

The RT_{PO} per stage for M-PC and M-PD It is also confirmed that secondary nucleation was the dominant mechanism in both cases, leading to a shift in the product CSD to smaller sizes (i.e. to the left) relative to the seed, and first- and second-stage PMSMPR product crystals. respectively. Process measurements were taken initially from the first-stage, followed by the second-stage, and finally the third-stage PMSMPR. The concentration of feed suspension

charged to the coupled and decoupled PMSMPR was 0.111 g PCM/g IPA. The SCO concentrations were 0.091 and 0.093 g PCM/g IPA, respectively, confirming the higher yield of M-PD relative to M-PC. Figure 5.14 (a) and (b) shows the operating trajectory in the phase diagram for M-PC and M-PD experiments. The profiles are slightly different with a more rapid decrease in concentration observed for M-PD from the first- through third-stage PMSMPR compared to the M-PC.

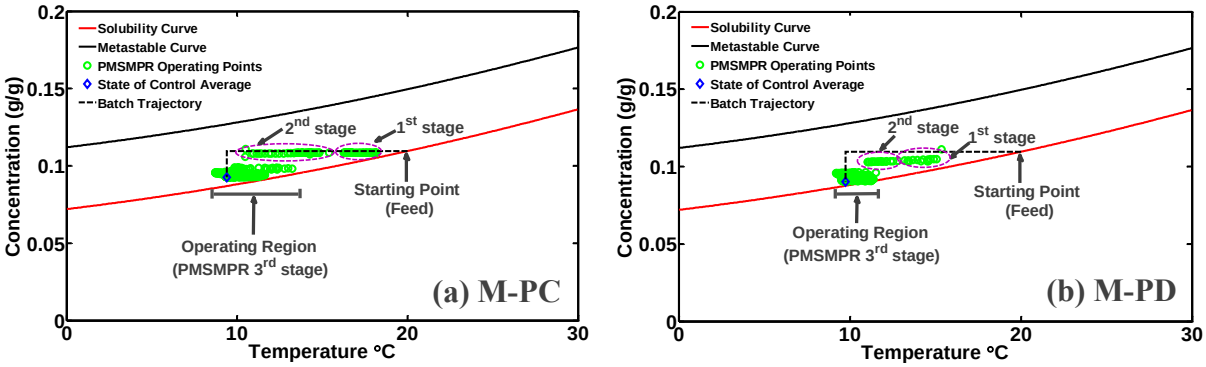

Figure 5.14: Process phase diagrams for the three-stage PMSMPR operated in (a) coupled (M-PC) and 9b) de-coupled (M-PD) modes, respectively.

The SWCLD plots, Figure 5.15 (a) – (d) show that there is little difference between the product CSD obtained from M-PC and MPD, with, exception that the latter gave narrow CSD relative to the former. It is also confirmed that secondary nucleation was the dominant mechanism in both cases, leading to a shift in the product CSD to smaller sizes (i.e. to the left) relative to the seed, and first- and second-stage PMSMPR product crystals.

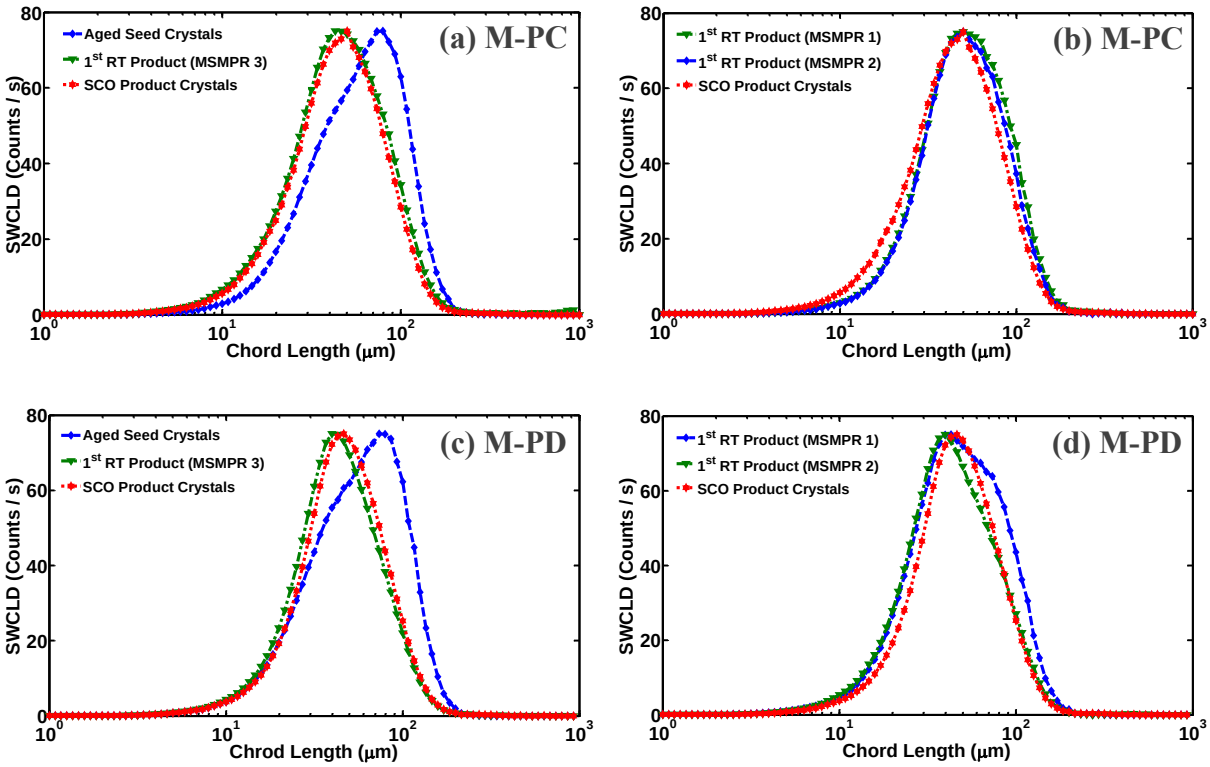

Figure 5.15: Comparison of FBRM SWCLD for three-stage PMSMPR operated in coupled (M-PC) and decoupled (M-PD) modes, respectively.

5.4 Conclusions

Periodic flow crystallisation in a novel PMSMPR was demonstrated as a feasible method of producing crystalline material with desired CQA, without encountering operating problems such as fouling, encrustation and blockage of transfer lines. Periodic flow crystallisation is a relatively new method whereby controlled disruptions are applied to the crystalliser primarily to increase the mean residence time and control crystal product attributes such as size and distribution. For the PMSMPR, conventional MSMPR operation is alternated with batch operation to increase the mean residence time. This operation illustrates a new paradigm of continuous operation whereby the process is in controlled state of operation (i.e. periodic steady-state or SCO) rather than steady-state. The application of an integrated array of PAT tools and in-house developed information system software CryPRINS within an IDS framework to the monitoring and characterisation of the PMSMPR was also demonstrated. The indicative CSDs for single-stage PMSMPR (operated with and without recycle stream), two-stage PMSMPR (operated without a recycle stream) and three-stage (coupled and decoupled flow) were determined from FBRM SWCLD data. The indicative mean crystal sizes were determined from FBRM SWMCL data. SCO was characterised using Raman, ATR-UV/vis, FBRM and PVM. The results indicate that the configuration of the PMSMPR (single-,

two- or three-stage), seeding strategy and the use of recycle stream (concentrated or non-concentrated) can affect the crystallisation outcome in terms of yield and mean crystal size attainable. The time taken to reach steady-state in the PMSMPR is more or less similar for all experiments except M-P2b, which was conducted using non-concentrated recycle and raw material seed, which was variable in size and shape. This result suggests that the seed properties can influence the time to achieving steady-state. With respect to configuration, the highest yield and mean product crystal size were obtained from the two-stage PMSMPR operated without a recycle stream. Furthermore, the crystal properties in terms of size and shape were noticeably better as observed from PVM and off-line microscope images of product crystals when compared to the product crystal from single-stage PMSMPR experiments. Of the single-stage PMSMPR configurations investigated, the largest mean crystal size was obtained from the system without recycle stream (M-P1). In comparison, the configuration with non-concentrated recycle stream (M-P3) gave a marginally smaller mean size. Although the single-stage PMSMPR with concentrated recycle stream (M-P4) gave a higher yield, the mean crystal size of the SCO product was markedly smaller. This is a further indication that concentrating the recycle stream improves process yield, but leads to smaller crystals due to increased secondary nucleation in the system. In all of the other PMSMPR experiments reported there was evidence of growth relative to the seed crystals used. However, the extent of crystal growth observed in all experiments, except M-P2b was marginal due to the strong influence of secondary nucleation on the crystallisation mechanism of PCM. The result from M-P2b showed a significant shift of the SCO product SWCLD to larger sizes relative to the seed crystals used. This result suggests that the seed properties can also influence the SCO product CSD. Agglomeration and growth were both evident in the SCO product as confirmed by PVM and microscope images. A batch crystallisation experiment was also conducted under similar conditions to that of the PMSMPR experiments for evaluation and comparison. As expected, the yield of the batch crystallisation process was higher than in all of the PMSMPR experiments. However, the product crystals were significantly smaller size, indicative of a broad CSD as confirmed by FBRM, PVM and off-line microscope image analysis. This was due to a significant amount of secondary nucleation in the batch system compared to the PMSMPR systems. Information from the batch crystallisation experiment gave further evidence that secondary nucleation is the dominant crystallisation mechanism of PCM even at low supersaturation levels. It was inferred from the observations in the batch crystallisation study, that PMSMPR is effective at controlling the extent of secondary nucleation leading to crystals of larger size compared to the seed materials used, albeit marginal in most cases. Three-stage PMSMPR experimental runs carried out in coupled and decoupled periodic flow modes, respectively gave comparable but smaller crystals relative to the seed materials used. It appears that under the experimental conditions employed,

secondary nucleation was favoured over crystal growth. Robust monitoring and temperature control using integrated PAT array and CryPRINS information systems software was also demonstrated for the periodic flow crystallisation in the PMSMPR. The results indicate that the combined used of PAT and information systems within an IDS framework can indicate when the periodic flow process attains SCO and also provides a better understanding of the parameters and operating procedures that influence the periodic operation. While the periodic operation was demonstrated here for seeded cooling crystallisation, a similar approach can be applied for anti-solvent or combined cooling and anti-solvent systems. The periods of alternating continuous and batch operation can also be tailored to accommodate systems belonging to different classes based on their growth and nucleation kinetics.

Chapter 6

Periodic Flow Crystallisation of Glycine: Example of a Fast Growing API

The novel concept of periodic flow crystallisation whereby controlled periodic disruptions are applied to the inlet and outlet flow of a MSMPR crystalliser was demonstrated in Chapter 5; various operating strategies were explored for the crystallisation of a slow growing active pharmaceutical ingredient (API), paracetamol (PCM). In this chapter, the same concept of periodic flow crystallisation in a mixed suspension mixed product removal (PMSMPR) crystalliser is exploited to achieve better control over the product CQA of a fast growing API glycine (GLY), whilst maintaining a "state of controlled operation" (SCO) in the design space. Experiments were conducted using glycine-water (GLY-H_2O) as a model system in single- and three-stage cascaded PMSMPR crystallisers. A dynamic model of the residence time distribution (RTD) was developed to demonstrate the periodic flow operation in terms of the extended mean residence time in periodic flow (RT_{PO}) and RTD broadening. Process models of the periodic flow crystallisations were also developed, with an aim to provide a better understanding and improve the performance of the PMSMPR. The modelling framework was based on the Process System Enterprise's gCRYSTAL 4.0 software. The crystallisation mechanisms and kinetics of the GLY-H_2O system were estimated from batch crystallisations. The process models were validated with experimental data from periodic flow crystallisations. Good agreement was observed between the model predictions and experimental data. Furthermore, larger crystals with mean size > 125 µm (i.e. larger than the highest sieved seed fraction: 75 – 125 µm) were obtained experimentally and in simulations, demonstrating the advantages of using periodic flow operation.

6.1 Introduction

The potential advantages of continuous crystallisation using cascaded multi-stage MSMPR crystallisers have been widely investigated [2], [11], [13], [25], [255], for example, steady-state operation for consistent product quality [11], [255], intensified production [87], [112], improved scalability [25], and reduction of equipment footprint, energy usage and capital cost. However, the challenges of insufficient mean residence time for crystal growth, fouling on the crystalliser walls and process monitoring equipment, transfer line blockages [13], particle settling and classification [25] and broadening of the crystal size distribution (CSD) in the conventional

MSMPR operation are still not well addressed. Tubular flow designs such as the continuous oscillatory baffled crystalliser (COBC) [20], [89] and plug flow crystalliser (PFC) [21] are promising alternatives. However, these technologies also suffer from issues with blockage of constricted orifices, encrustation on the vessel walls, slow attainment of controlled state of operation and operational instabilities [75], [256]. Furthermore, it is often difficult to adopt process analytical technologies (PAT) to COBC and PFC platforms [73] for the purpose of gaining process understanding. Other researchers have investigated novel configurations and/or operating strategies using MSMPR [32], [53], [82] and tubular flow devices [18], [257], [258]. For example, Griffin *et al* [53] modified a continuous MSMPR crystalliser by incorporating an "inverted" product classifier unit whereby small crystals are withdrawn as product, and larger crystals are recycled to a dissolver. In their studies, Ferguson *et al* [32], [51] and Lai *et al* [82] investigated a single-stage MSMPR design incorporating intermittent rapid product withdrawal in which a differential pressure is set-up across the system. Harji [257] designed a oscillatory mixed tubular vessel incorporating several baffles and channels; the model substance investigated was lactose monohydrate, and crystal sizes of ~50 µm were obtained. In the vast majority of the aforementioned studies there was a focus on producing small crystals (< 100 µm). While there are advantages to be gained from this approach, for example, in the development of inhalable pharmaceutical drugs, large crystal sizes (typically above 100 µm) are still required, for example, to improved filterability and for tablet and capsule formulations where controlled release is a requirement. Typically, seeded crystallisation approaches are applied to produce crystals of appropriate size and form due to tighter control over crystal growth and secondary nucleation mechanisms, leading to a desired CSD [259]–[261].

Periodic flow crystallisation using PMSMPR provides a promising alternative to the methods mention earlier, whereby (1) representative isokinetic slurry transfer can be achieved using intermittent increase in flow rates during transfer between stages, and (2) the mean residence time can be increased by having a tuneable holding (or batch) period between transfers. In the periodic operation, increased flow rates during transfer between PMSMPR stages helps to mitigate transfer line fouling and blockage without shortening the residence time of slurry inside the crystalliser. The work presented here also seeks to address some of the challenges encountered during continuous crystallisation development at laboratory scale using experimental approaches aided by the integrated PAT array and CryPRINS software within the IDS framework (described in Chapter 3) for process monitoring and temperature control in the PMSMPR crystalliser. Complementary off-line particle size analyses were carried out *viz*. laser diffraction using a Malvern MasterSizer® 2000 instrument, the experimental procedure employed was described in Chapter 3 Section 3.2.7. The seeded cooling crystallisations were

carried out in single- and multi-stage PMSMPRs applying coupled and decoupled operations (see Chapter 5). The work aims to demonstrate the application of the PMSMPR for control of particle size through the balance of growth and secondary nucleation for a fast growing model system (GLY-H_2O). Further aims were to determine the effect of seed properties (crystal size, shape and distribution), supersaturation and sample withdrawal method on the product CSD. The concept known as "state of controlled operation" (SCO) instead of "steady-state operation" is used to describe the periodic flow process [262]. A dynamic model was also developed for the RTD determination in the PMSMPR crystalliser to demonstrate the concept of periodic flow operation. Flowsheet process models were then developed for the periodic flow crystallisation of GLY using single- or three-stage PMSMPR crystallisers in order to provide a better understanding and improve the performance of SCO. The modelling framework was based on the Process Systems Enterprise's gCRYSTAL 4.0 platform wherein crystallisation mechanisms and kinetics of the model GLY-H_2O system were estimated from batch cooling crystallisation experiments from which solute concentration and CSD measurements were obtained. The models developed in gCRYSTAL were compared to experimental observations. The aim was to provide a benchmark periodic flow crystallisation that could contribute to the optimal design and control of PMSMPR crystallisers in the future.

6.2 Experimental Methods

The metastable zone width (MSZW) of GLY was first determined by using the polythermal method, for which unseeded batch cooling crystallisation experiments were carried out with initial concentrations ranging from 0.2801 to 0.4120g GLY/g H_2O (i.e. T_{sat} range 30 to 55 ^oC), and with constant cooling rates of 0.1 and 0.7 ^oC/min The crystalline product for the batch runs were isolated at a final temperature of either 25 or 6 ^oC. Note that no holding period was implemented up on reaching the final temperature. A stirring speed of 400 rpm was found to be sufficient for particle suspension, and applied to all experimental run reported in this chapter. The solubility data for GLY was obtained from literature, Mullin [263]. The MSZW can be thought of as a reflection of crystallisation mechanism and kinetics, that is, nucleation and crystal growth of a crystallising system. Hence, it has been widely used for crystallisation kinetic studies, for example, Mitchell *et al* [264], [265] estimated the primary nucleation and crystal growth kinetics for PCM crystallisation from ethanol. In this study, however, not only the MSZW data, but the complete experimental data sets of a series of batch cooling crystallisations were used to estimate the crystallisation kinetics, including primary nucleation, secondary nucleation, and crystal growth. A population balance model [230], [265] was developed and applied to estimate the kinetic parameters from four representative batch experiments, as shown in Table 6.1. The crystallisation kinetics obtained from these batch

experiments were independently verified by simulating single- or three-stage cascaded periodic flow crystallisations and comparing the results with experiments performed in the PMSMPR crystallisers described earlier.

Table 6.1: Summary of GLY batch MSZW experimental conditions.

Exp. No.	Initial Conc. C0 (g/g)	Cooling Rate (°C/min)	Sat. Temp., T_{sat} (°C)	Initial Temp. (°C)	Final Temp. (°C)	Batch Time (min)
BG-C1	0.4120	0.70	55	70.0	6.0	107.0
BG-C2	0.3248	0.65	40	50.0	6.0	90.0
BG-C3	0.3246	0.10	40	50.0	25.0	250.0
BG-C4	0.2801	0.55	30	40.0	6.0	93.0

6.2.1 Periodic and Continuous Flow Crystallisation Experiments

Figure 6.1 (a) and (b) provides schematic representations of the coupled and decoupled periodic flow operating regimes, respectively, showing the change in operating volume with time.

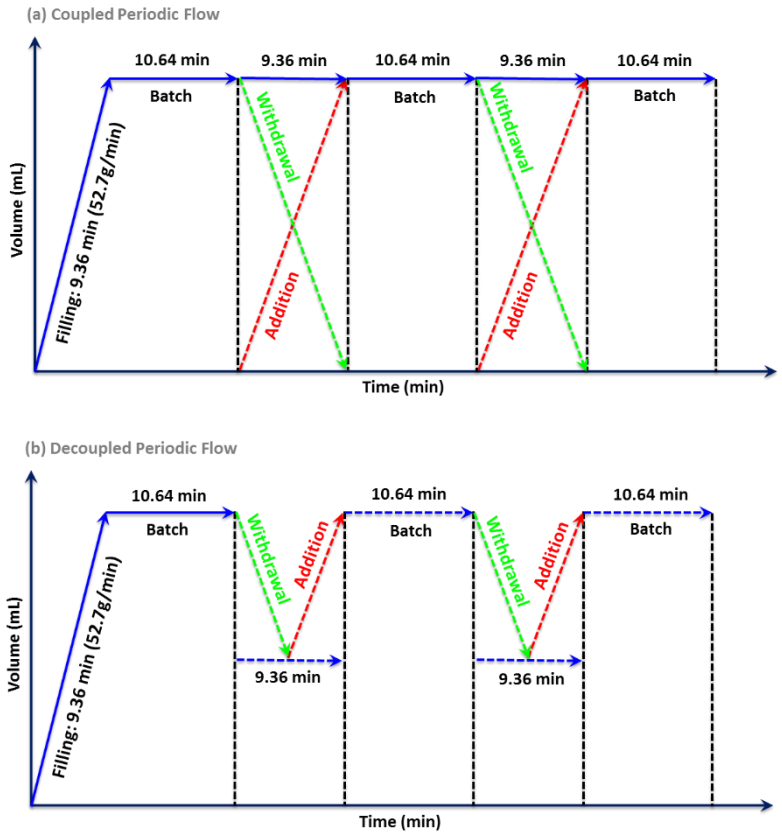

Figure 6.1: Schematic representations showing: (a) Coupled periodic flow operation of PMSMPR (constant operating volume); (b) Decoupled periodic flow operation of PMSMPR (variable operating volume due to asynchronous slurry addition and withdrawal).

The two approaches were investigated for the crystallisation of GLY in the single- and three-stage PMSMPR crystallisers. The operating volume of the crystalliser was set to 500 mL for both the decoupled and coupled operations. The coupled operation was performed as described in Chapter 5 for PCM crystallisation. However, a higher flow rate (52.7 g/mL) was employed for the addition/ withdrawal cycle to compensate for suspension density differences (i.e. PCM-IPA versus GLY-H_2O) and to have complete suspension of the GLY crystals in the transfer line to ensure rapid and isokinetic withdrawal. For the decoupled operation, half the volume of the crystalliser is removed at a rate of 52.7 g/min during the withdrawal cycle for a period of 4.68 min. This is immediately followed by the addition cycle (also 4.68 min), during which the vessel is refilled at the same flow rate and over the same time period as employed during the withdrawal cycle. Holding (or batch) periods of 10.64 min was implemented following the addition/ withdrawal cycle in both the coupled and decoupled operations, respectively.

Seed Preparation: The effect of seed properties was investigated during the periodic and continuous flow crystallisation of GLY using seed materials prepared as follows:

(1) Sieving recrystallised GLY to within size range < 75 µm ('broad CSD seed').
(2) Sieving recrystallised GLY to within size range 53 – 75 µm ('narrow CSD seed').
(3) Sieving recrystallised GLY to within size range 75 – 125 µm ('bimodal CSD seed').

Recrystallised material was used to prepare seed due to the better quality compared to seed prepared from pulverised raw material as demonstrated in Chapter 5. Figure 6.2 shows the Malvern CSDs of the three types of GLY seed materials used during the periodic flow crystallisation studies.

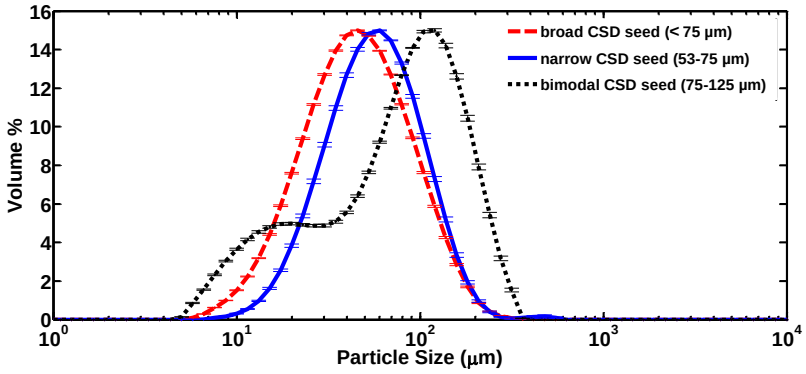

Figure 6.2: Malvern CSD for the three types of seed materials used in the study: broad CSD seed (< 75µm), narrow CSD seed (53 – 75 µm), and bimodal CSD seed (75 – 125 µm).

Periodic Flow Seeded Cooling Crystallisation in PMSMPR: Periodic flow crystallisation experiments were carried out using the PMSMPR described in Chapter 3, Section 3.6.2, Figure

3.19 (a) and (b). The process flow diagrams of the experimental set-ups used for the PMSMPR experiments are shown in Figure 6.3. Prior to start-up a fresh feed solution saturated at 20 °C (0.2278 ± 0.001 g GLY / g H_2O) was prepared in the 5 L feed vessel. The feed solution was then cooled to 19 °C, seeded with 2.5 % (28.47 g GLY) broad, narrow or bimodal CSD seed material and held for 30 min or until equilibration was observed, as determined by the FBRM D600 probe used. The holding period allows the seed suspension to equilibrate, and for crystal aging (by crystal growth and dissolution) [262] and surface healing via Ostwald ripening mechanism [252]. The supersaturation *S* of the feed steam was 1.0221 ± 0.003 (i.e. the average *S* of all experiments performed). At start-up the single-stage PMSMPR, Figure 6.3 (a), was cooled to 10 °C. Thereafter, feed suspension was added to give a SCO operating volume of ~500 mL by pumping at a rate of 52.7 g/min (pump 1) over a period of 9.36 min. This was then followed by a holding period in the PMSMPR of 10.64 min. Thereafter, periodic flow operation at a fixed rate of 52.7 g/min was initiated for 9.36 min, with cyclic holding periods of 10.64 min (coupled operation). For the decoupled periodic flow operation, the slurry addition and withdrawal cycles were each set to 4.68 min, and the holding period to 10.64 min. In the three-stage PMSMPR experiments, Figure 6.3 (b), the temperature of the first- (MSMPR 1), second- (MSMPR 2) and third- (MSMPR 3) stage of the PMSMPR were set to 17, 14 and 10 °C, respectively. The idea here is to implement a step-wise cooling profile, with an aim to reduce the supersaturation level gradually, and also increase the total mean RT_{PO} of slurry inside the PMSMPR, thus improving both the product mean crystal size and yield.

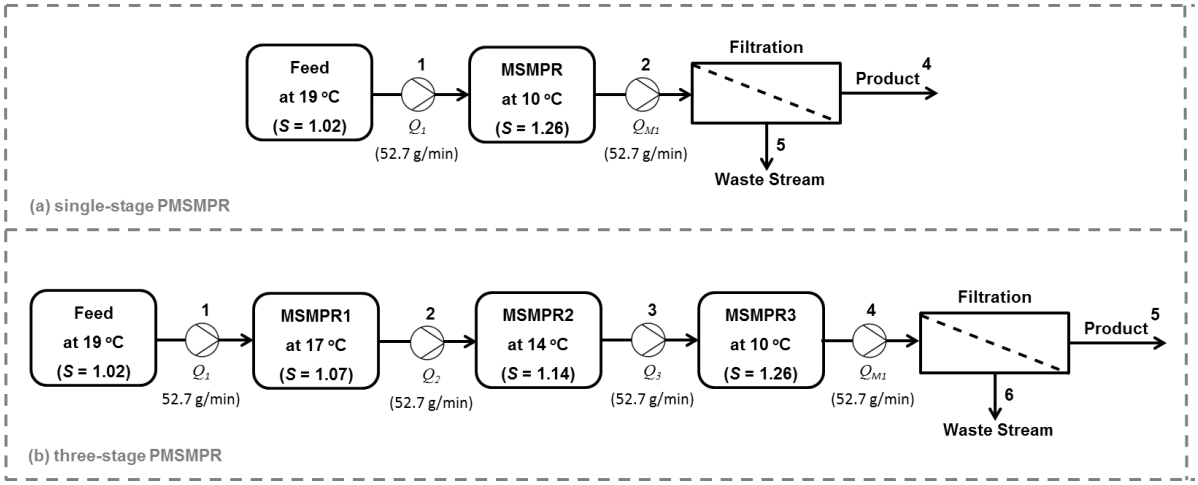

Figure 6.3: Flow diagrams showing the block configuration of: (a) single-stage PMSMPR; and (b) three-stage PMSMPR used during the periodic flow crystallisation studies.

The start-up procedure for the three-stage PMSMPR experiments was exactly the same as explained for the single-stage PMSMPRs. The three-stage PMSMPR units were operated in coupled or decoupled periodic flow crystallisation mode, Figure 6.1 (a) and (b). In the coupled operation, MSMPR 1 is filled with fresh feed suspension following the same procedure applied

for the single-stage PMSMPR described earlier. Coupled or decoupled periodic flow procedure was implemented soon after filling of the first-stage PMSMPR (MSMPR 1) until the second-stage (MSMPR 2) and third-stage (MSMPR 3) were filled. Thereafter, the coupled or decoupled periodic addition/withdrawal and batch operating cycles were continued for 10 or more RT_{PO}, that is, based on the last stage (MSMPR 3) only. The operating volume of each PMSMPR stage was ~500 mL. The sum of the addition/withdrawal and holding periods (mean RT_{PO}) of the single-stage PMSMPRs was 20 min. The RT_{PO} for each stage of the coupled three-stage PMSMPR was 20 min, therefore the total RT_{PO} was 60 min. In case of the decoupled periodic flow crystallisations (Figure 6.1 (b)) a rapid withdrawal of ~50 % of slurry from the crystalliser is implemented every cycle (flow rate: 52.7 g/min for 4.68 min), followed by rapid addition of fresh feed to refill the vessel, by employing the same flow rate/time interval. Once filled the vessel is allowed to operate in batch mode for 10.64 min. This results in a RT_{PO} of 20.00 min per PMSMPR stage, effectively giving a total RT_{PO} similar to the coupled operation. The periodic withdrawal, addition and batch operation cycles are repeated for the duration of each experimental run. Samples were taken at regular intervals from each stage during the coupled and decoupled PMSMPR experiments for off-line imaging and laser diffraction analyses. Table 6.2 provides a summary of the experimental conditions used for each of the PMSMPR experimental runs. Two sampling methods were employed during the study to determine the effect of slurry withdrawal location on the mean crystal size and CSD of product obtained from the PMSMPR. The first method, involved taking samples during the continuous operation period (cop) from each PMSMPR stage. For the second method, a representative sample was taken from the PMSMPR during the batch operation period (bop).

Table 6.2: Summary of experimental conditions used for the seeded cooling crystallisation of GLY in single- and three-stage PMSMPR crystallisers, respectively.

Experimental Conditions	M-G1	M-G2	M-G3	M-G4	M-G5	M-G6	M-G7
PMSMPR operation mode	C	C	C	DC	C	C	C
Sampling method	cop	cop/bop	cop	cop/bop	cop/bop	cop	cop/bop
Feed temperature (°C)	19	19	19	19	19	19	19
Feed concentration (g/g)	0.2288	0.2279	0.2278	0.2286	0.2278	0.2279	0.2279
PMSMPR temperature per stage (°C)	10	10	10	10	17; 14; 10	17; 14; 10	17; 14; 10
PMSMPR SCO mean concentration (c_o)	0.1868	0.1882	0.1842	0.1847	0.1888	0.1859	0.1874
Seed material (2.5 %)$^{++}$	broad	narrow	bimodal	bimodal	broad	narrow	Bimodal
Feed stream flow, Q_1 (g/min)	52.7	52.7	52.7	52.7	52.7	52.7	52.7
MSMPR 1 outlet flow, Q_2 (g/min)	n/a	n/a	n/a	n/a	52.7	52.7	52.7
MSMPR 2 outlet flow, Q_3 (g/min)	n/a	n/a	n/a	n/a	52.7	52.7	52.7
MSMPR 3 outlet flow, Q_{M1} (g/min)	52.7	52.7	52.7	52.7	52.7	52.7	52.7
Slurry withdrawal period (min)	9.36	9.36	9.36	4.68	9.36	9.36	9.36
Slurry addition period (min)	9.36	9.36	9.36	4.68	9.36	9.36	9.36
Holding (or batch) period (min)	10.64	10.64	10.64	15.32	10.64	10.64	10.64
Mean RT_{PO} (min)	20.00	20.00	20.00	20.00	60.00	60.00	60.00

M-G1, M-G2, M-G3 and M-G4 = single-stage PMSMPR; M-G5, M-G6 and M-G7 = three-stage PMSMPR; C = coupled operation; DC = decoupled operation; cop = sampling from outlet transfer line during continuous operation period; bop = sampling from bottom valve during batch operation period; n/a = not applicable.

Continuous Seeded Cooling Crystallisation of GLY in MSMPR: Continuous single- and three-stage MSMPR experiments were conducted under similar conditions to the periodic flow experiments described earlier. The saturation level of the feed (1.02 ± 0.03) and PMSMPR vessels were maintained at a similar level to the equivalent periodic flow experiments. Only 'bimodal CSD seed' (75 – 125 µm) seed was investigated for these studies. Flow rates employed were the same as that for the periodic flow experiments, therefore, the residence time of the continuous process was approximately half that of the coupled PMSMPR process. It was not possible to operate the continuous experiments at the low flow rates required to achieve comparable residence time to the periodic flow experiments due to the setting of particles, in particular, larger ones as determined by visual inspection of the transfer lines. Particle settling is attributed to the higher settling velocities of large particles compared to smaller ones [262].

Using the continuous MSMPR, there is a trade-off between the residence time and parameters such as product yield and crystal growth. To achieve sufficient product yield and crystal growth long residence time is a requirement. However, long residence time requires low flow rates between transfer lines, which can lead to classified product withdrawal due to particle settling. This then leads to the blockage of transfer lines, and hence frequent interruptions to the process that can cause erratic and unsteady-state (or uncontrolled) behaviour. Periodic sampling of the continuous flow process was conducted for off-line analyses and comparison with the PMSMPR operations. Experimental conditions for the continuous MSMPR runs are summarised in Table 6.3.

Table 6.3: Summary of experimental conditions used for the continuous seeded cooling crystallisation of GLY in single- and three-stage MSMPR crystallisers.

Experimental Conditions	M-CG1	M-CG2	M-CG3	M-CG4	M-CG5
Sampling method	cop	bop	cop	cop	bop
Feed temperature (°C)	19	19	19	19	19
Feed concentration (g/g)	0.2286	0.2275	0.2278	0.2287	0.2278
PMSMPR temperature per stage (°C)	10	10	10	17, 14, 10	17, 14, 10
MSMPR SCO mean concentration (c_0)	0.2074	0.2034	◊0.1962	◊0.1928	◊0.1970
Seed material (2.5 %)	bimodal	bimodal	bimodal	bimodal	bimodal
Feed stream flow, Q_1 (g/min)	52.7	52.7	52.7	52.7	52.7
MSMPR 1 outlet flow, Q_2 (g/min)	n/a	n/a	n/a	52.7	52.7
MSMPR 2 outlet flow, Q_3 (g/min)	n/a	n/a	n/a	52.7	52.7
MSMPR 3 outlet flow, Q_{M1} (g/min)	52.7	52.7	52.7	52.7	52.7
Mean RT_{PO} (min)	9.36	9.36	28.08	28.08	28.08

M-CG1, M-CG2 and M-CG3 = single-stage continuous MSMPR; M-CG4 and M-CG5 = three-stage continuous MSMPR; cop = sampling from outlet transfer line during continuous operation period; bop = sampling from bottom valve during batch operation period; ◊ = "steady-state operation" not achieved.

The mean residence time for continuous flow crystallisation in the MSMPR is the same as the addition/withdrawal cycle of the coupled PMSMPR operation. Due to the coupled addition/withdrawal of slurry applied during the coupled PMSMPR operation, the corresponding RTD would be as broad as that of continuous flow MSMPR crystallisation. However, the latter requires a vessel of about twice the operating volume of the former to achieve a comparable mean residence time. In this regard, the periodic flow operation shows

the benefits of reducing the equipment footprint and cost, compared to the continuous operation. The continuous flow single- and three-stage MSMPR crystallisations carried out in this study served as benchmarks to demonstrate the advantages of periodic flow crystallisation. For the continuous crystallisations, in all cases, the steady-state product slurry withdrawn during each experiment was filtered and the crystals collected for off-line image analysis and measurement of the CSD using laser diffraction.

6.3 Mathematical Modelling

6.3.1 Dynamic Model of Residence Time Distribution

The RTD in continuous flow MSMPR and periodic flow PMSMPR crystallisers were simulated taking into account the following assumptions: steady-state (i.e. in the continuous MSMPR), SCO (i.e. in the PMSMPR), transports at the inlet and the outlet takes place only by advection, and incompressible flow (i.e. closed boundary conditions). Although a continuously operated stirred tank crystalliser (STC) is usually assumed to attain perfect micro-mixing for liquid-solid phases in the vessel [83], the effect of macro-mixing due to addition and withdrawal of slurry plays a more critical role, in particular, shaping the final crystal attributes (e.g. crystal size, shape and CSD). Accordingly, the RTD of the slurry provides useful information on the mean residence time, and its corresponding standard deviation is often studied for many innovative continuous crystallisation techniques [266], [267]. Thus, a generic dynamic model was first developed for the RTD of a STC subject to different slurry addition and withdrawing operating patterns. The system governing equations of the RTD in a well-mixed stirred tank [268], [269] can be represented as follows:

$$\frac{\partial(VW)}{\partial t} = -\frac{\partial(VW)}{\partial \theta} + \sum_{i=1}^{m} v_i F_i - \sum_{j=1}^{n} v_j E_j \qquad 6.1$$

$$\frac{dV}{dt} = \sum_{i=1}^{m} v_i - \sum_{j=1}^{n} v_j \qquad 6.2$$

where t represents time (s); V is the operating volume (m^3); θ is the residence time inside the vessel(s); v_i is the feeding flowrate of the ith stream (m^3s^{-1}); v_j is the withdrawing flowrate of the jth stream (m^3s^{-1}); W (t, θ) is the corresponding RTD (s^{-1}); F_i (t, θ) is the RTD of the ith stream (s^{-1}); E_j (t, θ) is the RTD of jth exceeding stream (s^{-1}) and is identical to W(t, θ) for a well-mixed stirred tank. The corresponding initial and boundary conditions are:

$$W(0,\theta) = W_0(\theta) \quad 6.3$$

$$V(0) = 0 \quad 6.4$$

$$W(t,0) = 0 \quad 6.5$$

where $W_0(\theta)$ is the initial RTD in the vessel (s^{-1}). If the vessel starts from empty as in Eqn. 6.4, $W_0(\theta)$ is a Dirac delta function (or distribution), δ, such that W_0 is zero everywhere except at zero, with an integral of one over the entire residence time, θ. $F_i(t, \theta)$, is also a δ function if there is fresh feed into the vessel (used to characterise the impulse response curve). Owing to the simple convection term of $\partial\theta/\partial t = 1$, the backward finite difference method (BFDM) was used here to discretise the above partial differential equation (PDE) (1) and solve together with Eqn. 6.2 in MATLAB using "ode45".

6.3.2 Flowsheet Models of Periodic Flow Crystallisation Operation

Towards better process understanding and design of the novel periodic flow crystallisation in PMSMPR, rigorous population balance based mathematical modelling and flowsheet simulations were employed in this study by implementing the gCRYSTAL 4.0 software package, which offers various particle size change mechanisms and kinetics for characterisation of crystallisation processes, as well as convenient toolboxes for parameter estimation and process optimisation. The main steps involved in the implementation of gCRYSTAL for kinetic parameter estimation using the batch cooling crystallisation experiments and the simulation of periodic flow crystallisations is described. Firstly, the system information and material properties of GLY-H_2O, for example, molecular weights, densities and solubility that could be obtained elsewhere in the literature or chemical handbooks [270], were configured in the *"global specification"* module in gCRYSTAL. By adopting the *"Crystalliser MSMPR"* module in the model library, configurations of the batch STC were set-up according to the actual experimental conditions. In terms of the crystallisation mechanisms and kinetics, instead of using theoretical first-principles models for nucleation, crystal growth, and agglomeration, semi-empirical power-law kinetic models were used here for chemical engineering purposes. For example, a secondary nucleation model based on the work of Evans *et al*. [271] was used to describe the nucleation effect due to attrition. For crystal agglomeration, the A50 parameter was introduced to represent the combined effect of material strength, point of contact between two crystals and vessel geometry [272]. Details of the crystallisation mechanisms and kinetic models selected in gCRYSTAL are summarised in Table 6.4. Further information about the model equations can be found in the help documentation of the gCRYSTAL software and the references therein.

Table 6.4: Summary of the crystallisation mechanisms and kinetic models.

Mechanism	Kinetics	Options	Parameters
Primary nucleation	Customised power law kinetics	Relative supersaturation $(C-C_{sat})/C_{sat}$	▪ Rate constant ▪ Supersaturation order ▪ Activation energy ▪ Order with respect to solute concentration
Secondary nucleation	Evans kinetics	Collision type: Crystal-Impeller (CI)	▪ Rate constant ▪ Size above which crystals undergo attrition ▪ Order with respect to supersaturation
Crystal growth	Power law kinetics	Relative supersaturation $(C-C_{sat})/C_{sat}$	▪ Growth rate constant ▪ Order with respect to supersaturation ▪ Activation energy
Agglomeration	Mumtaz kinetics	-	▪ Agglomeration parameter (A50)

For the model development, data from the four unseeded experiments listed in Table 6.1 were imported into the gCRYSTAL folder of *"Experiments>Performed"*. Therein, the *in situ* measurements of GLY concentration and temperature, and off-line CSD measured by laser diffraction for each of the batch experiments were saved. "*Perfect control*" was chosen in the gCRYSTAL temperature controller so that the actual temperature profiles measured in the batch experiments could be imported as set points and were exactly tracked in the parameter estimation. Upon the successful input of the batch experimental data, the group of kinetic parameters listed in the Table 6.4 could be estimated using the "*Parameter Estimations*" tool in the software. Multiple tries of initial guesses were necessary to obtain a good agreement between model predictions and experimental measurements. In some cases, it was critical to re-examine the selected crystallisation mechanisms by referring to the experimental observations, for example, the effect of impeller stirring speed on nucleation based on FBRM total counts/s; and the effect of crystal agglomeration based on PVM and microscopy images.

Modelling of the periodic flow PMSMPR crystalliser was also implemented in gCRYSTAL 4.0 using multiple placements of transfer pumps and *"Crystalliser MSMPR"* stages in the flowsheet. A customised control module of the *"Intelligent Decision Support (IDS)*" framework was also developed in this study to logically switch on or off the pumps to realise the sequential start-up of a three-stage cascade of PMSMPR crystallisers, and to fulfil the periodic flow operating condition. Both single- and three-stage PMSMPR crystallisation simulations were performed according to the actual experimental operating conditions as described earlier in the experimental methods section. Their flowsheets are illustrated in Figure 6.4. Note that the same kinetic parameters estimated from the batch cooling crystallisations were incorporated here.

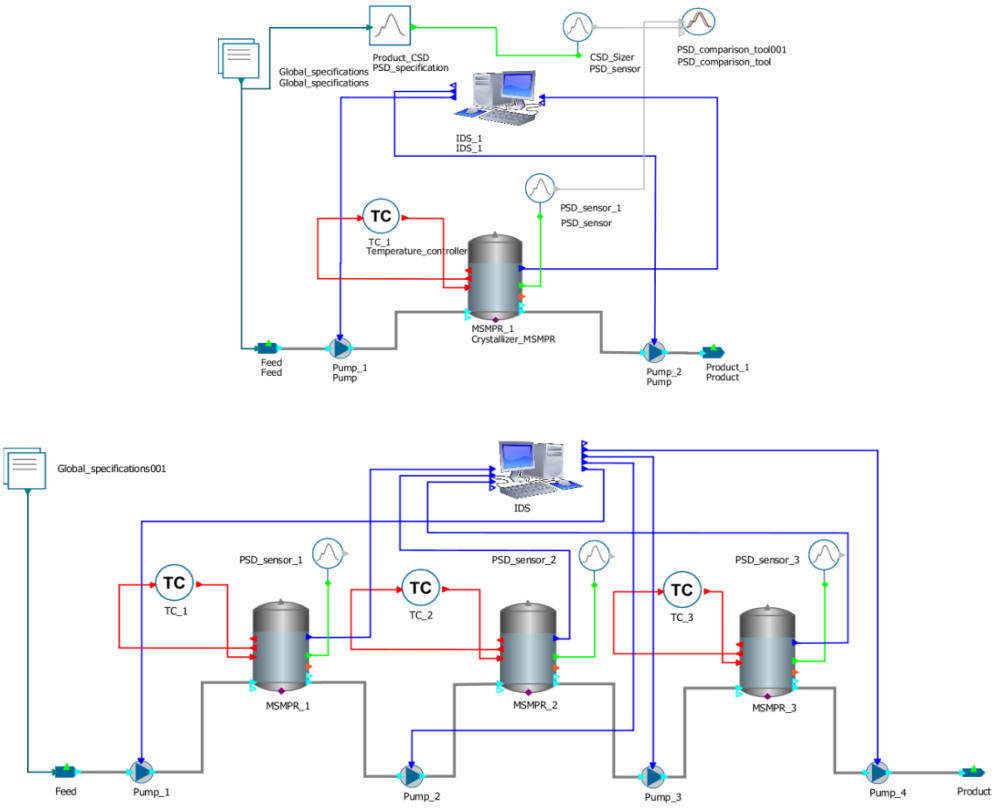

Figure 6.4: Flowsheet of the periodic flow crystallisation experiments: single-stage PMSMPR crystalliser (top); cascaded three-stage PMSMPR crystallisers.

Unlike the simulation of the unseeded batch crystallisations, seeded feed suspensions were used in the periodic flow PMSMPR crystallisations, which required the specification of initial seed loading and CSD in gCRYSTAL. This was done by importing the CSD measurements into the saved file "*Seed CSD.txt*" in the "*Miscellaneous Files*" folder. It is worth mentioning that conversion of the discrete histogram of laser diffraction CSD measurements of seed crystals to volume-based density distributions was required in the saved text file. In addition, proportional and integral (PI) controllers were introduced in the gCRYSTAL temperature controller. The parameters of "*Gain*" and "*Integral time*" were fine-tuned to agree well with the dynamic response of the temperature measured in the respective periodic flow experiments. This is because dynamic changes in temperature (for example, due to changes in liquid level and wall fouling) were possibly affected by the thermal capacity of the cooling jacket of each PMSMPR vessel.

6.4 Results and discussion

6.4.1 Residence Time Distribution in Periodic Flow Crystalliser

It would be of interest to demonstrate the RTD of periodic flow operation in the PMSMPR crystalliser and to compare it with that of a conventional continuous flow MSMPR crystalliser, when it is claimed that the periodic flow operation has the capability of extending the mean residence time without broadening the corresponding RTD. The dynamic RTD model reported in Section 6.3.1 has been applied to simulate the RTDs of a continuous flow MSMPR, and periodic flow PMSMPRs operated in coupled and decoupled modes, respectively. The operating principles were described earlier in the experimental methods section and depicted in Figure 6.1 (a) and (b). Their RTD results are shown in Figure 6.5. It was found that the coupled periodic flow operation approximately doubled the mean residence time, τ, from 9.17 min under continuous flow operation to a time-averaged value of 19.96 min, but with a much more broadened RTD, that is, the standard deviation, σ, of the distribution changed from 9.50 min to 19.91 min However, if one reduces the flow rates for feed addition and withdrawal in the continuous flow MSMPR, thereby doubling the mean residence time to 18.34 min, the corresponding standard deviation increases to 18.81 min On the other hand, if one compares the coefficient of variation (c.v.) of their respective RTDs, c.v. = σ/τ, the c.v. for continuous flow operation is 9.50/9.17 = 1.04, or 18.81/18.34 = 1.02; while the c.v. for coupled periodic flow operation is averaged at 19.91/19.96 = 1.00. In this respect, the coupled periodic flow operation did extend the residence time, but without broadening the RTD too much. For the decoupled periodic flow operation, the time-averaged mean residence time was increased to 35.05 min with a standard deviation of about 28.15 min, and c.v. of around 0.8031. This is because of the decoupling of pumping during addition and withdrawal of slurry, in such a way that minimises the possibility of direct washing-out of the fresh feeding suspension. However, the productivity of the decoupled periodic operation would be significantly affected because the interruption between withdrawal periods is prolonged and may merely show marginal advantages when compared to batch operation with respect to productivity. Furthermore, a very long time to a controlled state of operation (or SCO) is required during the start-up phase, based on the standard deviation of the RTD as shown in Figure 6.5. It should be emphasised once again that only half of the slurry in the crystalliser was withdrawn and subsequently refilled in the decoupled periodic flow operation (Figure 6.1). However, if larger volumes of slurry are involved, shorter mean residence times and narrower RTDs would be observed with limits approaching batch operation; while smaller volumes would result in longer residence time and broader RTD. In practice, the slurry withdrawal and refilling of the coupled or decoupled PMSMPR operation should be designed and optimised with profound process understanding. It therefore follows that

a systematic study and optimisation of the effect of RTD on CSD seem interesting and deserve more investigative effort. Future work may look to optimise the periodic flow operation for direct design and to tailor the RTD in order to achieve desired product CQAs.

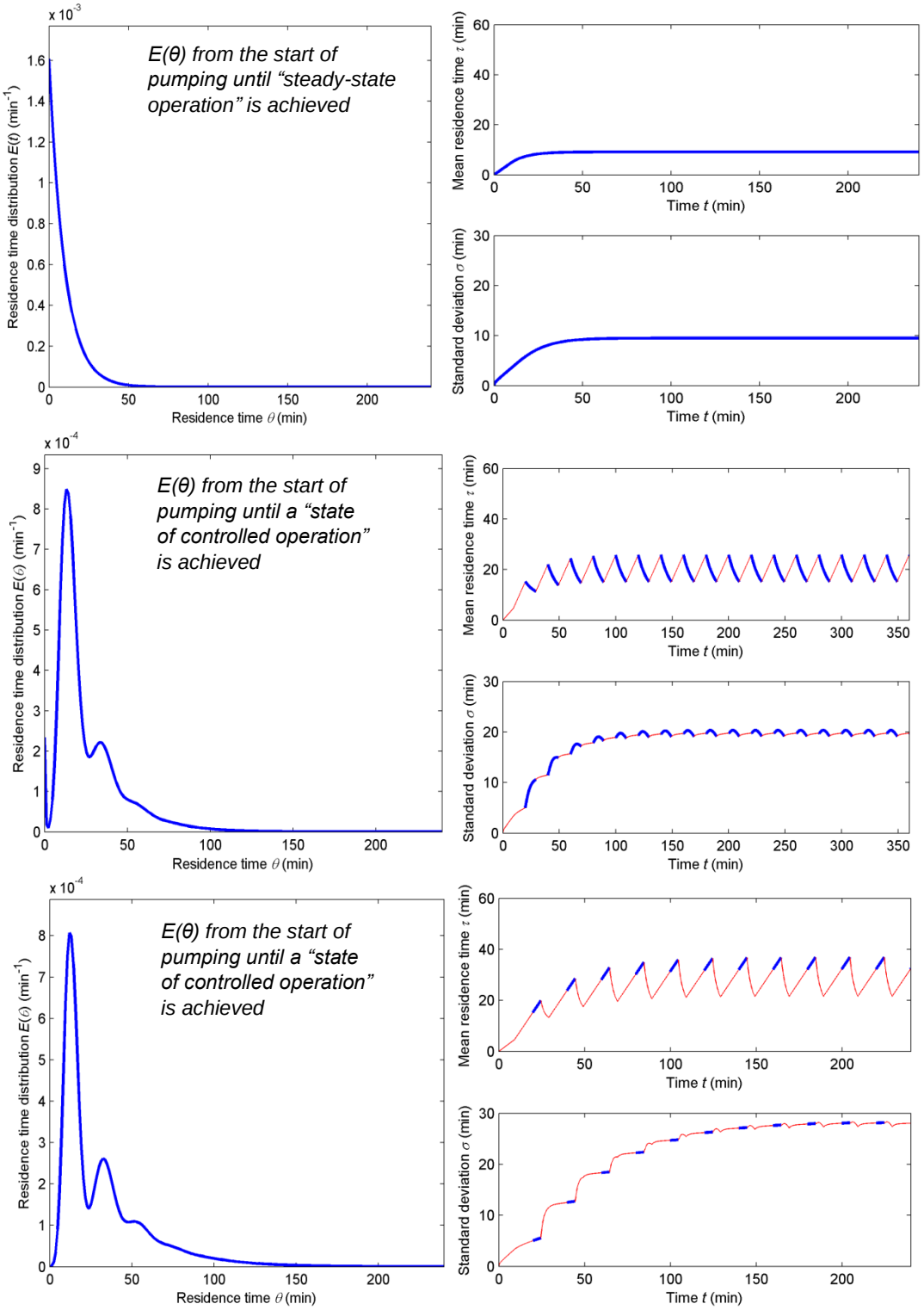

Figure 6.5: RTD of continuous MSMPR (top three), coupled periodic PMSMPR (middle three), and decoupled periodic PMSMPR (bottom three) crystallisers. Bold solid blue lines indicate final minutes of addition/withdrawal time period.

6.4.2 Comparison of Periodic and Continuous Flow Crystallisations

Single-stage periodic PMSMPR and continuous MSMPR Crystallisation Experiments: It is well-know that factors such as seeding strategy, residence time, and rate of supersaturation generation can significantly affect the mean product size and CSD in MSMPR crystallisers. In addition, the product withdrawal strategy can also influence the product mean size and CSD. In this study, the factors influencing product mean size and CSD mentioned earlier were experimentally investigated in the period flow process (PMSMPR). The effect of seed crystal properties on the product size and the time to achieve a "state of controlled operation" (SCO) was investigated by using the three types of seed materials mentioned in Section 6.2, applied at the same seed loading (2.5 wt%). Figure 6.6 (a) – (e) shows the process time diagrams for the single-stage periodic PMSMPR and continuous MSMPR experiments.

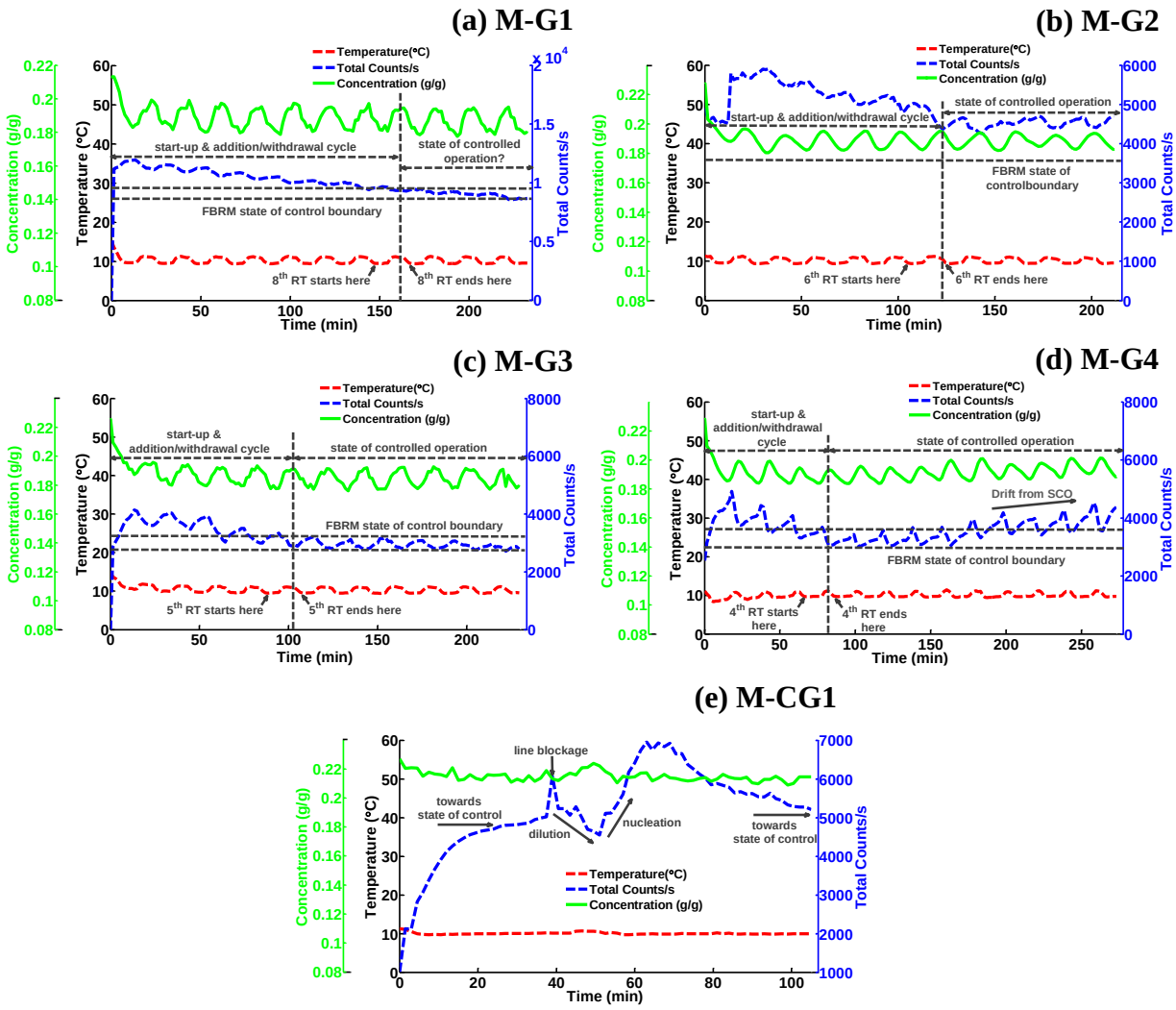

Figure 6.6: Process time diagrams for the single-stage coupled, (a) – (c) and decoupled, (d) PMSMPR experiments and equivalent continuous MSMPR experiment (e).

The effect of seed characteristics on the time to achieving SCO in the single-stage PMSMPR experiments is quite apparent from the change in FBRM counts/s. Two types of experiments were conducted, that is, coupled and decoupled periodic flow (Section 6.2.1). Broad, narrow and bimodal CSD seed were used for experiments M-G1 (a), M-G2 (b), M-G3 (c) and M-G4 (d) (Figure 6.6). The approach to SCO is fastest in the order M-G3 < M-G2 < M-G1 < M-G4, indicating that the seed properties (specifically size and CSD) and the mode of operation (coupled or decupled), affects the approach to a controlled state, with larger seed size leading to faster control. This appears to be a surface area effect, where by large seed crystals consume supersaturation at a slower more gradual rate compared to smaller seeds, which have a higher surface area (size dependent growth). Note that unlike batch operation, the periodic flow process does not operate at equilibrium. The time to a controlled state with respect to seed material is in the order bimodal CSD < narrow CSD < broad CSD seed. This is not entirely surprising since the mean size of the seed materials are in the order bimodal CSD > narrow CSD > broad CSD seed. Furthermore, aging of the seed and the Oswald's ripening process leads to preferential dissolution of fines and growth of large crystals at their expense. Although M-G4 appeared to achieve SCO early on based on FBRM and concentration measurements, there is an obvious drift from controlled operation that occurs from approximately 150 min, which is perhaps linked to the decoupled mode of operation. The RTD study, Section 6.4, showed that decoupled operation takes a longer time to achieve SCO. Table 6.5 shows the particle size of the crystalline seed materials before and after aging, as determined by Malvern Mastersizer® volume based mean particle size D[4, 3], and FBRM mean square weighted chord length (MSWCL) measurements and analyses. In addition to the seed material properties, the mode of periodic flow operation also affects the time to achieving SCO, with faster approach to control in the decoupled process.

Table 6.5: Summary of experimental results for the cooling crystallisation of GLY in single-stage periodic PMSMPR and continuous MSMPR crystallisers.

Parameters Measured	M-G1	M-G2	M-G3	M-G4	M-CG1
Seed material type	Broad	Narrow	Bimodal	Bimodal	Bimodal
Mean seed size before aging: D[4, 3] Malvern® (µm)	50 ± 0.2	61.8 ± 1.7	115.5 ± 1.6	119 ± 1.7	119 ± 1.7
Mean seed size after 30 min aging: D[4, 3] Malvern® (µm)	125.1 ± 1.2	171.5 ± 1.7	249.8 ± 4.2	232.4 ± 1.9	250.7 ± 2.2
Mean seed size after 30 min aging: FBRM MSWCL (µm)	53.1 ± 2.1	65.6 ± 1.3	79.9 ± 0.5	86 ± 0.4	84.2 ± 0.7
¥Mean product crystal size: D[4, 3] Malvern® (µm)	167.5 ± 3.3	220.0 ± 1.2	287.6 ± 1.6	519.0 ± 22.5	248.5 ± 8.8
Mean product crystal size: FBRM MSWCL (µm)	76.2 ± 1.1	95.3 ± 1.1	104.6 ± 0.8	114 ± 2.0	94.6 ± 1.4
% Yield of crystallisation (*Y*)	88.9	85.2	94.5	93.0	44.8

Experiments M-G3 and M-G4 were carried out under identical conditions using the same bimodal CSD seed, with the exception that the latter was operated in decoupled period flow mode. It would appear that there is a faster approach to control in M-G4 run, based on the concentration data. However, it is clear there is a significant drift in the FBRM total counts/s away from SCO operation due perhaps to the decoupling of the addition and withdrawal cycles leading to oscillations, and therefore a longer time to achieve control. This result would appear to agree with the predictions from the RTD simulations. The equivalent continuous MSMPR experiment carried out with bimodal CSD seed, Figure 6.6 (e) (M-CG1), did not achieved SCO due to line blockage issues, that is, despite the high flow rate and transfer velocities employed. This was perhaps a result of nucleation in the transfer lines leading to blockage at pump gears where the transfer tube is constricted. Table 6.5 also shows the percentage yield of crystallisation (*Y*), which is described in Chapter 5 and in [262]. The yield of crystallisation is similar for each of the single-stage PMSMPR experiments, and as expected the continuous single-stage MSMPR (M-CG1) show significantly lower yield. Figure 6.7 shows the operating trajectory though the phase diagram for a periodic flow PMSMPR (M-G3), and equivalent continuous MSMPR (M-CG1), which gives further evidence of the higher yield of crystallisation for the former case. The phase diagrams also give an insight into the crystallisation behaviour of both systems. In the periodic operation there are more oscillations in concentration relative to the continuous run.

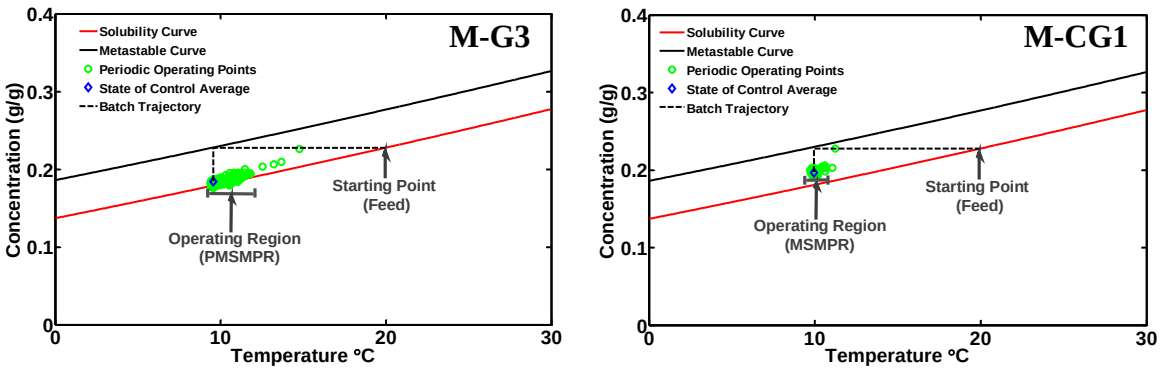

Figure 6.7: Process phase diagrams for PMSMPR (left, M-G3) and equivalent continuous MSMPR (right, M-CG1) crystallisations showing operating regions for each system.

The data in Table 6.5 further shows that for all seed materials used in the study, following the aging process, a larger mean size of particles is obtained compared to the pre-aged materials. The dramatic increase in mean crystal size is attributed not only to the growth of large particles at the expense of the smaller ones that dissolve, but also to two other factors: (1) the small but significant amount of supersaturation (1 ^{o}C) generated in the feed vessel at start-up (feed solution saturated at 20 ^{o}C, but held at 19 ^{o}C followed by addition of seeds); (2) aggregation of fine seed particles, which later form cemented agglomerates. This phenomenon was

evident particularly with finer seed materials, for example, the broad CSD (> 75 µm) seed. Evidence of the preferential agglomeration of the fine particles is shown in the microscope images of the aged seed materials (Figure 6.8). Of the aged seed materials, the bimodal CSD crystals show the least amount of agglomeration. On the other hand, a significant amount of agglomerates can be observed in the aged broad CSD seed material. Overall, the images appear to be consistent with an increase in mean crystal size of aged seed materials as determined by Malvern® and FBRM (Table 6.5). Relative to the aged seed crystals, significant crystal growth is observed for the product crystals obtained from each experiment as shown in Figure 6.9. The largest and most uniform crystals are obtained from M-G3 and M-G4 PMSMPR experiments in which the bimodal CSD seed material was used. The crystals exhibit the usual bipyramidal hexagonal prism morphology of the α-polymorphic form, which typically grows from aqueous solutions [273], [274].

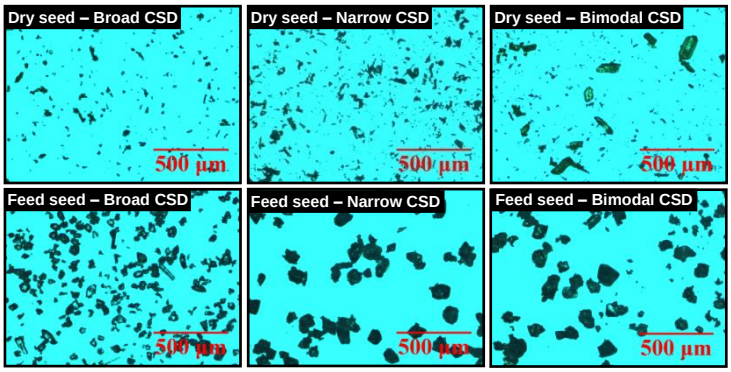

Figure 6.8: Microscope images of seed crystals used in the periodic PMSMPR and continuous MSMPR experiments: dry seed material before adding to feed vessel (first row); seed crystals obtained from feed vessel after 30 min aging (second row).

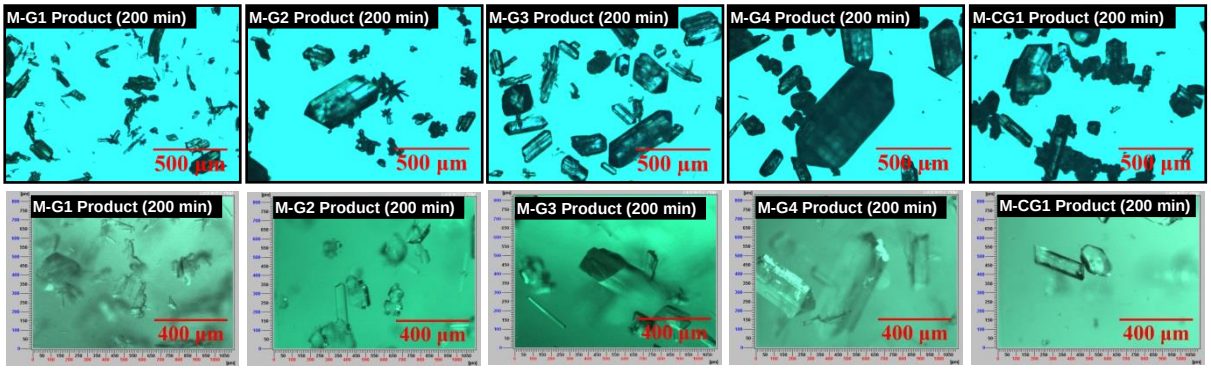

Figure 6.9: Microscope (first row) and PVM (second row) images of product crystals from the periodic PMSMPR and continuous MSMPR experiments.

The product crystals obtained from M-G1 (broad CSD seed) show variable shapes and have many agglomerates. In comparison, the product crystals from M-G2 have a well-defined

shape, but there is a mixture of large, small and agglomerated crystals. The crystalline products obtained from M-CG1 (continuous MSMPR), M-G3 (coupled PMSMPR) and M-G4 (decoupled PMSMPR) show similar well-defined crystal shapes and few agglomerates. The normalised product crystal CSD profiles obtained from laser diffraction measurements (Malvern Mastersizer®) on samples from each experimental run is show in Figure 6.10. For all experimental runs, crystal growth is observed as a shift of the CSD to the right relative to the aged seed materials. The product size is largest for the decoupled PMSMPR run (M-G4), while marginal growth is observed for the continuous MSMPR run (M-CG1). Collectively, the results presented indicate that glycine is a fast growing API, and that the kinetics of the crystallisation is suited to the PMSMPR operation. Furthermore, the quality of seed material can affect the extent of agglomeration and formation of well-defined crystals. In this section, the effect of seed properties on the time to achieve a SCO and on the product crystal size and quality was addressed. In the sections following, the effect of residence time, supersaturation, and product withdrawal strategy on the time to attain a SCO and CSD properties are discussed.

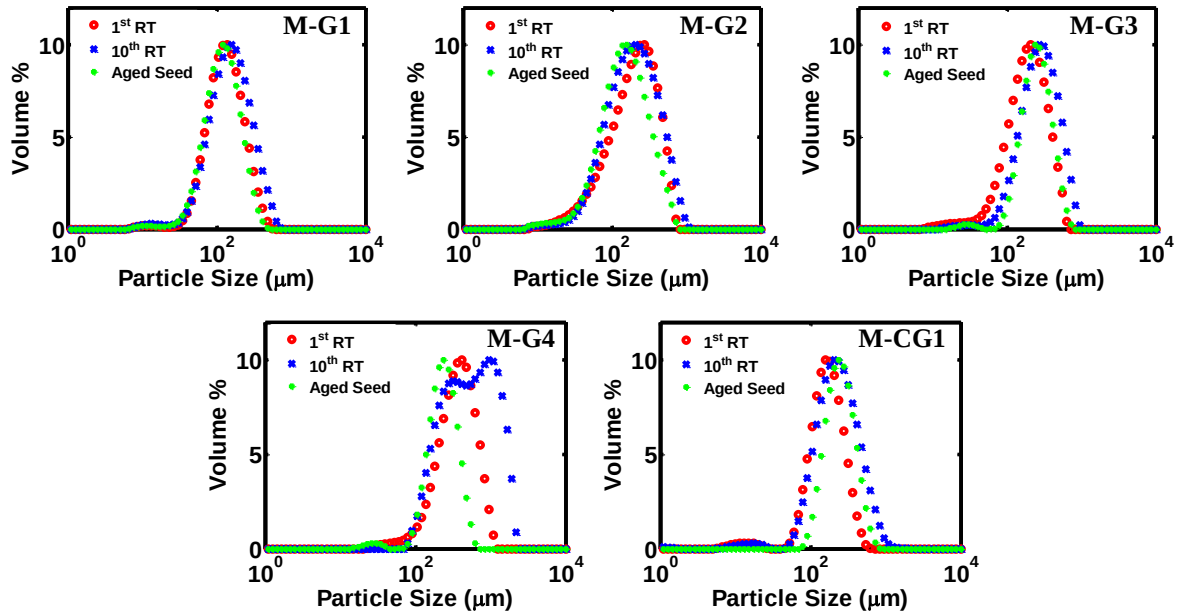

Figure 6.10: Normalised CSD profiles for the aged seed materials and 1st (20 min) and 10th (200 min) RT_{PO} product crystals obtained from the PMSMPR and continuous MSMPR experiments, data obtained by laser diffraction (Malvern Mastersizer®).

Three-Stage Periodic PMSMPR and Continuous MSMPR Crystallisations: The Time diagrams of the three-stage periodic PMSMPR and continuous MSMPR experimental runs are presented in Figure 6.11 (a) – (d), showing the FBRM counts/s and temperature recorded in the first- and third-stage of each experiment. Also shown are the FTIR ChemiGram and Raman concentration measurements from the second- and third-stage, respectively. The FTIR ChemiGram is generated from integrated absorbance over a specific frequency range, in this

case 1414 – 650 cm^{-1}. It shows the change in the relative absorbance of solution phase glycine from the accumulated spectra, which permits the monitoring of the time taken to attain SCO in the second-stage. In the three-stage operation, residence time increases threefold compared to the single-stage equivalents. There is also a more gradual change in supersaturation over the three stages, from 19 ^{o}C (feed vessel) to 17 ^{o}C (MSMPR 1), 14 ^{o}C (MSMPR 2) and 10 ^{o}C (MSMPR 3). SCO is observed for M-G5 (Figure 6.11 (a); broad CSD seed) and M-G6 (Figure 6.11 (b); narrow CSD seed), almost immediately from start-up to the end of each PMSMPR run. In the case of M-G7 (Figure 6.11 (c); bimodal CSD seed), SCO is achieved much later after ~104 min in all PMSMPR stages. Interestingly, the time taken to achieve SCO matches well with the equivalent single-stage PMSMPR (M-G3) experiment reported earlier.

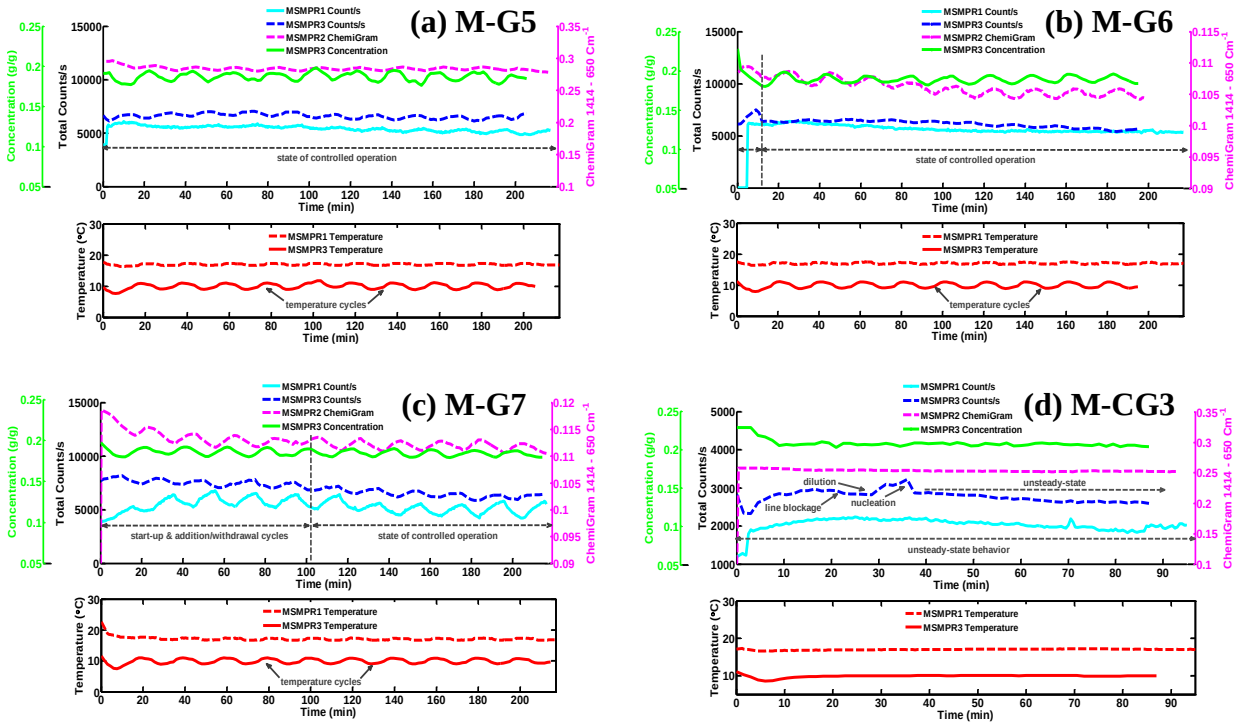

Figure 6.11: Process time diagrams for the three-stage cascade PMSMPR, (a) – (c) and equivalent continuous MSMPR (d) experiments.

The results suggest that the small amount of supersaturation generated at each PMSMPR stage is rapidly consumed when fine seed crystals (broad and narrow CSD) are used, leading to a much faster approach to a controlled state compared to when the bimodal CSD seed is used. Furthermore, it appears that not only the seed crystal properties (for example, mean size, shape and CSD) are affecting the time to achieving a SCO (also observed in the single-stage PMSMPR runs), but also the amount of supersaturation generated. For the equivalent continuous MSMPR experiment, steady-state was not observed due to line blockage issues, for the same reason as explained for the single-stage continuous MSMPR runs.

A summary of results from the three-stage experiments is present in Table 6.6. Interestingly, parameters such as mean product crystal size obtained from MSMPR 3, and the yield of crystallisation are very similar to the results observed for the single-stage experiments. The exception is the continuous three-stage MSMPR experiment (M-CG3), where the mean crystal size is smaller and the crystallisation yield much higher compared to the equivalent single-stage continuous MSMPR (M-CG1) run. Normally, one would expect a significant increase in mean crystal size and process yield in the three-stage operation due to the extended residence time. Regarding the mean product crystal size, it appears that despite the difference in the rate of supersaturation generation in the single- versus the three-stage PMSMPR operations, there is little effect on the crystal growth and nucleation rates. In the single-stage PMSMPR, supersaturation is generated rapidly, going from 19 ^{o}C (feed stream) to 10 ^{o}C saturation, that is, S = 1.23. For the three-stage PMSMPR, the change in S was more gradual, change from 1.04 (MSMPR 1) to 1.07 (MSMPR 2) and then 1.10 (MSMPR 3). However, for the continuous MSMPR operation, it appears that the rate of supersaturation generation is more significant. This explains why the product size and process yield for the continuous single- and three-stage MSMPRs are different. The results provide further evidence that the operating region in the phase diagram for the PMSMPR is different from that of the continuous MSMPR as indicated earlier (Figure 6.7; M-CG1).

Table 6.6: Summary of experimental results for the cooling crystallisation of GLY in three-stage periodic PMSMPR and continuous MSMPR crystallisers.

Parameters Measured	M-G5	M-G6	M-G7	M-CG3
Seed material type	Broad	Narrow	Bimodal	Bimodal
Mean seed size before aging: D[4, 3] Malvern® (µm)	50 ± 0.2	61.8 ± 1.7	115.5 ± 1.6	119 ± 1.7
Mean seed size after 30 min aging: D[4, 3] Malvern® (µm)	139.6 ± 2.2	170.8 ± 2.0	248.2 ± 0.4	214.8 ± 4.3
Mean seed size after 30 min aging: FBRM MSWCL (µm)	66.7 ± 3.0	70.2 ± 1.8	75.2 ± 1.9	82.6 ± 1.3
¥Mean product crystal size: D[4, 3] Malvern® (µm)	210.0 ± 4.3	216.8 ± 1.9	288.0 ± 14.7	227.9 ± 9.6
Mean product crystal size: FBRM MSWCL (µm)	83.3 ± 2.1	83.3 ± 2.7	103.5 ± 3.0	101.4 ± 5.4
% Yield of crystallisation (Y)	83.4	89.5	90.3	76.1

¥Mean product crystal size = samples taken from crystalliser outlet tube

Figure 6.12 shows the microscope images of the product crystals obtained from the first- through third-stage for each experimental run as well as real-time PVM images from the third-stage. As expected the largest and best quality crystals are obtained from M-G7 run due to the larger mean size of the seed crystals used (Table 6.6). The CSD profiles of seed crystals from the feed

and each of the three stages of the PMSMPR and continuous MSMPR experimental runs are shown in Figure 6.13. In all experimental runs, growth was observed progressively from the first to final-stage MSMPR, indicated by a shift in the distributions to the right relative to the aged seed materials. For the continuous MSMPR operation, there is a noticeable increase in fines through to the final stage (MSMPR 3), attributed to secondary nucleation (in MSMPR 1) and the short residence time of slurry in each stage of the process.

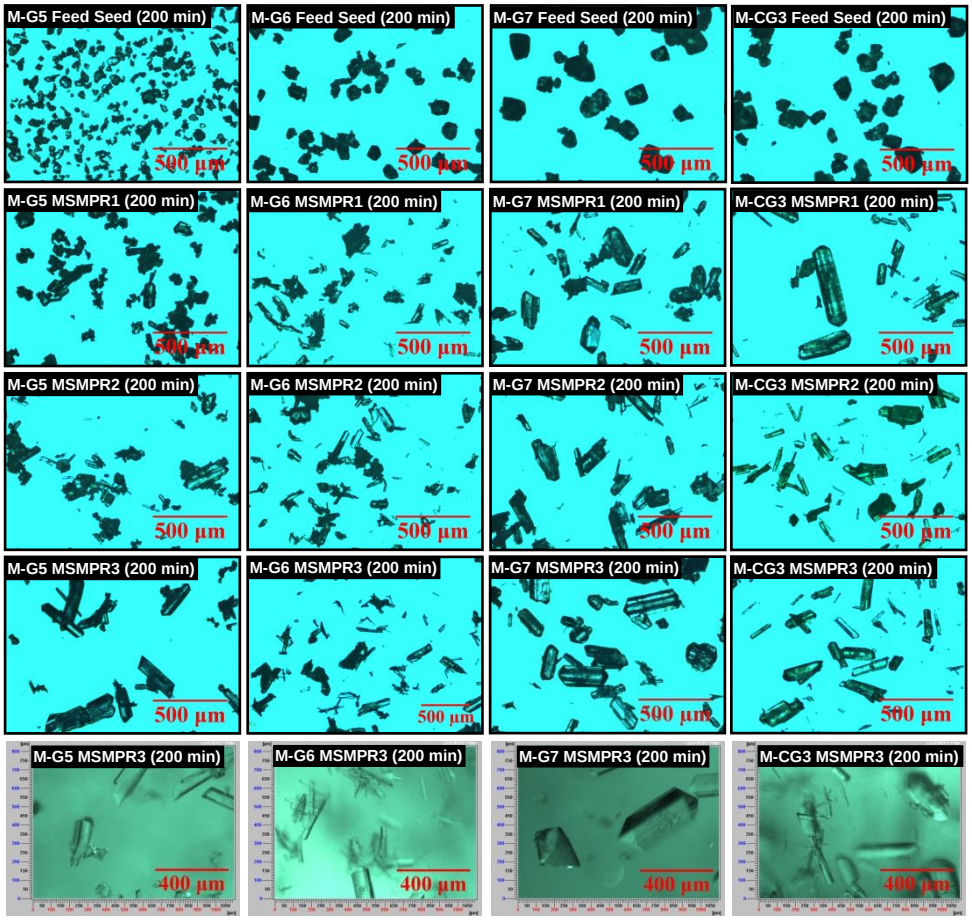

Figure 6.12: Microscope (rows 1 – 4) and PVM (last row) images of seed and product crystals from the PMSMPR and continuous MSMPR experiments.

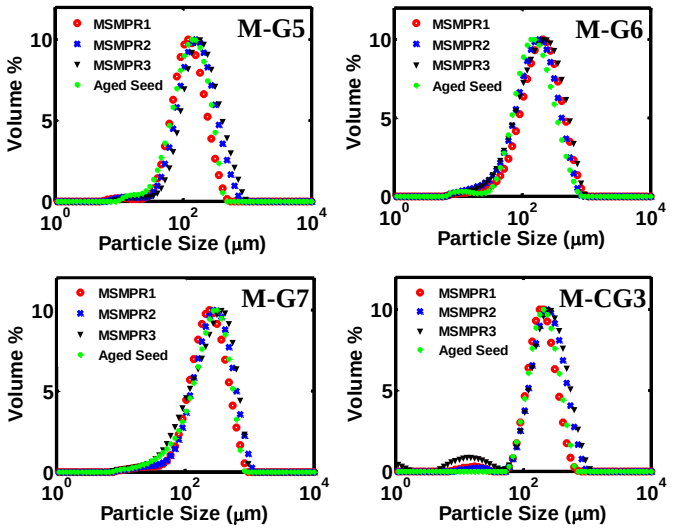

Figure 6.13: Normalised CSD profiles for the aged seed materials and the three stages of the PMSMPR and MSMPR experiments after 85 and 200 min, respectively, in the final stage. Data were obtained by laser diffraction using (Malvern Mastersizer®).

Effect of Sample Withdrawal Method on Product Crystal Properties: It was found that the sampling method employed is an important operational aspect of the PMSMPR. The way that slurry is collected can impact on the CSD and mean size of product crystals determined by the off-line laser diffraction (Malvern Mastersizer®). Furthermore, the sampling strategy can give an indication of the most suitable product withdrawal method to employ for PMSMPR and continuous MSMPR operations. Sampling of the PMSMPR was done in two ways: (1) withdrawal of a small amount of material from the outlet tube in the first minute of the continuous flow period (cop); (2) withdrawal from the bottom drain valve of the product vessel at the end of the holding operation period (bop) for PMSMPR operation. Continuous MSMPR experiments were sampled in a similar way for comparison. Table 6.7 provides a summary of results for each experimental run carried out using different seed material types. The data shows that the two sampling methods produce significantly different results. When samples were withdrawn from the outlet tube during the cop of the PMSMPR, the mean size determined by laser diffraction is markedly smaller compared to samples withdrawn during the batch operating period from the bottom drain valve, regardless of the properties of the initial seed material used. Four continuous MSMPR runs are included for comparison (M-CG1 – M-CG4). Evidently, the sample withdrawal location has a similar impact on the mean size. The CSD profiles and microscope images, Figure 6.14, for selected experiments provide evidence that the withdrawal method affects product crystal properties.

Table 6.7: Summary of results for two sampling methods investigated during the PMSMPR and continuous MSMPR experimental runs with bimodal CSD seed.

Exp. No.	Sampling Method	Seed Type	Particle Size: Malvern Mastersizer® (µm)			
			Aged Seed	MSMPR1	MSMPR2	MSMPR3
M-G2	cop	narrow	171.5 ± 1.7	220.0 ± 1.2	n/a	n/a
M-G2	bop	narrow	171.5 ± 1.7	357.8 ± 1.2	n/a	n/a
M-G4	cop	bimodal	232.4 ± 1.9	519.0 ± 22.5	n/a	n/a
M-G4	bop	bimodal	232.4 ± 1.9	683.9 ± 10.5	n/a	n/a
M-G5	cop	broad	139.6 ± 2.2	175.5 ± 4.4	215.3 ± 3.1	210.0 ± 4.3
M-G5	bop	broad	139.6 ± 2.2	201.8 ± 4.1	239.9 ± 7.7	348.3 ± 6.8
M-G7	cop	bimodal	248.2 ± 0.4	277.5 ± 1.7	288.8 ± 4.6	311.7 ± 3.5
M-G7	bop	bimodal	254.4 ± 8.7	277.3 ± 2.1	386.4 ± 2.5	696.8 ± 18.3
M-CG1	cop	bimodal	250.7 ± 2.2	248.5 ± 8.8	n/a	n/a
M-CG2	bop	bimodal	250.7 ± 2.2	708.6 ± 12.1	n/a	n/a
M-CG3	cop	bimodal	214.8 ± 4.3	198.6 ± 5.0	218.0 ± 4.8	227.9 ± 9.6
M-CG4	cop	bimodal	248.8 ± 4.2	235.3 ± 1.6	257.7 ± 0.9	342.2 ± 1.7

cop = sampling from outlet transfer line during continuous operation period; bop = sampling from bottom valve during batch operation period; n/a = not applicable.

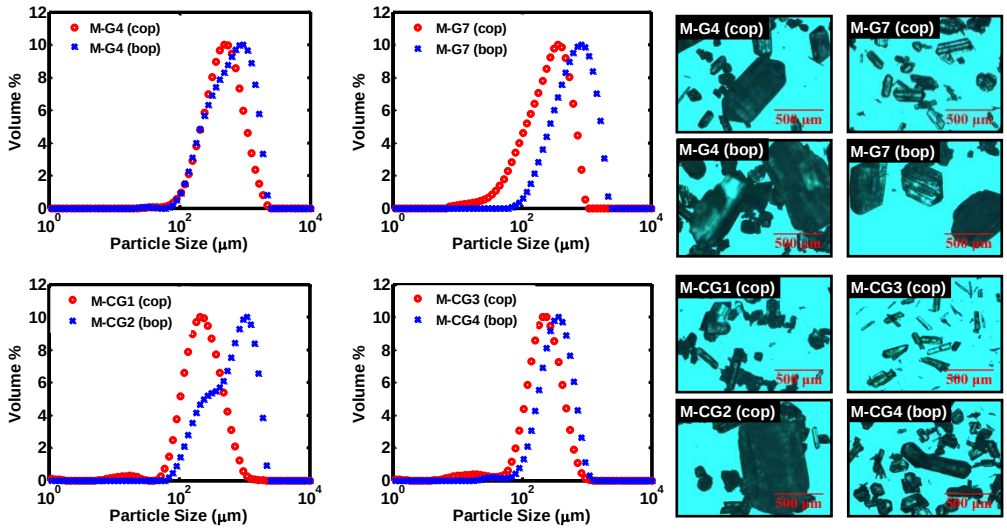

Figure 6.14: Normalised CSD profiles (left) and microscope images (right) of samples taken during the continuous operation period (cop) from outlet line and batch operation period (bop) from the bottom valve for the PMSMPR runs (M-G4 and M-G7). Samples were taken in a similar way during the MSMPR runs (M-CG1, M-CG2, M-CG3 and M-CG4).

The results from the slurry withdrawal study show there are large differences between the mean crystal size and CSD of samples taken from the transfer line tube and from the bottom valve of the continuous MSMPR and periodic flow PMSMPR crystallisers, respectively.

Consistently larger crystals were obtained when from the bottom valve withdrawal (bop) experiments. This reason for this is that large crystals due their mass and hence faster settling velocities are preferentially withdrawn when the bottom valve is released. This phenomenon occurs in spite of complete (or homogeneous) mixing in the crystalliser, since the law of gravity favours larger particles of greater mass being pull downward at a faster rate when the valve is released in comparison to smaller particles. Therefore, withdrawal from the bottom valve inadvertently leads to classification regardless of whether the bulk mixing in the crystalliser is complete or incomplete. On the other hand, withdrawal from the transfer line tube (cop) appears to be the best option for achieving representative isokinetic withdrawal and is therefore recommended on the basis that the bulk mixing conditions are better represented in terms of a complete distribution of particles pulled into the transfer line. However, further studies are required to demonstrate the physics and hydrodynamics that govern particle withdrawal: (1) from the vessel bottom valve, and (2) using a dip tube positioned above the impeller which is then connected to an outlet transfer line.

6.5 Process Modelling of Periodic Flow Crystallisation

6.5.1 Kinetic Parameter Estimation from Batch Experiments

The four unseeded batch crystallisation runs reported in Table 6.1, spanning a range of initial concentrations with different cooling rates were used to infer the major crystallisation kinetics. Since no significant crystal agglomeration was observed by PVM or microscopic image analysis for the batch experiments, see images inset, Figure 6.15, the agglomeration kinetics by “Mumtaz” in Table 6.4 was deactivated in the simulation and hence was not included in the parameter estimation at this stage. The final results of the parameter estimations are shown in Table 6.8 and Figure 6.15. Fouling on the Raman probe may occur due to the long operating time of over 4 hours in Batch 3, potentially resulting in slight uncertainties in the concentration predictions from the multivariate model (Chapter 3; Section 3.4.3), particular in the later stage. The same reasoning explains the deviation in Batch 4 concentration measurements recorded below the solubility limit in the later stage of the experiment (Figure 6.15). As a result, only the first half of Batch 4 was used for parameter estimation.

Table 6.8: Results of kinetic parameter estimations from four batch experiments.

Kinetics	Parameter	Estimate	Unit
Primary nucleation: Customised power law kinetics	Rate constant	1673.83 ± 22.82	LOG(#/s)
	Supersaturation order	4.23 ± 0.013	-
	Activation energy	1284.64 ± 147.4	J/mol
	Order with respect to solute concentration	3.41 ± 0.013	-
Secondary nucleation: Evans kinetics	Rate constant	16.40 ± 0.009	LOG(#/s)
	Size above when crystals undergo attrition	798.35 ± 1.174	μm
	Order with respect to supersaturation	1.00*	-
Crystal growth: Power law kinetics	Growth rate constant	$1.49\times10^{-5} \pm 3.52\times10^{-8}$	m/s
	Order with respect to supersaturation	1.71 ± 0.0010	-
	Activation energy	0.00*	J/mol
Agglomeration: Mumtaz kinetics	Agglomeration parameter (A50)	60.00×10^{-3}	N/m

*The final estimates hit the lower bound.

In general, reasonably good agreement was observed between the measured and the predicted data for the solute concentration and CSD measurements at the end of Batch 1 and 2 experiments. Uncertainties in the CSD may relate to the non-spherical and non-uniform crystal morphologies of the samples analysed by laser diffraction (i.e., crystal shape is approximated to that of a sphere), and the use of a single characteristic size for the one-dimensional population balance model in gCRYSTAL 4.0. Additionally, it is interesting to note that the major peak of the final product CSD for Batch 1 is due to mild primary nucleation when GLY concentration enters the metastable zone with moderate relative supersaturation of 0.25; while the minor peak in the small crystal size range is attributed to secondary nucleation caused by crystal-impeller collisions (which occurs at low supersaturation) and the existence of large crystals, as observed in Figure 6.15 microscope image inset, Batch 1. On the contrary, in Batch 2 more intensive primary nucleation was triggered and faster crystal growth rate observed later on, due to the higher relative supersaturation at 0.55 (notice the steep drop in concentration), which resulted in a broad CSD.

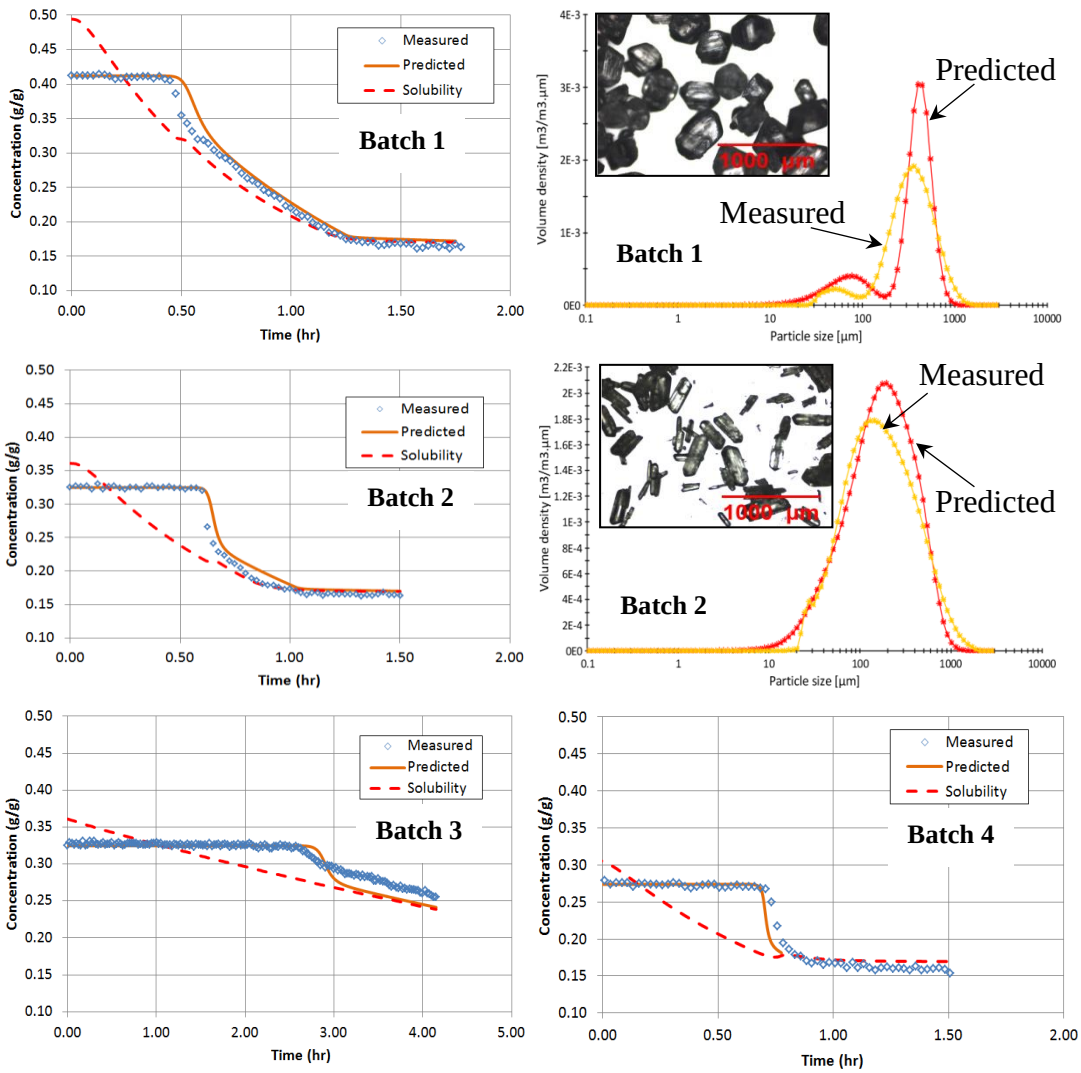

Figure 6.15: Kinetic parameter estimations using unseeded batch cooling crystallisations.

6.5.2 Model Validation Using Periodic Flow PMSMPR Experiments

Validation of the crystallisation mechanisms and kinetic parameters estimated from the batch experiments were considered using periodic flow crystallisation experiments that were conducted in either single- or cascaded three-stage PMSMPR crystallisers, as described in the earlier sections of this chapter. Two of the coupled periodic flow single-stage PMSMPR experiments were used, M-G1 (broad CSD seed) and M-G3 (bimodal CSD seed). In the unseeded batch crystallisation, the nuclei were generated initially by primary nucleation and were well dispersed in the slurry by stirring. In contrast, for the seeded PMSMPR crystallisations, in some cases a significant amount of agglomerates was observed from PVM and microscopic images. This was partly due to the seed preparation method whereby the material was ground and sieved to the desired size fraction. When these seed crystals were added to the feed vessel, initially they were found to agglomerate, especially the broad CSD

seed. The imperfect and rough surface of the seed crystals, which were reduced in size by grinding, may provide a low enough energy barrier for surface nucleation and bridging, thus leading to agglomeration of the crystals. For example, the initial seed and final crystals of M-G1 experiment were illustrated in Figure 6.8 (broad CSD) and Figure 6.9 (M-G1) earlier. For the purpose of this work, to account for the agglomeration kinetics, “Mumtaz kinetics” option in gCRYSTAL 4.0 was applied whenever agglomeration was observed in the PMSMPR experiments. In this regard, the agglomeration parameter (A50) was fine-tuned in the simulation of M-G1 to fit the CSD measurement at SCO while using the crystallisation kinetic parameters listed in Table 6.8. A value of 60 × 10^{-3} N/m for A50 resulted in good agreements for both GLY concentration and CSD measurements, as shown in Figure 6.16 for M-G1 experiment. Further to this, another independent verification of all the kinetic parameters obtained so far was demonstrated with M-G3, which was also affected by agglomeration; Figure 6.8 (bimodal CSD) and Figure 6.9 (M-G3). Although larger seed crystals with bimodal CSD seed were used in M-G3, the model predictions agreed well with the experimental CSD measurements, which provides further confirmation of the predictive capability of the crystallisation mechanism and kinetic parameters that were estimated here.

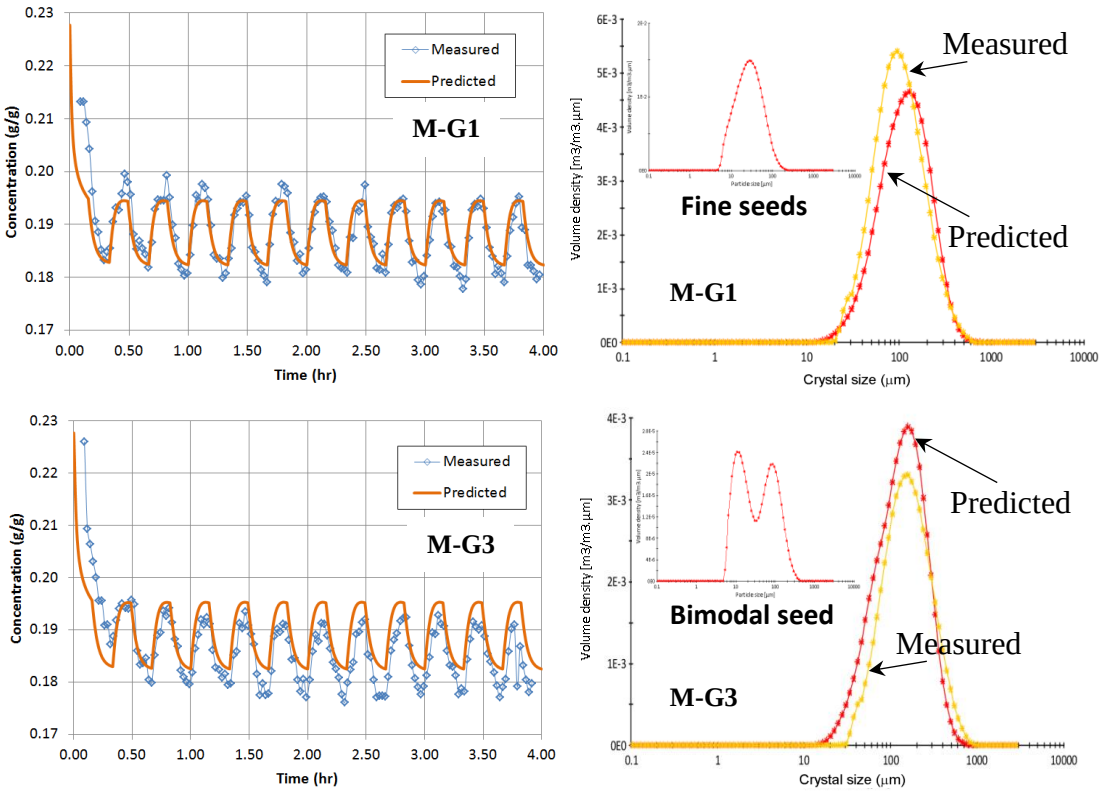

Figure 6.16: Comparison of predicted and measured data for period flow single-stage PMSMPR runs, M-G1 (‘fine seed’) and M-G3 (bimodal CSD seed). CSD measurements were taken at the start of pumping period (i.e., by cop method) after reaching SCO.

Validations with coupled periodic flow cascaded three-stage PMSMPR experiments, that is, M-G5* (broad CSD seed) and M-G7* (bimodal CSD seed), are shown in Figures 6.17, 6.18 and 6.19, where solute concentration was measured in the third-stage (MSMPR 3) only. Three samples were taken at the end of the holding period from each PMSMPR stage and analysed by laser diffraction. It should be noted that for a continuous flow MSMPR crystalliser, there is no concern when to take samples for off-line CSD measurement, so long as the system reaches steady-state. However, in a periodic flow operation, SCO is achieved *viz*. the system variables continuously varying in a limited range. Hence, in order to achieve better matches between predicted and measured CSD data, samples should be taken with special care. As the two periods of holding and addition/withdrawal are alternately applied during the operation it is better to take samples from the cascaded PMSMPR when the crystalliser reaches the end point of the holding period, that is, just before the start of the addition/withdrawal period, and in sequence from the third-, second and first-stage. In such a way, the crystalliser is most likely to achieve the best mixing conditions and also avoid the experimental perturbations caused by macro-mixing condition resulting from addition and withdrawal of slurry or from sampling the outlet streams. Furthermore, taking the samples from the vessel bottom valve is faster compared to sampling from the outlet stream transfer lines. The proposed sampling procedure has proven to be effective, with better matches between the model predictions and experiments.

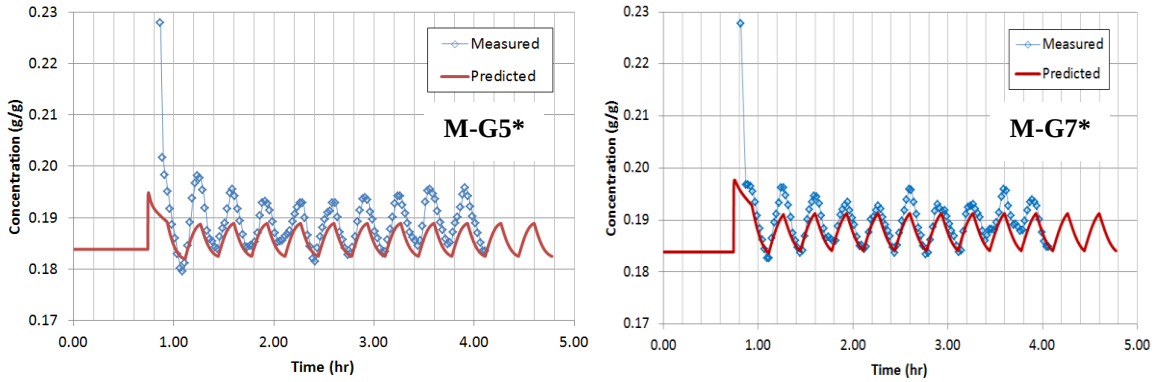

Figure 6.17: Comparison of predicted and measured solute concentration in the third-stage PMSMPR (MSMPR 3) for M-G5* and M-G7* experimental runs.

In spite of some uncertainties in the sampling and mixing conditions and the fact that the crystallisation kinetic parameters were previously estimated from batch crystallisation experiments without further tuning or re-estimations, the proposed model predicted the solute concentration and CSD very well, with the exception of sample 3-3 in Figure 6.19 (M-G7*) experiment. This may be a consequence of the large bipyramidal hexagonal prism shape crystals present, which exhibit varying aspect ratios. This phenomenon will be discussed further in Section 6.5.3.

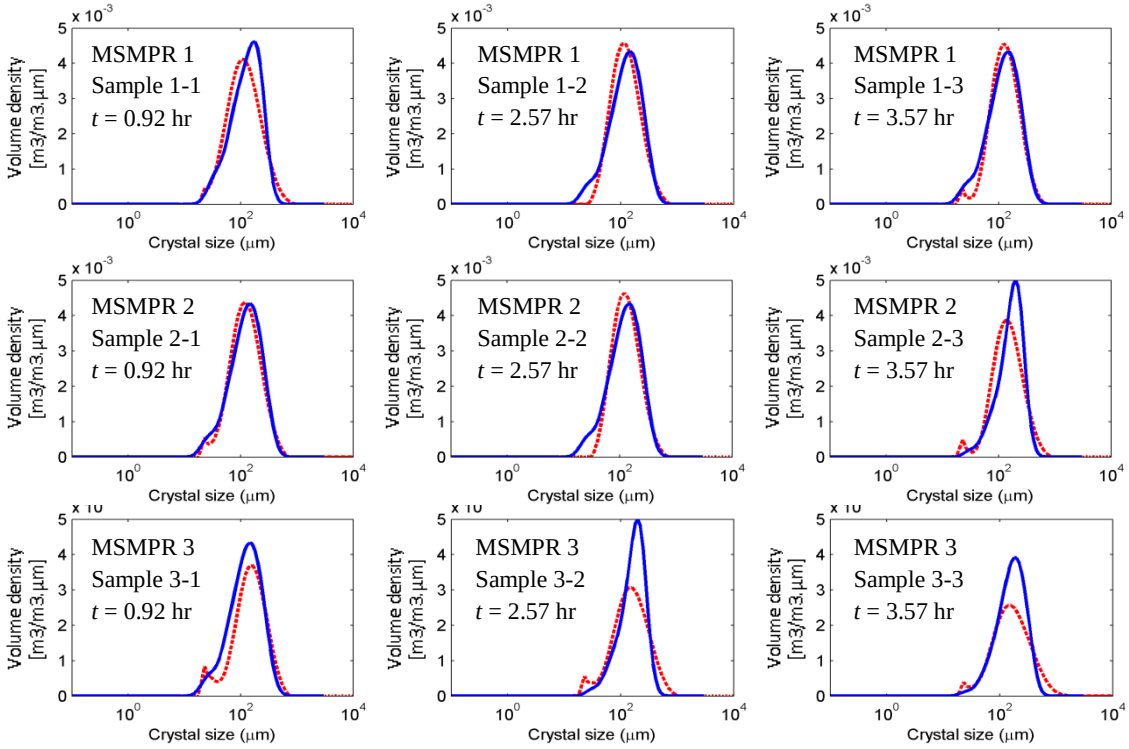

Figure 6.18: Comparison predicted and measured CSDs for M-G5* three-stage PMSMPR experiment (solid line: predicted; dash line: measured).

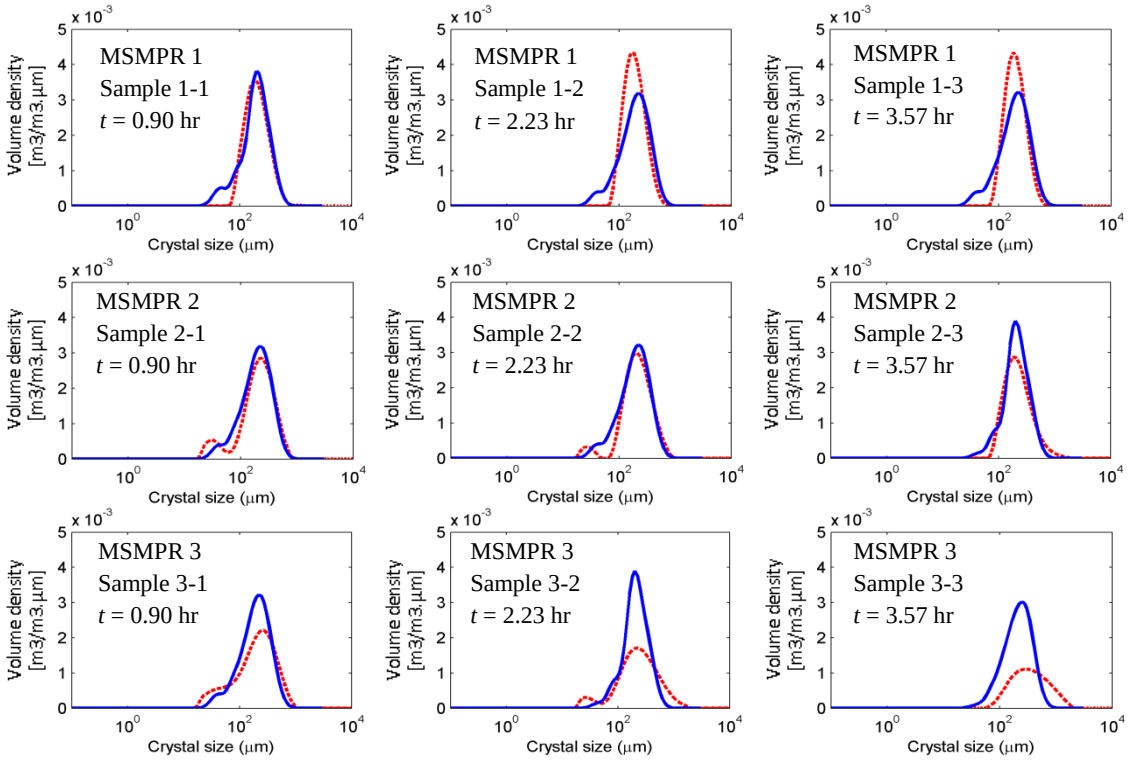

Figure 6.19: Comparison of predicted and measured CSDs for M-G7* three-stage PMSMPR experiment (solid line: predicted; dash line: measured).

In case of the model validation with decoupled periodic flow crystallisation, the single-stage PMSMPR, M-G4* (bimodal CSD seed) was used. The model predictions and their comparison to the experimental measurements, that is, solute concentration and CSD are illustrated in Figures 6.20 and 6.21, show good agreement, with the exception of sample 1-3. As mentioned above, this may be due to the existence of very large crystals with varying aspect ratios. Furthermore, as shown in the RTD profile (Figure 6.5) of the decoupled periodic PMSMPR, the process would take almost 4 hrs. to achieve SCO. Interestingly, in Figure 6.21, the three samples taken at 0.36, 2.00 and 2.70 h show a gradual increasing in the measured mean crystal size (357.8 µm, 601.8 µm, 683.9 µm, respectively) and broadening of the CSD, which is consistent with the increasing values of mean residence time and standard deviation in Figure 6.5.

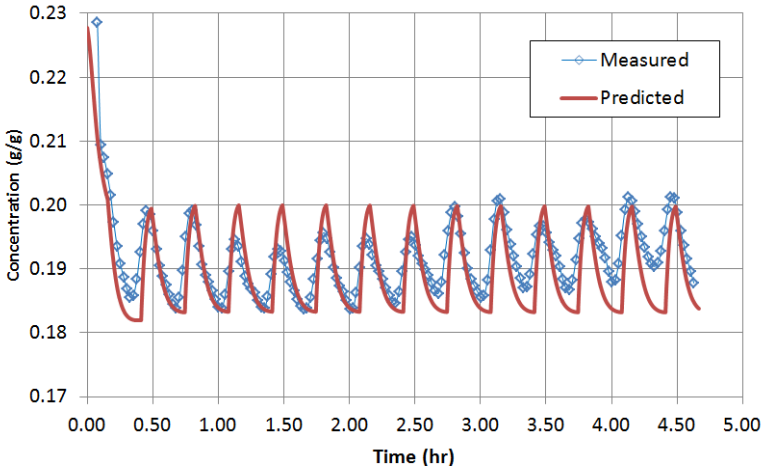

Figure 6.20: Comparisons of predicted and measured concentration for M-G4* decoupled flow single-stage PMSMPR experiment.

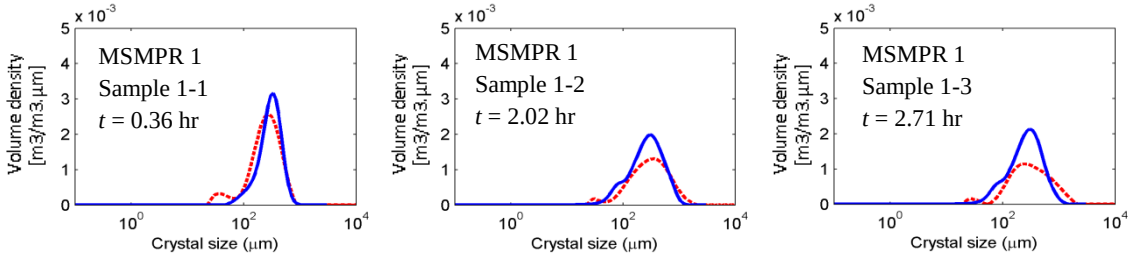

Figure 6.21: Comparison of predicted and measured CSD for M-G4* decoupled flow single-stage PMSMPR experiment (solid line: predicted; dash line: measured).

It is also interesting to compare periodic flow crystallisation in PMSMPR to continuous flow crystallisation in MSMPR. The product CSDs and model prediction for the coupled cascaded three-stage MSMPR crystallisers using bimodal CSD seed are shown in Figure 6.22. The mean residence time was doubled from 9.36 × 3 = 28.08 min in the continuous flow three-

stage MSMPR to 20.00 × 3 = 60.00 min in the coupled periodic flow three-stage PMSMPR, as discussed in the experimental methods section of this chapter. This corresponded to an increase in the experimentally measured volume-based mean particle size, $D[4, 3]_{exp}$, from 342.16 µm to 696.76 µm, while the corresponding predicted value, $D[4, 3]_{pred}$, showed an increase from 184.38 µm to 407.64 µm. Although the periodic flow operation has shown the benefits over the continuous flow operation, experimentally and in the simulations, there is a large mismatch between the measured and model predicted CSD. However, the mismatch is even greater for the continuous flow crystallisation. Besides the effect of crystal shape as mentioned for the mismatch of periodic flow CSD, the kinetic parameters estimated from the batch crystallisation experiments in this study may not be appropriate for the continuous MSMPR process since the mixing conditions are so different and may have played a critical role in the kinetic parameter estimation. The applicability of these crystallisation kinetics to the periodic flow operation may be due to the fact that this is a hybrid operation incorporating both batch and continuous operations.

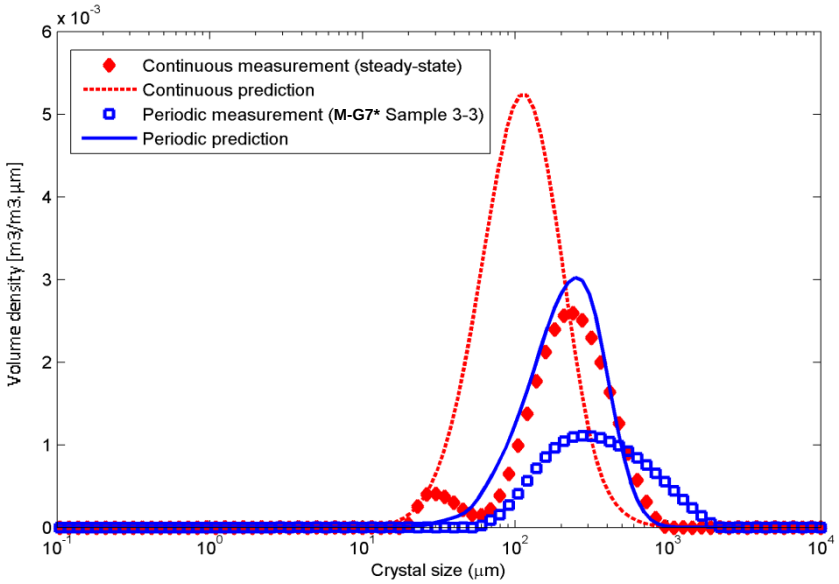

Figure 6.22: Comparisons of predicted and measured CSD for continuous and periodic flow operations in cascaded three-stage MSMPR and PMSMPR crystallisers, respectively.

6.5.3 Uncertainty Analyses and Summary

There has long been a concern with laser diffraction method for CSD measurement due to sometimes significant mismatches between experimental measurements and model predicted data (Su *et al* [275] and the references within). For the most part there is good agreement between the experimental CSD measurements and model predictions of the volume-based mean particle size *D[4, 3]*, as summarised in Table 6.9, but there are some significant

differences between $D[4, 3]_{exp}$ and $D[4, 3]_{pred}$ in some of the cases. In order to objectively reveal the model accuracy, the relative errors were calculated as:

$$Rel.error = \frac{D[4,3]_{pred} - D[4,3]_{exp}}{D[4,3]_{exp}} \times 100\ \% \qquad 6.6$$

Table 6.9 provides a summary of the experimental and predicted volume-based mean particle sizes for each of the evaluated experiments. The relative error in Eqn. 6 provides a reasonable and fair metric for evaluating the model prediction accuracy in each crystallisation experiment, provided that the CSD measurements are acquired in a similar way as reported in this work. In this regard, the model prediction capability was mostly good, except for the continuous flow crystallisation (rel. error of -46.11 %) and PMSMPR bop (rel. error of -23.09 to -41.49 %) experiments. For the continuous experiment, the difference in mixing conditions relative to the PMSMPR may have played a critical role. In case of the PMSMPR bop runs, classified withdrawal due to removal of slurry from the bottom valve is the crucial factor, which is reflected more prominently in the results from the last stage of the three-stage PMSMPR cascade experiments where the mean particle size is largest.

Table 6.9: Comparisons of volume-based mean particle size D_{43}

	Experiments	$D[4, 3]_{exp}$ (µm)	$D[4, 3]_{pred}$ (µm)	Rel. error
Batch	Sample at end Batch 1	498.99	454.62	-8.89 %
	Sample at end Batch 2	447.86	360.00	-19.62 %
	Sample at end Batch 3	-	321.99	-
	Sample at end Batch 4	-	319.27	-
M-G1	Controlled state average	167.48	183.21	9.39 %
M-G3	Controlled state average	287.64	216.60	-24.70 %
M-G5*	Sample 3-1	238.10	226.67	-4.80 %
	Sample 3-2	278.70	264.55	-5.08 %
	Sample 3-3	348.30	267.87	-23.09 %
M-G7*	Sample 3-1	364.41	362.34	-0.57 %
	Sample 3-2	519.54	409.39	-21.20 %
	Sample 3-3	696.76	407.64	-41.49 %
M-G4*	Sample 1-1	357.83	362.89	1.41 %
	Sample 1-2	601.78	431.65	-28.27 %
	Sample 1-3	683.88	418.52	-38.80 %
M-CG4	Steady-state	342.16	184.38	-46.11 %

The relative error shows an increasing trend in experiments M-G5*, M-G7*, and M-G4* when the crystals grow into large size domains, which results in an obvious mismatch in the mean *D[4, 3]* crystal size and CSD, for example, sample 3-3 in Figure 6.19 and sample 1-3 in Figure 6.21. One of the possible reasons argued was that the GLY crystals shows a bipyramidal hexagonal prism morphology with varying aspect ratios, as illustrated by the PVM images taken for M-G7* experiment in Figure 6.23, as an example. The adverse effect of varying aspect ratio on CSD measurements by laser diffraction method can be significant when the particles are large enough, which could also explain the increasing trend in relative prediction errors. In future work, a multiple dimensional population balance model would be necessary to reduce the prediction error and control the crystal shape, for example along the lines of Majumder and Nagy [276], Kwon *et al* [81], and Jiang *et al* [140]. Potentially, *in situ* PVM images which provide crystal shape and size measurements could provide the required information as demonstrated by Zhou *et al* [166]. Herein, it has been shown that the estimated crystallisation mechanism and kinetics from batch cooling crystallisation experiments give good predictive capability when tested on either coupled periodic flow crystallisation in single- and three-stage PMSMPR or decoupled periodic flow crystallisations in a single-stage PMSMPR, which proves that they can be implemented for process design, optimisation, and control.

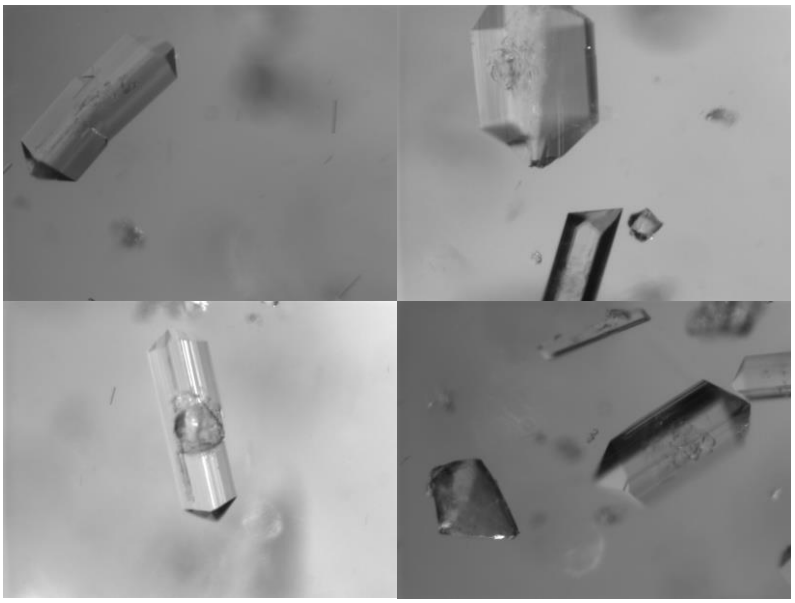

Figure 6.23: PVM images taken for the third-stage PMSMPR (MSMPR 3) of M-G7*.

6.6 Conclusions

The seeded cooling crystallisation of a fast growing API (GLY) was demonstrated using single- and three-stage cascaded configurations of the novel periodic flow PMSMPR crystalliser

operated in either coupled or decoupled mode. Conventional continuous MSMPR crystallisations were also conducted for comparison. The seed crystal properties (size, shape and CSD) affected the product size and overall quality and the time to achieve SCO in the single-stage PMSMPR, with larger seed sizes producing more uniform product crystals, and leading to a faster approach to a controlled state of operation. For cascaded three-stage crystallisations the opposite result was observed whereby the smaller seed crystals led to a faster approach to a controlled state of operation, that is, SCO in the PMSMPR. It appears that not only do the seed properties affect the approach to a controlled state, but also the rate of change of supersaturation. For the three-stage crystallisations, supersaturation was generated at a slower more gradual rate compared to the single-stage crystallisations. This leads to a more rapid approach to a controlled state of operation when fine seed material was used. There was no clear correlation between the yield of crystallisation and number of PMSMPR stages. However, the yield of crystallisation was significantly higher for PMSMPR crystallisations compared to the equivalent continuous MSMPR crystallisations in all cases. This was due to longer residence time for crystal growth in the former by introducing holding or batch operating cycles. The product crystals were also of better overall quality, having larger mean sizes and more uniform shape. The two different modes of PMSMPR operation demonstrated, that is, coupled and decoupled periodic flow showed markedly different results. Under decoupled periodic flow single-stage PMSMPR operation a longer time to SCO, and larger mean crystal sizes were observed based on FBRM counts/s measurements, compared to the equivalent coupled operation. Furthermore, the mean crystal size and CSD determined by laser diffraction did not show SCO behaviour. The results may be a reflection of the different mixing conditions and problems with flow control in the decoupled experiment.

The effect of sample collection point on mean product crystal size and CSD in the PMSMPR and continuous MSMPR operations was also investigated. For the PMSMPR crystallisations, samples taken from the crystalliser bottom valve during batch operation periods were of consistently larger size compared to samples taken from the crystalliser outlet transfer line during continuous operation periods. Laser diffraction analysis showed that the volume weighted mean sizes of crystals were significantly larger for the former case (343 - 709 µm) compared to the latter (161 - 519 µm). Sampling from the equivalent continuous MSMPR experimental runs confirmed that withdrawal from the bottom valve resulted in larger crystals compare to withdrawal at the crystalliser outlet transfer line. The straightforward explanation is that large crystals settle at a faster rate when product is withdrawn from the bottom valve. Arguably, withdrawal from the outlet transfer line leads to more representative product, in particular, where high withdrawal rates are employed that lead to high particle transfer velocities. The sampling results require further investigation to determine the best product

withdrawal strategy for the PMSMPR operation. The combined used of integrated PAT array in with CryPRINS information systems software package within the IDS framework led to effective monitoring and characterisation of the periodic flow process, and determination of when SCO was attained.

Simulation of the RTD profiles of the periodic flow operation (PMSMPR) was demonstrated and compared to that of the conventional continuous flow operation (MSMPR). The merit of extending the mean residence time without broadening the RTD too much in periodic flow operation makes it an attractive crystallisation system, especially since the mean residence time is an important design variable. Mathematical modelling and simulation of the periodic flow crystallisation processes using the single- and three-stage PMSMPR crystallisers (operated in coupled and decoupled modes) were demonstrated. The crystallisation mechanisms and kinetic parameters for GLY crystallised from water were estimated from unseeded batch crystallisation experiments and verified with periodic flow single- and three-stage PMSMPR experiments. Reasonably good agreements were obtained between the experimental measurements and model predictions for concentration and CSD evolution. The model uncertainties were analysed and future work suggested. Moreover, the advantages of periodic flow crystallisation were proven through both experiments and simulations.

Overall, results of this study indicate that coupled periodic flow crystallisation in the PMSMPR is the most efficient mode of operation, leading to better process control, faster approach to SCO and the mitigation of crystalliser wall fouling, crust formation and transfer line blockages. This is attributed to the intermittent operation which utilises high flow rates for isokinetic slurry transfer, whilst maintaining constant volume. In addition, the tuneable hold or batch cycle can lead to rapid desupersaturation (solute depletion) and crystal growth (system dependent), thereby producing more consistent particles (size and shape) relative to batch, MSMSR and decoupled PMSMPR operations.

Chapter 7

Periodic Flow Crystallisation of Co-Crystals Using PMSMPR: Case of Urea-Barbituric Acid

In this Chapter, periodic flow crystallisation of the polymorphic Urea-barbituric acid (UBA) co-crystal system is investigated. Pharmaceutical co-crystals are multi-component molecular systems typically formed through hydrogen bonding of a benign co-former molecule with the active pharmaceutical ingredient (API). Just as single component molecular systems can exhibit polymorphism due to the geometry of hydrogen bond donors and acceptors, the same is true for pharmaceutical co-crystals. In this study, the selective co-crystallisation of UBA forms I and III polymorphs is demonstrated, applying the novel periodic mixed suspension mixed product removal (PMSMPR) crystalliser described in Chapters 5 and 6. The PMSMPR was operated as a cascade of three-stage crystallisers. Three different start-up strategies were employed and their ability to produce selectively a particular polymorphic form of UBA evaluated. The experimental conditions for producing pure UBA form I were optimised, but the isolation of pure UBA form III remained elusive. The crystallisations were monitored using the integrated process analytical technologies (PAT) and CryPRINS informatics systems software within the IDS framework described in Chapter 3, to determine when a "state of controlled operation" (SCO) was achieved. Off-line characterisation of the UBA polymorphs was carried out using several solid-state characterisation techniques.

7.1 Introduction

Modification of the structure and molecular composition of an API by applying crystal engineering principles can lead to significant improvements to the stability, bioavailability and polymorphic properties of a drug. Pharmaceutical co-crystal formation has gained popularity in recent years as a feasible method for modifying APIs primarily to improve solubility and hence their bioavailability. Pharmaceutical co-crystallisation involves the formation of a crystal containing the API with a benign co-former molecule in specific stoichiometric ratios [277]. Similar to single component systems, co-crystals may exist in two or more polymorphic forms, which present an added complexity to the manufacture of these molecular systems for specialised use. This study looks at the selective co-crystallisation of UBA co-crystal polymorphs at laboratory scale using a PMSMPR crystalliser [262] operated in coupled periodic flow mode. The PMSMPR was configured and operated as a three-stage cascade in order to selectively

isolate the polymorphic forms of the UBA co-crystal system. There are three known polymorphs of UBA, as discovered by Krawczuk *et al* [278], [279] using small scale evaporative crystallisation techniques. The mole ratio of urea to barbituric acid (BA) is 1:1 for all three co-crystal polymorphic forms of UBA. Forms I and III exhibit similar physicochemical properties, such as solubility and melting points and often crystallise together as a mixture, from which it is really difficult to isolate either of the co-crystal forms. Form II appears to be metastable and is the most elusive of the three co-crystal forms [278], [279]. Figure 7.1 show the chemical structures of urea and BA, and the crystal structures of UBA forms I and III.

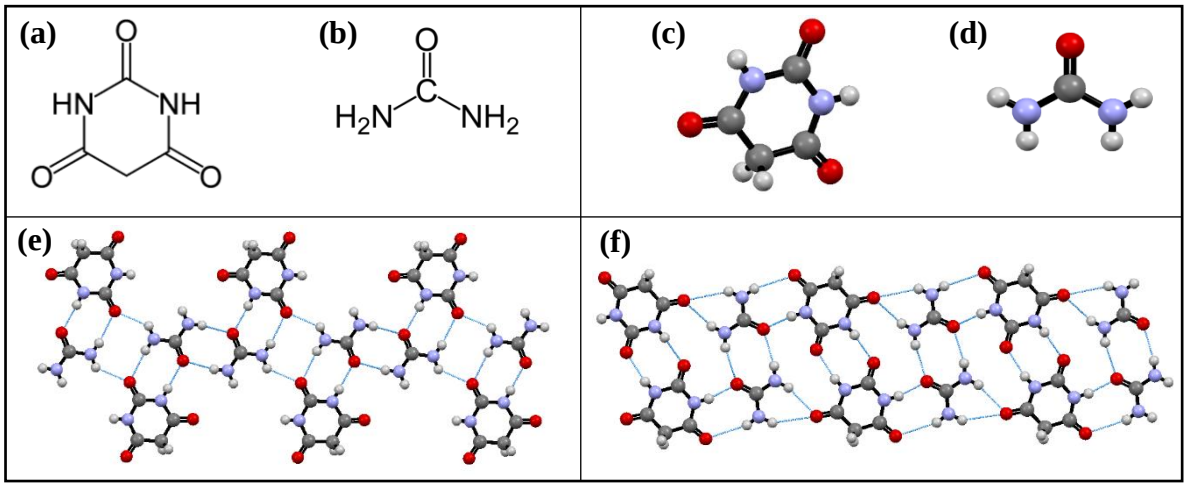

Figure 7.1: Chemical structures of BA (a) and (b) and urea (c) and (d), and crystal structures showing hydrogen bonding network of UBA form I (e) and UBA form III (f).

Anhydrous BA itself is known to form four polymorphs [277], [278], [280]; the crystal structures of form I and II have been determined by single crystal X-ray diffraction [277], [281]. Many of the derivatives of BA also crystallise in several different polymorphic forms [278] and are also capable of forming a variety of co-crystal polymorphs. Zerkowski *et al* [282]–[287] used BA derivatives such as barbital and a series of melamine derivatives to generate a range of different hydrogen bonded supramolecular motifs [288], [289], isolating and structurally characterising more than 60 co-crystals. These studies illustrate the potential diversity of co-crystal forms that can exist for a particular API. This diversity can offer exciting opportunities to develop novel and improved crystalline forms of APIs [288]. However, the preparation of co-crystals as described in the literature indicates the notoriously difficult situation these systems present [289].

Pharmaceutical co-crystals are typically discovered by solvent evaporation [290], [291], cooling crystallisation [292], [293], precipitation [294], dry grinding [293], [295]; solvent-assisted grinding [296] or sonication (applied to either to wet or dry solid mixtures) [297], [298]. However, cooling crystallisation is the most commercially feasible of these methods and can

afford superior control in preparation of co-crystals on an industrial scale. Polymorph control is critical in industrial crystallisation of fine chemicals [82], where the polymorphic form has a significant influence on the physical attributes of the material, and this can prove even more challenging for multi-component co-crystal systems. Therefore, from an industrial perspective, the polymorphic UBA co-crystal system proves particularly interesting and is utilised in this study as a model multi-component system to investigate polymorph control in multi-component cooling crystallisation using periodic flow operation. In this approach the concept of "state of controlled operation" (SCO) is used to describe the periodic flow process [262].

7.2 Experimental Methods

In this study, control over the crystallisation of UBA co-crystal polymorphs that exhibit similar physicochemical properties is demonstrated *viz* cooling co-crystallisation in periodic flow PMSMPR crystallisers. The concept of SCO instead of "steady-state" is used to describe when the periodic flow operation is under control. Figure 7.2 provides a comparison of the trajectory through the phase diagram for the crystallisation of UBA in batch, continuous flow MSMPR cascade and periodic flow PMSMPR cascade modes, respectively.

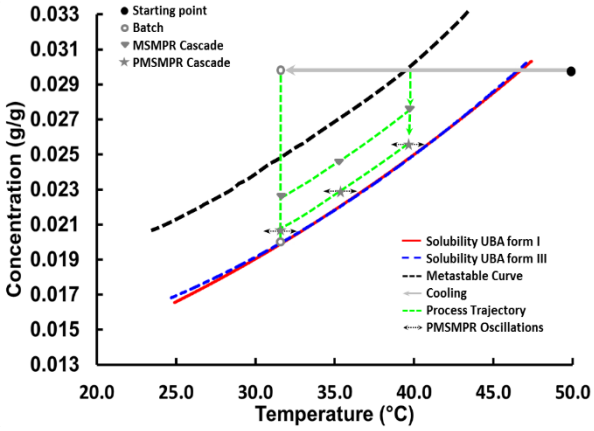

Figure 7.2: Phase diagram showing trajectory of batch, MSMPR and PMSMPR operations. UBA forms I and III in methanol.

7.2.1 Barbituric Acid and Co-Crystals Physicochemical Properties

Analyses of the solubilities and melting points of UBA forms I and III and their parent API, BA were carried out. These studies showed that UBA forms I and III have very similar physicochemical properties, but are markedly different from BA in this respect.

Solubility Studies in Methanol and Water: The Avantium benchtop Crystalline® with 8 parallel reactors was used for solubility determination *viz* turbidity measurements as described in

Chapter 3, Section 3.6.3. Figure 7.3 (a) and (b) show the solubility curves obtained for UBA forms I and III, and BA in methanol (MeOH) and water, respectively. The solubility curves for UBA form I and III are strikingly similar in both solvent systems.

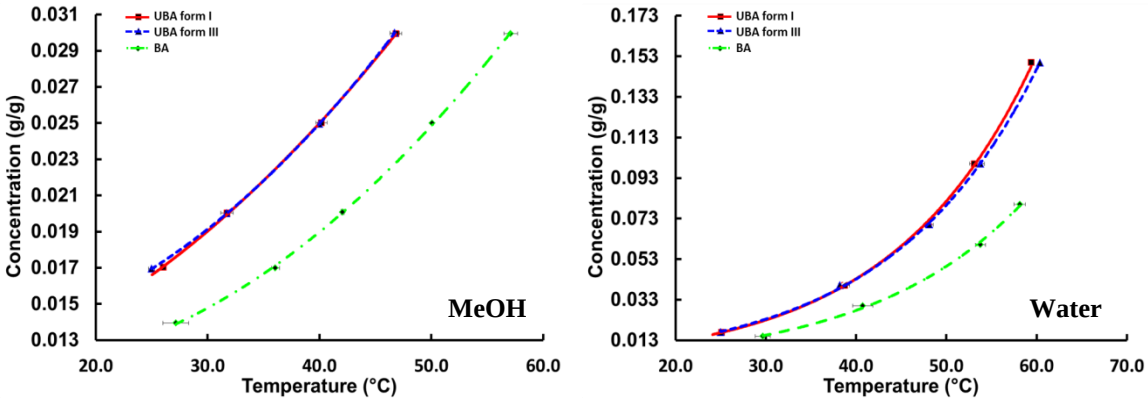

Figure 7.3: Solubility curves obtained in MeOH and water for UBA forms I and III and BA.

Melting Point Studies: Melting point studies were carried out using the TA Instrument Q10 Differential Scanning Calorimeter (DSC). Experimental conditions and data treatment were described in Chapter 3, Section 3.2.2. Different scan rates were implemented, ranging from 0.5 to 10 °C/min. Figure 7.4 show the DSC profiles for UBA forms I and III, and indicates the melting temperatures were 191.5 °C and 193.4 °C, respectively.

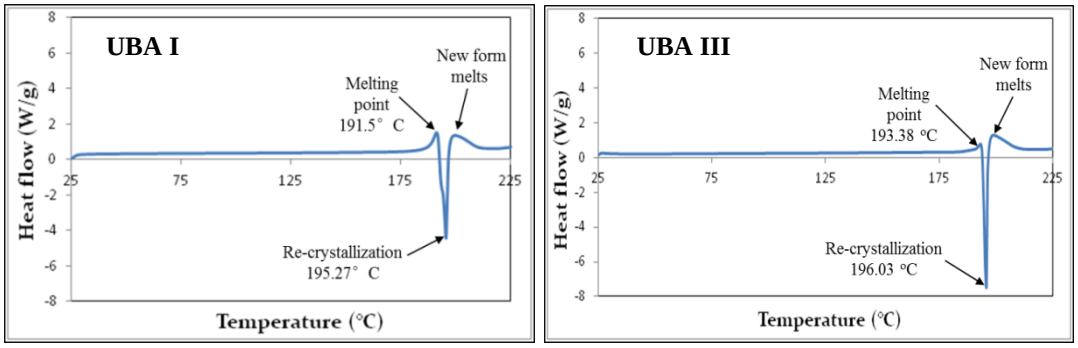

Figure 7.4: DSC profiles of UBA forms I (left) and III (right), 10 °C/min heating rate.

Recrystallisation points at 195.3 °C for UBA I and 196.0 °C for UBA III indicate that there may be a “high temperature” polymorph of the UBA co-crystal system that has not been previously isolated. Immediately following recrystallisation, a melt event is detected in both systems. These DSC profiles provide further evidence of similarities between UBA forms I and III. While the DSC results were interesting, the aim of the study was not structure elucidation. Work is ongoing as part of a separate project with collaborators from the University of Bath to isolate the suspected “high temperature” polymorph of UBA.

7.2.2 Off-line Solid-State Characterisations

To complement on-line PAT measurements, off-line solid-state techniques were used to aid characterisation of the batch, semi-batch and PMSMPR crystallisations of UBA co-crystals from MeOH. Samples were removed from each vessel at regular time intervals using a 10 mm ID glass pipette and transferred immediately onto a vacuum filter to minimise time for polymorph conversion. Samples were immediately washed with cold methanol to prevent cementation due to evaporation of the process liquor. Laser diffraction (particle size, shape and distribution), Powder X-ray diffraction (PXRD) and Raman microscopy (method reported in Chapter 3; PXRD and Raman results reported in Appendix II) analyses were carried out to identify the UBA co-crystal polymorph obtained from each experiment. UBA forms I and III exhibit characteristic morphologies under the crystallisation conditions employed in this study. Figure 7.5 shows microscope images of UBA forms I and III captured under normal and polarised light. UBA form I crystallises as semi-transparent crystals that readily agglomerate, exhibiting a rosette type morphology. UBA form III crystallises from MeOH as opaque crystals which show a greater tendency to agglomerate compared to UBA form I. The crystal agglomerates of UBA form III exhibits “coffee bean” type morphology.

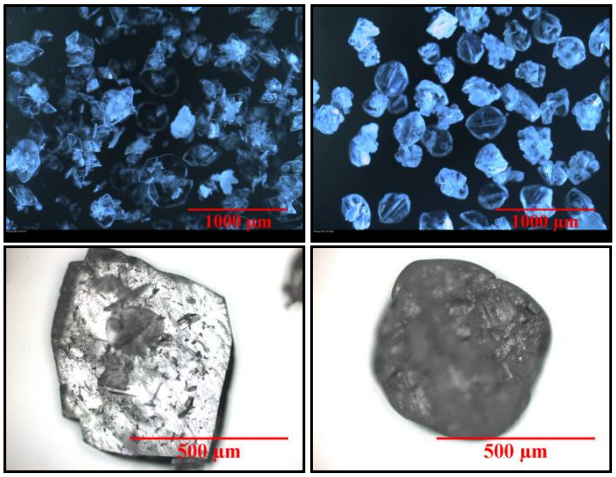

Figure 7.5: Polarised microscope images of UBA forms I (top left) and III (top right). Normal microscope images of UBA forms I (bottom left) and III (bottom right) single crystals.

7.2.3 Semi-Batch, Batch and Periodic Flow Crystallisation Studies

The crystalliser configurations used for the semi-batch, batch and periodic flow crystallisation experiments were presented in Chapter 3, Sections 3.6.1 and 3.6.2. The operating volume of the laboratory scale crystallisers was 500 mL. A number of smaller scale batch studies were also carried out at 5 mL volume. Stirrer speed was set to 450 rpm at 500 mL scale unless otherwise state. The approximate power per unit volume from the selected impeller speed was

0.084 kW/m^3. The selected impeller power input leads to homogeneous suspension of slurry inside each crystalliser, satisfying the MSMPR assumption. Due to fouling issues, data obtained from *in situ* Raman and ATR-UV/vis probes were not sufficiently reliable for characterising the systems studied.

Small Scale Co-Crystallisation Experiments: The small scale batch cooling co-crystallisation experiments were conducted using the Avantium Crystalline® system. Duplicate experiments were carried out using the 8 parallel reactors operated at five different cooling rates (0.05, 0.5, 1, 2 and 3 ^{o}C/min) and stirring speeds (400, 600, 800, 1000 and 1200 rpm). For each experimental run a suspension of urea and BA in MeOH was equilibrated at 20 ^{o}C for 30 min with stirring, followed by heating at a rate of 1^{o}C/min to 60 ^{o}C and holding for 60 min. The sample was then cooled at a pre-determined rate to a final temperature of 10 ^{o}C. Samples were collected, filtered and dried overnight at 40 ^{o}C and stored in borosilicate glass vials for subsequent solid-state characterisation.

Semi-Batch and Batch Co-Crystallisation Experiments: Experiments were carried out to guide later development of a three-stage periodic flow PMSMPR process. A number of seeded and unseeded co-crystallisation experiments were carried out to determine the most suitable conditions for obtaining UBA forms I and III, respectively. The crystalliser temperature was adjusted over different experimental runs to determine the effect on the polymorphic composition of the end product. A 2:1 mole ratio of urea:BA was used throughout this work due to the high solubility of urea in methanol. Without an excess of urea only the BA starting material crystallises. Therefore, it was necessary to ensure that urea concentration was high enough to encourage co-crystallisation with BA. The experiments were carried out in three ways:

1. Method 1 (batch): A 2:1 mole ratio solution of urea:BA was prepared in the 500 mL crystalliser (0.014 g urea/g MeOH and 0.015 g BA/g MeOH) at 55 °C.
2. Method 2 (semi-batch): 130 mL of urea (0.078 g urea/g methanol) solution and 400 mL of BA (0.018 g BA/g methanol) solution were prepared in separate vessels. Urea solution was then added to BA solution at a rate of 10 g/min to give a final solution composition of 2 moles urea to 1 mole BA.
3. Method 3 (semi-batch): The same solutions as in Method 2 above were prepared. However, urea solution was added rapidly to BA solution by manual addition to give a final solution composition of 2 moles urea to 1 mole BA.

Figure 7.6 shows the flow diagram of the semi-batch experimental configuration used in the co-crystallisation studies. Table 7.1 provides a summary of the experimental conditions employed during the batch and semi-batch co-crystallisation studies.

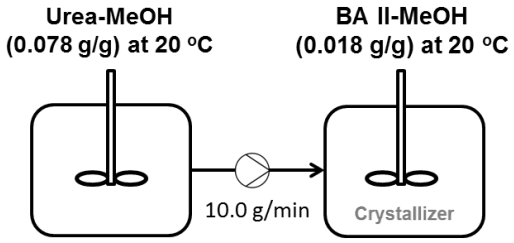

Figure 7.6: Flow diagram showing of the semi-batch configuration used for the co-crystallisation studies.

The batch experiments were carried out with seed addition *viz* Method 1, using 10 % of either UBA form III as seed (i.e. based on theoretical mass of UBA with 1:1 mole ratio of urea:BA in solution). The crystalliser containing urea-BA solution was cooled from 55 °C to the saturation temperature of UBA (43 °C) and seeded with 10 % UBA form III. The vessel was then cooled at a specific rate as indicated in Table 7.1 and then held at the specified final temperature. For the unseeded semi-batch experiments, urea and BA solutions were dissolved separately and held at either 30 or 35 °C. At the start of each experiment, urea was added to BA solution in the crystalliser (Method 2 or Method 3) held at the temperatures specified in Table 7.1.

Table 7.1: Experimental conditions employed for the batch and semi-batch co-crystallisations.

Exp. No.	Exp. Type	Exp. Method	Temperature (°C)				Exp. Time (h)	Cooling Rate (°C/min)	UBA Form Obtained
			Urea Soln.	BA Soln.	Start	Final			
1a	unseeded	3	30	30	10	10	#2.8	rapid	I
1b	unseeded	3	30	30	10	10	#2.8	rapid	I
2a	unseeded	2	30	30	10	10	#2.8	rapid	I
2b	unseeded	2	30	30	10	10	#2.8	rapid	*mix I-III
3a	unseeded	3	30	30	20	20	#2.8	rapid	I
3b	unseeded	3	30	30	20	20	#2.8	rapid	I
4a	unseeded	2	30	30	20	20	#2.8	rapid	•mix I-III
4b	unseeded	2	30	30	20	20	#2.8	rapid	•mix I-III
5a	unseeded	2	30	30	30	30	#2.8	n/a	◊mix I-III
5b	unseeded	2	30	30	30	30	#2.8	n/a	◊mix I-III
6a	unseeded	2	35	35	35	35	#2.8	n/a	◊mix I-III
6b	unseeded	2	35	35	35	35	#2.8	n/a	◊III
7a	unseeded	2	35	35	35	35	#2.8	n/a	◊III
7b	unseeded	2	35	35	35	35	#2.8	n/a	◊III
10	unseeded	2	30	30	30	30	1	n/a	◊mix I-III
11	unseeded	2	35	35	35	35	1	n/a	◊mix I-III
12	unseeded	2	35	35	35	23	ᵗ24	DNC	I
13	unseeded	2	30	30	30	30	1	n/a	•mix I-III
14	unseeded	2	30	30	30	30	1	n/a	‡mix I-III
15	seeded (III)	1	n/a	n/a	43	10	2.8	0.5	III
16	seeded (III)	1	n/a	n/a	43	10	2.8	0.5	▼mix I-III
17	seeded (III)	1	n/a	n/a	43	10	2.8	0.5	▼mix I-III
18	seeded (III)	1	n/a	n/a	43	10	2.8	0.5	•mix I-III
19	seeded (III)	1	n/a	n/a	43	10	14.3	0.06	I

(I) UBA form I; (III) UBA form III; #Sampling at 2.8 h followed by holding for 24 h; ‡dynamic nucleation control (DNC) [224], [260], [299] performed on final mixture for 24 h (set-point was 3000 ± 1000 counts/s); *mix I-III (prevalent form I, increasing with time); ▼mix I-III (prevalent form III, form I increases as temperature is decreased); ◊mix I-III (prevalent form III, form I increasing with time); ◊III (pure form III after 2.8 h, form I starts to appear after 24 h) and •mix I-III (~50:50 mixture of form I and form III).

Unseeded Periodic Flow Co-Crystallisation Experiments: These studies were carried out using the configurations described in the flow diagram of Figure 7.7 (Config. 1) and (Config. 2) below. The PMSMPR was configured with either four or five vessels depending on the method used to combine the urea co-former with the BA target material. In Config. 1, four vessels were arranged in series, consisting of a 6 L capacity feed vessel with premixed UBA solution and a cascade of three 500 mL PMSMPR crystallisers. Config. 2 consisted of a feed stream with two vessels, one 6 L (working volume 5.3 L) and one 1.3 L capacity containing

BA and urea solutions, respectively. The solutions were fed to a cascade of three 500 mL PMSMPR crystallisers. The temperature sets used over the three-stages of PMSMPR were tuned to obtain either pure UBA form I or III based on preliminary findings from the batch and semi-batch co-crystallisation runs.

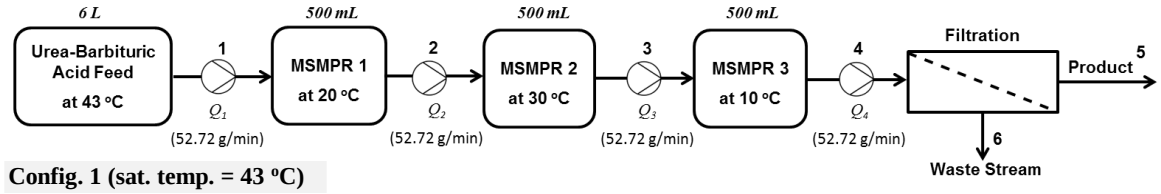

Config. 1 (sat. temp. = 43 °C)

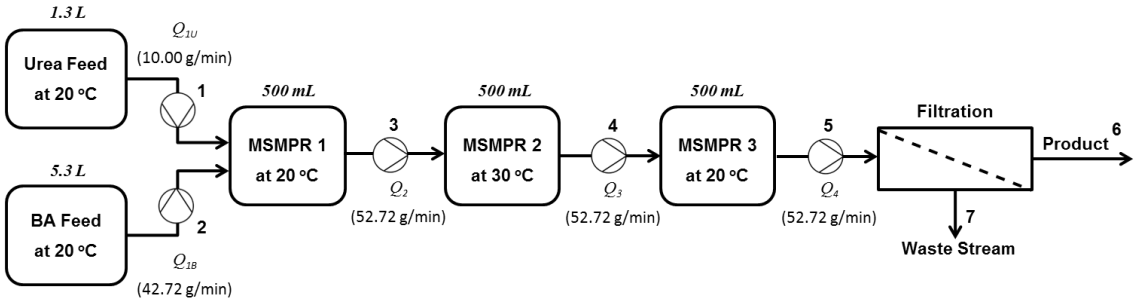

Config. 2 (sat. temp. urea = 43°C)

Figure 7.7: Flow diagram showing the configurations of the PMSMPR cascade units used during the unseeded periodic flow co-crystallisation study (sat. temp. = saturation temperature with respect to UBA co-crystal).

For Config. 1, 6 L of UBA solution (0.014 g urea/g methanol and 0.015 g BA/g methanol) was prepared in the feed vessel to give a 2:1 molar ratio of the urea:BA. The urea and BA starting materials were dissolved together at 55 °C, then cooled and held at 43 °C (saturation temperature of UBA at the specified concentration of feed solution). At start-up, all three PMSMPR crystallisers were initially empty and held at the pre-specified operating temperatures as shown Figure 7.7 (note that the conditions are indicative as a range of different temperature sets were investigated). UBA feed solution was pumped at a rate of 52.7 g/min for 7.40 min to the first-stage PMSMPR crystalliser (MSMPR 1, which acts as the nucleator stage). The MSMPR 1 was held at its pre-specified temperature for 12.60 min (holding period) before the resulting slurry was transferred to the second-stage (MSMPR 2). The third-stage (MSMPR 3) was filled from the MSMPR 2 in a similar way. A coupled periodic flow operating procedure (described in Chapters 5 and 6) was implemented once all vessels were filled and for the duration of each experimental run.

For Config. 2, solutions of 0.078 g urea/g methanol (1.3 L) and 0.018 g BA/g methanol (5.3 L), respectively, were prepared in separate feed vessels by heating the materials in each vessel to 30 °C and holding for 15 min to ensure complete dissolution. The two feed solutions were

then cooled to 20 ^{o}C and held at this temperature. The separate urea and BA streams were combined in either of two ways:

1. Method 1: Pumping concurrently at rates of 10.00 g/min (urea solution) and 42.72 g/min (BA solution), respectively to the first-stage PMSMPR for 7.40 min This resulted in a solution composition of 0.014 g urea/g methanol and 0.015 g BA/g methanol (2:1 molar ratio).

2. Method 2: BA solution pumped to the first-stage PMSMPR at a rate of 42.72 g/min for 7.40 min, followed by rapid manual addition of the required amount of urea solution, to give a 2:1 molar ratio of the urea to BA. Rapid manual addition was done only once (i.e. at start-up). Subsequent to this, a concurrent pumping procedure as described for Method 1 above was implemented for the duration of the experiment.

For each operation (i.e. Config. 1 or Config. 2), Method 1 or Method 2, the same overall feed rate flow was maintained (52.7 g/min). The solution(s) are mixed instantaneously on entering the first-stage, creating supersaturation for subsequent nucleation of UBA co-crystal(s). The nucleated suspension is held in the first-stage for 12.60 min following the procedure described for Config. 1. Subsequent transfer of slurry from the first- to the second-stage and from the second- to the third-stage employed the same operating procedure as described for Config. 1. For both Config. 1 and Config. 2, the sum of the addition/withdrawal and holding periods (20 min) represent the overall periodic flow mean residence time (RT_{PO}) in each stage of the PMSMPR cascade; hence, the total RT_{PO} is 60 min for all three stages combined.

Unseeded continuous crystallisation experiments were carried out for comparison with the periodic flow approaches described above. The continuous flow MSMPR cascade unit was configured as shown in Figure 7.7 (Config. 1). The continuous addition and withdrawal flow rates for each stage of the MSMPR cascade during the co-crystallisations were the same as those used in the periodic flow experiments. Therefore, the continuous flow mean residence time (RT) achieved per MSMPR stage was only 7.40 min, as opposed to 20 min. Table 7.2 gives a summary of the experimental conditions for each of the unseeded periodic and continuous flow co-crystallisations carried out during the study.

Table 7.2: Experimental conditions employed for the unseeded and periodic flow and continuous co-crystallisation experiments.

Expt. No.	Exp. Config.	Mixing Method	Expt. Type	Temperature (°C)		
				MSMPR 1	MSMPR 2	MSMPR 3
1	1	n/a	unseeded	20	30	10
2	2	ᵂ1	unseeded	20	30	20
3	2	ᵗ2	unseeded	20	30	20
4	2	ᵗ2	unseeded	15	10	5
5a	Conti	ᵂ1	unseeded	20	30	20
5b	Conti	ᵂ1	unseeded	20	30	20

n/a - not applicable; Conti - continuous co-crystallisation run; ᵂslow addition of urea to BA at 10 g/min from start-up to the end of experiment; ᵗrapid manual addition of urea to BA at start-up, thereafter addition rate of 10 g/min.

Seeded Periodic Flow Co-Crystallisation Studies: Figure 7.8 (Config. 3) shows the block configuration of the PMSMPR crystalliser used for the seeded co-crystallisation of UBA. Prior to start-up, 6 L of UBA solution (0.014 g urea and 0.015 g BA/g methanol, in a 2:1 mole ratio) was prepared in the feed vessel at 55 °C. The vessel was cooled to 43 °C and then seeded with 10 % UBA form I or III. The seed material used was either UBA form I or III obtained from prior batch cooling crystallisation experiments. The UBA seed suspension was held at 43 °C for 30 min prior to start-up to allow time for crystal healing and Ostwald's ripening [300]. Seed suspension was then pumped to the first-stage PMSMPR at a rate of 52.7 g/min for all experiments except for run 6 for which the flow rate was 41.7 g/min. Table 7.3 gives a summary of the experimental conditions for each of the seeded periodic flow co-crystallisation runs carried out during the study. Note that initial method development experiments were carried out at 41.7 g/min, however, due to particle settling (based on visual inspection) the higher flow rate of 52.7g/min was selected. A periodic operation as described for the unseeded experiments was employed during the seeded co-crystallisation study; the flow rates, slurry addition/withdrawal and holding periods were also the same.

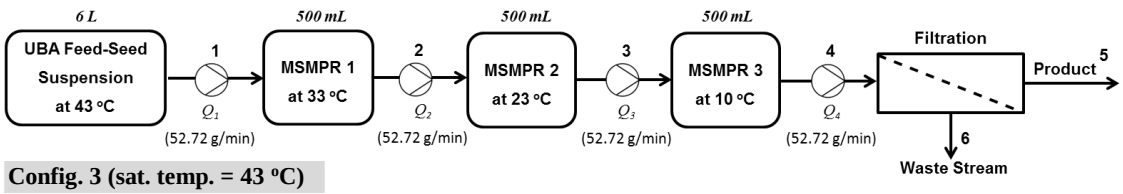

Figure 7.8: Flow diagram showing the block configuration of the PMSMPR cascade unit used during the seeded periodic flow co-crystallisation studies (sat. temp. = saturation temperature with respect to UBA).

Table 7.3: Experimental conditions employed for the seeded periodic flow and continuous co-crystallisation experiments.

Expt. No.	Exp. Config.	Expt. Type	Temperature (°C)		
			MSMPR 1	MSMPR 2	MSMPR 3
6	3	seeded (I)	27	17	10
7a	3	seeded (I)	33	23	10
7b	3	seeded (I)	33	23	10
8	3	seeded (III)	20	20	10
9	3	seeded (III)	35	30	25

(I) UBA form I co-crystal seed; and (III) UBA form III co-crystal seed.

7.3 Results and Discussion

7.3.1 Small Scale Batch Co-Crystallisation Experiments

The small scale experiments using the Avantium Crystalline® system produced pure UBA forms I and III, and mixtures over a range of mixing and cooling rates. A total of 50 experiments, which included duplicates were conducted; the results in terms of the polymorphic outcomes are presented in Table 7.4. The results from the small scale cooling co-crystallisation study did not show any obvious pattern in terms of the mixing and cooling rate effects on the polymorph outcomes, which is perhaps due to the high degree of similarity between energies of the two co-crystals (i.e. assumption based on their similar solubility profiles). However, the experiments did shed some light on the behaviour of the UBA co-crystal system at high and low stirring rates. Although, the results are not consistent over all the duplicate experimental runs as shown in Table 7.4, it appears that at very high stirring rates (800 – 1200 rpm), UBA form III is the more favoured polymorph. The inconsistencies observed during the small scale experimental runs can be attributed to nucleation on the walls of the reactor due to turbulent mixing, particularly at high stirring rates. This leads to the formation of crusts that then act as seed promoting secondary nucleation in the reactor. Another factor to take into account is that at small scale, the mixing behaviour is much different compared to large scale.

Table 7.4: Results from small scale batch (Avantium Crystalline®) co-crystallisation experiments.

Exp. No.	Cooling Rate (°C/min)	Stirring Rate (rpm)	UBA Form Obtained	
			Run 1	Run 2
1	0.05	400	mix I-III (prevalent III)	mix I-III (prevalent III)
2	0.05	600	mix I-III (prevalent III)	mix I-III (prevalent III)
3	0.05	800	mix I-III (prevalent I)	I
4	0.05	1000	*mix I-III (prevalent I)	n/a
5	0.05	1200	*mix I-III (prevalent III)	*mix I-III (prevalent III)
6	0.5	400	mix I-III	mix I-III (prevalent III)
7	0.5	600	I	III
8	0.5	800	*mix I-III (prevalent I)	III
9	0.5	1000	*mix I-III (prevalent I)	mix I-III (prevalent III)
10	0.5	1200	III	I, trace III
11	1	400	III	I, trace III
12	1	600	I	III
13	1	800	I, trace of III	*mix I-III (prevalent I)
14	1	1000	I, trace of III	III
15	1	1200	III	III, trace I
16	2	400	mix I-III (prevalent III)	I
17	2	600	*mix I-III (prevalent I)	III
18	2	800	I, trace of III	mix I-III (prevalent I)
19	2	1000	*mix I-III (prevalent I)	I
20	2	1200	I	mix I-III (prevalent III)
21	3	400	III	I
22	3	600	III	I
23	3	800	I	III
24	3	1000	I	*mix I-III (prevalent III)
25	3	1200	III, trace of I	mix I-III (prevalent III)

*Result affected by encrustation caused by splashing on vessel walls from vigorous stirring

7.3.2 Batch and Semi-Batch Co-Crystallisation Experiments

The complexity of separating polymorphic systems that exhibit similar properties (e.g. solubility, in the case of enantiotrophic systems) in continuous flow has recently been studied [52], [82]. Due to the unusual similarity in the physicochemical properties of UBA forms I and III co-crystal polymorphs has highlighted in Section 7.2.1, these systems present a unique challenge for separation in the periodic flow PMSMPR crystalliser. Therefore, a series of batch and semi-batch co-crystallisations were performed to identify conditions suitable for the selective crystallisation of UBA forms I and III, respectively. The outcome of the various batch and semi-batch co-crystallisations under different experimental conditions was presented earlier in Table 7.1. The results highlight batch-batch variabilities, however, UBA form I could

be isolated under certain conditions. For example, experiments 1a – 3b show that UBA form I was more favourably obtained at low temperatures and with rapid initial mixing of urea and BA (Method 2). However, isolation of UBA form III was more complex and required intensive investigation. It appears that UBA form III is favoured at high temperatures and with slow initial mixing of urea and BA. The co-crystallisation outcomes reported (Table 7.1) were based on off-line PXRD and Raman microscopy analyses on samples collected after each batch run. Experiments 11 – 14 were carried out under unseeded conditions using Method 2 whereby urea solution was added to BA solution at a rate of 10 g/min to give a solution composition of 2:1 moles urea:BA. The effect of manipulating three variables was investigated in these experiments: (1) the addition rate of urea solution, (2) the impeller stirring speed and (3) the process temperature. The urea addition rate can determine the local rate of supersaturation generation and also influences the initial mixing of urea and BA. The stirring speed affects mixing dynamics of the process, and hence the distribution of supersaturation. Finally, temperature is a crucial variable since there are some indications that the co-crystals polymorphs may be enantiotropic. In the preliminary small-scale experiments, UBA form III was found to be more stable at higher temperatures compared to UBA form I, hence the operating temperature range was restricted to between 30 – 35 °C in the lab scale batch and semi-batch operations. With respect to urea addition rate to BA, a slow rate (10 g/min) favours nucleation of UBA form III, whilst a fast rate favoured UBA form I. When impeller mixing speed was investigated, there was no clear relationship to the polymorphic outcome. For the majority of the unseeded semi-batch cooling co-crystallisation experiments, mixtures of UBA forms I and III were obtained. Pure UBA form III was the primary product soon after nucleation, with UBA I crystals appearing and increasing over time, as determined by off-line Raman and PXRD. This suggests a solution phase mediated transformation from UBA form III to I. Experiments 11 and 12 both resulted in predominantly UBA form III product, with only a trace of UBA form I detected. For experiment 12, step-wise rapid cooling (at -1.0^{o}C/min; holding at each step for 60 min) was undertaken from 35 °C to 32 °C, 28 °C and 23 °C, followed by application of dynamic nucleation control (DNC) for 24 h to examine the effect on the amount of UBA form I. Samples were taken at each step and after implementation of DNC. The amount of UBA form I was found to increase with each successive cooling step. The mixture was then held at 23 °C for 60 min, which led to a further slight increase in the amount of UBA form I, but with the mixture remaining predominantly UBA form III. DNC was conducted on this final mixture at 23 ^{o}C for 24 h to determine the effect of this temperature cycling approach on the polymorphic composition. DNC is a concept proposed by Nagy *et al*. [260], [299] and uses information on particle numbers (counts/s) provided by FBRM in a feedback control strategy that adapts the process temperature to promote dissolution, nucleation or crystal growth so that the desired quality of product is achieved, for example large crystals with a narrow crystal

size distribution (CSD) [299]. However, the objective here was to determine the effect of DNC cycles on the polymorphic composition of the mixture of UBA forms I and III. At the end of the DNC experiment, pure UBA form I was obtained, an indication that it is the more stable co-crystal polymorph. Experiments 15 – 19 were carried out under seeded conditions. For experiments 15 – 18 a cooling rate of -0.5 °C/min was implemented. Despite the similar operating conditions for these runs, different polymorphic outcomes were obtained, confirming that the batch crystallisation process is inherently variable. In experiment 19, a slower cooling rate (0.06 °C/min) was employed, and resulted in pure UBA form I product, although the experiment was initially seeded with UBA form III. The results from the small-scale batch, and lab scale batch and semi-batch experiments indicated that the co-crystallisation of urea with BA is very complex, producing mainly mixtures of UBA forms I and III co-crystals. These co-crystals exhibit strikingly similar physicochemical properties, which makes them difficult to isolate. It was therefore quite difficult to identify conditions in batch and semi-batch experiments that were suitable for obtaining the two co-crystal forms independently of each other.

7.3.3 Periodic and Continuous Flow Co-Crystallisation Experiments

Unseeded Co-Crystallisations: A number of unseeded periodic flow co-crystallisation experiments were carried out to determine the most suitable conditions for obtaining UBA forms I and III. The start-up method and the temperatures of the first- (MSMPR 1), second- (MSMPR 2) and third-stage (MSMPR 3) of the PMSMPR cascade were manipulated with the aim to obtain a desired polymorphic form of UBA co-crystal, with results as shown in Table 7.5. A typical goal in industrial crystallisation is to maximise yield whilst also improving filtration rates and avoiding downstream bottlenecks [155], [301]. The yield of co-crystallisation as presented in Table 7.5 is defined as:

$$Y = \frac{M_{UBA} - M_s}{c_o\, f_0 - c^* f_1} \times 100 \qquad (1)$$

where M_{UBA} and M_s are the mass flow of co-crystal product obtained from MSMPR 3 and seed crystals from the feed stream, respectively ($M_s = 0$ for unseeded experiments); c_o and c^* are, the feed stream concentration (g UBA/g MeOH; calculated on the basis of 1:1 co-crystal stoichiometry) and theoretical equilibrium concentration of UBA at the specified operating temperature in MSMPR 3, respectively; f_0 and f_1 are the mass flow rates of MeOH from the inlet and outlet streams of the PMSMPR, respectively. Since the inlet and outlet flow rates are equal when time averaged, then $f_0 = f_1 = M_{MeOH} Q_1$, where M_{MeOH} represents the mass

fraction of MeOH in each flow stream and Q_1 is the total mass flow rate of the inlet or outlet stream.

Table 7.5: Results of unseeded periodic and continuous flow co-crystallisation experiments.

Exp. No.	Exp. Config.	Mixing Method	Stage Temps. (°C)	Yield (%)	Product Size 1st RT (µm)^{Mal}	Product Size 10th RT (µm)^{Mal}	Product Size 1st RT (µm)^{FBRM}	Product Size 10th RT (µm)^{FBRM}	UBA Co-crystal Product
1	1	n/a	20/30/10	92	207	245	105	91	*mix I-III
2	1	ʷ1	20/30/20	100	183	244	101	88	*mix I-III
3	2	ᵗ2	20/30/20	86	190	223	101	87	I
4	2	ᵗ2	15/10/5	79	186	252	104	93	I
5a	Conti	ʷ1	20/30/20	66	202	259	104	92	♦mix I-III
5b	Conti	ʷ1	20/30/20	62	181	234	101	95	♦mix I-III

ʷslow addition of urea to BA at 10 g/min from start-up to the end of experiment; ᵗrapid manual addition of urea to BA at start-up, thereafter addition rate was 10 g/min; ^{Mal}Volume moment mean size ($D_{4,3}$) of dry product from MSMPR 3 analysed by laser diffraction; ^{FBRM}Square weighted mean chord length (SWMCL) of particles in MSMPR 3 obtained via *in situ* measurements with FBRM; *mix I-III (prevalent form I, increasing with time); ♦mix I-III (predominant form I with only traces of III); and n/a - not applicable.

The yields of co-crystallisation from experiments 3 and 4 were slightly lower (86 % and 79 %, respectively) compared to experiments 1 and 2 (100% and 92 %, respectively). This can be attributed to the supersaturation differences that exist between PMSMPR stages due to the different operating temperature of each stage. For example, in experiment 2 the level of undercooling going from stage 2 to 3 is -10 °C, this compares to a level of undercooling of -20 °C for experiment 1. In the former case equilibrium is approached more quickly compared to the latter case due to the lower level of undercooling between stages and hence low available supersaturation that is rapidly consumed by the crystals already present. Note that a lower yield than expected was observed for experiment 3, due perhaps to losses that occurred during the solid recover stage (filtration of the slurry collected from MSMPR 3). For experiment 5a and 5b, the yield of co-crystallisation was significantly less than that reported for experiments 1 – 4. This is attributed primarily to the shorter RT of the slurry in the crystalliser, due to the continuous operation (as opposed to periodic operation). It appears that the polymorphic outcome of co-crystallisation depends on the feeding regime employed for combining urea and BA in MSMPR 1 (Table 7.5), and the initial operating temperature. Equally important as well, is the operating temperature of subsequent PMSMPR stages, in particular MSMPR 2. When either a combined urea-BA feed stream (experiment 1) or separated flow with slow addition of urea to BA (experiment 2) is employed at temperatures of 20 °C or higher in MSMPR 1, a mixture of UBA form I and III was always observed. This was also confirmed by the semi-batch experiments conducted using a similar start-up strategy as the PMSMPR

experiments. This is perhaps due to better mixing, leading to a homogeneous solution, which allows equal chance of both co-crystal forms nucleating. This is a plausible conclusion since the two co-crystal forms display very similar physicochemical properties. On the other hand, it appears that rapid initial mixing of urea and BA streams in MSMPR 1 at operating temperatures of 20 ^{o}C and lower leads to the preferential formation of the UBA form I (experiment 4), although traces of UBA form III were also detected. This was also confirmed from the semi-batch experimental runs conduct under similar conditions.

Table 7.6: Evolution of UBA polymorphic form during experiments 1 – 5 for the first- through third-stage PMSMPR and MSMPR, analysed by off-line Raman spectroscopy and PXRD.

Sampling Time Exp. 1 – 4 (min)	MSMPR 1				
	Exp. 1	**Exp. 2**	**Exp. 3**	**Exp. 4**	**Exp. 5a**
30	mix I-III*	mix I-III♦	mix I-III♦	mix I-III♦	mix I-III* (11 min)
60	I	mix I-III♦	mix I-III♦	mix I-III♦	mix I-III* (22 min)
90	I	mix I-III♦	mix I-III♦	mix I-III♦	mix I-III♦ (33 min)
120	mix I-III*	mix I-III*	I	I	mix I-III* (45 min)
150	I	I	I	I	mix I-III♦ (56 min)
	MSMPR 2				
40	mix I-III*	mix I-III*	mix I-III*	mix I-III♦	mix I-III* (15 min)
70	mix I-III♦	mix I-III*	mix I-III*	mix I-III♦	mix I-III* (26 min)
100	mix I-III	mix I-III*	mix I-III*	mix I-III♦	mix I-III* (37 min)
130	I	mix I-III*	mix I-III♦	mix I-III♦	mix I-III♦ (48 min)
160	mix I-III♦	mix I-III*	mix I-III♦	I	I (60 min)
	MSMPR 3				
50	mix I-III*	mix I-III♦	mix I-III*	mix I-III♦	mix I-III* (19 min)
80	mix I-III*	mix I-III♦	mix I-III*	I	mix I-III* (30 min)
100	mix I-III*	mix I-III*	mix I-III*	I	mix I-III* (36 min)
120	mix I-III*	mix I-III*	mix I-III♦	I	mix I-III♦ (42 min)
140	mix I-III*	mix I-III♦	mix I-III♦	I	I (48 min)
160	I	mix I-III♦	mix I-III♦	I	mix I-III♦ (54 min)
180	mix I-III♦	I	I	I	I (60 min)
200	I	I	I	I	mix I-III♦ (66 min)
220	mix I-III♦	mix I-III♦	I	I	mix I-III♦ (72 min)

(I) UBA form I co-crystal; (III) UBA form III co-crystal; *mix I-III (prevalent form I, increasing with time); ♦mix I-III (prevalent form I with only traces of III); and I (form I only).

Table 7.5 also shows the product mean crystal size as determined by off-line particle size analysis *viz* laser diffraction and real-time *in situ* process monitoring with FBRM. The final product crystal sizes are similar for all experimental runs with no clear correlation between product crystal size and the process variables. Further discussion on the mean product size and CSD is provided late in this section. Periodic sampling of each PMSMPR stage was performed during the unseeded experiments (Table 7.5) in order to understand better the behaviour of the system. Samples were analysed using off-line Raman spectroscopy and PXRD. Evolution of the polymorphic outcome over time for experiments 1 – 5b, as determined by Raman spectroscopy and PXRD are presented in Table 7.6. For experiments 1, 2, 5a and

5b mixtures of UBA forms I and III were initially present, but as the reaction time progress there is a reduction in the amount of UBA form III, as UBA form I becomes the dominant polymorph. For experiment 3 and 4 Raman and PXRD confirmed that pure UBA form I was obtained from the final stage PMSMPR. The experimental results (Tables 7.5 and 7.6) indicate that increasing the temperature of MSMPR 2 leads to dissolution of the small amount of UBA form III initially formed in MSMPR 1 and propagated to subsequent stages of the PMSMPR. For experiment 4, there is a rapid transition from a mixture of UBA form I and III in MSMPR 1 to pure UBA form I in MSMPR 3. In this experiment, the temperature was progressively lowered in 5 °C steps from 15 °C in MSMPR 1 to 5 °C in MSMPR 3. This is an indication that rapid mixing of urea and BA at start-up and the high initial supersaturation generated in MSMPR 1 by cooling to 15 °C, favours the nucleation of UBA form I. Further cooling in subsequent stages of the PMSMPR then leads to a complete suppression of UBA form III crystallisation as UBA form I nucleates and grows.

The time diagrams for the FBRM counts/s and temperature profiles, Figure 7.9 (a) and (b), show that for all experiments a SCO is achieved in the early stages. Spikes in the time profiles of Figure 7.9 (a) indicate discontinuities where fouling of the FBRM probe was suspected and a cleaning procedure then implemented. For example, experiments 1 and 2 were most affected by fouling and crust formation compared to experiments 3, 4 and 5a. Interestingly, for the former two experiments, there was a mixture of co-crystals at all times, with significant amounts of UBA form III when compared to the latter three experiments. This suggests that fouling is more pervasive when UBA form III crystals are present in significant amounts, which can be correlated to the batch experiments discussed earlier where crust formation was observed. It appears that UBA form III has a greater tendency to stick on the sapphire probe window, (which appears to have an electrostatic charge surface charge [302]), compared to UBA form I.

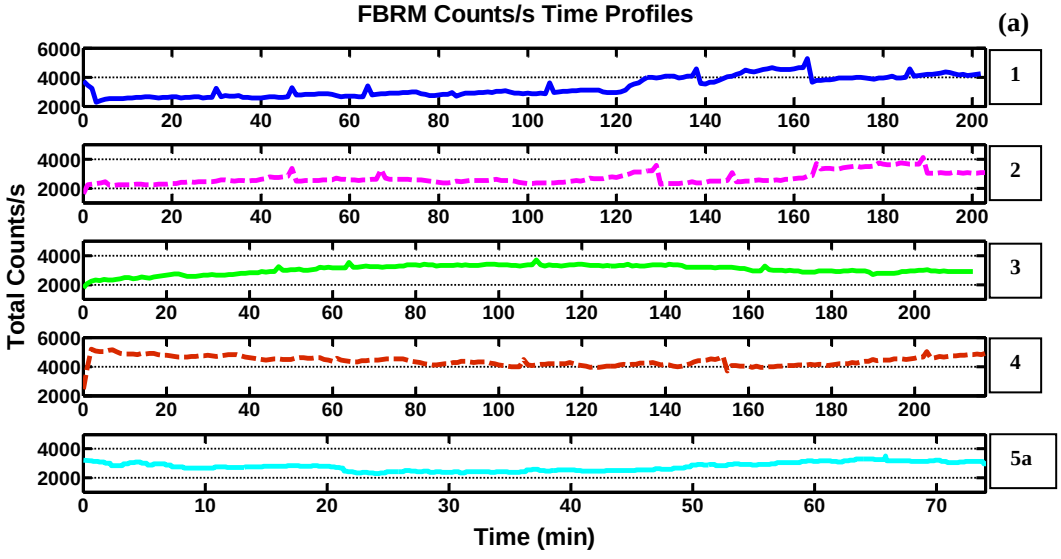

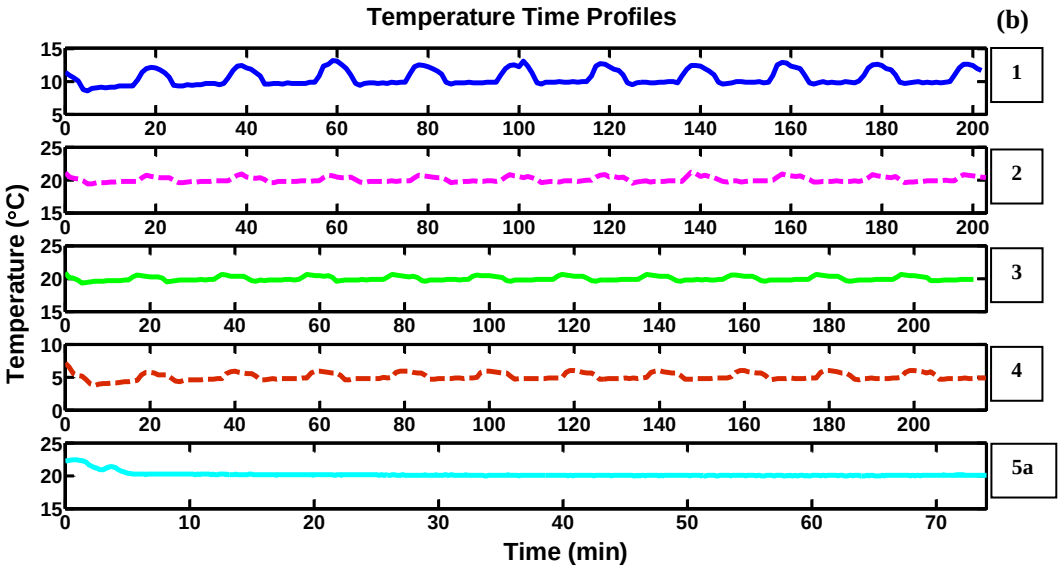

Figure 7.9: FBRM counts/s (a) and temperature (b) time profiles recorded in MSMPR 3 stage of the unseeded PMSMPR and MSMPR for experiments 1 – 4 and 5a. Spikes in the FBRM profiles indicate cleaning of the probe due to fouling. Temperature profiles reflect the periodic flow operation. Experiment 5a is a continuous MSMPR run included for comparison.

Fouling affected ATR-UV/vis to a greater extent compared to the other PAT probes, such that the signal was not stable and reliable, due to a need to clean the probe regularly. Evidence of this is given by ATR-UV/vis spectra collected during the periodic flow and batch co-crystallisation experiments, which show spectral distortion in the presence of UBA form III. Despite the incidence of fouling on the PAT probes, SCO was deemed to be achieved for all experimental runs, with sight drift toward the end of experiments 1, 2 and 5a. The ATR-UV/vis spectra captured subsequent to detection of fouling in these experiments were compared to pure Methanol, Methanol + Urea, and Methanol + Urea-BA spectra respectively, as shown in Figure 7.10. It is evident from the ATR-UV/vis spectra that UBA form III co-crystal had a tendency to stick on the sapphire probe window causing significant distortion of the signal. It has previously been reported that in the presence of solids, a small part of the ATR-UV/vis signal can be reflected resulting in baseline effects [145]. This effect becomes more pronounced after the onset of nucleation when solid particles have a greater tendency to stick on the probe window [303].

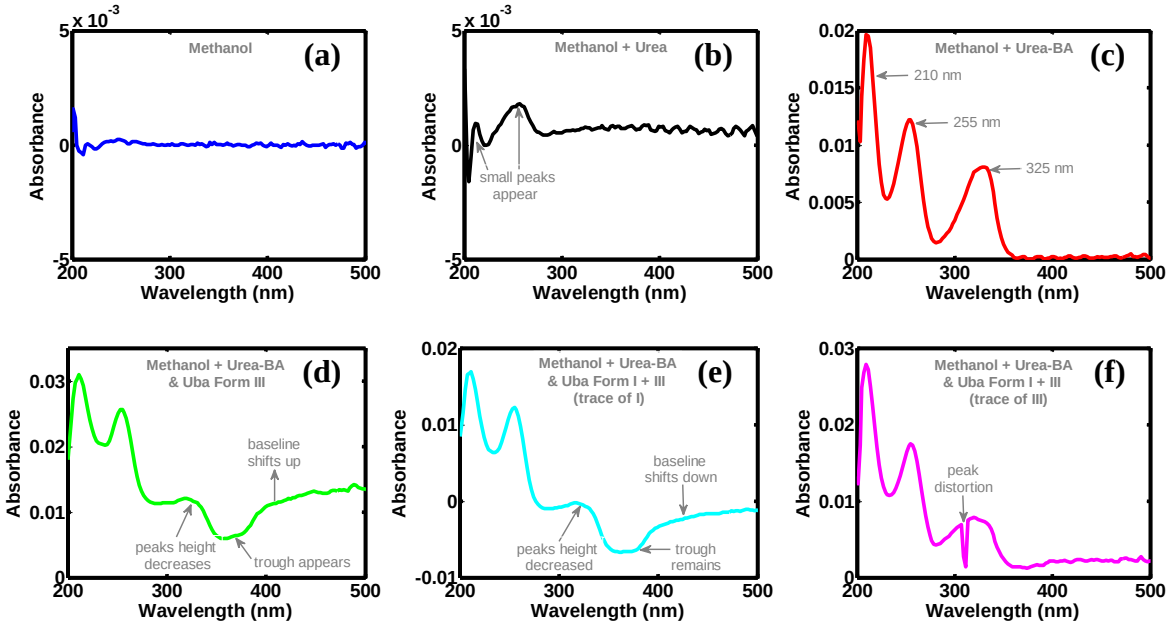

Figure 7.10: ATR-UV/vis signals for (a) Methanol; (b) Methanol + Urea; (c) Methanol + Urea-BA; (d) Methanol + Urea-BA solution and UBA Form III – experiment 15 (batch); (e) Methanol + Urea-BA solution and UBA Form I + III (trace of I) – experiment 16 (batch); and (f) Methanol + Urea-BA solution and UBA Form I + III (trace of III) – experiment 2 (periodic flow).

In situ PVM images captured from MSMPR 1 in real-time and off-line microscope images from MSMPR 3 (Figure 7.11) show the visual appearance of crystal growth over time. There is clear evidence of agglomeration of the UBA co-crystals from the PVM and microscope images, with UBA form I in particular having a tendency to agglomerate soon after nucleation. The apparent slight shifts to the left of the FBRM SWCLD plots (Figure 7.12) are not consistent with this visual evidence, indicating instead a slight reduction in particle size. Therefore, the FBRM results must be treated with caution, as it is well known that different particle sizing techniques can often give contradictory results [304]–[306] and the chord length measurements made in FBRM are highly dependent on the shape and roughness of particles scanned by the probe's laser beam. The PVM and microscope images (Figure7.11) show better agreement with the CSD data obtained from laser diffraction (Figure 7.13).

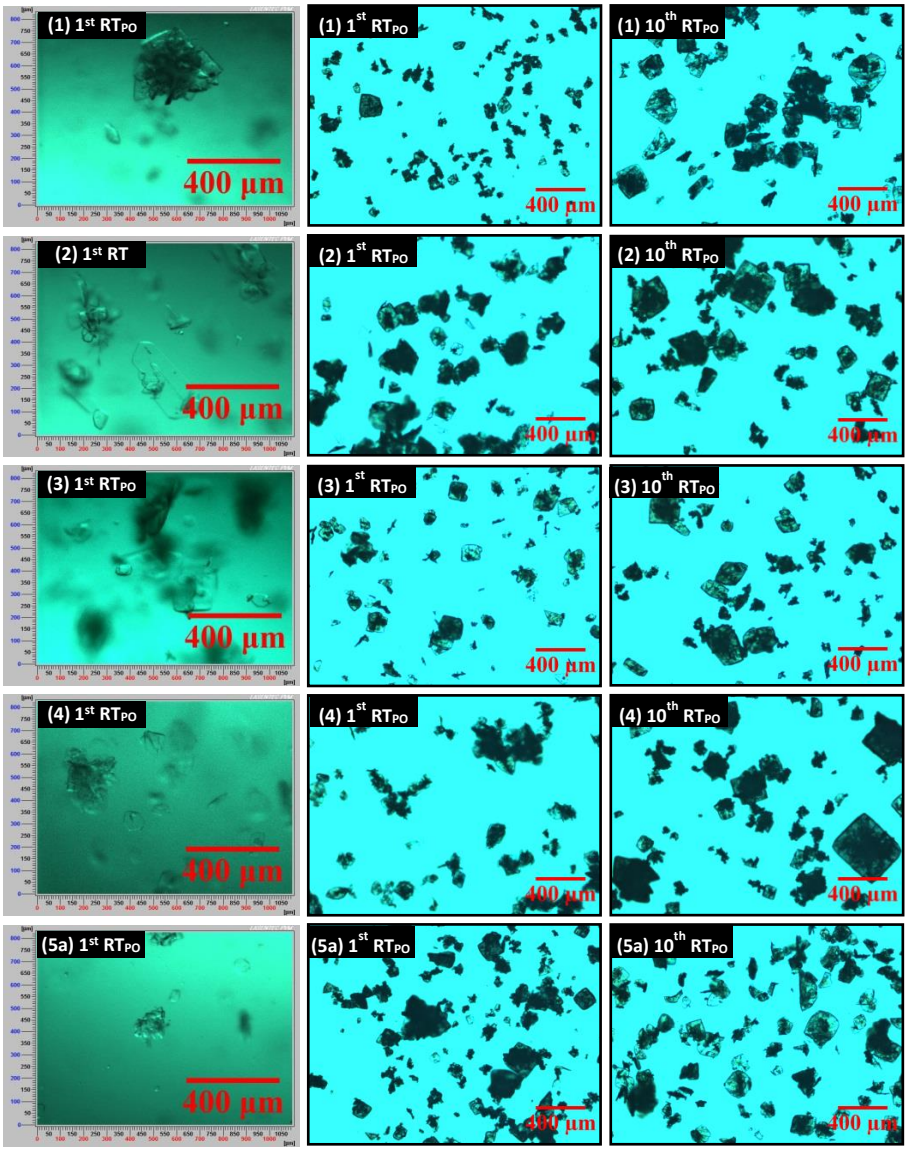

Figure 7.11: *In situ* PVM images (left) captured from MSMPR 1 and Off-line microscope images (right) of samples collected from MSMPR 3 for experiments 1 – 4 and 5a.

Together, these results show that crystal size increases from the 1st (20 min) to 10th (200 min) RT_{PO} in all PMSMPR experiments, mainly due to agglomeration, but also with evidence of crystal growth. From the PVM and microscope images in Figure 7.11, UBA form I crystals are identified as semi-transparent particles that often agglomerate forming rosette type structures. On the other hand, UBA form III crystals are more difficult to identify, but occur as dark agglomerated particles that appear to coat onto any UBA form I crystals present (see Figure 7.5). Evidence of the presence of UBA form III is seen in the microscope images for the 1st and 10th RT_{PO} of experiments 1 and 2. For experiments 3, 4 and 5a, there is little evidence of the presence of UBA form III in the 10th RT_{PO} samples. However, for experiment 5a there is evidence that UBA form III is present in the 1st RT_{PO} sample, but this is not the case for experiment 4. These

observations are in agreement with the off-line Raman and Powder XRD data presented earlier (Table 7.6).

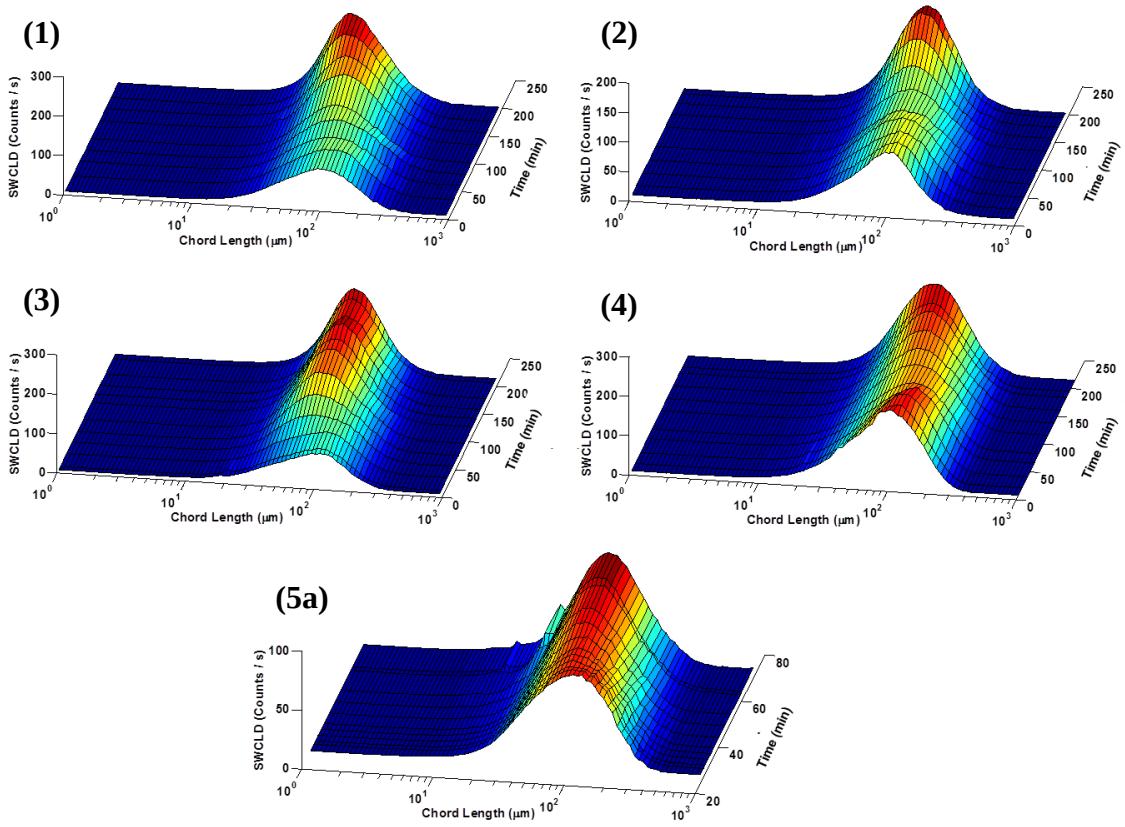

Figure 7.12: Evolution of FBRM SWCLD in MSMPR 3 stage for experiments 1 – 4 and 5a.

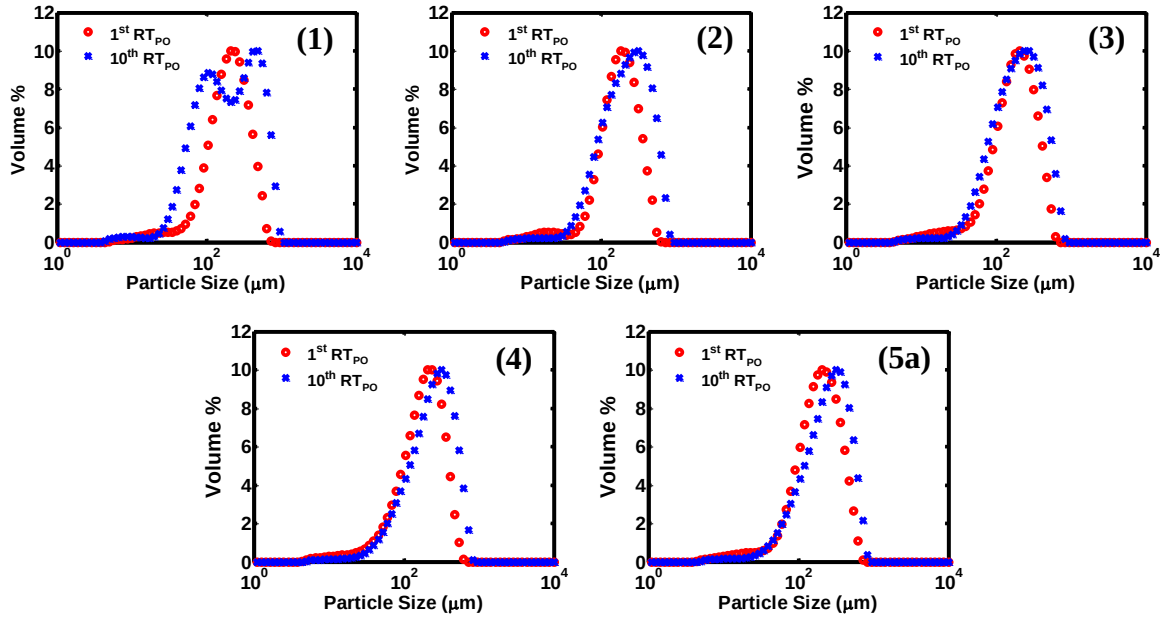

Figure 7.13: Normalised CSD profiles for the 1st and 10th RT_{PO} product of the third-stage PMSMPR (MSMPR 3) for experiments 1 – 4 and 5a, analyses by laser diffraction.

Seeded Co-Crystallisation Periodic Flow Experiments: A parallel strategy of seeded co-crystallisation in the PMSMPR was implemented for isolation of pure UBA forms I and III. Urea-BA feed solutions were seeded with the desired co-crystal form. Table 7.7 provides a summary of the experimental results obtained using the seeded co-crystallisation approach. The seeded experiments 6 – 9 were carried out using the periodic flow crystallisation approach in the PMSMPR cascade unit described in Section 7.2.3 (Figure 7.8). Different temperature sets were implemented across the stages of the PMSMPR based on the preliminary batch and semi-batch studies. In each case, the first-stage (MSMPR 1) does not behave as a nucleator vessel, which was the case in the unseeded experiments; instead secondary nucleation and growth are the main driving force. MSMPR 1 was fed with seed suspension from the 6 L feed vessel to promote secondary nucleation and growth. The feed solution (saturated at 43 °C) was seeded with 10 % of either UBA form I or III, ensuring modest fines dissolution whilst promoting growth and healing of the larger seed crystals *viz* aging and Ostwald ripening. Table 7.7 provides a summary of the results from each experimental run. The co-crystal polymorphic form at the end of each process was confirmed by Raman spectroscopy and PXRD.

The yields of co-crystallisation for experiments 6 – 9 shown in Table 7.7 reflects the experimental conditions that were applied during the study. High yields are achieved in the periodic operation because the mean RT_{PO} inside the PMSMPR crystalliser is extended with the holding period. Note that all experiments were seeded with 10 % co-crystal seed regardless of the polymorphic form. The yields of co-crystallisation of UBA form I for experiments 6, 7a, and 7b (seeded with UBA form I) are slightly different due to the different addition/withdrawal and holding periods, flow rates, and the temperature sets employed over the PMSMPR cascade. For experiment 6, the yield is lower due to: (1) the shorter holding period and lower flow rate, which caused settling of large crystals in the transfer line; and (2) the smaller temperature difference (7 °C) between MSMPR 2 and 3.

Table 7.7: Results for the seeded periodic flow co-crystallisation experiments.

Exp. No.	PMSMPR Stage Temps. (°C)	Process Yield (%)	Seeds Crystal Size (µm)^{Mal}	Product Size 1st RT (µm)^{Mal}	Product Size 10th RT (µm)^{Mal}	Seeds Crystal Size (µm)^{FBRM}	Product Size 1st RT (µm)^{FBRM}	Product Size 10th RT (µm)^{FBRM}	UBA Product
6	27/17/10	85	287 (I)	339	343	120	103	99	I
7a	33/20/10	94	278 (I)	217	279	110	108	123	I
7b	33/20/10	92	254 (I)	235	260	106	102	113	I
8	20/20/10	92	156 (III)	164	187	94	96	88	•mix I-III
9	35/30/25	100	193 (III)	173	245	101	101	103	•mix I-III

(I) UBA form I co-crystal seed; (III) UBA form III co-crystal seed; ^{Mal}Volume moment mean size ($D_{4,3}$) of dry product from MSMPR 3 analysed by laser diffraction; ^{FBRM}Square weighted mean chord length (SWMCL) of particles in MSMPR 3 obtained via *in situ* measurements with FBRM; •mix I-III (~50:50 mixture of form I and III).

The yield is higher for experiment 7a and 7b compared to experiment 6, due to the longer holding period and higher flow rate, leading to better suspension of crystals (based on visual observation); the larger temperature difference (10 ^{o}C) between MSMPR 2 and 3 led to a higher level of supersaturation in the final stage for crystal growth and secondary nucleation. For experiments 8 and 9, (seeded with UBA form III), the holding and addition/withdrawal periods and the flow rates were held constant. The only difference between these two experiments was the temperature change between the PMSMPR stages; the differences in yield may be attributed to the temperature change between MSMPR 1 and 2. These are the same in experiment 8, but not experiment 9, leading to further generation of supersaturation in the latter allowing enhanced crystal growth and nucleation. Raman and PXRD confirm that UBA form I was obtained from experiments 6, 7a and 7b, whereas mixtures of UBA form I and III were confirmed for experiments 8 and 9. For the former three experiments, seeding has ensured secondary nucleation of UBA form I in MSMPR 1. The resulting crystals are then grown in subsequent stages (MSMPR 2 and MSMPR 3). For experiment 6, temperatures were kept at 27 °C, 17 °C and 10 °C in MSMPR 1, MSMPR 2 and MSMPR 3, respectively. The temperatures employed in experiments 7a and 7b for each successive PMSMPR stage were 33 °C, 20 °C and 10 °C, respectively. The need to manipulate the temperature of each PMSMPR stage in this case was dictated by the trade-off between avoiding the blockage of transfer lines and achieving high product yield and crystal growth. The temperature set used during experiment 7a and 7b was found to be suitable for the purposes of avoiding blockage of the transfer lines. The narrowing of the temperature gap between the feed vessel and MSMPR 1 led to controlled secondary nucleation, thus preventing crystals clogging the transfer line to MSMPR 2. For experiments 8 and 9, a feed suspension of UBA form III was prepared and fed to MSMPR 1, with the aim of obtaining the pure co-crystal polymorph in the same manner as achieved in the successful outcome of experiments 6, 7a and 7b for UBA form I. However, for both experiments 8 and 9 mixtures of UBA forms I and III were obtained from MSMPR 3. As expected, UBA form III was the prevalent co-crystal form detected in the early stages of both experiments, that is, from start-up to the end of the 3rd RT (60 min). Table 7.8 shows the evolution of UBA co-crystal polymorphic form for experiments 8 and 9; the results are based on Raman and PXRD analyses.

Table 7.8: Evolution of UBA co-crystal polymorphic form in the final stage PMSMPR (MSMPR 3) during experiments 8 and 9, analyses by off-line Raman and PXRD.

Sampling Time (min)	UBA Co-crystal Form in MSMPR 3	
	Exp. 8	Exp. 9
1st (20 min)	◊mix I-III	◊mix I-III
2nd (40 min)	◊mix I-III	•mix I-III
3rd (60 min)	◊mix I-III	•mix I-III
4th (80 min)	•mix I-III	•mix I-III
5th (100 min)	•mix I-III	•mix I-III
6th (120 min)	•mix I-III	•mix I-III
7th (140 min)	•mix I-III	•mix I-III
8th (160 min)	•mix I-III	•mix I-III
9th (180 min)	•mix I-III	•mix I-III
10th (200 min)	•mix I-III	•mix I-III

◊mix I-III (prevalent form III, form I increasing with time); and •mix I-III (~50:50 mixture of form I and III).

The amount of UBA form I co-crystal in experiment 8 and 9 increased gradually with time. From the 3rd (60 min) – 10th (200 min) RT_{PO}, mixtures of UBA I and III were detected by off-line Raman and PXRD. A solution mediated transformation [165], [307], [308] takes place in each system, which results in an increase in the amount of UBA form I. Interestingly, for experiments 8 and 9, SCO was achieved after the 3rd and 2nd RT_{PO}, respectively, with an SCO polymorphic ratio of ~50:50, suggesting equal transformation between UBA forms I and III. The temperature set used in experiment 9 (35 °C, 30 °C and 25 °C for MSMPR 1, MSMPR 2 and MSMPR 3, respectively) was chosen to avoid this situation, by elevating the temperatures and maintaining small temperature step changes between each PMSMPR stage to suppress nucleation of UBA form I. However, this did not have an effect on the polymorphic outcome when compared to experiment 8.

The time diagrams for the FBRM counts/s and temperature profiles are shown in Figure 7.14 (a) and (b), respectively. The time profiles for each experiment are indicated by number. Similar to the unseeded co-crystallisation experiments, there are spikes in each of the FBRM counts/s time profiles due to the removal and cleaning of the probe whenever fouling was detected. Fouling was most frequently observed during experiments 6 and 9, in comparison to experiments 7a and 8. For experiment 6, the FBRM and other PAT probes were cleaned a total of 8 times. The frequent fouling of the probe was attributed to the low flow rate employed (41.7 g/min) compared to the other experiments (52.7 g/min). This resulted in the settling of larger crystals and the preferential propagation of smaller crystals in the transfer lines as observed from visual inspection. This resulted in an accumulation of fine crystals in the final stage MSMPR, which are more prone to sticking, aggregation and agglomeration. Experiment

6 was the first of a series of exploratory experiments to determine the minimum flow rate required to achieve particle suspension. A flow rate of 52.7 g/min was found to be a good particle suspension flow rate based on visual observations, and was therefore selected for all other experimental runs. In the case of experiment 9, a different scenario arises whereby significant fouling is observed despite the higher flow rate and smaller temperature step changes between the PMSMPR stages. The explanation for fouling in experiment 9 is the presence of UBA form III. During this experiment, the PAT probes were cleaned a total of 11 times due to persistent fouling. The effect of fouling from UBA form III on the ATR-UV/vis signal has previously been demonstrated. In the case of experiment 7a, only 3 incidences of fouling on the PAT probes were observed. During this experiment only UBA form I was detected, furthermore the flow rate employed between PMSMPR stages was sufficiently high compared to experiment 6 to prevent preferential propagation of smaller particles. In addition, the step changes in temperature between PMSMPR stages were smaller compared to experiment 6. For experiment 8, fouling on the PAT probes was detected 7 times, although this is not very obvious from the FBRM time profile. Similar to experiment 9, the occurrence of fouling is attributed to the presence of UBA form III, which has been shown to stick more readily to the probes, due perhaps to an attraction for the electrostatically charged surface of the sapphire windows (e.g. of the FBRM and ATR-UV/vis). The FBRM time profiles show that a SCO is achieved from the 2nd RT (40 min) in experiment 6 and is maintained until the 7th RT (140 min) where there begins a slight drift, marked by an increase in FBRM counts/s. For experiment 7a and 9 it takes approximately 30 min to achieve a SCO. However, for both of these experiments the system drifts from the SCO from approximately 95 min (experiment 7a) and 120 min (experiment 9) until the end. For experiment 8, SCO is achieved after approximately 80 min and is maintained until the end of the run. Also, the particle counts detected by FBRM are almost twice that observed in the other experiments. This is attributed to a significant amount of secondary nucleation in the early stages of the process due to the larger temperature gap (23 °C) between the feed and MSMPR 1. Consequently, the system is more sensitive to perturbations cause by the periodic operation and this leads to higher oscillation amplitudes observed in the FBRM signal compared to the other runs.

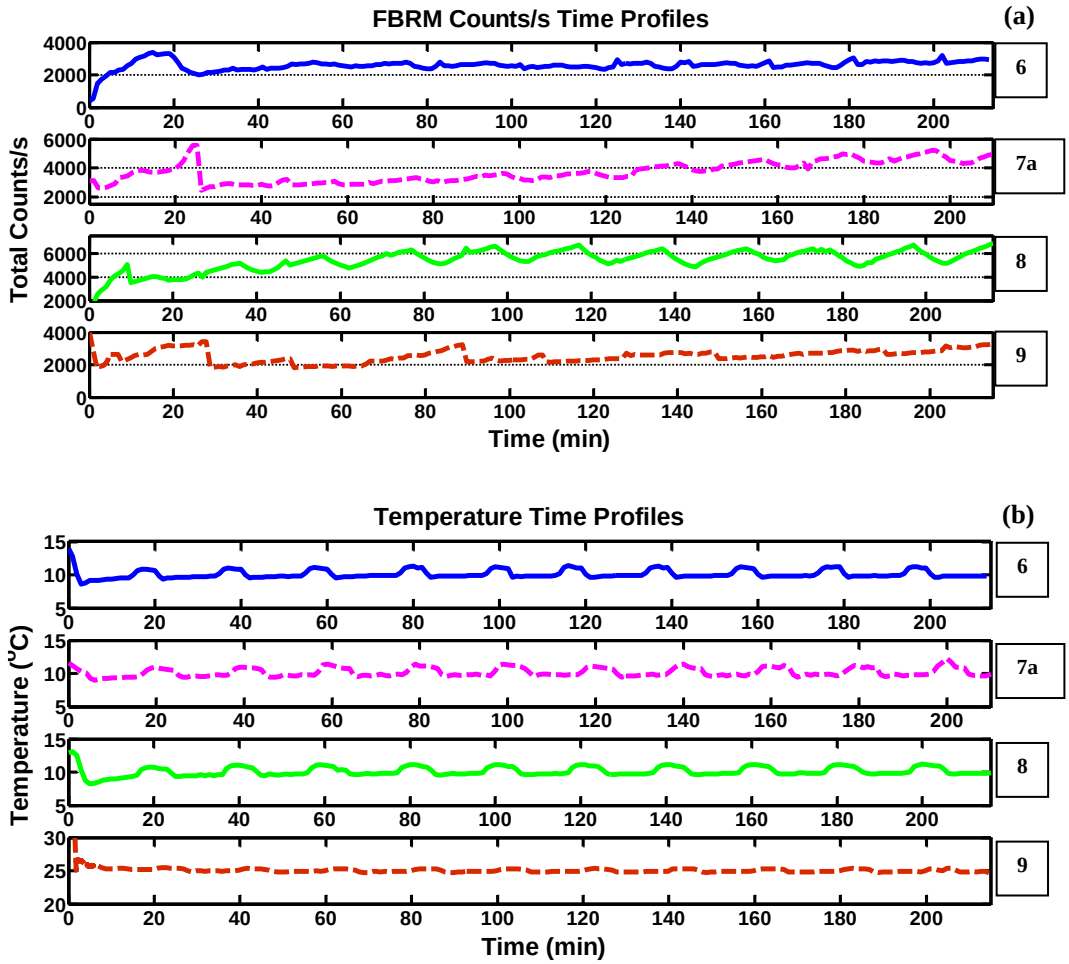

Figure 7.14: FBRM counts/s (a) and temperature (b) time profiles recorded in MSMPR 3 of the seeded PMSMPR for experiments 6 – 9.

The particle size and distribution results (Table 7.7; Figure 7.15), show clear evidence of crystal growth and/or agglomeration. As discussed earlier, these results were not fully consistent with the FBRM SWCLD; the CSD plots from the laser diffraction experiments are more reliable and are interpreted here. For all experiments, with the exception of run 7a there is a significant shift of the product CSD to the right compared to that of the seed crystals used. These observations agree with the mean crystal size obtained by laser diffraction analyses (Table 7.7) and the off-line microscope images of the seed and product crystals from MSMPR 3 shown in Figure 7.15.

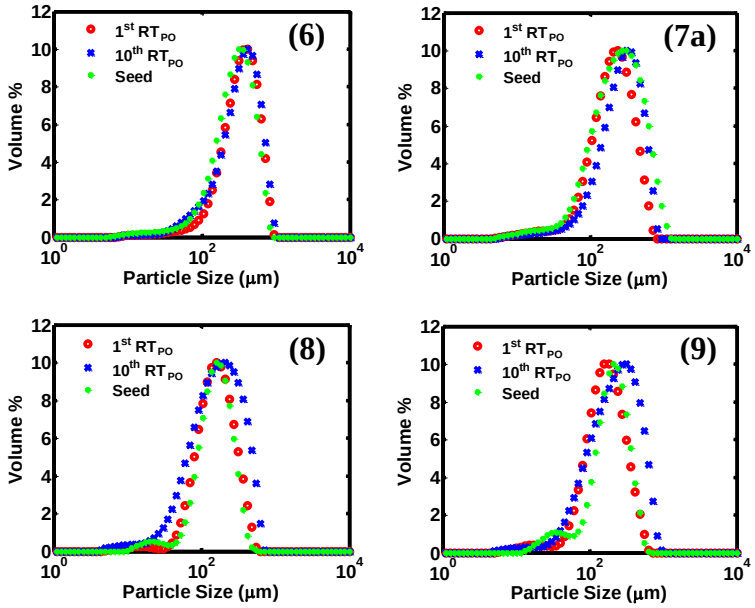

Figure 7.15: Normalised CSD profiles for the 1st (20 min) and 10th RT_{PO} (200 min) product of the third-stage PMSMPR (MSMPR 3) for experiments 6 – 9, analyses by laser diffraction.

The mean sizes of seed crystals for experiments 6 and 7a are quite similar with evidence of growth confirmed from microscope images (Figure 7.16). However, the CSD for experiment 7a is slightly broader compared to experiment 6. This is attributed to the seed properties at the start of each experiment. The seed CSD is slightly broader for experiment 7a, which may explain why the product CSD remains broad. It is also likely that the smaller temperature step between MSMPR 1 and MSMPR 2 and MSMPR 3 in experiment 6 (7 °C) compared to experiment 7a (10 °C) leads to lower supersaturation levels, reducing secondary nucleation and favouring more growth, thereby leading to maintenance of a narrow CSD. In experiment 7a, the temperature steps between each stage of the PMSMPR cascade are large, which is likely to contribute to more secondary nucleation compared, and hence broadening of the CSD. The CSD for the product of UBA form I appears to be narrower when compared to the CSD of mixtures of UBA form I and III (i.e. where UBA III is the more prevalent form present), which appear broader. This would suggest that the extent of secondary nucleation is greater when UBA III nucleates, thus, leading to a broadening of the CSD. Therefore, it would appear that laser diffraction could be used in a qualitative manner to determine when between UBA III is present in a mixture of the two co-crystal forms. For example, the significant broadening of the product CSD relative to the seed crystals for experiments 9 and 10 appears to be related to the presence of UBA form III. Off-line microscope images of the seed and product crystals from MSMPR 3 (Figure 7.16) agree with the CSD data obtained using the laser diffraction (Table 7.7; Figure 7.15).

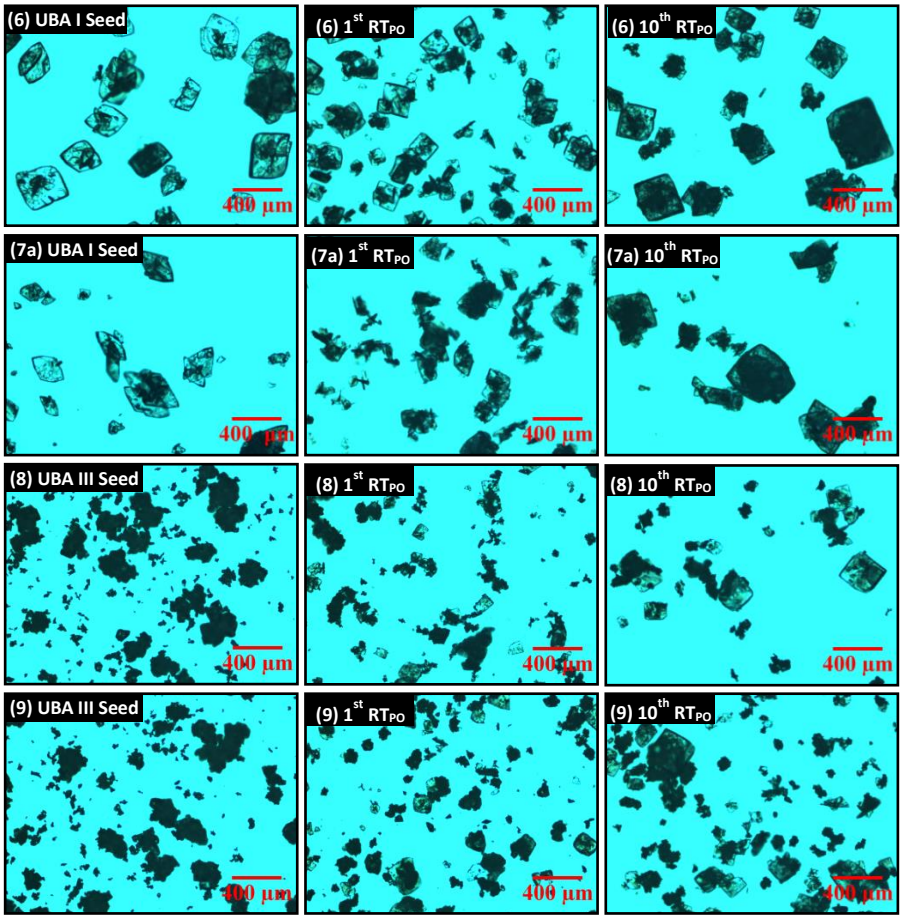

Figure 7.16: Off-line microscope images of the seed and product crystals from MSMPR 3 for experiments 6 – 9.

Overall, more consistent results in terms of polymorphism control were achieved using the periodic flow co-crystallisation approach reported in this study. The periodic flow PMSMPR process provided a different trajectory through the phase diagram compared to batch and continuous MSMPR, respectively. In each stage of the PMSMPR cascaded, the supersaturation oscillates, but in a controlled manner between narrow boundaries in the metastable zone. The operating boundaries of the periodic flow process can be expanded or reduced by manipulating the degree of undercooling, or the holding (batch) and/or addition/withdrawal (continuous) periods at each PMSMPR stage. This leads to additional degrees of freedom in operation that can be exploited to control the co-crystallisation as demonstrated in this study, when compared to batch and continuous MSMPR operations. The PMSMPR provides the flexibility of adjusting the supersaturation trajectory in the metastable zone to control the co-crystallisation outcome (i.e. polymorphic form), whilst producing consistent product in a relatively short time. This is not possible in batch operation without applying complex control strategies, for example, DNC [170], [224] and supersaturation control [31], [49] over very long periods. In comparison to continuous MSMPR operation, the periodic PMSMPR achieves much higher process yields (similar to batch operation) due to

the longer achievable RT, with the added advantage of controlling polymorphism, given that enough time is allowed for solution mediated transformation from one polymorphic form to another.

7.4 Conclusions

The co-crystallisation of the urea and BA to form UBA forms I and III co-crystal polymorphs was demonstrated under periodic flow conditions using a cascaded three-stage PMSMPR crystalliser. Batch and semi-batch co-crystallisations were used to identify conditions suitable for isolate pure UBA forms I and III. Significant variability from batch-to-batch was observed in both small scale batch (5 mL) and lab scale batch and semi-batch (500 mL) crystallisers. Continuous flow co-crystallisations in MSMPR were carried out for comparison with the periodic flow PMSMPR experiments. In the continuous experiments, mixtures of UBA forms I and III were consistently obtained. The PMSMPR provides a different operating trajectory through the phase diagram (i.e. it oscillates within a tight boundary) compared to batch and continuous processes, and has a tenable residence time that can be exploited for control over crystal growth and secondary nucleation. These system attributes can be exploited to manipulate the product crystal properties and lead to control over the crystallisation process. The PMSMPR was used to investigate the co-crystallisation of UBA forms I and III, which exhibit unusually similar physicochemical properties, for example, solubility and melting point. Pure UBA form I polymorph was successfully isolated, but pure UBA form III remained elusive. The periodic flow process seems to be a promising operating strategy for the isolation of pure polymorphs of APIs in the pharmaceutical industry. The study also demonstrated the application of PAT tools and CryPRINS informatics systems software to give information about the performance of the different crystallisation platforms studied. These tools were used together with off-line techniques (such as PXRD, Raman and laser diffraction) to characterise each process further. The information from these combined analyses confirmed that UBA is a complex polymorphic system. Despite this challenge, pure UBA form I could be isolated under strictly controlled conditions using the PMSMPR. Furthermore, the on-line PAT tools and off-line analytical methods are able to indicate when the process achieves SCO, that is, when transitory effects caused by the periodic but controlled disruptions are minimised. The reported results provide evidence that a PMSMPR cascade, with a suitably designed dissolution stage can produce consistently, the desired polymorphic form of the model co-crystal system, decreasing significantly product variability compared to batch operation.

Chapter 8

Design of Agrochemical Co-Crystallisation Processes: Isolation and Characterisation of 1:1 and 3:2 Co-Crystals of p-Toluenesulfonamide /Triphenylphosphine Oxide

In Chapter 7 the application of a periodic flow mixed suspension mixed product removal (PMSMPR) operation to selectively isolate polymorphs of a pharmaceutical co-crystal drug with similar physicochemical properties was examined. In this chapter, the selective crystallisation and characterisation of the stoichiometric forms of the agrochemical co-crystal system p-Toluenesulfonamide/Triphenylphosphine oxide (p-TSA-TPPO) is demonstrated using batch, semi-batch and PMSMPR crystallisers. Regions of the ternary phase diagram of p-TSA/TPPO/MeCN corresponding to the stability of the 1:1 and 3:2 co-crystal forms of p-TSA-TPPO were explored. In the batch study, solution mediated transformation of the co-crystals was monitored and directed towards the desired crystalline form using a Raman spectroscopy approach coupled with temperature cycling. A change in temperature can modify the relative stability of each co-crystal form or mixtures and induce a solvent mediated transformation towards the most stable species. The proposed strategy allows for obtaining the pure stoichiometric co-crystals, even when nucleation of a mixture occurs. Furthermore, mixtures of the two forms in specific ratios can be produced to better tailor the physical-chemical properties of the final product. In the semi-batch and PMSMPR studies better control over the co-crystal form was achieved compared to batch. The desired co-crystal form or mixture of forms could be produced consistently by manipulating the flow rates of the co-formers p-TSA and TPPO to these crystallisers. Raman, ATR-UV/vis and ATR-FTIR spectroscopy, FBRM and PVM were used as an integrated array with CryPRINS within the IDS framework to monitor and control the co-crystallisations. Complementary off-line solid-state techniques were used to characterise samples obtained from each process.

8.1 Introduction

In the agrochemical industry there is a need to develop and apply new active ingredient design strategies to deliver solutions for the discovery of agrochemicals that are fit for purpose in the 21st century [309]. For example, there is a need to reduce absolute usage of active

agrochemical ingredients (AAIs) to minimise environmental impact. To achieve this, a structure-based design approach to AAI production is required [310], [311]. Structure-based design is an iterative and multi-disciplinary process that is well established in the pharmaceutical industry. It has played an important role in the development of several registered drugs and clinical candidates [309], [311], for example, zanamivir [312], lopinavir–ritonavir and nelfinavir [313]. In contrast, structure-based design is a relatively new concept in the agrochemical industry, and there are currently no products on the market that are the direct result of this approach [309]. In recent years' structure-based design of multi-component molecular systems has gained popularity in the pharmaceutical sector as a viable alternative to traditional design approaches used to modify active pharmaceutical ingredients (APIs) for more effective performance. Modifications of the structure and molecular composition of an active ingredient by applying structure-based design principles can lead to significant improvements to the stability, solubility and release profile. This could lead to a reduction in use rates of AAIs, and hence a minimised environmental impact. For example, the release profile of an AAI could be controlled through the design of multi-component molecular systems such as co-crystals. Furthermore, multi-component systems offer the opportunity to delivery not just one, but two or more AAIs simultaneously, which could potentially minimise operating cost and equipment foot print through simplification of the manufacturing processes.

In this study, the selective co-crystallisation of two model AAIs, p-Toluenesulfonamide (p-TSA) and Triphenylphosphine oxide (TPPO) is demonstrated. p-TSA and its derivatives are widely used as raw materials for the synthesis of pesticides, drugs and fluorescent colorants [314], [315]. There are two known polymorphs of p-TSA: the α form (monoclinic) differs from the β form (triclinic) which has a unusual arrangement of layers [316]. TPPO finds use in the production of crop protection products, anti-fungal coatings, vitamins, and APIs [317], [318]. There are three known polymorphic forms of TPPO [319], [320], one orthorhombic and two monoclinic forms. Etter and Baures [320] were amongst the first to isolate co-crystals of TPPO. They were able to successfully co-crystallised TPPO with 15 different molecular entities, including of several derivatives of p-TSA. There are two known stoichiometric forms of the p-TSA-TPPO co-crystal system; composed of 1:1 and 3:2 mole ratios of p-TSA and TPPO respectively. Glidewell *et al.* [321], [322] isolated the 3:2 form of p-TSA-TPPO and reported on the crystal and molecular structures. The authors used a small scale reactive crystallisation method whereby triphenylphosphine (TPP) was reacted with Chloramine-T(n-Chloro p-Toluenesulfonamide sodium salt) in ethanol; the product was then recrystallised from anhydrous benzene. Croker *et al.* [323] isolated and reported the crystal structure of the 1:1 form of p-TSA-TPPO. In their work the ternary phase diagram for p-TSA/TPPO/MeCN was constructed at 20 ^{o}C. Subsequent studies examined the nucleation behaviour [324], isothermal suspension conversion [325] and

solution-mediated phase transformation [326] of the two co-crystal forms. The work presented here further examines the co-crystallisation of p-TSA-TPPO, but with the aid of PAT tools and CryPRINS within the IDS framework. Some aspects of this study were carried out as part of a personal development project (PDP). Specifically, solubility and multivariate calibration model development studies were carried out by MEng student Nyet Vun. The PDP project was supervised by the author of this Thesis who assisted the student with day-to-day planning of experimental work and interpretation of the results.

8.2 Experimental Methods

In the current work, the ternary phase diagram of p-TSA/TPPO/MeCN, Figure 8.1, developed by Croker *et al* [323] was explored in the regions where 1:1 and 3:2 p-TSA-TPPO co-crystal forms (Regions 1 and 2), and a mixture of both forms (Region 3) show stability. The aim is to demonstrate control over the co-crystallisation process in the different optimised crystalliser platforms, and to provide a comparative assessment of the performance of each platform.

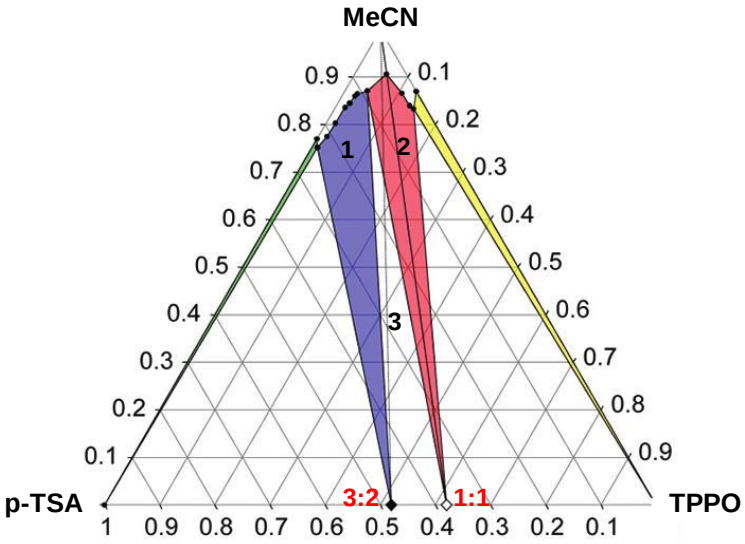

Figure 8.1: Ternary phase diagram for the p-TSA/TPPO/MeCN (axes in mass fraction) at 20 °C. Regions selected for this study: (1) 3:2 co-crystal form stable; (2) 1:1 co-crystal form stable; (3) Mixtures of 1:1 and 3:2 forms stable. Adopted from Croker et al. [323].

Figure 8.2 shows the chemical structures of the starting materials and crystal structures of the co-crystals. The structure of 1:1 p-TSA-TPPO consists of cyclic centrosymmetric aggregates in which two molecules of p-TSA are linked to two molecules of TPPO via two-point hydrogen bonds of the type :O·····H–N(SO_2Ph)–H·····O: as shown in Figure 8.2, with a lone pair of electrons on the oxygen of TPPO. The 3:2 p-TSA-TPPO co-crystal is also made up of cyclic centrosymmetric aggregates, but with three molecules of p-TSA linked to two molecules of

TPPO via a network of six linear hydrogen bonds of the type O·····H–N(SO_2Ph)–H·····O, with no lone pair electrons on the oxygen of TPPO.

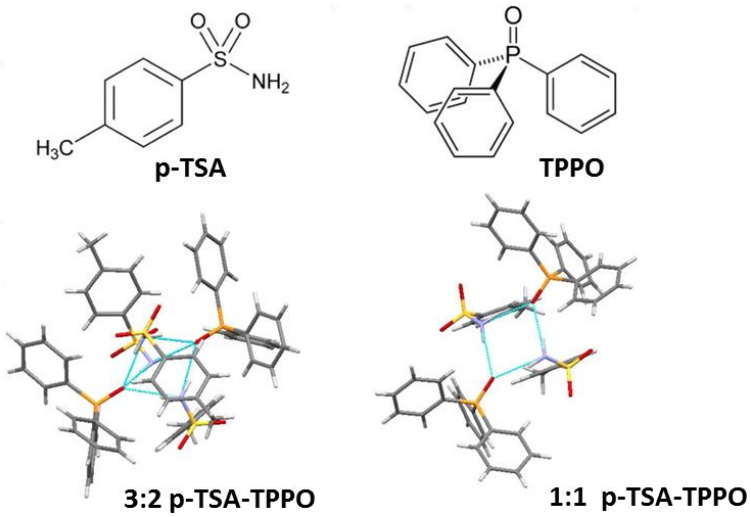

Figure 8.2: Chemical structures of p-TSA and TPPO (top) and crystal structures of 1:1 and 3:2 p-TSA-TPPO co-crystals (bottom). Adopted from Croker et al. [325].

Figure 8.3 shows the extended crystal structures of the two co-crystal forms, showing their distinctive molecular packing arrangements and hydrogen bonding network. Crystal structure calculations show that 1:1 and 3:2 p-TSA/TPPO [321], [323] belong to the monoclinic and trigonal crystallographic space groups, respectively. Figure 8.4 shows the SEM micrographs and microscope images of the two co-crystal forms obtained from experiments reported later in this chapter. The crystals of 1:1 and 3:2 p-TSA-TPPO show distinct crystal morphologies. 1:1 p-TSA-TPPO crystals have a rhombic shape, while 3:2 p-TSA-TPPO exhibits an elongated prismatic morphology.

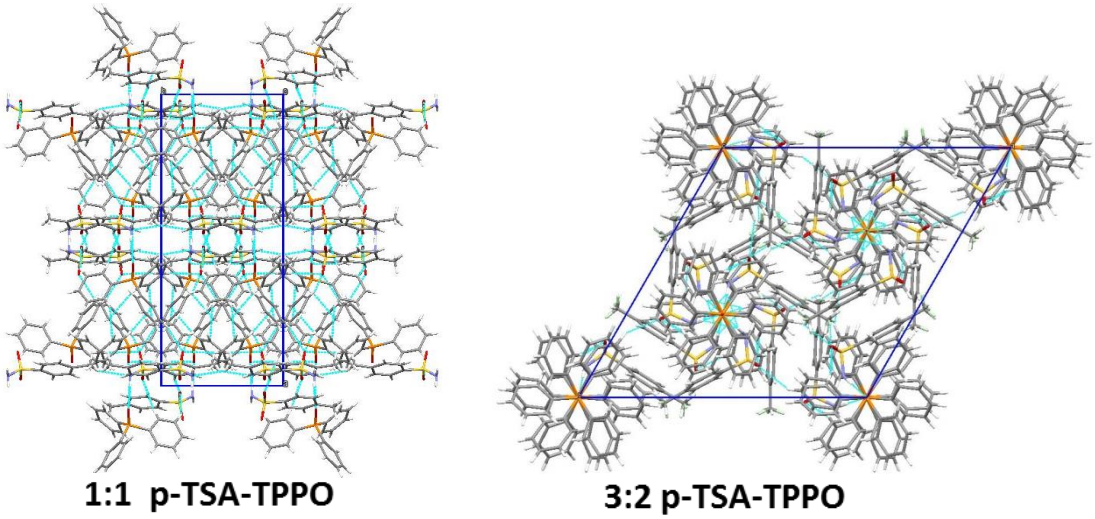

Figure 8.3: Extended crystal structures of 1:1 and 3:2 p-TSA-TPPO showing the distinctive molecular packing arrangement and hydrogen bonding networks [321], [323].

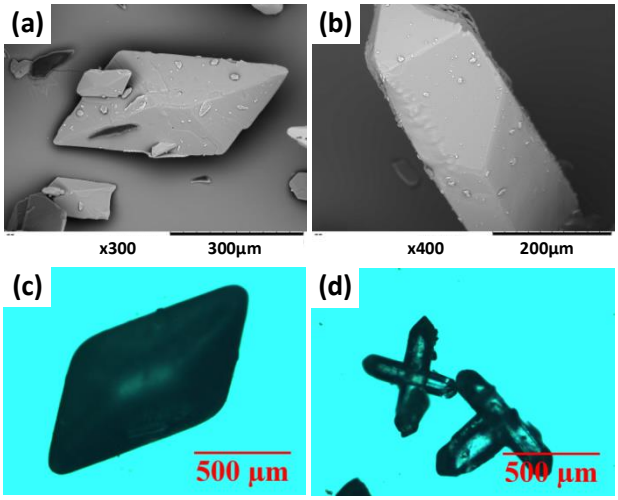

Figure 8.4: SEM micrographs (top) and microscope images (bottom) of 1:1 p-TSA-TPPO (a) and (c) and 3:2 p-TSA-TPPO (b) and (d) respectively.

8.2.1 Solubility and Supersaturation of Co-crystals

The co-crystallisation of p-TSA with TPPO from MeCN was carried out in batch, semi-batch and PMSMPR crystallisers as part of a proof of concept study using laboratory scale (500 mL) crystallisers. The solid ⇋ liquid equilibrium for 1:1 and 3:2 p-TSA-TPPO, respectively, can be written:

$$\text{p-TSA-TPPO}_{\text{solid}} \leftrightharpoons \text{p-TSA}_{\text{solution}} + \text{TPPO}_{\text{solution}} \qquad 8.1$$

$$(3\ \text{x p-TSA}) - (2\ \text{x TPPO})_{\text{solid}} \leftrightharpoons (3\ \text{x p-TSA})_{\text{solution}} + (2\ \text{x TPPO})_{\text{solution}} \qquad 8.2$$

The equilibrium concentrations of p-TSA and TPPO on dissolution of 1:1 p-TSA-TPPO and 3:2 p-TSA-TPPO are given by:

$$[\text{p-TSA}] = \frac{K_{sp\ 1:1}}{[\text{TPPO}]} \quad \text{(1:1 p-TSA-TPPO)} \qquad 8.3$$

$$[\text{p-TSA}] = \sqrt[3]{\frac{K_{sp\ 3:2}}{[\text{TPPO}]^2}} \quad \text{(3:2 p-TSA-TPPO)} \qquad 8.4$$

where K_{sp} is the solubility product, which only depends on the operating temperature, [p-TSA] and [TPPO] are respectively, the molar concentrations of p-Toluenesulfonamide and triphenylphosphine oxide. Since 3:2 p-TSA-TPPO exhibits incongruent dissolution [323], [326], with an intermediate step involving conversion to 1:1 p-TSA-TPPO, the solubility product

cannot simply be estimated from the molar concentrations of p-TSA and TPPO. For this reason, the solubility of 3:2 p-TSA-TPPO was not determined for this system during the study. The supersaturation ratio for 1:1 p-TSA-TPPO can be derived from the difference in chemical potential between the supersaturated and saturated solutions. The supersaturation ratio, σ, of 1:1 p-TSA-TPPO, by analogy with the definition of the supersaturation of salts [327], [328] can be represent as:

$$\sigma = \left[\frac{[\text{p-TSA}] \text{ x } [\text{TPPO}]}{K_{sp\ 1:1}}\right]^{1/2} \quad \text{(1:1 p-TSA-TPPO)} \qquad 8.5$$

Solubility Studies in MeCN: The solubility of a co-crystal, assuming congruent dissolution profile, can be expressed in terms of the mass ratio of solute (dissolved co-crystal) to solvent or the mole fraction of dissolved co-crystal in the solvent. The latter can be used to construct the solubility correlation similar to single component systems [263], and is evaluated using Eqn. 8.6:

$$x = \frac{m/M}{m/M + m_s/M_s} \qquad 8.6$$

where x is solubility in mole fraction, m is mass of dissolved co-crystal, M is molar mass of dissolved co-crystal, m_s is mass of solvent and M_s is molar mass of solvent. In this study, a modified version of the commonly used van't Hoff expression, Eqn. 8.7 [263], was applied. Taking into account the change in heat capacity, ΔC_p, of solute between its solid and supercooled-liquid forms [227], as well as the solubility parameter of solute and solvent [329], the following expression is derived:

$$ln(x\gamma) = -\frac{\Delta H_{m,fus}}{R}\left(\frac{1}{T_m} - \frac{1}{T}\right) \qquad 8.7$$

where γ is the activity coefficient, $\Delta H_{m,fus}$ is the enthalpy of fusion of solute (J/mol), T_m is the melting temperature of solute (K), T is the operating temperature (K) and R is the universal gas constant (8.314 J mol/K). Due to the complexity of determining the heat capacity of solute at its supercooled-liquid state, ΔC_p is assumed to be equivalent to the entropy of fusion of solute, which is the ratio of $\Delta H_{m,fus}$ / T_m, that is, Hildebrand's approximation [329], [330]. Taking into account the solubility parameters of the solute and solvent, respectively, Eqn. 8.8 can be modified as follows:

$$ln(x) = -\frac{\Delta H_{m,fus}}{RT_m} ln\frac{T_m}{T} - \frac{v\varphi^2\Delta\delta^2}{RT} \qquad 8.8$$

where v is the molar volume of solute in the liquid phase (cm^3/mol), φ is the volume fraction of solvent, $\Delta\delta$ is the difference in solubility parameters of solvent and solute ($J^{1/2}\,cm^{-3/2}$). Eqn. 8.8 can be further simplified to give Eqn. 8.9:

$$ln(x) = -Aln\left(\frac{B}{AT}\right) - \frac{C}{T} \qquad 8.9$$

where the constants A $\left(\frac{\Delta H_{m,fus}}{RT_m}\right)$ and B $\left(\frac{\Delta H_{m,fus}}{R}\right)$ are estimated using (differential scanning colorimetry) DSC, from which the thermochemical properties of the solute ($\Delta H_{m,fus}$ and T_m) can be estimated. The constant C $\left(\frac{v\varphi^2\Delta\delta^2}{R}\right)$ can be obtained by non-linear regression analysis. The solubility of solute in terms of mole fraction at any temperature can be determined using Eqn. 8.9 when the constants A, B and C are determined. These solubility values can be interconverted from mole fraction to mass ratio using Eqn. 8.10:

$$c = \left(\frac{x}{1-x}\right)\left(\frac{M}{M_s}\right) \qquad 8.10$$

the solubility (c) is expressed as the ratio of mass of solute to mass of solvent (g/g). The solubilities of p-TSA (MW = 171), TPPO (MW = 278) and 1:1 p-TSA-TPPO co-crystal in MeCN were determined gravimetrically in the temperature range 5 – 40 ^oC. The experimental apparatus and procedure used for the gravimetric solubility measurements was described in Chapter 3 Section 3.6.3. At each temperature, an excess of solid was added to 80 mL MeCN in the 100 mL vessel and equilibrated with constant stirring at 250 rpm for 3 h. The stirrer was then switched off, solids allowed to settle, and samples then taken according to the procedure described in Chapter 3 Section 3.6.3. Off-line Raman and ATR-FTIR spectroscopy measurements were carried out on each solid form to confirm whether any solid-state transformation occurred while the crystals were suspended in saturated solution. Three representative samples were taken per solubility measurement.

Thermochemical Studies by DSC: The thermochemical properties of p-TSA, TPPO and p-TSA-TPPO co-crystal were estimated based on DSC thermograms. The values of $\Delta H_{m,fus}$ and T_m obtained at 1 °C/min were expressed in Table .The values of $\Delta H_{m,fus}$ determined for p-TSA and TPPO at 298 K were in good agreement with the values reported by Flores *et al* [331] (p-TSA: 23.9 ± 0.3 kJ/mol) and Kirklin and Domalski [332] (TPPO: 17.9 ± 1.0 kJ/mol), as shown in Table 8.1.

Table 8.1: Thermochemical properties of materials estimated from DSC, at heating rate of 1 C/min.

Material	T_m (°C)	$\Delta H_{m,fus}$ at T_m (kJ/mol)	$\Delta H_{m,fus}$ at 298 K (kJ/mol)
p-TSA	139.1 ± 0.5	35.8 ± 2.0	25.9 ± 1.5
TPPO	158.4 ± 0.6	22.0 ± 1.3	15.2 ± 0.9
1:1 p-TSA-TPPO	136.8 ± 0.4	47.9 ± 2.1	34.8 ± 2.0

Solubility Estimation: The values of $\Delta H_{m,fus}$ and T_m obtained from DSC, together with Eqn. 8.9, were used to construct the predicted solubility curves for all three materials in MeCN over the temperature range of interest (5 – 40 °C). The comparison between measured (*m*) and predicted (*p*) solubility of the three materials are illustrated in Figure 8.5 (a) and (b) respectively.

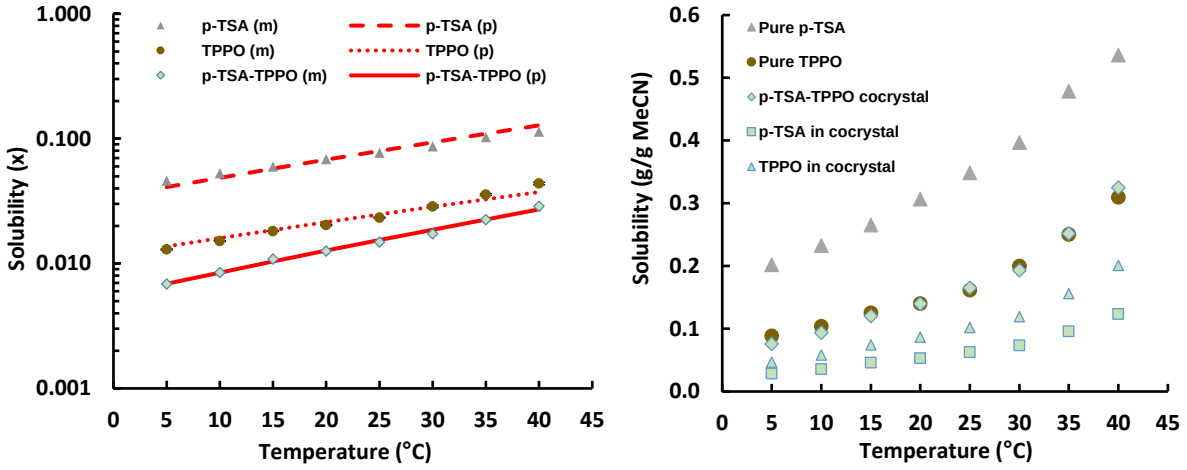

Figure 8.5: Solubility of investigated materials in terms of (a) mole fraction and (b) mass ratio at different temperature.

The predicted solubility agrees well with the measured values, resulting in reasonably good fits with sum of least square errors of 0.0464, 0.0452 and 0.0124 for the optimised regression of the predicted solubility of p-TSA, TPPO and 1:1 p-TSA-TPPO, respectively. The non-linear regression fits are expressed in Eqn. 8.11, 8.12, and 8.13 for p-TSA, TPPO and p-TSA-TPPO, respectively. The value of the constant C for the 1:1 p-TSA-TPPO was the least negative when compared to the values derived for p-TSA and TPPO. This implies that the Hildebrand solubility parameter, δ, of 1:1 p-TSA-TPPO is small relative to δ of MeCN; hence, it is more difficult to break the intramolecular hydrogen bonds (N-H···O=P) of the chemical structure. On the other hand, solute-solvent interactions between the single component systems p-TSA and TPPO can be more readily broken. In other words, the 1:1 p-TSA-TPPO co-crystal was much less soluble in MeCN compared to pure p-TSA and TPPO. The solubilities of pure p-TSA, TPPO and 1:1 p-TSA-TPPO in MeCN at 20 °C were: 0.307 ± 0.010, 0.141 ± 0.048 and 0.140 ± 0.004

g/g MeCN, respectively (derived from Figure 8.5 (b)), which are similar to results reported by Croker *et al* [323].

Evidently, the solubility of 1:1 p-TSA-TPPO is slightly lower than that of TPPO, and much lower than that of p-TSA. Other possible factors contributing to the lower solubility of the co-crystal compared to its constituent single molecules include possible differences in the dipole moment, dielectric constant and polarizability of the multi-component molecular system, which would influence nucleophilic and aromatic substitution between the solute and solvent molecules that affect solute-solvent interactions [321], [333]. The dissolution of 1:1 p-TSA-TPPO co-crystal resulted in an equivalent release of its constituent molecules in 1:1 molar ratio as shown in Figure 8.5 (b) *viz* congruent dissolution.

$$ln(x) = -10.5\ ln\left(\frac{412}{T}\right) - \frac{(-256)}{T} \quad 8.11$$

$$ln(x) = -7.53\ ln\left(\frac{431}{T}\right) - \frac{273}{T} \quad 8.12$$

$$ln(x) = -10.8\ ln\left(\frac{410}{T}\right) - \frac{215}{T} \quad 8.13$$

8.2.2 *In Situ* Solute Concentration Measurement of p-TSA and TPPO

Multivariate calibration models were developed using ATR-FTIR spectroscopy and ATR-UV/vis spectroscopy for real-time measurement of p-TSA and TPPO concentration. Details of the experimental and multivariate statistical data analysis were discussed in Chapter 3 Section 3.6.1. The ATR-UV/vis multivariate models gave superior prediction of p-TSA and TPPO concentrations compared to ATR-FTIR, and were therefore selected to monitor the co-crystallisation experiments. The application of multivariate calibration models to measure concomitantly the concentration of multiple species in the solution phase during crystallisation has previous been demonstrated with ATR-FTIR spectroscopy [138], [172], [292], [334]. The limitation of ATR-FTIR is that light absorbed by molecules in solution is harder to quantify due to scattering that occurs with each reflection of IR radiation in the internal element of the ATR crystal [335], as well as particle scattering effects from the solid-phase during crystallisation [172], [336]. Furthermore, it is well known that the ATR-FTIR signal can be affected by CO_2 absorption in its optical path length [337].

8.2.3 Batch Operating Conditions

Small scale batch co-crystallisation studies (1 – 50 mL) on the p-TSA-TPPO co-crystal system have previous been reported [6], [13], [30]. Batch co-crystallisation studies at a larger scale (500 mL) are presented here to examine aspects of process scalability of p-TSA-TPPO. A further aim of the study was to monitor and control the co-crystallisation of either 1:1 or 3:2 p-TSA-TPPO co-crystal. The experimental apparatus used was described in Chapter 3 Section 3.6.1 (Figure 3.18). The co-crystallisation runs were monitored using Raman, ATR-UV/vis, FBRM and PVM probes. Experiments were carried out in either of two ways, Method 1: simple linear cooling approach or Method 2: combined linear cooling and temperature cycling approach. For Method 1, the required amounts of p-TSA, TPPO and MeCN were added to the crystalliser and heated to 30, 60, 50 or 70 ^{o}C (depending on the amount of each starting materials used) at a rate of 1 ^{o}C/min. The vessel was the held for 15 min. to allow complete dissolution of the materials. For Method 2 the heating/cooling rate was set to either -0.02, -0.05, or 1.0 ^{o}C/min. For both Method 1 and 2, the heating/cooling rates were changed to influence the co-crystallisation outcome, which is similar to the effect of temperature cycling on polymorphic transformations [49]. Table 8.2 provides a summary of the experimental conditions used for the all the batch experiments.

For Method 1, the vessel was cooled to a final temperature of either 20 or 5 ^{o}C and held for 1 hour (Table 8.2; Exp. No. 1 – 11). At 20 ^{o}C the phase compositions of the co-crystals and other solid forms of p-TSA and TPPO are expected to follow the ternary phase diagram. However, when the temperature is varied, the phase compositions will also vary, since they are highly temperature dependent. Studies carried out using Method 2 (Table 8.2; Exp. No. 12 – 18) followed the same procedures as Method 1, except that temperature cycles were implemented soon after nucleation was detected. Regardless of the experimental conditions, a fixed impeller speed of 400 rpm was implemented (power per unit volume of 0.075 kW/m^{3}), which was sufficient to maintain crystals in suspension.

Table 8.2: Summary of experimental conditions employed during the batch crystallisation of p-TSA-TPPO co-crystals.

Exp. No.	p-TSA (g/g MeCN)	TPPO (g/g MeCN)	Temperature (°C)		Heating / Cooling Rate (°C/min)	Component Mass Fractions (M)			Region of Phase Diagram
			Initial	Final		p-TSA	TPPO	MeCN	
1	0.2987	0.1492	60	20	1.0 / -1.0	0.21	0.10	0.69	1 (3:2 form)
2	0.2997	0.1497	60	20	1.0 / -0.5	0.21	0.10	0.69	1 (3:2 form)
3*	0.2634	0.1247	60	20 5	1.0 / -1.0	0.19	0.09	0.72	1 (3:2 form)
4	0.5776	0.4202	70	5	1.0 / -1.0	0.29	0.21	0.5	1 (3:2 form)
5*	0.1147	0.1532	60	20 5	1.0 / -1.0	0.09	0.12	0.79	2 (1:1 form)
6	0.1154	0.1489	60	20	1.0 / -0.5	0.09	0.12	0.79	2 (1:1 form)
7	0.3793	0.6193	70	5	1.0 / -1.0	0.19	0.31	0.5	2 (1:1 form)
8	0.0706	0.1059	30	5	0.2 / -0.2	0.06	0.09	0.85	2 (1:1 form)
9	0.1156	0.1676	60	20	1.0 / -0.5	0.09	0.13	0.78	2 (1:1 form)
10	0.1115	0.1244	60	20	1.0 / -0.5	0.09	0.10	0.81	2 (1:1 form)
11	0.1084	0.0964	30	20	0.2 / -0.2	0.09	0.08	0.83	3 (mixture)
12	0.0833	0.1071	30	5	0.2 / -0.2	0.07	0.09	0.84	2 (1:1 form)
(13)	0.1728	0.0617	30	5	0.2 / -0.2	0.14	0.05	0.81	1 (3:2 form)
(14)	0.1484	0.1148	50	10 30	0.5 / -0.5	0.12	0.09	0.79	1 (3:2 form)
(15)	0.1492	0.1140	50	20 35 5	0.5 / -0.5	0.12	0.09	0.79	1 (3:2 form)
(16)	0.1054	0.0971	50	10 35	0.5 / -0.5	0.09	0.08	0.83	3 (mixture)
(17)	0.1282	0.1282	50	10	1.0 / -1.0	0.10	0.10	0.80	3 (mixture)
(18)	0.1049	0.0968	30	20	0.2 / -0.2	0.09	0.08	0.83	3 (mixture)

No brackets = Method 1 experiments; Brackets () = Method 2 experiments; *step heating from 20 to 5 °C implemented.

8.2.4 Semi-Batch Operating Conditions

A series of semi-batch development experiments were also performed to determine the most suitable conditions for the selective crystallisation of the 1:1 and 3:2 stoichiometric co-crystal forms of p-TSA-TPPO. The combination of p-TSA/TPPO/MeCN was varied on a mass fraction basis by changing the flow rates at which p-TSA and TPPO were charged to the crystalliser. Experiments were carried out using the experimental set-up described in Chapter 3 Section 3.6.1 (Figure 3.18) with slight modification to incorporate two solution feed vessels in the design as shown in Figure 8.6.

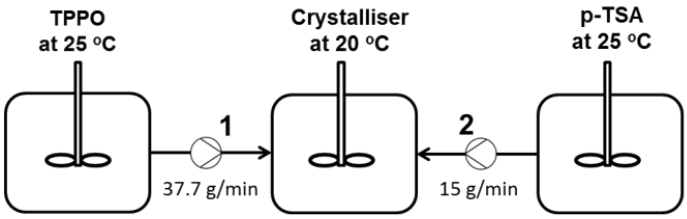

Figure 8.6: Flow diagram of the semi-batch experimental set-up used during the co-crystallisation studies (process conditions presented are indicative, since they were varied for each experimental run).

Experiments were monitored using the same PAT sensor array applied in the batch study. The required amount of p-TSA and TPPO were dissolved in separate vessels to generate undersaturated solutions according to Table 8.3. Solutions were prepared by heating suspensions of p-TSA and TPPO in MeCN to 30 °C (or 10 °C above saturation according to their respective solubility curves, Section 8.2) and holding for 15 min to allow complete dissolution of the materials. The resulting solutions were then cooled until just saturated (that is, 25 °C or 60 °C for experiment 26) and pumped separately to the 500 mL crystalliser, which was kept at a lower temperature (20 °C) to create supersaturation for nucleation of the co-crystal. At 20 °C, the suspension composition is expected to follow the ternary phase diagram with little to no variation. Any variation in the composition or co-crystal form obtain could therefore be linked to changes in the mass flow rate. The semi-batch experiments would later inform the development of a periodic flow crystallisation process. Calibrated Masterflex® pumps fitted with 3.1 mm ID tubing, and operated in time dispense mode were used to pump p-TSA/MeCN and TPPO/MeCN solutions to the crystalliser. The flow rates of p-TSA and TPPO solutions were varied from 15 to 32.7 g/min and 20 to 37.7 g/min, respectively. The targeted combined flow rate of the two streams was 52.7 g/min for each experimental run. Pumps were programmed to operate for 6.71 min, leading to the delivery of ~500 mL of combined p-TSA/TPPO/MeCN solution to the crystalliser, which was initially empty. For all experiments, the impeller speed of the crystalliser was set to 400 rpm. Table 8.3 gives a summary of the experimental conditions for each run.

Table 8.3: Summary of experimental conditions employed during the semi-batch co-crystallisation of p-TSA-TPPO co-crystals.

Exp. No.	p-TSA (g/g MeCN)	TPPO (g/g MeCN)	Solution Flow Rates (g/min)		Component Mass Fractions (M)			Region of Phase Diagram
			p-TSA soln.	TPPO soln.	p-TSA	TPPO	MeCN	
19	0.2987	0.1482	28	24.7	0.12	0.09	0.79	1 (3:2 form)
20	0.2987	0.1482	32.7	20.0	0.14	0.05	0.81	1 (3:2 form)
21	0.2987	0.1482	20.0	32.7	0.09	0.08	0.83	3 (mixture)
22	0.2987	0.1482	15.0	37.7	0.06	0.09	0.85	2 (1:1 form)
23	0.2987	0.1482	23.4	29.3	0.10	0.08	0.82	3 (mixture)
24	0.2987	0.1482	17.7	35	0.08	0.08	0.84	3 (mixture)
25	0.2987	0.1482	27.5	25.2	0.11	0.07	0.82	1 (3:2 form)
26	0.4625	0.2016	20.0	32.7	0.12	0.12	0.76	2 (1:1 form)

8.2.5 Periodic Flow Operating Conditions

Periodic flow co-crystallisation experiments were carried out using either a single-stage PMSMPR (without recycle stream) or a three-stage cascaded PMSMPR unit similar to the ones described in Chapter 3 Section 3.6.1 (Figure 3.19 (a) and (b)), with slight modification to incorporate two solution feed vessels in the design (similar to the semi-batch set-up). Other experimental conditions employed were the same as in the semi-batch study. Figure 8.7 shows the flow diagrams of the experimental set-up used for the single-stage PMSMPR and three-stage cascaded PMSMPR studies. The PMSMPR stages were operated either by coupled or decoupled slurry addition/withdrawal method described in previous chapters of this thesis. The flow rate for the slurry addition/withdrawal periods was 94.8 g/min. This was the maximum flow rate at which particles could be suspended based on visual observation. The hold cycle of the periodic flow operation was set to 5, 10 or 15 min to investigate the effect of holding time on the CSD. The slurry addition/withdrawal cycle was kept constant at 4.09 min for all experiments. The impeller speed of the crystalliser was set to either 450 or 500 rpm in each PMSMPR stage. The higher selected stirring speeds were required because of difficulties in achieving effective particle suspension, due to the very rapid growth of crystals into large size domains that eventually start to settle. The experimental conditions employed for the periodic flow crystallisation experiments are presented in Table 8.4.

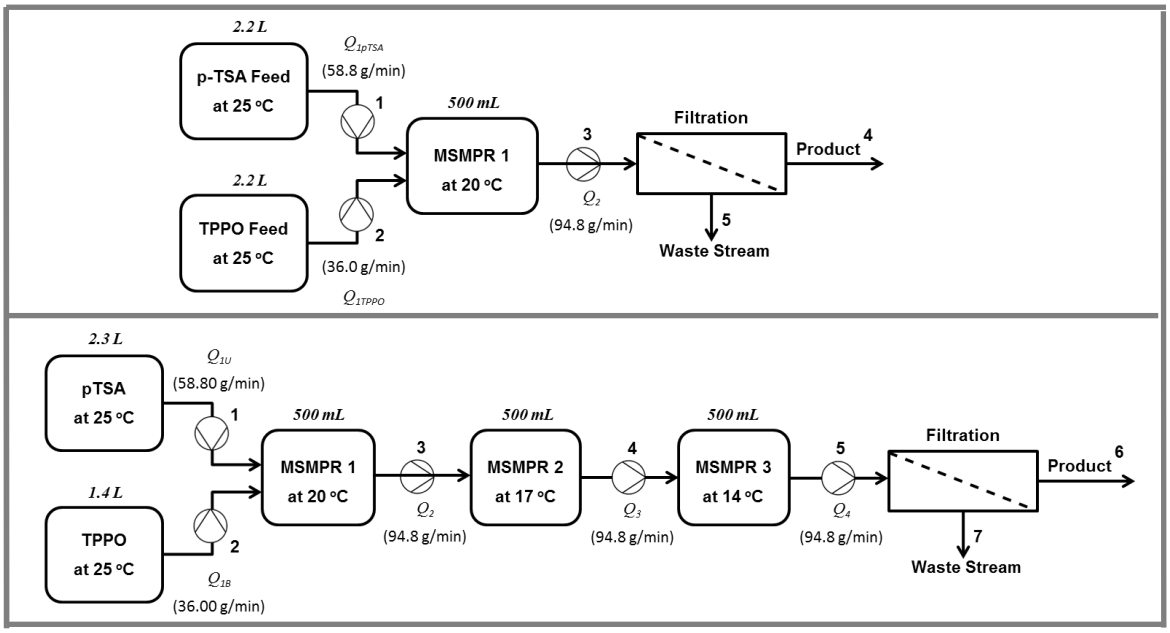

Figure 8.7: Flow diagrams of single-stage PMSMPR (top) and three-stage PMSMPR (bottom) configurations used during the co-crystallisation studies (process conditions are indicative as they and were varied for each experimental run).

Table 8.4: Summary of experimental conditions employed during the periodic flow crystallisation of p-TSA-TPPO co-crystals.

Exp. No.	Solution Flow Rates (g/min)		Component Mass Fractions (M)			Temperature (°C)			Region of Phase Diagram
	p-TSA soln.	TPPO soln.	p-TSA	TPPO	MeCN	MSMPR 1	MSMPR 2	MSMPR 3	
(27)^	32.7	20	0.14	0.05	0.81	5	n/a	n/a	1 (3:2 form)
(28)^	32.7	20	0.14	0.05	0.81	15	n/a	n/a	1 (3:2 form)
(29)	32.7	20	0.14	0.05	0.81	12.5	n/a	n/a	1 (3:2 form)
30	15.0	37.7	0.06	0.09	0.85	12.5	n/a	n/a	2 (1:1 form)
31	27.0	67.8	0.06	0.09	0.85	20	n/a	n/a	2 (1:1 form)
32	27.0	67.8	0.06	0.09	0.85	25	n/a	n/a	2 (1:1 form)
33	58.8	36.0	0.14	0.05	0.81	20	17	14	1 (3:2 form)
34	58.8	36.0	0.14	0.05	0.81	25	20	20	1 (3:2 form)
35	27.0	67.8	0.06	0.09	0.85	25	20	20	2 (1:1 form)
36	27.0	67.8	0.06	0.09	0.85	20	17	14	2 (1:1 form)

No brackets = coupled addition/withdrawal; Brackets () = decoupled addition/withdrawal; ^stirring set to 450 rpm, for all another experiments the stirring rate was set to 500 rpm.

8.2.6 Solid State Characterisation

Solid state characterization of raw materials (p-TSA and TPPO) their 1:1 and 3:2 p-TSA-TPPO co-crystal products were carried out using powder X-ray diffraction (PXRD), Raman

microscopy, ATR-FTIR spectroscopy, hot stage microscopy (HSM), DSC, scanning electron microscopy (SEM) and energy dispersive X-ray spectroscopy (EDS) and high performance liquid chromatography (HPLC). The operating principles and experimental procedures for each solid state technique were described in Chapter 3 Section 3.2. Patterns of co-crystal samples from each experimental run were compared to in-house developed reference samples of 1:1 and 3:2 p-TSA-TPPO that were prepared according to the procedures of Croker *et al*. [323], [324].

PXRD, Raman Microscopy, ATR-FTIR and DSC Analyses: Figure 8.8 (a) – (d) shows the patterns obtained from PXRD (a), Raman microscope (b), ATR-FTIR (c), and DSC (d) solid state characterizations of p-TSA, TPPO and 1:1 and 3:2 p-TSA-TPPO co-crystal reference materials, respectively. For each material analysed, the patterns show distinctive features that were exploited to identify subsequent samples collected from different experimental runs during the study.

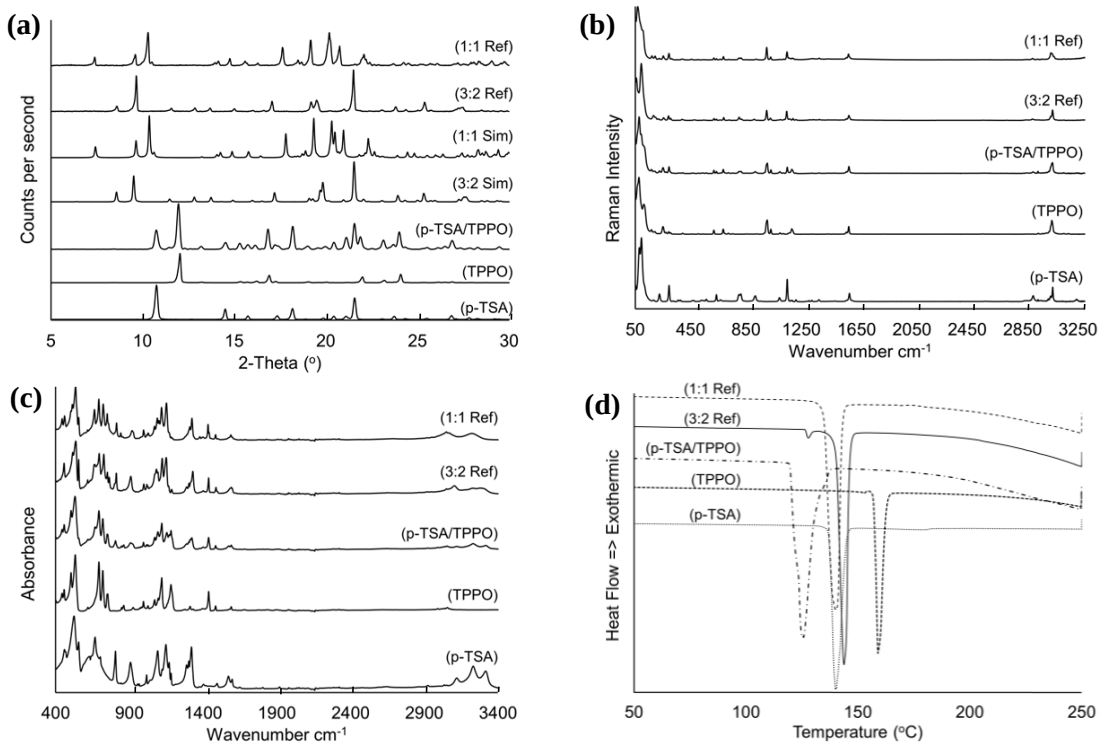

Figure 8.8: Solid state characterization results for p-TSA and TPPO raw materials, and d simulated and reference patterns for 1:1 and 3:2 p-TSA-TPPO. (a) PXRD patterns (b) Raman spectra; (c) ATR-FTIR spectra; and (d) DSC patterns.

Clear differences are observed between the co-crystal forms and their respective starting materials and physical mixture. For example, The PXRD patterns show distinctive broad (1:1 p-TSA-TPPO) and sharp (3:2 p-TSA-TPPO) peaks in the 2-Theta (°) positions 7 – 10 and 17 – 22. The Raman spectra show differences in peak width and position in the regions 3180 –

2855, 1150 – 890, and 780 – 480 cm^{-1}. In terms of the ATR-FTIR signal, 1:1 and 3:2 p-TSA-TPPO both show distinctive broad peaks in the region 3400 – 3100 cm^{-1}. Distinctive differences between the two forms are also observed in the fingerprint region from 1500 to 400 cm^{-1}. The DSC patterns also show the clear difference between the melt of the two co-crystals, their parent compounds and physical mixture. The melts for the different crystalline phases are observed at approximately 140 ^{o}C (1:1 p-TSA-TPPO), 144 ^{o}C (3:2 p-TSA-TPPO), 139 ^{o}C (p-TSA) and 159 ^{o}C (TPPO). Interestingly, the physical mixture of p-TSA and TPPO shows a very broad endotherm from approximately 121 – 140 ^{o}C. It is unclear why there is such a significant shift in the endotherm for the physical mixture of the two compounds. DSC scans from replicate runs showed a similar profile, which suggests that heating the two substances together leads either to the lowering of both of their melting points or the formation of different crystalline phase, which has a lower melting point. However, these hypotheses require further investigation that is beyond the scope of the current study.

HSM Analyses: Hot stage microscopy (HMS) studies were carried out on samples of 1:1 and 3:2 p-TSA-TPPO from selected experimental runs. Figure 8.9 (a) and (b) show the images captured from 100 ^{o}C until 148 ^{o}C (left) and DSC scans (right) for the melting of 3:2 and 1:1 p-TSA-TPPO. The HMS patterns show melting in the temperature ranges 141 – 148 ^{o}C, and 139 – 143 ^{o}C for 3:2 p-TSA-TPPO, and 1:1 p-TSA-TPPO, respectively, which is in good agreement with DSC where melting points of 143.7 ^{o}C and 139.9 ^{o}C were recorded for the respective co-crystal forms. The additional endothermic event at 128.2 ^{o}C observed in the 3:2 co-crystal DSC profile is mostly likely residual starting material since this peak seems to correspond to the melt of physical mixture of p-TSA and TPPO as shown in Figure 8.8 (d).

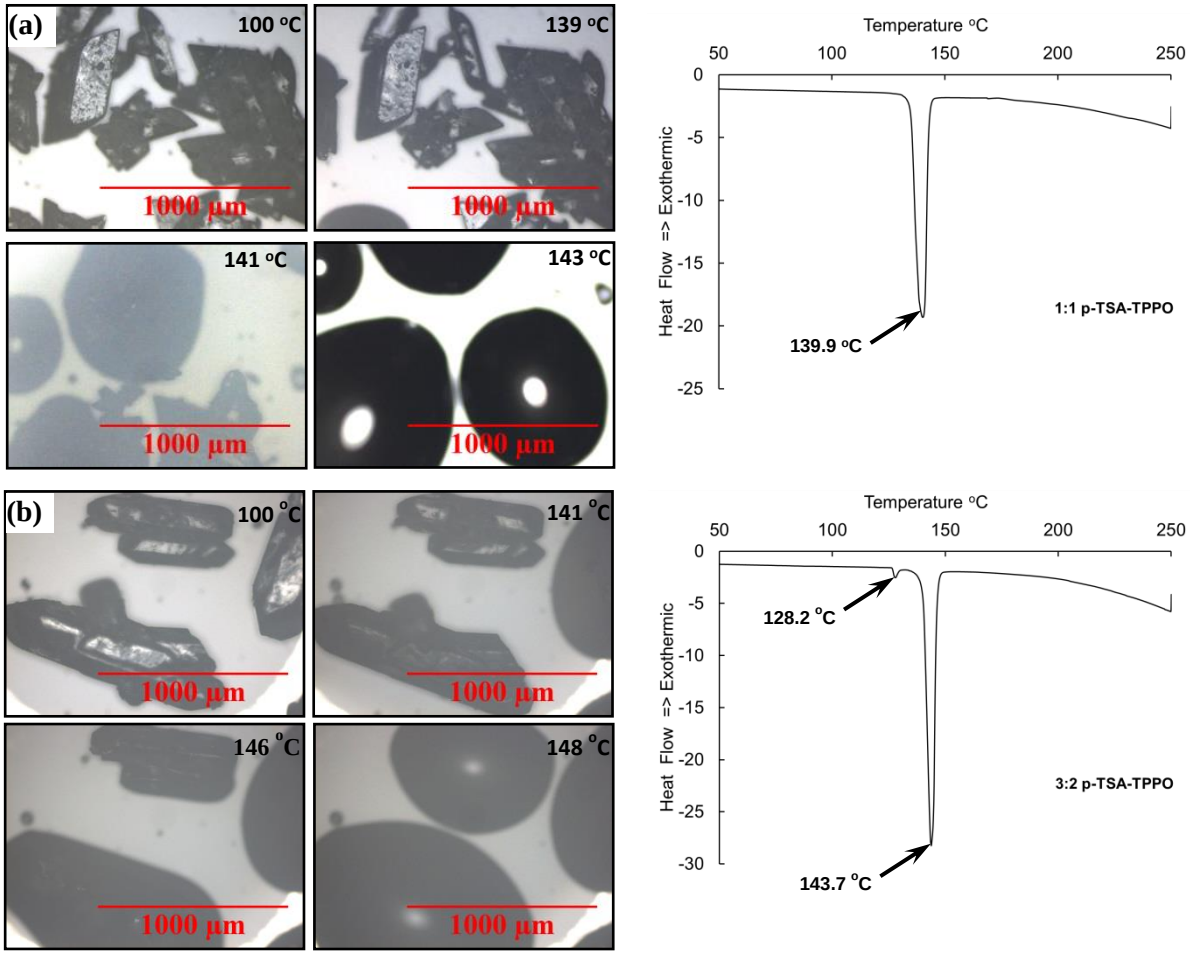

Figure 8.9: Hot stage microscopy images (left), (a) 1:1 p-TSA-TPPO and (b) 3:2 p-TSA-TPPO; and respective DSC scans (right) for each sample.

SEM/EDS Analyses: The crystalline products from selected experiments were analysed by SEM/EDS. Figure 8.10 (a)-(d) show the SEM micrographs (x60) of 1:1 p-TSA-TPPO, 3:2 p-TSA-TPPO and mixture of the two co-crystal forms. The distinct morphology of the 1:1 and 3:2 p-TSA-TPPO is evident from the SEM micrographs. In particular, Figure 8.10 (e) (x300) and (f) (x400) show clearly the rhombic and rod shapes of 1:1 and 3:2 p-TSA-TPPO, respectively. The 3:2 p-TSA-TPPO samples Figure 8.10 (c) and (d) obtained from two different experimental runs show a clear distinction in crystal size and is attributed to a difference in the mass fraction composition of materials in the batch crystalliser (or the supersaturations). This leads to different crystal sizes, which suggests that the mass fraction composition of materials in the crystalliser can be adjusted to control the mean size and CSD of the final product. Using equations 8.5, and taking the equilibrium solubility at the operating temperature (based on solubility data) into account, the supersaturation with respect to 1:1 p-TSA-TPPO for these two experiments works out to 2.94 (c) and 1.77 (d), respectively. It appears that the growth of the crystals is extremely fast and is favoured at low supersaturation (d) compared to high supersaturation (c), which is expected. However, the supersaturation of the former is still quite

high, which suggest that the 3:2 co-crystal phase is extremely fast growing as crystals greater than 1 mm size were obtained.

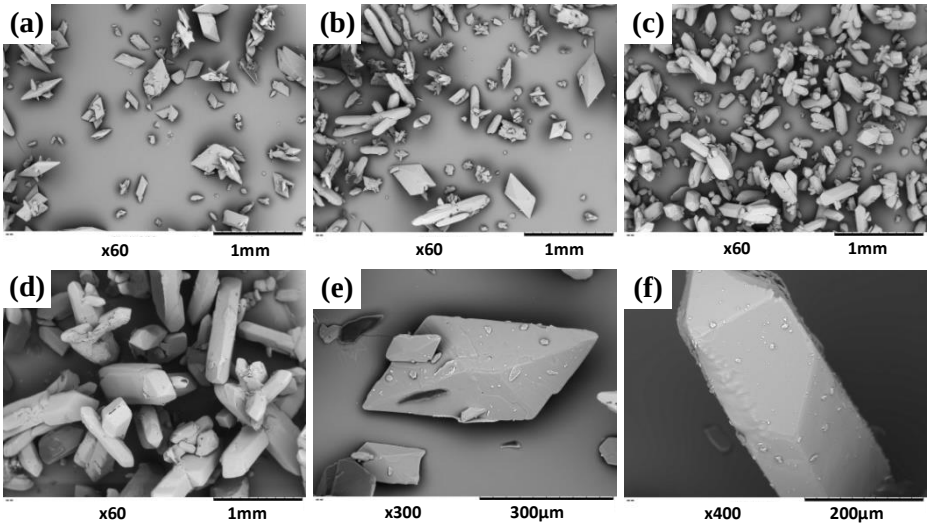

Figure 8.10: SEM micrographs of (a) 1:1 p-TSA-TPPO (x60); (b) mixture of 1:1 and 3:2 p-TSA-TPPO (x60); (c) and (d) 3:2 p-TSA-TPPO (x60); and (e) 1:1 p-TSA-TPPO (x300) and (f) 3:2 p-TSA-TPPO (x400) crystals.

EDS analyses were carried out on single crystals of 1:1 and 3:2 p-TSA-TPPO to determine the elemental composition of the crystal surface, and therefore can be used to confirm the co-crystal form present. Unlike HPLC, EDS is not able to determine the ratio of p-TSA:TPPO in the bulk sample, since the technique can only probe small regions on individual crystal faces. Figure 8.11 shows the ESD spectra obtained from single crystals of 1:1 and 3:2 p-TSA-TPPO, respectively. The spectra show that five elements were detected, oxygen (O), carbon (C), nitrogen (N), phosphorous (P) and sulphur (S). Table 8.5 provides a summary of the EDS results showing the elemental composition of the 1:1 and 3:2 p-TSA-TPPO co-crystal forms, respectively. The data confirms the stoichiometric purity of co-crystal forms, and proves that EDS is a useful tool for phase identification. It was not possible to quantify the amount of hydrogen in the respective 1:1 and 3:2 p-TSA-TPPO co-crystal samples, since EDS is not very sensitive to lighter elements. With the exception of nitrogen and phosphorous, the EDS measurements matched well with the theoretical values. EDS is a useful analytical tool that can be applied to distinguish between the 1:1 and 3:2 stoichiometric co-crystal forms of p-TSA-TPPO and complements other solid-state techniques such as PXRD, Raman and ATR-FTIR spectroscopy.

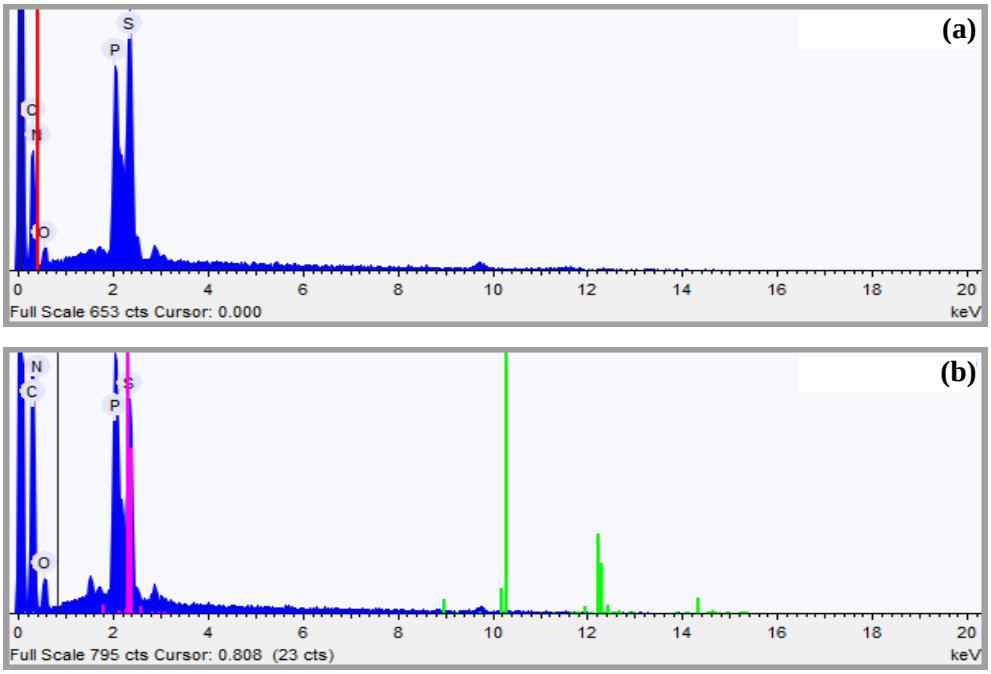

Figure 8.11: EDS spectra of (a) 1:1 and (b) 3:2 p-TSA-TPPO single crystals.

Table 8.5: EDS measurements on single crystals of 1:1 and 3:2 p-TSA-TPPO.

Elements	1:1 p-TSA-TPPO Theoretical (wt%)	1:1 p-TSA-TPPO EDS Meas. (wt%)	3:2 p-TSA-TPPO Theoretical (wt%)	3:2 p-TSA-TPPO EDS Meas. (wt%)
Carbon	70.6	70.4	67.6	67.5
Nitrogen	3.3	3.8	4.1	2.2
Oxygen	11.3	9.4	12.6	10.6
Phosphorous	7.3	8.2	6.1	8.3
Sulphur	7.5	8.0	9.5	8.2

HPLC Analyses: The purity and stoichiometric composition of the 1:1 and 3:2 p-TSA-TPPO co-crystal forms was confirmed by HPLC, applying a univariate calibration model developed by preparing different mass fractions of the starting materials (p-TSA and TPPO) in MeCN and finding the ratio between the areas of the resolved peaks of both components. Figure 8.12 shows the calibration curve used to determine the relative amount of p-TSA and TPPO in samples obtained from each experimental run.

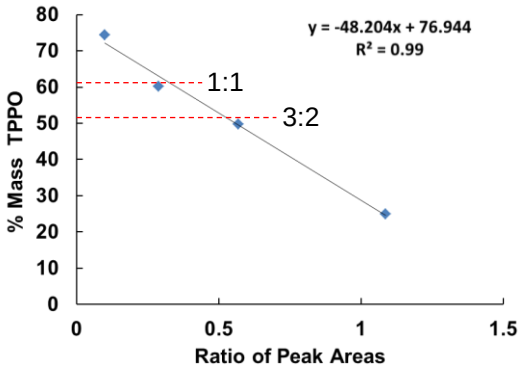

Figure 8.12: Univariate HPLC calibration model used to determining the purity and stoichiometry of 1:1 and 3:2 p-TSA-TPPO co-crystal forms.

8.2.7 *In situ* Process Monitoring and Characterisation

Real-time in process characterizations were carried out applying *in situ* Raman and ATR-FTIR spectroscopy to clear solutions and suspensions of 1:1 and 3:2 p-TSA-TPPO, respectively. Figure 8.13 shows the regions selected from *in situ* Raman spectroscopy for identification of the different phases. Results from each of the co-crystallisation runs were routinely correlated with HPLC measurements on samples taken at different intervals in order to confirm the identity of the solid forms present. Where necessary, other off-line measurement techniques, as described earlier in Section 8.2.6, were also employed to validate the results from the in situ process measurements and HPLC, for example, in cases where a mixture of different crystalline forms were suspected. This study highlights the complementarity of off-line and *in situ* process measurements. Furthermore, the application of both methods provides a robust analysis of the co-crystallisation process as well as valuable information for process scale-up. The Raman bands in the regions 200 – 350, 600 – 700, 1050 – 1250 and 1550 – 1610 cm^{-1} corresponding respectively to vibration modes of aromatic ring wagging (233 – 262 cm^{-1}), C-N bending (289 – 304 cm^{-1}), ring deformation (629 – 640 cm^{-1}), C-C ring stretching and C-S stretching (1083 – 1110 cm^{-1}), P=O symmetric and asymmetric stretching (1130 – 1200 cm^{-1}) and aromatic ring vibrations (1560 – 1620 cm^{-1}).

It has been shown so far that off-line solid-state and *in situ* characterisation techniques can be applied effectively to distinguish between the different crystalline forms of p-TSA and TPPO, including their stoichiometric co-crystal forms. This information can be applied not only to distinguish between crystalline forms, but also to inform the development of effective crystallisation control strategies in batch, semi-match and periodic flow crystallisers.

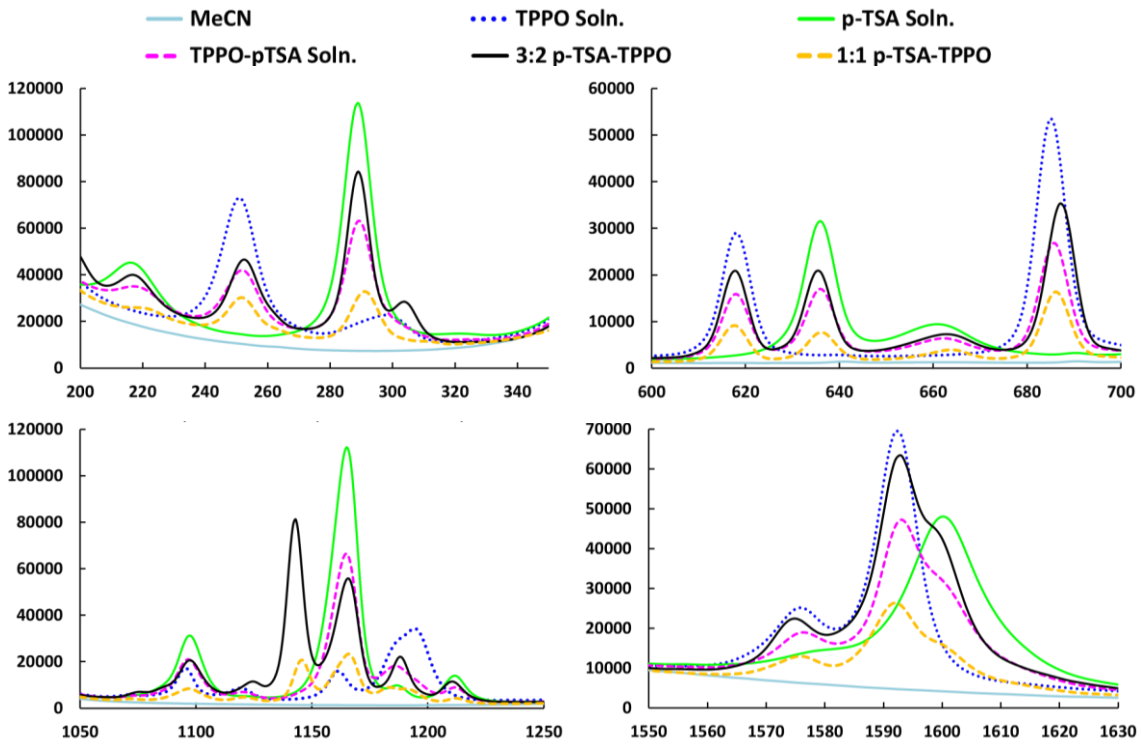

Figure 8.13: Regions of *in situ* Raman spectra used to differentiate between solution and solid phases of the p-TSA/TPPO/MeCN system.

8.2.8 Quantitative Raman Spectroscopy: Complementary Off-line and On-line Analyses

The aim of this study was to develop a multivariate calibration model to quantify the amount of 1:1 and 3:2 p-TSA-TPPO in samples collected from experimental runs where temperature cycles were implemented. In order to construct the multivariate calibration model dry mixtures with different proportions (i.e. 0, 20, 40, 60, 80 and 100 %) of pure 1:1 and 3:2 p-TSA-TPPO obtained from previous experimental runs were prepared and analysed using the Raman PHAT probe as described in Chapter 3, Section 3.2.3. The experimental procedure involved mixing (i.e. without grinding to avoid co-crystal transformation) and spreading evenly each calibration standard onto a paper sample holder in a circular shape (~ 5.5 mm diameter) and then mounting it on to the PHAT probe stage. The PHAT probe used had a spot size of 6mm and working distance of 250 mm a total of five measurements were taken for each calibration standard. Between each measurement the sample was remixed and spread as described earlier. The collected spectra were pre-processed using SNV normalisation routine to minimise the signal noise caused by the different scattering patterns of small and large particles. Figure 8.14 below shows the SNV pre-processed spectra at different concentrations of 1:1 and 3:2 p-TSA-TTPO. The concentrations ranged from 100 % (sample 1) to 0 % (sample 6) 1:1 p-TSA-TPPO. As the composition of 1:1 and 3:2 p-TSA-TPPO changes from samples

1 to 6, changes in spectral shifts are observed in the regions 1200 – 1177, 950 – 890, 440 – 370 and 350 – 150 cm^{-1}.

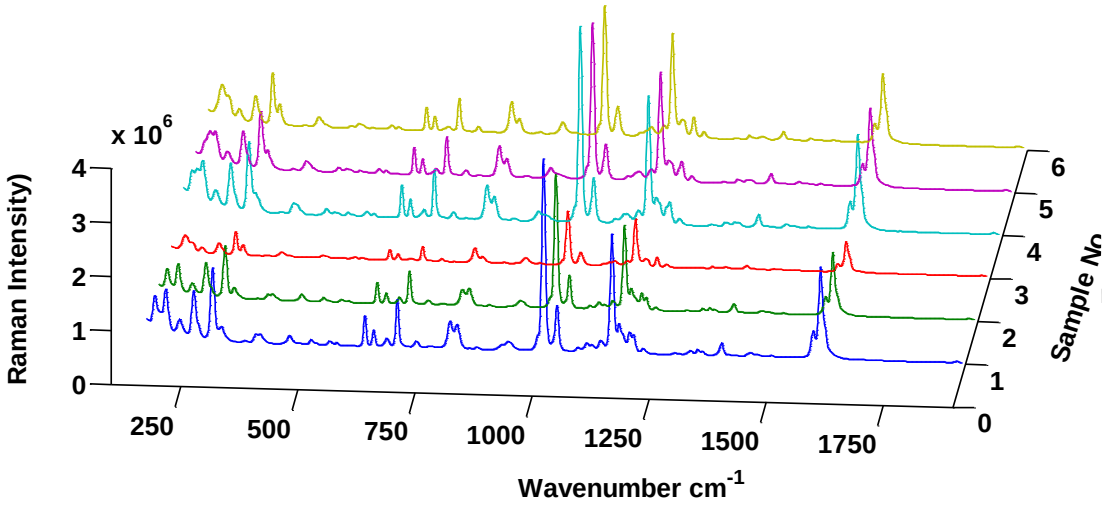

Figure 8.14: Spectra of calibration standards collected using Raman PHAT probe.

PLSR and PCR multivariate calibration techniques were applied to the pre-processed spectra; the resulting models were then validate using spectra of samples collected from subsequent experimental runs. The PHAT probe measurements were then correlated with *in situ* Raman MR immersion probe (described in Chapter 3, Section 3.3.1) measurements to further extend the capability of the multivariate model to real-time quantification of the crystalline co-crystal form. Further details on this aspect of the study are provided in the discussion section following.

The best methods for assessing the co-crystals on a quantitative basis are HPLC (with univariate model) and Raman PHAT probe (with multivariate model). The limitation of the HPLC method is the inability to determine accurately the composition of the co-crystals when a mixture is present due to the requirement to dissolve the crystals before analysis. The Raman PHAT probe method on the other hand can be applied to determine the composition of mixtures as the samples are analysed in solid form. The other techniques described earlier in Section 8.2.6 were used qualitatively (off-line Raman (microscopy), off-line ATR-FTIR, PXRD, DSC and HSM) or semi-quantitatively (EDS) to identify the crystalline forms of p-TSA and TPPO and provided useful information about the crystalline forms on initial assessment of samples prior to their quantitative analysis.

8.3 Results and Discussions

8.3.1 Batch Co-Crystallisation Monitoring and Control

The batch cooling co-crystallisations of p-TSA with TPPO to give stoichiometric 1:1 and 3:2 p-TSA-TPPO co-crystal forms, as per the ternary phase diagram, were monitored by applying integrated PAT and CryPRINS informatics system tools within the IDS framework to extract information pertaining to the stability of each co-crystal form under different operating conditions. A further aim was to optimise the batch process for the selective crystallisation of each co-crystal form, achieved by tuning either the starting composition of p-TSA/TPPO/MeCN or the crystallisation temperature profile. Figure 8.15 (a) and (b) shows the process time diagrams obtained from monitoring the crystallisation of 1:1 and 3:2 p-TSA-TPPO during experiment 5 and 3 (Table 8.2), respectively using FBRM, ATR-UV/vis and ATR-FTIR spectroscopy. Also shown are the microscope images of the crystalline products.

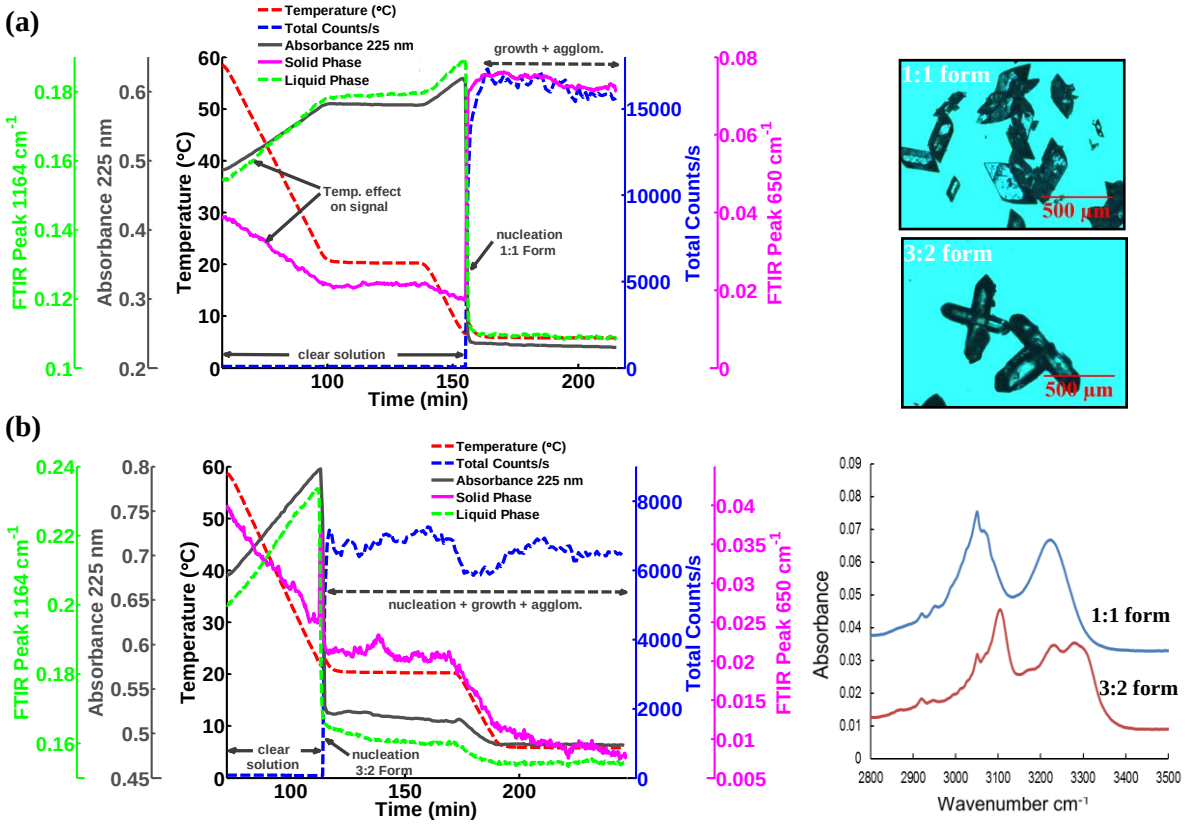

Figure 8.15: Schematic showing the process time diagrams with temperature, ATR-UV/vis, ATR-FTIR and FBRM signals for the crystallisation of: (a) 1:1 p-TSA-TPPO – experiment 5; (b) 3:2 p-TSA-TPPO – experiment 3; along with microscope images (top right) and off-line ATR-FTIR spectra (bottom right) of samples collected at the end of both processes.

As expected, 1:1 p-TSA-TPPO show a distinct rhombic morphology, while the 3:2 form exhibits the characteristic elongated prismatic morphology, Figures 8.4 and Figure 8.15 (top left). The infrared spectra of the two co-crystal forms, Figure 8.15 (bottom right), also show distinct differences in the regions associated with the C-H stretching (2900 – 3000 cm^{-1}) and N-H stretching (3000 – 3400 cm^{-1}) vibration frequencies, respectively. Off-line Raman, XRD, DSC and HPLC also confirmed the purity of each co-crystal form. The time diagrams, Figure 8.15 (a) and (b), are annotated to indicate where important events occurred during each co-crystallisation run. Signals from the PAT tools show good agreement with respect to the detection of nucleation, although the *in situ* ATR-UV/vis and ATR-FTIR signals are affected by temperature. Nucleation of 1:1 p-TSA-TPPO, Figure 8.15 (a), is not observed until cooling toward 5 ^{o}C (final temperature was ~6.5 ^{o}C). On the other hand, nucleation of 3:2 p-TSA-TPPO, Figure 8.15 (b), occurs at ~21 ^{o}C. The contrasting results were due to the difference in mass fraction composition of p-TSA/TPPO/MeCN in each experimental run, that is, and 0.19/0.09/0.72 (experiment 3) and 0.09/0.12/0.79 (experiment 5). The corresponding σ values for the experiments 3 and 5 were 2.69 and 2.29, respectively. Note that the cooling rate was held constant for both experiments and the overall temperature profile was the same. These experiments were found to be reproducible, in terms of the co-crystal outcome. In addition to detecting signal from the solution phase, the ATR-FTIR probe was also able to detect the solid phase signal, albeit at the lower limit of the instrument (650 cm^{-1}) when 1:1 p-TSA-TPPO nucleated. This is not entirely surprising since it is well known that *in situ* ATR-FTIR can be affected by particle scattering [29], [143], and to a much greater extent than *in situ* ATR-UV/vis, which shows much less sensitivity [303]. However, the ATR-FTIR signal cannot be properly interpreted for experiment 3 in which 3:2 p-TSA-TPPO was the product obtained. The signal was found to change in almost exactly the same way as the temperature profile, with the exception of a sudden spike at the 650 cm^{-1} peak position at ~110 min. This sudden spike was consistent with a sudden increase in FBRM counts/s and a simultaneous drop in ATR-UV/vis absorbance, with confirmation of the presence of crystals obtained via real-time PVM imaging. The change in behaviour of the 650 cm^{-1} peak signal may be attributed to material sticking on the probe window leading to the observed dramatic change in signal. Furthermore, peaks that are close to the limits of the ATR-FTIR range (for the study the instrument had a range 650 – 2800 cm^{-1}) are often not consistent due to small signal to noise ratio, and therefore their reliability for interpretation of process behaviour is strongly cautioned. In fact, the signal changes for the ATR-FTIR probe as observed in experiment 3 were not repeatable.

The mass fraction of MeCN was fixed to 0.50 for experiments 4 and 7 (Table 8.2) and the amount of p-TSA and TPPO varied according to the recipe by Croker et al. [323] for obtaining pure 3:2 and 1:1 p-TSA-TPPO respectively by cooling crystallisations at 50 mL scale. For

experimental runs 4 and 7, pure 3:2 and 1:1 p-TSA-TPPO, respectively, were obtained as confirmed by off-line analysis (HPLC, Raman microscopy, off-line ATR-FTIR, EDS and DSC). However, due to the high solubility of p-TSA and TPPO in MeCN, it seems impractical to consider scale-up of the co-crystallisation process applying the conditions used for experimental runs 4 and 7, since the high viscosity of the slurry at these high concentrations leads to poor mixing and suspension of the crystals. Furthermore, speciality agro chemicals are often highly toxic and expensive, plus the bulk storage of materials could pose health and environmental risks [309]. Therefore, the co-crystallisation was investigated at much lower concentrations of p-TSA and TPPO in MeCN (see Table 8.2), exploiting the upper most regions (toward MeCN) of the ternary phase diagram. Table 8.6 provides a summary of the outcomes in terms of co-crystal form obtained, based on-line (*in situ* Raman) and off-line (Raman microscopy, off-line ATR-FTIR, EDS and DSC) analyses.

Consistent results in terms of co-crystal form were obtained for all investigated compositions of p-TSA/TPPO/MeCN, that is, with the exception of experiments 11 and (18). These two experiments were identical linear runs (note that temperature cycling was applied to (18) later) that were expected to yield a mixture of 1:1 and 3:2 p-TSA-TPPO. Instead, 1:1 p-TSA-TPPO and 3:2 p-TSA-TPPO were obtained from experiment 11 and (18), respectively. This is likely due to operation of the process in the region of the ternary diagram (Figure 8.1) in the narrow region where the boundaries between stable 1:1 p-TSA-TPPO (Region 2), a mixture (Region 3) and stable 3:2 p-TSA-TPPO are really close. Although one would expect to obtain a mixture of co-crystals under the prevailing operating conditions, the outcome perhaps highlights the potential variability issues that can arise in the batch process. However, it must be noted that the experimental conditions reflect the dynamics of the crystallisation kinetics of the co-crystal system. The ternary phase diagram on the other hand reflects the thermodynamic stability at a fixed temperature of 20 ^{o}C. If the crystalliser was held for a long period (e.g. 24 hrs.) at 20 ^{o}C, then perhaps a mixture of the two co-crystals would have prevailed in experiments 11 and (18). However, other control strategies can be explored to achieve the desired crystallisation outcome over a shorter time period, namely temperature cycling as demonstrated for experiment (18) later. Temperature cycling using active polymorphic feedback control based on *in situ* Raman spectroscopy is a promising method recently explored by Simone et al. [49] to eliminate the undesired polymorphic form of orthoaminobenzoic acid (OABA) and then grow the desired form. In this study, a simple temperature cycling method was employed to eliminate one co-crystal form and grow the desired form. Temperature cycling was implemented for experiments (13) and (18). The 1:1 co-crystal form is desired since the 3:2 form exhibits incongruent dissolution behaviour in MeCN [323], [326]. These experiments also shed light on the stability and by extension the thermodynamics of the crystallisation of 1:1

and 3:2 p-TSA-TPPO, respectively. The temperature cycles in experiments (13) and (18) were implemented based on the *in situ* Raman signal of peaks associated with the 1:1 and 3:2 co-crystal form, respectively.

Figure 8.16 shows the process time diagram for the crystallisation of 3:2 p-TSA TPPO during experiment (18) and the subsequent transformation to 1:1 p-TSA-TPPO. The mixture was heated up and subjected to a complex temperature profile with ramped heating and cooling cycles (Figure 8.16), the same temperature profile was used for experiment (13). The final product obtained from experiments (13) and (18) was pure 1:1 p-TSA-TPPO, as confirmed by on-line Raman spectroscopy and off-line solid state characterization methods (HPLC, PXRD, Raman microscopy and ATR-FTIR) described earlier.

Table 8.6: Summary of co-crystallisation outcomes for selected experiments, co-crystal form was determined by on-line and off-line measurements.

Exp. No.	p-TSA (g/g MeCN)	TPPO (g/g MeCN)	Component Mass Fractions (M)			HPLC Ratio p-TSA/TPPO	p-TSA-TPPO Co-crystal Form	Region in Ternary Phase Diagram
			p-TSA	TPPO	MeCN			
3	0.2634	0.1247	0.19	0.09	0.72	1.005	3:2	1 (3:2 form)
4	0.5776	0.4202	0.29	0.21	0.50	1.470	3:2	1 (3:2 form)
5	0.1147	0.1532	0.09	0.12	0.79	1.034	1:1	2 (1:1 form)
7	0.3793	0.6193	0.19	0.31	0.50	1.002	1:1	2 (1:1 form)
8	0.0706	0.1059	0.06	0.09	0.85	1.000	1:1	2 (1:1 form)
11	0.1084	0.0964	0.09	0.08	0.83	1.006	1:1	3 (mixture)
12	0.0833	0.1071	0.07	0.09	0.84	1.002	1:1	2 (1:1 form)
(13)	0.1728	0.0617	0.14	0.05	0.81	1.477 => 1.002	3:2 => 1:1	1 (3:2 form)
(18)	0.1049	0.0968	0.09	0.08	0.83	1.463 => 0.998	3:2 => 1:1	3 (mixture)

() Temperature cycles implemented; => Conversion from 3:2 to 1:1 p-TSA-TPPO.

Figure 8.16 also shows the point where the first sample was taken from the process (arrow 1; image S1). The sample taken was confirmed to be pure 3:2 p-TSA-TPPO by both on-line and off-line measurements. Following on from that point is the dissolution of 3:2 p-TSA-TPPO (arrow 2, image S2), which is marked by a decrease in the FBRM counts/s and the 2nd derivative of Raman peak signal at 304 cm^{-1} (indicative of the presence of 3:2 p-TSA-TPPO). Subsequent to this event, nucleation of 1:1 p-TSA-TPPO occurs (arrow 3), marked by a sudden increase in FBRM counts/s and the 2nd derivative of Raman peak signal 1145 cm^{-1} (indicative of the presence of 1:1 p-TSA-TPPO). This is followed by slight dissolution as the temperature continues to increase in the heating cycle (arrow 4). At ~270 min. there is a rapid increase in the FBRM counts/s and simultaneous increase in the 2nd derivative 1145 cm^{-1} peak signal (arrow 5; image S3) due to implementation of a temperature cooling cycle. This is attributed to secondary nucleation of 1:1 p-TSA-TPPO as the amount of 3:2 p-TSA-TPPO

diminishes. The relative solubility of each co-crystal phases plays an important role in the conversion between forms. The 3:2 co-crystal is known to undergo incongruent dissolution, whereby there is a transformation step involving the formation and subsequent dissolution of 1:1 p-TSA-TPO [308]. The temperature cooling step implemented from ~334 to 490 min. (cooling rate of -0.2 ^{o}C/min) led to further secondary nucleation of 1-1 p-TSA-TPPO (arrow 7). The microscope image of sample 3, Figure 8.16 (S3), shows there is a mixture of 3:2 and 1:1 p-TSA-TPPO. The presence of a mixture was also confirmed by off-line solid-state characterizations and HPLC analysis. Following this, a temperature heating step was implemented (heating rate of 0.2 ^{o}C/min) to dissolve 3:2 p-TSA-TPPO (arrow 8; image S3). This was then followed by another cooling step to nucleate and grow 1:1 p-TSA-TPPO (arrow 10; image S4).

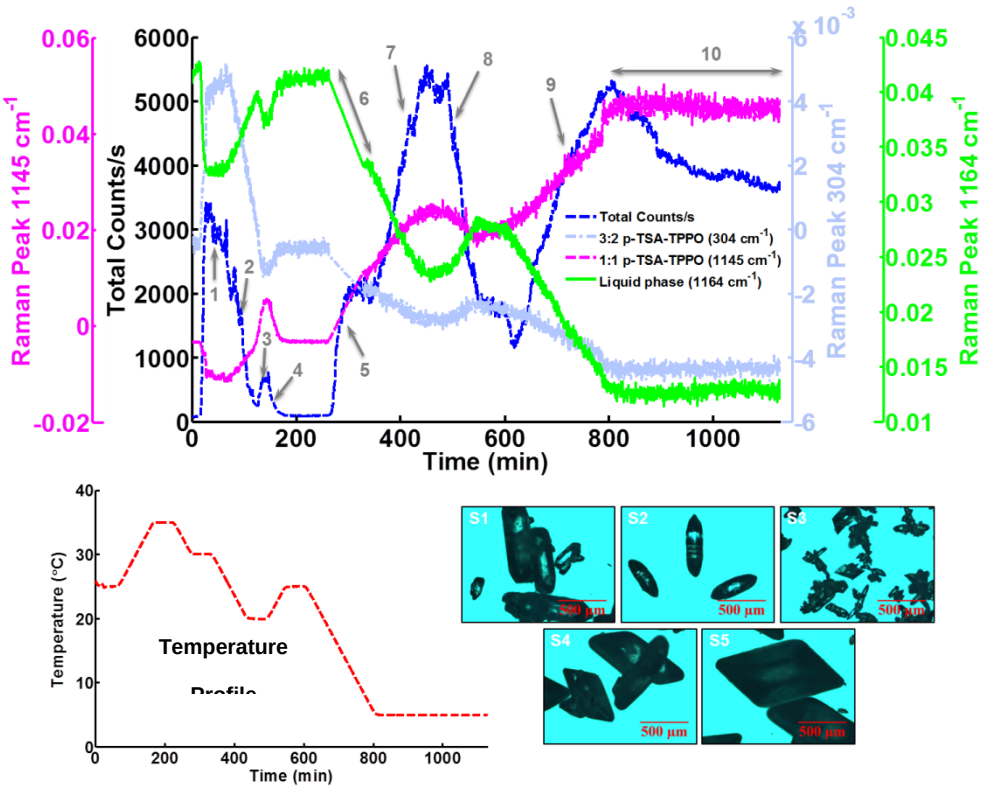

1 = Sample 1 at 57 min.	5 = Sample 3 at 272 min.	9 = Nucleation event.
2 = Sample 2 at 109 min.	6 = Signal loss/fluorescence	10 = Sample 5 at 1137 min.**
3 = Nucleation event	7 = Nucleation event	**growth/agglomeration/
4 = Dissolution event	8 = Sample 4 at 177 min.	settling observed.

Figure 8.16: Process time diagram for experiment (18) showing the changes in FBRM count/s and *in situ* Raman 2nd derivative signals (top), temperature profile implemented (bottom left) and microscope images of samples (bottom right).

The final sample collected at the end of the batch (image S5) was found to be pure 1:1 p-TSA-TPPO. As demonstrated earlier, increasing the process temperature soon after nucleation of 3:2 p-TSA-TPPO leads to its dissolution and subsequent transformation to 1:1 p-TSA-TPPO.

The 1:1 co-crystal then starts to increase in amount *viz* secondary nucleation. The switching from heating to a cooling cycle soon after the detection of 1:1 p-TSA-TPPO leads to an increase in the amount of this co-crystal form and further reduction in the amount of 3:2 p-TSA-TPPO. The work presented here is a proof of concept study whereby the mass faction composition and temperature cycling are applied to control the co-crystallisation process in order to obtain the desired stoichiometric form of the p-TSA-TPPO co-crystal system. It has been demonstrated that the co-crystal form can be controlled by manipulating the composition of p-TSA, TPPO and MeCN, as previously demonstrated by Croker *et al*. [323], [326] in small scale studies. The stoichiometric purity of the final co-crystal was assured by implementation of a complex array of on-line and off-line monitoring and characterization techniques.

8.3.2 *In situ* Quantitative Analysis of Co-Crystallisation Process Using Raman Spectroscopy

In the previous section the implementation of temperature cycles based on signals from *in situ* Raman spectroscopy was investigated. In this study the Raman control approach was investigated in greater detail by applying multivariate statistical methods. The Raman spectra obtained in the presence of solids (i.e. after the crystallisation of the respective 1:1 and 3:2 co-crystal forms or mixtures thereof) using the MR immersion probe for a series of experimental runs reported earlier in Section 8.3.1, (i.e. experiments 8, 11 and (13)), were pre-processed viz. the application of 2nd derivative with Savitzky-Golay smoothing filter using the iC Raman (version 4.1) software interface which was connected to the Kaiser RamanRXN2 Hybrid spectrometer used in this study (see Chapter 3). In experiments 8, 11 and (13), 1:1 p-TSA-TPPO, 3:2 p-TSA-TPPO and a mixture of 1:1 and 3:2 p-TSA-TPPO, respectively, were obtained on crystallisation. The 2nd derivative spectra of each experimental data set was further analysed to identify any trends related to the different co-crystal compositions obtained. Figure 8.17 show the specific regions of the overlaid 2nd derivative spectra for the three experimental runs that were tracked. The spectra collected soon after nucleation was detected are the ones displayed.

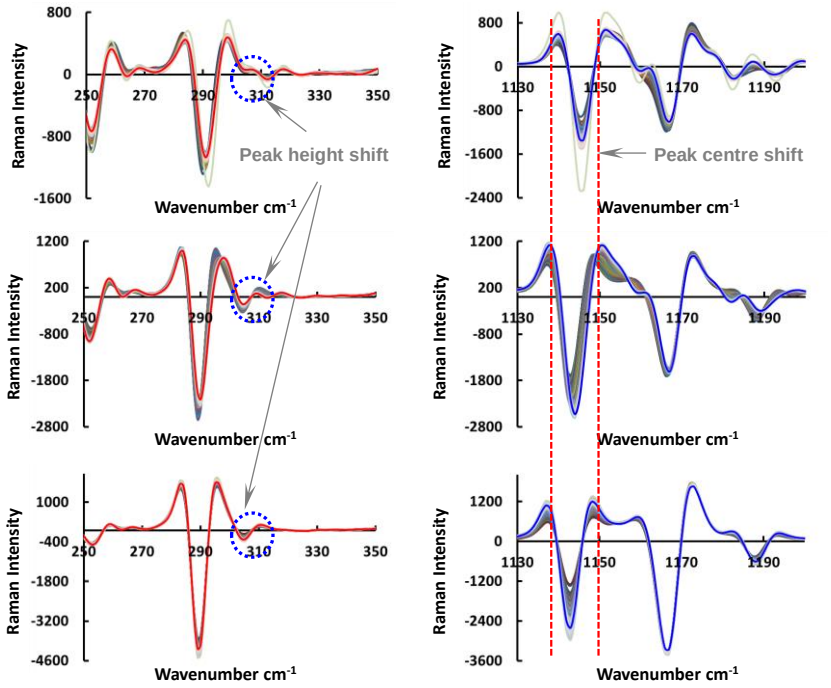

Figure 8.17: Selected regions of 2nd derivative pre-processed spectra for experiments 8 (top; 1:1 p-TSA-TPPO), 11 (middle; mixture), and (13) (3:2 p-TSA-TPPO).

The region from 308 – 300 cm^{-1}, which occurs as a small negative peak was found to be useful for tracking 3:2 p-TSA-TPPO. The peak appears when 3:2 p-TSA-TPPO nucleates as pure form or as a mixture with 1:1 p-TSA-TPPO and increases in intensity as the amount of 3:2 p-TSA-TPPO increases. On the other hand, when 1:1 p-TSA-TPPO nucleates as pure form the peak at 308 – 300 cm^{-1} is absent. The region from 1149 – 1137 cm^{-1}, which encompasses a large negative peak, was another region of interest that was tracked during this study. The centre position of this peak was found to shift position toward higher wavenumbers (i.e. toward 1149 cm^{-1}) whenever 1:1 p-TSA-TPPO nucleated. Conversely, the centre position shifted towards lower wavenumbers (i.e. toward 1137 cm^{-1}) whenever 3:2 p-TSA-TPPO nucleated. Tracking of the peak centre position in the region from 1149 – 1137 cm^{-1} was found to be more reliable for the purposes of detecting transformation events involving the two co-crystal forms. Based on the centre position of this peak, a decision can be made to trigger heating or cooling cycles to convert from between the two co-crystal forms, akin to dynamic feedback control of the process. A number of experimental runs were conducted with temperature cycling to investigate the solution mediated transformation events from 3:2 p-TSA-TPPO to 1:1 p-TSA-TPPO and vice versa. Samples were taken during each temperature cycle and analysed by using off-line techniques, including HPLC, ATR-FTIR, Raman Microscopy and Raman spectroscopy using a PHAT probe accessory fitted to the Kaiser RamanRXN2 Hybrid spectrometer (Chapter 3, Section 3.2.3). The results of these experimental runs in terms of co-crystallisation outcome are presented in Table 8.7 below.

Table 8.7: Summary of experimental results obtained with temperature cycling.

Exp. No.	p-TSA (g/g MeCN)	TPPO (g/g MeCN)	Component Mass Fractions (M)			HPLC Ratio p-TSA/TPPO	p-TSA-TPPO Co-crystal Form	Region in Ternary Phase Diagram
			p-TSA	TPPO	MeCN			
(14)	0.1484	0.1148	0.12	0.09	0.79	1.486	3:2 => 1:1	1 (3:2 form)
(15)	0.1492	0.1140	0.12	0.09	0.79	1.151	mix >> 3:2	1 (3:2 form)
(16)	0.1054	0.0971	0.09	0.08	0.79	1.294	mix >>> 1:1	3 (mixture)
(17)	0.1384	0.1136	0.11	0.09	0.8	1.182	mix >>> 1:1	3 (mixture)

() Temperature cycles implemented; => Conversion from 3:2 to 1:1 p-TSA-TPPO; >> Conversion from mixture to 3:2 p-TSA-TPPO; >>> Conversion from mixture to 1:1 p-TSA-TPPO.

Figure 8.18 (a) and (b) show the time diagrams with PAT sensor signals from ATR-UV/vis, FBRM, PVM and Raman for experiment 14. Several events were detected by the PAT sensors during the cooling crystallisation with temperature cycling. The first event labelled (1) involves the simultaneous dissolution of the raw materials p-TSA and TPPO. The second event (2) marks the nucleation of a p-TSA-TPPO co-crystal which is detected as an increase in FBRM and PVM count/s, in Figure 8.18 (a). This event was also detected by Raman spectroscopy, Figure 8.18 (b), whereby there is an increase in the second derivative signal of the peak height and centre position between 308 – 300 cm^{-1} and 1149 – 1137 cm^{-1}, respectively. The sudden increase in peak height signal between 308 – 300 cm^{-1} is an indication that 3:2 p-TSA-TPPO was the co-crystal form that nucleated. Simultaneously, the centre position of the peak signal between 1149 – 1137 cm^{-1} experiences a shift towards ~1142 cm^{-1}, which also confirms the presence of 3:2 p-TSA-TPPO. A simultaneous decrease in intensity of the peak height at 1186 cm^{-1} (the solution peak) indicates that the concentrations of the starting materials (p-TSA and TPPO) are decreasing. This is expected since the materials are co-crystallising with each other. A fluorescence (or interference) event can be seen in the Raman signal of the peak positions 308 – 300 cm^{-1} and 1186 cm^{-1}. However, it appears that this event did not have an effect on the 1149 – 1137 cm^{-1} peak centre position Raman signal. This was therefore seen as the more reliable Raman signal to track compared to the two others mentioned previously.

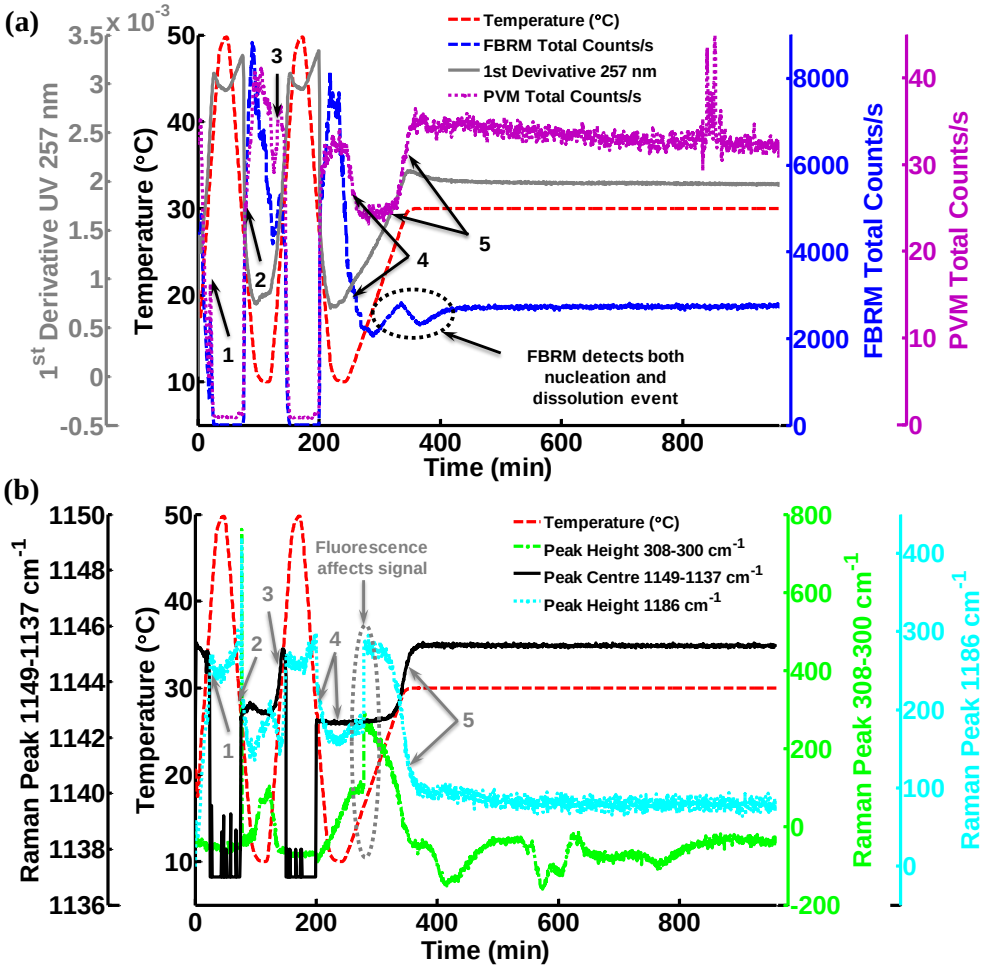

Figure 8.18: Process time diagrams showing the changes in temperature and (a) ATR-UV/vis, FBRM counts/s and PVM counts/s; and (b) Second derivative Raman signals for peak centre shift between 1149 – 1137 cm^{-1} and peak height shifts at 308 – 300 cm^{-1} and 1186 cm^{-1} during experiment (14). 1 = raw materials dissolution; 2 = nucleation of 3:2 p-TSA-TPPO; 3 and 4 = dissolution of 3:2 p-TSA-TPPO and nucleation of 1:1 p-TSA-TPPO; and 5 = transformation of 3:2 to 1:1 p-TSA-TPPO

The third (3) and fourth (4) events that were detected mark the dissolution of 3:2 p-TSA-TPPO and subsequent nucleation of 1:1 p-TSA-TPPO during the first and second temperature cycles, respectively. This solution-mediated transformation event was detected as subtle changes in the FBRM and PVM signals (i.e. shape decrease and subsequent increase in counts/s). The Raman peak position at 1149 – 1137 cm^{-1} confirmed that 3:2 p-TSA-TPPO was the co-crystal form that crystallised during the first two temperature cycles and that it started to transform on heating to 1:1 p-TSA-TPPO. The transformation was detected as a sharp rise in the signal towards 1145 cm^{-1} (i.e. shift of the peak centre position towards higher wavenumbers). Subsequent to this, the fifth (5) event indicates a more gradual increase in the Raman signal of the peak centre position between 1149 – 1137 cm^{-1} as a third temperature cycle is implemented. The cooling and heating rates for this third cycle were slower (-0.2 / 0.2

°C/min) compared to the first two cycles (-0.5 / 0.5 °C/min). The cooling and heating rates were made slower in order to better detect the solution mediated transformation event during the heating cycle. With slower heating it was much easier to detect the transformation from 3:2 p-TSA-TPPO to 1:1 p-TSA-TPPO, although the relative compositions of the two co-crystal forms could not be quantified. It is interesting to note that the change in FBRM signal between 290 and 410 min. Indicates that secondary nucleation of 1:1 p-TSA-TPPO is taking place, marked by a sudden increase in counts/s during the heating phase. This was quickly followed by a sudden decrease in counts/s nearing the end of the heating cycle, which suggests slight dissolution (or perhaps agglomeration) of 1:1 p-TSA-TPPO. These events are attributed to the solution mediated transformation from 3:2 to 1:1 p-TSA-TPPO. Figure 8.19 below shows microscope images of samples collected at different time intervals during experiment (14), which confirms the events reported earlier.

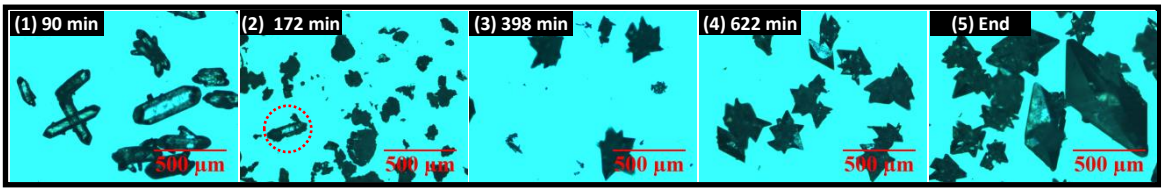

Figure 8.19: Microscope images of samples collected from experiment (14). Circled particle show the early stages of transformation from 3:2 to 1:1 p-TSA-TPPO.

Image (1) shows the distinctive elongated prismatic morphology typically exhibited by 3:2 p-TSA-TPPO. Image (2) show crystals with poor crystal habit, an indication of the onset of transformation from 3:2 to 1:1 p-TSA-TPPO. Subsequent images, (3), (4) and (5) indicate the presence of 1:1 p-TSA-TPPO crystals, which show the distinctive rhombic morphology. Figure 8.20 (a) and (b) show the off-line ATR-FTIR and Raman microscope spectra of the samples collected during experiment (14) along with the reference spectra. These spectra further confirm the findings discussed earlier for experiment (14). The ATR-FTIR spectra, Figure 8.20 (a), in the region 3350 to 2900 cm^{-1} show the distinctive features of pure 1:1 and 3:2 p-TSA-TPPO (i.e. based on the reference materials). The peaks observed in this region for both co-crystal forms are a result of the vibration frequencies associated the amine ($-NH_2$) group of p-TSA. It appears the different hydrogen bonding interactions of the $-NH_2$ with TPPO leads to the distinctive peak positions and peak broadening/distortions observed this region. For example, there is a shift in peak positions toward lower wavenumbers for 1:1 p-TSA-TPPO relative to 3:2 p-TSA-TPPO. Furthermore, 3:2 p-TSA-TPPO shows peak boarding/distortion in the region 3350 – 3200 cm^{-1}, while the same can be said for 1:1 p-TSA-TPPO in the region 3130 – 2930 cm^{-1}. The reference materials of 1:1 and 3:2 p-TSA-TPPO show prominent peaks with centre positions at 3224 cm^{-1}, 3106 and 3050 cm^{-1}. Analysis of the sample spectra relative to the reference spectra indicate that sample (1) is pure 3:2 p-TPP-TPPO, sample (2) is a

mixture of 1:1 and 3:2 p-TSA-TPPO and samples (3), (4) and (5) are pure 1:1 p-TSA-TPPO. The Raman results, Figure 8.20 (b), complement well the ATR-FTIR results explained earlier. The peak shifts (i.e. boarding/distortion) between 3090 – 3030 results confirm that sample (1) is 3:2 p-TSA-TPPO, sample (2) is a mixture of 1:1 and 3:2 p-TSA-TPPO, and samples (4) and (5) are both 1:1 p-TSA-TPPO. The spectrum of sample (3) has similar features to 1:1 p-TSA-TPPO, but there is some distortion in the region between 3070 – 3060 cm^{-1}. This is an indication that this sample may have trace amounts of 3:2 p-TSA-TPPO, which were not detected with off-line ATR-FTIR. HPLC analysis on this sample gave a ratio of 1.288, which confirms the Raman microscope results. This compares to a value of 1.352 observed for sample (2), which was confirmed as a mixture by all the solid-state techniques employed. Note that the HPLC method gives a semi-quantitatively determination of the co-crystal composition and cannot be used to determine the amount of each co-crystals present in mixtures. It is interesting to note that the microscope images did not show any evidence of the presence of 3:2 p-TSA-TPPO in sample (3), as confirmed by visual inspection. Therefore, a quantitative method is required to give a more accurate representation of the co-crystal composition of samples. The quantitative method was developed using off-line and on-line Raman spectroscopy to determine the relative amounts of the two co-crystals as described in Section 8.2.8 and below.

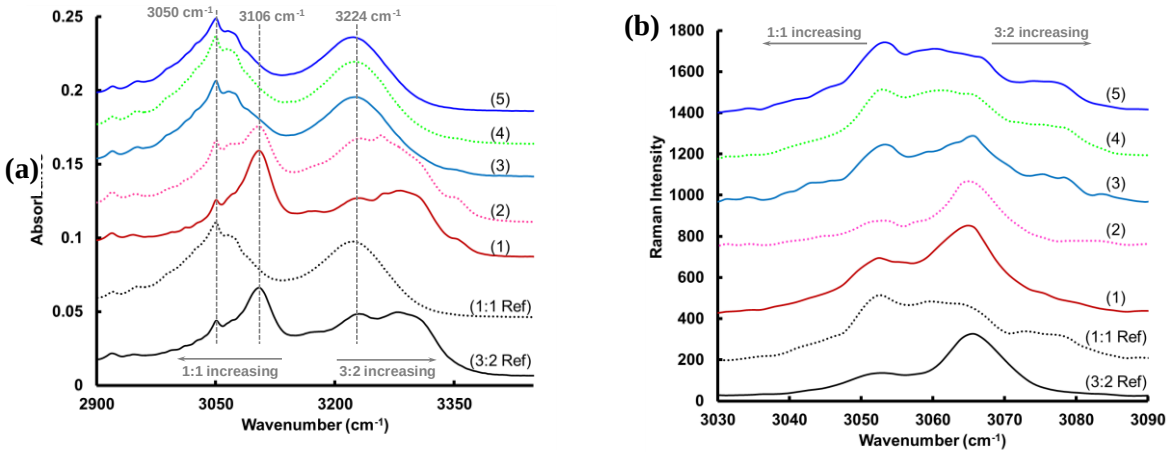

Figure 8.20: Off-line ATR-FTIR (left) and Raman (right) spectra showing the peak shifts/distortions for the transformation of 3:2 to 1:1 p-TSA-TPPO.

***Quantitative Method Using Raman PHAT and MR Immersion Probe*:** It was useful to correlate the off-line multivariate calibration method developed with the Raman PHAT probe to *in situ* Raman measurements to be able to quantify the amount of each co-crystal in real-time, in particular, when transformation events are taking place. This provides a useful means of determining the end-point of these transformation events and is a useful guide to determine when to stop the crystallisation process. Table 8.8 below shows the performance indices of

the PLSR and PCR multivariate models that were developed using the Raman PHAT probe as described in Section 8.2.8. The models were trained on spectra obtained from mixtures of know composition of 1:1 and 3:2 p-TSA-TPPO and were able to interpret the data from measurements of samples taken from each experiment well. Both models showed similar accuracy, hence both were used to test the co-crystal composition of unknown samples.

Table 8.8: Summary of performance indices for the best PLSR and PCR models

Model Type	Pre-Processing Applied	No. C*	RMSEP	R^2	% Error	Remarks
PLSR	SNV	2	0.0389	0.9893	± 3.8	optimum
PCR	SNV	2	0.0375	0.9889	± 3.8	optimum

C* = number of components

The performance of the multivariate calibration model developed using the Raman PHAT probe was checked against samples collected from experimental runs (15), (16) and (17), listed in Table 8.7. In these experiments, several temperature cycles were implemented intentionally to create the conditions for solution-mediated transformation from 3:2 to 1:1 p-TSA-TPPO and vice versa. The decision to implement cooling or heating steps was based on the signal observed from the *in situ* Raman MR immersion probe. As explained earlier the second derivative of the peak centre positon in the region 1149 – 1137 cm^{-1} was found to be the most reliable for detecting the respective 1:1 and 3:2 co-crystal forms of p-TSA-TPPO. Therefore, this signal was tracked and used as the decision variable to switch between heating and cooling cycles in order to trigger solution mediated transformation of the two co-crystals. Figure 8.21 below shows the time diagram for experiment (15), arrows and numbers indicate where samples were taken. The sampling frequency was necessary to capture the transformation events and correlate the process signal to the presence of a specific co-crystal form or mixture of forms. Nucleation of a mixture of 1:1 and 3:2 p-TSA-TPPO was observed in this experiment, although 3:2 p-TSA-TPPO was expected. This was attributed to batch-to-batch variability often encountered in batch operations. A co-crystal mixture was confirmed by the *in situ* Raman measurement at the peak centre position 1149 – 1137 cm^{-1} and by off-line solid-state analyses (discussed below).

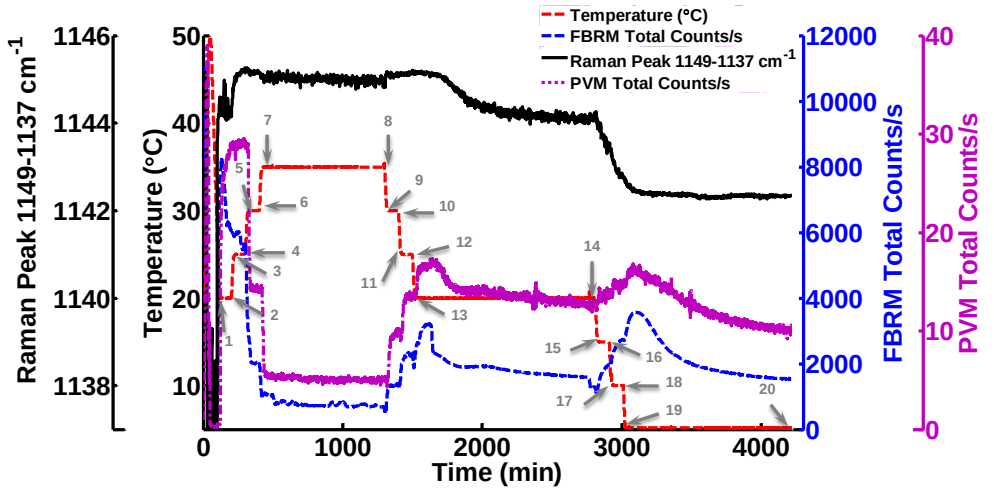

1 = Sample 1 at 103 min.	8 = Sample 8 at 495 min.	15 = Sample 15 at 2821 min.
2 = Sample 2 at 193 min.	9 = Sample 9 at 1300 min.	16 = Sample 16 at 2905 min.
3 = Sample 3 at 214 min.	10 = Sample 10 at 1393 min.	17 = Sample 17 at 2919 min.
4 = Sample 4 at 295 min.	11 = Sample 11 at 1410 min.	18 = Sample 18 at 3050 min.
5 = Sample 5 at 313 min.	12 = Sample 12 at 1495 min.	19 = Sample 19 at 3354 min.
6 = Sample 6 at 390 min.	13 = Sample 13 at 1513 min.	20 = Sample 20 at 4219 min.
7 = Sample 7 at 415 min.	14 = Sample 14 at 2919 min.	

Figure 8.21: Time diagram of experiment (15) showing the change in Raman signal (peak centre position between 1149 – 1137 cm^{-1}), FBRM and PVM particle counts/s.

Figure 8.21 shows that stepwise heating of the process vessel to 35 °C led to the gradual transformation of the mixture to 1:1 p-TSA-TPPO. Subsequent stepwise cooling from 35 to 20 °C led to the opposite result, whereby gradual transformation from 1:1 to 3:2 p-TSA-TPPO is observed. Further cooling to 5 °C led to further conversion to 3:2 p-TSA-TPPO as the equilibrium composition of the mixture keeps shifting with cooling. These results indicate that 1:1 p-TSA-TPPO is the thermodynamic co-crystal form and 3:2 p-TSA-TPPO is the kinetic form. The PLSR and PCR multivariate models were also applied to samples collected from experimental run (16); the process time diagram for this shown in Figure 8.22. Points where samples were collected are indicated with arrows. Points where important transformation events from 3:2 to 1:1 p-TSA-TPPO and vice versa were detected by the PAT probes are also indicated. The transformation events were detected by FBRM, PVM and Raman probes. However, the Raman MR immersion probe was the most sensitive to the process changes. This experiment provided evidence of a correlation between the off-line Raman PHAT probe and the *in situ* Raman MR immersion probe process measurements.

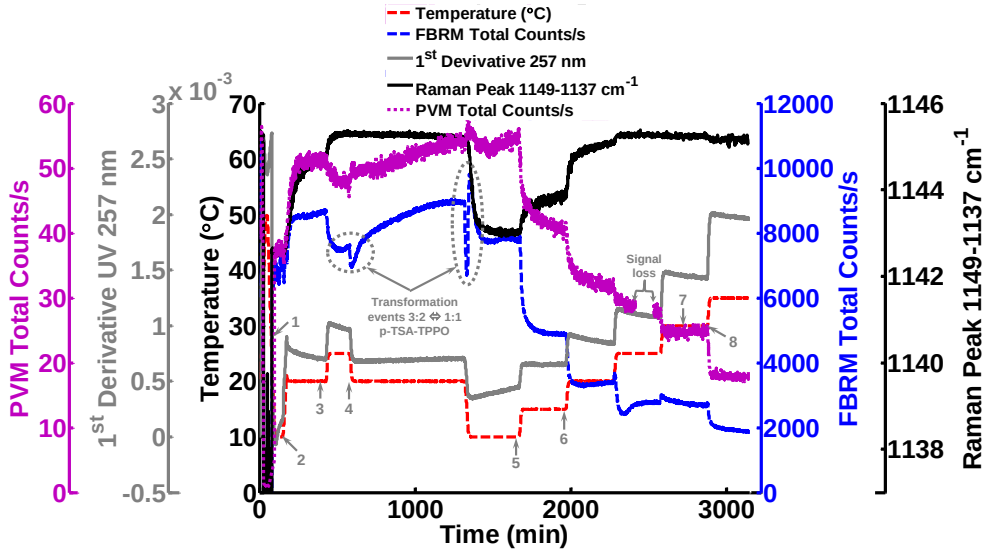

1 = Sample1 at 91 min	4 = sample 4 at 576 min	7 = Sample 2779 at
2 = Sample 2 at 151min	5 = Sample 5 at 1165 min.	8 = Sample 2856 at
3 = Sample 3 at 420 min	6 = Sample 6 at 1977min.	

Figure 8.22: Time diagram of experiment (16) showing the change in Raman signal (peak centre position between 1149 – 1137 cm^{-1}), ATR-UV/vis, FBRM and PVM particle counts/s.

Figure 8.23 (a) and (b) shows the change in composition of the various samples of the co-crystal mixture with time for experiments (15) and (16), respectively, as determined by apply the PLSR and PCR multivariate models developed with the Raman PHAT probe. Both calibration models gave similar predictions of the composition of co-crystal mixtures at the different sampling periods for both experimental runs. The models confirm that a mixture of 1:1 and 3:2 p-TSA-TPPO nucleated in experiment (15) and that the co-crystal mixture is transformed to 1:1 p-TSA-TPPO after ~500 min., which concurs with the discussions earlier relating the second derivative signal of the *in situ* MR immersion probe (i.e. the peak centre shift between 1149 – 1137 cm^{-1}) to the co-crystal composition.

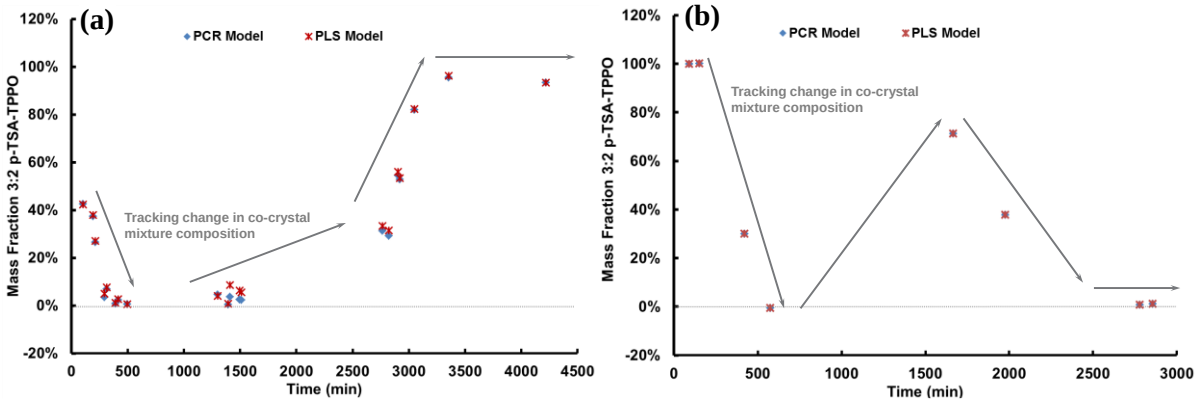

Figure 8.23: Change in co-crystal composition for experiment (15) as determined by off-line Raman PHAT probe *viz* multivariate PLSR and PCR calibration models.

For experiment (16), the calibration models predicted that pure 3:2 p-TSA-TPPO was formed initially, which was then converted to a mixture of 1:1 and 3:2 p-TSA-TPPO and finally to pure 1:1 p-TSA-TPPO. Figure 8.24 shows the correlation diagram of the *in situ* Raman MR immersion probe measurement for peak centre position shifts between 1149 – 1137 cm^{-1} and the co-crystal composition as determined by off-line measurement using the PHAT probe with the multivariate calibration models for experiments (14), (15) and (16).

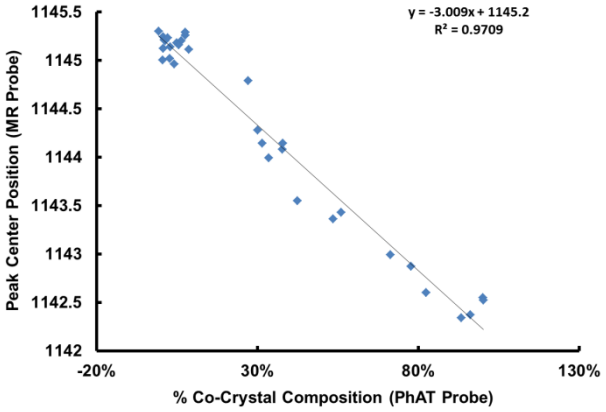

Figure 8.24: Correlation diagram showing the relationship between Raman *in situ* MR probe and PHAT probe measurements.

The correlation coefficient indicates that there is good agreement between the two Raman measurements. With this information, it is therefore possible to quantitatively determine the amount of each co-crystal form present at any given time in the process using the *in situ* probe. An illustration of this point is presented in Figure 8.25, which shows experimental run (17) with several temperature cycles. Notice that despite the implementation of identical temperature cycles that different co-crystal outcomes were observed, that is, based on the Raman MR immersion probe measurements. This experiment was carried out in the region of the ternary phase where a mixture was expected to nucleate. It highlights, the variability that can sometimes occur in a batch process. Off-line analysis using the PHAT probe can be applied to validate the experimental observations from the in situ measurements. These two approaches, that is, on-line and offline measurement serve as a robust means of tracking and quantifying the changes which occur when phase transformation events take place. This has been clearly demonstrated from the results presented earlier. Further validation of the results present came from the analysis of samples by Raman microscopy, off-line ATR-FTIR and HPLC.

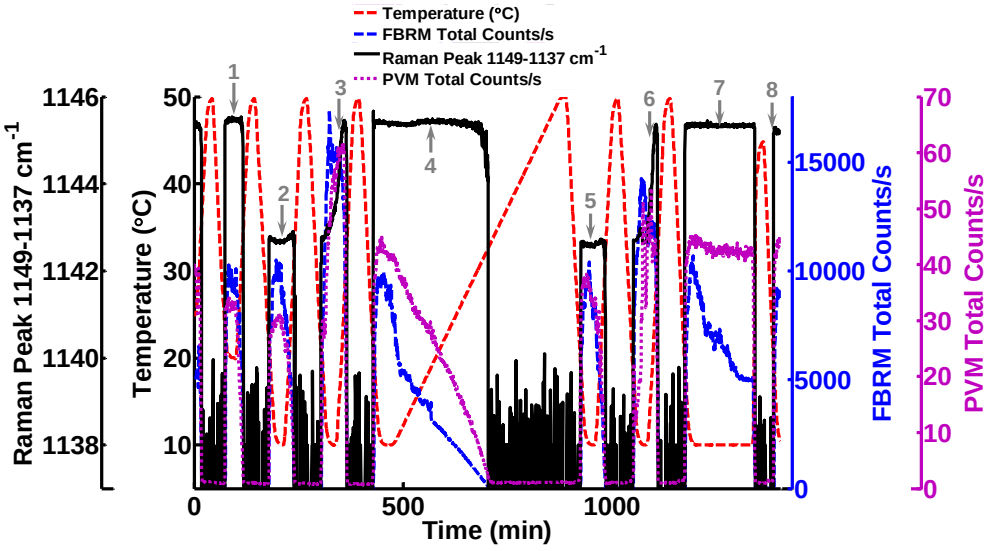

1 = 1:1 form nucleates	4 = 1:1 form nucleates	7 = 1:1 form nucleates
2 = 1:1 and 3:2 mixture	5 = 1:1 and 3:2 mixture	8 = 1:1 form nucleates
3 = Mixture => 1:1 form	6 = Mixture => 1:1 form	

Figure 8.25: Time diagram showing changes in co-crystal composition for experiment (17) as determined by *in situ* Raman MR immersion probe.

8.3.3 Semi-Batch Co-Crystallisation Monitoring and Control

The semi-batch co-crystallisation of p-TSA with TPPO was explored under flow conditions whereby a fixed concentration of the two starting materials dissolved in MeCN are pumped separately and then combined and mixed in a batch crystalliser (see Figure 8.6). In this study the flow rates of the two components were adjusted to crystallise the desired stoichiometric form of the p-TSA-TPPO co-crystal system. This operating strategy offers a promising alternative to batch, and could potential lend itself to further development into a continuous or periodic flow co-crystallisation operation. Table 8.9 provides a summary of the co-crystallisation outcomes for each of the semi-batch experimental runs.

Table 8.9: Summary of co-crystallisation outcomes for the experiments 19 – 26, co-crystal form determined by on-line and off-line measurements.

Exp No.	Mass Fractions (M) in Crystalliser			HPLC Ratio p-TSA/TPPO	p-TSA-TPPO Co-Crystal Form	Region of Phase Diagram
	p-TSA	TPPO	MeCN			
19	0.12	0.09	0.79	1.479	3:2	1 (3:2 form)
20	0.14	0.05	0.81	1.522	3:2	1 (3:2 form)
21	0.09	0.08	0.83	1.313	1:1 + 3:2	3 (mixture)
22	0.06	0.09	0.85	1.002	1:1	2 (1:1 form)
23	0.10	0.08	0.82	1.475	3:2	3 (mixture)
24	0.08	0.08	0.84	1.333	1:1 + 3:2	3 (mixture)
25	0.11	0.07	0.82	1.475	3:2	1 (3:2 form)
26	0.12	0.12	0.76	1.021	1:1	2 (1:1 form)

Figure 8.26 (a) and (b) shows the process time diagrams with temperature profile and on-line PAT signals from FBRM (solid phase), ATR-UV/vis (solution phase), ATR-FTIR (solution phase) and Raman (co-crystal form and solution phase monitoring) for experiment 19. The co-crystal form obtained from this experiment was pure 3:2 p-TSA-TPPO as confirmed by both on-line (Raman MR immersion probe) and off-line (HPLC, PXRD, Raman microscope and ATR-FTIR) measurements. Experiments 20 – 25 (Table 8.9) were carried out under similar process conditions to experiment 19, meaning the process temperature (varying from 25 ^{o}C to 20 ^{o}C) and concentrations of p-TSA (0.2987 g/g MeCN) and TPPO (0.1492 g/g MeCN) in the feed vessels were exactly the same. The main difference between these runs is the mass flow rate of p-TSA and TPPO from the feed vessels (Figure 8.9) to the crystalliser. The results show that by changing the mass flow rate of either p-TSA or TPPO, one can change the mass fraction composition of materials in the crystalliser and thereby control the co-crystallisation outcome. When the flow rate is adjusted so that the mass fractions of p-TSA and TPPO are similar, the resulting mixture falls into Region 3 of the ternary diagram and hence two co-crystal forms were obtained, for example, as observed from experiments 21 and 24 (Table 8.9).

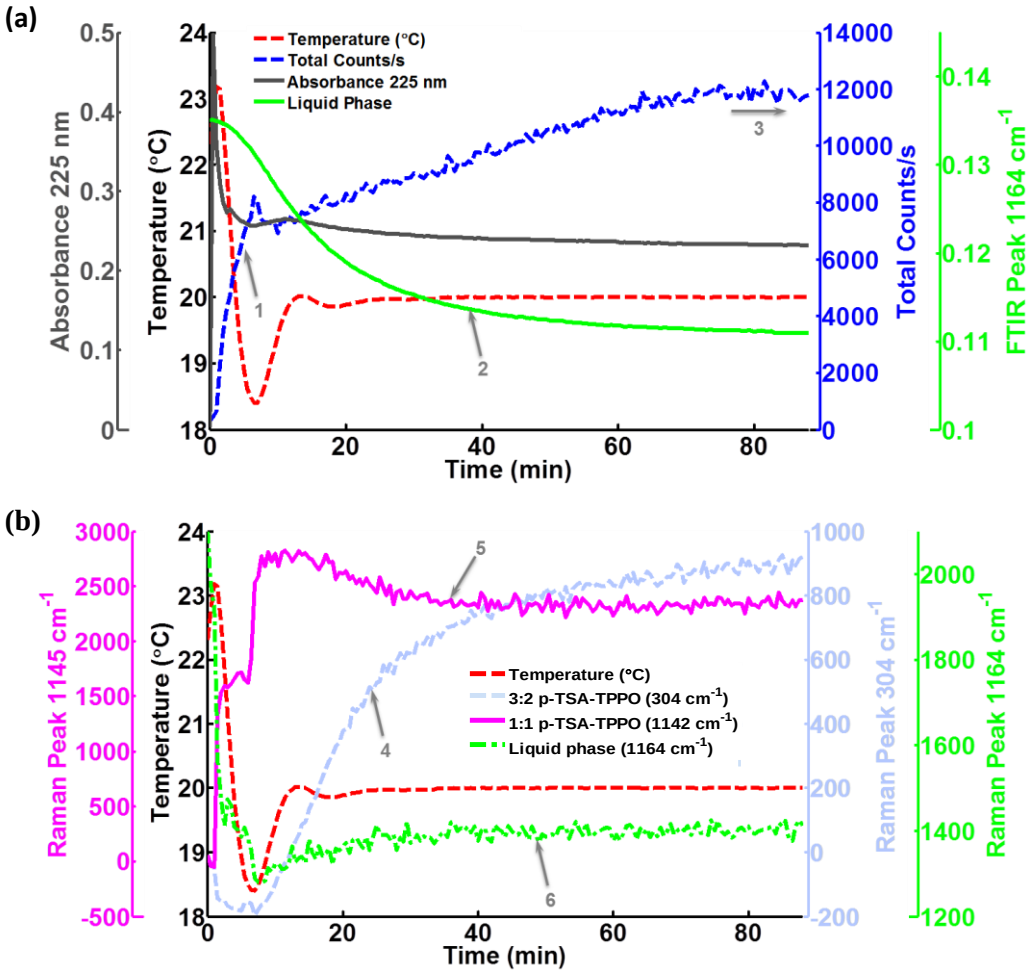

Figure 8.26: Process time diagrams of experiment 19 showing the temperature profile, (a) FBRM total particle counts/s (solid phase monitoring) and the change in absorbance and peak intensity readings from ATR-UV/vis and ATR-FTIR probes used to monitor the liquid phase; and (b) changes in the 2nd derivative Raman peak intensities associated with 1:1 and 3:2 p-TSA-TPPO, and the liquid phase. Arrows show respectively, nucleation (FBRM counts/s) (1), decreasing solute in solution phase (2), crystal growth (3), increasing 3:2 p-TSA-TPPO peak (4), 1:1 p-TSA-TPPO peak (5), and change in solution phase (6).

Indeed, the semi-batch co-crystallisation experiments were more consistent in terms of co-crystallisation outcomes when compared to the batch runs described earlier (Section 8.3.1). Moreover, slight changes in the mass flow rate of either p-TSA or TPPO can alter the co-crystallisation outcome favouring either 1:1 or 3:2 p-TSA-TPPO or a mixture. However, these changes can be avoided if the flow rates are controlled appropriately.

Principal component analysis (PCA) is often used in chemometrics to extract the dominant patterns from chemical data. The result is a complementary set of scores and loadings that can be used to visualise trends in the data [188]. PCA analysis was performed on the Raman spectra obtained when pure 1:1 and 3:2 p-TSA-TPPO and mixture of the two co-crystals forms

nucleated; a total of 390 spectra obtained from batch experiments 8, 11, 12 (13) and (18), and semi-batch experiments 19, 21 and 22 were analysed. Figure 8.27 shows the scores plot of principal components 1 and 2 obtained from the analysis. It shows there are three clusters of data corresponding to each of the three co-crystallisation outcomes observed in the studies presented here.

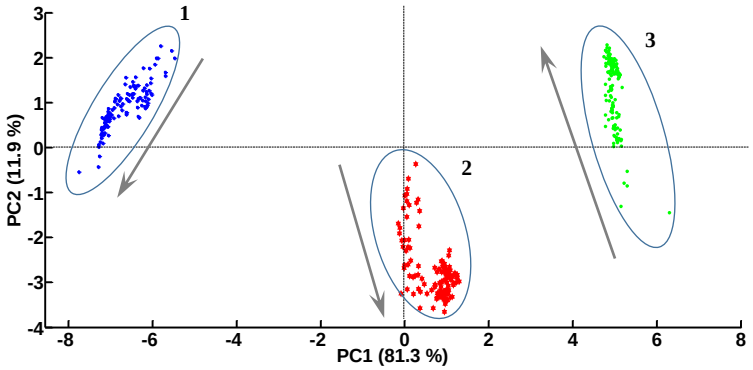

Figure 8.27: PCA scores plot of Raman spectra from different experiments, cluster 1 (3:2 p-TSA-TPPO), cluster 2 (mixtures of 1:1 and 3:2 p-TSA-TPPO) and cluster 3 (1:1 p-TSA-TPPO). Arrows show the direction of increasing amounts of solids as the crystallisations progress.

Analysis of the PCA scores plot allows for the further identification and confirmation of the co-crystal form obtained from each experiment and shows the diversity of applications possible using the *in situ* Raman MR immersion probe. PC1 and PC2 combined represent 93.2 % of the spectral variance. Clusters 1, 2 and 3 represent co-crystal forms were 3:2 p-TSA-TPPO, mixture of 1:1 and 3:2 p-TSA-TPPO and 1:1 p-TSA-TPPO, respectively. Arrows show the direction of increasing amount of solids as the crystallisation progresses. PCA can be used as an additional tool to monitor and characterise the co-crystallisation process, providing valuable information pertaining to the crystalline form that nucleates and grows. It could be used qualitatively as an initial screening method to support the development of the co-crystallisation with *in situ* Raman MR immersion probe.

8.3.4 Periodic Flow Co-Crystallisation Monitoring and Control

The semi-batch experiments reported earlier were used as a guide to inform the development periodic flow crystallisation approaches for producing pure 1:1 and 3:2 p-TSA-TPPO, respectively. Table 8.10 below provides a summary of the co-crystallisation outcomes for experiments carried out in single-stage and three-stage PMSMPR configurations (Section 8.2.5; Figure 8.7). In all experimental runs the co-crystal form obtained was the form expected based on the operating region in the ternary phase diagram (Figure 8.1).

Table 8.10: Summary of experimental conditions employed during the periodic flow crystallisation of p-TSA-TPPO co-crystals.

Exp. No.	Component Mass Fractions (M)			Temperature (°C)			p-TSA-TPPO Co-Crystal Form	Region of Phase Diagram
	p-TSA	TPPO	MeCN	MSMPR 1	MSMPR 2	MSMPR 3		
(27)^	0.14	0.05	0.81	5	n/a	n/a	3:2	1 (3:2 form)
(28)^	0.14	0.05	0.81	15	n/a	n/a	3:2	1 (3:2 form)
(29)	0.14	0.05	0.81	12.5	n/a	n/a	3:2	1 (3:2 form)
30	0.06	0.09	0.85	12.5	n/a	n/a	1:1	2 (1:1 form)
31	0.06	0.09	0.85	20	n/a	n/a	1:1	2 (1:1 form)
32	0.06	0.09	0.85	25	n/a	n/a	1:1	2 (1:1 form)
33	0.14	0.05	0.81	20	17	14	3:2	1 (3:2 form)
34	0.14	0.05	0.81	25	20	20	3:2	1 (3:2 form)
35	0.06	0.09	0.85	25	20	20	3:2	2 (1:1 form)
36	0.06	0.09	0.85	20	17	14	3:2	2 (1:1 form)

No brackets = coupled addition/withdrawal; Brackets () = decoupled addition/withdrawal; ^stirring set to 450 rpm, for all other experiments the stirring rate was set to 500 rpm.

Figure 8.28 below shows the process time diagrams and FBRM statistical trends of the single-stage PMSMPR experiments (27)^, (28)^ and (29). For each of these experiments the process was operated in Region 3 of the ternary phase diagram where 3:2 p-TSA-TPPO shows stability. In each case the decoupled periodic flow method was applied. A state of controlled operation (SCO) was not achieved in any of these experiments due to issues with particle settling during the crystallisations (confirmed by visual observation). This was due to the fast growth rate of the system leading to the formation of millimetre size particles elongated prismatic particles (Figure 8.4). The operating temperatures were selected to control supersaturation and investigate the best operating condition that led a balance between growth and secondary nucleation. For example, the operating temperatures for experiments (27)^, (28)^, (29) as indicated in Table 8.10 led to supersaturation levels of 3.28, 2.50 and 2.74 (i.e. with respect to 1:1 p-TSA-TPPO), respectively. Due to the fast crystal growth rate of 3:2 p-TSA-TPPO, predominantly large crystals were observed for each experiment, which had a tendency of settling to the bottom of the crystalliser.

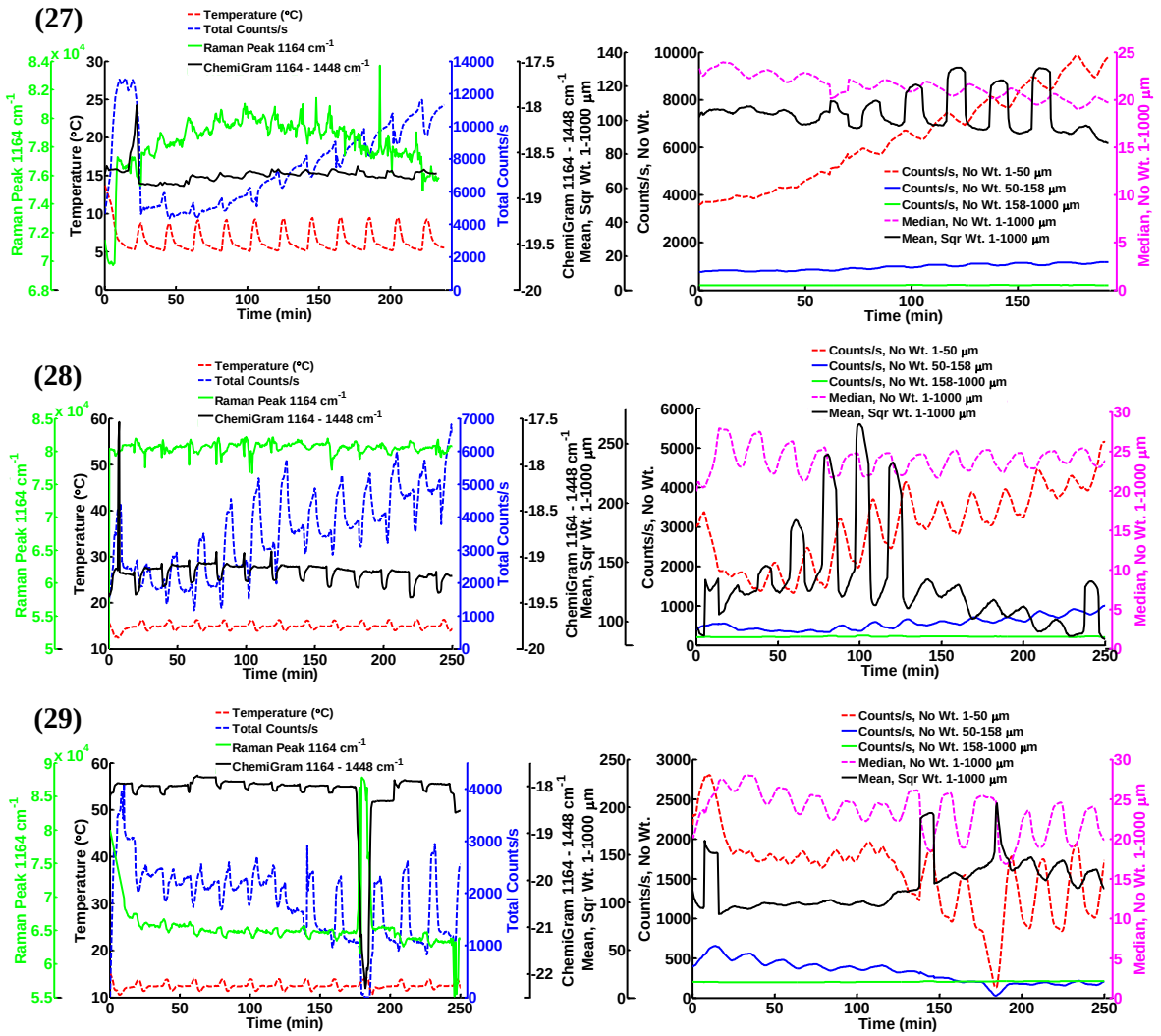

Figure 8.28: Time diagrams (left) and FBRM statistics (right) for experiments (27), (28) and (29).

The time diagrams of the FBRM trends show the no weighted statistics for the median and mean square weighted chord length (MSWCL) and the no weighted counts/s for different particle size ranges corresponding to small (1 – 50 µm) and medium (50 – 158 µm) and large (316 – 1000 µm) particles. The FBRM data are complex, indicating on the one hand persistent secondary nucleation for experiments (27)^ and (28)^, seen as an increase in the 1 – 50 µm counts/s and marginal decrease in the median and MSWCL, respectively. On the other hand, this could be an indication of particles settling, such that smaller particles are detected preferentially due to their low settling velocities compared to larger ones. Hence, the stirring rate (which was already high) was adjusted stirring rate adjusted from 450 rpm (experiments (27)^ and (28)^) to 500 rpm (experiment (29)), but significant effect on particle suspension was observed. Stirring rates above 500 rpm led to bubbles and vortex formation which were not desirable when transfer of material out of the crystalliser by pumping, due to inconsistencies flow rates. Another interpretation of the results could be the measurement of short chords by the

FBRM due to an increase in the length of the 3:2 p-TSA-TPPO crystals as they grow to become elongated prisms. Interestingly, for experiment (29), there is a decrease in the 1 – 50 µm with a simultaneous, but slight decrease in the median, but increase in the MSWCL. This result differs from experiment (27)^ and (28)^, due to blockage problems encountered in this experiment, which lead to the disturbances observed in the signals. The microscope images of the product crystals obtained from experiments (27)^, (28)^ and (29) are shown in Figure 8.29 below. The images show that for all three experimental runs, millimetre size crystals are present. Evidently, larger crystals were observed for experiments (28)^ which operated at a lower supersaturation level compared to (27)^ and (29).

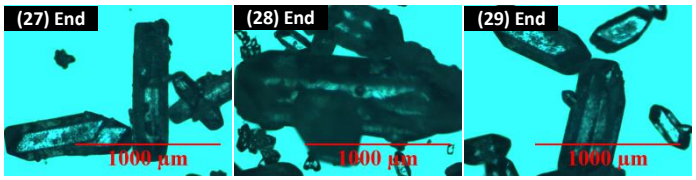

Figure 8.29: Microscope images of crystals from experiment (27)^, (28)^ and (29).

Figure 8.30 below shows the process time diagram and FBRM statistics for experiment 30. The coupled period flow method was employed for this experiment, due to the issues observed during the decoupled PMSMPR runs reported in earlier chapters of this thesis, for example, the longer time taken to achieve SCO compared to coupled PMSMPR operation. For experiment 30, the multivariate models built for concentration measurement of the two AAIs (p-TSA and TPPO) concomitantly (Chapter 3, Section 3.6.1) were employed. The process time diagram shows that for this experiment, SCO was attained at ~100 min. However, there is significant oscillation of the FBRM total counts/s for the attainment of SCO onwards. The FBRM counts/s oscillates between 8500 and 11900 counts/s. The high amplitudes are a result of the competing secondary nucleation and growth. Figure 8.31 shows the images of product crystals collected at 100, 180 and 250 min, respectively. The microscope images support the suggestion that the two crystallisation mechanisms are in competition as there is a mixture of large and fine crystals for all samples collected during SCO operation. Experiments 31 and 32 reported in Table 8.10 were not completed due to significant blockage issues arising due to the very large crystals obtained in these from these runs. This can be attributed to the lower operating supersaturation whereby crystal growth is promoted over secondary nucleation. The supersaturation level for experiment 30 was 2.51, compared to 1.86 and 1.49 for experiments 31 and 32, respectively.

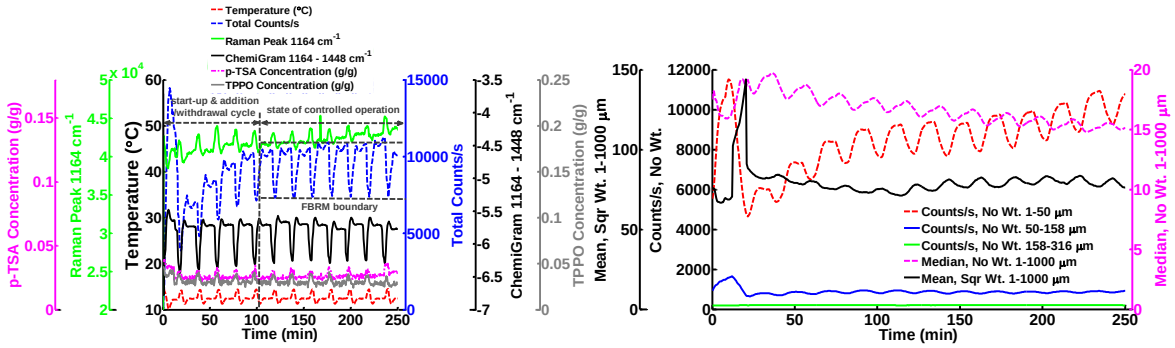

Figure 8.30: Time diagram (left) and (FBRM statistics (left) for experiment 30.

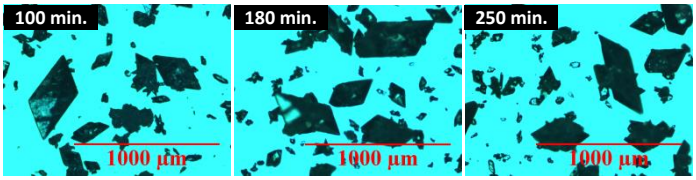

Figure 8.31: Microscope images of crystals from experiment 30.

Several PMSMPR three-stage experiments were carried out in coupled periodic flow mode to investigate control over the supersaturation generation and thus try to manipulate the crystal size for both the 1:1 and 3:2 co-crystal forms, as highlighted in Table 8.10, for all of these experiments the expected co-crystal form was obtained. This is an indication of the consistent results that can be obtained with the PMSMPR operation in comparison to the batch runs reported on earlier. However, the significant issue of particle size control for each of the co-crystal forms could not be achieved in three-stage PMSMPR. It may be that further investigation is required and process modelling and optimisation implemented in order to identify the conditions for producing smaller crystals consistently.

8.4 Conclusions

In this chapter, the cooling co-crystallisation of p-TSA with TPPO AAI ingredients to form pure 1:1 and 3:2 p-TSA-TPPO stoichiometric co-crystals or their mixtures from MeCN was demonstrated in laboratory scale batch, semi-batch and single- and three-stage cascaded PMSMPR crystallisers. Monitoring and control of the selective co-crystallisations was achieved with the aid integrated PAT array within the IDS. Three regions of the ternary phase diagram of p-TSA/TPPO/MeCN corresponding to the formation of the pure co-crystals as well as mixtures were explored by changing the mass fraction compositions of p-TSA/TPPO/MeCN in the crystallisers investigated. In the batch study, there were some consistent results. However, batch-to-batch variability issues were occasionally encountered. It was demonstrated that if appropriate strategies are implemented using PAT tools that the crystallisation can be controlled

and directed towards the desired outcome. This was demonstrated *viz* the implementation of temperature cycles to convert from the 3:2 to 1:1 co-crystal form and vice versa. The temperature was changed based on *in situ* Raman spectroscopy, validated with off-line Raman measurements. Using the *in situ* Raman method, transformation of the co-crystal forms could be tracked. Furthermore, quantitative information on the proportions of 3:2 to 1:1 p-TSA-TPPO was also obtained by application of multivariate methods to the *in situ* (MR immersion probe) and off-line (PHAT probe) Raman data. The temperature cycling approach is presented as a proof of concept approach for the control of crystalline form during co-crystallisation, which prior to now was only been demonstrated for polymorphic single component molecular systems. The study demonstrates the use of PAT to monitor the transformation events for a co-crystallisation process in which solution mediated transformation from one stoichiometric crystalline form to another occurs. The information obtained was used to aid the control of the batch co-crystallisation process in order to obtain the desired crystalline form when operating at different temperatures outside the range of the ternary phase diagram. Semi-batch co-crystallisation studies were also carried out for comparison with the batch method. In these experimental runs solutions of fixed concentrations of the two AAIs (p-TSA and TPPO) were prepared in separate vessels. In this proof of concept study, the co-crystallisation was controlled by changing the flow rate of the dissolved materials to the crystalliser. It was demonstrated that by changing the flow rates, the mass fraction of components sent to the crystalliser could be controlled, thereby controlling the outcome of the co-crystallisation. This operation is a promising alternative to batch, providing better control over the co-crystallisation outcome and could potentially be developed into a continuous or periodic flow co-crystallisation process. Periodic flow experiments were performed in single- and three-stage cascaded crystallisers, respectively. While consistent results were observed and the desired co-crystal form produced in consecutive experimental runs, there were significant issues with control over the product particle size. This led to settling and transfer line blockage issues in the single and three-stage PMSMPR operations. These issues could not be resolved over the timeline of the study, therefore further work is recommended along the lines of process modelling and optimisation aimed at identifying better supersaturation conditions which would avoid the formation of very large crystals. The studies presented in this chapter show that on-line PAT tools complemented by off-line solid state characterization techniques can be applied together to gain a better understanding of the crystallisation behaviour of p-TSA-TPPO co-crystal system. This led to the development of robust control strategies using either temperature or flow rate control to influence the co-crystallisation outcome.

Main Conclusions

In this thesis, the dynamics of batch crystallisation, a novel continuous MSMPR configuration and a novel operating strategy in MSMPR, known as periodic flow crystallisation (PMSMPR) were investigated and compared. The dynamics of these processes are vastly different and hence there are differences in the way supersaturation is generated as a result of the different trajectories through the phase diagram. The PMSMPR method of operation involves periodic transfer of slurry (addition and withdrawal) at high flow rates. The PMSPPR is therefore characterised by periodic withdrawal of product slurry. Different concepts in crystallisation control using batch, semi-batch, MSMPR and PMSMPR platforms were demonstrated for the crystallisation of different molecular systems that exhibit different crystallisation kinetics and crystalline forms. The various crystallisation platforms were applied to crystallise: (1) slow growing PCM-IPA system, (2) fast growing GLY-H_2O system, (3) UBA polymorphic co-crystal system and, (4) p-TSA-TPPO stoichiometric co-crystals. Optimised batch and continuous MSMPR experiments indicated that different crystal CQA were attainable for the slow-growing PCM-IPA system in each platform. However, the continuous MSMPR which was operated at steady-state shows more consistency in the product crystal CQA. Inevitably, the yield of crystallisation in a single-stage MSMPR was much lower compared to batch, but the productivity of crystallisation is significantly higher. The yield was improved by using a multi-stage MSMPR cascade. Issues were encountered with fouling, transfer line blockages and encrustation in the continuous MSMPR. The use of an additive, HPMC, was investigated to control the continuous crystallisation process. While the additive effectively controlled the crystallisation and led to faster establishment of a steady-state operation, suppression of the growth and nucleation kinetics of PCM was evident, which reduces the yield of the MSMPR. In an industrial context, it is foreseeable that additives from the list of substances generally regarded as safe (GRASS) could be used to control the crystallisation outcome thereby leading to in spec product of desired CQA. However, the amount of additive to be applied requires careful consideration, due to the potential effects on the crystallisation kinetics as demonstrated in this thesis

In order to alleviate the issues encountered in the continuous MSMPR, an alternative crystallisation strategy was investigated *viz*. periodic flow operation. This novel operating strategy involves combining the best aspects of batch and continuous MSMPR operation to improve the crystallisation outcomes for PCM-IPA system, and opens up the possibility of using flow crystallisation for other slow-growing systems. Due to the slow growth kinetics of PCM, the tuneable batch (or holding) period in the periodic mixed suspension mixed product removal (PMSMPR) operation is important, since mean the residence time of material can be

extended significantly relative to continuous MSMPR operation, whilst narrowing the RTD slightly. A novel concept referred to as “periodic steady-state” was introduced to describe when the PMSMPR operation reached a state of controlled operation. Periodic steady-state is defined as a state of a system that maintains itself despite the transitory effects caused by periodic, but controlled disruptions applied to the system (i.e. “state of controlled operation”). The work also illustrated the concept of “state of controlled operation” instead of “steady-state operation” as a state that can characterize periodic (or continuous) operation. The PMSMPR was configured as either a single-, two-, or three-stage unit and operated for up to 11 mean residence times without blockage or encrustation problems. The number of PMSMPR stages, seed properties (size, shape and distribution), mode of operation (i.e. coupled or decoupled) and use of recycle stream were the main variables that influenced the periodic operation, significantly affecting the extent of secondary nucleation and growth. Seed material selection was shown to affect the product distribution with “fine” high surface area seed leading to broader CSD compared to “coarse” low surface area seed. This has implications for the filtration, formulation and ultimately the therapeutic properties of a drug product, and it demonstrates the importance of selecting the appropriate seed recipe for a crystallisation process.

Adjustment of the PMSMPR holding period could also affect the product distribution, however this parameter was not investigated in this study. It is expected that this could have a significant effect on the particle attributes and CSD in the PMSMPR operation. For example, longer holding times could lead to greater yield, larger crystals, narrow CSD and allow for polymorphic transformations to achieve completion. Based on the results from the PMSMPR studies presented in this thesis, the best operating strategies for a slow growing system are: seeding with well-defined crystalline material, long residence times (i.e. depending on the observed growth kinetics) and coupled multi-stage PMSMPR (consisting of at least three-stages). For fast growing systems that same strategies apply, except that a short residence time is should be targeted and a maximum of two PMSMPR stages used in coupled periodic flow mode. The stage temperatures of the PMSMPR for fast or slow growing systems should be carefully selected to find a balance between growth and secondary nucleation. The choice of conditions will depend on the target product CQA, which should be clearly defined at the outset. The choice of recycle depends on the whether material conservation is important for a given process (which will be driven by the economics factors) and the impurity profile of the starting material. In the case of polymorphic systems or where different crystalline forms exist for a given material, a systematic approach is recommended, first using batch crystallisation to assess the system dynamics and then deciding on a suitable approach for periodic flow crystallisation in PMSMPR.

The periodic flow crystallisation operation was further demonstrated as a proof-of-concept for the crystallisation of GLY-H_2O system. GLY is a fast growing API which shows markedly different crystallisation kinetics (nucleation and growth) from PCM. In this study, the effect of seed properties, product withdrawal strategy, rate of supersaturate generation and decoupled or coupled periodic flow operation on the product crystal CQA were investigated and found to influence the crystallisation outcome to varying extents. The properties of the seed crystals appear to the most significant variable affecting the product size, shape and CSD. In this study, dynamic models of the residence time distribution in continuous MSMPR and periodic flow PMSMPR crystallisers were developed. The model demonstrated the periodic flow operation in terms of extended mean residence time and slightly narrower residence time distribution. In addition, process models of periodic flow process were developed with an aim to provide a better understanding and improve the performance of the operation. The modelling framework was based on the Process System Enterprise's gCRYSTAL software, wherein the crystallisation mechanisms and kinetics of the GLY-H_2O system were estimated from batch cooling crystallisation experiments. Experiments of periodic flow crystallisations were also conducted in single- / three-stage MSMPR crystallisers to validate the process models. Good agreements were obtained between the model predictions and the experimental measurements. Importantly, significant larger crystals were obtained experimentally and in simulation compared to the batch or continuous MSMPR systems, demonstrating the advantages of using periodic flow operation.

Control over polymorphism is critical in industrial crystallisation of fine chemicals since the polymorphic form has a significant influence on the physical attributes of the material. This can prove even more challenging for multi-component co-crystal systems. Polymorph control of the UBA co-crystal system, which has three know polymorphic forms was investigated in three-stage cascaded periodic flow PMSMPR crystallisers. Different start-up strategies were explored and their ability to produce selectively a particular polymorph of UBA was investigated. The experimental conditions for producing pure UBA form I was optimised in the PMSMPR cascade. However, pure UBA form III remained elusive (i.e. it was difficult to obtain consistently), while UBA form II was never observed due to stability issues with this metastable polymorph. It may be that here are too many input variables to consider and perhaps only process modelling and simulation can give the best conditions for optimisation in order to improve the crystallisation outcomes for the UBA co-crystal system. Furthermore, UBA forms I and III showed strikingly similar physicochemical properties (e.g. solubility and melting points) and it was unclear which of the co-crystal form was more stable. However, despite these challenges UBA form I was isolated using either seeding (with pure form I) or by fast mixing of urea and barbituric acid solutions at low temperatures (below 30 ^oC) in PMSMPR. A

cascade of PMSMPR was required to give a longer residence time for complete transformation to UBA form I. Relative to batch and continuous crystallisations, the periodic flow process was more consistent in producing UBA form I. Furthermore, the study demonstrated that periodic flow operation can provide an alternative trajectory in the phase diagram which can lead to desired crystallisation outcomes if tuned appropriately by selecting the batch and continuous operating periods.

Finally, the selective co-crystallisation of two model active agro-chemical ingredients, p-TSA and TPPO was demonstrated in batch, semi-batch and periodic flow crystallisers. Regions of the p-TSA/TPPO/MeCN ternary phase diagram that corresponded to the stability of the respective stoichiometric co-crystal forms of p-TSA-TPPO, that is, 1:1 and 3:2 (mole ratio) were explored. Batch-to-batch variability issues were encounter for the batch studies, however, the implementation of temperature cycles triggered by quantitative Raman spectroscopy which detected the stoichiometric form being produced and led to better control over the co-crystallisation form obtained and allowed for investigation of the solution mediated transformation from 3:2 to 1:1 p-TSA-TPPO and vice-versa. On the other-hand, the semi-batch and PMSMPR studies gave much more consistent control over the co-crystal form relative to batch, with a feed mixture in the appropriate region of the phase diagram and without the need for temperature cycling. The desired co-crystal form was produced consistently by manipulating the flow rates of the co-formers (i.e. p-TSA and TPPO) to the semi-batch or PMSMPR crystallisers. Due to the very fast growth kinetics of the co-crystals, large crystals (millimetre size) were obtained that had a tendency to settle. This phenomenon led to classified withdrawal in the PMSMPR and stochastic behaviour, which eventually resulted in blockage of transfer lines.

The crystallisations mentioned earlier were monitored using the integrated process analytical technologies (PAT) and CryPRINS informatics systems software within an IDS framework to determine when equilibrium (batch operation), steady-state (continuous MSMPR operation) or “state of controlled operation” (SCO) (periodic flow PMSMPR operation) is achieved. The online methods were supported by off-line solid-state (e.g. PXRD, DSC, Raman and ATR-FTIR spectroscopy) and wet chemistry methods (e.g. HPLC). The results presented in this thesis illustrate the use of PAT and information system tools together to determine when batch, continuous and periodic operations reach a controlled state of operation. These tools provided a better understanding of the variables and operating procedures influencing these operations. The need for an integrated array of PAT sensors was driven by the need to grasp a holistic understanding of the process, since the results from a single PAT sensor cannot be interpreted unambiguously. PAT sensors must also be selected carefully in order to capture the most

useful information about a given system. In this thesis *in situ* Raman spectroscopy was used extensively and can be considered one of the most powerful tools for information gathering since it has the capability to sense multiple solution components, plus solid phase properties (i.e. polymorphs and other crystalline forms). FBRM and PVM were used extensively as they both give useful information on how the particles evolve during a crystallisation process. *In situ* ATR-UV/vis was useful for monitoring solution phase (conjugated systems only) without interference from the solid phase. The use of *in situ* ATR-FTIR was also investigate, however, this was the least useful technique for solution phase monitoring due primarily to the requirement for high solute concentrations, but also to the slight but noticeable effect of particle scattering on the process signal and the sensitivity of the fibre optic cable to the slight movements or disturbance.

Another significant aspect of this thesis was the use of PAT tools (i.e. spectroscopy techniques only) for the development of multivariate calibration models. Most notable was the use of Raman spectroscopy to monitor and quantify solute concentration and composition of solid phase. Raman is the most promising technique for multivariate data analysis, due to the ability to quantify solution and solid phase composition.

Recommendations

The modified continuous MSMPR operation and novel periodic flow operating strategy presented in this thesis could be explored further for the crystallisation of a wider range of compounds.

The design of the modified continuous MSMPR crystalliser could be optimised by developing the simulation and process models for the system. In particular, investigation of the hydrodynamic and population balance models together could shed light on ways to improve their performance. Due to the complexity of the system, it is difficult to explore process optimisation experimentally, hence initial modelling and simulation *in silico*, with later experimental validation is necessary. In addition, a cascade of MSMPR could be investigated for controlled supersaturation generation and more stable operation. MSMPR cascade can give (a) better yields, and (b) allows more degrees of freedom (i.e. the various stage temperatures and possible stage residence times) to tailor product properties.

There were some problems with the product CSD for GLY-H_2O system, either due to the kinetic parameters used in the simulations or the limited range of the crystallisation experiments performed, which led to undesirable mismatch for the cascaded three-stage PMSMPR operation. Further investigation is therefore required to improve either the model predictions or expand the range of experimental conditions. Besides the analysis of the possible reasons for the mismatch in the CSD, future work could consider benchmark experiments of conventional continuous MSMPR crystallisation upon which the benefits of periodic flow crystallisation processes could be demonstrated more clearly in terms of crystal attributes, yield and productivity. Model identification is an important consideration, for example in the case of GLY crystallisation further work is required to (a) expand the range of data collected experimentally and (b) investigate different model assumptions with respect to phenomena such as agglomeration, secondary nucleation, breakage, and so on.

The periodic flow crystallisation process also requires further investigation and characterisation at laboratory scale to determine the effect of batch holding and continuous withdrawal cycles on the system stability and product CQA, as well as to investigate the most effective start-up procedures and the time to achieve a “state of controlled operation”. While the crystallisation kinetics were estimated for GLY based on batch experimental data and the population balance models for the system developed, process optimisation was not investigated. This is an essential step to perform in order to identify the best operating conditions for the crystallisation of product with desired CQA. Process simulation

(demonstrate for GLY system in this thesis) is required as a route to optimisation since it gives useful information about the crystallisation mechanism and kinetics.

Aspects of parameter estimation, process modelling and simulation could also be investigated for the co-crystal systems presented in this thesis. This will inform process optimisation steps that can lead to further demonstration of the periodic flow crystallisation concept.

Further investigations of the polymorphism control in the PMSMPR are required, in particular for single component molecular systems (which were not covered in this thesis).

References

[1] U. Vollmer, “H-∞ Control of a Continuous Crystallizer,” *Control Eng. Pract.*, vol. 9, pp. 837–845, 2001.

[2] J. Chen, B. Sarma, J. M. B. Evans, and A. S. Myerson, “Pharmaceutical Crystallization: Published as Part of the Crystal Growth & Design 10th Anniversary Perspective,” *Cryst. Growth Des.*, vol. 11, pp. 887–895, 2011.

[3] B. Kratochvíl, “Solid Forms of Pharmaceutical Molecules,” *Glas. Amorph. Nano-Crystalline Mater.*, pp. 1–8, 2011.

[4] P. Barrett, B. Smith, W. Joerg, V. Bracken, B. O’Sullivan, and D. O’Grady, “A Review of the Use of Process Analytical Technology for the Understanding and Optimization of Production Batch Crystallization Processes,” *Org. Process …*, vol. 9, no. 3, pp. 348–355, 2005.

[5] N. S. Tavare, *Industrial Crystallization: Process Simulation Analysis and Design*. New York: Plenum Press, 1995.

[6] A. S. Myerson, *Handbook of Industrial Crystallization*, 2nd ed. Butterworth Heinemann, 2002.

[7] S. D. Schaber, D. I. Gerogiorgis, R. Ramachandran, J. M. B. Evans, P. I. Barton, and B. L. Trout, “Economic Analysis of Integrated Continuous and Batch Pharmaceutical Manufacturing: A Case Study,” *Ind. Eng. Chem. Res.*, vol. 50, no. 17, pp. 10083–10092, Sep. 2011.

[8] H. Zhang, J. L. Quon, A. J. Alvarez, J. M. B. Evans, A. S. Myerson, and B. L. Trout, “Development of Continuous Anti-Solvent/Cooling Crystallization Process using Cascaded Mixed Suspension, Mixed Product Removal Crystallizers,” *Org. Process Res. Dev.*, vol. 16, no. 5, pp. 915–924, May 2012.

[9] A. D. Randolph and M. A. Larson, *Theory of Particulate Processes*. New York: Academic Press, 1971.

[10] K. Plumb, “Continuous Processing in the Pharmaceutical Industry,” *Chem. Eng. Res. Des.*, vol. 83, no. 6, pp. 730–738, Jun. 2005.

[11] R. Maria, D. B. Alves, C. Augusto, D. I. Gerogiorgis, and P. I. Barton, “Steady-State Optimization of a Continuous Pharmaceutical Process,” *Comput. Aided Chem. Eng.*, vol. 27, pp. 927–932, 2009.

[12] M. Sen, A. Rogers, R. Singh, A. Chaudhury, J. John, M. G. Ierapetritou, and R. Ramachandran, “Flowsheet optimization of an integrated continuous purification-processing pharmaceutical manufacturing operation,” *Chem. Eng. Sci.*, vol. 102, pp. 56–66, Oct. 2013.

[13] A. J. Alvarez, A. Singh, and A. S. Myerson, “Crystallization of Cyclosporine in a Multistage Continuous MSMPR Crystallizer,” *Cryst. Growth Des.*, vol. 11, no. 10, pp. 4392–4400, Oct. 2011.

[14] H. Leuenberger, “New trends in the production of pharmaceutical granules: batch versus continuous processing,” *Eur. J. Pharm. Biopharm.*, vol. 52, no. 3, pp. 289–296, Nov. 2001.

[15] S. Buchholz, “Future manufacturing approaches in the chemical and pharmaceutical

industry," *Chem. Eng. Process. Process Intensif.*, vol. 49, no. 10, pp. 993–995, Oct. 2010.

[16] M. Sen, A. Chaudhury, R. Singh, J. John, and R. Ramachandran, "Multi-scale flowsheet simulation of an integrated continuous purification-downstream pharmaceutical manufacturing process.," *Int. J. Pharm.*, vol. 445, no. 1–2, pp. 29–38, Mar. 2013.

[17] T. Vetter, C. L. Burcham, and M. F. Doherty, "Regions of attainable particle sizes in continuous and batch crystallization processes," *Chem. Eng. Sci.*, vol. 106, pp. 167–180, Mar. 2014.

[18] R. J. P. Eder, S. Radl, E. Schmitt, S. Innerhofer, M. Maier, H. Gruber-Woelfler, and J. G. Khinast, "Continuously Seeded, Continuously Operated Tubular Crystallizer for the Production of Active Pharmaceutical Ingredients," *Cryst. Growth Des.*, vol. 10, no. 5, pp. 2247–2257, May 2010.

[19] S. Y. Wong, A. P. Tatusko, B. L. Trout, and A. S. Myerson, "Development of Continuous Crystallization Processes Using a Single-Stage Mixed-Suspension, Mixed-Product Removal Crystallizer with Recycle," *Cryst. Growth Des.*, p. A–G, Oct. 2012.

[20] X.-W. Ni, S. Lawton, G. Steele, L. Zhao, and I. Laird, "Continuous Crystallization of Pharmaceuticals Using a Continuous Oscillatory Baffled Crystallizer," *Org. Process Res. Dev.*, vol. 13, no. 6, pp. 1357–1363, 2009.

[21] A. J. Alvarez and A. S. Myerson, "Continuous Plug Flow Crystallization of Pharmaceutical Compounds," *Cryst. Growth Des.*, vol. 10, no. 5, pp. 2219–2228, May 2010.

[22] B. J. Ridder, A. Majumder, and Z. K. Nagy, "Population Balance Model-Based Multiobjective Optimization of a Multisegment Multiaddition (MSMA) Continuous Plug-Flow Antisolvent Crystallizer," *Ind. Eng. Chem. Res.*, vol. 53, no. 11, pp. 4387–4397, Mar. 2014.

[23] A. Majumder and Z. K. Nagy, "Fines Removal in a Continuous Plug Flow Crystallizer by Optimal Spatial Temperature Profiles with Controlled Dissolution." pp. 1–23, 2013.

[24] J. L. Quon, H. Zhang, A. J. Alvarez, J. M. B. Evans, A. S. Myerson, and B. L. Trout, "Continuous Crystallization of Aliskiren Hemifumarate," *Cryst. Growth Des.*, vol. 12, no. 6, pp. 3036–3044, Jun. 2012.

[25] R. Whelan, M. Barrett, H. Hao, and B. Glennon, "Laboratory-Scale MSMPR Classification and Withdrawal Techniques," in *11th International Conference on Chemical & Process Engineering*, 2013, pp. 1–4.

[26] FDA, "Guidance for Industry Q10 Pharmaceutical Quality System," 2009.

[27] L. X. Yu, R. A. Lionberger, A. S. Raw, R. D'Costa, H. Wu, and A. S. Hussain, "Applications of process analytical technology to crystallization processes," *Adv. Drug Deliv. Rev.*, vol. 56, no. 3, pp. 349–369, 2004.

[28] S. Banerjee and N. Bhatwadekar, "Process Analytical Technology (PAT) : Boon to Pharmaceutical Industry," *Pharm. Inf.*, vol. 6, no. 6, pp. 238–247, 2008.

[29] R. D. Braatz and Z. K. Nagy, "Advances and new directions in crystallization control.," *Annu. Rev. Chem. Biomol. Eng.*, vol. 3, pp. 55–75, Jan. 2012.

[30] Z. K. Nagy, G. Févotte, H. Amer, and L. L. Simon, "Recent advances in the monitoring, modelling and control of crystallization systems," *Chem. Eng. Res. Des.*,

vol. 91, no. 10, pp. 1903–1922, Jul. 2013.

[31] Z. K. Nagy, M. Baker, N. Pedge, and G. Steele, “Supersaturation and Direct Nucleation Control of an Industrial Pharmaceutical Crystallisation Process Using a Crystallisation Process Informatics System,” in *Proc. Int.Workshop Ind. Cryst., 18th, Sept 7–9.*, 2011, pp. 101–6.

[32] S. Ferguson, G. Morris, H. Hao, M. Barrett, and B. Glennon, “Characterization of the anti-solvent batch, plug flow and MSMPR crystallization of benzoic acid,” *Chem. Eng. Sci.*, vol. 104, pp. 44–54, Dec. 2013.

[33] M. J. Mollan and M. Lodaya, “Continuous Processing in Pharmaceutical Manufacturing,” 2004.

[34] J. Kossik, “Pharmaceutical Facility Could Boost Capacity and Slash Costs by Trading in Certain Batch Operations for Continuous Versions,” *Pharmaceutical Manufacturing*, 2003.

[35] FDA, “Guidance for Industry PAT — A Framework for Innovative Pharmaceutical Development, Manufacturing and Quality Assurance,” 2004.

[36] H. Kidwell, “Quality by Design - the new manufacturing paradigm,” *Pharmafile*, 2011.

[37] Z. N. Orosianikov, “Continuous Crystallization of Products of Raw Sugar Factories and Refineries,” *Deut. Zuckerind*, vol. 33, pp. 851–852, 1908.

[38] H. Zhang, R. Lakerveld, P. L. Heider, M. Tao, M. Su, C. Testa, A. D’Antonio, P. I. Barton, R. D. Braatz, B. L. Trout, A. S. Myerson, K. F. Jensen, and J. M. B. Evans, “Application of continuous crystallization in an integrated continuous pharmaceutical pilot plant,” *Cryst. Growth Des.*, vol. 14, pp. 2148–2157, Mar. 2014.

[39] R. Lakerveld, B. Benyahia, P. Heider, H. Zhang, R. D. Braatz, and P. Barton, “Averaging Level Control to Reduce Off-Spec Material in a Continuous Pharmaceutical Pilot Plant,” *Processes*, vol. 1, no. 3, pp. 330–348, Nov. 2013.

[40] Girish Malhotra, “The Path Towards Continuous Processing: Opportunities Exist for Increased Revenues, Profits and Innovation,” *Pharma Process*, p. 27 (8) 16–20, 2010.

[41] J. A. DiMasi, H. G. Grabowski, and R. W. Hansen, “Innovation in the Pharmaceutical Industry: New Estimates of R&D Costs,” *J. Health Econ.*, 2016.

[42] J. a. DiMasi, R. W. Hansen, and H. G. Grabowski, “The price of innovation: New estimates of drug development costs,” *J. Health Econ.*, vol. 22, no. 2, pp. 151–185, 2003.

[43] G. S. Calabrese, S. Park, and S. Pissavini, “From batch to continuous flow processing in chemicals manufacturing,” *AIChE J.*, vol. 57, no. 4, pp. 828–834, 2011.

[44] K. Plumb, “Quality BY DESIGN,” *IChemE: the chemical engineer*, London, pp. 36–38, Feb-2013.

[45] FDA, “US Food and Drug Administration, Center for Drug Evaluation and Research, 21 Code of Federal Regulations, Parts 210 and 211 Current Good Manufacturing Practice for Manufacturing, Processing, Packing, or Holding of Drugs,” 2015. [Online]. Available: http://www.accessdata.fda.gov/scripts/cdrh/cfdocs/cfcfr/CFRSearch.cfm?CFRPart=210&showFR=1. [Accessed: 19-Sep-2015].

[46] FDA, “FDA Perspective on Continuous Manufacturing,” 2012. [Online]. Available: http://www.fda.gov/downloads/AboutFDA/CentersOffices/OfficeofMedicalProductsand

Tobacco/CDER/UCM341197.pdf. [Accessed: 19-Sep-2015].

[47] FDA, “Regulatory Expectations of Executive Management,” 2012. [Online]. Available: http://www.fda.gov/downloads/Drugs/DevelopmentApprovalProcess/Manufacturing/UCM324353.pdf. [Accessed: 19-Sep-2015].

[48] A. N. Saleemi, “Strategic feedback control of pharmaceutical crystallization systems,” Loughborough University, 2011.

[49] E. Simone, A. N. Saleemi, N. Tonnon, Z. K. Nagy, Ali N. Saleemi, N. Tonnon, and Z. K. Nagy, “Active polymorphic feedback control of crystallization processes using a combined raman and ATR-UV/Vis spectroscopy approach,” *Cryst. Growth Des.*, vol. 14, pp. 1839–1850, 2014.

[50] Y. Yang, L. Song, and Z. K. Nagy, “Automated Direct Nucleation Control in Continuous Mixed Suspension Mixed Product Removal Cooling Crystallization,” *Cryst. Growth Des.*, vol. 15, no. 12, pp. 5839–5848, Dec. 2015.

[51] S. Ferguson, F. Ortner, J. Quon, L. Peeva, A. Livingston, B. L. Trout, and A. S. Myerson, “Use of Continuous MSMPR Crystallization with Integrated Nanofiltration Membrane Recycle for Enhanced Yield and Purity in API Crystallization,” *Cryst. Growth Des.*, vol. 14, no. 2, pp. 617–627, Feb. 2014.

[52] T.-T. C. Lai, J. Cornevin, S. Ferguson, N. Li, B. L. Trout, and A. S. Myerson, “Control of Polymorphism in Continuous Crystallization via Mixed Suspension Mixed Product Removal Systems Cascade Design,” *Cryst. Growth Des.*, vol. 15, no. 7, p. 150605082543003, Jun. 2015.

[53] D. W. Griffin, D. a. Mellichamp, and M. F. Doherty, “Reducing the mean size of API crystals by continuous manufacturing with product classification and recycle,” *Chem. Eng. Sci.*, vol. 65, no. 21, pp. 5770–5780, Nov. 2010.

[54] R. Peña and Z. K. Nagy, “Process Intensification through Continuous Spherical Crystallization Using a Two-Stage Mixed Su spension Mixed Product Removal (MSMPR) System,” *Cryst. Growth Des.*, vol. 15, no. 9, pp. 4225–4236, Sep. 2015.

[55] K. Tahara, M. O’Mahony, and A. S. Myerson, “Continuous Spherical Crystallization of Albuterol Sulfate with Solvent Recycle System,” *Cryst. Growth Des.*, p. 150917073857008, 2015.

[56] S. H. Chung, D. L. Ma, and R. D. Braatz, “Optimal model-based experimental design in batch crystallization,” *Chemom. Intell. Lab. Syst.*, vol. 50, no. 1, pp. 83–90, Jan. 2000.

[57] Q. Su, B. Benyahia, Z. K. Nagy, and C. D. Rielly, “Mathematical Modeling, Design, and Optimization of a Multisegment Multiaddition Plug-Flow Crystallizer for Antisolvent Crystallizations,” *Org. Process Res. Dev.*, 2015.

[58] R. J. P. Eder, S. Schrank, M. O. Besenhard, E. Roblegg, H. Gruber-Woelfler, and J. G. Khinast, “Continuous Sonocrystallization of Acetylsalicylic Acid (ASA): Control of Crystal Size,” *Cryst. Growth Des.*, vol. 12, no. 10, p. 120828144735000, Aug. 2012.

[59] A.-T. Nguyen, Y. L. Joo, and W.-S. Kim, “Multiple Feeding Strategy for Phase Transformation of GMP in Continuous Couette–Taylor Crystallizer,” *Cryst. Growth Des.*, vol. 12, pp. 2780–2788, 2012.

[60] M. D. Johnson, S. A. May, J. R. Calvin, J. Remacle, J. R. Stout, W. D. Diseroad, N. Zaborenko, B. D. Haeberle, W.-M. Sun, M. T. Miller, and J. Brennan, “Development and Scale-Up of a Continuous, High-Pressure, Asymmetric Hydrogenation Reaction,

Workup, and Isolation," *Org. Process Res. Dev.*, vol. 16, no. 5, pp. 1017–1038, May 2012.

[61] T. D. White, K. D. Berglund, J. M. Groh, M. D. Johnson, R. D. Miller, and M. H. Yates, "Development of a Continuous Schotten–Baumann Route to an Acyl Sulfonamide," *Org. Process Res. Dev.*, vol. 16, no. 5, pp. 939–957, May 2012.

[62] A. G. Bosma, "ISPT experiments with continuous crystallization highly promising," The European Federation of Pharmaceutical Industries and Associations, 2010.

[63] T. Lee, H. R. Chen, H. Y. Lin, and H. L. Lee, "Continuous Co-Crystallization As a Separation Technology: The Study of 1:2 Co-Crystals of Phenazine–Vanillin," *Cryst. Growth Des.*, p. 121107094029005, Nov. 2012.

[64] S. Byrn, M. Futran, H. Thomas, E. Jayjock, N. Maron, R. F. Meyer, A. S. Myerson, M. P. Thien, and B. L. Trout, "Achieving continuous manufacturing for final dosage formation: challenges and how to meet them. May 20-21, 2014 Continuous Manufacturing Symposium.," *J. Pharm. Sci.*, vol. 104, no. 3, pp. 792–802, Mar. 2015.

[65] D. Barrasso, S. Oka, A. Muliadi, J. D. Litster, C. Wassgren, and R. Ramachandran, "Population Balance Model Validation and Predictionof CQAs for Continuous Milling Processes: toward QbDin Pharmaceutical Drug Product Manufacturing," *J. Pharm. Innov.*, vol. 8, no. 3, pp. 147–162, Jul. 2013.

[66] C. Vervaet and J. P. Remon, "Continuous granulation in the pharmaceutical industry," *Chem. Eng. Sci.*, vol. 60, no. 14, pp. 3949–3957, Jul. 2005.

[67] M. Baumann and I. R. Baxendale, "The synthesis of active pharmaceutical ingredients (APIs) using continuous flow chemistry.," *Beilstein J. Org. Chem.*, vol. 11, no. 1, pp. 1194–219, Jan. 2015.

[68] L. Malet-Sanz and F. Susanne, "Continuous Flow Synthesis. A Pharma Perspective," *J. Med. Chem.*, vol. 55, no. 9, pp. 4062–4098, May 2012.

[69] Eric Palmer, "Vertex, J&J, GSK, Novartis all working on continuous manufacturing facilities," *FiercePharma Manufacturing*, 2015. [Online]. Available: http://www.fiercepharmamanufacturing.com/story/vertex-jj-gsk-novartis-all-working-continuous-manufacturing-facilities/2015-02-09. [Accessed: 26-Sep-2015].

[70] Q. Su, Z. K. Nagy, and C. D. Rielly, "Pharmaceutical crystallisation processes from batch to continuous operation using MSMPR stages: Modelling, design, and control," *Chem. Eng. Process. Process Intensif.*, vol. 89, pp. 41–53, Mar. 2015.

[71] D. M. Zarkadas and K. K. Sirkar, "Antisolvent Crystallization in Porous Hollow Fiber Devices," *Chem. Eng. Sci.*, vol. 61, no. 15, pp. 5030–5048, Aug. 2006.

[72] D. M. Zarkadas and K. K. Sirkar, "Cooling Crystallization of Paracetamol in Hollow Fiber Devices," *Ind. Eng. Chem. Res.*, vol. 46, no. 10, pp. 2928–2935, May 2007.

[73] S. Ferguson, G. Morris, H. Hao, M. Barrett, and B. Glennon, "In-situ Monitoring and Characterization of Plug Flow Crystallizers," *Chem. Eng. Sci.*, vol. 77, pp. 105–111, Jul. 2012.

[74] S. Ferguson and B. Glennon, "Design of Plug Flow Crystallizations," *Cryst. Growth Des.*, 2012.

[75] R. J. P. Eder, E. K. Schmitt, J. Grill, S. Radl, H. Gruber-Woelfler, and J. G. Khinast, "Seed Loading Effects on the Mean Crystal Size of Acetylsalicylic Acid in a Continuous-flow Crystallization Device," *Cryst. Res. Technol.*, vol. 46, no. 3, pp. 227–237, Mar. 2011.

[76] J. S.-I. Kwon, M. Nayhouse, P. D. Christofides, and G. Orkoulas, “Modeling and control of crystal shape in continuous protein crystallization,” *Chem. Eng. Sci.*, vol. 107, pp. 47–57, Apr. 2014.

[77] G. Hou, G. Power, M. Barrett, B. Glennon, G. Morris, and Y. Zhao, “Development and characterization of a single stage MSMPR crystallization process with a novel transfer unit,” *Cryst. Growth Des.*, pp. 1–34, Feb. 2014.

[78] G. Hou, B. Glennon, G. Morris, M. Barrett, Y. Zhao, and G. Power, “Design and Characterization of a Continuous Stirred Tank Crystallizer,” in *AIChE 12th Annual Meeting*, 2012.

[79] C. J. Callahan and X.-W. Ni, “Probing into Nucleation Mechanisms of Cooling Crystallization of Sodium Chlorate in a Stirred Tank Crystallizer and an Oscillatory Baffled Crystallizer,” *Cryst. Growth Des.*, vol. 12, no. 5, pp. 2525–2532, May 2012.

[80] M. Jiang, Z. Zhu, E. Jimenez, C. D. Papageorgiou, J. Waetzig, A. Hardy, M. Langston, and R. D. Braatz, “Continuous-flow tubular crystallization in slugs spontaneously induced by hydrodynamics,” *Cryst. Growth Des.*, vol. 14, no. 2, pp. 851–860, 2014.

[81] J. Sang-Il Kwon, M. Nayhouse, G. Orkoulas, and P. D. Christofides, “Crystal shape and size control using a plug flow crystallization configuration,” *Chem. Eng. Sci.*, vol. 119, pp. 30–39, 2014.

[82] T.-T. C. Lai, S. Ferguson, L. Palmer, B. L. Trout, and A. S. Myerson, “Continuous Crystallization and Polymorph Dynamics in the l-Glutamic Acid System,” *Org. Process Res. Dev.*, vol. 18, no. 11, pp. 1382–1390, Nov. 2014.

[83] J. Scully and P. J. Frawley, “Computational Fluid Dynamics Analysis of the Suspension of Nonspherical Particles in a Stirred Tank,” *Ind. Eng. Chem. Res.*, vol. 50, no. 4, pp. 2331–2342, Feb. 2011.

[84] S. Mascia, P. L. Heider, H. Zhang, R. Lakerveld, B. Benyahia, P. I. Barton, R. D. Braatz, C. L. Cooney, J. M. B. Evans, T. F. Jamison, K. F. Jensen, A. S. Myerson, and B. L. Trout, “End-to-End Continuous Manufacturing of Pharmaceuticals: Integrated Synthesis, Purification, and Final Dosage Formation,” *Angew. Chemie Int. Ed.*, vol. 52, no. 47, pp. 12359–12363, Nov. 2013.

[85] G. Power, G. Hou, V. K. Kamaraju, G. Morris, Y. Zhao, and B. Glennon, “Design and optimization of a multistage continuous cooling mixed suspension, mixed product removal crystallizer,” *Chem. Eng. Sci.*, Feb. 2015.

[86] M.-R. Chen and M. A. Larson, “Crystallization Kinetics of Calcium Nitrate Tetrahydrate from MSMPR Crystallizer,” *Chem. Eng. Sci.*, vol. 40, no. 7, pp. 1287–1294, 1985.

[87] S. Ferguson, G. Morris, H. Hao, M. Barrett, and B. Glennon, “Characterization of Batch, Plug Flow and MSMPR crystallisation of Benzoic Aicd,” 2013.

[88] E. Poiesz and I. Laird, “Technoproject CS0108 Oscillatory Baffled Flow Crystallisation,” Utrecht NL, 2011.

[89] X.-W. Ni, “Continuous Oscillatory Baffled Reactor Technology,” *Innov. Pharm. Technol.*, pp. 8–12, 2006.

[90] M. Sultana, “Microfluidic Systems for Continuous Crystallization of Small Organic Molecules,” Massachusetts Institute of Technology, 2010.

[91] M. Sultana and K. Jensen, “Microfluidic Continuous Seeded Crystallization: Extraction of Growth Kinetics and Impurity Impact on Morphology,” *Cryst. Growth Des.*, pp. 1–17, 2012.

[92] K. K. Sirkar and D. M. Zarkadas, “Solid Hollow Fiber Cooling Crystallization Systems and Methods,” *US Pat. App. 11/259,184*, 2010.

[93] K. K. Sirkar and D. M. Zarkadas, “Solid Hollow Fiber Cooling Crystallization Methods,” *US Pat. App. 12/819,857*, 2011.

[94] C. Brechtelsbauer and F. Ricard, “Reaction Engineering Evaluation and Utilization of Static Mixer Technology for the Synthesis of Pharmaceuticals,” *Org. Process Res. …*, no. 11, pp. 541–545, 2001.

[95] M. Stahl, B. L. Aslund, and Å. C. Rasmuson, “Reaction Crystallization Kinetics of Benzoic Acid,” *AIChE*, vol. 47, no. 7, 2001.

[96] J. M. Hacherl, E. L. Paul, and H. M. Buettner, “Investigation of Impinging-Jet Crystallization with a Calcium Oxalate Model System,” *AIChE J.*, vol. 49, no. 9, pp. 2352–2362, Sep. 2003.

[97] G. I. Taylor, “Stability of a Viscous Liquid Contained between Two Rotating Cylinders,” *Philos. Trans. R. Soc. A Math. Phys. Eng. Sci.*, vol. 223, no. 605–615, pp. 289–343, Jan. 1923.

[98] J. R. Méndez del Río and R. W. Rousseau, “Batch and Tubular-Batch Crystallization of Paracetamol: Crystal Size Distribution and Polymorph Formation,” *Cryst. Growth Des.*, vol. 6, no. 6, pp. 1407–1414, Jun. 2006.

[99] K. Ekambara and J. B. Joshi, “Axial mixing in laminar pipe flows,” *Chem. Eng. Sci.*, vol. 59, no. 18, pp. 3929–3944, Sep. 2004.

[100] J. Garside and M. B. Shah, “Crystallization Kinetics from MSMPR Crystallizers,” *Ind. Eng. Chem. Process Des. Dev.*, vol. 19, no. 4, pp. 509–514, 1980.

[101] A. G. Jones, J. Budz, and J. W. Mullin, “Crystallization Kinetics of Potassium Sulfate in an MSMPR Agitated Vessel,” *AIChE J.*, vol. 32, no. 12, pp. 2002–2009, Dec. 1986.

[102] J. Mydlarz and A. G. Jones, “An Assessment of MSMPR Crystallization Kinetics Data for Systems Modeled by Size-Dependent Crystal-Growth Rate-Functions,” *Chem. Eng. J.*, vol. 55, pp. 69–80, Aug. 1994.

[103] M. A. Larson, E. T. White, K. A. Ramanarayanan, and K. A. Berglund, “Growth rate dispersion in MSMPR crystallizers,” *AIChE J.*, vol. 31, no. 1, pp. 90–94, Jan. 1985.

[104] K. A. Ramanarayanan, “Effects of Growth Rate Dispersion and Residence Time Distribution on the CSD from a Continuous Crystallizer,” *AIChE Annu. Meet.*, 1985.

[105] D. T. Moore, H. Sai, K. W. Tan, D.-M. Smilgies, W. Zhang, H. J. Snaith, U. Wiesner, and L. A. Estroff, “Crystallization kinetics of organic-inorganic trihalide perovskites and the role of the lead anion in crystal growth.,” *J. Am. Chem. Soc.*, vol. 137, no. 6, pp. 2350–2358, Jan. 2015.

[106] M. Zahedi, N. Roohpour, and A. K. Ray, “Kinetic study of crystallisation of sol–gel derived calcia–alumina binary compounds,” *J. Alloys Compd.*, vol. 582, pp. 277–282, Jan. 2014.

[107] S. K. Sikdar and A. D. Randolph, “Secondary Nucleation of Two Fast Growth Systems in a Mixed Suspension Crystallizer: Magnesium Sulfate and Citric Acid Water Systems,” *AIChE J.*, vol. 22, no. 1, pp. 110–117, Jan. 1976.

[108] C. Jinyang and L. Shuzhong, “Study on the Kinetics of Crystallization of Glutamic Acid in the MSMPR Crystallizer from the Industrial Fermentation Broth,” *J. Tsinghua Univ.*, vol. 33, no. 6, pp. 60–66, 1996.

[109] A. Alamdari and F. Tabkhi, “Kinetics of Hexamine Crystallization in Industrial Scale,” *Chem. Eng. Process. Process Intensif.*, vol. 43, no. 7, pp. 803–810, Jul. 2004.

[110] E. Kougoulos, A. G. Jones, and M. W. Wood-Kaczmar, “Estimation of Crystallization Kinetics for an Organic Fine Chemical Using a Modified Continuous Cooling Mixed Suspension Mixed Product Removal (MSMPR) Crystallizer,” *J. Cryst. Growth*, vol. 273, no. 3–4, pp. 520–528, Jan. 2005.

[111] H. Hao, J. Wang, Y. Wang, and B. Hou, “Crystal Growth Models of Dexamethasone Sodium Phosphate in a MSMPR Reactive Crystallizer,” *Chinese J. Chem. Eng.*, vol. 13, no. 3, pp. 350–354, 2005.

[112] B. Wierzbowska, K. Piotrowski, J. Koralewska, A. Matynia, N. Hutnik, and K. Wawrzyniecki, “Crystallization of Vitamin C in a Continuous DT MSMPR Crystallizer – Size Independent Growth Kinetic Model Approach,” *Cryst. Res. Technol.*, vol. 43, no. 4, pp. 381–389, Apr. 2008.

[113] K. A. Jackson, “On the Theory of Crystal Growth: The Fundamental Rate Equation,” *J. Cryst. Growth*, vol. 5, no. 1, pp. 13–18, 1969.

[114] C. F. Abegg, J. D. Stevens, and M. A. Larson, “Crystal Size Distributions in Continuous Crystallizers when Growth Rate is,” 1968.

[115] D. E. Kile and D. D. Eberl, “On the origin of size-dependent and size-independent crystal growth: Influence of advection and diffusion,” *Am. Mineral.*, vol. 88, no. 10, pp. 1514–1521, 2003.

[116] C. D. Rielly and A. J. Marquis, “A Particle’s Eye View of Crystallizer Fluid Mechanics,” *Chem. Eng. Sci.*, vol. 56, no. 7, pp. 2475–2493, Apr. 2001.

[117] J. Cheng, C. Yang, Z.-S. Mao, and C. Zhao, “CFD Modeling of Nucleation, Growth, Aggregation, and Breakage in Continuous Precipitation of Barium Sulfate in a Stirred Tank,” *Ind. Eng. Chem. Res.*, vol. 48, no. 15, pp. 6992–7003, Aug. 2009.

[118] Y. Yang and Z. K. Nagy, “Application of nonlinear model predictive control in continuous crystallization systems,” in *Proceedings of the American Control Conference*, 2015, pp. 4282–4287.

[119] Y. Yang and Z. K. Nagy, “Advanced control approaches for combined cooling/antisolvent crystallization in continuous mixed suspension mixed product removal cascade crystallizers,” *Chem. Eng. Sci.*, vol. 127, pp. 362–373, May 2015.

[120] Y. Yang and Z. K. Nagy, “Combined Cooling and Antisolvent Crystallization in Continuous Mixed Suspension, Mixed Product Removal Cascade Crystallizers: Steady-State and Startup Optimization,” *Ind. Eng. Chem. Res.*, vol. 54, no. 21, pp. 5673–5682, Jun. 2015.

[121] K. Galan, M. J. Eicke, M. P. Elsner, H. Lorenz, and A. Seidel-Morgenstern, “Continuous Preferential Crystallization of Chiral Molecules in Single and Coupled Mixed-Suspension Mixed-Product-Removal Crystallizers,” *Cryst. Growth Des.*, vol. 15, no. 4, pp. 1808–1818, Apr. 2015.

[122] Y.-T. Tseng and J. D. Ward, “Critical seed loading from nucleation kinetics,” *AIChE J.*, p. n/a–n/a, Feb. 2014.

[123] R. Geyyer, A. Kienle, and S. Palis, “Robust control of continuous crystallization processes,” *IFAC-PapersOnLine*, vol. 48, no. 11, pp. 598–603, 2015.

[124] A. Mersmann, *Crystallization Technology Handbook*, 2nd ed. New York: Marcel Dekker, Inc., 1995.

[125] N. V. V. S. S. Raman, U. R. Mallu, and H. R. Bapatu, “Analytical Quality by Design Approach to Test Method Development and Validation in Drug Substance Manufacturing,” *J. Chem.*, vol. 2015, pp. 1–8, Jan. 2015.

[126] FDA, “ICH guideline Q11 on development and manufacture of drug substances (chemical entities and biotechnological/biological entities).” pp. 1–27, 2011.

[127] L. L. Simon, H. Pataki, G. Marosi, F. Meemken, K. Hungerbühler, A. Baiker, S. Tummala, B. Glennon, M. Kuentz, G. Steele, H. J. M. Kramer, J. W. Rydzak, Z. Chen, J. Morris, F. Kjell, R. Singh, R. Gani, K. V. Gernaey, M. Louhi-Kultanen, J. O’Reilly, N. Sandler, O. Antikainen, J. Yliruusi, P. Frohberg, J. Ulrich, R. D. Braatz, T. Leyssens, M. von Stosch, R. Oliveira, R. B. H. Tan, H. Wu, M. Khan, D. O’Grady, A. Pandey, R. Westra, E. Delle-Case, D. Pape, D. Angelosante, Y. Maret, O. Steiger, M. Lenner, K. Abbou-Oucherif, Z. K. Nagy, J. D. Litster, V. K. Kamaraju, and M.-S. Chiu, “Assessment of Recent Process Analytical Technology (PAT) Trends: A Multiauthor Review,” *Org. Process Res. Dev.*, vol. 19, no. 1, pp. 3–62, Jan. 2015.

[128] A. Chanda, A. M. Daly, D. A. Foley, M. A. LaPack, S. Mukherjee, J. D. Orr, G. L. Reid, D. R. Thompson, and H. W. Ward, “Industry Perspectives on Process Analytical Technology: Tools and Applications in API Development,” *Org. Process Res. Dev.*, vol. 19, no. 1, pp. 63–83, 2015.

[129] S. Bordawekar, A. Chanda, A. M. Daly, A. W. Garrett, J. P. Higgins, M. A. LaPack, T. D. Maloney, J. Morgado, S. Mukherjee, J. D. Orr, G. L. Reid, B.-S. Yang, and H. W. Ward, “Industry Perspectives on Process Analytical Technology: Tools and Applications in API Manufacturing,” *Org. Process Res. Dev.*, p. 150831134504003, Aug. 2015.

[130] A. M. Thayer and C&EN Houston, “Real-Time Monitoring,” *CEN.ACS.ORG*, pp. 8–12, Nov-2014.

[131] W. Chew and P. Sharratt, “Trends in process analytical technology,” *Anal. Methods*, vol. 2, no. 10, p. 1412, Oct. 2010.

[132] A. S. Rathore, R. Bhambure, and V. Ghare, “Process analytical technology (PAT) for biopharmaceutical products.,” *Anal. Bioanal. Chem.*, vol. 398, no. 1, pp. 137–54, Sep. 2010.

[133] Z. Chen, D. Lovett, and J. Morris, “Process analytical technologies and real time process control a review of some spectroscopic issues and challenges,” *J. Process Control*, vol. 21, no. 10, pp. 1467–1482, Dec. 2011.

[134] H. Wu, Z. Dong, H. Li, and M. Khan, “An Integrated Process Analytical Technology (PAT) Approach for Pharmaceutical Crystallization Process Understanding to Ensure Product Quality and Safety: FDA Scientist’s Perspective,” *Org. Process Res. Dev.*, vol. 19, no. 1, pp. 89–101, Jan. 2015.

[135] H. Wu, M. White, R. Berendt, R. D. Foringer, and M. Khan, “Integrated Process Analytical Technology Approach for Nucleation Induction Time Measurement and Nucleation Mechanism Assessment for a Dynamic Multicomponent Pharmaceutical Antisolvent Crystallization System,” *Ind. Eng. Chem. Res.*, vol. 53, no. 4, pp. 1688–1701, Jan. 2014.

[136] E. Simone, Ali N. Saleemi, and Z. K. Nagy, “Application of Quantitative Raman Spectroscopy for the Monitoring of Polymorphic Transformation in Crystallization Processes Using a Good Calibration Practice Procedure,” *Chem. Eng. Res. Des.*, vol. 92, pp. 594–611, Dec. 2014.

[137] M. F. Roberto, T. I. Dearing, S. Martin, and B. J. Marquardt, “Integration of Continuous Flow Reactors and Online Raman Spectroscopy for Process Optimization,” *J. Pharm. Innov.*, vol. 7, no. 2, pp. 69–75, May 2012.

[138] Z. Q. Yu, P. S. Chow, R. B. H. Tan, and W. H. Ang, “Supersaturation Control in Cooling Polymorphic Co-Crystallization of Caffeine and Glutaric Acid,” *Cryst. Growth Des.*, vol. 11, no. 10, pp. 4525–4532, Oct. 2011.

[139] S. Khan, C. Y. Ma, T. Mahmud, R. Y. Penchev, K. J. Roberts, J. Morris, L. Özkan, G. White, B. Grieve, A. Hall, P. Buser, N. Gibson, P. Keller, P. Shuttleworth, and C. J. Price, “In-process monitoring and control of supersaturation in seeded batch cooling crystallisation of l-glutamic acid: From laboratory to industrial pilot plant,” *Org. Process Res. Dev.*, vol. 15, no. 3, pp. 540–555, 2011.

[140] M. Jiang, X. Zhu, M. C. Molaro, M. L. Rasche, H. Zhang, K. Chadwick, D. M. Raimondo, K. K. K. Kim, L. Zhou, Z. Zhu, M. H. Wong, D. O’Grady, D. Hebrault, J. Tedesco, and R. D. Braatz, “Modification of crystal shape through deep temperature cycling,” *Ind. Eng. Chem. Res.*, vol. 53, no. 13, pp. 5325–5336, 2014.

[141] A. N. Saleemi, C. D. Rielly, and Z. K. Nagy, “Monitoring of the combined cooling and antisolvent crystallisation of mixtures of aminobenzoic acid isomers using ATR-UV/vis spectroscopy and FBRM,” *Chem. Eng. Sci.*, vol. 77, pp. 122–129, Jul. 2012.

[142] E. Aamir, Z. K. Nagy, and C. D. Rielly, “Evaluation of the Effect of Seed Preparation Method on the Product Crystal Size Distribution for Batch Cooling Crystallization Processes,” *Cryst. Growth Des.*, vol. 10, no. 11, pp. 4728–4740, Nov. 2010.

[143] S. S. Kadam, E. van der Windt, P. J. Daudey, and H. J. M. Kramer, “A Comparative Study of ATR-FTIR and FT-NIR Spectroscopy for In-Situ Concentration Monitoring during Batch Cooling Crystallization Processes,” *Cryst. Growth Des.*, vol. 10, no. 6, pp. 2629–2640, Jun. 2010.

[144] Y. Roggo, P. Chalus, L. Maurer, C. Lema-Martinez, A. Edmond, and N. Jent, “A review of near infrared spectroscopy and chemometrics in pharmaceutical technologies.,” *J. Pharm. Biomed. Anal.*, vol. 44, no. 3, pp. 683–700, Jul. 2007.

[145] E. Simone, A. N. Saleemi, and Z. K. Nagy, “Raman, UV, NIR, and Mid-IR Spectroscopy with Focused Beam Reflectance Measurement in Monitoring Polymorphic Transformations,” *Chem. Eng. Technol.*, vol. 37, no. 8, pp. 1305–1313, Aug. 2014.

[146] H. Wu and M. Khan, “THz spectroscopy: An emerging technology for pharmaceutical development and pharmaceutical Process Analytical Technology (PAT) applications,” *Journal of Molecular Structure*, vol. 1020. pp. 112–120, 2012.

[147] Y. Du, H. Zhang, J. Xue, H. Fang, Q. Zhang, Y. Xia, Y. Li, and Z. Hong, “Raman and terahertz spectroscopical investigation of cocrystal formation process of piracetam and 3-hydroxybenzoic acid,” *Spectrochim. Acta Part A Mol. Biomol. Spectrosc.*, vol. 139, pp. 488–494, Mar. 2015.

[148] K. L. Nguyen, T. Friscić, G. M. Day, L. F. Gladden, and W. Jones, “Terahertz time-domain spectroscopy and the quantitative monitoring of mechanochemical cocrystal formation.,” *Nat. Mater.*, vol. 6, no. 3, pp. 206–9, Mar. 2007.

[149] C. Gendrin, Y. Roggo, and C. Collet, “Pharmaceutical applications of vibrational chemical imaging and chemometrics: a review.,” *J. Pharm. Biomed. Anal.*, vol. 48, no. 3, pp. 533–53, Nov. 2008.

[150] Z. Wu, O. Tao, X. Dai, M. Du, X. Shi, and Y. Qiao, “Monitoring of a pharmaceutical

blending process using near infrared chemical imaging," *Vib. Spectrosc.*, vol. 63, pp. 371–379, Nov. 2012.

[151] P.-Y. Sacré, C. De Bleye, P.-F. Chavez, L. Netchacovitch, P. Hubert, and E. Ziemons, "Data processing of vibrational chemical imaging for pharmaceutical applications.," *J. Pharm. Biomed. Anal.*, vol. 101, pp. 123–40, Dec. 2014.

[152] E. Kougoulos, A. G. Jones, K. H. Jennings, and M. W. Wood-Kaczmar, "Use of Focused Beam Reflectance Measurement (FBRM) and Process Video Imaging (PVI) in a Modified Mixed Suspension Mixed Product Removal (MSMPR) Cooling Crystallizer," *J. Cryst. Growth*, vol. 273, no. 3–4, pp. 529–534, Jan. 2005.

[153] L. L. Simon, T. Merz, S. Dubuis, A. Lieb, and K. Hungerbuhler, "In-situ monitoring of pharmaceutical and specialty chemicals crystallization processes using endoscopy–stroboscopy and multivariate image analysis," *Chem. Eng. Res. Des.*, vol. 90, no. 11, pp. 1847–1855, Nov. 2012.

[154] A. Bluma, T. Höpfner, P. Lindner, C. Rehbock, S. Beutel, D. Riechers, B. Hitzmann, and T. Scheper, "In-situ imaging sensors for bioprocess monitoring: state of the art.," *Anal. Bioanal. Chem.*, vol. 398, no. 6, pp. 2429–38, Nov. 2010.

[155] B. Smith, "White Paper: Best Practices for Crystallization Development." Mettler Toledo AutoChem Inc., pp. 1–9, 2013.

[156] J. W. Chew, P. S. Chow, and R. B. H. Tan, "Automated in-line technique using FBRM to achieve consistent product quality in cooling crystallization," *Cryst. Growth Des.*, vol. 7, no. 8, pp. 1416–1422, 2007.

[157] T. Leyssens, C. Baudry, and M. L. Escudero Hernandez, "Optimization of a Crystallization by Online FBRM Analysis of Needle-Shaped Crystals," *Org. Process Res. Dev.*, vol. 15, no. 2, pp. 413–426, Mar. 2011.

[158] A. N. Saleemi, G. Steele, N. I. Pedge, A. Freeman, and Z. K. Nagy, "Enhancing Crystalline Properties of a Cardiovascular Active Pharmaceutical Ingredient Using a Process Analytical Technology Based Crystallization Feedback Control Strategy.," *Int. J. Pharm.*, vol. 430, no. 1–2, pp. 56–64, Jul. 2012.

[159] N. Gherras and G. Fevotte, "On the use of process analytical technologies and population balance equations for the estimation of crystallization kinetics. A case study," *AIChE J.*, vol. 58, no. 9, pp. 2650–2664, Sep. 2012.

[160] C. Schaefer, C. Lecomte, D. Clicq, A. Merschaert, E. Norrant, and F. Fotiadu, "On-line Near Infrared Spectroscopy as a Process Analytical Technology (PAT) Tool to Control an Industrial Seeded API crystallization.," *J. Pharm. Biomed. Anal.*, vol. 83, pp. 194–201, Sep. 2013.

[161] N. A. F. A. Samad, G. Sin, K. V. Gernaey, and R. Gani, "Introducing uncertainty analysis of nucleation and crystal growth models in Process Analytical Technology (PAT) system design of crystallization processes," *Eur. J. Pharm. Biopharm.*, vol. 85, no. 3, pp. 911–929, 2013.

[162] E. Simone, W. Zhang, and Z. K. Nagy, "Application of Process Analytical Technology-Based Feedback Control Strategies To Improve Purity and Size Distribution in Biopharmaceutical Crystallization," *Cryst. Growth Des.*, vol. 15, no. 6, pp. 2908–2919, 2015.

[163] H. Hao, M. Barrett, Y. Hu, W. Su, S. Ferguson, B. Wood, and B. Glennon, "The Use of in Situ Tools To Monitor the Enantiotropic Transformation of p -Aminobenzoic Acid Polymorphs," *Org. Process Res. Dev.*, vol. 16, no. 1, pp. 35–41, Jan. 2012.

[164] J. Cornel, C. Lindenberg, and M. Mazzotti, “Quantitative Application of in Situ ATR-FTIR and Raman Spectroscopy in Crystallization Processes,” *Ind. Eng. Chem. Res.*, vol. 47, no. 14, pp. 4870–4882, Jul. 2008.

[165] G. G. Z. Zhang, D. Law, E. A. Schmitt, and Y. Qiu, “Phase transformation considerations during process development and manufacture of solid oral dosage forms.,” *Adv. Drug Deliv. Rev.*, vol. 56, no. 3, pp. 371–90, Feb. 2004.

[166] Y. Zhou, X. Doan, and R. Srinivasan, “On-Line Monitoring of Particle Shape and Size Distribution in Crystallization Processes through Image Analysis,” in *17th European Symposium on Computer Aided Process Engineering – ESCAPE17 V.*, 2007, pp. 1–6.

[167] M. Fujiwara, Z. K. Nagy, J. W. Chew, and R. D. Braatz, “First-principles and direct design approaches for the control of pharmaceutical crystallization,” *J. Process Control*, vol. 15, no. 5, pp. 493–504, Aug. 2005.

[168] G. X. Zhou, M. Fujiwara, X. Y. Woo, E. Rusli, H.-H. Tung, C. Starbuck, O. Davidson, Z. Ge, and R. D. Braatz, “Direct design of pharmaceutical antisolvent crystallization through concentration control,” *… growth Des.*, 2006.

[169] P. Billot, M. Couty, and P. Hosek, “Application of ATR-UV Spectroscopy for Monitoring the Crystallisation of UV Absorbing and Nonabsorbing Molecules,” *Org. Process Res. Dev.*, vol. 14, no. 3, pp. 511–523, May 2010.

[170] A. N. Saleemi, C. D. Rielly, and Z. K. Nagy, “Comparative Investigation of Supersaturation and Automated Direct Nucleation Control of Crystal Size Distributions using ATR-UV/vis Spectroscopy and FBRM,” *Cryst. Growth Des.*, vol. 12, no. 4, pp. 1792–1807, Apr. 2012.

[171] N. Gherras, E. Serris, and G. Févotte, “Monitoring industrial pharmaceutical crystallization processes using acoustic emission in pure and impure media.,” *Int. J. Pharm.*, vol. 439, no. 1–2, pp. 109–19, Dec. 2012.

[172] L. Derdour, G. Févotte, F. Puel, and P. Carvin, “Real-time evaluation of the concentration of impurities during organic solution crystallization,” *Powder Technol.*, vol. 129, no. 1–3, pp. 1–7, Jan. 2003.

[173] C. A. Marasco, “Pharma’S Process Analytical Technology,” *C&EN Washingt.*, vol. 83, no. 8, pp. 201–206, 2005.

[174] G. Févotte, “In Situ Raman Spectroscopy for In-Line Control of Pharmaceutical Crystallization and Solids Elaboration Processes: A Review,” *Chem. Eng. Res. Des.*, vol. 85, no. 7, pp. 906–920, Jan. 2007.

[175] P. T. Mah, S. J. Fraser, M. E. Reish, T. Rades, K. C. Gordon, and C. J. Strachan, “Use of low-frequency Raman spectroscopy and chemometrics for the quantification of crystallinity in amorphous griseofulvin tablets,” *Vib. Spectrosc.*, vol. 77, pp. 10–16, Mar. 2015.

[176] A. Lust, C. J. Strachan, P. Veski, J. Aaltonen, J. Heinämäki, J. Yliruusi, and K. Kogermann, “Amorphous solid dispersions of piroxicam and Soluplus®: Qualitative and quantitative analysis of piroxicam recrystallization during storage,” *Int. J. Pharm.*, vol. 486, no. 1–2, pp. 306–314, May 2015.

[177] X. Zhou, V. Razmovski-Naumovski, and K. Chan, “A multivariate analysis on the comparison of raw notoginseng (Sanqi) and its granule products by thin-layer chromatography and ultra-performance liquid chromatography,” *Chin. Med.*, vol. 10, no. 1, p. 13, 2015.

[178] G. Smith, A. Hussain, N. I. Bukhari, and I. Ermolina, “Quantification of residual crystallinity in ball milled commercially sourced lactose monohydrate by thermo-analytical techniques and terahertz spectroscopy.,” *Eur. J. Pharm. Biopharm.*, vol. 92, pp. 180–91, May 2015.

[179] I. Singh, P. Juneja, B. Kaur, and P. Kumar, “Pharmaceutical Applications of Chemometric Techniques,” *ISRN Anal. Chem.*, vol. 2013, pp. 1–13, Oct. 2013.

[180] L. L. Simon, K. Abbou Oucherif, Z. K. Nagy, and K. Hungerbuhler, “Bulk video imaging based multivariate image analysis, process control chart and acoustic signal assisted nucleation detection,” *Chem. Eng. Sci.*, vol. 65, no. 17, pp. 4983–4995, Sep. 2010.

[181] L. Eriksson, T. Byrne, E. Johansson, J. Trygg, and C. Vikström, *Multi- and Megavariate Data Analysis*, First Edit. UMETRICS Academy, 2003.

[182] C. Rosen, *A chemometric approach to process monitoring and control-with applications to wastewater treatment operation*. 2001.

[183] K. R. Beebe, R. J. Pell, and M. B. Seasholtz, *Chemometrics : A Practical Guide*. New York: Wiley-Interscience, 1998.

[184] M. Otto, *Chemometrics: Statistics and Computer Application in Analytical Chemistry*. Weinheim, Germany: Whiley-VCH Verlag GmbH, 1998.

[185] N. R. Draper and H. Smith, *Applied Regression Analysis*, Third Edit. New York: Wiley-Interscience, 1998.

[186] H. Hotelling, “Analysis of a complex of statistical variables into principal components.,” *J. Edu. Psych.*, vol. 24, pp. 417–441, 1933.

[187] K. Pearson, “On lines and planes of closest fit to systems of points in space,” *Philos. Mag. Ser. 6*, vol. 2, no. 11, pp. 559–572, Nov. 1901.

[188] S. Wold, K. Esbensen, and P. Geladi, “Principal component analysis,” *Chemom. Intell. Lab. Syst.*, vol. 2, no. 1–3, pp. 37–52, Aug. 1987.

[189] R. A. Fisher and W. A. Mackenzie, “Studies in crop variation. II. The manurial response of different potato varieties,” *J. Agric. Sci.*, vol. 13, pp. 311–329, Mar. .

[190] N. Kettaneh, A. Berglund, and S. Wold, “PCA and PLS with very large data sets,” *Comput. Stat. Data Anal.*, vol. 48, no. 1, pp. 69–85, 2005.

[191] M. Scholz, “Approaches to analyse and interpret biological profile data,” University of Postdam, Germany, 2006.

[192] Y. S. Thakare and S. B. Bagal, “Performance Evaluation of K-means Clustering Algorithm with Various Distance Metrics - ProQuest,” *Int. J. Comput. Appl.*, vol. 110, no. 11, pp. 12–16, 2015.

[193] D. Yu and L. Deng, “Gaussian Mixture Models,” in *Automatic Speech Recognition*, London: Springer-Verlag, 2015, pp. 13–21.

[194] M. Daszykowski, B. Walczak, and D. . Massart, “Looking for natural patterns in data,” *Chemom. Intell. Lab. Syst.*, vol. 56, no. 2, pp. 83–92, May 2001.

[195] J. A. Lopes, P. F. Costa, T. P. Alves, and J. C. Menezes, “Chemometrics in bioprocess engineering: process analytical technology (PAT) applications,” *Chemom. Intell. Lab. Syst.*, vol. 74, no. 2, pp. 269–275, Dec. 2004.

[196] S. Matero, “Chemometric methods in pharmaceutical tablet development and

manufacturing unit operations," University of Eastern Finland, 2010.

[197] S. Wold, M. Sjöström, and L. Eriksson, "PLS-regression: A basic tool of chemometrics," *Chemom. Intell. Lab. Syst.*, vol. 58, no. 2, pp. 109–130, 2001.

[198] S. Wold, A. Ruhe, H. Wold, and W. J. Dunn, III, "The Collinearity Problem in Linear Regression. The Partial Least Squares (PLS) Approach to Generalized Inverses," *SIAM J. Sci. Stat. Comput.*, vol. 5, no. 3, pp. 735–743, Sep. 1984.

[199] S. Wold, N. Kettaneh, and K. Tjessem, "Hierarchical multiblock PLS and PC models for easier model interpretation and as an alternative to variable selection," *J. Chemom.*, vol. 10, no. 5–6, pp. 463–482, Sep. 1996.

[200] S. de Jong, B. M. Wise, and N. L. Ricker, "Canonical partial least squares and continuum power regression," *J. Chemom.*, vol. 15, no. 2, pp. 85–100, Feb. 2001.

[201] A. E. Hoerl and R. W. Kennard, "Ridge Regression: Biased Estimation for Nonorthogonal Problems," *Technometrics*, Apr. 2012.

[202] J. a Westerhuis, T. Kourti, and J. F. MacGregor, "Analysis of multiblock and hierarchical PCA and PLS models," *J. Chemom.*, vol. 12, no. 5, pp. 301–321, 1998.

[203] J. A. Lopes, J. C. Menezes, J. A. Westerhuis, and A. K. Smilde, "Multiblock PLS analysis of an industrial pharmaceutical process," *Biotechnol. Bioeng.*, vol. 80, no. 4, pp. 419–427, 2002.

[204] P. D. Wentzell and L. V. Montoto, "Comparison of principal components regression and partial least squares regression through generic simulations of complex mixtures," *Chemom. Intell. Lab. Syst.*, vol. 65, no. 2, pp. 257–279, 2003.

[205] B. Hemmateenejad, M. Akhond, and F. Samari, "A comparative study between PCR and PLS in simultaneous spectrophotometric determination of diphenylamine, aniline, and phenol: Effect of wavelength selection.," *Spectrochim. Acta. A. Mol. Biomol. Spectrosc.*, vol. 67, no. 3–4, pp. 958–65, Jul. 2007.

[206] B. D. Cullity, *Elements of X-ray diffraction 2nd edition*. Reading, MA, USA: Addison-Wesley Publishing Company Inc., 1978.

[207] P. Gill, T. T. Moghadam, and B. Ranjbar, "Differential Scanning Calorimetry Techniques: Applications in Biology and Nanoscience," *J. Biomol.*, vol. 21, no. 4, pp. 167–193, 2010.

[208] D. J. Gardiner and P. R. Graves, *Practical Raman Spectroscopy*. Berlin, Heidelberg: Springer Berlin Heidelberg, 1989.

[209] K. Downard, *Mass Spectrometry: A Foundation Course*. Cambridge: Royal Society of Chemistry, 2004.

[210] Malvern Instruments Limited, "A Basic Guide to Particle Characterization," *White Paper*, pp. 1 – 26, 2012.

[211] Horiba, "A Guidebook to Particle Size Analysis," Horiba Instruments, Inc., Irvine, 2013.

[212] R. Bro, "Multivariate calibration: What is in chemometrics for the analytical chemist?," *Anal. Chim. Acta*, vol. 500, no. 1, pp. 185–194, 2003.

[213] H. Hojjati and S. Rohani, "Measurement and prediction of solubility of paracetamol in water-isopropanol solution. Part 1. Measurement and data analysis," *Org. Process Res. Dev.*, vol. 10, no. 519, pp. 1101–1109, 2006.

[214] H. Mark and J. W. Jr, “Derivatives in Spectroscopy: Part I — The Behavior of the Derivative,” vol. 18, no. April, 2003.

[215] H. Mark and J. W. Jr, “Derivatives in Spectroscopy: Part IV — Calibrating with Derivatives,” *Spectroscopy*, vol. 19, no. 1, pp. 44–51, 2004.

[216] J. Huang, S. Romero-Torres, and M. Moshgbar, “Practical Considerations in Data Pre-treatment for NIR and Raman Spectroscopy,” *American Pharmaceutical Review*, 2010.

[217] Bruker, “Multivariate Calibration: A Practical Guide for Method Development in Analytical Chemistry.” Bruker Optik GmbH, pp. 1–115, 2006.

[218] M. R. H. A. Bakar, “Process Analytical Technology Based Approaches for the Monitoring and Control of Size and Polymorphic Form in Pharmaceutical Crystallisation Processes,” Loughborough University, 2010.

[219] P. W. Hansen, “Pre-processing method minimizing the need for reference analyses,” *J. Chemom.*, vol. 15, no. 2, pp. 123–131, 2001.

[220] R. M. Balabin, R. Z. Safieva, and E. I. Lomakina, “Comparison of linear and nonlinear calibration models based on near infrared (NIR) spectroscopy data for gasoline properties prediction,” *Chemom. Intell. Lab. Syst.*, vol. 88, no. 2, pp. 183–188, Sep. 2007.

[221] B. M. Wise and R. T. Roginski, “Model Maintenance: the unrecognized cost in PAT and QbD,” *Chim. Oggi-Chemistry Today*, vol. 33, no. 2, pp. 38–43, 2015.

[222] K. Janné, J. Pettersen, N. O. Lindberg, and T. Lundstedt, “Hierarchical principal component analysis (PCA) and projection to latent structure (PLS) technique on spectroscopic data as a data pretreatment for calibration,” *J. Chemom.*, vol. 15, no. 4, pp. 203–213, 2001.

[223] K. Faber and B. R. Kowalski, “Propagation of measurement errors for the validation of predictions obtained by principal component regression and partial least squares,” *J. Chemom.*, vol. 11, no. 3, pp. 181–238, 1997.

[224] A. N. Saleemi, C. D. Rielly, and Z. K. Nagy, “Automated Direct Nucleation Control for In Situ Dynamic Fines Removal in Batch Cooling Crystallization,” *CrystEngComm*, vol. 14, no. 6, pp. 2196–2203, 2012.

[225] O. Narducci, A. G. Jones, and E. Kougoulos, “Continuous crystallization of adipic acid with ultrasound,” *Chem. Eng. Sci.*, vol. 66, no. 6, pp. 1069–1076, Mar. 2011.

[226] L. L. Simon and A. S. Myerson, “Continuous Antisolvent Plug-Flow Crystallization of a Fast Growing API,” in *Associazione Italiana Di Ingegneria Chimica (AIDIC)*, 2011, pp. 3–6.

[227] R. A. Granberg and Å. C. Rasmuson, “Solubility of Paracetamol in Pure Solvents,” *J. Chem. Eng. Data*, vol. 44, no. 6, pp. 1391–1395, Nov. 1999.

[228] D. B. Patience, “Crystal engineering through particle size and shape monitoring, modeling, and control,” University of Wisconsin-Madison, 2002.

[229] M. Fujiwara, P. S. Chow, and R. D. Braatz, “Paracetamol crystallization using laser backscattering and ATR-FTIR spectroscopy: Metastability, agglomeration, and control,” *Cryst. Growth …*, vol. 2, no. 5, pp. 363–370, 2002.

[230] Z. K. Nagy, M. Fujiwara, X. Y. Woo, and R. D. Braatz, “Determination of the Kinetic Parameters for the Crystallization of Paracetamol from Water Using Metastable Zone

Width Experiments," *Industrial & Engineering Chemistry Research*, Feb-2008. [Online]. Available: http://dx.doi.org/10.1021/ie060637c. [Accessed: 26-Jul-2012].

[231] N. R. Rao and A. Narasaraju, "Rapid separation and determination of process-related substances of paracetamol using reversed-phase HPLC with photo diode array as a detector.," *Anal. Sci.*, vol. 22, no. 2, pp. 287–92, Feb. 2006.

[232] O. Calinescu, I. A. Badea, L. Vladescu, V. Meltzer, and E. Pincu, "HPLC separation of acetaminophen and its impurities using a mixed-mode reversed-phase/cation exchange stationary phase," *J. Chromatogr. Sci.*, vol. 50, no. 4, pp. 335–342, 2012.

[233] J. Vojta, P. Hanzlík, A. Jedlička, and P. Coufal, "Separation and determination of impurities in paracetamol, codeine and pitophenone in the presence of fenpiverinium in combined suppository dosage form.," *J. Pharm. Biomed. Anal.*, vol. 102, pp. 85–92, Jan. 2015.

[234] T. Németh, P. Jankovics, J. Németh-Palotás, and H. Koszegi-Szalai, "Determination of paracetamol and its main impurity 4-aminophenol in analgesic preparations by micellar electrokinetic chromatography.," *J. Pharm. Biomed. Anal.*, vol. 47, no. 4–5, pp. 746–9, Aug. 2008.

[235] C. Akay, I. T. Degim, and A. Sayal, "Simultaneous determination of acetylsalicylic acid, paracetamol, and their degradation and toxic impurity products by HPLC in pharmaceutical dosage forms," *TURKISH J. …*, vol. 38, no. 2, pp. 167–173, 2008.

[236] E. McEvoy, S. Donegan, J. Power, and K. Altria, "Application of MELC and MEEKC for the Analysis of Paracetamol and Related Impurities in Suppositories," *Chromatographia*, vol. 68, no. 1–2, pp. 49–56, May 2008.

[237] P. J. Frawley, N. A. Mitchell, C. T. Ó'Ciardhá, and K. W. Hutton, "The effects of supersaturation, temperature, agitation and seed surface area on the secondary nucleation of paracetamol in ethanol solutions," *Chem. Eng. Sci.*, vol. 75, pp. 183–197, Jun. 2012.

[238] W.-S. Kim, "Application of Taylor Vortex to Crystallization," *J. Chem. Eng. JAPAN*, vol. 47, no. 2, pp. 115–123, 2014.

[239] L. L. Simon, Z. K. Nagy, and K. Hungerbuhler, "Comparison of external bulk video imaging with focused beam reflectance measurement and ultra-violet visible spectroscopy for metastable zone identification in food and pharmaceutical crystallization processes," *Chem. Eng. Sci.*, vol. 64, no. 14, pp. 3344–3351, Jul. 2009.

[240] L. L. Simon, K. A. Oucherif, Z. K. Nagy, and K. Hungerbuhler, "Histogram Matching, Hypothesis Testing, and Statistical Control-Chart-Assisted Nucleation Detection Using Bulk Video Imaging for Optimal Switching between Nucleation and Seed Conditioning Steps," *Ind. Eng. Chem. Res.*, vol. 49, no. 20, pp. 9932–9944, Oct. 2010.

[241] T. Togkalidou, H.-H. Tung, Y. Sun, A. Andrews, and R. D. Braatz, "Solution Concentration Prediction for Pharmaceutical Crystallization Processes Using Robust Chemometrics and ATR FTIR Spectroscopy," *Org. Process Res. Dev.*, vol. 6, no. 3, pp. 317–322, May 2002.

[242] H. Wen, K. R. Morris, and K. Park, "Synergic effects of polymeric additives on dissolution and crystallization of acetaminophen.," *Pharm. Res.*, vol. 25, no. 2, pp. 349–58, Feb. 2008.

[243] M. N. Femi-Oyewo and M. S. Spring, "Studies on paracetamol crystals produced by growth in aqueous solutions," *Int. J. Pharm.*, vol. 112, no. 1, pp. 17–28, 1994.

[244] J. S. Capes and R. E. Cameron, “Effect of polymer addition on the contact line crystallisation of paracetamol,” *CrystEngComm*, vol. 9, no. 1, p. 84, Dec. 2007.

[245] C. Thompson, M. C. Davies, C. J. Roberts, S. J. B. Tendler, and M. J. Wilkinson, “The effects of additives on the growth and morphology of paracetamol (acetaminophen) crystals.,” *Int. J. Pharm.*, vol. 280, no. 1–2, pp. 137–150, Aug. 2004.

[246] L. Li, D. Lechuga-Ballesteros, B. A. Szkudlarek, and N. Rodríguez-Hornedo, “The Effect of Additives on Glycine Crystal Growth Kinetics,” *J. Colloid Interface Sci.*, vol. 168, pp. 8–14, 1994.

[247] Á. Borsos, A. Majumder, and Z. K. Nagy, “Model development and experimental validation for crystal shape control by using tailored mixtures of crystal growth modifiers,” *Computer Aided Chemical Engineering*, vol. 33, no. 2009. pp. 781–786, 2014.

[248] R. I. Ristic, S. Finnie, D. B. Sheen, and J. N. Sherwood, “Macro- and Micromorphology of Monoclinic Paracetamol Grown from Pure Aqueous Solution,” *J. Phys. Chem. B*, vol. 105, no. 38, pp. 9057–9066, Sep. 2001.

[249] H. Wen, K. R. Morris, and K. Park, “Hydrogen bonding interactions between adsorbed polymer molecules and crystal surface of acetaminophen.,” *J. Colloid Interface Sci.*, vol. 290, no. 2, pp. 325–35, Oct. 2005.

[250] A. D. Randolph and M. A. Larson, “Transient and steady state size distributions in continuous mixed suspension crystallizers,” *AIChE J.*, vol. 8, no. 5, pp. 639–645, Nov. 1962.

[251] J. Nyvlt, O. Söhnel, M. Matachová, and M. Broul, “The kinetics of industrial crystallization,” *AIChE J.*, vol. 32, no. 7, pp. 1231–1231, Jul. 1986.

[252] A. D. McNaught and A. Wilkinson, *IUPAC Compendium of Chemical Terminology*, 2nd ed. 2006.

[253] B. O. Sullivan, B. Smith, and G. Baramidze, “Recent Advances for Seeding a Crystallization Process A Review of Modern Techniques Crystallization Development.” Mettler Toledo, Columbia, USA, pp. 3–12, 2013.

[254] N. Doki, N. Kubota, A. Sato, and M. Yokota, “Effect of cooling mode on product crystal size in seeded batch crystallization of potassium alum,” *Chem. Eng. J.*, vol. 81, no. 1–3, pp. 313–316, Jan. 2001.

[255] S. Ferguson, “Continuous Crystallization of Pharmaceutical Compounds.” 2009.

[256] H. Gros, T. Kilpio, and J. Nurmi, “Continuous Cooling Crystallization from Solution,” *Powder Technol.*, vol. 121, pp. 106–115, 2001.

[257] B. Harji, “Crystallisation Process and Apparatus,” WO/2011/051,728, 2011.

[258] R. J. P. Eder, M. O. Besenhard, S. Schrank, E. Roblegg, H. Gruber-Woelflera, and J. G. Khinast, “API Crystallization in a Continuous-Flow Equipment,” in *Associazione Italiana Di Ingegneria Chimica (AIDIC)*, 2011, pp. 1–4.

[259] V. Liotta and V. Sabesan, “Monitoring and Feedback Control of Supersaturation Using ATR-FTIR to Produce an Active Pharmaceutical Ingredient of a Desired Crystal Size,” *Org. Process Res. Dev.*, 2004.

[260] M. R. H. A. Bakar, Z. K. Nagy, and C. D. Rielly, “Seeded batch cooling crystallization with temperature cycling for the control of size uniformity and polymorphic purity of sulfathiazole crystals,” *Org. Process Res. Dev.*, vol. 13, no. 3, pp. 1343–1356, 2009.

[261] M. R. H. A. Bakar, Z. K. Nagy, and C. D. Rielly, “Optimal seed recipe design for crystal size distribution control for batch cooling crystallisation processes,” *Chem. Eng. Sci.*, vol. 65, no. 11, pp. 3602–3614, Jun. 2010.

[262] K. A. Powell, C. D. Rielly, Z. K. Nagy, and A. N. Saleemi, “Periodic Steady-State Flow Crystallization of a Pharmaceutical Drug Using MSMPR Operation,” *Chem. Eng. Process. Process Intensification.*, 2015.

[263] J. W. Mullin, *Crystallization*, Fourth. Oxford: Butterworth-Heinemann, 2001.

[264] N. A. Mitchell and P. J. Frawley, “Nucleation kinetics of paracetamol–ethanol solutions from metastable zone widths,” *J. Cryst. Growth*, vol. 312, no. 19, pp. 2740–2746, Sep. 2010.

[265] N. a. Mitchell, C. T. Ó’Ciardhá, and P. J. Frawley, “Estimation of the growth kinetics for the cooling crystallisation of paracetamol and ethanol solutions,” *J. Cryst. Growth*, vol. 328, no. 1, pp. 39–49, Aug. 2011.

[266] N. Reis, A. A. A. Vicente, J. A. A. Teixeira, and M. R. Mackley, “Residence times and mixing of a novel continuous oscillatory flow screening reactor,” *Chem. Eng. Sci.*, vol. 59, no. 22–23, pp. 4967–4974, Nov. 2004.

[267] N. Reis, A. a. A. A. Vicente, and J. A. Teixeira, “Liquid backmixing in oscillatory flow through a periodically constricted meso-tube,” *Chem. Eng. Process. Process Intensif.*, vol. 49, no. 7, pp. 793–803, Jul. 2010.

[268] P. V. Danckwerts, “Continuous flow systems. Distribution of residence times,” *Chem. Eng. Sci.*, vol. 50, no. 24, pp. 3857–3866, 1995.

[269] E. L. Paul, V. Atiemo-obeng, and S. M. Kresta, *Handbook of Industrial Mixing*. 2004.

[270] J. W. Mullin, *Crystallization*, 4th Editio. Oxford: Wiley, 2001.

[271] T. W. Evans, A. F. Sarofim, and G. Margolis, “Models of secondary nucleation attributable to crystal-crystallizer and crystal-crystal collisions,” *AIChE Journal.*, vol. 20, no. 5, pp. 959–966, 1974.

[272] H. S. Mumtaz, M. J. H. Member, N. A. S. Member, and W. R. P. Member, “Orthokinetic Aggregation During Precipitation: A Computational Model for Calcium Oxalate Monohydrate,” *IchemE*, vol. 75, pp. 152–159, 1997.

[273] I. Weissbuch, V. Y. Torbeev, L. Leiserowitz, and M. Lahav, “Solvent effect on crystal polymorphism: why addition of methanol or ethanol to aqueous solutions induces the precipitation of the least stable beta form of glycine.,” *Angew. Chem. Int. Ed. Engl.*, vol. 44, no. 21, pp. 3226–9, May 2005.

[274] S. Gnanasambandam and R. Rajagopalan, “Growth morphology of α-glycine crystals in solution environments: an extended interface structure analysis,” *CrystEngComm*, vol. 12, no. 6, p. 1740, May 2010.

[275] Q. Su, M.-S. Chiu, and R. D. Braatz, “Modeling and Bayesian parameter estimation for semibatch pH-shift reactive crystallization of l -glutamic acid,” *AIChE J.*, vol. 60, no. 8, pp. 2828–2838, Aug. 2014.

[276] A. Majumder and Z. K. Nagy, “Prediction and control of crystal shape distribution in the presence of crystal growth modifiers,” *Chem. Eng. Sci.*, vol. 101, pp. 593–602, 2013.

[277] T. C. Lewis, D. A. Tocher, and S. L. Price, “An Experimental and Theoretical Search for Polymorphs of Barbituric Acid: The Challenges of Even Limited Conformational

Flexibility," *Cryst. Growth Des.*, vol. 4, no. 5, pp. 979–987, Sep. 2004.

[278] M. Gryl, A. Krawczuk, and K. Stadnicka, "Polymorphism of urea-barbituric acid co-crystals.," *Acta Crystallogr. B.*, vol. 64, no. Pt 5, pp. 623–32, Oct. 2008.

[279] M. Gryl, A. Krawczuk-Pantula, and K. Stadnicka, "Charge-density analysis in polymorphs of urea-barbituric acid co-crystals.," *Acta Crystallogr. B.*, vol. 67, no. Pt 2, pp. 144–54, Apr. 2011.

[280] D. Braga, M. Cadoni, F. Grepioni, L. Maini, and K. Rubini, "Gas-solid reactions between the different polymorphic modifications of barbituric acid and amines," *CrystEngComm*, vol. 8, no. 10, p. 756, 2006.

[281] W. Bolton, "The crystal structure of anhydrous barbituric acid," *Acta Crystallogr.*, vol. 16, no. 3, pp. 166–173, Mar. 1963.

[282] J. A. Zerkowski, C. T. Seto, D. A. Wierda, and G. M. Whitesides, "The design of organic structures in the solid state: hydrogen-bonded molecular 'tapes,'" *J. Am. Chem. Soc.*, vol. 112, no. 24, pp. 9025–9026, Nov. 1990.

[283] J. A. Zerkowski, C. T. Seto, and G. M. Whitesides, "Solid-state structures of rosette and crinkled tape motifs derived from the cyanuric acid melamine lattice," *J. Am. …*, no. 18, pp. 5473–5475, 1992.

[284] Folkers John P., J. A. Zerkowski, Laibinis Paul E., C. T. Seto, and Whitesides George M., *Supramolecular Architecture*, vol. 499. Washington, DC: American Chemical Society, 1992.

[285] J. A. Zerkowski, J. P. Mathias, and G. M. Whitesides, "New Varieties of Crystalline Architecture Produced by Small Changes in Molecular Structure in Tape Complexes of Melamines and Barbiturates," *J. Am. Chem. Soc.*, vol. 116, no. 10, pp. 4305–4315, May 1994.

[286] J. A. Zerkowski and G. M. Whitesides, "Steric Control of secondary, solid-state architecture in 1:1 complexes of melamines and barbiturates that crystallize as crinkled tapes," *J. Am. Chem. Soc.*, vol. 116, no. 10, pp. 4298–4304, May 1994.

[287] J. A. Zerkowski, J. C. MacDonald, C. T. Seto, D. A. Wierda, and G. M. Whitesides, "Design of Organic Structures in the Solid State: Molecular Tapes Based on the Network of Hydrogen Bonds Present in the Cyanuric Acid.cntdot.Melamine Complex," *J. Am. Chem. Soc.*, vol. 116, no. 6, pp. 2382–2391, Mar. 1994.

[288] A. V Yadav, A. S. Shete, A. P. Dabke, P. V Kulkarni, and S. S. Sakhare, "Co-crystals: a novel approach to modify physicochemical properties of active pharmaceutical ingredients.," *Indian J. Pharm. Sci.*, vol. 71, no. 4, pp. 359–70, Jul. 2009.

[289] R. Prasad and M. Rakesh, "Pharmaceutical cocrystallization: a review," *Int J Pharm Chem …*, vol. 1, no. 3, pp. 725–736, 2012.

[290] P. P. Bag, M. Patni, and C. Malla Reddy, "A kinetically controlled crystallization process for identifying new co-crystal forms: fast evaporation of solvent from solutions to dryness," *CrystEngComm*, vol. 13, no. 19, p. 5650, Sep. 2011.

[291] M. C. Sarraguça, P. R. Ribeiro, A. Santos, M. C. Silva, and J. a Lopes, "A PAT approach for the on-line monitoring of pharmaceutical co-crystals formation with near infrared spectroscopy.," *Int. J. Pharm.*, vol. 471, no. 1–2, pp. 478–484, Jun. 2014.

[292] E. Gagniere, D. Mangin, and F. Puel, "Cocrystal formation in solution: in situ solute concentration monitoring of the two components and kinetic pathways," *Cryst. Growth Des.*, vol. 9, no. 8, pp. 3376–3383, 2009.

[293] M. B. Hickey, M. L. Peterson, L. A. Scoppettuolo, S. L. Morrisette, A. Vetter, H. Guzmán, J. F. Remenar, Z. Zhang, M. D. Tawa, S. Haley, M. J. Zaworotko, and O. Almarsson, “Performance comparison of a co-crystal of carbamazepine with marketed product.,” *Eur. J. Pharm. Biopharm.*, vol. 67, no. 1, pp. 112–9, Aug. 2007.

[294] Y.-H. Luo, C.-G. Zhang, B. Xu, and B.-W. Sun, “A cocrystal strategy for the precipitation of liquid 2,3-dimethyl pyrazine with hydroxyl substituted benzoic acid and a Hirshfeld surfaces analysis of them,” *CrystEngComm*, vol. 14, no. 20, p. 6860, Sep. 2012.

[295] K. Chadwick, R. Davey, and W. Cross, “How does grinding produce co-crystals? Insights from the case of benzophenone and diphenylamine,” *CrystEngComm*, vol. 9, no. 9, p. 732, Aug. 2007.

[296] A. Ainouz, J.-R. Authelin, P. Billot, and H. Lieberman, “Modeling and prediction of cocrystal phase diagrams.,” *Int. J. Pharm.*, vol. 374, no. 1–2, pp. 82–9, Jun. 2009.

[297] J. R. G. Sander, D.-K. Bucar, R. F. Henry, J. Baltrusaitis, G. G. Z. Zhang, and L. R. MacGillivray, “A red zwitterionic co-crystal of acetaminophen and 2,4-pyridinedicarboxylic acid.,” *J. Pharm. Sci.*, vol. 99, no. 9, pp. 3676–83, Sep. 2010.

[298] T. Friščić, S. L. Childs, S. A. A. Rizvi, and W. Jones, “The role of solvent in mechanochemical and sonochemical cocrystal formation: a solubility-based approach for predicting cocrystallisation outcome,” *CrystEngComm*, vol. 11, no. 3, p. 418, Feb. 2009.

[299] M. R. H. A. Bakar, Z. K. Nagy, A. N. Saleemi, and C. D. Rielly, “The Impact of Direct Nucleation Control on Crystal Size Distribution in Pharmaceutical Crystallization Processes,” *Cryst. Growth Des.*, vol. 9, no. 3, pp. 1378–1384, Mar. 2009.

[300] H. F. Wilhelm Ostwald, Max Bodenstein, Klaus Clusius, Karl Friedrich Bonhoeffer, *Zeitschrift für physikalische Chemie, Volume 22*. Akademische Verlagsgesellschaft Geest & Portig, 1897.

[301] S. Kim, B. Lotz, M. Lindrud, K. Girard, T. Moore, K. Nagarajan, M. Alvarez, T. Lee, F. Nikfar, M. Davidovich, S. Srivastava, and S. Kiang, “Control of the Particle Properties of a Drug Substance by Crystallization Engineering and the Effect on Drug Product Formulation,” *Org. Process Res. Dev.*, vol. 9, no. 6, pp. 894–901, Nov. 2005.

[302] J. P. Fitts, X. Shang, G. W. Flynn, T. F. Heinz, and K. B. Eisenthal, “Electrostatic surface charge at aqueous/alpha-Al2O3 single-crystal interfaces as probed by optical second-harmonic generation.,” *J. Phys. Chem. B*, vol. 109, no. 16, pp. 7981–6, Apr. 2005.

[303] D. R. Thompson, E. Kougoulos, A. G. Jones, and M. W. Wood-Kaczmar, “Solute concentration measurement of an important organic compound using ATR-UV spectroscopy,” *J. Cryst. Growth*, vol. 276, no. 1–2, pp. 230–236, Mar. 2005.

[304] A. Abbas, D. Nobbs, and J. a Romagnoli, “Investigation of on-line optical particle characterization in reaction and cooling crystallization systems. Current state of the art,” *Meas. Sci. Technol.*, vol. 13, no. 3, pp. 349–356, Mar. 2002.

[305] A. F. T. Silva, A. Burggraeve, Q. Denon, P. Van der Meeren, N. Sandler, T. Van Den Kerkhof, M. Hellings, C. Vervaet, J. P. Remon, J. A. Lopes, and T. De Beer, “Particle sizing measurements in pharmaceutical applications: comparison of in-process methods versus off-line methods.,” *Eur. J. Pharm. Biopharm.*, vol. 85, no. 3 Pt B, pp. 1006–18, Nov. 2013.

[306] C. Bosquillon, C. Lombry, V. Preat, and R. Vanbever, “Comparison of particle sizing

techniques in the case of inhalation dry powders.," *J. Pharm. Sci.*, vol. 90, no. 12, pp. 2032–41, Dec. 2001.

[307] K. Sato, "Polymorphic transformations in crystal growth," *J. Phys. D. Appl. Phys.*, vol. 26, no. 8B, pp. B77–B84, Aug. 1993.

[308] A. Maher, D. M. Croker, Å. C. Rasmuson, and B. K. Hodnett, "Solution Mediated Polymorphic Transformation: Form II to Form III Piracetam in Ethanol," *Cryst. Growth Des.*, vol. 12, no. 12, pp. 6151–6157, Dec. 2012.

[309] C. Lamberth, S. Jeanmart, T. Luksch, and A. Plant, "Current challenges and trends in the discovery of agrochemicals.," *Science*, vol. 341, no. 6147, pp. 742–6, Aug. 2013.

[310] C. M. Henry, "Structure-Based Drug Design," *Chemical and Engineering News: Science and Technology*, vol. 79, no. 23, Washington, pp. 67–74, 2001.

[311] I. D. Kuntz, "Structure-Based Strategies for Drug Design and Discovery," *Science (80-.).*, vol. 257, no. 5073, pp. 1078–1082, Aug. 1992.

[312] J. N. Varghese, "Development of neuraminidase inhibitors as anti-influenza virus drugs," *Drug Dev. Res.*, vol. 46, no. 3–4, pp. 176–196, Mar. 1999.

[313] S. Walmsley, B. Bernstein, M. King, J. Arribas, G. Beall, P. Ruane, M. Johnson, and D. Johnson, "Lopinavir–Ritonavir versus Nelfinavir for the Initial Treatment of HIV Infection," *N Engl J Med*, vol. 346, pp. 2039–2046, 2002.

[314] A. Ajibola, P. Gago-Ferrero, V. L. Borova, M. E. Dasenaki, A. A. Bletsou, and N. S. Thomaidis, "Benzosulfonamides in wastewater: method development, occurrence and removal efficiencies.," *Chemosphere*, vol. 119 Suppl, pp. S21–7, Jan. 2015.

[315] M. Farahi, B. Karami, and H. M. Tanuraghaj, "Efficient synthesis of a new class of sulfonamide-substituted coumarins," *Tetrahedron Lett.*, vol. 56, no. 14, pp. 1833–1836, Apr. 2015.

[316] T. N. Drebushchak, N. A. Pankrushina, A. N. Mikheev, and M. K. A. Thumm, "Crystalline products of tolbutamide decomposition in water after microwave treatment," *CrystEngComm*, vol. 15, no. 18, p. 3582, Apr. 2013.

[317] R. K. Palmer, K. Atwal, I. Bakaj, S. Carlucci-Derbyshire, M. T. Buber, R. Cerne, R. Y. Cortés, H. R. Devantier, V. Jorgensen, A. Pawlyk, S. P. Lee, D. G. Sprous, Z. Zhang, and R. Bryant, "Triphenylphosphine oxide is a potent and selective inhibitor of the transient receptor potential melastatin-5 ion channel.," *Assay Drug Dev. Technol.*, vol. 8, no. 6, pp. 703–13, Dec. 2010.

[318] S. M. Richoll and I. Colón, "Determination of triphenylphosphine oxide in active pharmaceutical ingredients by hollow-fiber liquid-phase microextraction followed by reversed-phase liquid chromatography.," *J. Chromatogr. A*, vol. 1127, no. 1–2, pp. 147–53, Sep. 2006.

[319] A. L. Spek, "Structure of a second monoclinic polymorph of triphenylphosphine oxide," *Acta Crystallogr. Sect. C Cryst. Struct. Commun.*, vol. 43, no. 6, pp. 1233–1235, Jun. 1987.

[320] M. C. Etter and P. W. Baures, "Triphenylphosphine oxide as a crystallization aid," *J. Am. Chem. Soc.*, vol. 110, no. 2, pp. 639–640, Jan. 1988.

[321] G. Ferguson and C. Glidewell, "The reactions of triphenylphosphine The reactions of triphenylphosphine and triphenylarsine with chloramine-T, sodium N-chlorotoluene-p-sulphonamide: crystal and molecular structure of triphenylphosphine oxide–toluene-p-sulphonamide (2/3)," *J. Chem. Soc. Perkin Trans. 2*, no. 12, pp. 2129–2132, Jan.

1988.

[322] G. Ferguson, A. J. Lough, and C. Glidewell, “The reactions of triarylphosphines and triarylarsines with chloramines B and T: crystal and molecular structures of triphenylarsine oxide-benzenesulphonamide (1 : 1) hemi-acetone solvate and tri-m-tolylphosphine oxide-toluene-p-sulphonamide (1 : 1),” *J. Chem. Soc. Perkin Trans. 2*, no. 12, p. 2065, Jan. 1989.

[323] D. M. Croker, M. E. Foreman, B. N. Hogan, N. M. Maguire, C. J. Elcoate, B. K. Hodnett, A. R. Maguire, Å. C. Rasmuson, and S. E. Lawrence, “Understanding the p -Toluenesulfonamide/Triphenylphosphine Oxide Crystal Chemistry: A New 1:1 Cocrystal and Ternary Phase Diagram,” *Cryst. Growth Des.*, vol. 12, no. 2, pp. 869–875, Feb. 2012.

[324] D. M. Croker, R. J. Davey, Å. C. Rasmuson, and C. C. Seaton, “Nucleation in the p -Toluenesulfonamide/Triphenylphosphine Oxide Co-crystal System,” *Cryst. Growth Des.*, vol. 13, no. 8, pp. 3754–3762, Aug. 2013.

[325] D. M. Croker and Å. C. Rasmuson, “Isothermal Suspension Conversion as a Route to Cocrystal Production: One-Pot Scalable Synthesis,” *Org. Process Res. Dev.*, vol. 18, no. 8, pp. 941–946, Aug. 2014.

[326] D. M. Croker, R. J. Davey, Å. C. Rasmuson, and C. C. Seaton, “Solution mediated phase transformations between co-crystals,” *CrystEngComm*, vol. 15, no. 11, p. 2044, Feb. 2013.

[327] N. Rodríguez-Hornedo, S. J. Nehm, K. F. Seefeldt, Y. Pagan-Torres, and C. J. Falkiewicz, “Reaction crystallization of pharmaceutical molecular complexes.,” *Mol. Pharm.*, vol. 3, no. 3, pp. 362–367, Jan. 2006.

[328] E. Gagniere, D. Mangin, F. Puel, A. Rivoire, O. Monnier, E. Garcia, and J. Klein, “Formation of co-crystals: Kinetic and thermodynamic aspects,” *J. Cryst. Growth*, vol. 311, no. 9, pp. 2689–2695, Apr. 2009.

[329] S. H. Neau, G. L. Flynn, and S. H. Yalkowsky, “The influence of heat capacity assumptions on the estimation of solubility parameters from solubility data,” *Int. J. Pharm.*, vol. 49, no. 3, pp. 223–229, Feb. 1989.

[330] M. Belmares, M. Blanco, W. A. Goddard, R. B. Ross, G. Caldwell, S.-H. Chou, J. Pham, P. M. Olofson, and C. Thomas, “Hildebrand and Hansen Solubility Parameters from Molecular Dynamics with Applications to Electronic Nose Polymer Sensors,” *J Comput Chem*, vol. 25, pp. 1814–1826, 2004.

[331] H. Flores, E. Adriana Camarillo, and P. Amador, “Enthalpies of combustion and formation of benzenesulfonamide and some of its derivatives,” *J. Chem. Thermodyn.*, vol. 47, pp. 408–411, Apr. 2012.

[332] D. R. Kirklin and E. S. Domalski, “Enthalpies of combustion of triphenylphosphine and triphenylphosphine oxide,” *J. Chem. Thermodyn.*, vol. 20, no. 6, pp. 743–754, Jun. 1988.

[333] M. R. J. Dack, *Solutions and Solubilities. Part II, in: Techniques of Chemistry, Vol. VIII*. New York; London: Wiley-Interscience, 1976.

[334] Z. Q. Yu, P. S. Chow, and R. B. H. Tan, “Operating Regions in Cooling Cocrystallization of Caffeine and Glutaric Acid in Acetonitrile,” *Cryst. Growth Des.*, vol. 10, no. 5, pp. 2382–2387, May 2010.

[335] A. R. Hind, S. K. Bhargava, and A. McKinnon, “At the solid/liquid interface: FTIR/ATR

— the tool of choice," *Adv. Colloid Interface Sci.*, vol. 93, no. 1–3, pp. 91–114, Oct. 2001.

[336] G. Yang, L. Zhou, and C. Liu, "Glycine canonical and zwitterionic isomers within zeolites.," *J. Phys. Chem. B*, vol. 113, no. 30, pp. 10399–402, Jul. 2009.

[337] T. Togkalidou, M. Fujiwara, S. Patel, and R. D. Braatz, "Solute concentration prediction using chemometrics and ATR-FTIR spectroscopy," *J. Cryst. Growth*, vol. 231, no. 4, pp. 534–543, 2001.

Appendix 1

1.1. A1. Generic Multivariate Model Development Code (GLY-H_2O)

```
clc;
clear;
load StepwiseVariables7 % variable selection using forward multiple linear
regression (MLR)
tic

% Calibration model training data set
data=xlsread('Calibration_Model_Data.xlsx','Training_Set'); % Reads data
from Excel
X=data(2:120,in); % Selected variables from MLR
y=data(2:120,3328); % Concentration values for model training data
[n,p]= size(X); % Gives size of the temperature and spectral data matrix

% Preprocessing
meanX=mean(X); % Calculates the mean spectrum
[X] = msc(X,mean(X)); % Multiplicative scatter correction pre-processing
[X] = savgol(X,7,3,1); % Derivative pre-processing
[X_Scaled,mx,stdx]=autoscale(X,[],[]); % Auto-scaling of spectra +
temperature
[y_Scaled,my,stdy]=autoscale(y,[],[]); % Auto-scaling of assigned
concentration values

% PLS model
 [Xloadings,Yloadings,Xscores,Yscores,betaPLS3,PLSPctVar,PLSmsep,stats] =
plsregress(X_Scaled,y_Scaled,7,'CV',10); % Performs PLS regression with
components

figure (1), plot(1:7,cumsum(100*PLSPctVar(2,:)),'-bo');
xlabel('Number of PLS components');
ylabel('Percent Variance Explained in Y'); % The plot shows how much
variance is explained by each PLS factor
yfitPLS = [ones(n,1) X_Scaled]*betaPLS3 *stdy + my; % Calculates
concentration of the test data with the developed model
yval=[ones(n,1) X_Scaled]*betaPLS3;

% PCR Model
[PCALoadings,PCAScores,PCAVar] = princomp(X_Scaled); % Builds PCR model
betaPCR = regress(y_Scaled-mean(y_Scaled), PCAScores(:,1:10)); % Change no.
"10" here to change no. of components
betaPCR = PCALoadings(:,1:10)*betaPCR *stdy + my; % This should be same as
in previous line
betaPCR = [mean(y_Scaled) - mean(X_Scaled)*betaPCR; betaPCR];
yfitPCR = [ones(n,1) X_Scaled]*betaPCR;

figure (2), plot(100*cumsum(PCAVar(1:10))/sum(PCAVar(1:10)),'r-^'); %
Variance plot
xlabel('Number of PCR components');
ylabel('Percent Variance Explained in Y');

PCRmsep=sum(crossval(@pcrsse,X,y,'KFold',10),1)/n; % Calculates PCR RMSEP
and Cross Validation
```

```
save MainModel betaPLS3 meanX mx stdx my stdy % Saves model parameters

% PRESS Plot
figure (3), plot(0:10,PLSmsep(2,:),'b-o',0:10,PCRmsep,'r-^'); % Predicted
Residual Error Sum of Squares (PRESS) plot was used to evaluate the quality
of the method
xlabel('Number of components');
ylabel('Estimated Mean Squared Prediction Error');
legend({'PLSR' 'PCR'},'location','NE');

% Principal Component Analysis
figure (4) % PCA plot
pcclusters = clusterdata(PCAScores(:,1:10),7);
gscatter(PCAScores(:,1),PCAScores(:,2),pcclusters); % For generating Scores
scatter plot.
xlabel('PC1');
ylabel('PC2');

figure (5), plot(y,yfitPLS,'bo'); % Plots actual vs predicted
concentrations (PLS model)
xlabel('Observed Response');
ylabel('Fitted Response');
legend({'PLSR with 7 Components'},  ...
    'location','NW');

figure (6), plot(y,yfitPCR,'r^'); % Plots actual vs predicted
concentrations (PCR model)
xlabel('Observed Response');
ylabel('Fitted Response');
legend({'PCR with 10 Components'},  ...
    'location','NW');

% Error calculation PCR/PLS
TSS = sum((y-mean(y)).^2);
RSS_PLS = sum((y-yfitPLS).^2);
rsquaredPLS = 1 - RSS_PLS/TSS
RSS_PCR = sum((y-yfitPCR).^2);
rsquaredPCR = 1 - RSS_PCR/TSS

% Model validation
data=xlsread('Validation Data.xlsx','Validation_Set');
X2=data(2:179,in); % Validataion data
y2=data(2:179,3328); % Concentration values for validation data

% Pre-processing of validation data
[X2] = msc(X2,meanX);
[X2] = savgol(X2,7,3,1);
[n,p]=size(X);
[X2_Scaled]=autoscale(X2,mx,stdx);

yvalPLS = [ones(size(X2_Scaled,1),1) X2_Scaled]*betaPLS3 *stdy+my; % Auto-
scaling relative to training data set
yvalPCR = [ones(size(X2_Scaled,1),1) X2_Scaled]*betaPCR *stdy+my; % Auto-
scaling relative to training data set

figure (7), plot(y2,yvalPLS,'bo',y,yfitPLS,'r^'); % Plots actual vs
predicted concentrations for PLS model
xlabel('Observed Response');
```

```
ylabel('Fitted Response');
legend({'PLSR with 7 Components'},  ...
'location','NW');

figure (8), plot(y2,yvalPCR,'bo',y,yfitPCR,'r^'); % Plots actual vs
predicted concentrations for PCR mode
xlabel('Observed Response');
ylabel('Fitted Response');
legend({'PCR with 3 Components'},  ...
'location','NW');

% Error calculation PCR/PLS
TSS = sum((y2-mean(y)).^2);
RSS_PLS = sum((y2-yvalPLS).^2);
rsquaredPLS = (1 - RSS_PLS/TSS);
RSS_PCR = sum((y2-yvalPCR).^2);
rsquaredPCR = (1 - RSS_PCR/TSS);

% Root mean squared error of prediction calculation
 PLSrmsep=sqrt(sum((y2-yvalPLS).^2)/178) %RMSEP for PLS model
PCRrmsep=sqrt(sum((y2-yvalPCR).^2)/178) %RMSEP for PCR model

% Applying the model for prediction of an unknown data set
data=xlsread('Prediction_Data.xlsx','Prediction_Set');
X3=data(2:179,in); % Prediction data

[X3] = msc(X3,meanX);
[X3] = savgol(X3,7,3,1);
[n,p]=size(X);
[X3_Scaled]=autoscale(X3,mx,stdx);

yvalPLS = [ones(size(X3_Scaled,1),1) X3_Scaled]*betaPLS3 *stdy+my;
yvalPCR = [ones(size(X3_Scaled,1),1) X3_Scaled]*betaPCR *stdy+my;

toc
```

1.2. A1. Statistical Plots for Multivariate Models (GLY-H_2O)

Figure 1.1. A1 below show the statistical plots derived from the PLSR and PCR multivariate calibration models developed using the codes in Section 1.1. A1.

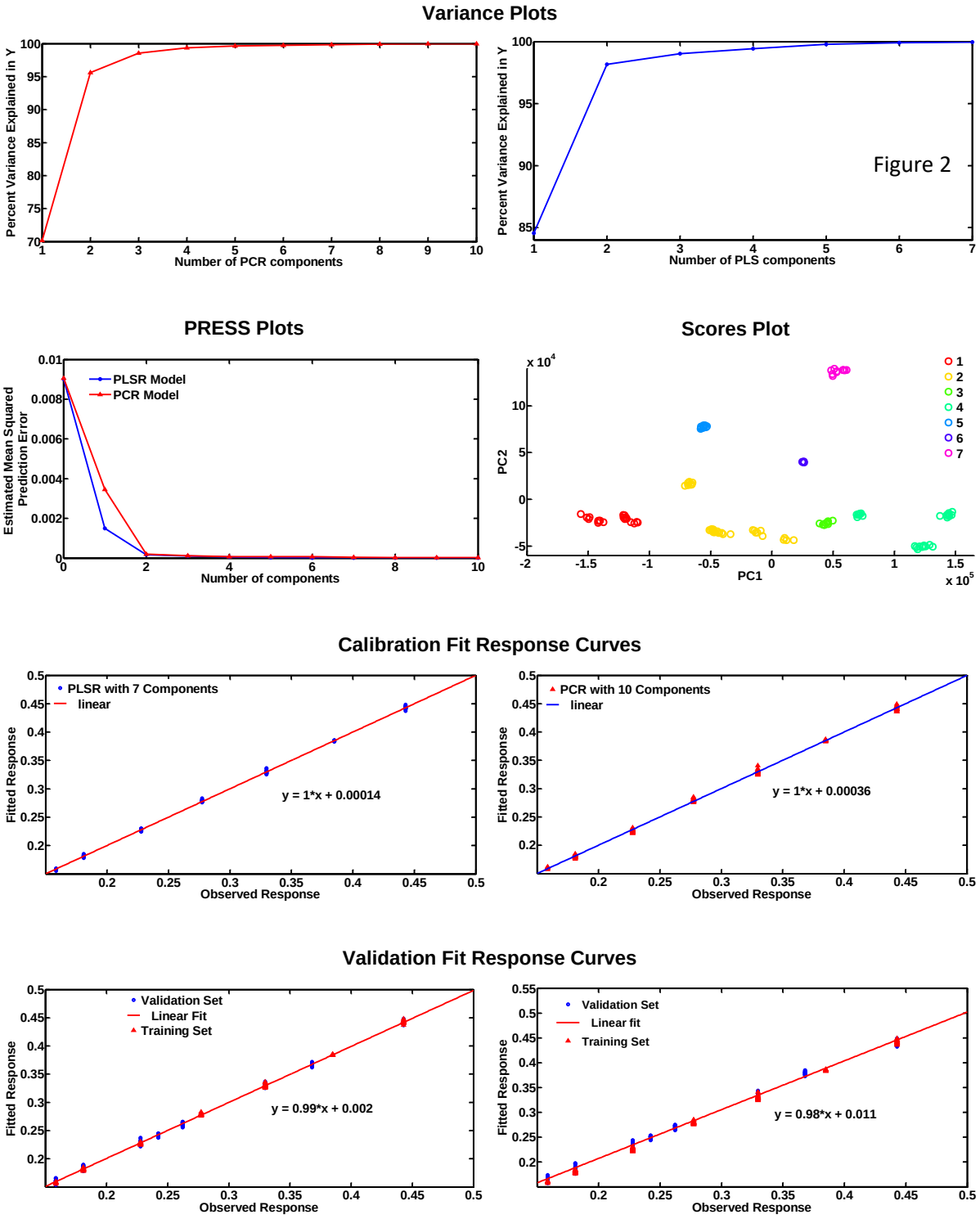

Figure 1.1. A1: Statistical plots derived from the PCR and PLS multivariate calibration models.

Appendix 2

2.1. A2. Urea-Barbituric Acid Co-Crystal Studies in PMSMPR: Raman Spectra

Raman spectroscopy and PXRD are complementary solid state characterization techniques; hence both were used to monitor the UBA polymorphic form during each experiment reported in the paper. Figure 2.1. A2, experiments 1 – 4 and (5) and Figure 2.2. A2, experiments 6 – 9 shows Raman spectra of samples taken from the third-stage PMSMPR (MSMPR 3) after 50 min (a) and 220 min (b), for unseeded and seeded co-crystallization experiments.

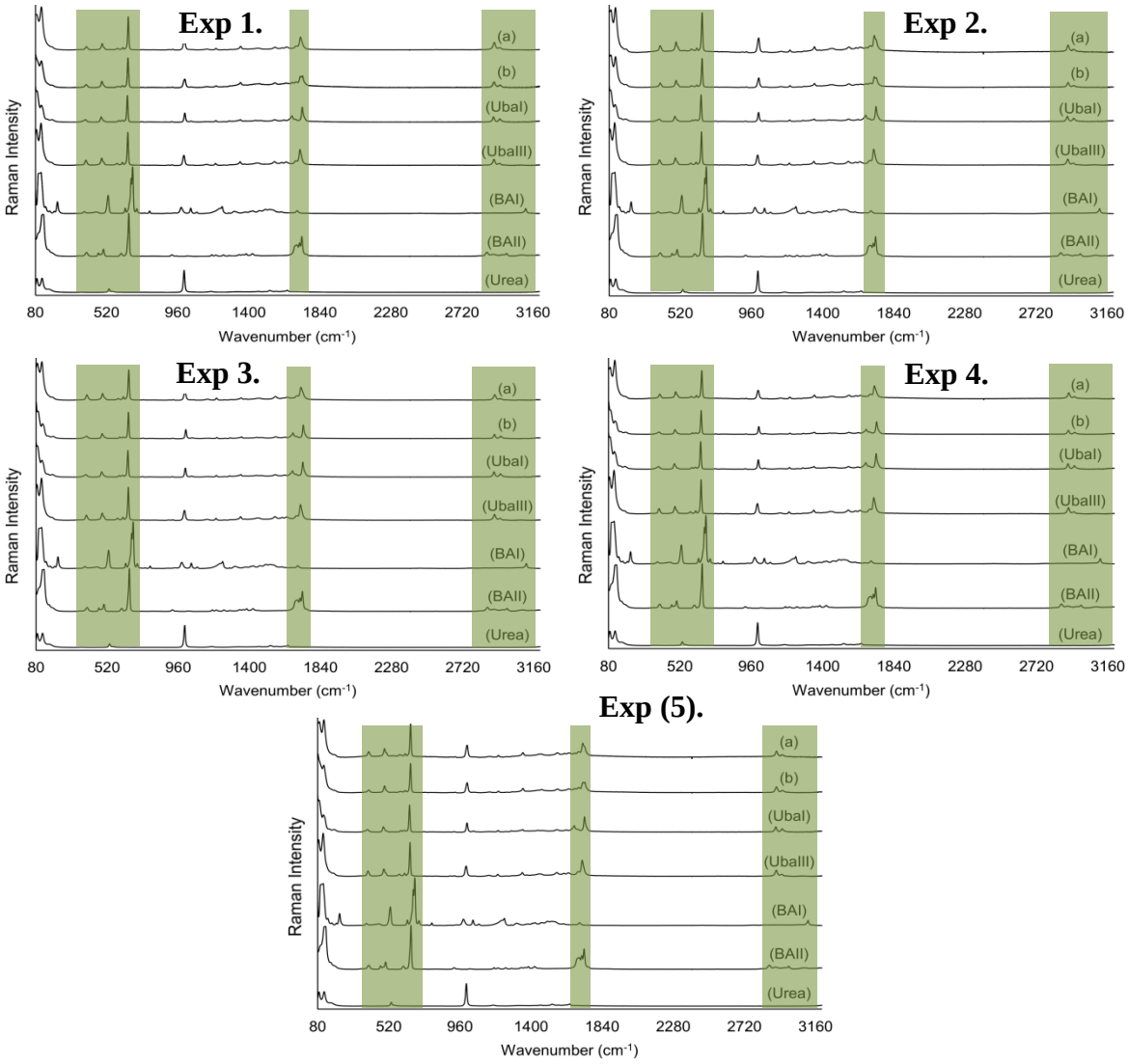

Figure 2.1. A2: Raman spectra of samples taken from each PMSMPR stage during experiments 1 – 4 and (5), reference patterns for UBA forms I and III; BA forms I and II; urea; a) MSMPR 3 at 50 min and b) MSMPR 3 at 220 min.

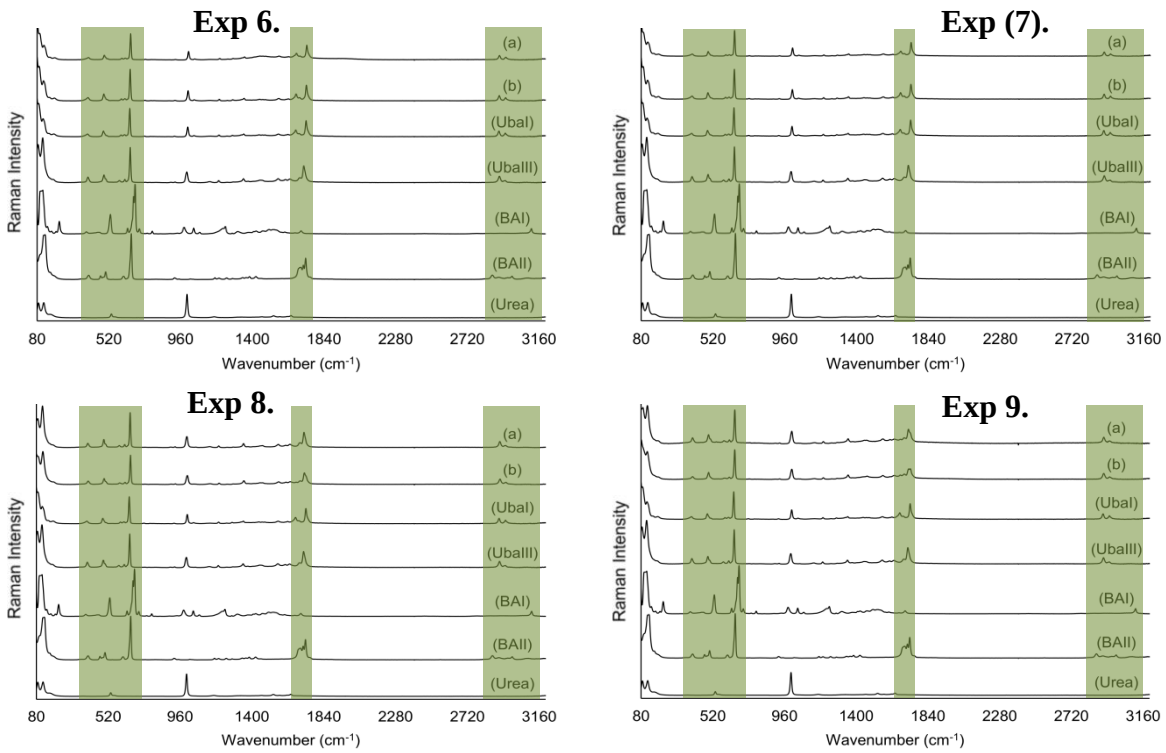

Figure 2.2. A2: Raman spectra of samples taken from each PMSMPR stage during experiments 6 – 9, reference patterns for UBA forms I and III; BA forms I and II; urea; a) MSMPR 3 at 50 min and b) MSMPR 3 at 220 min.

Highlighted regions in Figure 2.1. 2A and Figure 2.2. 2A were used for polymorph identification: 367 – 681 cm^{-1} (aliphatic chain vibrations), 1624 – 1775 cm^{-1} (C=O stretching) and 2885 – 2990 cm^{-1} (C-H stretching).

2.1. A2. Urea-Barbituric Acid Co-Crystal Studies in PMSMPR: PXRD Patterns

Figure 2.3. A2, experiments 1 – 4 and (5) and Figure 2.4. A2, experiments 6 – 9 shows the PXRD patterns of samples taken from each PMSMPR stage at different time intervals. The PXRD patterns captured well the change in polymorphic composition in each stage of the PMSMPR, particularly in the region 23 – 31° 2θ. Two peaks present at 27° and 29° 2θ, which are unique peaks in the patterns of UBA form III and UBA form I, respectively, indicate a mixture of UBA form I and III is initially produced. As the PMSMPR progresses the peak at 27° 2θ is no longer present and there is an increase in the intensity of the peak at 29° 2θ, which signifies the conversion to UBA form I.

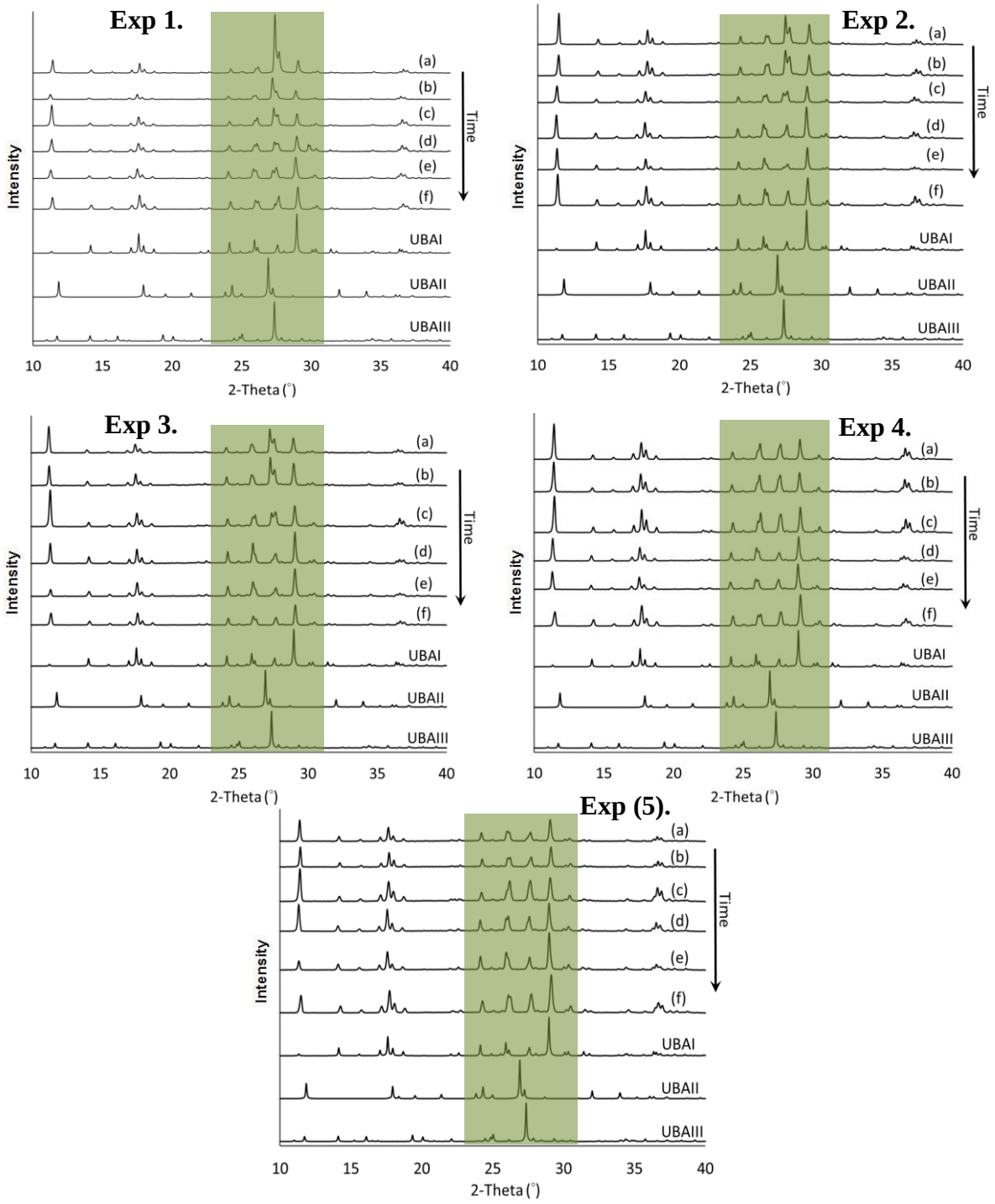

Figure 2.3. 2A: PXRD of samples taken from each PMSMPR stage during experiments 1 – 4 and (5), showing simulated patterns for UBA forms I, II and III calculated from single crystal X-ray data collected at room temperature; a) MSMPR 1 at 30 min., b) MSMPR 2 at 40 min, c) MSMPR3 at 50 min., d) MSMPR 1 at 150 min., e) MSMPR 2 at 160 min. and f) MSMPR 3 at 220 min.

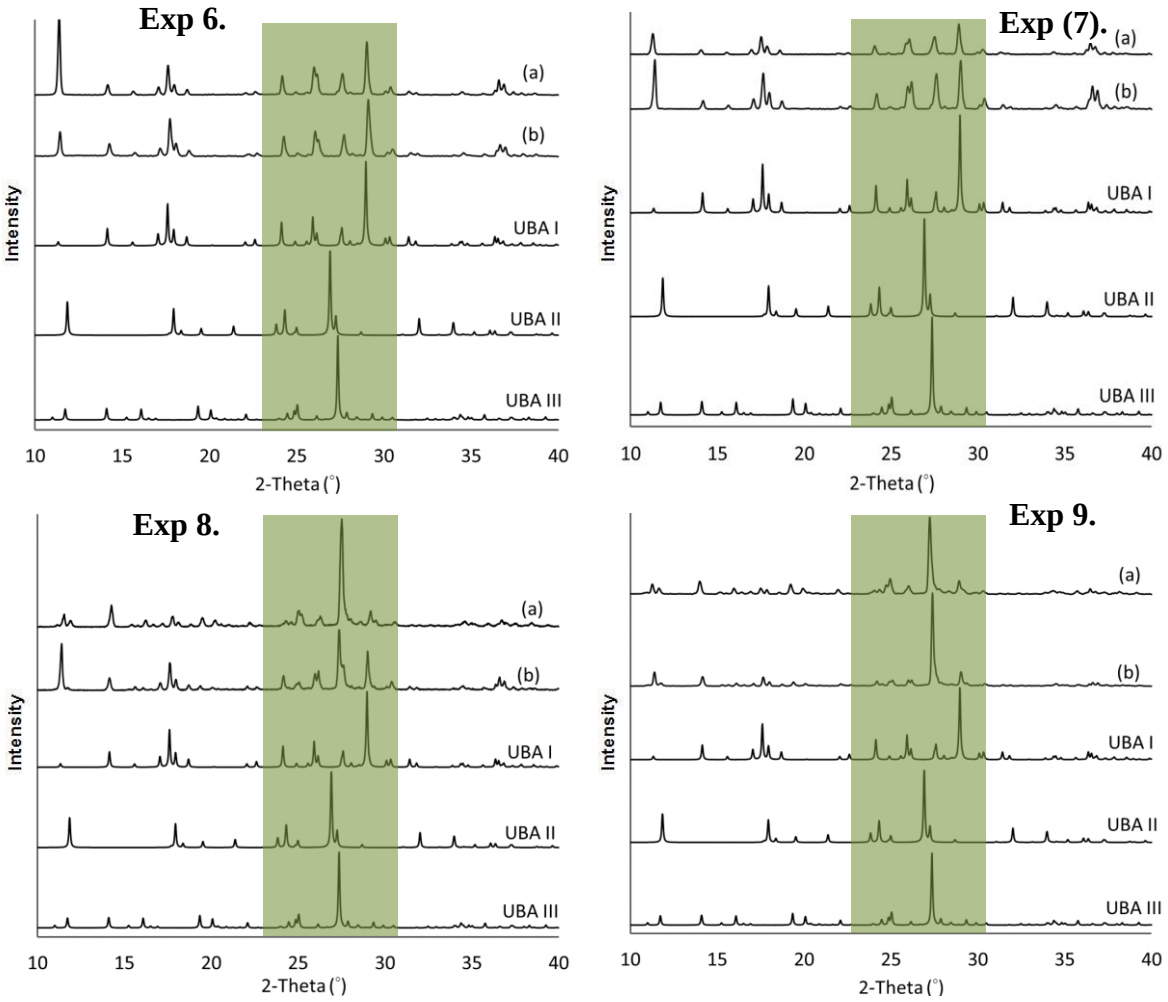

Figure 2.4. A2: PXRD of samples taken from the PMSMPR cascade during experiments 6 – 9, showing simulated patterns for UBA forms I, II and III calculated from single crystal X-ray data collected at room temperature; a) MSMPR 3 at 50 min. and b) MSMPR 3 at 220 min.

Publications

Journal Articles

1. Powell, K. A., Rielly, C. D., Nagy, Z. K., & Saleemi, A. N. (2015). Periodic Steady-State Flow Crystallization of a Pharmaceutical Drug Using MSMPR Operation. Chemical Engineering & Processing: Process Intensification. http://doi.org/10.1016/j.cep.2015.01.002

2. Powell, K. A., Bartolini, G., Wittering, K. E., Saleemi, A. N., Wilson, C. C., Rielly, C. D., & Nagy, Z. K. (2015). Toward Continuous Crystallization of Urea-Barbituric Acid: A Polymorphic Co-Crystal System. Crystal Growth & Design. http://doi.org/10.1021/acs.cgd.5b00599

3. Powell, K. A., Saleemi, A. N., Rielly, C. D., Nagy, Z. K., & Saleemi, A. N. (2015). Monitoring Continuous Crystallization of Paracetamol in the Presence of an Additive Using an Integrated PAT Array and Multivariate Methods. Organic Process Research & Development. http://doi.org/10.1021/acs.oprd.5b00373

4. Powell K. A., Croker D. M., Rielly C. D. and Nagy Z. K. (2016) PAT-based Design of Agrochemical Co Crystallization Processes: A Case-Study for the Selective Crystallization of 1:1 and 3:2 Co Crystals. http://dx.doi.org/10.1016/j.ces.2016.06.005

Articles in Review

1. Powell K. A., Su Q., Rielly C. D. and Nagy Z. K. (2016). Experimental Evaluation of a Novel Periodic Flow Crystallization Process Using MSMPR Operation Part I: Example of a Fast Growing Active Pharmaceutical Ingredient.

2. Su Q., Powell K. A., Rielly C. D. and Nagy Z. K. (2016). Mathematical Evaluation of a Novel Periodic Flow Crystallization Process Using MSMPR Operation Part II: Example of a Fast Growing Active Pharmaceutical Ingredient.

3. Powell K. A., Rielly C. D. and Nagy Z. K. (2016) A Hierarchical Approach to Multivariate Model Development.

4. Powell K. A., Simone E., Croker D. M., Rielly C. D. and Nagy Z. K. (2016) A Raman Spectroscopy Approach to On-line Quantitative Analysis of Stoichiometric Co Crystal Forms of p Toluenesulfanomide/Triphenylphosphine.

Conference Articles

1. Powell K. A., Croker D. M., Rielly C. D. and Nagy Z. K. (2015). PAT-based Design of Agrochemical Co Crystallization Processes: a Case-Study for the Selective Crystallization of 1:1 and 3:2 Co-Crystals of p-Toluenesulfanomide/ Triphenylphosphine, BACG London, UK

2. Powell K. A., Saleemi A. N., Rielly C. D. and Nagy Z. K. (2014). Periodic Flow Crystallization of Fast & Slow Growing APIs in MSMPR: Characterization with Integrated PAT and Information System, Conference Proceedings, BIWIC Rouen, France.

3. Powell K. A., Saleemi A. N., Rielly C. D. and Nagy Z. K. (2014) Periodic Flow Crystallization of Fast and Slow Growing Active Pharmaceutical Ingredients in a MSMPR Crystallizer, Conference Proceedings, BACG Leeds, UK.

4. Powell K. A., Saleemi A. N., Rielly C. D. and Nagy Z. K. (2013). Application of Combined Process Analytical Technologies for the Monitoring of Continuous Crystallisation of Paracetamol, Conference Proceedings, BIWIC Odense, Denmark.

5. Powell K. A., Onyemelukwe I., Saleemi A. N., Rielly C. D. and Nagy Z. K. (2013). Monitoring Paracetamol Crystallisation in a Single Stage MSMPR Crystalliser with Recycle Using in situ Process Raman, FBRM and PVM, Conference Proceedings, BACG Manchester, UK.

Poster Presentations

1. Powell K. A., Simone E., Croker D. M., Rielly C. D. and Nagy Z. K. (2015). Monitoring Phase Transitions in a Co-Crystallisation Process Using in Situ Quantitative Raman, CMAC Open Day Glasgow, UK.

2. Powell K. A., Saleemi A. N., Rielly C. D. and Nagy Z. K. (2014). Crystallization of Fast and Slow Growing Active Pharmaceutical Ingredients in a Periodically Operated MSMPR Crystallizer, Manufacturing the Future Glasgow UK.

3. Powell K. A., Saleemi A. N., Rielly C. D. and Nagy Z. K. (2014). Integrated Process Analytics for Real-time Monitoring of a Novel Periodic Flow Crystallization Process, EuroPact Conference Barcelona, Spain.

4. Powell K. A., Saleemi A. N., Rielly C. D. and Nagy Z. K. (2014). Characterizing Periodic Steady-state Flow Crystallization of a Pharmaceutical Drug Using Integrated Process Analytical Technologies (PAT), ISIC Conference Toulouse, France.

5. Powell K. A., Saleemi A. N., Rielly C. D. and Nagy Z. K. (2014). Integrated Process Analytics for Real-time Monitoring of a Novel Periodic Flow Crystallization Process, ChemEng Day Manchester, UK.

6. Powell K. A., Saleemi A. N., Rielly C. D. and Nagy Z. K. (2013). Monitoring and Control of Continuous and Periodic Flow Crystallization in MSMPR Using PAT and an In-house Developed Information System Software (CryPRINS), CMAC Research Away Day, Crieff Hydro, UK.

7. Powell K. A., Saleemi A. N., Rielly C. D. and Nagy Z. K. (2013). Periodic Steady-State Flow Crystallisation of Paracetamol Using MSMPR: A novel approach to achieve desired crystal properties, CMAC Open Day Glasgow, UK.

8. Powell K. A., Saleemi A. N., Rielly C. D. and Nagy Z. K. (2013) Application of Process Analytical Technologies to Continuous Crystallisation of Active Pharmaceutical Ingredients, Loughborough Research Conference Loughborough, UK.

9. Powell K. A., Saleemi A. N., Rielly C. D. and Nagy Z. K. (2013). From Batch To Continuous Crystallisation of Pharmaceutical Drugs, Loughborough Workers Conference Loughborough, UK.

Awards

1. Doctoral Trainee Annual Research Prize (2015). CMAC Open Day, Technology Innovation Centre, Glasgow, UK.

2. Best Poster Prize. (2013). For the work: *"Periodic Steady-State Flow Crystallisation of Paracetamol Using MSMPR: A novel approach to achieve desired crystal properties"*, CMAC Open Day Glasgow Science Centre, Glasgow, UK.